

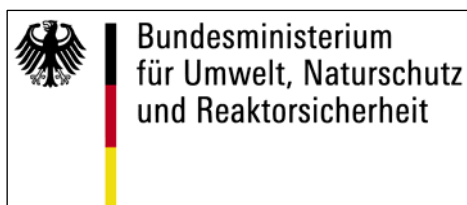
Proceedings of the 2nd International Conference on Transport, Atmosphere and Climate (TAC-2)

Aachen, Germany, and Maastricht, The Netherlands,
22 to 25 June 2009



Edited by

Robert Sausen, Peter F.J. van Velthoven, Claus Brüning and Anja Blum



Ministerie van Verkeer en Waterstaat



<http://www.pa.op.dlr.de/tac/proceedings.html>

Edited by

Robert Sausen¹, Peter F.J. van Velthoven², Claus Brüning³ and Anja Blum¹

Oberpfaffenhofen, August 2010

¹ Institut für Physik der Atmosphäre, Deutsches Zentrum für Luft- und Raumfahrt e.V., Oberpfaffenhofen, Germany

² Royal Netherlands Meteorological Institute, AE De Bilt, The Netherlands

³ European Commission, DG Research, Directorate Environment, Unit 'Climate Change and Environmental Risks', Brussels, Belgium

Foreword

The "2nd International Conference on Transport, Atmosphere and Climate (TAC-2)" held in Aachen (Germany) and Maastricht (The Netherlands), 2009, was organised with the objective of updating our knowledge on the impacts of transport on the composition of the atmosphere and on climate, three years after the TAC conference in Oxford (United Kingdom).

The TAC-2 conference covered all aspects of the impact of the different modes of transport (aviation, road transport, shipping etc.) on atmospheric chemistry, microphysics, radiation and climate, in particular:

- engine emissions (gaseous and particulate),
- emission scenarios and emission data bases for transport,
- near-field and plume processes, effective emissions,
- transport impact on the chemical composition of the atmosphere,
- transport impact on aerosols,
- contrails, contrail cirrus, ship tracks,
- indirect cloud effects (e.g., aerosol-cloud interaction),
- radiative forcing,
- impact on climate,
- metrics for measuring climate change and damage,
- mitigation of transport impacts by technological changes in vehicles and engines,
- mitigation of transport impacts by operational means.

The conference was also a forum for dialogue of the QUANTIFY⁴ and ATTICA⁵ project participants with the wider scientific community. While QUANTIFY was a research project, ATTICA's main objective was to produce assessment reports on the atmospheric impact of the different modes of transport (aviation, shipping, land transport) and on metrics to compare the climatic impacts. The ATTICA reports will be published in *Atmospheric Environment* in 2010.

The conference benefited from substantial financial support from the German Bundesministerium für Umwelt, Naturschutz und Reaktorsicherheit⁶, from the Dutch Ministerie van Verkeer en Waterstaat⁷, and the European Commission's DG Research, to whom the organizers are extremely grateful.

Prof. Dr. Robert Sausen
DLR, Institut für Physik der Atmosphäre
Oberpfaffenhofen
D-82234 Wessling
Germany

tel.: +49-8153-28-2500
fax: +49-8153-28-1841
email: robert.sausen@dlr.de

Dr. Peter van Velthoven
Koninklijk Nederlands Meteorologisch Instituut
P.O. box 201
NL-3730 AE De Bilt
The Netherlands

tel.: +31-30-2206419
fax: +31-30-2210407
email: velthove@knmi.nl

⁴ QUANTIFY was an EC funded Integrated Project entitled "Quantifying the Climate Impact of Global and European Transport Systems", see also <http://ip.quantify.eu>.

⁵ ATTICA was an EC funded Specific Support Activity entitled "European Assessment of Transport Impacts on Climate Change and Ozone Depletion", see also <http://ssa-attica.eu>.

⁶ Federal Ministry for the Environment, Nature Conservation and Nuclear Safety

⁷ Ministry of Transport, Public Works and Water Management

Program Committee

Prof. Robert Sausen, DLR, Germany (chair)
Dr. Peter van Velthoven, KNMI, The Netherlands (co-chair)
Dr. Claus Brüning, EC, Belgium
Prof. Horst Friedrich, DLR, Germany
Dr. Jan Fuglestad, CICERO, Norway
Dr. Pieter Hammingh, PBL, The Netherlands
Mr. Falk Heinen, BMU, Germany
Prof. Rolf Henke, RWTH, Germany
Prof. Ivar Isaksen, UiO, Norway
Dr. Dietrich Knörzer, EC, Belgium
Prof. David S. Lee, MMU, United Kingdom
Prof. Joyce Penner, University of Michigan, USA
Dr. Ernie Weijers, ECN, The Netherlands
Prof. Christos Zerefos, NKUA, Greece

Table of Contents

Foreword	3
Program Committee	4
Table of Contents	5
Conference Agenda	9
List of Posters	14
Opening address at the Second International Conference on Transport, Atmosphere and Climate, TAC-2,	16
Extended Abstracts	19

Emissions

An Overview of the NASA Alternative Aviation Fuel Experiment (AAFEX) <i>Andreas Beyersdorf, Bruce Anderson, AAFEX Science Team</i>	21
Effects of Alternative Fuels on Hydrocarbon and Particle Emissions from Aircraft Engines <i>R.C. Miake-Lye, E.C. Wood, M.T. Timko, Z. Yu, S.C. Herndon, B. Lee, G. Santoni, W.B. Knighton</i>	26

Impact of atmospheric composition I

Transport and Transformation of Air Pollution from Road and Ship Transport - Joint Analysis of Regional Scale Impacts and Interactions <i>G. Gadzhev, K. Ganev, G. Jordanov, N. Miloshev, A. Todorova, D. Syrakov, M. Prodanova</i>	33
Characterisation of particulate matter and gaseous emissions from a large ship diesel engine <i>Jana Moldanová, Erik Fridell, Olga Popovicheva, Benjamin Demirdjian, Victoria Tishkova, Alessandro Faccinnetto, Cristian Focsa</i>	38

Clouds and cloud effects

Trends in man-made and natural cirrus clouds for the period 1984-2004 <i>Kostas Eleftheratos, Christos S. Zerefos, Patrick Minnis</i>	45
Ice nucleation on soot in contrails and cirrus: laboratory view <i>O.B. Popovicheva, P. J. DeMott, K. A. Koehler, S. M. Kreidenweis, M. D. Petters, C. M. Carrico N.Shonija, E.Kireeva</i>	51
Detection of young contrails – selected results from the CONCERT (CONtrail and Cirrus ExpeRimenT) campaign <i>C. Voigt, *, U. Schumann, T. Jurkat, D. Schäuble, H. Schlager, M. Lichtenstern, M. Scheibe, T. Hamburger, A. Petzold, F. Arnold **, A. Dörnbrack, F. Holzäpfel, J.-F. Gayet, C. Goubeyre, M. Krämer, M. Kübbeler, J. Meyer, J. Schneider, J. Schmale, H. Eichler, W. Frey, S. Molleker, S. Borrmann</i>	57
Quantitative forecast model of contrail formation and prospects of its application <i>V.T. Dedesh, R.Kh. Tenishev, S.N. Kiose, V.V. Popov, E.G. Pavlova, I.V. Voronich, M.A. Lavrov, V.P. Mogilnikov, A.I. Lanshin, A.A. Evstigneev, A.N. Nevzorov, O.B. Popovicheva</i>	63
A Contrail Cirrus Prediction Tool <i>U. Schumann</i>	69
A global ship track climatology from ATSR-2: January 1999 – January 2001 <i>A. M. Sayer, R. G. Grainger, E. Campmany</i>	75

Impact on climate I

Risk assessment of contrail formation using AIRS, MOZAIC and AERO2k databases <i>N. Lamquin, C.J. Stubenrauch, S. Cros, H. Smit</i>	80
Aviation emissions under climate stabilization at 450ppmv and below <i>H. J. Preston, L. L. Lim, D. S. Lee and P. D. Hooper</i>	86
Global temperature change from the transport sectors: Historical development and future scenarios <i>R.B. Skeie, J.S. Fuglestad, T. Berntsen, M.T. Lund, G. Myhre, K. Rypdal</i>	93
Indications of Distinctive Efficacies for Transport Related Ozone Perturbations <i>M. Ponater, S. Dietmüller, N. Stuber, K.P. Shine, E.J. Highwood, G. Rädcl</i>	95

Impact on atmospheric composition II

Investigation of NO ₂ Pollutions on Board of Research Aircraft (Some Results of QUANTIFY and POLARCAT Field Campaigns) <i>N. Sitnikov, V. Sitnikova, A. Ulanovskiy, A. Lukyanov, H. Schlager, A. Roiger, M. Scheiber, M. Lichtenstern and P. Stock, F. Ravegnani</i>	102
High resolution simulations of aircraft condensation trails: Contrails Evolution and Diffusion <i>Sarrat, C., R. Paugam¹, R. Paoli, D. Cariolle, L. Nybelen</i>	108
The Effect of Ice Particles on the Tropospheric Ozone Budget via Heterogeneous Conversion processes <i>J. E. Williams, G.-J. van Zadelhoff and P.F.J. van Velthoven</i>	112

Impact on climate II

Short-haul Flights and Climate Change: What are the Effects and Potential Alternatives? <i>R. Kaur, C. Dey</i>	119
Exploring the uncertainties involved in calculating temperature response from the transport sector <i>L.L. Lim, H.J. Preston, D.S. Lee</i>	126

Metrics and mitigation

Abatement strategies to reduce air pollution from transport in Germany <i>U. Kugler, J. Theloke, B. Thiruchittampalam, T. Gefler, M. Uzbasich, R. Köble, R. Friedrich, P. Builtes, H. Denier van der Gon, R. Stern, W. Jörß, U. Dämmgen, J. Appelhans</i>	134
ECATS - Mission of Association for an environmentally compatible air transport system <i>S. Matthes, G. Erhardt, K. Gierens, A. Petzold, P. Brok, M. Hagström, C. Helmig, Ivar S. Isaksen, P. Laroche, X. Vancassel, D. Lee, D. Raper, T. Panidis, K. Mathioudakis, T. Tsalavoutas, R. Kurtenbach, P. Wiesen, C. Wilson, P. Habisreuther, K. Schäfer, N. Zarzalis</i>	140

Poster sessions

B. Impact on atmospheric composition

SPIDER model simulations of aircraft plume dilution <i>N. Dotzek, S. Matthes, and R. Sausen</i>	146
ECHAM5 simulations with the $\text{HO}_2 + \text{NO} \rightarrow \text{HNO}_3$ reaction <i>K. Gottschaldt, C. Voigt¹, B. Kärcher</i>	153
Long-term 3D Simulation of Aviation Impact on Ozone Precursor Chemistry using MOZART-2 <i>J. Hurley,</i>	157
QUANTIFY model evaluation of global chemistry models: carbon monoxide <i>C. Schnadt Poberaj[*], J. Staehelin, R. Bintania, P. van Velthoven, O. Dessens, M. Gauss, I.S.A. Isaksen, V. Grewe, P. Jöckel, P. Hoor, B. Koffi, D. Hauglustaine, D. Olivie</i>	163

C. Clouds and cloud effects

Properties of Ice-Supersaturated Layers Based on Radiosonde Data Analysis <i>S. L. Baughcum, M. Y. Danilin, L. M. Miloshevich, A. J. Heymsfield</i>	169
Condensation Trails in the regional Climate Model CCLM <i>A. Ferrone, P. Marbaix, R. Lescroart, J.-P. van Ypersele</i>	174
Some evidence of aviation fingerprint in diurnal cycle of cirrus over the North Atlantic <i>K. Graf, H. Mannstein, B. Mayer, U. Schumann</i>	180
Aviation and ship soot as freezing nuclei of water/sulfate cloud droplets <i>E. Kireeva, O. Popovicheva, N. Persiantseva, N. Shonija, T. Khokhlova</i>	186
Large Eddy Simulation of Persistent Contrails <i>A.D. Naiman, S.K. Lele, F. Ham, J.T. Wilkerson, M.Z. Jacobson</i>	191
Uptake of nitric acid in ice crystals in persistent contrails <i>D. Schauble, C. Voigt, B. Kärcher, P. Stock, H. Schlager, M. Krämer, C. Schiller, R. Bauer, N. Spelten, M. de Reus, M. Szakáll, S. Borrmann, U. Weers, T. Peter</i>	197
Peculiarities of airplane vortex wakes and condensation trails interaction and their mathematical modeling <i>A.N. Zamyatin, V.T. Dedesh, R.L. Kagarmanov, A.I. Zhelannikov</i>	203

D. Impact on climate

Do radiative forcings of methane and ozone cancel out? - A case study from the last IMO Greenhouse gas study <i>Jérôme Hilaire, Ruben Rodriguez de Leon, David S. Lee</i>	217
Aerosol optical properties <i>D.M. Peters, R.G. Grainger, G. Thomas</i>	222
Distinctive Efficacies of the Components Contributing to Total Aviation Climate Impact <i>M. Ponater[*]</i>	227
Aviation NO_x Global Warming Potential <i>Agnieszka Skowron, David S. Lee, Jane Hurley</i>	233

E. Metrics and mitigation

Vertical spatial scales of ice supersaturation and probability of ice supersaturated layers in low resolution profiles of relative humidity	239
<i>N.C. Dickson¹, K. Gierens², H.L. Rogers¹, R.L. Jones¹</i>	
Impact on air quality of a 90 km/h speed limit during PM10 episodes	244
<i>P. Viaene, W. Lefebvre, K. Van de Vel, S. Janssen, G. Cosemans, K. De Ridder, I. De Vlieger, C. Mensink, L. Schrooten, J. Vankerkom, F. Fierens, T. Van Mierlo, F. Blommaert</i>	
Participants Photo	248
Participants List	249
Index of Authors	257

Conference Agenda

Sunday, 21 June 2009

18:00 Registration

20:00 End of Sunday registration time

Monday, 22 June 2009

08:00 Registration

Opening Ceremony

Chair: Sausen

08:45 Ministerialdirigent Hubert Steinkemper, Bundesministerium für Umwelt, Naturschutz und Reaktorsicherheit, Germany

Opening Address

09:00 Dr. Claus Brüning, European Commission

Opening Address

09:15 Dr. Frits Brouwer, Director-General, Koninklijk Nederlands Meteorologisch Instituut, The Netherlands

Opening Address

09:25 Prof. Dr. Ulrich Schumann, Deutsches Zentrum für Luft- und Raumfahrt e.V., Germany

Opening Address

09:35 Prof. Dr. Robert Sausen,

Introduction to Aachen and Maastricht

10:00 *Poster setup / Coffee*

Emissions

Chair: N. Dotzek

10:30 R. Kurtenbach, E. Anamaterou, C. Helmis, C. Heyder, M. Hoffmann, C. Jahn, A. Niedojadlo, M. O'Connor, K. Schäfer, G. Sgouros and P. Wiesen: *Airport air quality study in Athens. Gaseous and particle emissions from commercial aircraft at take-off condition*

10:50 B. Anderson and A. Beyersdorf: *An overview of the NASA Alternative Aviation Fuel Experiment (AAFEX)*

11:10 P. Whitefield, D. Hagen, P. Lobo and R. C. Miake-Lye: *Emissions from alternate aviation fuels and their environmental impact*

11:30 K. S. Patel, Y. Nayak, and M. Georg: *Polycyclic aromatic hydrocarbon road dust pollution in India*

11:50 R. C. Miake-Lye, E. C. Wood, M. T. Timko, Z. Yu, W. B. Knighton and S. C. Herndon: *The effects of alternative fuels on the composition of hydrocarbon and particle emissions from aircraft engines*

12:10 H. Hemmer, T. Otten, M. Plohr and A. Döpelheuer: *Emission characteristics of future ultrahigh-bypass-ratio aero engines*

Impact on atmospheric composition I**Chair: J. Penner**

- 12:30 O. Dessens, A. Anger, T. Barker, H. Rogers, R. Jones and J. Pyle (solicited): *Effect of climate control on air pollution: Methodology and preliminary results from one-way coupling of an energy-environment-economy model and atmospheric chemistry model in decarbonising international transport*
- 13:10 Lunch
- 14:40 T. Halenka, P. Huszar and M. Belda: *On the resolution sensitivity of transportation emission impacts – Application in effective emission concept for ships*
- 15:00 J. Moldanová and L. Persson: *Importance of subscale processes in modelling emissions from shipping*
- 15:20 G. Gadzhev, K. Ganev, D. Syrakov, G. Jordanov, M. Prodanova, N. Miloshev and A. Todorova: *Transport and transformation of air pollution from road and ship transport – Joint analysis of regional-scale impacts and interactions*
- 15:40 V. Matthias, I. Bewersdorff, A. Aulinger and M. Quante: *Enhanced aerosol formation due to ship emissions in the North Sea regions*
- 16:00 V. Eyring, I. Isaksen, T. Berntsen, W. Collins, J. Corbett, O. Endresen, R. Grainger, J. Moldanová, H. Schlager and D. Stevenson: *Transport impacts on atmosphere and climate: Shipping*
- 16:20 Posters / Coffee
- 16:50 S. Dalsøren, M. S. Eide, O. Endresen, G. Gravir, A. Mjelde and I. S. A. Isaksen: *Update on emissions and environmental impacts from the international fleet of ships*
- 17:10 J. Moldanová, E. Fridell, O. Popovicheva, A. Faccinetto and C. Focsa: *Characterisation of particulate matter and gaseous emissions from a large ship diesel engine*
- 17:30 K. S. Patel and S. Gupta: *Environment impact of the extreme particulate in aerosol and their impact*
- 17:50 M. Prather: *Uncertainties in calculating aviation's impact on global atmospheric chemistry*
- 18:10 End of presentations
- 19:00 Icebreaker (Krönungssaal, Rathaus Aachen)

Chair: F. Heinen**Tuesday, 23 June 2009**

08:30 Registration

Clouds and cloud effects**Chair: C. Brüning**

- 09:00 J. Penner and M. Wang: *Effects of aircraft aerosols on cirrus clouds, tropopause temperatures, and water transport to the stratosphere*
- 09:20 U. Burkhardt: *Climate impact of contrail cirrus*
- 09:40 K. Eleftheratos, C. Zerefos and P. Minnis: *Update of man-made and natural trends in cirrus clouds*
- 10:00 M. Vazquez-Navarro, H. Mannstein and B. Mayer: *Lifecycle of contrails*
- 10:20 O. Popovicheva and P. DeMott: *Ice nucleation on soot in contrails and cirrus*
- 10:40 Posters / Coffee

Chair: K. Gierens

- 11:10 P. Minnis, R. Palikonda, D. Duda and P. Heck: (solicited) *Microphysical properties of contrails derived from satellite measurements*
- 11:40 C. Voigt, T. Jurkat, U. Schumann, D. Schäuble, H. Schlager, A. Petzold, D. Delhayé, A. Dörnbrack, F. Arnold, M. Krämer, J.-F. Gayet, J. Schmale, J. Schneider, S. Borrmann, H. Eichler and the CONCERT team: *Detection of contrails from various aircraft – Overview of the CONCERT (CONtrail and Cirrus ExpeRiment) campaign*

- 12:00 V. Dedesh, R. Tennishev, S. Kiose, V. Popov, E. Pavlova, I. Voronich, M. Lavrov, V. Mogilnikov, A. Zamyatin, R. Kagarmanov, A. Lanshin, A. Evstigneev, A. Nevzorov and O. Popovicheva: *Quantitative forecast model of the formation conditions of steady contrails and prospects of its appliance*
- 12:20 U. Schumann: *A contrail cirrus prediction tool*
- 12:40 A. M. Sayer and R. G. Grainger: *A global ship track climatology from ATSR-2: June 1995 – January 2001*
- 13:00 Lunch

Poster session**Chair: N. Dotzek**

- 14:30 Posters on display: *Authors in attendance*
- 16:00 Posters / *Coffee*

Impact on climate I**Chair: P. Hammingh**

- 16:30 B. Kärcher, U. Burkhardt, P. Minnis and S. Unterstrasser: *Impact of microphysical variability on contrail cirrus optical depth and radiative forcing*
- 16:50 N. Lamquin, C. J. Stubenrauch, S. Cros and H. Smit: *Risk assessment of contrail impact on climate using AIRS, MOZAIC and Aero2K databases*
- 17:10 Y. Balkanski, G. Myhre, G. Rädel and K. Shine: *Direct radiative effect of aerosols emitted by transport: From road, shipping and aviation*
- 17:30 H. Preston, L. L. Lim, D. S. Lee and P. Hooper: *Transport emissions and climate stabilization*
- 17:50 R. B. Skeie, J. S. Fuglestad, T. Berntsen, M. T. Lund, G. Myhre and K. Rypdal: *Global temperature change from the transport sectors: Historical development and future scenarios*
- 18:10 M. Ponater, N. Stuber, K. P. Shine, E. Highwood, G. Rädel and S. Dietmüller: *Indications of distinctive efficacies for transport-related ozone perturbations*
- 18:30 End of presentations

Wednesday, 24 June 2009

- 08:00 Registration

Impact on atmospheric composition II**Chair: T. Berntsen**

- 08:30 D. Cariolle, R. Paoli, D. Hauglustaine, D. Caro, B. Cuenot and R. Paugam: *Introduction of plume chemistry into large-scale atmospheric models*
- 08:50 N. Sitnikov, H. Schlager, V. Sitnikova, F. Ravagnani, A. Ulanovskiy, A. Lukjanov, A. Roiger, M. Scheibe, M. Lichtenstern and P. Stock: *Investigation of NO₂ pollutions on board of research aircraft (some results of QUANTIFY and POLARCAT field campaigns)*
- 09:10 R. Paoli, R. Paugam, L. Nybelen, C. Sarrat and D. Cariolle: *High-resolution numerical simulations of physico-chemical processes in aircraft wakes*
- 09:30 M. Uphoff and K. H. Schlutzen: *Sensitivity of model results depending on parameterisation of aircraft-induced mixing in a mesoscale model*
- 09:50 S. C. Herndon, E. C. Wood, M. T. Timko, Z. Yu, W. B. Knighton and R. C. Miake-Lye: *The evolution of aircraft engine emissions in the atmosphere*
- 10:10 Posters / *Coffee*
- 10:40 J. Williams, G.-J. van Zadelhoff and P. van Velthoven: *The effect of ice particles on the tropospheric ozone budget via heterogeneous conversion processes*

Impact on climate II**Chair: U. Schumann**

- 11:00 R. Kaur and C. Dey: *Short-haul flights and climate change: What are the effects and potential alternatives?*
- 11:20 M. Z. Jacobson, J. T. Wilkerson, A. D. Naiman and S. K. Lele: *Quantifying the effects of aircraft on climate with a model that treats the subgrid evolution of contrails from all commercial flights worldwide*
- 11:40 *End of presentations*
- 12:00 *Bus transport to Maastricht*
- 13:00 *Lunch (room Napoleon)*

Chair: B. Bregman

- 14:00 Staatssecretaris Tineke Huizinga, Ministerie van Verkeer en Waterstaat, NL: *Welcome address*
- 14:15 Dr. Claus Brüning, EC: *Atmospheric research in the 7th Framework Programme of the EU*
- 14:25 Hein Haak, Climate and Seismology, Koninklijk Nederlands Meteorologisch Instituut, The Netherlands: *Welcome address*
- 14:35 Prof. Robert Sausen, Deutsches Zentrum für Luft- und Raumfahrt: *The impact of transport on climate*
- 15:00 Henk van Hoorn, Ministerie van Verkeer en Waterstaat, NL: *Overview National Transportation Policy of The Netherlands*
- 15:15 Sibrand Hassing, Ministerie van Verkeer en Waterstaat, NL: *Ship emissions and the Road to Copenhagen*
- 15:30 *Coffee*
- 16:00 *Panel Discussion*
- 16:45 *Press conference / Buses to Valkenburg*
- 17:30 *Last bus to Valkenburg*
- 17:30 *Guided tour Fluweelengrot / Ruins*
- 18:45 *Buses to Berg en Terblijt*
- 19:00 *Conference Dinner*
- 22:30 *Buses to Aachen*

Chair: R. Sausen**Thursday, 25 June 2009**

- 08:30 Registration

Impact on climate III**Chair: B. Bregman**

- 09:00 D. S. Lee, D. W. Fahey, P. M. Forster, P. J. Newton, R. C. N. Wit, L. L. Lim, B. Owen and R. Sausen: *Aviation and global climate change in the 21st century*
- 09:20 L. Wilcox, B. Hoskins and K. Shine: *Water vapour emissions from aircraft*
- 09:40 C. Fichter, M. Ponater, V. Grewe and R. Sausen: *Air traffic climate effects in dependency of emission location and altitude*
- 10:00 L. Lim, H. Preston, D. S. Lee: *Exploring the uncertainties involved in calculating temperature response from the transport sector*
- 10:20 S. Unterstrasser and K. Gierens: *Numerical simulations of contrail-to-cirrus transition – The impact of radiation*
- 10:40 *Posters / Coffee*
- 11:10 N. Dotzek: *Technical information concerning your proceedings contribution*

Metrics and mitigation**Chair: J. Moldanová**

- 11:20 J. Fuglestvedt, K. P. Shine, J. Cook, D. S. Lee, A. Stenke, R. Skeie, G. J. M. Velders and I. A. Waitz: (solicited) *Comparing climate impacts of transportation*
- 12:00 R. Egelhofer, D. Schmitt and K. Shine: *Aircraft design driven by climate change*
- 12:20 P. Hammingh: *Effects of biofuels on emissions of air pollutants*
- 12:40 U. Kugler, J. Theloke, P. Builtjes, R. Stern, W. Jörß, R. Köble, B. Thiruchittampalam, T. Geftler, M. Uzbasich, R. Friedrich, U. Dämmgen and J. Appelhans: *Abatement strategies to reduce air pollution from transport in Germany*

13:00 *Lunch***Chair: R. Miake-Lye**

- 14:30 T. Berntsen, J. Fuglestvedt and K. Rypdal: *Climate effects of passenger cars: Gasoline versus diesel*
- 14:50 H. Mannstein, K. Gierens, K. Graf, A. Waibel, S. Meilinger, A. Seifert and C. Köhler: *Smart aircraft routing – a possibility for mitigation?*
- 15:10 S. Matthes: *ECATS - Mission of Association for an environmental compatible air transport system*
- 15:20 M. Gupta: *Aviation Climate Change Research Initiative (ACCRI): The Next Steps*

Closing Session**Chair: R. Sausen**

- 15:30 *Summary, conclusions, awards, ...*
- 16:00 *Coffee*
- 16:30 *End of meeting*

List of Posters

A. Emissions

- A.01 J. Borken-Kleefeld, H. Steller, G. de Ceuster, F. Vanhove, M. Eide, O. Endresen, H. Behrens, D. Lee, B. Owen, T. Meretei, K. Rypdal, R. Skeie, J. van Aardenne, G. Erhardt and R. Sausen: *QUANTIFY transport emission scenarios up to 2100*
- A.02 J. Moldanová, E. Fridell, O. Popovicheva, A. Faccineto and C. Focsa: *Characterisation of particulate matter and gaseous emissions from a large ship diesel engine*
- A.03 A. Okhapkin and A. Shustov: *Simulation and forecasting of the civil aircraft pollutants above the territory of Russia*
- A.04 A. Paxian, V. Eyring, W. Beer, R. Sausen and C. Wright: *Bottom-up emission inventory for international shipping*
- A.05 V. Tishkova, B. Demirjian, D. Ferry, O. Popovicheva, N. Persiantseva, E. Kireeva, N. Shonija, N. Zubareva, J. Moldanova and E. Fridell: *Ship exhaust characterization: Micro-structure, elemental composition, surface chemistry*

B. Impact on atmospheric composition

- B.01 A. Akachat: *Atmospheric pollution and particulate matter concentration at petrol station in semi-urban site*
- B.02 B. Ambade and K. S. Patel: *Chemical composition of rainwater in Raipur*
- B.03 A. J. Badyda: *The multifarious influence of vehicular traffic on the municipal environment*
- B.04 K. Dahlmann, V. Grewe, M. Ponater and S. Matthes: *Trends in ozone concentration caused by emissions from fossil fuel combustion and natural sources*
- B.05 O. Dessens, P. Hoor, M. Gauss, I. S. A. Isaksen, B. Koffi, M. Prather, Q. Tang, P. van Velthoven and J. A. Pyle: *Transport modes impact on atmospheric chemistry: 2000 to 2100 SRES A1 scenario*
- B.06 N. Dotzek, S. Matthes and R. Sausen: *SPIDER model simulations of aircraft plume dilution*
- B.07 K. Gottschaldt, C. Voigt and B. Kärcher: *ECHAM5/Messy simulations with the HO₂ + NO → HNO₃ reaction*
- B.08 J. Hurley and D. S. Lee: *Impact of aviation emissions from multi-year MOZART simulations*
- B.09 V. K. Jena and S. Gupta: *Assessment of chemical composition of atmosphere and its impact*
- B.10 T. Jurkat, C. Voigt, F. Arnold, H. Schlager, M. Lichtenstern and H. Aufmhoff: *Sulfuric acid formation in jet aircraft exhaust - In-flight ion trap CIMS investigations of different aircraft*
- B.11 M. Köhler, G. Rädcl, K. P. Shine, H. L. Rogers and J. A. Pyle: *Regional growth in aircraft NO_x emissions and related atmospheric impacts*
- B.12 R. C. Pike and J. A. Pyle: *Air-quality impacts of large-scale biofuel use: What can a global model tell us about our future decisions?*
- B.13 C. Schnadt Poberaj, R. Bintanja, B. Koffi, O. Dessens, S. Dalsoren, M. Gauss, V. Grewe, P. Hoor, I. Isaksen, D. Olivié, J. Staehelin and P. Van Velthoven: *QUANTIFY Activity 3: Model evaluation of global chemistry models*

C. Clouds and cloud effects

- C.01 S. L. Baughcum, M. Y. Danilin, L. M. Mioshevich and A. J. Heymsfield: *Properties of ice-supersaturated regions based on radiosonde analysis*
- C.02 S. Dietmüller, M. Ponater, R. Sausen and S. Pechtl: *Some evidence against a significant contrail impact on diurnal temperature range*
- C.03 A. Ferrone, P. Marbaix and J.-P. van Ypersele: *Simulation of aircraft-induced cloudiness in the regional climate model CCLM*
- C.04 K. Graf, B. Mayer, H. Mannstein and U. Schumann: *Aviation fingerprint in diurnal cycle of cirrus over the North Atlantic*

- C.05 E. Kireeva, O. Popovicheva, N. Persinatseva and N. Shonija: *Aviation and ship soot as freezing nuclei of water/sulphate cloud droplets*
- C.06 A. D. Naiman, F. Ham, S. K. Lele, J. T. Wilkerson and M. Z. Jacobson: *Large-eddy simulation of persistent contrails*
- C.07 G. Rädcl, K. Shine and R. Forbes: *Predicting persistent contrails using the ECMWF integrated forecast system*
- C.08 D. Schäubel, C. Voigt, B. Kärcher, P. Stock, H. Schlager, M. Krämer, C. Schiller, R. Bauer, N. Spelten, M. de Reus, M. Szakall, S. Borrmann, U. Weers and T. Peter: *Airborne measurements of the nitric acid partitioning in persistent contrails*
- C.09 S. Unterstrasser, I. Sölch and K. Gierens: *Numerical models for contrail and contrail cirrus simulation*
- C.10 G. M. Whelan, F. Cawkwell, H. Mannstein and P. Minnis: *The use of meteorological data to improve automated contrail detection in satellite imagery over Ireland*
- C.11 A. Zamyatin, V. Dedesh, A. Zhelannikov and R. Kagarmanov: *Peculiarities of airplane vortex wakes and condensation trails interaction and their mathematical modelling*

D. Impact on climate

- D.01 A. Abdellatif: *Sensitivity of climate models*
- D.02 H. H. Asadov and N. M. Suleymanov: *New formulation of atmospheric turbidity factor given by Linke*
- D.03 T. Berntsen and J. Fuglestedt: *Global temperature responses to current emissions from the transport sectors*
- D.04 V. Grewe, M. Plohr, G. Cerino, M. Di Muzio, Y. Deremaux, M. Galerneau, P. de Saint Martin, T. Chaika, A. Hasselrot, U. Tengzelius and V. Korovkin: *Small supersonic transport aircraft (S4TA) – Is the impact upon the atmosphere acceptable? Results from the HISAC project*
- D.05 J. Hilaire and D. S. Lee: *Quantifying the impacts of shipping NO_x emissions on tropospheric chemistry and climate*
- D.06 D. Olivie, D. Cariolle, H. Teyssèdre, D. Saint-Martin and F. Kärcher: *Climate impact of transport sectors modelled with an atmosphere-ocean general circulation model*
- D.07 D. Peters and R. G. Grainger: *Aerosol optical properties*
- D.08 G. Pitari and D. Iachetti: *Radiative forcing from particle emissions by future supersonic aircraft*
- D.09 M. Ponater: *Distinctive efficacies for the components contributing to total aviation climate impact*
- D.10 R. Rodriguez de Leon and D. S. Lee: *Uncertainties in the radiative properties of cirrus in climate models*
- D.11 A. Skowron, D. S. Lee, J. Hurley and R. R. De Leon: *How realistic is a negative NO_x GWP?*

E. Metrics and mitigation

- E.01 A. Agha and M. S. Tamannai: *Fuel cells: A sustainable approach meeting future energy demands*
- E.02 J. Borken-Kleefeld, T. Berntsen and J. Fuglestedt: *Comparing the climate impact of passenger and freight transport modes*
- E.03 O. Deuber: *A matter of choice! Role of metrics in climate policies in aviation*
- E.04 N. Dickson, K. Gierens, H. Rogers and R. Jones: *Vertical spatial scales of ice supersaturation*
- E.05 C. Fichter, M. Ponater, D. S. Lee, V. Grewe, K. Obermaier and R. Sausen: *Effects of global mean flight altitude changes*
- E.06 S. Matthes and K. Gierens: *ECATS - Towards an Environmental Compatible Air Transport System - Research contributions*
- E.07 S. Matthes, V. Grewe and R. Sausen: *REACT4C : A novel concept for environmentally friendly flight routing*
- E.08 P. Viaene, K. Van de Vel, W. Lefebvre, S. Janssen, F. Blommaert, G. Cosemans, K. De Ridder, I. De Vlieger, F. Fierens, C. Mensink, L. Schrooten, J. Vankerkom and T. Van Mierlo: *Impact on air quality of a 90 km/h speed limit during PM₁₀ episodes*

Opening address at the Second International Conference on Transport, Atmosphere and Climate, TAC-2,

Aachen/Maastricht, June 22-25, 2009,

by dr. Frits J.J. Brouwer, Director-General of the Royal Netherlands Meteorological Institute

Mister Chairman, Ladies and Gentlemen,

On behalf of KNMI (the Dutch acronym for: Royal Netherlands Meteorological Institute), being the co-organizer of this TAC-2, I bid you a warm welcome at this conference!

Maybe first a few words about KNMI. As the National Met Service, we are an agency of the Ministry of Transport and Water Management. Being an agency means that we have an own budget scheme and are not directly involved in political issues. Our budget is about 55 MEuro, and some 450 people are employed at KNMI. Being the National Met Service, we have of course a number of operational tasks, such as issuing warnings and alarms for high impact weather. But I am also very proud that about one third of KNMI staff is academic staff and thus devoted to the scientific understanding of weather and climate issues. A major product of this are e.g. the climate scenarios that KNMI issues about every 5 years. These are the official basis for the national policies on e.g. water management, physical planning, health issues, etc.

Now back to TAC-2! Infrastructure is the most vital economic network in the Netherlands. As you probably know, our economically most valuable regions are located below sea level. Last year our Vice Minister, Staatssecretaris Tineke Huizinga - who will speak to you by video on Wednesday afternoon -, set up a commission to advise the Dutch government how to make the Dutch water management climate proof. The commission took into account the possibility that our country will be exposed to a sea level rise of 1.3 m over the next century. Not that such an extreme climate projection will not easily become reality, but it provides a benchmark to make our country climate proof.

To work towards climate adaptation, the Dutch government initiated national programmes to develop a sustainable infrastructure and transport system. At the same time our transport sector has to fulfil the Kyoto Protocol targets and the National Emission Ceilings Directive as part of the European Thematic Strategy on Air Pollution. In addition to the contribution to the concentration of (greenhouse) gases and aerosols in the atmosphere, noise is another important variable for the transport sector, in particular in our urbanised regions. Highways and airports cause noise exposure above threshold levels. KNMI investigates the relationship between such exposures and climate change, to help designing more sustainable infrastructure and traffic systems as part of an integrated adaptation and mitigation strategy.

Our kind of knowledge provides the necessary scientific basis. The relationship between transport emissions and the climate system, the delivery of solid and consistent climate scenarios, the translation of these scenarios into policy proof concepts, and in particular the continuation of climate observations are all crucial elements in such a scientific basis.

Last week KNMI successfully launched the world's first NO₂ sonde at the start of the CINDI Campaign, which hopefully provides reliable in situ NO₂ vertical profiles in the future. These unique measurements complement space-borne NO₂ observations by e.g. the OMI instrument (the Ozone Monitoring Instrument on NASA's EOS/AURA-satellite). I'm sure this conference will show some examples where OMI NO₂ data are involved, illustrating the value of these data. KNMI is proud of its role as PI (Principal Investigator) in the development of the OMI instrument and in providing and analysing the data.

This development illustrates the necessity for innovation in climate science. Without innovations and basic climate research, every adaptation and mitigation strategy to tackle climate change will fail. Note e.g. that satellite data are the eye in the sky; they act as a global watch over the effectiveness of the Kyoto Protocol and mitigation options in the transport sector.

KNMI realises its crucial position and increases its effort to create an effective relationship between science and our national climate and transport policy. We have to transform our observations (in combination with our modelling) to make implementation of climate and transport policy successful. In other words, we have to act as a climate service. The importance of regional climate services increases. The Third World Climate Conference of the WMO (World Meteorological Organisation) which will take place in August/September this year, recognizes this development and will recommend the set up of a global framework on climate services, together with an international Task Force.

Most of the world's economy is found in Mega-cities, most of them located in regions vulnerable to climate change. The infrastructure and transport form the vital networks. Their relation with climate change is one of the most important future research subjects. This conference covers this subject right in the heart!

This year the road to Copenhagen is probably the most heavily used road. I hope that the traffic on this road leads to a solid successor of Kyoto. I also hope that science remains the basis of the new protocol and those that will follow. Conferences such as these, contribute significantly to a better understanding of the contribution of transport to the volume of greenhouse gases and provide the necessary information for the right discussion on this sensitive subject.

I'm therefore honoured to co-open this conference and I wish you all a very interesting and successful, but also a pleasant, time in Aachen and Maastricht!

Thank you for your attention.

Extended Abstracts

An Overview of the NASA Alternative Aviation Fuel Experiment (AAFEX)

Andreas Beyersdorf, Bruce Anderson^{*}
NASA Langley Research Center

AAFEX Science Team

Keywords: Aircraft Exhaust, Fischer-Tropsch Fuels, Volatile Aerosol Formation

ABSTRACT: The NASA Alternative Aviation Fuel Experiment (AAFEX) was conducted at NASA's Palmdale, CA aircraft facility in January-February, 2009 to investigate the effects of synthetic fuels on: 1) engine performance; 2) engine and auxiliary power unit (APU) gas and particle emissions and characteristics; and 3) volatile aerosol formation in aging exhaust plumes. The NASA DC-8, which has CFM-56 engines, was used as the test platform and the test fuels included standard JP-8 along with two synthetic fuels produced from natural gas and coal feedstocks using the Fischer-Tropsch (FT) process. AAFEX included participants from the Air Force Research Lab at Wright-Patterson, Arnold Engineering Development Center, Aerodyne Research Inc., Carnegie-Mellon, the EPA, Harvard, Missouri Science and Technology, Montana State University, NASA, the University of California, and United Technologies. During AAFEX, the aircraft was parked in an open-air run-up facility and complete sets of gas and particle emission measurements were made as a function of engine thrust. To delineate fuel-matrix related changes in emissions from those caused by variations in ambient conditions, samples were alternately drawn from the exhaust of the left inboard engine, which always burned JP-8, and the right inboard engine, which burned either standard JP-8 or one of the test fuels. To examine plume chemistry and particle evolution in time, samples were drawn from inlet probes positioned 1, 30, and 145 m downstream of the aircraft's engines. An instrumented vehicle also periodically profiled the exhaust plume from 30 to 300 m downstream to document temporal changes in exhaust composition. Engine runs were conducted in early morning and mid afternoon to examine the effects of ambient temperature on emission parameters. Results indicate that burning synthetic fuels substantially reduces particle emissions from both the aircraft engines and APU.

1 INTRODUCTION

The production of liquid fuel from coal and natural gas feedstocks dates back to the early twentieth century. However, only recently has the possibility for the use of these alternative fuels in aircraft been widely studied (Corporan *et al.*, 2007). The increased interest is the result of the possibility of these fuels to increase aviation fuel sources, increase fuel security and reduce particulate emissions. This contribution details preliminary results from the Alternative Aviation Fuel Experiment (AAFEX) which studied particulate and gaseous emissions from an aircraft fueled with fuels made via the Fischer-Tropsch (FT) process. Previous experiments have been performed on alternative fuels but this NASA sponsored experiment provides a large data set of measurements on an in-use aircraft that is completely publically accessible.

The primary goal of AAFEX was to determine the change in gaseous and particulate emissions when a FT fuel is burned in comparison to regular JP-8 fuel. Measurements were not only made of fresh emissions near the exhaust plane but also downwind plumes to determine the effects of aging on aerosol concentrations and composition. The composition of aerosols emitted by aircraft engines should change dramatically as they age. Because of high temperatures at the exhaust plane the aerosol is composed primarily of soot. As the plume ages it also cools allowing condensation of volatile

^{*} Corresponding author: Bruce Anderson, NASA Langley Research Center, Science Directorate, Mail Stop 483, Hampton, VA 23681. Email: bruce.e.anderson@nasa.gov

species. This increase in volatile aerosols should be highly dependent on the ambient temperature with cooler temperatures promoting greater volatile aerosol formation.

In addition to the engine tests, the exhaust from auxiliary power units (APUs) was analyzed. These small engines provide the power needed for the start-up of the aircraft engines. However, despite their widespread use, they currently have very limited regulation. The aircraft studied had a Garrett AiResearch GTCP85-98CK power unit which is typical of those found on mid-size aircraft (such as the DC-8 studied).

2 EXPERIMENTAL DESIGN

The experiment was performed at the NASA Dryden Aircraft Operations Facility in Palmdale, California from January 20 – February 3, 2009 with participants from the Air Force Research Lab at Wright-Patterson, Arnold Engineering Development Center, Aerodyne Research Inc., Carnegie-Mellon, the EPA, Harvard, Missouri Science and Technology, Montana State University, NASA, the University of California, and United Technologies. The large collaboration allowed for a variety of measurements and comparison between similar measurements to determine optimal sampling methods. Many of the experimental techniques were similar to those used during the Aircraft Particle Emissions Experiment (APEX; Wey *et al.*, 2007).

The test aircraft was a DC-8 aircraft with four CFM-56 engines. The aircraft was parked on the tarmac and exhaust inlet probes were placed at 1, 30 and 144 meters behind the exhaust planes of the #2 and #3 engines (left and right inboard, respectively). Samples collected at 1 m were diluted with a concentric flow of dry nitrogen to prevent condensation of water and low-volatility exhaust components, whereas samples drawn into the downstream probes were typically diluted by a factor of 20 or more with background air and were thus processed without additional dilution. Stainless steel sample lines carried the exhaust stream to trailers located off the aircraft's right wing which housed instruments to measure CO₂, CO, NO, NO₂, HONO, SO₂ and CH₄ along with particle number densities, size distributions, mass loadings and composition.

During testing, the #2 and #3 engines were set at 8 different power settings over the range from 4% to 100% of maximum rated thrust (fuel flow rates of 1000-7600 lbs per hour), which corresponds to the range from ground idle to take-off. The standardized power for ground idle is 7%; however it is typical for aircraft to idle at powers closer to 4%. The right engine was fuelled with one of five test fuels: regular JP-8, an FT fuel made from natural gas (FT-1), a FT fuel made from coal (FT-2), and 50/50 blends of the FT fuels with JP-8 (Blend 1 and Blend 2). The JP-8 had an aromatic content of 19% and sulphur content of 2200 ppm while the pure FT fuels were essentially aromatic hydrocarbon and sulphur free; the Blends had concentrations of these components that were about halfway between the two extremes. The left engine was fueled with JP-8 throughout all experiments. The exhaust was alternatively sampled from the engines with the left engine acting as a reference.

Tests were performed between 5:00 and 16:00 local time. During the AAFEX timeframe the temperature ranged from about -5 at sunrise to 20°C in the mid-afternoon. Experiments were planned such that each fuel was analyzed twice with one of the tests early in the morning and the other in the afternoon. Emissions were characterized at all three sampling distances; the 1 and 30 m gas phase measurements are discussed by Miake-Lye *et al.* (this issue) whereas Herndon *et al.* (this issue) analyze the downwind gas-phase observations in greater detail.

3 RESULTS

At power settings above ground idle, the aircraft engines are extremely efficient, converting over 99% of the carbon in the fuel into carbon dioxide (CO₂). This species is easily measured and thus provides a convenient parameter against which to normalize trace species emissions. The fuels consumed during AAFEX contained about 86% carbon, which yielded CO₂ emission indices (EI) of around 3160g CO₂/kg fuel burned. The EI of species, X, is thus given by $EI_X = [dX/dCO_2] * [M_X/M_{CO_2}] * T * R * 3160/P$, where dX and dCO₂ are the enhancements of the species concentra-

tions above ambient levels, M_x and M_{CO_2} are their molecular weights, T is the sample temperature in Kelvin, R is the gas constant, and P is sample pressure.

As shown in Figure 1, the direct exhaust (1m) showed a marked decrease in both aerosol number and mass when burning the alternative fuels. At low power (4-45%), aerosol number and mass EIs decreased by over 90% when burning the FT fuels in comparison to the JP-8. Values for the blended fuels were intermediate between the FT and JP-8 fuels. At higher powers, there is less of a reduction for the alternative fuels. However, even at maximum rated thrust the reduction is over 60% for the FT fuels. Because of the high temperatures of the exhaust, the aerosol mass is composed almost entirely of black carbon (BC; Figure 2). A shift is also seen in the size of the particles with smaller sized particles seen for the alternative fuels.

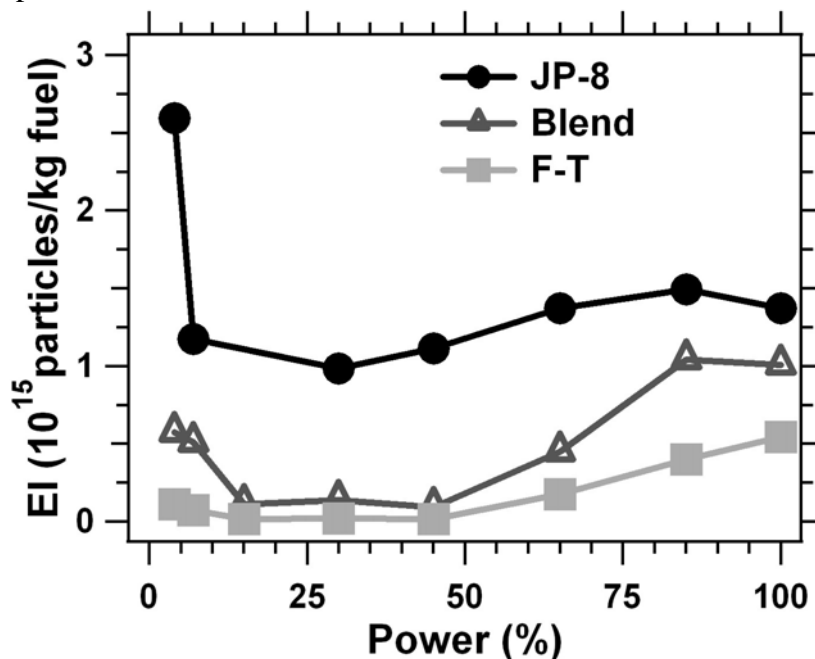


Figure 1. Aerosol emission indices 1m behind the #3 engine when fueled with JP-8, blended (average of both) and FT (average of both) fuels. Similar reductions are seen in the aerosol mass EIs.

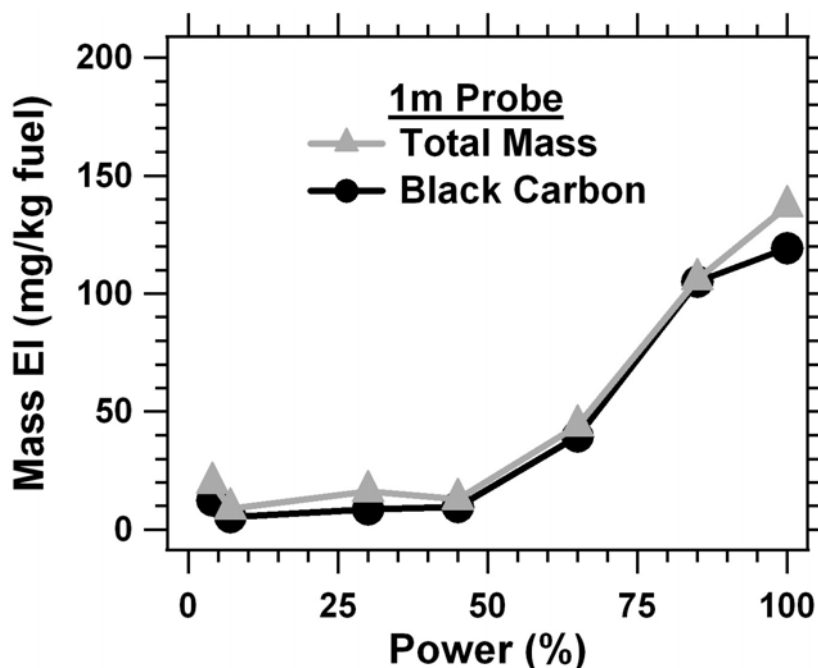


Figure 2. Black carbon and total aerosol mass emission indices measured 1m behind the engine when burning JP-8 fuel.

As the exhaust plume ages the temperature decreases and semi-volatile species begin to condense, either to form new particles or coatings on existing soot particles. As shown in Figure 3,

black carbon accounts for a majority of the total aerosol mass EI in the 1 m samples. However, at 30m the total aerosol mass is significantly greater than black carbon mass with the difference between the two measurements attributable to volatile aerosols (Figure 3). The volatile aerosols are most prevalent at low engine power, coincident with the peak in gas phase hydrocarbon emissions. As the power increases, the engines produce less hydrocarbons and the mass of volatile aerosols decreases. This volatile aerosol mass was determined to be highly temperature dependent (Figure 4) with a decrease in emission index of 10 mg/kg fuel per degree temperature at 4% power. As the power increases there is less of a dependence on ambient temperature and at 100% power volatile aerosol mass has no dependence on temperature.

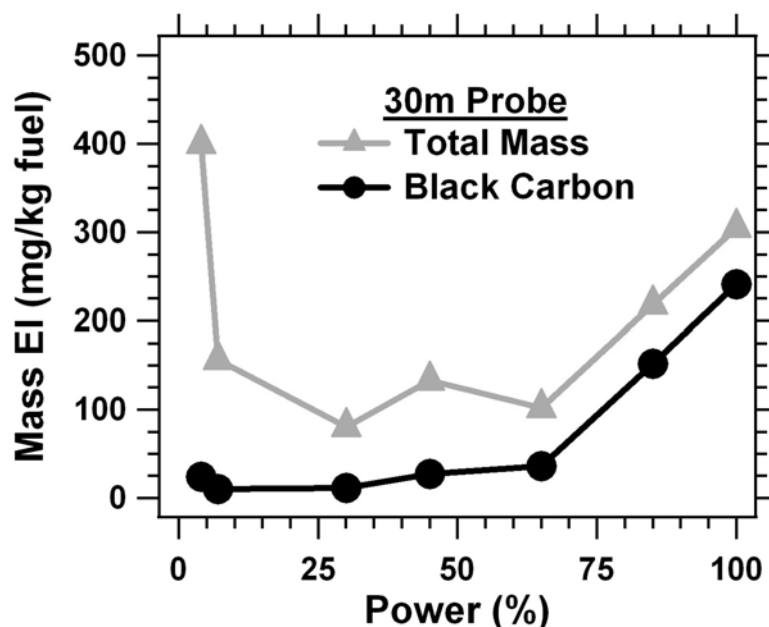


Figure 3. Black carbon and total aerosol mass emission indices measured 30m behind the engine when burning JP-8 fuel. Comparison to Figure 2 shows similar black carbon EIs but an increased total aerosol EI indicative of volatile aerosol formation.

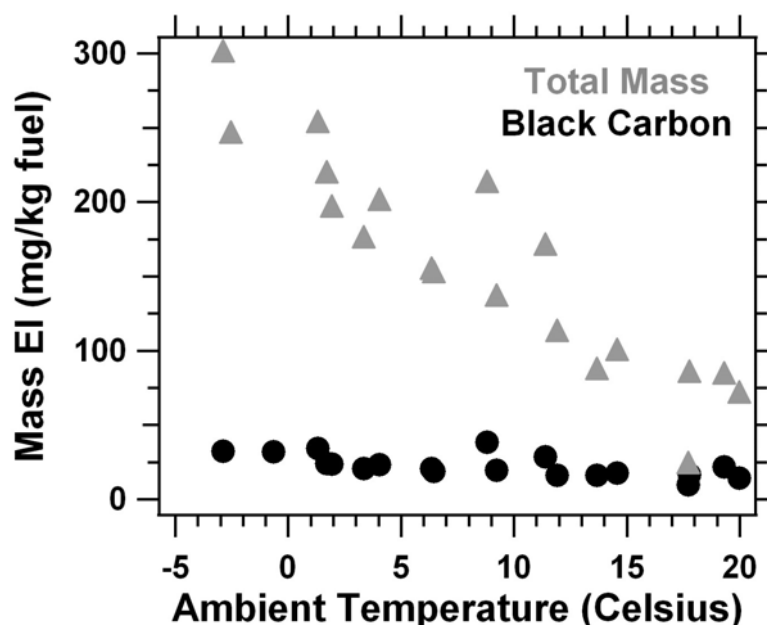


Figure 4. Black carbon and total aerosol mass emission indices measured 30m behind the engine when burning JP-8 fuel as a function of ambient temperature.

Emissions from the on-board APU were measured as it burned either JP-8 or FT-2 fuel. The APU running on JP-8 fuel had black carbon emission indices on the order of 200-500 mg/kg fuel burned. These values are 20 times greater than emitted by the aircraft engine running at idle. A significant reduction in both black carbon and organic mass was seen when burning the FT fuel (Figure 5).

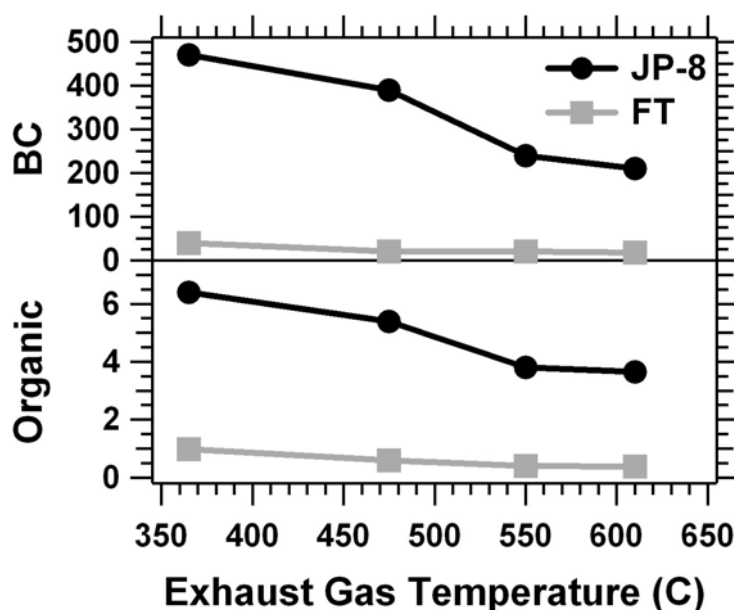


Figure 5. Aerosol mass emission ratios for black carbon (top) and organic compounds (bottom).

4 PRELIMINARY CONCLUSIONS

The driving force in the use of FT fuels as an aviation fuel is the goal of reducing dependence on foreign oil. However, a beneficial side effect of this is a potential decrease in particulate emissions. Significant decreases on the order of 90% were seen in aerosol emissions when using the pure Fischer-Tropsch fuels. During the test, no marked differences were seen in engine performance between the fuels. However, fuel leaks occurred in the aircraft fuel system and tanker trucks when the pure FT fuels were used due to the absence of aromatic compounds, which have been shown to increase seal swell (DeWitt *et al.*, 2009). No leaks were seen when the right engine was fuelled with the blended fuels. For this and other reasons, the initial alternative fuels used for aviation will likely be blends with normal jet fuel.

It should be noted that the Fischer-Tropsch process to make these alternative fuels typically produces a large amount of CO₂. Thus the use of FT fuels for aviation may reduce aerosol emissions but will not decrease CO₂ emissions. However, it is possible that carbon sequestration techniques will be able to eliminate the CO₂ emissions associated with FT fuel production (Jaramillo *et al.*, 2008). In addition, the reduction of aromatic and sulphur content in non-synthetic fuels are likely to produce similar particulate emission reductions.

5 ACKNOWLEDGEMENTS

We would like to thank the sponsorship of NASA, the support of the NASA Dryden Aircraft Operations Facility and the entire AAFEX science team.

REFERENCES

- Corporan, E., M.J. DeWitt, V. Belovich, R. Pawlik, A.C. Lynch, J.R. Gord, and T.R. Meyer, 2007: Emissions Characteristics of a Turbine Engine and Research Combustor Burning a Fischer-Tropsch Jet Fuel. *Energy & Fuels* 21, 2615-2626.
- DeWitt, M.J., E. Corporan, J. Graham, and D. Minus, 2008: Effects of Aromatic Type and Concentration in Fischer-Tropsch Fuel on Emissions Production and Material Compatibility. *Energy & Fuels* 22, 2411-2418.
- Jaramillo, P., W.M. Griffin, and H.S. Matthews, 2008: Comparative Analysis of the Production Costs and Life-Cycle GHG Emissions of FT Liquid Fuels from Coal and Natural Gas. *Environmental Science & Technology* 42, 7561-7565.

Effects of Alternative Fuels on Hydrocarbon and Particle Emissions from Aircraft Engines

R.C. Miake-Lye^{*}, E.C. Wood, M.T. Timko, Z. Yu, S.C. Herndon
Aerodyne Research, Inc., Billerica, USA

B. Lee, G. Santoni
Harvard University, Cambridge, MA USA

W.B. Knighton
Montana State University, Bozeman, MT USA

Keywords: aircraft emissions, alternative fuel, particles, volatile particles, organics, Fischer-Tropsch

ABSTRACT: Alternatives to fossil, petroleum-based jet fuels are being considered for a variety of economic and environmental reasons. The possible alternatives usually result in a change in the detailed hydrocarbon make-up of the fuels, which might be anticipated to result in changes in the emissions released when burning these fuels. Several recent measurement campaigns have examined the gas-phase hydrocarbon emissions and the volatile contributions to particulate emissions from aircraft gas turbine engines. Preliminary results from the Alternative Aviation Fuel EXperiment (AAFEX) are presented that quantify the speciation of hydrocarbon emissions, especially at low power operation, and the organic and sulfate contributions to volatile particulate emission across the range of operating conditions. The measured differences suggest that alternative fuels can have significant impact on the emissions resulting from their use as aviation fuels.

1 INTRODUCTION

Alternatives to petroleum-based fuels may provide economic and environmental benefits relative to the continued use of fossil fuels. Using alternative fuels for aviation will require the fuel to satisfy all of the technical specifications needed for safety and operability across the range of conditions experienced during flight. While a major motivation for considering alternative fuels is the reduced emissions of carbon dioxide (CO₂) as a green house gas, the question naturally arises as to whether other emissions may also be affected by substituting alternative fuels for the traditional petroleum-based fuel sources. Other emissions, both gaseous and particulate, have been receiving increasing attention even in the context of aviation using petroleum fuels due to their potential impacts on both climate change and on local air quality. Especially since the fuel sulfur content and the detailed hydrocarbon speciation of alternative fuels are expected to be different from that of petroleum-based fuels, studies have been carried out to determine the emissions of aircraft engines when burning alternative fuels (e.g. Corporan et al., 2007).

In January 2009, a NASA-led field campaign called Alternative Aviation Fuel EXperiment (AAFEX) was carried out at NASA Dryden facilities in Palmdale, California using two Fischer-Tropsch fuels and comparing with a standard JP-8 fuel. This mission was reviewed by A. Beyersdorf and B. Anderson at the TAC-2 conference (see agenda in this proceedings), where the range of conditions, fuels, and measurements performed are described. The present extended abstract provides results from the measurements made by the Aerodyne team, which included members from Aerodyne, Montana State University, and Harvard University. These results are preliminary, given that the first AAFEX science team meeting was held one week prior to the TAC-2 conference at which these results were presented. On-going analysis is continuing and more complete reports and presentations at an AIAA meeting in January 2010 will be available in the near future.

The comparison of data for the different fuels requires careful consideration of comparable op-

^{*} Corresponding author: R.C. Miake-Lye, Aerodyne Research, Inc., 45 Manning Road, Billerica, MA, USA.
Email: rick@aerodyne.com

erational points. Clearly for very extreme changes in the emissions, like the observed decreases in black carbon particle emissions, effects of the fuel properties on emissions are unequivocal. However for more subtle changes and for accurate quantification of the effects on emissions, the determination of the equivalent engine power setting when using different fuels will require more detailed analysis. In specific, when the different fuels have differing energy content, on either a mass or volume basis, using standard mass flow rates for determining the power condition may be insufficient. Thus the power setting might be better interpreted on the basis of the amount of energy being provided per second by the fuel, for example, rather than the more usual mass per second. Similarly, when reporting the emissions numbers, the traditional practice of reporting the mass of emission per mass of fuel burned (as an “Emission Index” in g/kg-fuel) may need to be amended to account for the differing fuel energy contents as well. Due to the preliminary nature of the data reported here, such analysis has not yet been included, and thus further refinement of the quantification of these emissions will be required.

The range of measurements reported here are similar to what has been used in recent field missions such as the APEX1-3 campaigns (C.C. Wey *et al.*, 2007, Timko 2009a,b) with some important additions. For gaseous species, we again measured CO, speciated organics, NO, NO₂, NO_x, and HONO with significant refinements in some our measurement approaches, and methane (CH₄) was also measured. For particulate emissions, black carbon mass (Multi-Angle Absorption Photometer: MAAP), particle number (Condensation Particle Counter: CPC), particle size (Scanning Mobility Particle Sizer: SMPS), and particle volatile contribution composition (Aerosol Mass Spectrometer: AMS) were all measured. The AMS measures the size-dependent volatile contributions to the emitted particles, primarily based on the coatings on the black carbon soot particles due to the size sensitivity limits of the AMS of about 30 nm – 800 nm in the mass based-size distribution. In essence, the AMS provides information mostly about the organic and sulfate coatings on the soot particles, since those are the primary volatile constituents seen in aircraft exhaust.

2 GASEOUS EMISSIONS

The speciation of the emitted organics of petroleum fuels (Spicer *et al.*, 1992, 1994, Anderson *et al.*, 2006, Yelvington *et al.*, 2007, Knighton *et al.*, 2007) has been measured to be a largely invariant profile of a range of species which is highest at the lowest idle conditions and that is mostly been reduced to immeasurably small values at power greater than about 30% power. Carbon monoxide (CO) as another product of incomplete combustion also demonstrates this rapid drop off with increasing power, and both CO and the emitted organics have a significant temperature dependence, decreasing with increasing ambient temperature. These features are also seen with the two alternative fuels, and the differences between the FT fuels and JP-8 suggests a small decrease in these products of incomplete combustion near idle for the FTs, but this may be confounded by temperature effects and effects of the varying fuel energy content and will require further analysis.

A more marked difference is noticed in comparing the speciation of the organic emissions. Both of the FT fuels had very low fuel aromatic content. This has impact on the emitted species as shown in Figure 1. The value of benzene emission index (EI in g/kg fuel) is plotted versus formaldehyde in the left panel and against ethene in the right. For petroleum fuels, the ratio of benzene to HCHO (or C₂H₄) is largely invariant, and the plot gives a single slope near 0.16 for HCHO (or 0.13 for C₂H₄). For the two FT fuels, the slope is markedly lower in both panels, which is due to the lower aromatic content of the FT fuels resulting in lower benzene emissions relative to HCHO or C₂H₄. Interestingly, while the benzene is lower for both FT fuels relative to that of JP-8, the slope changes are somewhat different for HCHO vs C₂H₄ (c.f. left and right panels) indicating that even the relative amounts of HCHO and C₂H₄ depend on which fuel is considered.

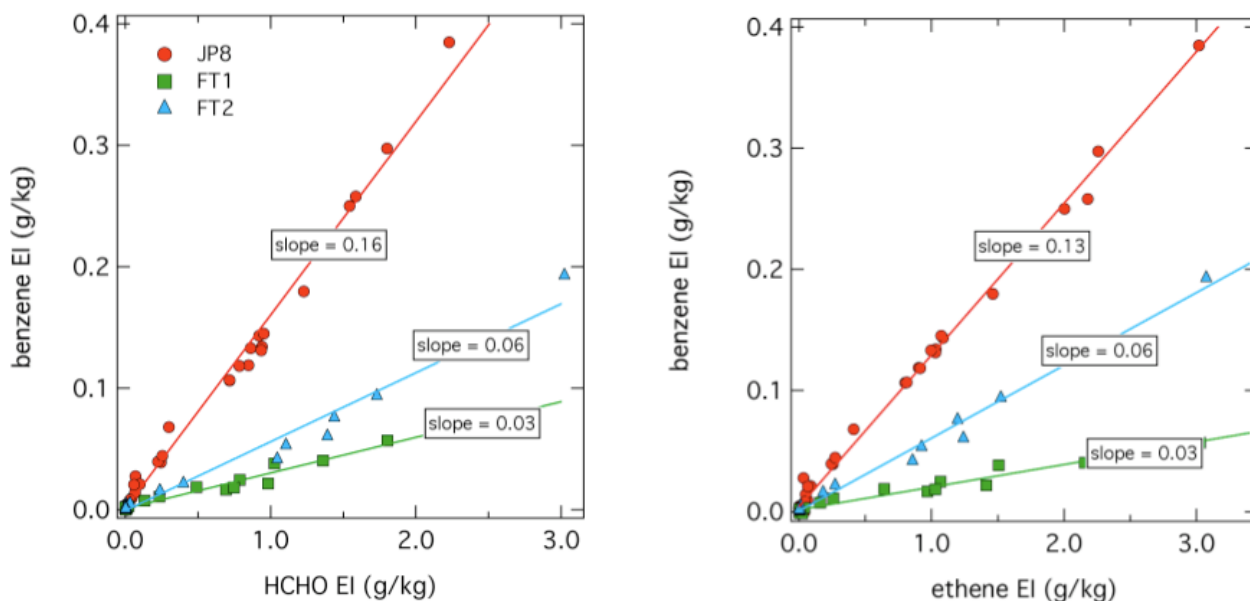


Figure 1. Benzene Emissions Index (EI) plotted versus formaldehyde (HCHO) EI, left panel, and versus ethene (C_2H_4), right panel, indicating that the relative amount of benzene compared to HCHO or C_2H_4 is less for the FT fuels. In addition, the relative amounts of HCHO vs C_2H_4 is also affected since the two FT fuels have different behaviors in the right and left panels.

While benzene is a smaller contributor to the organic profile for the FT fuels, the contribution does not scale simply with the aromatic content, suggesting benzene may be produced in the combustion process even in when very low aromatics are present in the fuel itself, as shown in Figure 2. Here benzene is ratioed to HCHO for a number of recent emissions studies, and the two AAFEX FT fuels represent the left most points in the fuel analysis range.

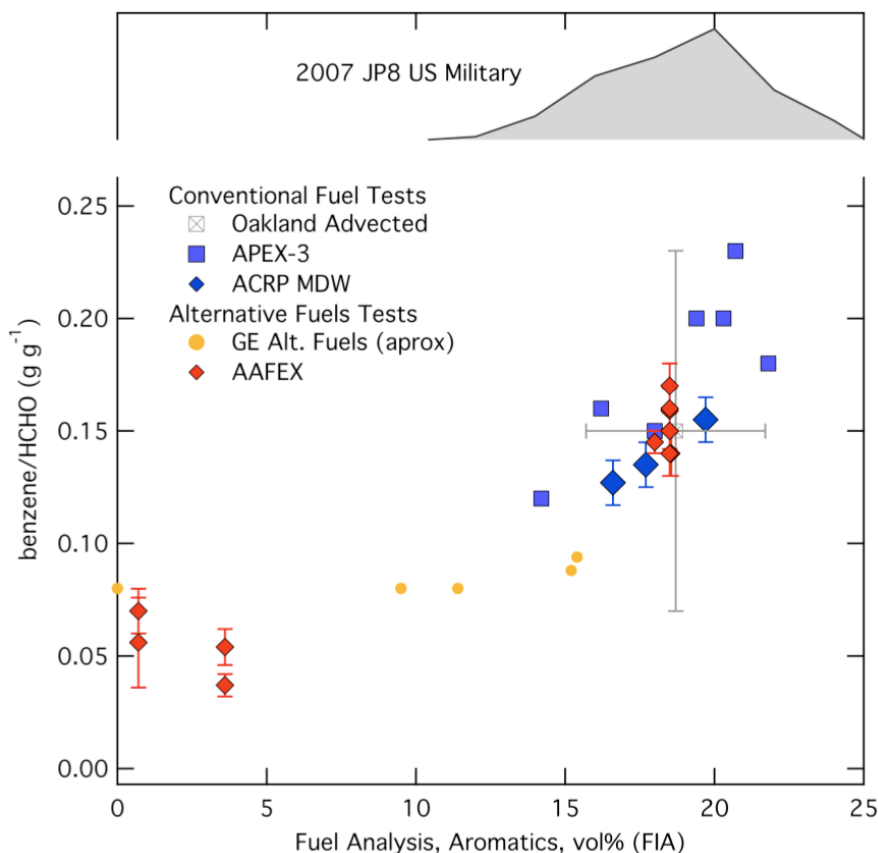


Figure 2. Benzene to HCHO ratio versus fuel aromatic content, indicating that benzene drops as aromatic content is reduced, but the benzene does not approach zero even as fuel aromatics go to zero.

Emissions of oxides of nitrogen (NO_x , NO_y) are important both for climate impact and for local air quality. NO , NO_2 , and HONO were all measured in AAFEX. While one might expect that NO_x emissions would be primarily dependent on the power condition properly accounting for fuel energy content, it is possible that difference in chemical kinetics in the flame zone could depend on the fuel HC mixture by affecting flame peak temperature and structure in the combustor. Since NO_x productions is non-linear in combustor temperature, this could affect the NO_x produced. Proper quantification will require careful analysis accounting for the fuel energy content as discussed in the introduction, but Figure 3a shows that the NO_x EI at 85% power is lower for the two FT fuels compared the JP-8 fuel. It will be important to assess whether the FT fuels produce less NO_x for operation at these higher power settings.

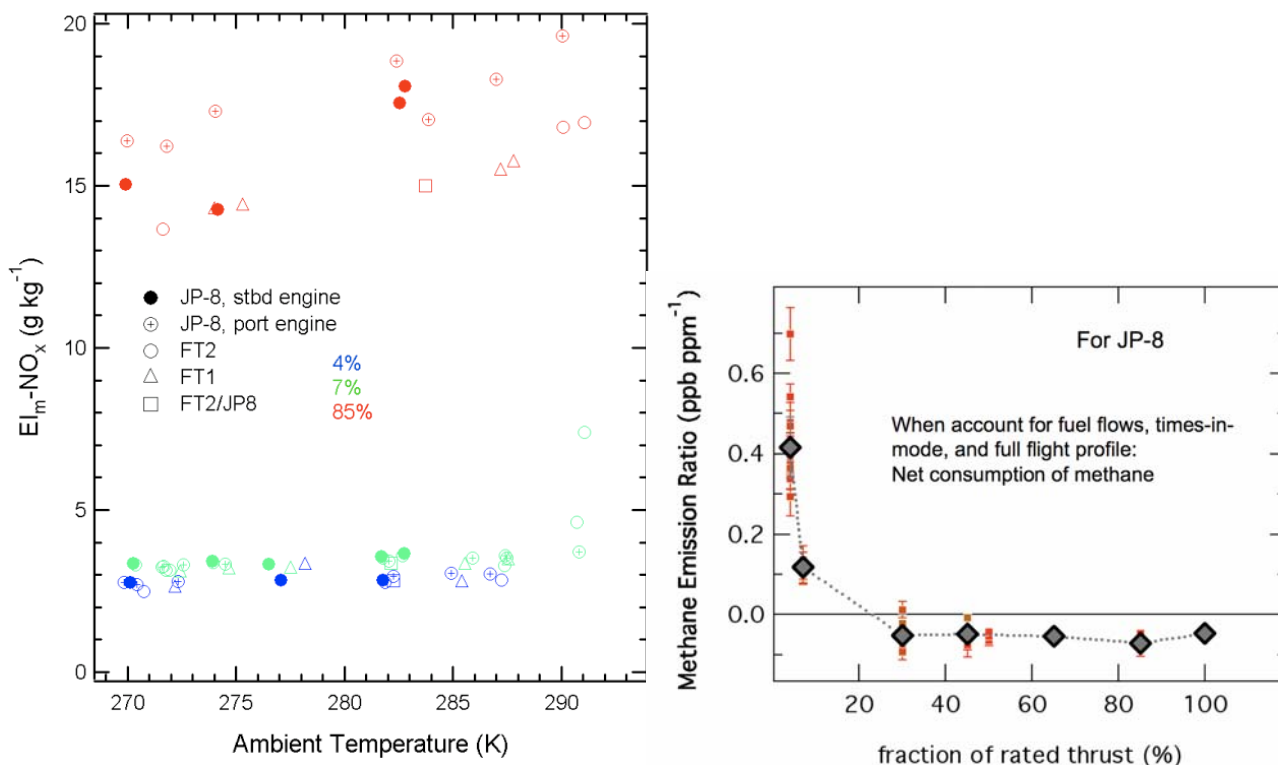


Figure 3a (left) NO_x EI vs ambient Temperature for idle and 85% power. FT fuels (triangles and squares) are lower than the JP-8 fuel.

Fig 3b (right) Methane emission ratio (ppb methane per ppm CO_2) as a function of engine power.

Improvements in measuring HONO allowed a more accurate speciation of the emitted NO_y family of species. This resulted in an upward refinement of the fraction of HONO in the NO_y speciation. NO_2 continues to be measured as the dominant NO_y emission at idle, which will take on increasing significance as NO_2 regulations become tighter and/or more widespread.

Methane was also measured as part of the suite of gaseous measurements, and largely corroborated the methane measurements made by Spicer *et al.* (1992). More detailed power dependence has been mapped out in the AAFEX study (Figure 3b), and measurements at both downwind locations and the engine exit plane were performed. The important point to note is that while CH_4 is emitted at idle conditions, the exhaust concentrations are lower than ambient for engine powers of 30% and above, which indicates that ambient methane is being consumed for most power conditions. When one considers the fuel flow and time in mode for a typical aircraft operation, it is clear that methane is being consumed in net by this engine.

3 PARTICLE EMISSIONS

The most notable effect of the FT fuels on particle emissions is the pronounced decreases in black carbon particles, with the fractional decrease largest at the lowest engine powers. This was reported at length by Whitefield *et al.* at TAC-2 (see elsewhere in these proceedings) and these results were

confirmed in the MAAP, CPC, and SMPS data taken by the Aerodyne team. These results were presented at TAC-2 and will be documented in forthcoming reports.

The particle mass EI measured at 1 and 30 m downstream of the engine exit is shown in Figure 4 for JP-8 and cold ambient temperatures (near 0 °C). When comparing MAAP black carbon data to total mass data taken from an integrating particle size distribution (EEPS data courtesy of Bruce Anderson, NASA and David Liscinsky, UTRC, where a density of unity is assumed to convert to mass), it is noted that the black carbon mass does not change from 1 to 30 m and represents most of the total mass for engine powers greater than about 30% power. However at idle, the total mass is much greater than the black carbon mass, indicating a substantial volatile component. Interestingly, the total mass at idle is not much different than that at take-off, yet at idle most of the mass is due to volatile contributions, while at take-off most of the mass is black carbon/non-volatile PM.

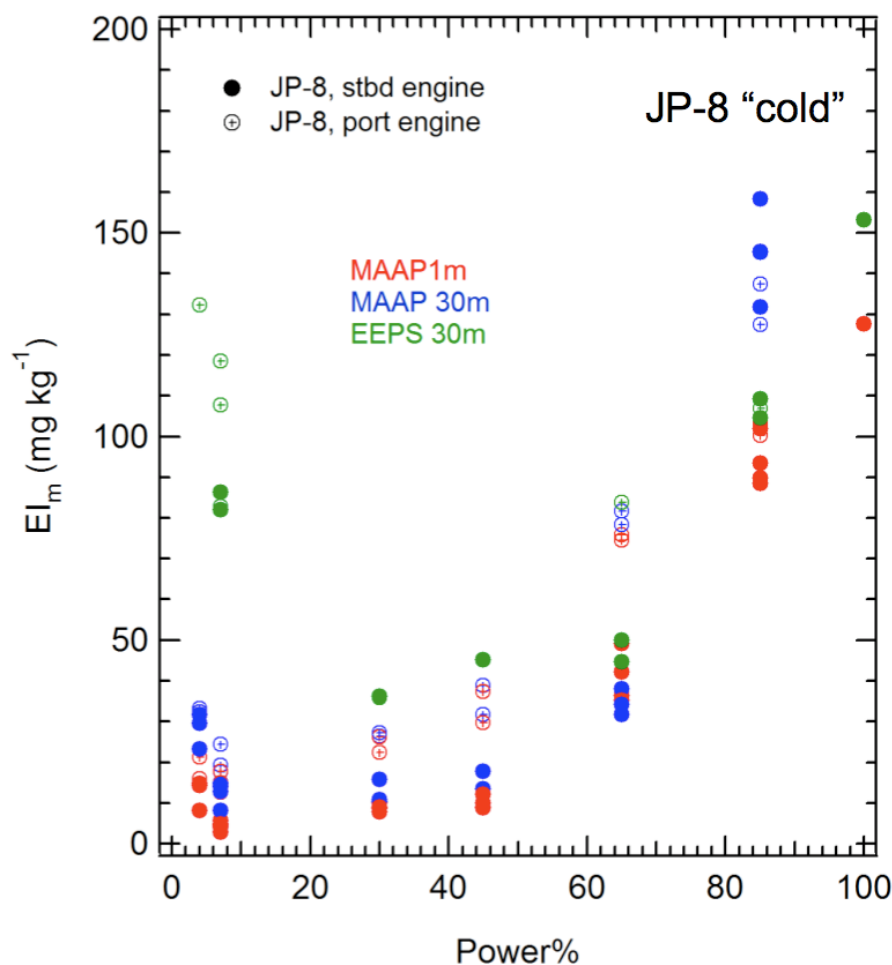


Figure 4. Particle Mass EI versus engine power for measurements at 1 and 30 m downstream of the engine exit. Both black carbon mass (red: 1 m and blue: 30 m) and total mass (green: 30 m, EEPS data courtesy Bruce Anderson, NASA and Dave Liscinsky, UTRC) show the changing volatile/non-volatile particle composition versus power.

Figure 5 uses the AMS to quantify the volatile contributions at 30 m downstream. The left panel (Fig. 5a) shows the particle bound sulfate versus engine power for the several fuels. Sulfate is absent for the FT fuels, which is consistent with the lack of sulfur in those fuels. The JP-8 shows a rising trend with engine power, which is indicative of the increasing soot surface area as the soot increases with engine power. As discussed elsewhere (Timko *et al.*, 2009b, Onasch *et al.*, 2009), the total particulate sulfate likely has less of a power dependence, since the AMS is not measuring sulfate in small volatile particles that are important at low engine powers.

Figure 5b shows the equivalent data for organic contributions to volatile PM at 30 m downstream. The organics decrease dramatically with power, which is even more noticeable when one includes the AMS's lack of sensitivity to small particle mass. The FT fuels and the FT mixture lie below the JP-8, indicating that organic contributions to the PM mass are less for these fuels. This may be explained, similarly to the gas-phase benzene effects, as being a result of the lower aromatic

content of the FT fuels, however one must also account for the fact that the available soot surface area is also significantly lower for the FT fuels. While the particle phase organics are significantly lower, both fuel aromatic content and available soot surface area for condensation may play a role in that reduction.

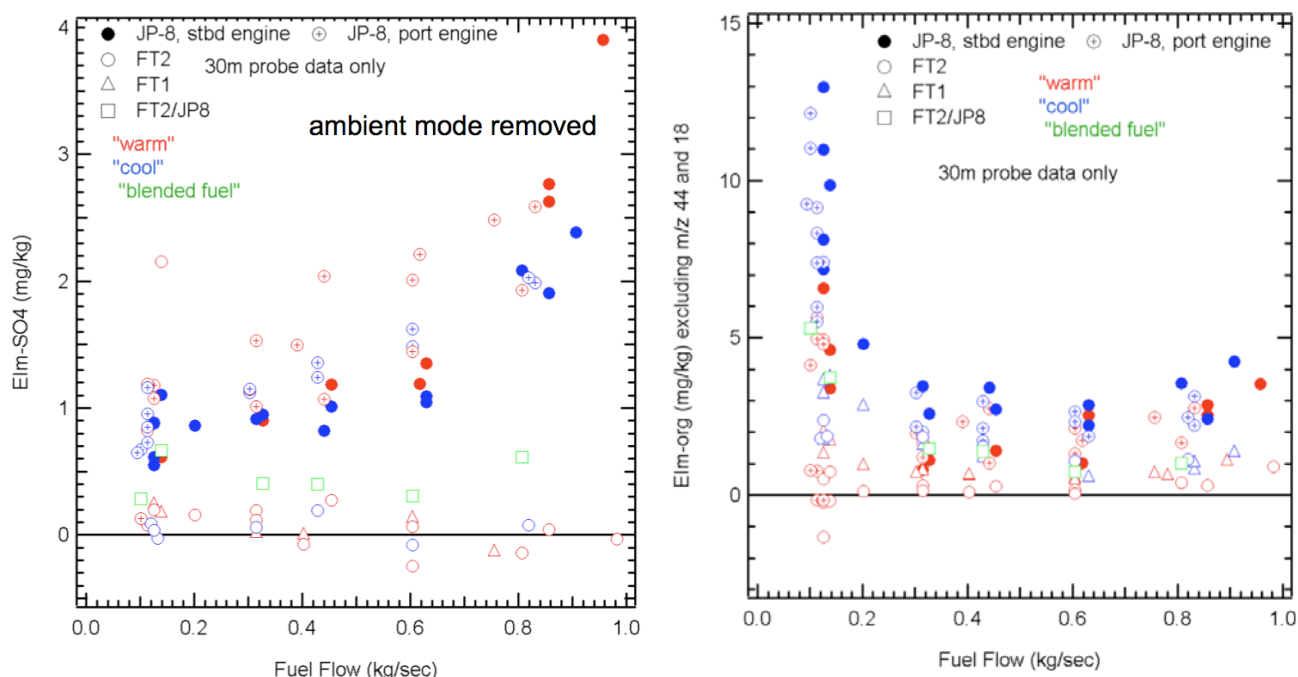


Figure 5. Volatile PM mass contributions measured at 30 m downstream of the engine exit. Fig 5a (left panel) shows sulfate contributions, which are essentially absent for FT fuels. Fig 5b (right panel) shows organic contributions, which are lower for FT fuels relative to JP-8.

4 CONCLUSIONS

The alternative FT fuels explored in AAFEX indicate that the low fuel sulfur content and low aromatic content of these fuels have impact on the gaseous and particulate emission from an aircraft gas turbine engine. The hydrocarbon speciation profile depends on fuel type, and notably aromatic species emissions (e.g. benzene) are lower relative to major emissions like formaldehyde and ethene (which also change somewhat relative to one another). At AAFEX, the NO_y speciation was measured more accurately for all fuels, and further analysis is required to determine if the use of alternative fuels could affect the total NO_x emissions, after properly accounting for fuel energy content. Methane emissions were measured and the data confirm that modern gas turbine engines have CH_4 emissions at idle, but consume CH_4 at higher power, resulting in a net CH_4 consumption for a full flight profile. This methane result applies to all fuels.

FT fuel resulted in significant reductions of non-volatile (soot) and volatile (sulfate, organic) emissions with FT fuel. The volatile contributions, and especially what is measured by the AMS, are coupled to the non-volatile (soot) particle emissions through the soot particle providing surface area for the volatile species to condense. Thus, at higher power where there is more soot, more of the volatile PM appears as coatings on the soot. At lower powers, more of the volatile PM is contained in particles smaller than the AMS can measure. Organic contributions decrease with increasing engine power, and the FT fuels have lower organic PM contributions than the JP-8. Sulfate is not detected for the FT fuels as a direct consequence of their very low fuel sulfur content.

ACKNOWLEDGMENTS

Sponsorship of NASA and the FAA (via PARTNER CoE and the MS&T Center of Excellence for Aerospace Particulate Emission Reduction Research) is gratefully acknowledged. Support from and interaction with the AAFEX mission team, especially NASA (LaRC, DFRC, GRC), MS&T, UTRC, US EPA, and US Air Force (AFRL/UDRI, AEDC) contributed to the mission success.

REFERENCES

- Anderson, B. E., Chen, G., and Blake, D. R., 2006, Hydrocarbon Emissions from a modern commercial airliner,” *Atmospheric Environment*, 40, 3601–3612.
- Corporan, E., DeWitt, M.J., Belovich, V., Pawlik, R., Lynch, A.C., Gord, J.R., Meyer, T.R., 2007, Emissions characteristics of a turbine engine and research combustor burning a Fischer-Tropsch jet fuel, *Energy & Fuel*, 21, 2615-2626.
- Knighton W.B., T.M. Rogers, B.E. Anderson, S.C. Herndon, P.E. Yelvington, and R.C. Miake-Lye, 2007, *J. of Propulsion and Power*, 23, 949-958.
- Onasch, T.B., J.T. Jayne, S. Herndon, D.R. Worsnop, R.C. Miake-Lye, I.P. Mortimer, and B.E. Anderson, 2009. Chemical properties of aircraft engine particulate exhaust emissions sampled during aircraft particle emissions experiment, accepted for publication in *J. Propulsion and Power*.
- Wey, C.C., B.E. Anderson, C. Wey, R.C. Miake-Lye, P. Whitefield, and R. Howard, 2007 Overview of the Aircraft Particle Emissions Experiment. *J. Propulsion and Power*, 23, 898-905.
- Spicer, C.W., M.W. Holdren, D.L. Smith, D.P. Hughes, and M.D. Smith, 1992, Chemical composition of exhaust from aircraft turbine engines, *J. Eng. For Gas Turbines and Power*, 114, 111-117.
- Spicer, C.W., M.W. Holdren, R.M. Riggan, and T.F. Lyon, 1994, Chemical composition and photochemical reactivity of exhaust from aircraft turbine engines, *Annales Geophysicae*, 12, 944-955.
- Timko, M.T., S.C. Herndon, E.C. Wood, T.B. Onasch, M.J. Northway, J.T. Jayne, M.R. Canagaratna, R.C. Miake-Lye and W.B. Knighton, 2009a: Gas turbine engine emissions Part 1. Hydrocarbons and nitrogen oxides. accepted for publication in *J. Engineering for Gas Turbines and Power*.
- Timko, M.Y., T.B. Onasch, M.J. Northway, J.T. Jayne, M. Canagaratna, S.C. Herndon, E.C. Wood, R.C. Miake-Lye and W.B. Knighton, 2009b: Gas turbine engine emissions Part 2. Chemical properties of particulate matter. accepted for publication in *J. Engineering for Gas Turbines and Power*.
- Yelvington, P.E., S.C. Herndon, J.C. Wormhoudt, J.T. Jayne, R.C. Miake-Lye, W.B. Knighton, and C. Wey, 2007, Chemical speciation of hydrocarbon emissions from a commercial aircraft engine, *J. of Propulsion and Power*, 23, 912-918.

Transport and Transformation of Air Pollution from Road and Ship Transport - Joint Analysis of Regional Scale Impacts and Interactions

G. Gadzhev*, K. Ganev, G. Jordanov, N. Miloshev, A. Todorova
Geophysical Institute, Bulgarian Academy of Sciences, Sofia, Bulgaria

D. Syrakov, M. Prodanova
National Institute of Meteorology and Hydrology, Bulgarian Academy of Sciences, Sofia, Bulgaria

Keywords: transport and transformation, regional scale, road and ship transport emissions

ABSTRACT: The objective of the present work is to study the dilution and transformation processes and the interaction of the plumes generated by road and ship transport. The numerical simulations are carried out with the US EPA MODELS-3 system. A large number of numerical experiments were carried out, which makes it possible to distinguish the relative contribution of different air pollution factors. Careful and detailed analysis of the obtained results can outline the influence of the domain specific physiographic characteristics, road and ship emission impacts and meteorology conditions on the pollution characteristics

1 INTRODUCTION

The objective of the present work is to study the regional scale dilution and chemical transformation processes of pollutants generated by road and ship transport. More precisely the study aims at clarifying the interaction between the pollution from road and ship emissions their mutual impacts and contribution to the overall pollution.

It is expected the results of the current work to give some clues for specification of the “effective emission indices” linking emission inventories to the emissions to be used as input in large scale models.

2 METHODOLOGY

The US EPA Models-3 system (Dudhia, 1993, Grell et al., 1994, Byun et al., 1998, Byun and Ching, 1999, Byun and Schere, 2006) was chosen as a modelling tool. US NCEP Global Analyses data was used for meteorological background input: The data is with 1×1 degree grid resolution covering the entire globe, the time resolution is 6 hours. The Models-3 system nesting abilities were applied for downscaling the problem to a resolution of 30 km for the domain discussed further.

Two sets of emission data are used in the present study:

- The data set created by Visschedijk and Denier van der Gon (2005) was used for the all the emissions but those from ship transport;
- The ship transport emissions were taken from the inventory created by Wang et al. (2007).

More details about emission processing (introducing temporal profiles, speciation, etc.) can be seen in Syrakov et al. (in press).

* Corresponding author: G. Gadzhev, Geophysical Institute, Bulgarian Academy of Sciences, Acad. G.Bonchev str., block 3, Sofia 1113, Bulgaria. Email: ggadjev@geophys.bas.bg

The study was based on joint analysis of the results from the following emission scenarios:

- Simulations with all the emissions in the simulation domain, corresponding arbitrary (concentration, deposition, columnar value, process contribution, etc.) characteristic ϕ denoted by ϕ_{all} ;
- Simulations with the emissions from road transport excluded, corresponding arbitrary characteristic ϕ denoted by $\phi_{no,road}$;
- Simulations with the emissions from ship transport excluded, corresponding arbitrary characteristic ϕ denoted by $\phi_{no ship}$;
- Simulations with the emissions from both road and ship transport excluded, corresponding arbitrary characteristic ϕ denoted by $\phi_{no road \& ship}$.

The most natural properties, which can be constructed from these scenarios are the relative (in %) contributions of road/ship emissions to the formation of the characteristic ϕ :

$$\phi_{road} = \frac{\phi_{all} - \phi_{no road}}{\phi_{all}} \cdot 100 \text{ and } \phi_{ship} = \frac{\phi_{all} - \phi_{no ship}}{\phi_{all}} \cdot 100 . \quad (1)$$

Some more “sophisticated” properties, like impact of road transport on the pollution from ship emissions (the ratio $\phi_{ship}|_{road}$ of pollution from ship emissions when road emissions are also excluded to pollution from ship emissions, but with road emissions present) or vice versa ($\phi_{road}|_{ship}$) can also be defined:

$$\phi_{ship}|_{road} = \frac{\phi_{no road} - \phi_{no road \& ship}}{\phi_{all} - \phi_{no ship}} \cdot 100 \quad \text{and} \quad \phi_{road}|_{ship} = \frac{\phi_{no ship} - \phi_{no road \& ship}}{\phi_{all} - \phi_{no road}} \cdot 100 . \quad (2)$$

MM5 and CMAQ simulations were carried out for the periods January 2001-2005 and July 2001-2005.

Averaging the fields over the respective month produces a diurnal behavior of given pollution characteristic, which can be interpreted as “typical” for the month (respectively season). The characteristic, which will be mostly demonstrated and discussed as an example further in this paper is the surface concentration c . Moreover, what will be shown and discussed concerns not only separate pollutants, but also some aggregates like nitrogen compounds (GNOY=NO + NO₂ + NO₃ + 2*N₂O₅ + HONO + HNO₃ + PNA), organic nitrates (ORG_N=PAN + NTR), hydrocarbons (HYDC=PAR + ETH + OLE + TOL + XYL + ISO), CAR_PHE= FORM + ALD2 + MGLY + CRES, aerosol NH₄, SO₄ and H₂O, PM_{2.5} and PM_{coarse}=PM₁₀-PM_{2.5}.

The Models-3 “Integrated Process Rate Analysis” option is applied to discriminate the role of different dynamic and chemical processes for the pollution from road and ship transport. The processes that are considered are: advection, diffusion, mass adjustment, emissions, dry deposition, chemistry, aerosol processes and cloud processes/aqueous chemistry.

3 RESULTS AND DISCUSSION

The respective “typical” concentrations can be also averaged for the day and these will be (due to the volume limitations) most of the illustrations demonstrated, like on Figure 1.

The impact of road/ship emissions is rather complex and will take a lot of pages to be described. One could not help but notice, however, how well displayed the configurations of most intensive ship/road transport are. Due to the none-linearity of the processes their impact can be negative as well. Some big cities and the main ship routs are particularly well displayed as sinks in the July ozone plots.

The impact of road/ship emissions for a “typical” January day is again very complex. The difference, both qualitative and quantitative between “summer” and “winter” fields is quite evident (due to volume limitations not demonstrated in the present paper) for all the species, thou the configurations of most intensive ship/road transport are again very well displayed.

Ship/road emission relative contribution does have diurnal course, which is well displayed by Figure 2. Again the temporal behavior is complex and can not be described by some general statements. The most intensive ship/road sources are well visible as sinks and the sink locations do not

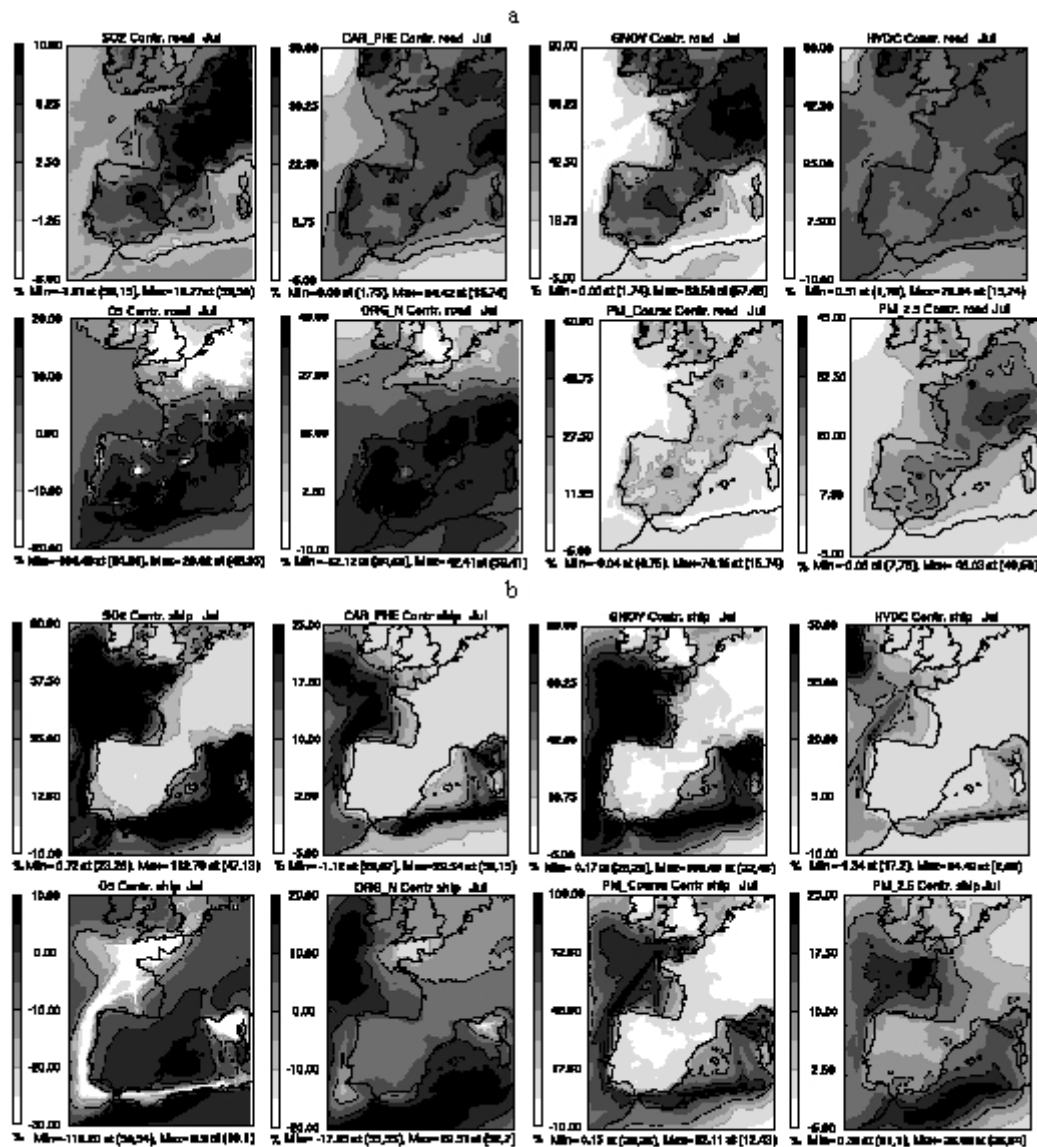


Figure 1. Averaged for a "typical" day in July fields of C_{road} [%] (a) and C_{ship} [%] (b) for ozone, PM_{2.5}, nitrogen compounds, hydrocarbons, CAR_PHE, PM_{coarse}, organic Nitrates and SO₂

have dramatic diurnal change. The temporal variations of shape and location of areas with positive impact to the ozone levels generated by ship/road transport emissions are more prominent. The more complex and sophisticated "road-to-ship" and "ship-to-road" contributions are illustrated in Figure 3. It is really hard to describe the plot, but they are a very good demonstration of how complex the interactions of the pollutants are and how strange and surprising the impact of one of the types of transport to the air pollution by the other is. The absolute value of these contributions in some points could be very large, but generally for most of the compounds the contributions vary within relatively narrow margins around 100%. The corresponding plots for January are of course different, but the most general features mentioned above are valid as well.

To better understand the interaction of pollutants from road and ship transport, one should closely examine the contributions of different processes to the total pollution, in particular the "road-to-ship" and "ship-to-road" contributions to the respective processes. That is why the CMAQ "Integrated Process Rate Analysis" option was applied and the "portions" of the major processes which form the hourly concentration changes were calculated. The process "portions" $\Delta c^{(proc.)}$ can be treated like the concentrations and respective "road", "ship", "road-to-ship" and "ship-to-road" contributions can be estimated.

Plots of the horizontal fields of the “road-to-ship” ($\Delta c_{ship}^{(chem)} \Big|_{road}$) and “ship-to-road” ($\Delta c_{road}^{(chem)} \Big|_{ship}$) contributions to the chemical transformation processes “portion” of the surface ozone the hourly change concentrations are shown in Figure 4. The very complex and “mosaic” texture of the plots can hardly be discussed in details. This is simply an illustration of how discouragingly complex the mutual impacts of pollution from different source types is and how difficult the answer of a question “What is the impact of the pollution from road transport to the chemical transformation of the ozone from ship transport?” or vice versa could be.

4 CONCLUSIONS

The numerical experiments performed produced a huge volume of information, which have to be carefully analyzed and generalized so that some final conclusions could be made. The conclusions that can be made at this stage of the studies are that the transport type/processes interactions are indeed very complex.

The results produced by the CMAQ “Integrated Process Rate Analysis” demonstrate the very complex behavior and interaction of the different processes – process contributions change very quickly with time and these changes for the different points on the plane hardly correlate at all. The analysis of the behavior of different processes does not give simple answer of the question what the impact of pollution from given source type to the process, which form the pollution from another source type, could be. The “Integrated Process Rate Analysis” is a fruitful approach, however, so an attempt should be made the evaluation and analysis of the processes to be presented in a more general way.

5 ACKNOWLEDGEMENTS

The present work is supported by EC through 6FP NoE ACCENT (GOCE-CT-2002-500337) and QUANTIFY (GOG-003893), SEE-GRID-SCI project, contract № FP7 –RI-211338, COST Actions 728, as well as by the Bulgarian National Science Fund (grants № D002-161/2008 and D002-115/2008).

The contacts within the framework of the NATO Sfp Grant ESP.EAP.SFPP 981393 were extremely simulating as well.

Deep gratitude is due to US EPA, US NCEP and EMEP for providing free-of-charge data and software. Special thanks to the Netherlands Organization for Applied Scientific research (TNO) for providing us with the high-resolution European anthropogenic emission inventory.

REFERENCES

- Byun, D. and J. Ching, 1999: Science Algorithms of the EPA Models-3 Community Multiscale Air Quality (CMAQ) Modeling System. EPA Report 600/R-99/030, Washington DC.
- Byun, D., J. Young, G. Gipson, J. Godowitch, F.S. Binkowski, S. Roselle, B. Benjey, J. Pleim, J. Ching, J. Novak, C. Coats, T. Odman, A. Hanna, K. Alapaty, R. Mathur, J. McHenry, U. Shankar, S. Fine, A. Xiu, and C. Jang, 1998: Description of the Models-3 Community Multiscale Air Quality (CMAQ) Modeling System, 10th Joint Conference on the Applications of Air Pollution Meteorology with the A&WMA, 11-16 January 1998, Phoenix, Arizona, 264-268.
- Byun, D. and K.L. Schere, 2006: Review of the Governing Equations, Computational Algorithms, and Other Components of the Models-3 Community Multiscale Air Quality (CMAQ) Modeling System. Applied Mechanics Reviews 59, 51-77
- Dudhia, J. 1993: A non-hydrostatic version of the Penn State/NCAR Mesoscale Model: validation tests and simulation of an Atlantic cyclone and cold front. Mon. Wea. Rev. 121, 1493-1513.
- Grell, G.A., J. Dudhia, and D.R. Stauffer, 1994: A description of the Fifth Generation Penn State/NCAR Mesoscale Model (MM5). NCAR Technical Note, NCAR TN-398-STR, 138 pp.

- Syrakov, D., K. Ganev, M. Prodanova, N. Miloshev, G. Jordanov. 2009. Background Pollution Forecast over Bulgaria, to appear in Lirkov, S. Margenov, and J. Wasniewski (Eds.), LSSCD2009, Lecture Notes in Computer Sciences (accepted, in press), 0302-9743
- Visschedijk A.J.H. and H.A.C. Denier van der Gon. 2005: Gridded European Emission Data for NO_x, SO₂, NMVOC, NH₃, CO, PM₁₀, PM_{2.5} and CH₄ for year 2000, TNO Report B&O-A R 2005/106 version 2, Apeldoorn, The Netherlands.
- Wang, C., J.J. Corbett, and J. Firestone. 2007: Improving Spatial Representation of Global Ship Emissions Inventories, Environmental Science & Technology, Web Release Date: 01-Dec-2007;(Article) DOI: 10.1021/es0700799, 2007.

Characterisation of particulate matter and gaseous emissions from a large ship diesel engine

Jana Moldanová*, Erik Fridell

IVL, Swedish Environmental Research Institute, Göteborg, Sweden

Olga Popovicheva

SINP, Moscow State University, 119991, Moscow, Russia

Benjamin Demirdjian, Victoria Tishkova

CINaM, UPR CNRS 3118, Campus de Luminy, Marseille, France

Alessandro Faccinetto, Cristian Focsa

Laboratoire de Physique des Lasers, Atomes et Molécules (UMR 8523), Université de Lille 1, 59655 Villeneuve d'Ascq, France

Keywords: Ship emissions, Particulate matter, chemical composition, elemental composition, microphysical characteristic, NOX, CO, SO₂, hydrocarbons

ABSTRACT: Composition of exhaust from a large cargo vessel was investigated onboard a ship during the Quantify field campaign in June 2007. The emitted particulate matter (PM) properties were investigated along with composition of the gas-phase emissions. Mass, size distribution, chemical composition and microphysical structure of the PM were investigated. The emission factor for PM was 5.3 g/(kg fuel). The mass size distribution showed a bimodal shape with two maxima: one in the accumulation mode with mean particle diameter DP around 0.5 µm and one in the coarse mode at DP around 7 µm. The PM composition was dominated by organic carbon (OC), ash and sulphate while the elemental carbon (EC) composed only a few percent of the total PM. Increase of the PM in exhaust upon cooling was associated with increase of OC and sulphate. Laser analysis of the adsorbed phase in the cooled exhaust showed presence of a rich mixture of polycyclic aromatic hydrocarbon (PAH) species with molecular mass 178 – 300 amu while PM collected in the hot exhaust showed only four PAH masses. Microstructure and elemental analysis of ship combustion residuals indicated three distinct morphological structures with different chemical composition: soot aggregates, significantly metal polluted; char particles, clean or containing minerals; mineral and/or ash particles. Additionally, organic carbon particles of unburned fuel or/and lubricating oil origin were observed. Hazardous constituents from the combustion of heavy fuel oil such as transitional and alkali earth metals (V, Ni, Ca, Fe) were observed in the PM samples.

1 INTRODUCTION

Emissions of exhaust gases and particles from seagoing ships contribute significantly to the anthropogenic burden, thereby affecting the chemical composition of the atmosphere, local and regional air quality and climate. According to the global estimates shipping emits between 0.9 and 1.7 million tons of particulate matter annually. The fact that nearly 70 % of ship emissions occur within 400 km from land implies potential of these emissions to significantly affect air quality in coastal areas (Endresen et al., 2003, Eyring et al., 2005). Global-scale model study of Corbett et al. (2007) has shown a maximum increase of PM_{2.5} due to shipping by 2 µg/m³. This study also indicated that shipping-related PM emissions on a global scale are responsible for around 60 000 cardiopulmonary and lung cancer deaths annually.

The radiative forcing of PM emitted by shipping is rather complex: radiative forcing of black carbon is positive, while radiative forcing of sulphate particles is negative (Endresen et al., 2003; Eyring et al., 2007; Lauer et al., 2007). The particles also affect the life cycle and radiative proper-

* Corresponding author: Jana Moldanová, IVL, Swedish Environmental Research Institute, Box 5302, SE – 400 14, Göteborg, Sweden. Email: janam@ivl.se

ties of the marine stratus clouds at the top of the marine boundary layer and contribute with a negative radiative forcing. Current estimates indicate that the present-day net radiative forcing caused by ship emissions (including the gaseous species) could be negative (Endresen *et al.*, 2003; Eyring *et al.*, 2007; Lauer *et al.*, 2007).

The particles emitted from large marine diesel engines fuelled with residual oil represent a variety of compositions and sizes. Despite of many indications of their important role, both as air pollutant and for the climate change, information on emissions of ship-exhaust particles, such as detailed characterisation of chemical composition, microphysical characteristic and description of transformation processes in the marine environment, is only sparse. The ship-exhaust particles are composed by elemental, organic and inorganic carbon, sulphate and ash as well as nitrates. Quantification of aerosol mass emitted from the low-speed marine diesel engines has been investigated by few studies (Lyyräinen *et al.*, 1999; Cooper, 2003; Sinha *et al.*, 2003; Chen *et al.*, 2004; Petzold *et al.*, 2008; Fridell *et al.*, 2008). Size distributions are available both for ship plumes (e.g. Hobbs *et al.*, 2000; Petzold *et al.*, 2004) and for fresh emissions (e.g. Lyyräinen *et al.*, 1999; Petzold *et al.*, 2008; Fridell *et al.*, 2008). Microphysical and chemical studies of the PM generated by combustion of residual fuels have shown that the PM is composed of two different types of particles: graphitic soot aggregates in the size range tenths to hundred nm and larger carbon-rich char particles in size range of few μm containing also sulphur and other inorganic species (Ca, V, Ni, Fe) (Lyyräinen *et al.*, 1999; Chen *et al.*, 2005).

In this study we report properties of particles sampled in the exhaust of the main engine on a large cargo vessel together with their individual microphysical and chemical characteristics. Results from sampling both in hot and in diluted/cooled-exhaust gas are presented and the formation of particles during cooling of the exhaust is discussed. Composition of gaseous emissions was investigated to give a more complete picture of composition of the emissions.

2 METHODS

2.1 *Measurement campaign*

The measurements were performed in June 2007 as a part of a field campaign organized within the EU project QUANTIFY. The aim of the campaign was to investigate plume and corridor effects of ship emissions. The measurements were performed in area of the Celtic Sea, the English Channel and the North Sea. The campaign involved both measurements from the research aircraft that performed surveys in the ship corridors as well as plume chasing of a designated ship and measurements onboard this vessel. The onboard measurements presented here were performed on a combined Ro-Ro and container ship. The vessel was built in 1985 and is 292 m long and 32 m wide. The overall height is 52 m and the height from the sea level to the funnel top is 39 m. Further technical parameters of the ship engine and the cruise as speed, power, temperature and flux of the exhaust gases are presented in Table 1.

Table 1. Technical parameters of the ship and ship engine operation specific for the measurements performed 14/6 2007. The exhaust flow is given at normalized conditions (273.14 K, 1013.25 hPa)

Gross tonnage	58 438
Net tonnage	21 660
Main diesel engine	
Kincaid B&W 6L90 GBE	20 200 kW, 97 rpm *
Thrusters	2 × 1 398 kW
Full sea speed	17.5 knots (32.4 km/h)
Fuel consumption at sea	HFO ** 3.2-3.4 m ³ /h
Brake Power Load, %	84
Brake Power, Main Engine, MW	17.0
Speed, km/h	31.5
Calculated Fuel Consumption, kg/h	3 263
Calculated Fuel Consumption, g/kWh	194
Exhaust temperature after the engine, °C	330
Exhaust flow, main engine, Nm ³ /h	110 000
Exhaust flow speed, m/s	25

* rpm: rotations per minute, ** HFO: Heavy-Fraction Oil (residual oil)

Fuel analyses, one performed on routine basis after the fuel purchase on behalf of the ship owner and one performed on a fuel sample taken directly from the engine during the campaign have shown the following elemental composition: 86.5 % (mass) C, 0.7% O, 0.34% N, 1.9 % S, 107 mg/kg V, 35 mg/kg Ni, 5 mg/kg Si, 3 mg/kg Ca. The ash content was 0.03 % (mass).

2.2 Measured parameters and methodologies

The analysed exhaust from the 20.2 MW main engine was sampled through 3 holes in the exhaust pipe positioned c.a. 25 m behind the engine and 40 meters before the funnel exit plane. Properties of the particulate matter were investigated in the hot exhaust gas sampled directly in the exhaust pipe, in a diluted and cooled gas sampled in the dilution system, or in both, as indicated later in the text. The partial flow dilution system was used to mix the hot-exhaust gas with ambient air (26-30°C, 30% RH) and cool to around 40°C. The dilution factor was determined by continuous CO₂ measurements (International Organisation of Standardisation, 1996), and varied between 8 and 10. In addition, concentration of NO_x, HC, CO, CO₂, O₂ and SO₂, as well as humidity, temperature and the gas flow were measured. More details about the sampling are described in Moldanová *et al.* (2009).

The size distribution of particles in the hot diesel exhaust was probed using a cascade impactor (Andersen Mark III Particle Sizing Stack Sampler) with eight stages and 47 mm diameter quartz filter. The impactor stages have cut-offs between about 10 and 0.2 µm. The filters were analysed gravimetrically. The total particle mass was measured using glass fibre, quartz and Teflon filters in the partial flow dilution system and quartz filters in the hot exhaust. The filters were analysed gravimetrically. Analyses of reference filters sampled behind the dilution system showed contribution of the background PM to the exhaust gas concentration by about 0.2%.

The morphology, microstructure and composition of individual carbonaceous particles on samples taken in hot and cooled exhaust were investigated by various electron microscopy techniques, including transmission electron microscopy (TEM) with the phase-contrast imaging method, energy-dispersive X-ray spectroscopy (EDS), and selected area electron diffraction (SAED) (Demirdjian *et al.*, 2007). The surface composition (especially in terms of adsorbed PAHs) of the carbonaceous material deposited on filters exposed in hot and cooled exhaust was investigated by two-step laser mass spectrometry (L2MS) (Bouvier *et al.*, 2007; Mihešan *et al.*, 2008).

Evolved Gas Analyses (EGA) by thermal-optical analyzer (Johnson *et al.*, 1981; Birch and Cary, 1996) for determination of the sum of organic carbon and carbonates (OC) and of the elemental carbon (EC) content and ion-chromatographic analyses for determination of the sulphate content were performed at NILU laboratory on quartz filter samples. The samples were taken both from the hot exhaust and from the diluted exhaust.

Concentrations of a number of other gas constituents were measured continuously in the hot exhaust at point B. Nitrogen oxides (Horiba PG-250 chemiluminescence instrument), carbon monoxide and carbon dioxide (Horiba PG-250 NDIR), oxygen (Horiba PG-250 galvanic cell), total hydro-

carbons (Bernath Atomic BA 3006 FID), and sulphur dioxide (Horiba PG-250 NDIR) were monitored. The temperature and humidity of the inlet air were monitored. The exhaust gas flow was measured with a pitot tube at point A. The exhaust temperature in the hot exhaust was 300°C, and in the dilution system 40°C. Engine data were obtained from the ship's instrumentation. Further details of the individual measurement techniques are given in Moldanová et al. (2009) and references therein.

3 RESULTS AND DISCUSSION

3.1 Exhaust composition and PM properties

A summary of measured emission indices of the engine, emission rates and concentrations of exhaust components are given in Table 2. The indices were calculated from measured concentrations and from the exhaust flow and fuel consumption presented in Table 1. Emission The emission factor for NO_x is on the low side of the span of values of the global average EF_{NO_x} for cargo ships, is lower for CO and significantly lower for hydrocarbons (EF comparison this work/global average values for cargo ships (in g/kg fuel): EF_{NO_x}: 73.4/67.9–87; EF_{CO}: 2.2/4.7–7.4; EF_{HC}: 0.36/2.4–6.6). However, since emission factors are known to vary between ships, these results are not surprising. The SO₂ emission factor may be deduced directly from the sulphur content in the fuel assuming all sulphur is oxidized into SO₂ in the combustion chamber. Such a calculation gave 39.4 g/(kg fuel), a value close to emission factor 39.3 g/(kg fuel) obtained from the SO₂ measurements.

The PM emission factors, emission rates and concentrations given in Table 2 for the hot and for the diluted exhaust are calculated from gravimetric analysis of the total particle mass on filters. The value for the hot exhaust is an average of three samples, the value for the diluted exhaust is an average of five samples. The increase in PM observed after the dilution reflects condensation growth of particles during cooling from about 300°C to 40°C.

Table 2. Emission factors EF, emission rates Er and concentrations C in exhaust from the main diesel engine operating under conditions as listed in Table 1 (84% power load) and using the HFO. Concentrations are given at normalized conditions (273.14 K, 1013.25 hPa).

Exhaust component	EF g/kWh	EF g/kg fuel	Er kg/hr	C g/Nm ³
NO _x	14.22	73.4	241.7	2.20
CO ₂	667	3 441	11 339	103.1
CO	0.42	2.17	7.1	0.065
HC	0.07	0.36	1.2	0.011
O ₂	1270	6 553	21 590	196.3
SO ₂	7.62	39.32	129.5	1.18
SO ₃	0.11	0.57	1.9	0.017
Benzene	0.012	0.06	0.21	0.002
PM	0.29	1.49	4.86	0.044
PM*	1.03	5.31	17.43	0.158
OC*	0.30	1.58	5.15	0.047
EC [†]	0.02	0.13	0.42	0.004
Ash [†]	0.19	0.98	3.19	0.029
Sulphate*	0.15	0.76	2.47	0.022

*after cooling in the dilution system, †average hot exhaust and diluted exhaust

The mass particle size distribution measured in the hot exhaust is presented in Figure 1. It is a fit for the PM mass data from the stage-impactor measurement. The hot-exhaust mass distribution shows clearly two main modes: one in the accumulation mode at diameter DP around 0.5 µm and one in the coarse mode at DP around 7 µm. The coarse particles around 7 µm constitute a major mode of the ship-exhaust particulates' mass size distribution. Exhaust particulate residuals from medium-speed diesel engines operated with HFO investigated by Lyyrinen et al. (1999) also demonstrated the bimodal mass size distribution with the main mode at 0.1 µm and a second mode at about 10 µm. The presence of coarse particles along with fine aerosols is probably associated with HFO combustion and may be explained by the various nature and composition of the ship-exhaust par-

ticulates. The findings of TEM observations can confirm this assumption. This size distribution is strongly different from typical automobile diesel soot where the mean diameter around $1\ \mu\text{m}$ is emphasized (Kerminen et al., 1997). The difference is due to very different chemical composition and physical properties of the marine HFO and car diesel fuel and different conditions of combustion.

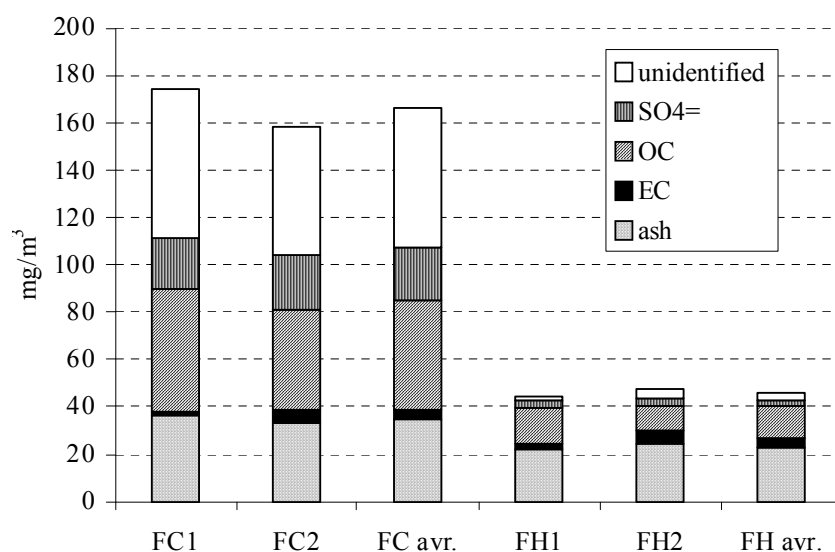


Figure 1. Particle mass size distribution measured on stage impactor in the hot exhaust gas.

The composition of PM with respect to the content of EC, OC (is OC + carbonate), sulphate and fly ash is presented in Figure 2. Organic matter (OM) was calculated from organic carbon via the relationship $\text{OM} = 1.2 \times \text{OC}$ (Petzold et al., 2008). Figure 2 shows clearly that OM and sulphate increase after the cooling of the exhaust gas while content of EC and ash remains unchanged, which is consistent with the expected condensation of H_2SO_4 and hydrocarbons due to the cooling of the exhaust gas. The unidentified PM in Figure 2 represents a fraction obtained by subtracting the sum of OC, EC, fly ash (from the EGA analysis) and sulphate (from the ion chromatography) from the total PM concentration on the filter obtained by gravimetry. Part of this mass may be water associated with sulphate.

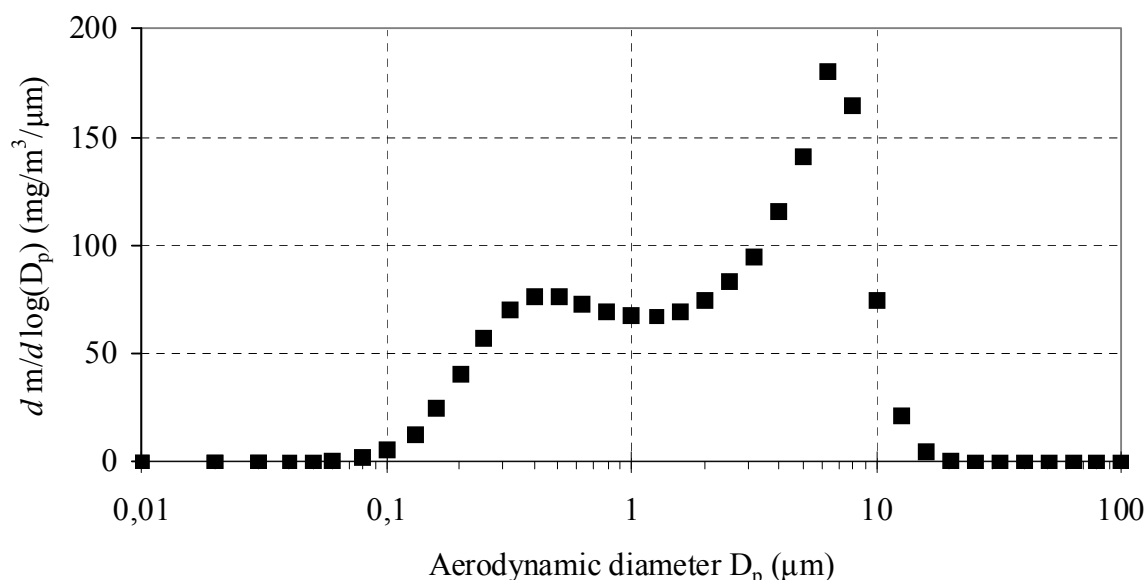


Figure 2. Composition of PM (as mg/m^3 exhaust gas) collected on filters in the diluted (FC) and hot (FH) exhaust gas. FC1, FC2, FCavr. and FH1, FH2, FHavr. are individual filter samples and their average values collected in the diluted and hot exhaust, respectively.

The emission factors derived for EC and ash in Table 2 are calculated as an average from filter samples taken both in the hot and in the cooled exhaust while emission factors for OC and sulphate were derived only from filter samples taken in the cooled exhaust with much higher content of these species. For EC, ash and OC our results are consistent with values derived from data published by

Petzold *et al.* (2008) (0.174, 1.18 and 0.28 g/kg of OC, EC and sulphate, respectively) and Agrawal *et al.* (2008) (0.08, 1.22 and 0.58). The L2MS analysis have shown that the high OC-content of the PM collected in the cooled exhaust is accompanied also by much more rich composition of PAH species comparing to few PAH species observed in PM collected in the hot exhaust. The emission factor for sulphate derived from the FC samples was substantially lower than factors derived from Agrawal *et al.* (2008) and Petzold *et al.* (2008). The difference was due to a lower conversion ratio of S^{IV} to S^{VI} in the exhaust (Moldanová *et al.*, 2009). Emission factor 5.3 g/(kg fuel) for the total PM (EF_{PM}) obtained from our measurements was lower than EF_{PM} 6-7 g/(kg fuel) obtained in Petzold *et al.* (2008).

3.2 Microphysical properties of individual particles

In general, microstructure and elemental analysis of ship combustion residuals sampled in the hot and diluted exhaust indicate three distinct morphological structures with quite different chemical composition: Soot aggregates, significantly metal polluted; Char particles, clean and containing minerals; Mineral and/or ash particles. The soot aggregates dominate in the sub-micrometer fraction. Vanadium, nickel and sulphur are gathered within the soot matrix forming composite submicron particles. Spherically shaped char particles are abundant in the micrometer size fraction. They can be found as almost clean spherical carbonaceous particles or mixed with alkali-earth compounds, e.g. V, Ni, Ca, included in partly burnt carbonaceous matrix. Spherically or irregularly shaped mineral and/or ash particles have typically size 200 nm to 10 μ m. They are characterized by a dominant content of Ca, V and Ni and by having mineral dust structure of elongated prismatic crystals related to mineral compounds. Their formation may be explained by coalescence of molten grains of minerals during combustion. Additionally, organic carbon particles with a size of about 100 nm, of unburned fuel or/and lubricating oil origin, were observed.

Sulphur was detected by EDS analysis in almost all individual particles. Soot particles contain on average the smallest amount of sulphur, typically less than 1% and also have lower content of O, V and other inorganic elements. The highest S content is associated with large amount of V and other inorganic elements from the parent fuel oil in char particles. These composition differences are consistent with formation mechanisms of particles; since the char particles do not undergo evaporation – condensation process, inorganic elements from parent oil fuel are more readily preserved there.

The ship-emitted PM with surfaces covered with transition metals and organics has a potential to cause reverse health effects. Armstrong *et al.* (2004) have shown potential impact of PAHs on human health. Study by Mudway *et al.* (2004) have shown that the residual oil using diesel exhaust particles cause higher oxidative stress on epithelial lining fluid in lungs than particles not having their surface covered with oxidants. The oxidative stress increases the relative health risk of the PM.

REFERENCES

- Agrawal, H., Malloy, Q. G. J., Welch, W. A., Miller, J. W., Cocker, D. R., 2008. In-use gaseous and particulate matter emissions from a modern ocean going container vessel. *Atmospheric Environment* 42, 5504–5510.
- Armstrong, B., Hutchinson, E., Unwin, J., Fletcher, T., 2004. Lung Cancer Risk after Exposure to Polycyclic Aromatic Hydrocarbons. *Environmental Health Perspectives* 112, 970-978.
- Birch, M. E., Cary, R. A., 1996. Elemental carbon-based method for monitoring occupational exposures to particulate diesel exhaust. *Aerosol Science and Technology* 25, 221-241.
- Bouvier, Y., Mihean, C., Ziskind, M., Therssen, E., Focsa, C., Pauwels, J.F., Desgroux, P., 2007. Molecular species adsorbed on soot particles issued from low sooting methane and acetylene laminar flames: A laser-based experiment. *Proceedings of the Combustion Institute* 31 (2007) 841-849.
- Chen, Y. Z., Shah, N., Huggins, F. E., Huffman, G. P., 2004. Investigation of the microcharacteristics of PM_{2.5} in residual oil fly ash by analytical transmission electron microscopy. *Environmental Science and Technology* 38, 6553-6560.
- Chen, Y. Z., Shah, N., Raun, A., Huggins, F. E., Huffman, G. P., 2005. Electron microscopy investigation of carbonaceous particulate matter generated by combustion of fossil fuels. *Energy Fuels* 19, 1644–1651.
- Cooper, D. A., 2003. Exhaust emissions from ships at berth. *Atmospheric Environment* 37, 3817–3830.
- Corbett, J. J., Winebrake, J. J., Green, E. H., Kasibhatla, P., Eyring, V., Lauer A., 2007. Mortality from Ship Emissions: A Global Assessment. *Environmental Science and Technology* 41, 8512–8518.

- Demirdjian B., Ferry D., Suzanne J., Popovicheva O. B., Persiantseva N. M. and Shonija N. K., 2007. Heterogeneities in the microstructure and composition of aircraft engine combustor soot: impact on the water uptake. *Journal of Atmospheric Chemistry* 56, 83-103, doi: 10.1007/s10874-006-9043-9.
- Endresen, Ø., Sørgård, E., Sundet, J. K., Dalsøren, S. B., Isaksen, I. S. A., Berglen, T. F., Gravir, G., 2003. Emission from international sea transportation and environmental impact. *Journal of Geophysical Research* 108, 4560, doi:10.1029/2002JD002898.
- Eyring, V., Köhler, H. W., van Aardenne, J., Lauer, A., 2005. Emissions from International Shipping: 1. The last 50 Years. *Journal of Geophysical Research* 110, D17305, doi:10.1029/2004JD005619.
- Eyring, V., Stevenson, D. S., Lauer, A., Dentener, F. J., Butler, T., Collins, W. J., Ellingsen, K., Gauss, M., Hauglustaine, D. A., Isaksen, I. S. A., Lawrence, M. G., Richter, A., Rodriguez, J. M., Sanderson, M., Strahan, S. E., Sudo, K., Szopa, S., van Noije, T. P. C., Wild, O., 2007. Multi-model simulations of the impact of international shipping on atmospheric chemistry and climate in 2000 and 2030. *Atmospheric Chemistry and Physics* 7, 757-780.
- Fridell, E., Steen, E. and Peterson, K., 2008. Primary particles in ship emissions, *Atmospheric Environment*, **42**, 1160.
- Hobbs, P. V., Garrett, T. J., Ferek, R. J., Strader, S. R., Hegg, D. A., Frick, G. M., Hoppel, W. A., Gasparovic, R. F., Russell, L. M., Johnson, D. W., O'Dowd, C., Durkee, P. A., Nielsen, K. E., and Innis, G., 2000. Emissions from ships with respect to their effects on cloud. *Journal of Atmospheric Science* 57, 2570-2590.
- International Organisation of Standardisation, 1996. ISO 11042F – Gas turbines – Exhaust gas emission – Parts 1 and 2.
- Johnson, R.I., Jitendra, J.S., Cary, R. A., Huntzicker, J. J., 1981. An automated thermal-optical method for analysis of carbonaceous aerosol. In: Macias ES, Hopke PK, Eds., ACS Symposium Series No. 167, *Atmospheric Aerosol: Source/Air Quality Relationships*. American Chemical Society, Washington, D.C.
- Kasper, A., Aufdenblatten, S., Forss, A., Mohr, M. and Burtscher, H., 2007. Particulate Emissions from a Low-Speed Marine Diesel Engine. *Aerosol Science and Technology* 41, 24 – 32.
- Kerminen, V. M., Mäkelä, T. E., Ojanen, C. H., Hillamo, R. E., Vilhunen, J. K., Rantanen, L., Havers, N., von Bohlen, A., and Klockow, D., 1997. Characterization of the particulate phase in the exhaust from a diesel car. *Environmental Science and Technology*, 31, 1883-1889.
- Lauer, A., Eyring, V., Hendricks, J., Jöckel, P., Lohmann, U., 2007. Effects of ocean-going shipping on aerosols and clouds. *Atmospheric Chemistry and Physics* 7, 5061-5079.
- Lyyrinen, J., Jokiniemi, J., Kauppinen, E. I., and Joutsensaari, J., 1999. Aerosol characterisation in medium-speed diesel engines operating with heavy fuel oils. *Journal of Aerosol Science*, 30, 771-784.
- Mihesan, C., Ziskind, M., Therssen, E., Desgroux, P., Focsa, C., 2008. Parametric study of polycyclic aromatic hydrocarbon laser desorption. *Journal of Physics: Condensed Matter* 20, 025221.
- Mudway, I.S., Stenfors, N., Duggan, S. T., Roxborough, H., Zielinski, H., Marklund, S. L., Blomberg, A., Frew, A. J., Sandstrom, T., Kelly, F. J., 2004. An in vitro and in vivo investigation of the effects of diesel exhaust on human airway lining fluid antioxidants. *Archives of Biochemistry and Biophysics* 423, p. 12.
- Petzold, A., Feldpausch, P., Fritzsche, L., Minikin, A., Lauer, P., Kurok, C., and Bauer, H., 2004. Particle emissions from ship engines. *Journal of Aerosol Science*, Abstracts of the European Aerosol Conference, S1095-S1096.
- Petzold, A., Hasselbach, J., Lauer, P., Baumann, R., Franke, K., Gurk, C., Schlager, H., and Weingartner, E., 2008. Experimental studies on particle emissions from cruising ship, their characteristic properties, transformation and atmospheric lifetime in the marine boundary layer. *Atmospheric Chemistry and Physics* 8, 2387-2403.
- Sinha, P., Hobbs, P. V., Yokelson, R. J., Christian, T. J., Kirchstetter, T. W., Brientjes, R., 2003. Emissions of trace gases and particles from two ships in the southern Atlantic Ocean. *Atmospheric Environment* 37, 2139-2148.

Trends in man-made and natural cirrus clouds for the period 1984-2004

Kostas Eleftheratos^{*}, Christos S. Zerefos

Laboratory of Climatology & Atmospheric Environment, University of Athens, Greece

Patrick Minnis

NASA Langley Research Center, Hampton VA, USA

Keywords: Cirrus clouds, trends

ABSTRACT: This study compares trends in man-made and natural cirrus clouds with aviation flown distance and with trends in natural parameters over the tropical and middle latitudes i.e., over regions dominated by dynamics in comparison with regions where microphysics explains most of the variance in cirrus cloud cover. Results presented in this study generally confirm earlier findings on possible effects of aviation on cirrus cloud positive trends over congested air traffic regions. More specifically, the longitudinal distribution of cirrus cloud trends from 1984 to 2004 is positively correlated (+0.6) with the spatial distribution of aviation flown distance over the northern middle latitudes and not over the tropics. In the tropics it is shown that cirrus cloud trends are correlated with trends in vertical velocities and with trends in relative humidity.

1 INTRODUCTION

Aircraft flying at high altitudes may form contrails. Contrails are line shaped clouds forming behind an aircraft if the ambient air is cold enough (Schumann, 1996). In dry air the contrails dissipate quickly, and their impact is of minor importance, but in moist air which is super-saturated with respect to ice, the contrails spread and grow with the uptake of ambient water vapour, and become contrail-cirrus (Schumann, 2005). Contrail-cirrus would not exist without the prior formation of contrails (i.e., Gierens, 2006). Figure 1 shows some examples of linear persistent contrails and contrail-cirrus in the atmosphere based on observations from ground. This kind of cirrus formation occurs in regions with high air traffic (i.e., North America, North Atlantic, Europe).

Recent studies (i.e., Minnis et al., 2001; Zerefos et al., 2003; Minnis et al., 2004; Stubenrauch and Schumann, 2005; Stordal et al., 2005; Mannstein and Schumann, 2005; Krebs, 2006) have examined the possible influence of air traffic emissions on cirrus cloud positive trends using various methods and different datasets for different periods of records. Major findings of those studies were summarized in Gierens (2006). For example, in central Europe it was found that the observed positive trends in cirrus due to aircraft are about 1-2% cover per decade. Mannstein and Schumann (2005) had estimated ~3% additional cloud coverage due to aircraft over Europe, which is about ten times higher than the coverage by linear contrails (~0.3%) alone. However, their conclusion that the coverage by additional cirrus clouds in Europe is about 10 times higher than by linear contrails is no longer supported (Mannstein and Schumann, 2007).

As air traffic increases (~5% per year), manmade (aviation) cirrus clouds are expected to increase. These additional clouds contribute to the greenhouse effect (i.e., Minnis et al., 2004; Sausen et al., 2005). However, present knowledge of the coverage and radiative forcing of manmade cirrus clouds is still poor. This kind of cirrus cloud might be responsible for up to a doubling of the present estimate of aviation radiative forcing. If this is true, then the contribution of aviation to the total anthropogenic radiative forcing (which is ~3.5% for 1992 aircraft operations) might be doubled.

^{*} *Corresponding author:* Kostas Eleftheratos, Laboratory of Climatology & Atmospheric Environment, Faculty of Geology & Geoenvironment, University of Athens, 15784 Athens, Greece. Email: kelef@geol.uoa.gr



Figure 1. Examples of linear persistent contrails and contrail-cirrus in the atmosphere.

This study compares changes in contrail-cirrus and natural cirrus clouds with aviation travelled distance and with changes in natural parameters. Correlations are sought over the tropical and middle latitudes i.e., over regions dominated by dynamics in comparison with regions where microphysics explains most of the variance in cirrus cloud cover. The main purpose is to relate and to attribute long-term changes in cirrus cloud cover to natural and anthropogenic (aviation-related) sources. The natural parameters used in this study are vertical velocities and relative humidity at 300 hPa. The level of 300 hPa was considered in this study as a standard level for highflying air traffic in the northern middle latitudes.

2 DATA SOURCES

The cloud data set analysed in this study was produced by the International Satellite Cloud Climatology Project (Rossow and Schiffer, 1999). The data are based on observations from a suite of operational geostationary and polar orbiting satellites. Visible radiances are used to retrieve the optical thickness of clouds and infrared radiances to retrieve cloud top temperature and pressure. The D2 dataset used in this study has a spatial resolution of 280 km (2.5° at the equator) and provides monthly averages of cloud properties of fifteen different cloud types. The cloud types are derived based on radiometric definitions that rely on cloud optical thickness and cloud top pressure. Cirrus clouds are defined as those with optical thickness less than 3.6 and cloud top pressure less than 440 hPa. In this study we made use of the cirrus cloud data for the period 1984-2004.

The ISCCP cloud properties have been tested extensively both against other satellite cloud retrievals and against surface cloud observations (Rossow and Schiffer, 1999). In the latest (D-series) version of the ISCCP dataset, changes in the retrieval thresholds and the inclusion of an ice microphysics model for retrieval of optical thicknesses and top temperatures of cold clouds, have improved the agreement of cirrus cloud amounts with both surface observations (Rossow and Schiffer,

1999) and High-Resolution Infrared Sounder (HIRS) data (Stubenrauch et al., 1999). An underestimation of ISCCP cirrus clouds amounts ($\sim 5\%$ at northern middle latitudes) compared to HIRS results is caused by missed detection of very thin clouds (Stubenrauch et al., 1999; Rossow and Schiffer, 1999). Moreover, high cloud amounts from this data set have been compared with those from SAGE II (Liao et al., 1995). It has been shown that the frequency of high-level clouds from SAGE II is about 3 times higher than the cloud amount from ISCCP with little seasonal variation. Despite this large systematic difference it was noted that the correlation between the zonal mean curves is high, 0.88 (99.99% confidence level) for July and 0.82 (99.99% confidence level) for January, which strengthens our results.

Vertical velocities and relative humidity at 300 hPa were analysed using the NCEP Reanalysis datasets for the period 1984-2004. NCEP provides mean monthly gridded values of various atmospheric and surface parameters on $2.5^\circ \times 2.5^\circ$ grid boxes and on global scale. We made use of the monthly daily means which are monthly means from base times 0000, 0600, 1200 and 1800 UTC (<http://www.cdc.noaa.gov/data/gridded/data.ncep.reanalysis.html>).

To overcome the effect of seasonal variations in the estimated trends, all trends were calculated after removing variations related to the seasonal cycle of the data. Cirrus cloud data were deseasonalized by subtracting the long-term monthly mean (1984-2004) pertaining to the same calendar month. All trends were evaluated as to their statistical significance by applying the t-test of each trend against the null hypothesis of no-trend for the appropriate number of degrees of freedom. CCC data for the years 1991 and 1992 were not used in our analysis in order to minimize artificial satellite cloud retrievals after the eruption of Mt. Pinatubo in 1991 (Rossow and Schiffer 1999; Luo et al., 2002).

3 RESULTS AND DISCUSSION

Figure 2 shows the spatial distribution of aviation travelled distance at 9760–11590 m height in the wintertime (January, February and March) (in km). Regions with heavy air traffic (more than 40,000 travelled km) are shown by dark grey and black colours while regions with lower air traffic (less than 40,000 km) are shown by light grey colours. In the northern middle latitudes (35° – 55° N), congested air traffic regions are found over the US, Europe, and Japan, and over the North Atlantic and North Pacific Oceans. In the tropics (5° – 25° N), regions with high air traffic are mainly observed over the Southeast Asia air traffic corridors and over the Caribbean Sea.

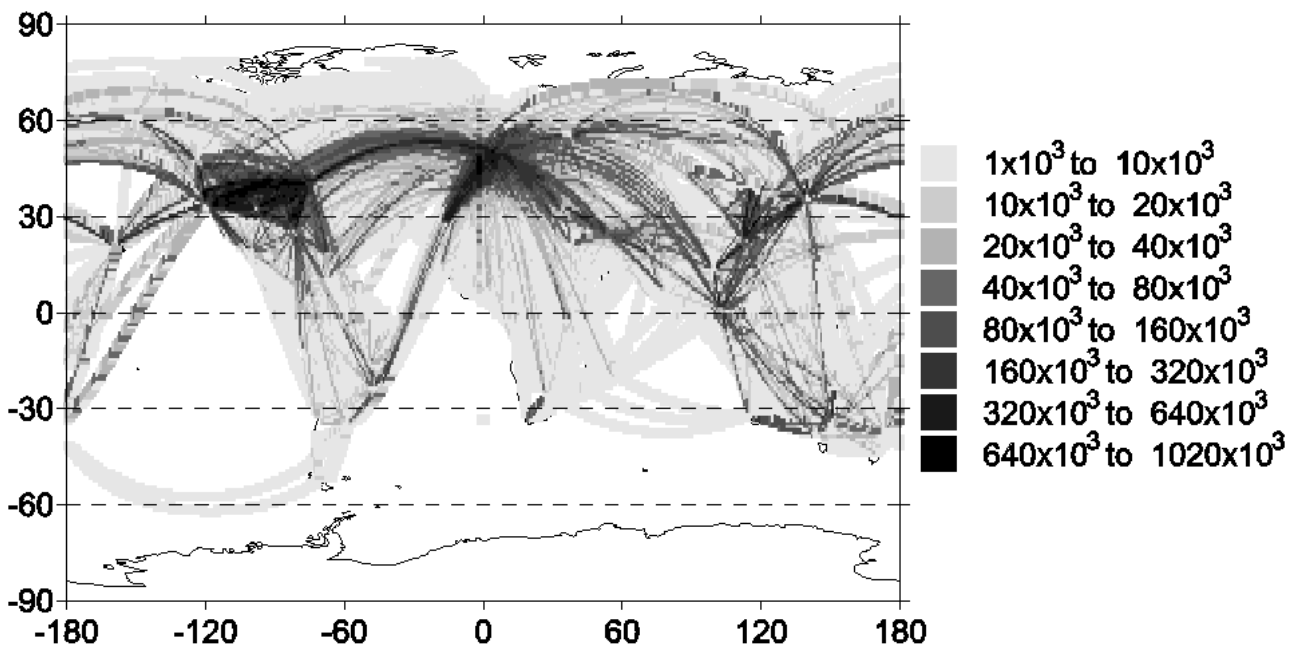


Figure 2. Travelled distance by aviation at 9760–11590 m height in 2000 in the wintertime (January, February and March) (in km/month).

In order to investigate whether cirrus cloud trends are correlated with air traffic, aiming at quantifying changes in cirrus cloudiness due to contrail formation by aviation, we have spatially correlated the cirrus cloud trends with travelled distance by aviation over areas that correspond to different air traffic load: (a) over the high air traffic northern middle latitudes (35° - 55° N) and (b) over low air traffic tropical regions between (5° - 25° N). Cirrus cloud trends could also be related to dynamical and thermo-dynamical variability. As a tracer of dynamics (convective activity) in the upper troposphere we made use of the monthly vertical velocities at 300 hPa (VV300). As a tracer of thermo-dynamical variability over the studied areas we analysed trends in relative humidity at 300 hPa (RH300). Figure 3 (upper panel) shows the longitudinal distributions of cirrus cloud trends from 1984 to 2004 and of aviation travelled distance in 2000 for the cold period (January, February and March).

As can be seen from Fig. 3a the longitudinal distribution of CCC trends over the northern middle latitudes is well correlated with travelled distance by highflying air traffic (correlation coefficient, $R = +0.6$), which agrees with the results presented by Zerefos et al. (2003). The positive correlation between the two variables suggests that the apparent increase of thin cirrus coverage, about 1.4% over North America and 0.5% over Europe, could be possibly related to contrail formation by aviation. Over East Asia on the other hand, there are negative trends in CCC which are related to negative trends seen in relative humidity (Zerefos et al., 2007). Negative trends over East Asia were also found by Minnis et al. (2004) who analysed cirrus/high clouds from ground-based data. For the summertime we note that the largest increases in CCC are found over the North Atlantic flight corridor ($\sim 2.1\%$ per decade) (not shown here).

At lower latitudes (5° - 25° N), where air traffic density is lower, the correlation between cirrus trends and aviation is insignificant (Fig. 3b). However the longitudinal variability of CCC is as high as that over the middle latitudes. This is not a paradox and can be explained by the fact that in tropical latitudes, cirrus clouds are formed primarily from vertical water vapour transport by convective processes (Zerefos et al., 2003). As a result, tropical cirrus amounts are controlled by local temperature conditions and moisture sources and any trend in those conditions would leave a signature on the cirrus cloud field. Therefore, the tropical cirrus trends could reflect trends in the local temperature and moisture field. In the middle latitudes, on the other hand, cirrus cloud formation is largely controlled by baroclinic processes that are to a great extent independent of local conditions and depend on global wave patterns. Therefore, any localized modulation of middle latitude cirrus cloud properties would be related more strongly to microphysical rather than dynamical condition changes (Zerefos et al., 2003). The results are shown in Figs. 3c, 3d, and in Figs. 3e, 3f where it appears that the observed trends in cirrus clouds are significantly correlated with corresponding trends in VV300 and RH300 over the tropics (-0.4 and $+0.8$, respectively) but not over the middle latitudes.

Our findings on the positive trends in cirrus clouds over the US, North Atlantic and Europe due to air traffic are consistent with those published by Zerefos et al. (2003), Minnis et al. (2004), Stordal et al. (2005), Stubenrauch and Schumann (2005) and Eleftheratos et al. (2007) even though there are considerable differences among the examined datasets and periods of records.

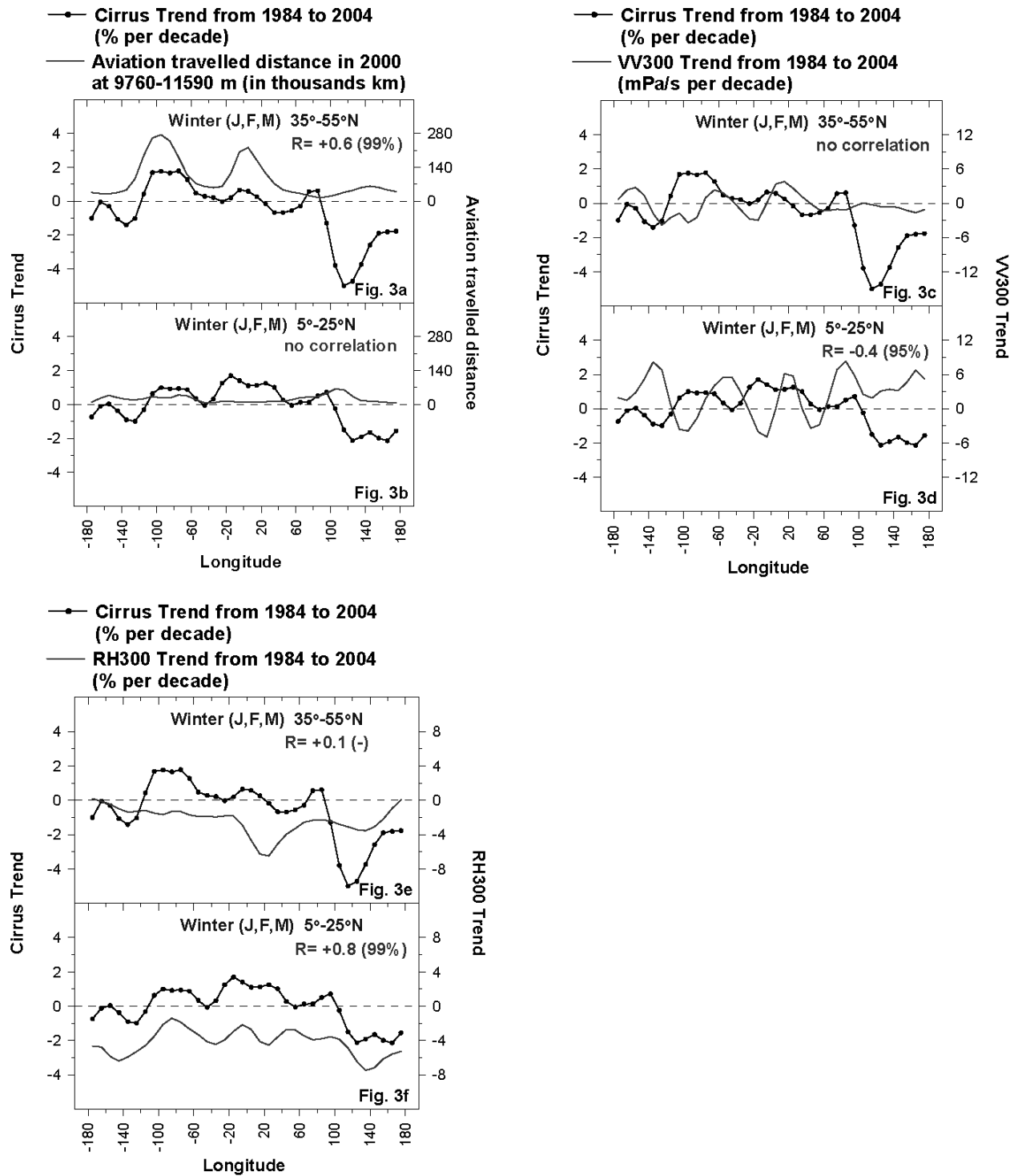


Figure 3. (Upper left panel) Longitudinal distribution of cirrus trends from 1984 to 2004 in the wintertime (Jan, Feb, Mar) versus the spatial distribution of aviation travelled distance in 2000 over: (a) heavy air traffic regions (35°-55°N), and (b) over low air traffic regions (5°-25°N). (Upper right panel) Same as in upper left panel but for cirrus trends and VV300 trends, respectively. (Lower left panel) Same as in upper left panel but for cirrus trends and RH300 trends, respectively.

4 CONCLUSIONS

Long-term changes in cirrus cloud cover from ISCCP satellite data have been correlated with aviation flown distance and compared with changes in natural parameters (vertical velocities and relative humidity at 300 hPa) over the middle and tropical latitudes. Results presented in this study generally confirmed earlier findings on possible effects of aviation on cirrus cloud positive trends over congested air traffic regions. More specifically, the longitudinal distribution of cirrus cloud

trends from 1984 to 2004 was found to be positively correlated (+0.6) with the spatial distribution of aviation flown distance over the northern middle latitudes and not over the tropics. In the tropics over the regions studied, trends in cirrus cloud cover were found to be significantly correlated with trends in the vertical winds (−0.4) and with trends in relative humidity (+0.8).

5 ACKNOWLEDGMENTS

This study was conducted within the FP6 Integrated Project QUANTIFY (003893-GOCE) funded by EC. *NCEP Reanalysis data were provided by the NOAA/OAR/ESRL PSD, Boulder, Colorado, USA, from their web site at <http://www.cdc.noaa.gov/>.*

REFERENCES

- Eleftheratos, K., C.S. Zerefos, P. Zanis, D.S. Balis, G. Tselioudis, K. Gierens, and R. Sausen, 2007: A study on natural and manmade global interannual fluctuations of cirrus cloud cover for the period 1984–2004. *Atmos. Chem. Phys.* 7, 2631–2642.
- Gierens, K., 2007: Contrails, contrail cirrus, and ship tracks. *Proceedings of the TAC-Conference*, June 26 to 29, 2006, Oxford, UK, 214–220.
- Krebs, K., 2006: Analyse des Einflusses des Flugverkehrs auf die natürliche Zirkusbewölkung über Europa, Nordafrika und dem Nordatlantik. *Dissertation*, Ludwig-Maximilians Universität München, 211pp (in German).
- Luo, Z., W.B. Rossow, T. Inoue, and C.J. Stubenrauch, 2002: Did the Eruption of the Mt. Pinatubo Volcano Affect Cirrus Properties?. *J. Climate* 17, 2806–2820.
- Mannstein, H., and U. Schumann, 2005: Aircraft induced contrail cirrus over Europe. *Meteorol. Z.* 14, 549–554.
- Mannstein, H., and Schumann, U., 2007: Corrigendum to “Aircraft induced contrail cirrus over Europe”. *Meteorol. Z.* 16, 131–132.
- Minnis, P., J.K. Ayers, R. Palikonda, D.R. Doelling, U. Schumann, and K. Gierens, 2001: Changes in cirrus cloudiness and their relationship to contrails. *Proceedings American Meteorology Society*, Boston, USA, No. 11.9, 239–242.
- Minnis, P., J.K. Ayers, R. Palikonda, and D. Phan, 2004: Contrails, Cirrus Trends, and Climate. *J. Climate* 17, 1671–1685.
- Rossow, W.B., and R.A. Schiffer, 1999: Advances in understanding clouds from ISCCP. *Bull. Amer. Meteor. Soc.* 80, 2261–2287.
- Sausen, R., I. Isaksen, V. Grewe, D. Hauglustaine, D.S. Lee, G. Myhre, M.O. Köhler, G. Pitari, U. Schumann, F. Stordal, and C. Zerefos, 2005: Aviation radiative forcing in 2000: An update on IPCC (1999). *Meteorol. Z.* 14, 555–561.
- Schumann, U., 1996: On conditions for contrail formation from aircraft exhausts. *Meteorol. Z.* 5, 4–23.
- Schumann, U., 2005: Formation, properties and climatic effects of contrails. *Comptes Rendus Physique* 6, 549–565.
- Stordal, F., G. Myhre, E.J.G. Stordal, W.B. Rossow, D.S. Lee, D.W. Arlander, and T. Svendby, 2005: Is there a trend in cirrus clouds cover due to aircraft traffic?. *Atmos. Chem. Phys.* 5, 2155–2162.
- Stubenrauch, C.J., W.B. Rossow, F. Cheruy, A. Chedin, and N.A. Scott, 1999: Clouds as seen by satellite sounders (3I) and imagers (ISCCP), Part I, Evaluation of cloud parameters. *J. Climate* 12, 2189–2213.
- Stubenrauch, C.J., and U. Schumann, 2005: Impact of air traffic on cirrus coverage. *Geophys. Res. Lett.* 32, L14813, doi: 10.1029/2005GL022707.
- Zerefos, C.S., K. Eleftheratos, D.S. Balis, P. Zanis, G. Tselioudis, and C. Meleti, 2003: Evidence of impact of aviation on cirrus cloud formation. *Atmos. Chem. Phys.* 3, 1633–1644.
- Zerefos, C.S., K. Eleftheratos, P. Zanis, D.S. Balis, and G. Tselioudis, 2007: Search for Man-Made Cirrus Contrails over Southeast Asia. *Terr. Atmos. Ocean. Sci.* 18(3), 459–474.

Ice nucleation on soot in contrails and cirrus: laboratory view

O.B. Popovicheva^{*},

Institute of Nuclear Physics, Moscow State University, Moscow, Russia

P. J. DeMott, K. A. Koehler, S. M. Kreidenweis, M. D. Petters, C. M. Carrico

Department of Atmospheric Science, Colorado State University, Fort Collins, CO, USA

N. Shonija, E. Kireeva

Chemical Department, Moscow State University, Moscow, Russia

Keywords: aircraft particulates, soot, ice nucleation, contrail, cirrus

ABSTRACT: Laboratory studies of water uptake and ice nucleation (for temperatures $\leq -40^{\circ}\text{C}$) are presented for combustion particles of a wide range of physico-chemical properties, from hydrophobic through a range of hydrophilicity, to hygroscopic ones. Different mechanisms of water interactions with aircraft-generated soot aerosols of various compositions are considered for contrail and cirrus formation conditions. The findings generally confirm that heterogeneous ice nucleation is a function of surface oxidation of hydrophilic soot, hydrophobic soot initiates the ice phase from water vapor only at water supersaturated conditions while hygroscopic soot behaves in a manner reflecting homogeneous freezing with particles containing soluble matter.

1 INTRODUCTION

The climate impacts of aircraft particulate emission is highly uncertain because of the poor knowledge of soot aerosols ability to influence cloud formation and thus soot lifetime with respect to nucleation scavenging and precipitation removal, as well as to affect cloud optical properties and radiative balance. Contrail observations supported by theoretical estimates based on simple models of plume evolution suggest that contrails only form at high relative humidities, when liquid saturation with respect to water is reached in the plume (Karcher et al., 1998). The specific ice nucleation activity of aircraft-generated soot particles and their impact on threshold contrail formation conditions is still an important open question. An estimate of the maximum number concentration contribution of aircraft-generated soot particles results in an increase of the potential ice nuclei (IN) number concentration of up to 50 % at the main aircraft flight altitude (Hendricks et al., 2005). A potentially strong soot indirect effect has also been inferred when including such additional numbers of heterogeneous freezing ice nuclei along with the predominant sulfate homogeneous freezing process in microphysical models of cirrus clouds (DeMott et al., 1997). However, the state of scientific understanding of microphysical and chemical processes at the surface of soot aerosols that cause ice nucleation is still poor. Contrail formation models assume ice nucleation on initially hydrophobic soot particles which require the activation by plume processing while hygroscopic properties are considered for BC aerosols in the global simulations (Hendricks et al., 2005). Long-term research progress requires the development of new concepts and laboratory approaches with respect to aviation-emitted aerosol impacts on ice cloud formation.

Advanced QUANTIFY (Popovicheva et al., 2008a) and previous PartEmis (Petzold et al., 2005) studies have proven the highly heterogeneous nature of aircraft-generated soot aerosols with respect to both physical (size, morphology, porosity) and chemical (composition, impurities) properties, in dependence on engine design, operation conditions, and fuel content. Data of different characterization campaigns shows the dominant mass of BC over organic and sulfates especially at high engine power (Herndon et al., 2007), H_2SO_4 coverage of a few monolayer at high fuel sulfur content, non-volatile OC at low combustion temperature (Petzold et al., 2005), and the high water soluble fraction (WSF) and many surface functionalities responsible for water interactions (Popovicheva et al.,

^{*} *Corresponding author:* Olga Popovicheva, Institute of Nuclear Physics, Moscow State University, 119991, 119991, Moscow, Russia. Email: polga@mics.msu.su

2004). Moreover, examination of characteristics of soot collected at background testing facilities for typical engines showed a main fraction of soot with low O, S content, probably relating to hydrophobic particles, and a fraction containing impurities with high O, S, Fe content which may be assigned to hydrophilic or even hygroscopic particles (Popovicheva et al., 2004). Therefore we may conclude that aircraft engine generates soot aerosols with properties which may vary from hydrophobic, through hydrophilic to hygroscopic, in dependence on surface chemistry and amount of hydrophilic impurities.

This work reports the laboratory measurements of water uptake and ice nucleation on various characterized soots with a wide range of physico-chemical properties. Different ice nucleation behaviors depending on temperature and soot particle hydrophilicity reflect a variety of particle interactions with water at low temperatures. These studies contribute toward clarifying the relationship between the extent of soot hydrophilicity and IN activated fraction at atmospheric conditions. Fractions of hydrophobic, hydrophilic and hygroscopic soot particles predicted to activate within a plume at contrail formation conditions are reported with the purpose of relating these to general observations of the contrail formation conditions. Also, the apparent range of soot hydrophilicity that is most favorable for heterogeneous ice nucleation at the cirrus formation conditions is proposed.

2 WATER UPTAKE QUANTIFICATION

Quantification of atmospheric impacts stemming from water interactions with soot particles of various origin, including emitted from aircraft engines, requires identification of hydrophobic and hydrophilic soots. Therefore, water uptake measurements are performed in laboratory on well-characterized soots available for atmospheric studies (Popovicheva et al., 2008a). Differing characteristics were achieved through generation by three different combustion sources; three soots from natural gas pyrolysis and soot from a turbulent diffusion flame in an aircraft engine combustor. Comparative analysis of water adsorption isotherms on soots of various compositions allows suggesting a concept of quantification (Popovicheva et al., 2008b). Systematic analysis demonstrates two mechanisms of water/soot interaction, namely, the bulk dissolution into soot water soluble coverage (absorption mechanism) and the water molecule adsorption on surface active sites (adsorption mechanism). Water uptake on hygroscopic soot takes place by the absorption mechanism: it significantly exceeds the formation of many surface layers. If soot particles are made mostly from elemental carbon and/or have a water insoluble organic coverage, they are classified as non-hygroscopic. Low water adsorption on some active sites following cluster formation is a typical mechanism of water interaction with hydrophobic soot. If the water film extending over the surface is formed due to cluster confluence it is suggested that soot is hydrophilic.

Thermal soot (TS) particles produced from natural gas combustion are classified as hydrophobic with a surface of low polarity. Graphitized Thermal soot (GTS) particles are proposed for comparison as extremely hydrophobic and of very low surface polarity. In contrast, oxidation of TS soot leads to an increase in the density of active water adsorption sites and the extent of surface polarity, thus to production of hydrophilic Thermal Oxidized soot (TOS). Aircraft engine soot (AEC), produced from burning TC1 kerosene in a gas turbine engine combustor, exhibit hygroscopic properties. Due to the presence of water soluble organic and inorganic material (near 3.5% sulfates) many AEC particles can be covered by water layers even below water saturation conditions.

3 ICE NUCLEATION ON SOOT

The present study seeks direct evidence for IN activity at environmentally-relevant water supersaturations and for ice nucleation behaviours at contrail and cirrus formation conditions, using this set of soots of varying and well-characterized physical and chemical characteristics. Laboratory measurements of ice nucleation were performed at conditions that simulate those in the atmosphere; a continuous flow diffusion chamber (CFDC) was used to scan the relative humidity conditions needed for IN activation at temperatures typical for the upper troposphere (down to -600C) (Koehler et al., 2009). Soot was dispersed using a fluidized bed generator and then size-selected by the DMA prior to being introduced to the CFDC.

Hydrophobic TS soot particles, having some active sites for water adsorption, may activate ice nucleation at $-40\text{ }^{\circ}\text{C}$ only in the water supersaturated regime (see for details Koehler et al., 2009). A strong increase in the nucleated fraction, up to 10% of the particles frozen, occurred only above $\sim 102\% RH_w$. At $-57\text{ }^{\circ}\text{C}$, ice nucleation occurs on a small fraction (<1 in 1000) of TS soot starting at $RH_w < RH_{Koop}$. Heterogeneous freezing appears as the most likely explanation for small ice nucleated fraction at RH_w well below water saturation. Larger proportions of the 200 nm than the 100 nm particles are typically activated for the same T and RH_w conditions.

Extremely hydrophobic GTS soot particles with limited active sites are observed to initiate the ice phase only at water supersaturated conditions, $RH_w > 102\%$, at both -40 and $-51.5\text{ }^{\circ}\text{C}$. Ice nucleation did not occur until the particles were exposed to water supersaturations approaching presumably those high enough to condense water onto the particles. Ice formation was observed only on $\sim 1\%$ of the particles at up to several percent water supersaturation. Although onset of detectable ice formation was observed at a slightly lower RH_w at $-51\text{ }^{\circ}\text{C}$ than at $-40\text{ }^{\circ}\text{C}$, similar activated fractions were observed at both temperatures.

The fraction of particles initiating ice formation is shown in Figures 1,2 for hydrophilic and hygroscopic soot particles, respectively. The sizes of dry particles and the scheme of specific water interaction (at left) are included in the figures. The “Koop lines (KL)” in each figure indicate the conditions for which homogeneous freezing of 200 nm ammonium sulfate particles is predicted for the CFDC residence times. Hydrophilic TOS particles have many active sites which may grow water clusters and form the water film on the surface; 200 nm TOS particles display onset ice nucleation conditions close to RH_{Koop} at $-40\text{ }^{\circ}\text{C}$ (see Fig.1). By $101\% RH_w$, the frozen fraction exceeds 20%. At $-51.5\text{ }^{\circ}\text{C}$, 10^{-4} of the TOS particles activated by $RH_w = 85\%$. More efficient ice nucleation occurring in this lower- RH regime, up to $\sim RH_{Koop}$ must proceed via a heterogeneous mechanism. In contrast to the behaviors of TS soot, however, ice formation on TOS particles displayed a steep increase in the region $RH_{Koop} < RH_w < 100\%$, leading to activated fractions of TOS exceeding 10% by $RH_w = 100\%$.

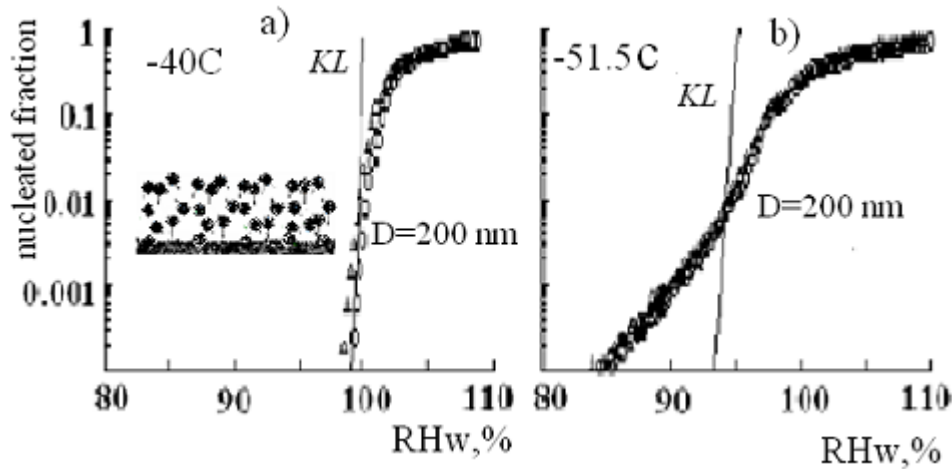


Figure 1. Ice nucleation of hydrophilic TOS soot particles at a) $-40\text{ }^{\circ}\text{C}$, b) $-51.5\text{ }^{\circ}\text{C}$.

Hygroscopic AEC soot activates ice formation at $-40\text{ }^{\circ}\text{C}$ near the predicted point for homogeneous freezing of pure dissolved solute (see Fig.2). More than 10% of the particles froze for $RH_w = 102\%$. Similarly, at $-57\text{ }^{\circ}\text{C}$, both 250 nm size-selected particles and the polydisperse particle distribution showed significant increases in ice nucleated fraction near the homogeneous freezing nucleation threshold. In comparison to the non-hygroscopic soot particles, the AEC particles nucleated ice several to ten times more efficiently at -40 and $-57\text{ }^{\circ}\text{C}$ for $RH_w > RH_{Koop}$, with $\sim 4\%$ of particles frozen at water saturation and 10% frozen at $102\% RH_w$ in both cases. These observations appear at least consistent with the dissolution of water in the soluble coverage of a large fraction of these particles, leading to homogeneous freezing, while the other fraction may be less hydrophobic.

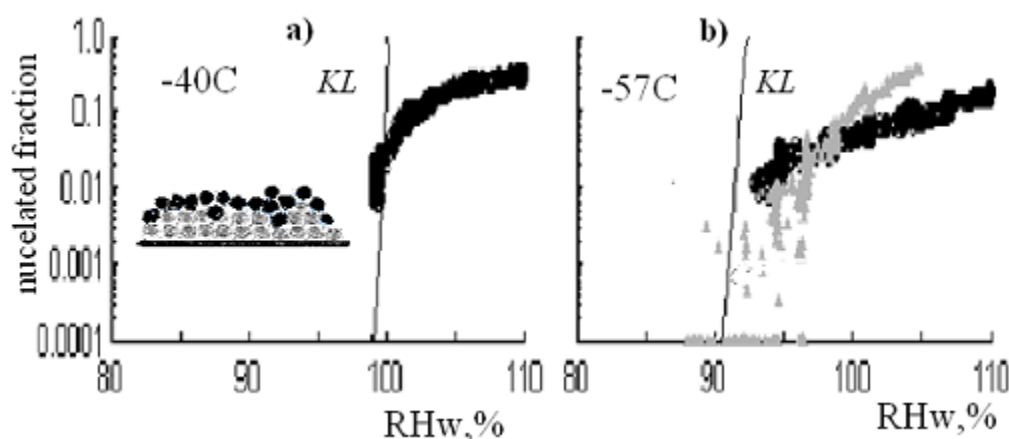


Figure 2. Ice nucleation of hygroscopic AEC soot particles at a) -40°C , b) -57°C .

4 CONTRAIL AND CIRRUS FORMATION

Experimental results suggest that the ability of soot particles of various physico-chemical properties to act as freezing nuclei in the atmosphere is related to their mechanism of interaction with water vapor. Specifically, processes that promote water uptake can facilitate ice nucleation at cirrus temperatures. This finding may be applied for aircraft contrail and cirrus formation with the hypothetical assumption that aircraft engines generate and emit into the atmosphere soot particles with a spectrum of hygroscopic properties.

Thus, we apply the obtained data for an aircraft plume situation assuming three different type of soot particle emitted and the CFDC RH uncertainty of 3%: hydrophobic, hydrophilic and hygroscopic as schematically shown in Figure 3. In the plume soot particles with different extents of hydrophilicity interact with water in accord with their water absorbability, and at the moment water saturation is exceeded we may conclude that about 10 to 50% of hydrophilic particles can freeze heterogeneously, at least 4 to 20% of hygroscopic particles (taking into account the example of AEC soot) may homogeneously freeze, and virtually no ice nucleation would occur on hydrophobic particles. At least 10% water supersaturation is needed to activate all hydrophilic particles and possibly more to freeze high proportions of hydrophobic aerosols. In general, this scenario is in accord with previously observations indicating that water saturation is needed for contrail formation whenever ice crystals are formed on exhaust soot (Karcher et al., 1998). Below water saturation very small numbers of soot particles may act as IN but significantly above water saturation all emitted soot aerosols of any surface properties have to serve as nuclei for contrail formation.

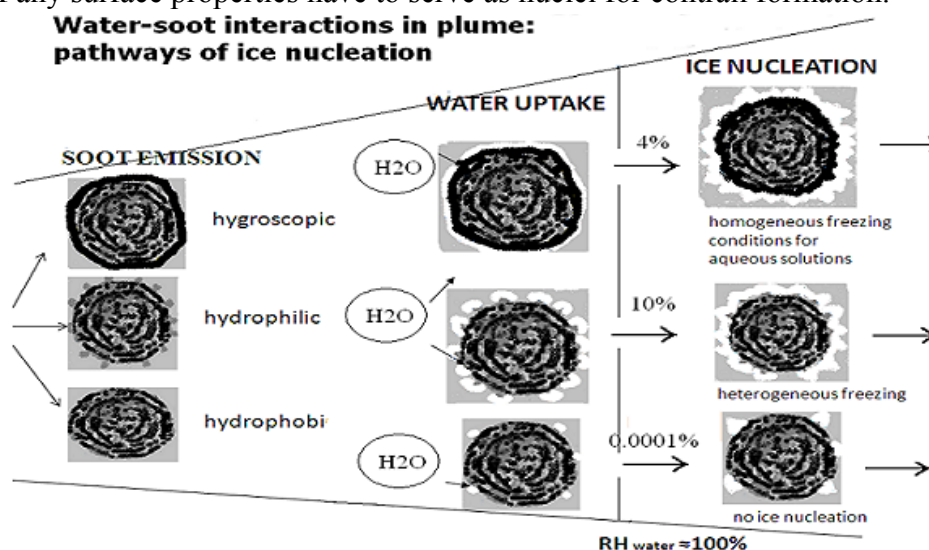


Figure 3. Scheme of pathways of ice nucleation on soot emitted in aircraft plume.

If we consider the effects of the possible physico-chemical nature of soot aerosols and order of magnitude number concentration estimates of BC in the atmosphere we can assume that hydropho-

bic soot particles should not alter cirrus cloud formation due to requiring high water supersaturations for ice nucleation at temperatures below -40°C . For soot particles that have developed a surface coverage of significant amounts of water soluble material, ice nucleation may be limited to occurring only at relative humidities near to or exceeding values required for homogeneous freezing of similar sizes of soluble particles in the upper troposphere. Their freezing is then indistinguishable from that of other particles containing water soluble species and they must compete with these other particles. Only special circumstances could allow hygroscopic soot particles to alter cirrus properties by acting as centres for homogeneous freezing. This could occur in situations where soot particles dominate aerosol numbers overall or especially at larger particle sizes. In this case, they would be the first ones to freeze in the homogeneous freezing regime, but cloud microphysical and radiative properties might not be altered.

A greater impact on cirrus formation and properties is expected if soot particles act as heterogeneous ice nuclei at lower RH_w than required for homogeneous freezing. In this case, the number concentration of ice nuclei required to dominate ice formation in competition with homogeneous freezing depends on the dynamics (updraft) driving cirrus formation. Below -40°C and below RH_{Koop} , ice formation occurred within 1 in 100 oxidized soot particles. Considering previous parcel modeling studies (DeMott et al., 1997), background upper tropospheric soot concentrations of 0.1 to 1 cm^{-3} would be predicted to have no impact to very modest impacts on natural cirrus formation if 10^{-4} to 10^{-2} fractions of the particles serve as freezing nuclei at $RH_w < RH_{Koop}$. These impacts would be restricted to cloud formation in the synoptic scale regime of vertical motions (under several cm s^{-1}), and are not expected for the stronger mesoscale motions present in cirrus generating cells. However, depending on the type of soot present or its transformation through oxidative processing, the impact of heterogeneous freezing nuclei on cirrus formation could be quite significant for higher soot concentration scenarios, such as those that occur when cirrus form in air masses affected by aged aircraft exhaust plumes or biomass smoke plumes.

5 CONCLUSIONS

Ice nucleation behaviors in relation to water uptake were investigated for soots whose properties ranged from hydrophobic to hygroscopic at the conditions of contrail and cirrus formation. It is found that hydrophobic soot initiates the ice phase from water vapor only at water supersaturated conditions while hydrophilic soot with oxidized surface and hygroscopic soot with a soluble coverage display ice nucleation onset at slightly lower conditions, in general agreement with contrail formation observations. Based on current results, hydrophobic soot may not impact ice nucleation in atmosphere, while highly hygroscopic soot should mimic the homogeneous ice nucleation behaviors of any other hygroscopic particles in the upper troposphere. Surface polarity of hydrophilic soots from various combustion sources (including aircraft) is considered to support the most effective heterogeneous ice nucleation mechanism by ice germ growth on hydrophilic nucleation sites in cirrus clouds forming below water saturation.

ACKNOWLEDGEMENTS

This study was supported by the EC within the Integrated project QUANTIFY (Contract No.003893 GOCE), Project ISTC 3097. Partial support was also provided by the National Aeronautics and Space Administration under Grant #NNG06GF00G, the U.S. Department of Energy's Office of Science (BER) through the Western Regional Center of the National Institute for Climatic Change Research (Contract #MPC35TA-A1) and the U. S. National Science Foundation via Grant ATM-0521643.

REFERENCES

DeMott, P. J., D. C. Rogers and S. M. Kreidenweis, 1997: The susceptibility of ice formation in upper tropospheric clouds to insoluble aerosol components. *J. Geophys. Res.*, 102, 19575-19584.

- Hendricks, J., B. Karcher, U. Lohmann, and M. Ponater, 2005: Simulating the global atmosphere black carbon cycle: a revisit to the contribution of aircraft emissions. *Geophys. Res. Lett.*, 32, L12814, doi:10.1029/2005GL022740.
- Herndon, S.C., T.B. Onasch, J.T. Jayne, E.C. Wood, P.E. Yelvington, J. Wormhoudt, M.J. Northway, P. Mortimer, D.R. Worsham, M.S. Zahniser, D.D. Nelson, J.H. Shorffer, J.B. McManus and R.C. Miake-Lye. Aircraft emission characterization. in R. Sausen, et al. (eds): *Proceedings of an International Conference on Transport, Atmosphere and Climate (TAC)*, Luxemburg: Office for Official Publications of the European Communities, ISBN 92-79-045583-0, 320pp.
- Karcher, B., R. Busen, A. Petzold, F. P. Schroder, U. Schumann and E. J. Jensen, 1998: Physicochemistry of aircraft-generated liquid aerosols, soot, and ice particles-2. Comparison with observations and sensitivity studies. *J. Geophys. Res.*, 103, 17129-17147.
- Koehler, K., P. DeMott, S. Kreidenweis, O. Popovicheva, M. Petters, C. Carrico, E. Kireeva, T. Khokhlova, N. Shonija, 2009: Cloud condensation nuclei and ice nucleation activity of hydrophobic and hydrophilic soot particles. *Phys. Chem. Chem.*, 11, 7906 – 7920.
- Petzold A., Gysel M., Vancassel, Hitzemberger R., Puxbaum H., Vrochicky S., Weingarnter E., Baltensperger U., and Mirabel P., 2005: On the effect of organic matter and sulfur-containing compounds on the CCN activation of combustion particles, *Atmospheric Chemical Physics*, 5, 3187-3203.
- Popovicheva, O.B., N.M., Persiantseva, E.E., Lukhovitskaya, N.K., Shonija, N.A. Zubareva, B. Demirdjian, D. Ferry, and J. Suzanne, 2004: Aircraft engine soot as contrail nuclei. *Geophys. Res. Lett.*, 31, L11104. doi:10.1029/2003GL018888.
- Popovicheva, O. B., N. M. Persiantseva, N. K. Shonija, P. DeMott, K. Koehler, M. Petters, S. Kreidenweis, V. Tishkova, B. Demirdjian and J. Suzanne, 2008: Water interaction with hydrophobic and hydrophilic soot particles. *Phys. Chem. Chem. Phys.*, 10, 2332-2344.
- Popovicheva, O.B., Persiantseva, N.M., Tishkova, V., Shonija, N.K., and Zubareva, N.A., 2008b. Quantification of water uptake by soot particles. *Environmental Research Letters* 3, doi:10.1088/1748-9326/3/2/025009

Detection of young contrails – selected results from the CONCERT (CONtrail and Cirrus ExpeRimenT) campaign

C. Voigt^{*,**}, U. Schumann, T. Jurkat, D. Schäuble, H. Schlager, M. Lichtenstern, M. Scheibe, T. Hamburger, A. Petzold, F. Arnold^{***}, A. Dörnbrack, F. Holzäpfel
Deutsches Zentrum für Luft- und Raumfahrt (DLR) – Institut für Physik der Atmosphäre Oberpfaffenhofen, Germany

^{**} also at *Johannes-Gutenberg-Universität, Institut für Physik der Atmosphäre, 55099 Mainz, Germany*

^{***} also at *Max-Planck Institut für Kernphysik, Atmospheric Physics Division, Heidelberg, Germany*

J.-F. Gayet, C. Gourbeyre

Université Blaise Pascal Clermont Ferrand, LaMP UMR 6016 CNRS, 63177 Aubière, France

M. Krämer, M. Kübbeler, J. Meyer

Forschungszentrum Jülich, Institut für Chemie und Dynamik der Geosphäre, ICG 1, 52425 Jülich, Germany

J. Schneider, J. Schmale, H. Eichler, W. Frey, S. Molleker, S. Borrmann

Johannes-Gutenberg-Universität, Institut für Physik der Atmosphäre, 55099 Mainz, Germany

Keywords: contrail, aircraft emissions, optical depth

ABSTRACT: Large uncertainties remain in estimating the climate impact from contrails. In particular it is unknown, whether the aircraft type has an influence on contrail properties. Therefore, microphysical and radiative properties of contrails were detected with the DLR research aircraft Falcon during the CONCERT campaign in October/ November 2008. During 12 mission flights over Western Europe 22 contrails from 11 different aircraft were probed and the ice particle number density, size, extinction, contrail dimension as well as trace gas fields were measured. Here we focus on the 14 minutes sampling of the contrail of an A319. The 1 to 3 min old contrail was detected in the vortex regime. It was observed at an altitude of 10.6km and a temperature of 216K in ice sub-saturated air ($82\% < \text{RHI} < 98\%$). Particle concentration, extinction, and ice water content decrease within the sampling period due to contrail ageing and dilution. A vertical contrail depth of 122m has been estimated from the measurements and agrees with vortex descent simulations. Micro- and macro-physical contrail observations allow for the quantification of the contrail optical depth, playing a crucial role for the estimate of contrail radiative forcing.

1 INTRODUCTION

Contrails are produced through mixing of the hot and humid aircraft exhaust with the cold ambient air when saturation with respect to liquid water is reached. Ice may nucleate in the aerosol below the contrail formation threshold temperature (Schumann, 1996), whereby liquid plume particles compete with the exhaust soot for the formation of contrail ice crystals. If the ambient air is ice-supersaturated, the initially line shaped contrail will develop into a persistent contrail cirrus deck. Atmospheric and plume specific processes acting on different scales result in a variability of contrail properties that can be quantified using probability distribution functions (Kärcher et al., 2009). Lee et al., (2009) present a first attempt to include such a variability of contrail properties in global climate simulations. Including aircraft induced cloudiness, they derive a net median aviation radiative forcing in 2005 of 4.9% (2–14%, 90% likelihood range) of the total anthropogenic radiative forcing. Thereby, the key parameter in determining the climate impact from contrails is the contrail optical depth.

* *Corresponding author:* Christiane Voigt, Deutsches Zentrum für Luft- und Raumfahrt (DLR) – Institut für Physik der Atmosphäre, Oberpfaffenhofen, D-82234 Wessling, Germany. Email: Christiane.Voigt@dlr.de

The contrail optical depth τ can be calculated from the effective ice crystal radii, the number density, the ice water content (IWC) and the contrail depth. Still, in situ and remote sensing data on these micro- and macro-physical contrail properties in the vortex regime are sparse. Reasons for the lack of contrail data are that the detection of numerous small aerosol and ice particles with different refractive indices poses a challenge for accurate in situ measurements. Further, the resolution of satellite instruments often inhibits the observation of young contrails with ages of few minutes from space.

Few studies investigate microphysical properties of young contrails. Mean ice crystal effective radii derived from in situ data show values of 0.5 to 1 μm initially (Heymsfield et al., 1998), increasing due to condensation to values of up to 5 μm at 30min contrail age (Schröder et al., 2000). Mean ice crystal concentrations larger than 1000 cm^{-3} have been detected in 5 and 8s old contrails decreasing by dilution to concentrations of a few 100 cm^{-3} (Schröder et al., 2000) or less than 100 cm^{-3} (Febvre et al., 2009) over the first 3min of age. The ice water content in a range of 1 to 6 mg m^{-3} in young contrails has occasionally been probed at temperatures near 218K (Schröder et al., 2000; Febvre et al., 2009). Arbitrary sampling of contrails in thin cirrus clouds at temperatures near 217K leads to IWC values of 1 to 3 mg m^{-3} (Schäuble et al., 2009). Another study reports values of up to 18 mg m^{-3} at 236K (Gayet et al., 1996). Contrail widths of 1 to 3km have been derived for less than 30min old contrails from Lidar measurements above Germany (Freudenthaler et al., 1995).

Given the sparsity of in situ measurements of contrail microphysical properties, here we report on a new set of contrail observations. The measurements were performed in November 2008 with the DLR research aircraft Falcon. During the CONCERT campaign (CONtrail and Cirrus ExpeRimenT) numerous contrails were sampled in ice sub- and supersaturated air ($50 < \text{RHI} < 130\%$). In total 22 contrails from 11 different commercial airliners were probed, including an A380, several A340 and B737 and a number of smaller aircraft such as an A319. As the data evaluation is still ongoing, we focus here exemplarily on a 14 minutes sampling event of the contrail of an A319 above Northern Germany, which is suitable for statistical data analysis. We derive particle concentrations, ice water content, and contrail depth from our data and compare them to results from vortex descent simulations.

2 FALCON INSTRUMENTATION



Figure 1. Deployment of the DLR research aircraft Falcon during the CONCERT – campaign (CONtrail and Cirrus ExpeRimenT) in October/November 2008.

During the CONCERT campaign a set of particle and trace gas instruments was deployed on the DLR research aircraft Falcon. The particle size distribution of large particles (20 μm - 1mm) was detected with a 2DC probe, the particle shape (2.3 μm pixel size) with a cloud particle imager (CPI)

and the scattering phase function of cloud particles ($3\mu\text{m}$ - $\sim 1\text{mm}$) using a polar nephelometer (Gayet et al., 2006, Febvre et al., 2009). A forward scattering spectrometer (FSSP 300) probe detected the particle number density and size distribution of small particles in the size range 0.3 to $20\mu\text{m}$ diameter (Petzold et al., 1997). The particle size distribution was evaluated assuming spherical particles and a refractive index of 1.33 for ice. During the first phase of the CONCERT campaign, an aerosol mass spectrometer (Schneider et al., 2006) was integrated in the Falcon instead of the FSSP.

The trace gas instrumentation consisted of a Lyman- α fluorescence Fast In situ Stratospheric Hgrometer FISH (Schiller et al., 2008) with a backward-facing inlet sampling water vapour with an uncertainty of 8%. In addition, nitric oxide and the sum of reactive nitrogen species NO_y were measured with a chemiluminescence instrument (Schlager et al., 1997) with an uncertainty of 8%. A chemical ionization ion trap mass spectrometer was operated to detect sulfur dioxide (SO_2) and nitrous acid HONO with an uncertainty of 30%. Contrails from different source aircraft were frequently probed with this instrumentation during the CONCERT campaign. Below we investigate data from a flight on 19 November 2008, where microphysical and chemical properties of the contrail of an A319 were measured for 14 minutes.

3 DETECTION OF CONTRAILS

Contrails were mainly probed above optically visible cirrus clouds, as this sampling strategy was found to be very effective. Predictions for high clouds or of the IWC from ECMWF analyses were used to send the aircraft into a cirrus region and the flight altitude was then adjusted based on contrail observations of the pilots. The contrail formation altitude was communicated to German Air Traffic Control, and commercial airliners flying in that region were asked to change their flight altitude to contrail formation altitudes. Then the Falcon was directed behind the airliners and contrails were detected at 5 to 85 nautical miles distance corresponding to contrail ages of 55 to 600s.

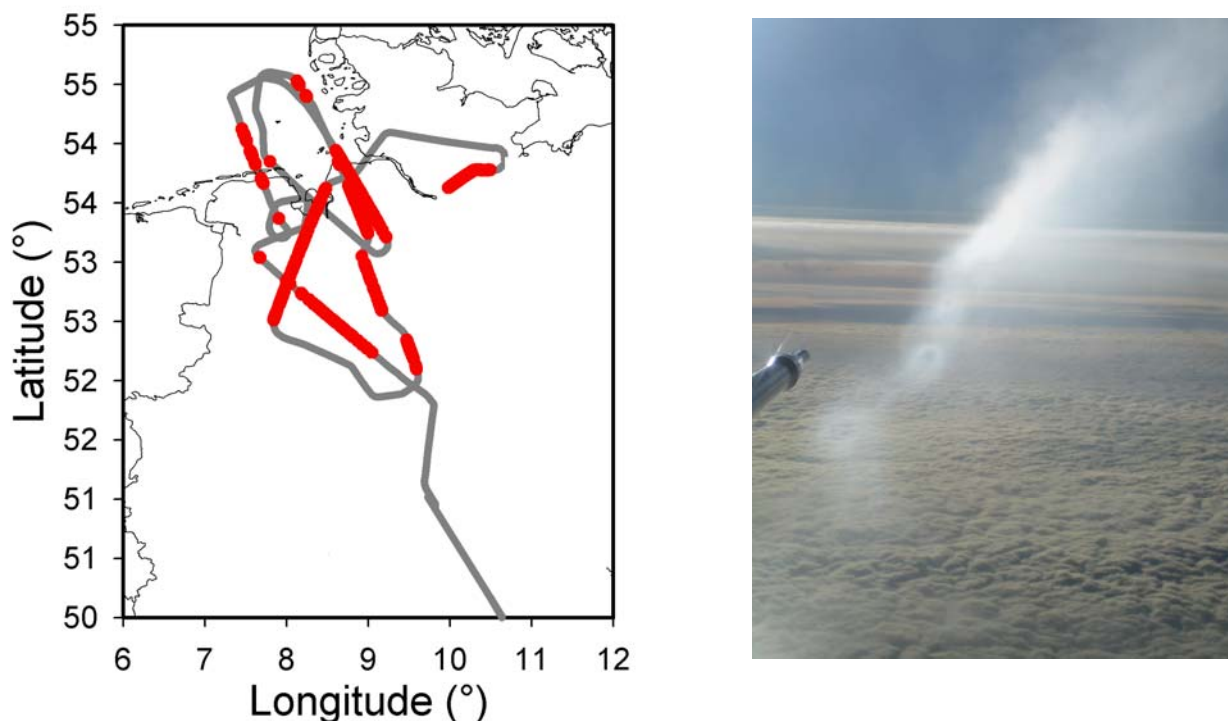


Figure 2, left panel. Flight path of the Falcon on 19 November 2009 (gray). Contrails are marked in red.

Figure 2, right panel. Photo of the contrail of the A319 which was probed by the instruments on the Falcon. The primary and the secondary wake, other contrails, and the nose boom of the Falcon can be seen.

On 19 November 2008 the Falcon five times probed the contrail of an A319, which was operating on that day exclusively as a contrail producing source aircraft. The Falcon took off in Oberpfaffenhofen, performed measurements within contrails above Northern Germany at altitudes between

10.1 and 10.8 km and landed in Hamburg. The Falcon flight track, 5 contrail encounters of the A319 and contrail samplings of other aircraft are shown in Figure 2. Some contrail segments formed above cirrus clouds as seen on the photo in the right panel of Figure 2. Note that the primary and secondary wakes of the A319, contrails from other aircraft, and the nose boom of the Falcon are shown.

Measurements during the longest contrail penetration of 14 minutes from 53°N, 8°W to 54°N, 9°W are presented in Figure 3. Simultaneous peaks in the concentrations of reactive nitrogen, sulphur dioxide and particle number density are indications for a contrail encounter.

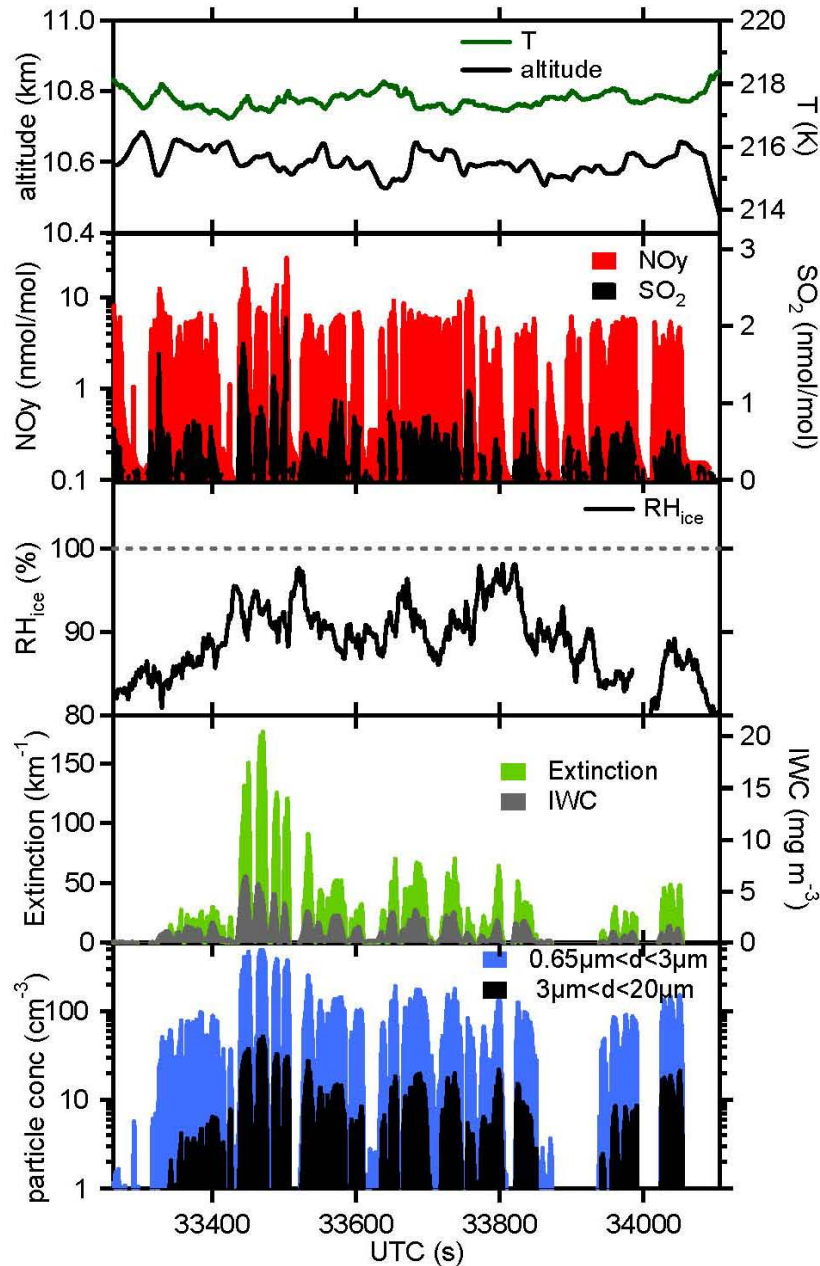


Figure 3. Sequence of 14 minutes of measurements in the contrail of an A319 performed on 19 November 2008 above Northern Germany. Temperature, altitude, trace gas mixing ratios of NO_y , SO_2 and RHI are shown in the upper three panels. The lower panels show contrail particle properties, i.e. the ice water content, the extinction of particles $> 3\mu\text{m}$, and the particle concentrations in the cloud mode ($3\mu\text{m} < d < 20\mu\text{m}$) and the haze mode ($0.65\mu\text{m} < d < 3\mu\text{m}$). The contrail age increases from 77 to 184 s within the sampling sequence.

The contrail sequence was measured at an altitude of 10.6 km and a temperature of 217.6 K. Up to 27 nmol/mol NO_y were observed in the contrail with average NO_y concentrations of 6 nmol/mol. Such concentrations have been detected previously in the primary and secondary wake of aircraft (Schlager et al., 1997). SO_2 mixing ratios up to 2 nmol/mol were measured with an average of

290 pmol/mol and background concentrations of about 80 pmol/mol. The air was slightly sub-saturated with respect to ice ($98 > \text{RHI} > 82\%$), suggesting that the contrail was evaporating.

Total ambient particle concentrations of up to 546 cm^{-3} for particles in the size range $0.65 < d < 20 \mu\text{m}$ have been detected by the FSSP. The particle concentration shows a substantial variability within the contrail and decreases within the measurement period due to dilution of the aging contrail. Particles $> 3 \mu\text{m}$ exhibit an extinction up to 170 km^{-1} decreasing with contrail age. The ice water content in the range of 7 to 1 mg m^{-3} has been derived from a combination of FSSP and CIP data.

We calculated the age of the contrail from the positions of the Falcon and the A319 and meteorological parameters by matching the advected contrail with the Falcon flight path. The contrail was 77 s old at the beginning of the sampling and 184 s at the sampling end. Contrail dynamics for contrail with ages of 1 to 3 min is described by the vortex regime.

Besides microphysical contrail properties such as particle number density, size and ice water content, we also evaluate contrail profiles and estimate the vertical contrail depth from our measurements. The data will allow us to derive the contrail optical depth.

4 CONTRAIL PROFILE

Engine emissions are captured by the wake vortices forming behind the aircraft. Due to momentum conservation, the primary vortices descent within the first 1 to 3 min transporting a large fraction of the emissions including particles downwards. The air is adiabatically heated during its downward transport, which can result in a (partial) evaporation of ice particles in subsaturated conditions with respect to ice. A small fraction of the emissions including particles remains near its emission altitude in the secondary wake. Depending on ambient saturation ratios and descent depths, the primary and/or the secondary wake might survive the vortex phase and evolve into a persistent contrail. A profile taken in the A319 contrail near 33420 s UT (101 s contrail age) is shown in Figure 4.

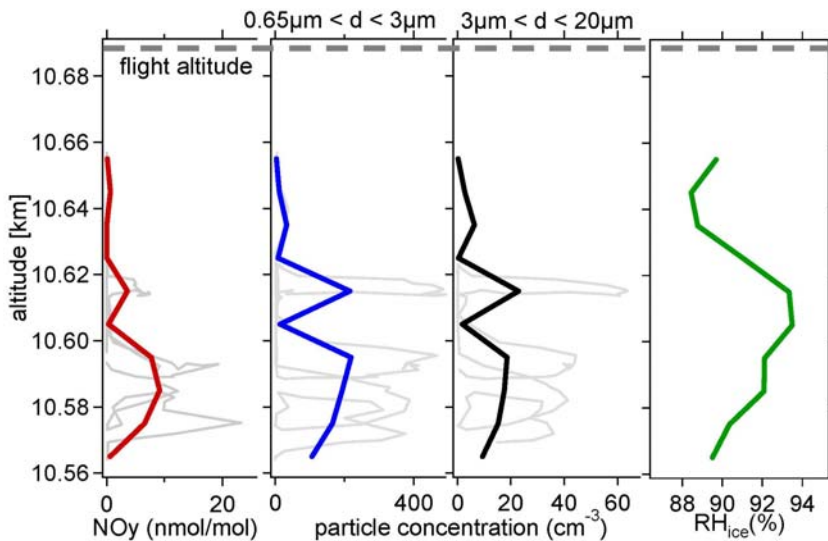


Figure 4. Profile of the NO_y mixing ratios, particle concentrations of the haze mode ($0.65 \mu\text{m} < d < 3 \mu\text{m}$), the cloud mode ($3 \mu\text{m} < d < 20 \mu\text{m}$), and RHI in the contrail of an A319 measured on 19 November 2008 at 33420 s UT. Thick lines are averages of the individual measurements (gray lines) in 10 m altitude intervals.

From the contrail profile, we estimate a vertical contrail depth of 122 m, which is in agreement with simulations of the wake vortex descent of an A319 of 124 m using the P2P model under standard ambient conditions (Holzäpfel et al., 2003).

5 CONCLUSIONS AND OUTLOOK

The CONCERT campaign provides an extensive and detailed data set on microphysical and optical contrail properties from 11 different aircraft, amongst them an A380, four A340, several B737, A319 and smaller aircraft. The data have been used for model validation (Schumann, 2009). The measurements of particle number density, size and contrail dimensions of the A319 will be used to derive contrail optical depths. Long sampling times in the contrail will allow for a statistical data analysis. The next step is to compare the contrail optical depths of the A319 to contrail samplings from other aircraft with the aim to investigate the impact of aircraft type on contrail properties. The results including a statistical data analysis will appear soon in a refereed journal.

REFERENCES

- Febvre, G., J.-F. Gayet, A. Minikin, H. Schlager, V. Shcherbakov, O. Jourdan, R. Busen, M. Fiebig, B. Kärcher, and U. Schumann, 2009: On optical and microphysical characteristics of contrails and cirrus, *J. Geophys. Res.*, 114, D02204, doi:10.1029/2008JD010184.
- Freudenthaler, V., F. Homburg, and H. Jäger, 1995: Contrail observations by ground-based scanning Lidar: Cross-sectional growth, *Geophys. Res. Lett.*, 22, 3501–3504.
- Gayet J.-F., V. Shcherbakov, H. Mannstein, A. Minikin, U. Schumann, J. Ström, A. Petzold, J. Ovarlez and F. Immler, 2006: Microphysical and optical properties of midlatitudes cirrus clouds observed in the southern hemisphere during INCA, *Q. J. R. Meteorol. Soc.*, 132, 1–30.
- Heymsfield, A. J., R.P. Lawson, and G.W. Sachse, 1998: Growth of ice crystals in a precipitating contrail, *Geophys. Res. Lett.*, 25, 1335–1338, 1998.
- Holzäpfel F., 2003: A Probabilistic Two-Phase Wake Vortex Decay and Transport Model, *Journal of Aircraft*, 40, 2, 323–331.
- Kärcher, B., U. Burkhardt, S. Unterstrasser, and P. Minnis, 2009: Factors controlling contrail cirrus optical depth, *Atmos. Chem. Phys.*, 9, 6229–6254.
- Lee, D., D. W. Fahey, P. M. Forster, P. J. Newton, R. C.N. Wit, L. L. Lim, B. Owen and R. Sausen, 2009: Aviation and global climate change in the 21st century, *Atmos. Environ.*, 43, 3520–3537.
- Petzold, A., et al., 1997: Near-field measurements on contrail properties from fuels with different sulfur content, *J. Geophys. Res.*, 102, 29867–29881.
- Schäuble, D., C. Voigt, B. Kärcher, P. Stock, H. Schlager, M. Krämer, C. Schiller, R. Bauer, N. Spelten, M. de Reus, M. Szakall, S. Borrmann, U. Weers, and T. Peter, 2009: Airborne measurements of the nitric acid partitioning in persistent contrails, *Atmos. Chem. Phys. Discuss.*, 9, 14165–14187.
- Schlager, H., P. Konopka, P. Schulte, U. Schumann, H. Ziereis, F. Arnold, M. Klemm, D. Hagen, P. Whitefield, J. Ovarlez, 1997: In situ observations of air traffic emission signatures in the North Atlantic flight corridor, *J. Geophys. Res.*, 102, 10739–10750.
- Schiller, C., M. Krämer, A. Afchine, N. Spelten, and N. Sitnikov, 2008: Ice water content of Arctic, midlatitude, and tropical cirrus, *J. Geophys. Res.*, 113, D24208, doi:10.1029/2008JD010342.
- Schneider, J., S. Hings, N. Hock, S. Weimer, S. Borrmann, M. Fiebig, A. Petzold, R. Busen, B. Kärcher, Aircraft-based operation of an aerosol mass spectrometer: Measurements of tropospheric aerosol composition, *J. Aerosol Sci.*, 37, 839–857, doi: 10.1016/j.aerosci.2005.07.002, 2006.
- Schröder, F., B. Kärcher, C. Duroure, J. Ström, A. Petzold, J.-F. Gayet, B. Strauss, P. Wendling, and S. Borrmann, 2002: On the transition of contrails into cirrus clouds, *J. Atmos. Sci.*, 57, 464–480.
- Schumann, U., 1996: On conditions for contrail formation from aircraft exhausts, *Meteorol. Z.*, 5, 4–23.
- Schumann, U., 2009: A Contrail Cirrus Prediction Tool, *Intern. Conf. on Transport, Atmosphere and Climate*, Aachen and Maastricht, EUR, in press.

Quantitative forecast model of contrail formation and prospects of its application

V.T. Dedesh*, R.Kh. Tenishev, S.N. Kiose, V.V. Popov, E.G. Pavlova, I.V. Voronich, M.A. Lavrov, V.P. Mogilnikov
Gromov Flight Research Institute (GFRI), Zhukovsky, Russia

A.I. Lanshin, A.A. Evstigneev
Baranov Central Institute of Aviation Motors (CIAM), Moscow, Russia

A.N. Nevzorov
Central Aerologic Observatory, Moscow, Russia

O.B. Popovicheva
Lomonosov Moscow State University (MSU), Moscow, Russia

Keywords: aircraft, contrails, cirrus clouds, forecast model

ABSTRACT: A complex methodic and quantitative model were developed for quantitative valuation and forecast of formation conditions and characteristics of contrails, in cruise flights of civil airplanes with different types of jet engines using specially equipped flying testbed Tu-154 prober/generator. The methodic uses uniform and 2D mixing of the exhaust engine jet and atmosphere. The data, obtained during the flight experiments proved the reliability of the methodic.

1 MOTIVATION

Influence of aviation on the environment is not limited only by the greenhouse gases. Contrail formation according to some researches can at least as important as CO₂. But in previous researches of contrails there were several aspects preventing us from clear understanding of the subject. First of all, characteristics of engine exhaust jet are appreciated by total heat equivalent and their values for given engines and airplanes are determined approximately. Then, peculiarities of bypass engines without mixing chamber and turboprop engines are not considered at all. Moreover, contrail formation conditions are considered only qualitatively, that prevents from direct influence estimation of deviations of engine and atmosphere characteristics on contrail characteristics and formation conditions.

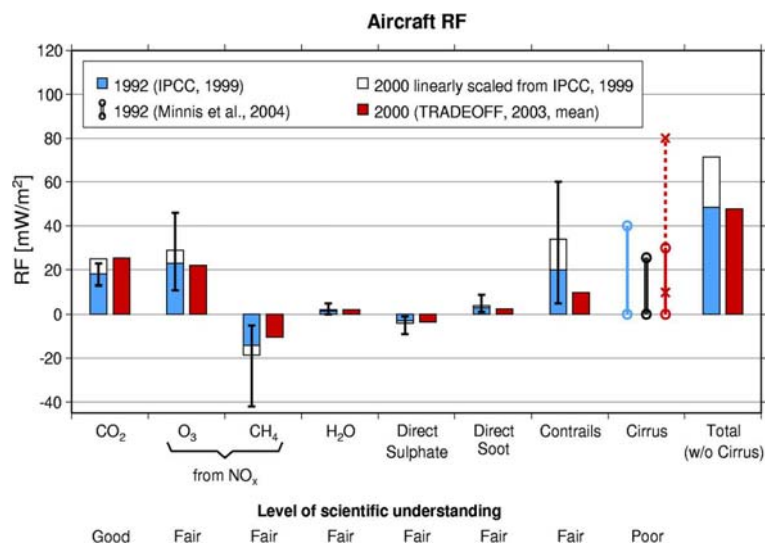


Figure 1. Radiative forcing from aircraft.

* Corresponding author: V.T.Dedesh, Gromov Flight Research Institute, 140182, Russian Federation, Moscow Region, Zhukovsky-2. Email: kd3@aha.ru

1.1 The model

Complex quantitative model was proposed. As a criteria of contrail formation and existence, index of maximum humidity supersaturation h_{Σ} is used, consisting of two parts: $h_{\Sigma} = h_m + e_{amb}$, where h_m = maximum supersaturation towards water while mixing exhaust jet with dry atmosphere, depending practically from engine characteristics, ambient temperature and pressure; and e_{amb} = atmosphere humidity on the flight altitude. The methodic, developed by the GFRI specialists differs in facts that engine exhaust jet characteristics are estimated directly from results of a special experiment or calculation and exhaust jet and atmosphere mixing is estimated with consideration of peculiarities of bypass engines and possible influence of engine flow-around at 2D mixing on equivalent mixing line while assuming uniform mixing of engine jet and atmosphere.

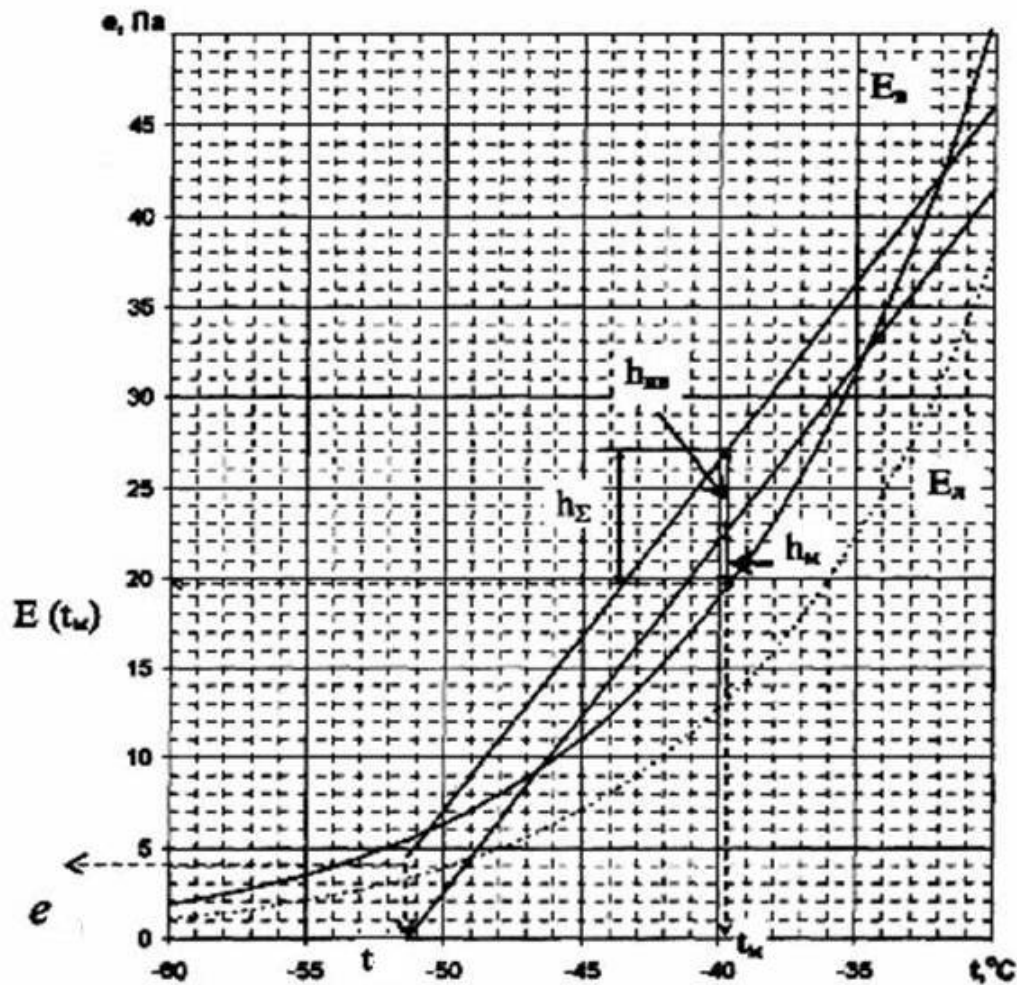


Figure 2. Quantitative supersaturation index.

1.2 The testbed

To prove the validity of the criteria and to adjust the methodic, flying testbed Tu-154 was used. It was equipped with special measuring means to measure cloud and contrail characteristics. The emphasis was done on the humidity of the air. It was measured by an aircraft condensation hygrometer (SKG) and by an on-board sorption hygrometer (BSIV). Water content of atmosphere and contrails was measured by the measurer of water content (IVOKS). Temperature values came from the resistance temperature detector (ET-17). For in-flight observation of condensation trail formation a periscope (TS-27AMSh) and a video camera were installed. For registration of formation borders and lifetime of condensation trails in solo and twin flights following devices are used: videotheodolitic system “Opal”, “Jantar” and also specialized camera for video and photo recording from earth.



Figure 3. Sensors on the flying testbed Tu-154M.

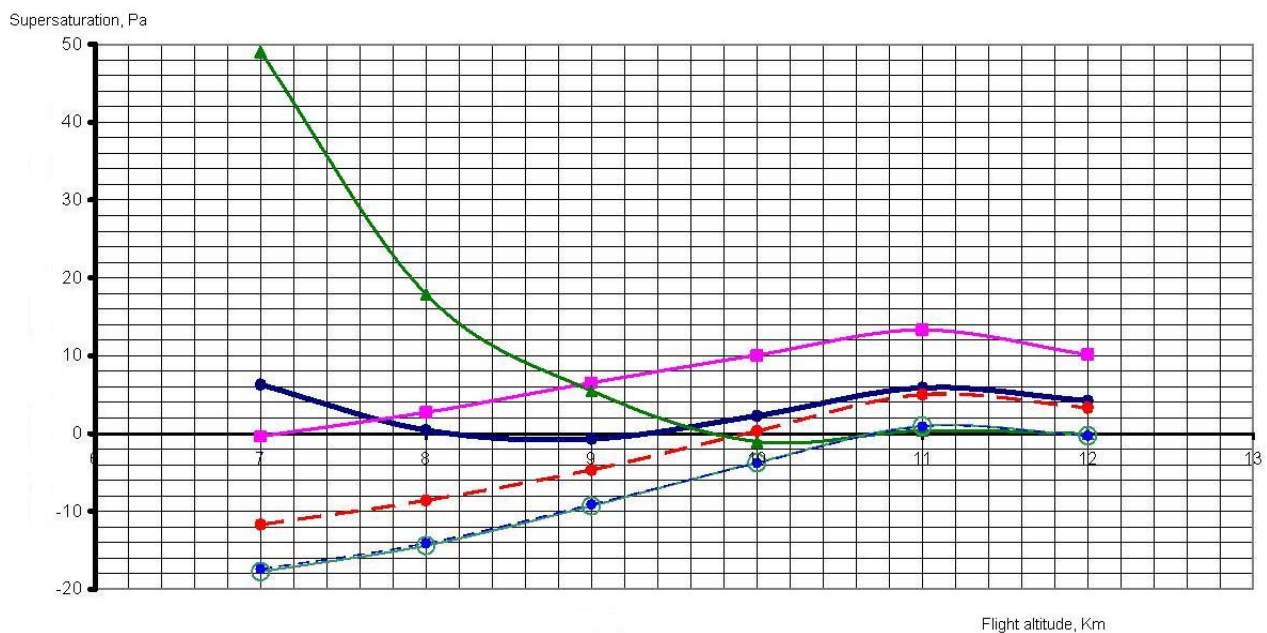


Figure 4. Calculation results for the D-30KU engine.

On the heights $H = 7 \dots 8$ km scatter of characteristics can be caused by higher temperatures of ambient air and their greater deviations from ISA standard or by greater range of margin values of humidity (partial pressure) between its saturations over water and ice. Above mentioned factors give more favourable conditions for carrying out experiments aimed at identification of the forecast model with supersaturation index $h_{\Sigma} = h_m + e_{amb}$ on formation and existence of contrails.

1.3 The 2D model

For examination of contrail formation processes of mixing of a jet from a modern bypass engine with concurrent flow a calculation methodic was developed. This methodic is based on solution of full system of gas dynamic equations considering turbulence. Main geometric and gas dynamic parameters are pointed out, physical and mathematical models of current are determined, calculation model is developed, technology of quantitative modelling is worked out.

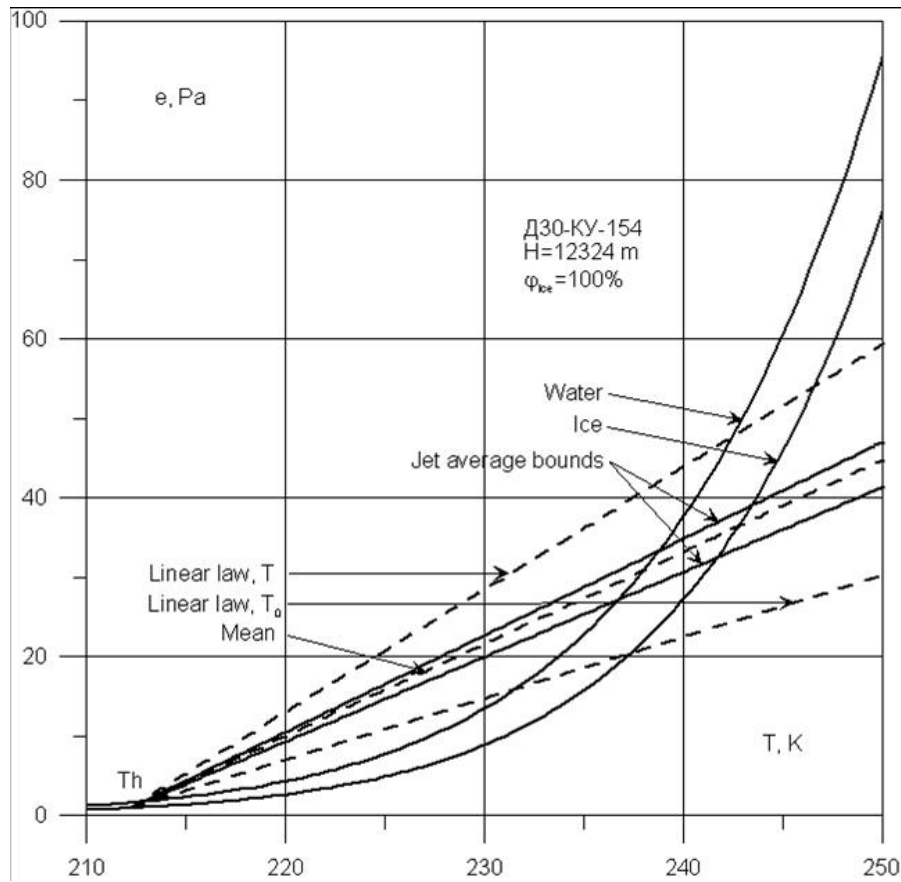


Figure 5. Uniform mixing line, calculated using 2D model.

Basing on these results, specification is done of quantitative forecast model of contrail formation conditions at uniform mixing of engine exhaust jet with atmosphere. Method of calculation mixing line gradient values is also proposed, considering both full and static temperatures of engine exhaust jet. Method of uniform mixing and methodic of calculation mixing line gradient values were used to calculate values of sum supersaturation index over water and ice considering both full and static temperatures of engine exhaust jet after engine mixing chamber.

$$B_0 = \frac{B_0(T_{mix}^*) + B_0(T_{mix})}{2} \quad (1)$$

The conducted comparison showed that quantitative humidity supersaturation index calculated basing on the improved methodic, where average temperature in the mixing chamber ($T_{mix.av}$) is used, is more adequate to contrail formation conditions according to saturation curves over water and ice in comparison with the previous methodic ($T_{mix.abs}$) used up to the present.

According to engines without mixing chamber investigations of contrail formation conditions were also done. Research carried out using the developed model showed that averaged mixing line exists for engine with open fan.

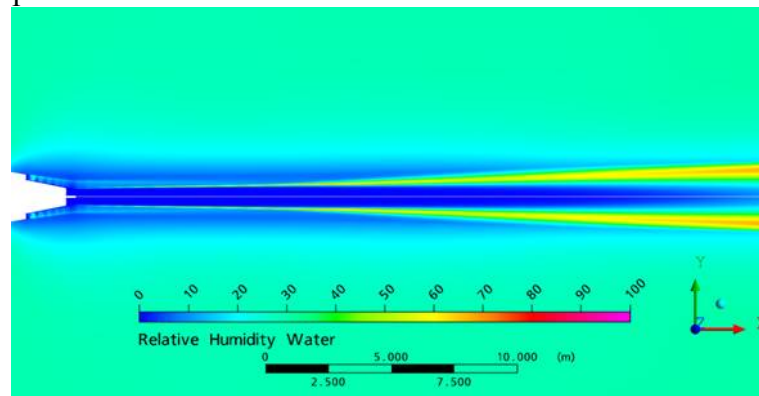


Figure 6. 2D calculation for engine with open fan.

2 RESULTS

The forecast model allows estimating characteristic and equivalent influence on h_{Σ} of engine characteristics and atmospheric pressure (flight altitudes); temperature and humidity on steady contrail formation conditions. Calculations of humidity supersaturation indexes h_{Σ} and its identification with experimental results showed that: two altitude borders of formation of steady contrails are possible for aircrafts flying in various air conditions. These borders depend from engine characteristics, temperature deviations from ISA temperatures $\pm 10^{\circ}\text{C}$; evaluation of equivalent influence in border region on high altitude can show change of the borders, where steady contrails can be formed, at changes of T_{amb} , ambient humidity and engine mode; in number of cases steady contrail formation was observed at $h_{\Sigma} < h_{\Sigma\text{boundary}}$ at $\Delta h_{\Sigma} = h_{\Sigma\text{boundary}} - h_{\Sigma}$, corresponding to the interval between saturation curves over water and ice ($\Delta e = e_{\text{water}} - e_{\text{ice}}$), that can be explained by presence of crystallisation centres (soot, etc.)

Methodic of 2D mixing of engine jet and atmosphere is developed and tested on different engine types. It allows to estimate characteristics of mixing, including geometrical, averaging parameters, temperature T_{mix} and humidity in cross-sections.

Method is shown of calculating values of mixing line gradient (that can be used for calculating h_{Σ}) basing on the analysis of calculation of contrail formation conditions done for bypass jet engines with mixing chamber and open fan.

Using both T_4^* and $T_{4\text{stat}}$ of jet engines with mixing chambers for estimation humidity supersaturation index is more adequate to contrail (ice particles) formation conditions and saturation curves over water and ice, than using only T_4^* . Calculations of humidity supersaturation indexes h_{Σ} using T_{mid} for bypass engines with mixing chamber and its identifications with results of experiment on the Tu-154 FTB with D-30KU engines showed that for these engines at boarder $h_{\Sigma} > 0$ contrails are steady.

$$T_{\text{mid}} \approx \frac{T_4^* + T_{4\text{static}}}{2} \quad (2)$$

$$B_0 = \frac{B_0(T_{\text{mix}}^*) + B_0(T_{\text{mix}})}{2} \quad (3)$$

3 CONCLUSION

The performed works and obtained results, when applied and developed, can essentially amplify works done in this field by specialists of European organisations. They are of great interest for ecological estimations of emission influence of specific aircrafts with different engines on contrail formation in cruise flights and possible influence on Earth climate, as well as for development of recommendations on flight organization on different routes (local, regional and international) with the object of reducing of this effect, considering peculiarities of atmosphere in specific regions, on specific air routes and in different seasons.

In case if characteristics of alternative fuels are available, it is also possible to use the methods developed to estimate their effect on contrail formation and existence during airplane cruise flights.

Conducted researches show that it is efficient to use the experience of complex researches and handling of jobs by different specialists according to consistent schedule in order to improve the efficiency of the further work.

4 ACKNOWLEDGMENTS

This work was partly funded by the International Science and Technology Center in the frames of the ISTC Project #3097.

REFERENCES

- Dedesh V.T., R.Kh.Tenishev, N.A.Dankovtsev, A.P.Leut, E.G.Pavlova, A.N.Nevzorov, S.N.Kiose, V.V.Popov, A.I.Lanshin, 2005: Forecast and identification methodology of influence of jet engine characteristics on condensation trails formation in cruise flights, International conference Aircraft engines of the XXI century, CIAM, Moscow, Russia.
- Dedesh V.T., R.Kh.Tenishev, N.A.Dankovtsev, A.P.Leut, E.G.Pavlova, S.N.Kiose, V.V.Popov, M.A.Grigoryev, A.N.Nevzorov, 2006: Need in developing flight research methodics of formation and existence of condensation trails of jet airplanes in cruise flights, Ninth international exhibition Engines-2006, ASSAD, Moscow, Russia.
- Dedesh V.T., R.Kh.Tenishev, N.A.Dankovtsev, A.P.Leut, E.G.Pavlova, S.N.Kiose, V.V.Popov, A.I.Lanshin, M.A.Grigoryev, A.N.Nevzorov, 2006: GFRI experience in carrying out flight experiments on aircraft engines influence on atmospheric pollution, International aeronautics seminar Europe-Russia, Brussels, Belgium.
- Fischter K., S.Markwart, R.Sausen, 2005: Influence of cruise flight altitude on condensation trails and corresponding radiation, Meteorologische Zeitschrift, vol. 14, No. 4, 563-572.
- Manstein G., U.Schumann, 2005: Cirrus clouds over Europe, formed by aircraft condensation trails, Meteorologische Zeitschrift, vol. 14, No. 15, 549-554.
- Mathes S., 2005: Impact of aviation on the environment in global scale, AERONEN III Work materials №17 Results of the seminar on air transport systems, Stockholm, Sweden.
- Schumann U., 1996: On condensation trail of aircraft exhaust jet formation conditions, Meteorologische Zeitschrift, N.F. 5, 4-23.

A Contrail Cirrus Prediction Tool

U. Schumann*

Deutsches Zentrum für Luft- und Raumfahrt (DLR) – Institut für Physik der Atmosphäre Oberpfaffenhofen, Germany

Keywords: contrails, contrail cirrus, simulation

ABSTRACT: An new “Contrail Cirrus Prediction Tool” (CoCiP) has been developed to simulate contrail cirrus resulting from a single flight as well as from a fleet of cruising aircraft, flight by flight, regionally or globally. The method predicts contrail cirrus for given air traffic and weather prediction data. The method describes the life cycle of each contrail individually using a Lagrangian Gaussian plume model with simple bulk contrail ice properties, without feedback to meteorology. Contrails are initiated when the Schmidt-Appleman criterion is satisfied and when the ambient atmosphere is humid enough to allow for contrail persistence. The initial plume properties reflect properties of the originating aircraft. The evolution of individual contrails of cruising aircraft is computed using wind, temperature, humidity, and ice water content from numerical weather prediction (NWP) output. The plume trajectory follows horizontal and vertical wind. The model simulates shear and turbulence driven spreading, ice water content as a function of ice supersaturation, and some ice particle loss processes (turbulent mixing, aggregation and sedimentation). Radiative cloud forcing is estimated for the sum of all contrails using radiative fluxes without contrails from NWP output. The tool is kept simple to allow for efficient contrail simulations. The method has been tested for case studies with some comparisons to observations. The most critical input parameter is the NWP humidity field. The results compare favourably with observations and support interpretations of insitu, satellite and lidar observed aviation impact on cirrus clouds. CoCiP can be used to predict and minimize the climate impact of contrails.

1 INTRODUCTION

Because of the general awareness of climate change and the growth of traffic, aviation caused environmental concerns which were discussed with respect to the fleet of civil aviation since the early 1990’ (Schumann, 1994; IPCC, 1999). Despite considerable scientific progress in predicting the climate impact of aviation, still major uncertainties remain, in particular with respect to contrail cirrus (IPCC, 2007; Lee et al., 2009). The range of radiative forcing from present aviation induced contrails scatter by a factor of larger ten (from 3 to 120 W/m²). Observed increases in cloudiness may be attributed to aviation, but the observations miss physical explanation and other explanations cannot be ruled out. Contrail and cirrus formation is a highly nonlinear process. The contrail cirrus formation depends strongly on the scale transition from the plumes with fresh soot and young contrails into spread cirrus layers. Early studies concentrated on line-shaped contrails, but contrails develop dynamically into cirrus at time scales of hours during which the line-shaped structure is lost. This scale transition requires a model that follows the history of all the contrails from the global fleet of aircraft from origin shortly after engine exit until the end of their lifetime due to sublimation or sedimentation. This paper describes a recently developed model for this purpose. The model is based on a Gaussian plume model as suggested a long time ago (Schumann and Konopka, 1994).

* *Corresponding author:* Ulrich Schumann, Deutsches Zentrum für Luft- und Raumfahrt (DLR) – Institut für Physik der Atmosphäre, D-82234 Oberpfaffenhofen, Germany. Email: ulrich.schumann@dlr.de.

2 THE MODEL

The contrail cirrus prediction (CoCiP) model is designed to analyze and predict contrail cirrus cover and the related radiative forcing from air traffic. The model simulates contrail cirrus resulting from a fleet of cruising aircraft, flight by flight, regionally or globally. The concept is illustrated by an example, see Figure 1.

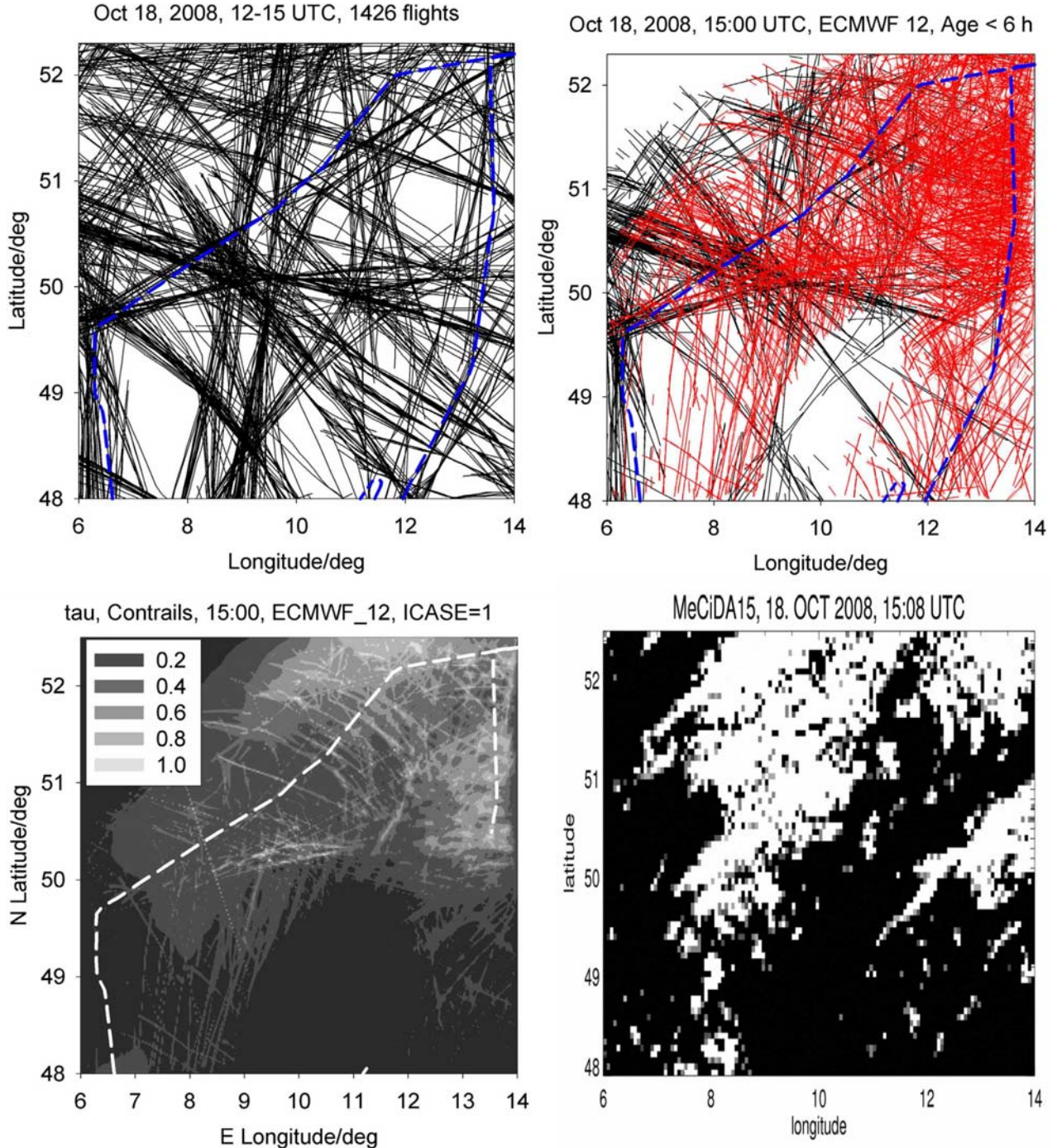


Figure 1. Example CoCiP output: Contrail pattern as computed for a $8^\circ \times 4.2^\circ$ (680×470 km 2) region over Germany, for a case study (Oct 18, 2008, 15 UTC), for which contrails were observed visually and by lidar measurements with the Falcon research aircraft (flight path shown as blue or white dashed curve). Top left: flight paths of air traffic from all 1426 flights above 7.3 km altitude (FL 240) over Germany between 13 and 15 UTC that day. Top right: Flight segments causing contrails during recent 6 h which contribute to contrail cover at 15 UTC (black), and contrail plumes centre line (full red) together with their left and right boundaries (dashed red; closely near the centre lines). Bottom left: solar optical depth of these contrails (from CoCiP) superposed on cirrus (from ECMWF output). Bottom right: Cirrus cloud cover (white) computed by K. Graf with the MeCiDa algorithm (Krebs et al., 2007) from Meteosat data at the given time.

The method computes the contrail cirrus cover for a given time instant for given weather data and for given data of air traffic for the past covering all contrails with life times of up to six hours (in Fig 1) or about a day (for larger domains). The model requires input in terms of wind vector, temperature, humidity, and ice water content fields as available from numerical weather prediction (NWP) or climate model output, as a function of time and three dimensions (3d) in space (typical time intervals: 1-3 h; typical spatial resolution: 0.25-1 degree horizontally, 20 levels vertically from 120-500 hPa for Germany). In addition, the model requires the irradiances for outgoing longwave radiation (OLR) and short-wave reflected radiation (RSR) at top of the atmosphere (TOA) as a function of horizontal coordinates and time. The traffic data need to be provided, flight by flight, as waypoint sequences (3 space coordinates and time) together with the aircraft type. The tool is kept simple to allow for efficient global contrail simulations. The example requires about 10 s computing time on a single processor Laptop.

The model treats each exhaust plume as a Gaussian plume (Konopka, 1995; Schumann et al., 1995; Dürbeck and Gerz, 1996). The model assumes that any mass specific concentration c in the plume has the distribution $c(x,y,z,t) = (C_0/A) \exp(-(1/2)\mathbf{x}^T \boldsymbol{\sigma}^{-1} \mathbf{x})$, where C_0 is the mass per unit length in the contrail, A is the plume cross-section area, \mathbf{x} is the vector of space coordinates relative to the plume centre ($\mathbf{x}=(x,y,z)$, x in flight direction, y cross-flight direction, z vertical direction), and $\boldsymbol{\sigma}(\mathbf{x},t)$ is the positive definite symmetric concentration-covariance matrix with matrix diagonal elements σ_{yy} and σ_{zz} , and diagonal elements $\sigma_{yz} = \sigma_{zy}$. $A = \iint \exp[-(1/2)\mathbf{x}^T \boldsymbol{\sigma}^{-1} \mathbf{x}] dy dz = 2\pi [\det(\boldsymbol{\sigma})]^{1/2}$. The initial plume has an elliptical cross-section with effective width B and depth D , $\sigma_{yy} = B^2/8$, $\sigma_{zz} = D^2/8$, so that the initial cross-section area is $A = (\pi/4) B D$.

The model distinguishes 3 model phases: Phase 0: initial plume conditions just after engine exit; phase 1: initial plume conditions at the end of the wake vortex period (accounting for wake vortex downwash); Phase 2: plume evolution until dry-out because of ambient subsaturation or until sedimentation of the particles below the lower boundary of the computational domain (typically at 5 km altitude).

In phase 0, contrails form when the Schmidt-Appleman criterion is satisfied, i.e. when the ambient temperature T is below a critical temperature T_{LC} (Schumann, 1996) which is a function of fuel properties and the overall propulsion efficiency $\eta = (V F)/(m_F Q)$, with thrust F , true air speed V , fuel consumption per unit distance m_F and combustion heat Q , and ambient temperature T , absolute ambient humidity q , and pressure p as computed for the given time t and position \mathbf{x} by bilinear interpolation in the NWP output fields. Contrails are assumed to persist when the relative humidity over ice (RHi) is larger than a critical value RHi_{crit} , which should be 100 % for good NWP input data. The ECMWF model output predicts supersaturated air masses fairly realistically (Tompkins et al., 2007). The COSMO-DE model output shows practically no supersaturation. Therefore, we run the model for this example with both input data with $RHi_{crit} = 0.9$.

The initial contrail depth is assumed to be proportional to the wake vortex maximum downwash Δz_w . This downwash is determined from a parameterization of P2P model results (Holzäpfel, 2006). The parameterization is a function of aircraft parameters (mass, speed, span width) and atmospheric parameters (Brunt Väisälä frequency, density, and turbulent dissipation rate). The aircraft parameter values are taken from the BADA data set of EUROCONTROL.

For microphysics, we assume saturation inside the contrail plume. The initial ice water content IWC in the plume at stage 0 is set to the amount of water mass per volume in the ambient air above ice saturation. The specific water mass in the plume is the sum of ambient humidity and the amount of water emitted from the engine and mixed over the plume cross-section. During the wake vortex phase, the plume sinks and heats up adiabatically. This leads to a reduction of the saturation water mass and hence to a loss of IWC, which is computed within CoCiP accordingly.

The initial number of ice particles N per unit length is assumed to be determined by fuel consumption m_F and the soot number emission index EI_{soot} ; this is consistent with recent model results (Kärcher and Yu, 2009) and the few available measurements (Schumann et al., 2002). The soot emission index is estimated according to earlier studies (Petzold et al., 1999; Eyers et al., 2005). During the wake vortex period, part of the ice particles sublimate because of the adiabatic warming and turbulent mixing with ambient air (Sussmann and Gierens, 1999). Loss factors have been computed by large eddy simulations (Kärcher et al., 2009). However, from comparisons to observed data, we got the impression that these factors are too low. Therefore we instead assume that the ratio of N in phase 1 relative to N in phase 0 is proportional to corresponding ratio of IWC.

In the evolution phase (2) of the contrails we follow the plumes in a Lagrangian manner. The plume position follows horizontal and vertical wind as analysed from the NWP data. In addition, the vertical position changes with the mean sedimentation speed of the bulk of the ice particles. We also have foreseen a rising motion component due to radiative heating. For given winds from NWP, advection is computed using a second-order Runge-Kutta scheme.

The change in plume cross-section with time as a function of vertical velocity shear S , and vertical and horizontal diffusivities D_{yy} and D_{zz} is integrated analytically (Konopka, 1995). The diffusivities are functions of plume scales, total shear S_T and stratification N_{BV} ($D_{zz} = 0.4 w^2 / N_{BV}$; $w = 0.1$ m/s as the vertical turbulent velocity fluctuations), $D_{yy} = 0.1 D^2 S_T$. The shear diffusivity D_{yz} is set to zero. The shear value S (perpendicular to the plume axis) and S_T (total) are computed from differences of the corresponding wind speeds at the next available levels above and below the contrail. Since the grid spacing Δz is often large compared to the contrail depth D , we allow for an enhancement factor $f(\Delta z/D)$ (Adelfang, 1971), where $f(r) = (1/2)(1+r^m)$. The exponent m is close to $2/3$ for Kolmogorov type turbulence (dependence on wavenumber k as $k^{-5/3}$) and close to 0 for 2d turbulence (k^{-3}). Here, we assume $m = 1/2$. We also have foreseen enhanced turbulent diffusivities due to radiative heating.

During integration we assume that any ice supersaturation within the air mass entrained with growing cross-section $A(t)$ into the contrail plume gets converted to ice water content $IWC_s(t)$ immediately, leaving saturated ($RH_i = RH_{crit}$) humidity inside the contrail. Accordingly, we integrate the ice water content such that the plume ice water budget is conserved except for mixing with the humidity from ambient air. The volume mean ice particle radius r is computed locally from IWC and number N of ice particles per unit length, or n per unit volume $n = N/A$, so that $(4/3) \pi r^3 n \rho_{ice} = IWC$ ($\rho_{ice} = 917$ kg/m³ as ice bulk density). We assume that the number of ice particles remains constant unless specific particle loss processes like agglomeration or turbulent phase changes reduce the number of particles. Hence the number of ice particles follows from $dN/dt = (dN/dt)_{agg} + (dN/dt)_{turb}$. Further we use the assumptions $(dN/dt)_{agg} = -E_a 8 \pi r^2 V_t N^2/A$, and $(dN/dt)_{turb} = -E_T (D_{yy}/\max(D,B)^2 + D_{zz}/d_{eff}^2) N$, where V_t is the sedimentation velocity of particles with radius r , and $d_{eff} = A/B$, and E_a and E_T are free model parameters of order unity. These relationships are justified by dimensional analysis.

The solar optical depth τ of the contrail is computed from $\tau = 3 Q_{ext} IWC d_{eff}/(4 \rho_{ice} r_{eff})$, with extinction coefficient $Q_{ext} = 2$ and optically effective radius $r_{eff} = C_\tau r$. The factor $C_\tau \approx 0.9$ depends on the particle habits and the particle size distribution function; its value is quite uncertain. The values of τ and r_{eff} form the input to a radiative forcing (RF) model which computes the RF from contrails for given OLR and RSR at TOA fit to forward calculations with libRadtran (Schumann et al., 2009).

3 APPLICATION EXAMPLES

The model has been applied to weather and traffic conditions over Germany and the North Atlantic (first global tests have also been performed) for the following case studies: 1) comparison to insitu measurements of NO_x , ice and soot particle concentrations in the contrails of six (small and large) different aircraft, at plume ages of 60 to 600 s, during the experiment CONCERT, Nov 19, 2008 (Voigt et al., 2009); 2) comparison to lidar measurements of the extinction coefficient of cirrus and contrail cirrus particles at altitudes 6-11 km along a flight path of the Falcon over Germany on Oct 18, 2008 (Schumann and Wirth, 2009); and 3) comparisons to cirrus cover and outgoing longwave radiation data obtained from Meteosat for Germany (see Fig 1) or the North Atlantic in the time period August 11-14 2005. The results show: CoCiP computes a dilution with time which agrees favourable with the NO_x measurements (Voigt et al., 2009) and with previous data (Schumann et al., 1998). The number of ice particles and soot particles computed by CoCiP compares reasonably with insitu measurements during CONCERT. The results do fit only after taking the specific aircraft properties into account. There are no indications of additional ice formation after the initial soot-controlled contrail formation. The diurnal cycle of cirrus cover and OLR computed for 3 days in the NAR shows the order of magnitude with respect to the amplitudes of cirrus cover and of OLR as derived from Meteosat (Graf et al., 2009). Also the delay time between traffic maximum and cirrus cover maximum is in the same range of 3 to 5 h as observed. Parameter studies indicate that changes of most model parameters have less than linear impact on integral results like net radiative

forcing. A somewhat larger sensitivity is found for the critical relative humidity, and the parameters limiting the plume life time. The SW RF is strongly sensitive to the assumed particle habits.

For example, Figure 1 shows the 848 contrails (1069 contrail segments) that are computed to exist in the region shown at 15 UTC this day. The contrails formed from 2816 flights during the 6 h before this time. The average contrail age is 2.25 h. About 38 % of all flights (628626 flight km) in that period formed contrails. The mean fuel flow rate of contrail forming aircraft was 3.8 kg/km. The mean contrail width is 3180 m, the mean contrail length 134 km. More than 92 % of the contrails formed inside the thin cirrus, i.e. in air masses containing positive ice water content, according to ECMWF. Contrails contained 5.3×10^{11} /m ice particles per unit plume length. The mean optical depth τ was 0.054. One contrail reached $\tau = 1.1$. Not accounting for overlap of the various contrails, the cover with thin contrail cirrus would be 110 %, mostly optical thin ($\tau < 0.03$). The fraction of cirrus with optical depth larger 0.4 (larger 0.05) was 4.5 % (35.5 %) without contrails and 9 % (50.6 %) with contrails, i.e. 15 % of the sky was covered with contrail cirrus of $\tau > 0.05$. The contrail induced RF is 3.8 W/m² in the LW, -4.5 W/m² in the SW, and -0.64 W/m² net. Hence, contrails were cooling in this case. The computed contrail cover agrees - not ideally but qualitatively - with the cirrus cover derived from Meteosat (see Fig. 1). The remaining differences are mainly because of deviations of the computed RH_i from the NWP data compared to reality. Best performance was obtained with ECMWF forecasts from 12 UTC that day.

4 CONCLUSIONS

A new Contrail Cirrus Prediction Tool (CoCiP) has been developed to simulate and predict contrail cirrus from a fleet of aircraft, flight by flight, regionally or globally. The model has been developed in the last year and parts are still under development. So far, the model has been tested in parameter studies in comparison with insitu, lidar, and satellite data. The most critical parameters concern the NWP humidity and the life time of contrails (sedimentation, turbulent particle loss). The results indicate that most contrails occur inside thin cirrus in the upper troposphere. The radiative forcing by contrail cirrus is far larger than estimated from line shaped contrails and may be negative at least regionally. Contrail climate impact can be reduced by proper air traffic management. The model will next be used for global evaluation of contrail cirrus RF. We plan to run it for several years and compare it with Meteosat observations. Moreover we plan for tests with research aircraft (HALO and Falcon) in a cirrus experiment “ML-CIRRUS”. The model will also be applied within the project UFO (Mannstein and al., 2009). In the future, the model may be coupled to other global models (with aerosols & chemistry) to assess the total aviation climate impact. For example it may be used to study renucleation effects from contrail-processed soot emissions. The model may be extended with plume chemistry to compute the effective chemical emissions. Higher order microphysics cloud physics may be included. The same principle approach may be used to simulate ship trails.

5 ACKNOWLEDGMENTS

The author gratefully acknowledges contributions from coworkers, in particular: K. Graf, B. Mayer, H. Mannstein, U. Hamann, R. Meerkötter (help with Meteosat, MeCiDa, LibRadTran), M. Wirth, S. Rahm (lidar), C. Voigt, T. Jurkat, H. Schlager et al. (CONCERT), F. Holzäpfel (P2P model), A. Dörnbrack, C. Keil, J. Dahl, and A. Tafferner (for access to NWP data), and K. Gierens, I. Sölch, and S. Unterstraßer (modelling). Moreover, important meteorological data and air traffic data were provided by DWD, ECMWF, DFS, and EUROCONTROL. This research is part of the DLR-project “Climate-compatible Air Transport System” (CATS).

REFERENCES

- Adelfang, S. I., 1971: On the relations between wind shears over various altitude intervals. *J. Appl. Meteorol.*, 10, 156-159.
- Dürbeck, T. and T. Gerz, 1996: Dispersion of aircraft exhausts in the free atmosphere. *J. Geophys. Res.*, 101, 26007-26015.

- Eyers, C. J., D. Addleton, K. Atkinson, et al., 2005: AERO2k Global Aviation Emissions Inventories for 2002 and 2025.
- Graf, K., H. Mannstein, B. Mayer, and U. Schumann, 2009: Aviation fingerprint in diurnal cycle of cirrus over the North Atlantic. *Intern. Conf. on Transport, Atmosphere and Climate*, Aachen and Maastricht, EUR, this volume.
- Holzäpfel, F., 2006: Probabilistic Two-Phase Aircraft Wake-Vortex Model: Further Development and Assessment. *J. Aircraft*, **43**, 700-708.
- IPCC, 1999: *Aviation and the Global Atmosphere*. Cambridge Univ. Press, 373 pp.
- IPCC, 2007: *Climate Change 2007: The Physical Science Basis. Contribution of Working Group I to the Fourth Assessment Report of the Intergovernmental Panel on Climate Change*. Cambridge Univ. Press, 996 pp.
- Kärcher, B., U. Burkhardt, S. Unterstrasser, and P. Minnis, 2009: Factors controlling contrail cirrus optical depth. *Atmos. Chem. Phys.*, **9**, 6229-6254.
- Kärcher, B. and F. Yu, 2009: Role of aircraft soot emissions in contrail formation. *Geophys. Res. Lett.*, **36**, L01804.
- Konopka, P., 1995: Analytical Gaussian solutions for anisotropic diffusion in a linear shear flow. *J. Non-Equilib. Thermodyn.*, **20**, 78-91.
- Krebs, W., H. Mannstein, L. Bugliaro, and B. Mayer, 2007: Technical note: A new day- and night-time Meteosat Second Generation Cirrus Detection Algorithm MeCiDA. *Atmos. Chem. Phys.*, **7**, 6145-6159.
- Lee, D. S., G. Pitari, V. Grewe, et al., 2009: Transport impacts on atmosphere and climate: Aviation. *Atmos. Env.*, 1-57.
- Mannstein, H. and al., 2009: Smart aircraft routing – a possibility for mitigation? *Intern. Conf. on Transport, Atmosphere and Climate*, Sausen, Ed., EUR.
- Petzold, A., A. Döpelheuer, C. A. Brock, and F. Schröder, 1999: In situ observation and model calculations of black carbon emission by aircraft at cruise altitude. *J. Geophys. Res.*, **104**, 22171-22181.
- Schumann, U., 1994: On the effect of emissions from aircraft engines on the state of the atmosphere. *Ann. Geophysicae*, **12**, 365-384.
- Schumann, U., 1996: On conditions for contrail formation from aircraft exhausts. *Meteorol. Z.*, **5**, 4-23.
- Schumann, U., F. Arnold, R. Busen, J. Curtius, B. Kärcher, J. Curtius, A. Petzold, H. Schlager, F. Schröder, and K. H. Wohlfrom, 2002: Influence of fuel sulfur on the composition of aircraft exhaust plumes: The experiments SULFUR 1-7. *J. Geophys. Res.*, **107**, AAC 2-1 - AAC 2-27.
- Schumann, U. and P. Konopka, 1994: A simple estimate of the concentration field in a flight corridor. *Impact of Emissions from Aircraft and Spacecraft upon the Atmosphere. Proc. of an Intern. Sci. Colloquium, Köln (Cologne), Germany, April 18-20, 1994*, Schumann and Wurzel, Eds., DLR-Mitt. 94-06, 354-359.
- Schumann, U., P. Konopka, R. Baumann, R. Busen, T. Gerz, H. Schlager, P. Schulte, and H. Volkert, 1995: Estimate of diffusion parameters of aircraft exhaust plumes near the tropopause from nitric oxide and turbulence measurements. *J. Geophys. Res.*, **100**, 14147-14162.
- Schumann, U., B. Mayer, K. Graf, H. Mannstein, and R. Meerkötter, 2009: A parametric radiative forcing model for cirrus and contrail cirrus. *ESA Atmospheric Science Conference, Special Publication SP-676 (6 pages)*, Barcelona, Spain, 7-11 September 2009, 1-6.
- Schumann, U., H. Schlager, F. Arnold, R. Baumann, P. Haschberger, and O. Klemm, 1998: Dilution of Aircraft Exhaust Plumes at Cruise Altitudes. *Atmos. Env.*, **32**, 3097 - 3103.
- Schumann, U. and M. Wirth, 2009: Optical depth of cirrus and embedded contrails from airborne Lidar and models *Geophysical Research Abstracts*, *EGU2009-5128*, **11**, 1.
- Sussmann, R. and K. Gierens, 1999: Lidar and numerical studies on the different evolution of vortex pair and secondary wake in young contrails. *J. Geophys. Res.*, **104**, 2131-2142.
- Tompkins, A., K. Gierens, and G. Rädcl, 2007: Ice supersaturation in the ECMWF Integrated Forecast System. *Q. J. R. Meteorol. Soc.*, **133**, 53-63.
- Voigt, C., U. Schumann, T. Jurkat, and al., 2009: Detection of young contrails – selected results from the CONCERT (CONtrail and Cirrus ExpeRimenT) campaign. *Intern. Conf. on Transport, Atmosphere and Climate*, Aachen and Maastricht, EUR, this volume.

A global ship track climatology from ATSR-2: January 1999 – January 2001

A. M. Sayer^{*}, R. G. Grainger

Atmospheric, Oceanic and Planetary Physics, Department of Physics, University of Oxford, UK

E. Campmany

NASA Goddard Institute for Space Studies, New York, USA

Keywords:

ABSTRACT: Two years (January 1999 – January 2001) of data from the Along-Track Scanning Radiometer 2 (ATSR-2) aboard the satellite ERS-2 have been processed with an automatic ship track detection algorithm. The distribution of detected tracks shows similar patterns and magnitudes to another satellite-derived dataset and is consistent with locations of shipping lanes. Most tracks are detected in the North Pacific and North Atlantic, between March and August. The derived track masks have been used with ATSR-2 data from the Oxford-RAL Aerosol and Clouds (ORAC) retrieval scheme to reveal differences between track and non-track clouds. Water clouds which are part of a ship track show an approximate 50% increase in optical depth as compared to background cloud conditions (30 km or more from tracks), and a decrease in effective radius of similar magnitude. This is consistent with the first aerosol indirect (Twomey) effect.

1 INTRODUCTION

The aerosol present in the exhaust of ships can act as cloud condensation nuclei (CCN) and seed clouds in clear-sky situations, or alternatively the increase in CCN can modify the properties of existing clouds. Such resulting ship tracks are easily visible in aerial or satellite imagery, although their global spatial extent and impact on cloud properties are less well-known. Hence it is of interest to be able to quantify them.

In this work the application of an algorithm for the automatic detection of ship tracks from near-infrared Along-Track Scanning Radiometer 2 (ATSR-2) imagery, combined with retrievals of cloud microphysical properties derived from the same instrument, is discussed. The ATSR-2 instrument was launched in 1995 on the satellite ERS-2 and measures radiance at 7 wavelengths in the visible and infrared; nadir-view measurements from the 0.67, 0.87, 1.6, 10.8 and 12.0 μm channels are used in the track detection and cloud retrieval algorithms. At present, data from January 1999 to January 2001 have been processed with the ship track detection algorithm.

2 TRACK DETECTION AND FILTERING

The automated ship-track detection algorithm is described in detail by Campmany et al., (2009). It uses ATSR-2 1.6 μm data gridded to 3 km by 4 km pixels to find straight ‘ridgelets’ of higher intensity than their neighbours. These ridgelets are then connected via a set of connectivity rules, and are deemed to be ship tracks if sufficiently long. Additional constraints, such as the absolute 1.6 μm intensity of the pixels and their infrared brightness temperatures, are employed to ensure that the detected ridgelets represent low-lying cloud.

Detected tracks are then filtered using data from the Oxford-RAL Aerosol and Clouds (ORAC) retrieval scheme, processed under the framework of the Global Retrieval of ATSR Cloud Parameters and Evaluation (GRAPE) project (Poulsen et al., in prep., Sayer et al., in prep.). The ORAC data provides (with associated uncertainty estimates and quality control information) for each

^{*} Corresponding author: Andrew Sayer, University of Oxford – Clarendon Laboratory, Parks Road, Oxford, OX1 3PU. Email: sayer@atm.ox.ac.uk

cloudy pixel estimates of the cloud optical depth, effective radius, water path, and cloud-top pressure (also converted to height and temperature), along with information on whether the cloud consists of water droplets or ice crystals. The track detection is performed at 3 km by 4 km resolution as the retrieval of cloud properties is performed at this scale. The ORAC algorithm has been applied to the whole ATSR-2 dataset and is currently being applied to the similar Advanced ATSR (AATSR) instrument, launched in 2002 as the successor instrument to ATSR-2.

Pixels flagged as potential tracks by the automatic algorithm are then confirmed as track pixels if they correspond to successful water cloud retrievals with a cloud-top height lower than 1 km. This extra step helps to remove false positives from the detections.

3 DISTRIBUTION OF DETECTED TRACKS

The annual mean fractional coverage of ship tracks is shown in Figure 1. Tracks are most frequently detected in the Northern Atlantic and Pacific oceans, where annual mean coverage may reach 0.3 % in some regions. This distribution of tracks is consistent with known heavy shipping traffic in these regions (Endrensen et al., 2003) although shipping lanes elsewhere in the world without track detections are a consequence of the meteorology, with track formation requiring low warm, moist air. The distribution is also consistent with the results of Schreier et al., (2007) who detected ship tracks in AATSR data for the year 2004.

Track frequency was found to exhibit a seasonal cycle, with more tracks detected in the Summer hemisphere (particularly in the Northern Hemisphere between March and August). This is again consistent with Schreier et al., (2007); as shipping traffic does not show this seasonal behaviour, this is further evidence for the meteorological dependence of ship track occurrence.

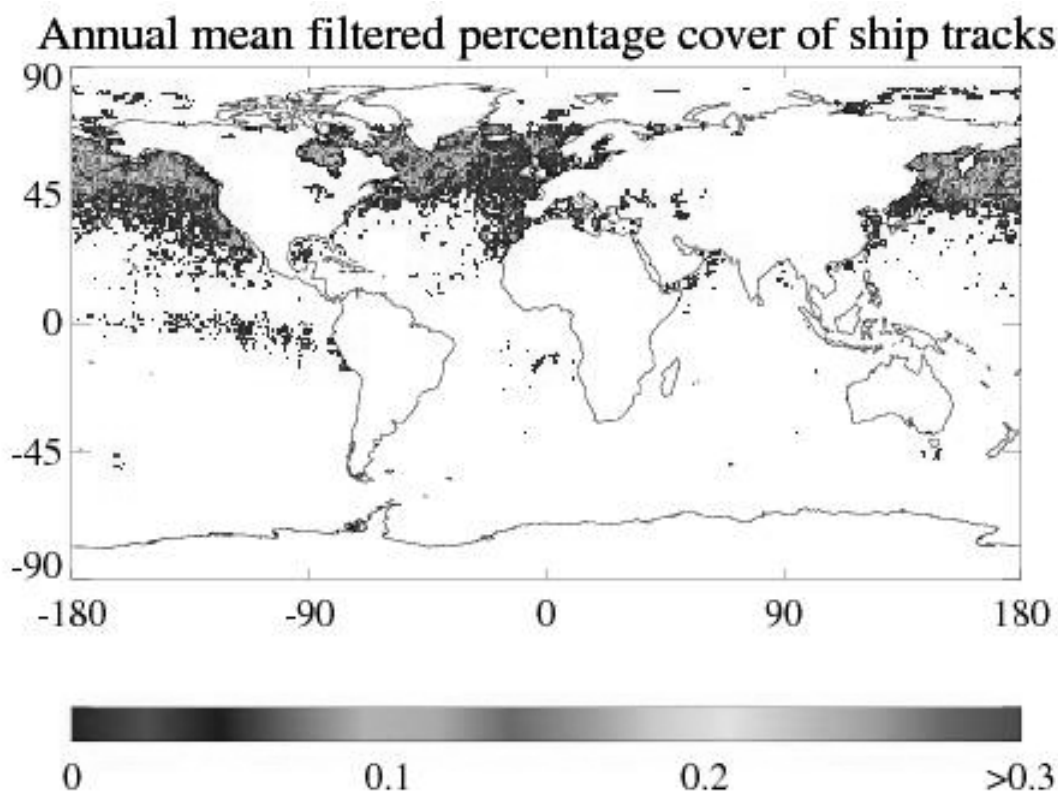


Figure 1. Annual mean percentage cover of ship tracks determined for the period January 1999-January 2001, after the automated detection algorithm and ORAC cloud retrieval filter have been applied.

4 PROPERTIES OF TRACK AND NEAR-TRACK CLOUDS

Together with the track mask, the ORAC cloud retrieval data enable the comparison of ship track properties with those of nearby cloud. This allows the assessment of the impact of shipping on ex-

isting cloud decks (although does not directly inform about the properties of new clouds seeded in otherwise cloud-free conditions).

For each orbit containing ship tracks, the mean cloud optical depth, effective radius, and liquid water path are calculated for retrievals flagged as being parts of tracks. Then, the same calculation is done for water cloud retrievals at increasing distances from the nearest pixel flagged as a track, in 4 km distance increments (e.g. 0–4 km, 4–8 km). Finally the ratio between the mean cloud property for track pixels and that for cloud properties for each distance increment are found. As ship tracks tend to be geographically clustered and so subject to similar background meteorological conditions, calculating these means on an orbit basis, rather than the more difficult task of by individual tracks, is not expected to influence the comparison.

This process is repeated for each orbit containing tracks to form a mean distance profile; Figure 2 shows the relative cloud optical depth moving away from tracks, Figure 3 the relative cloud effective radius, and Figure 4 the relative cloud water path. These figures show that the tracks have a higher cloud optical depth and lower effective radius than background conditions (where the background, taken at the point at which the curves flatten, is approximately 30 km from the nearest track pixel). The tracks show an enhancement of the order of 50 % in optical depth and decrease of a similar amount (although not quite as pronounced) in effective radius as compared to these background values. This result is consistent with the first aerosol indirect effect (also called the Twomey effect or cloud albedo effect) that the aerosol from the ship's exhaust leads to a higher number of smaller cloud droplets.

The liquid water path, shown in Figure 4, is approximately constant but shows a hint of enhancement near tracks. Liquid water path is calculated from the product of optical depth and effective radius and this enhancement is an indicator of the stronger response of cloud optical depth than effective radius. It is not clear whether the enhancement is real, which could be due to increased water content from convective rising of air in the ship's path, or a retrieval artefact.

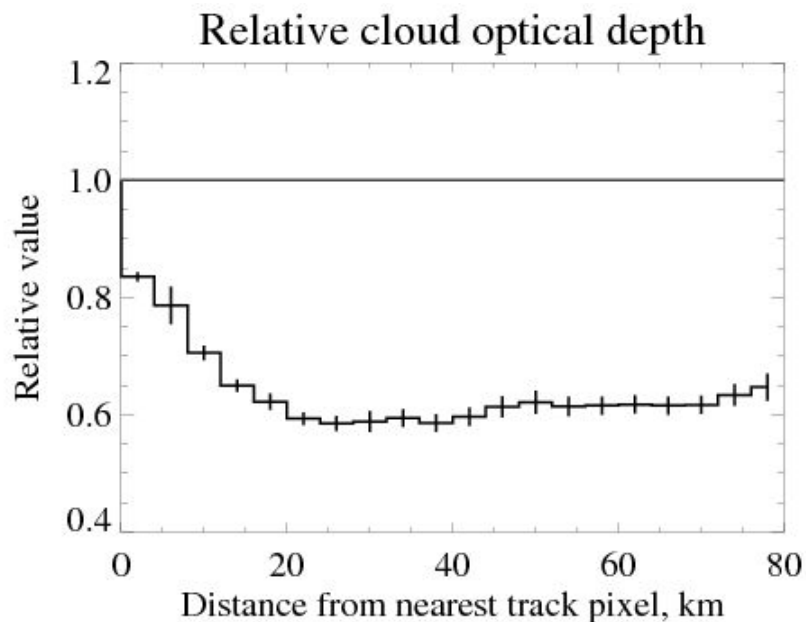


Figure 2. Relative cloud optical depth as a function of distance from nearest track pixel. The error bars indicate the standard error on each distance increment. The solid grey line indicates a ratio of 1.

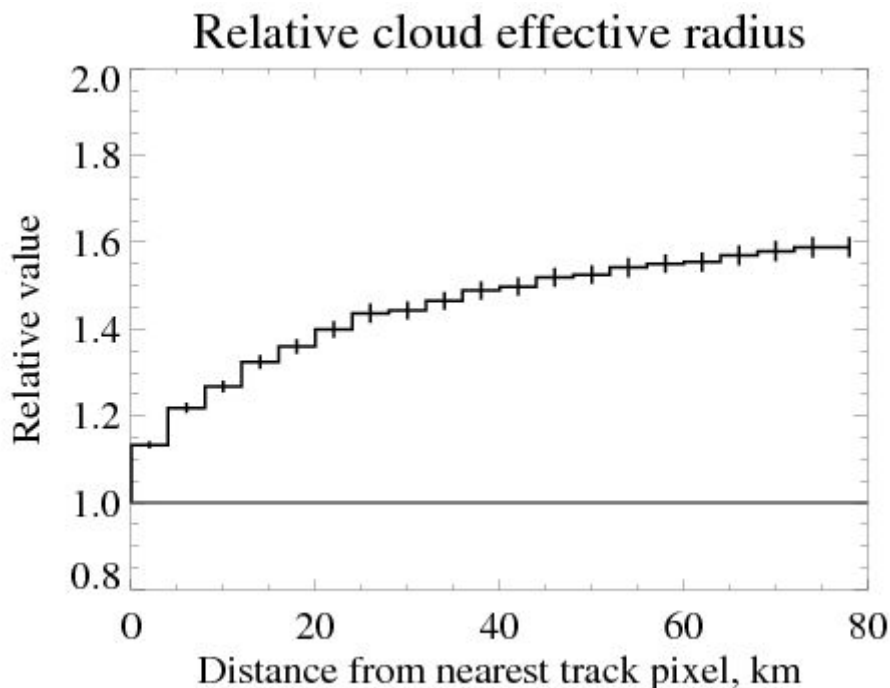


Figure 3. Relative cloud effective radius as a function of distance from nearest track pixel. The error bars indicate the standard error on each distance increment. The solid grey line indicates a ratio of 1.

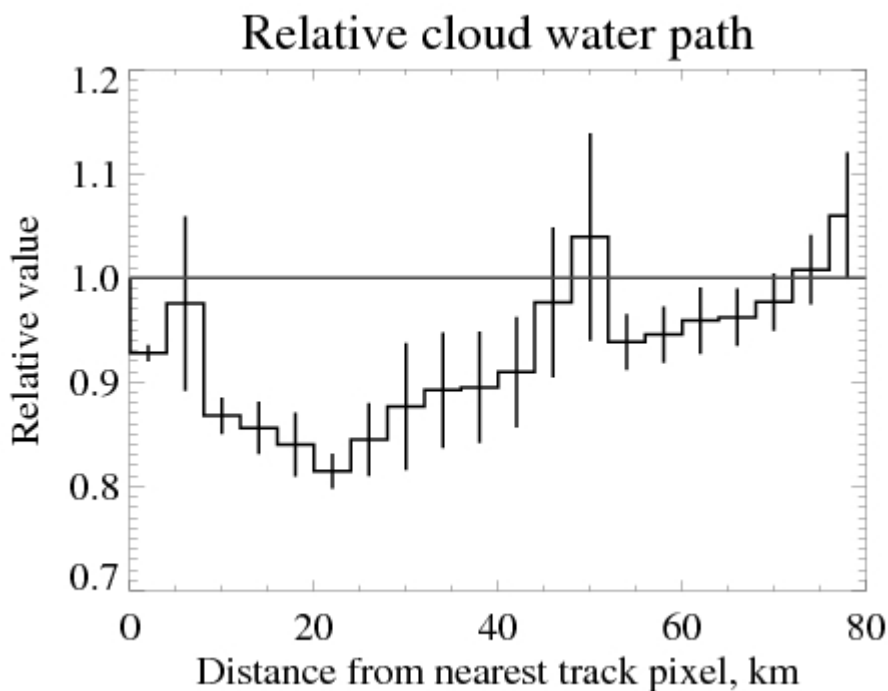


Figure 4. Relative cloud liquid water path as a function of distance from nearest track pixel. The error bars indicate the standard error on each distance increment. The solid grey line indicates a ratio of 1.

5 CONCLUSIONS

An automatic algorithm for the detection of ship tracks has been applied to two years of data from ATSR-2. The distribution of detected tracks is consistent with known patterns of shipping, and another satellite dataset of ship track frequency.

The change of cloud optical depth, effective radius and liquid water path has been examined as a function of distance from ship tracks. This revealed an approximate 50 % increased of optical depth

and a decrease of effective radius of slightly smaller magnitude as compared to background conditions 30 km or more away. This is a signature of the first aerosol indirect effect on clouds. Liquid water path showed signs of a small enhancement in and near tracks although the reasons for this are not certain.

Although at an early stage, this work demonstrates the capability to monitor ship track occurrence and properties from space. In the future this algorithm will be improved and applied to the whole (A)ATSR record to give a 13-year or longer record of ship tracks, which could be used to further investigate aerosol indirect effects, examine trends in shipping and ship-induced cloudiness and estimate the radiative forcing of ship tracks.

REFERENCES

- Campmany, E., R. G. Grainger, S. M. Dean, and A. M. Sayer, 2009: Automatic detection of ship tracks in ATSR-2 satellite imagery. *Atmos. Chem. Phys.*, *9*, 1899-1905.
- Endresen, O., E. Sørsgard, J. K. Sundet, S. B. Dalsøren, I. S. Isaksen, T. F. Berglen, and G. Gravir, 2003. Emission from international sea transportation and environmental impact. *J. Geophys. Res.*, *108*, D17.
- Poulsen, C. A., E. Campmany, R. G. Grainger, A. M. Sayer, R. Siddans, and G. E. Thomas, in prep. The GRAPE cloud retrieval algorithm.
- Sayer, A. M., E. Campmany, R. G. Grainger, C. A. Poulsen, R. Siddans, and G. E. Thomas, in prep. Validation of GRAPE cloud products.
- Schreier, M., H. Mannstein, V. Eyring, and H. Bovensmann, 2007. Global ship track distribution and radiative forcing from 1 year of AATSR data. *Geophys. Res. Lett.*, *34*, L17814.

Risk assessment of contrail formation using AIRS, MOZAIC and AERO2k databases

N. Lamquin^{*}, C.J. Stubenrauch, S. Cros

Laboratoire de Météorologie Dynamique, Ecole Polytechnique, CNRS/IPSL, Palaiseau, France

H. Smit

Forschungszentrum Jülich, Institut für Chemie der belasteten Atmosphäre (ICG2), Jülich, Germany

Keywords: potential contrail occurrence, satellite observations

ABSTRACT: Ice supersaturation is a condition for contrails to persist and to induce additional cloud coverage. We use 6 years of the Atmospheric InfraRed Sounder (AIRS) data to determine the frequency of occurrence of potential persistent contrails over the globe. Since the relative humidity is retrieved over atmospheric layers of about 2 km depth, we use collocated data from the Measurements of OZone and water vapour by in-service AIRbus airCRAFT experiment (MOZAIC) to develop a correction algorithm for a better estimation of the frequency of ice supersaturation using the AIRS data. In addition, the AIRS cloud properties, retrieved at Laboratoire de Météorologie Dynamique (LMD), help to determine the occurrence of situations where persistent contrails would have the highest radiative impact. The AERO2k database, a global monthly inventory of aircraft traffic for the year 2002, is used to provide insight of the role played by the air traffic density.

1 INTRODUCTION

Condensation trails from aircrafts have a potential impact on the Earth's radiation budget by forming ice clouds in the upper troposphere. Ice supersaturation is a condition for contrails to persist and to induce additional high cloud coverage. We use atmospheric profiles of specific humidity and temperature from AIRS L2 data to determine relative humidity RH_i over pressure layers with a depth of 50 or 100 hPa (corresponding to about 2 km) in the upper troposphere. Since humidity can only be determined as an integrated property over an atmospheric layer from IR sounders, where the depth of the layers depends on the spectral resolution of the instrument, this prevents the detection of ice supersaturated portions shallower than the vertical resolution. By collocating the AIRS relative humidity profiles with measurements from the MOZAIC experiment, the latter were taken at specific flight levels, we were able to develop a correction algorithm for a better estimation of the frequency of ice supersaturation when using the AIRS data. This algorithm determines the probability of ice supersaturation occurrence within a given AIRS profile, even when the integrated relative humidity determined by AIRS is lower than saturation (100%). The AIRS-LMD cloud property retrieval (Stubenrauch et al., 2008, 2009) helps to identify situations where persistent contrails would have the highest radiative impact (over clear and mostly clear situations). Frequency of occurrence of these situations is determined over the AIRS pressure layers in the upper troposphere. The AERO2k database, a global monthly inventory of aircraft traffic for the year 2002, is used to integrate these frequencies by means of the density of the global air traffic. It identifies regions and seasons with highest risk of persistent contrail formation, where the impact on climate is the largest.

2 DATA HANDLING

Since May 2002 the AIRS instrument (Chahine et al., 2006) onboard the polar orbiting satellite Aqua provides very high spectral resolution measurements of Earth emitted radiation in three spectral bands (3.74-4.61 micron, 6.20-8.22 micron and 8.80-15.40 micron) from 2378 channels, at 1:30

^{*} *Corresponding author:* Nikolas Lamquin, Laboratoire de Météorologie Dynamique CNRS/IPSL CNRS/IPSL LMD Ecole Polytechnique 91128 Palaiseau France Email: nicolas.lamquin@gmail.com

and 13:30 local time. The spatial resolution of these measurements is 13.5 km at nadir. Nine AIRS measurements (3x3) correspond to one footprint of the Advanced Microwave Sounder Unit (AMSU). AIRS L2 standard products include temperature at 28 pressure levels from 0.1 hPa to the surface and water vapour mixing ratios in 14 pressure layers from 50 hPa to the surface (Susskind et al., 2003, 2006). These atmospheric profiles were retrieved from cloud-cleared AIRS radiances (Chahine et al., 2006) within each AMSU footprint, at a spatial resolution of about 45 km. We use version 5 of AIRS L2 data and retrieve relative humidity RH_i in five pressure layers, 150-200, 200-250, 250-300, 300-400, and 400-500 hPa, as in Lamquin et al., 2009. Cloud properties (pressure and effective emissivity) have been retrieved at LMD and evaluated with CALIPSO data (Stubenrauch et al., 2008, 2009). This cloud climatology covers the whole globe over a period from 2003 - 2008 and also allows a distinction between clear and cloudy situations. This enables us to consider climatological situations nesting potential contrails where they have the highest radiative impact (over mostly clear areas).

The MOZAIC experiment (Marenco et al., 1998) gathered temperature, pressure and water vapor from commercial airplanes measurements over the period August 1994 - December 2007. Compared to the relative humidity determined from AIRS over pressure layers, these measurements were taken at specific levels (at flight altitudes). For detecting ice supersaturation in the upper troposphere we will use relative humidity over ice RH_{im} as derived in Gierens et al. (1999). We have collocated these data with the AIRS data to determine a correction algorithm for the detection of ice supersaturation within the AIRS data. The implementation of this algorithm gives a better estimation of the occurrence of ice supersaturation and therefore of potential persistent contrails. The EU Fifth Framework Programme project AERO2k (Eyers et al., 2004) provides a global monthly inventory of flown distance for civil and military aircrafts in a 1° latitude x 1° longitude grid and with a vertical resolution of 500 feet (about 150 m) for the year 2002. From these data we have determined the air traffic density within the AIRS pressure layers over which our analyses are made.

3 AIRS-MOZAIC SYNERGY FOR A BETTER ESTIMATION OF THE FREQUENCY OF OCCURRENCE OF ICE SUPERSATURATION

Kahn et al. (2008) and Lamquin et al. (2008) have shown that the AIRS vertical resolution limits the estimation of ice supersaturation occurrence within a pressure layer. Lamquin et al. (2009) suggest a s-shaped probability function of the occurrence of ice supersaturation within an atmospheric pressure layer as function of the relative humidity averaged over the whole layer (in this case RH_{ia}). Such an s-function is certainly dependent on the vertical resolution. The collocation of ice supersaturation detected by MOZAIC at a certain level with the relative humidity determined from AIRS over a pressure layer permits to build such a function. We introduce uncertainties based on the MOZAIC uncertainties of $\pm 10\%$ and the relationship found (Fig.1) is shown for occurrences of RH_{im} higher than 90, 100 or 110% (Fig. 1).

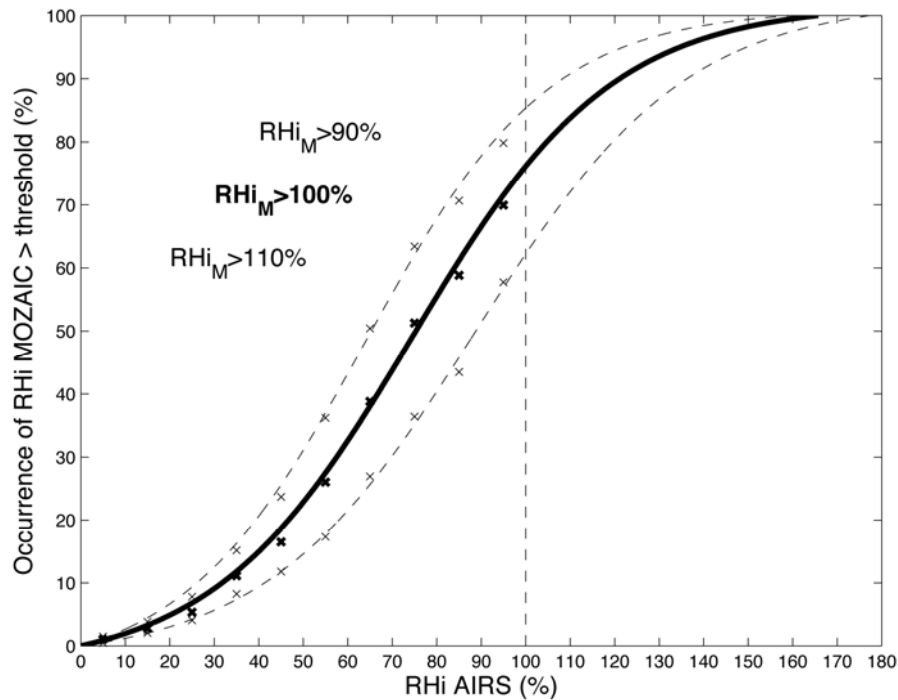


Figure 1: S-shaped functions of the probability of occurrence of ice supersaturation detected by MOZAIC as a function of the relative humidity determined from AIRS. Thresholds for the detection of ice supersaturation are 90%, 100%, or 110 %.

We observe the following: 1) a significant probability of occurrence of ice supersaturation within the AIRS pressure layer is found even when RH_{ia} is smaller than 100%. This is expected as Kahn et al. (2008) and Lamquin et al. (2008) have already shown that very shallow ice clouds are concomitant with low RH_{ia} . 2) the occurrence of ice supersaturation found by MOZAIC is only about 75% for RH_{ia} values around saturation. This can first be explained by the fact that the MOZAIC flight level does not always coincide with the altitude of the ice supersaturation layer within the AIRS pressure layer. In addition, there can be an effect of the uncertainties related to the determination of the relative humidity within the AIRS data. Lamquin et al. (2009) show that this uncertainty can reach 30% for RH_{ia} around saturation.

The s-function is then applied to the AIRS data in order to estimate the ice supersaturation occurrence over each AIRS pressure layer between 150 and 500 hPa. A weighting by the average flight altitude from the AERO2k database provides an integrated view of ice supersaturation occurrence at air traffic flight altitude (here over clear and partly cloudy situations, Fig.2). The map compares well to the results of Gierens et al. (2000) and extends their result to the whole globe.

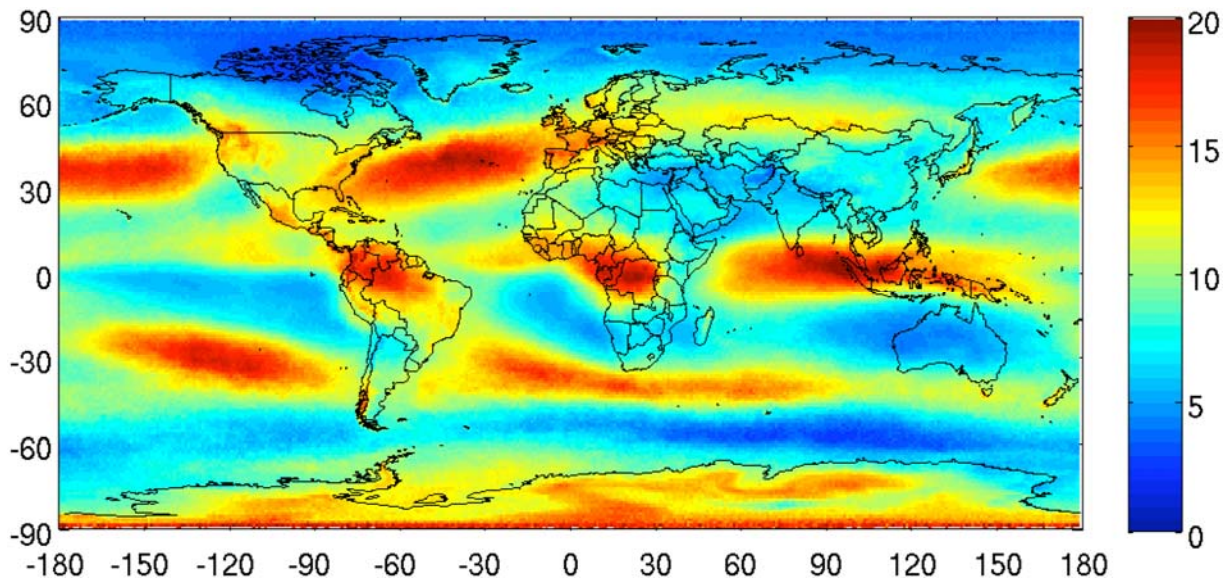


Figure 2: Global frequency of occurrence of ice supersaturation for clear and partly cloudy situations over the years 2003-2008 and integrated by the mean flight altitude in the upper troposphere.

4 RISK ASSESSMENT OF CONTRAIL FORMATION

Persistent contrails have the largest radiative effect over clear skies or situations with a low cloud amount (Stuber and Forster, 2007). It is possible to establish a separation between low and high cloudiness using the AIRS cloud properties. This, in addition to the Schmidt-Appleman criterion for the formation of contrails (Schumann, 1996), leads to a global climatology of the frequency of occurrence of persistent potential contrails as proposed, for example, in Sausen et al. (1998). Again, the results (Fig.3) are produced over AIRS pressure layers and the average flight altitude provides an integrated view of the global potential persistent contrail frequency of occurrence. The results compare well to Sausen et al. (1998).

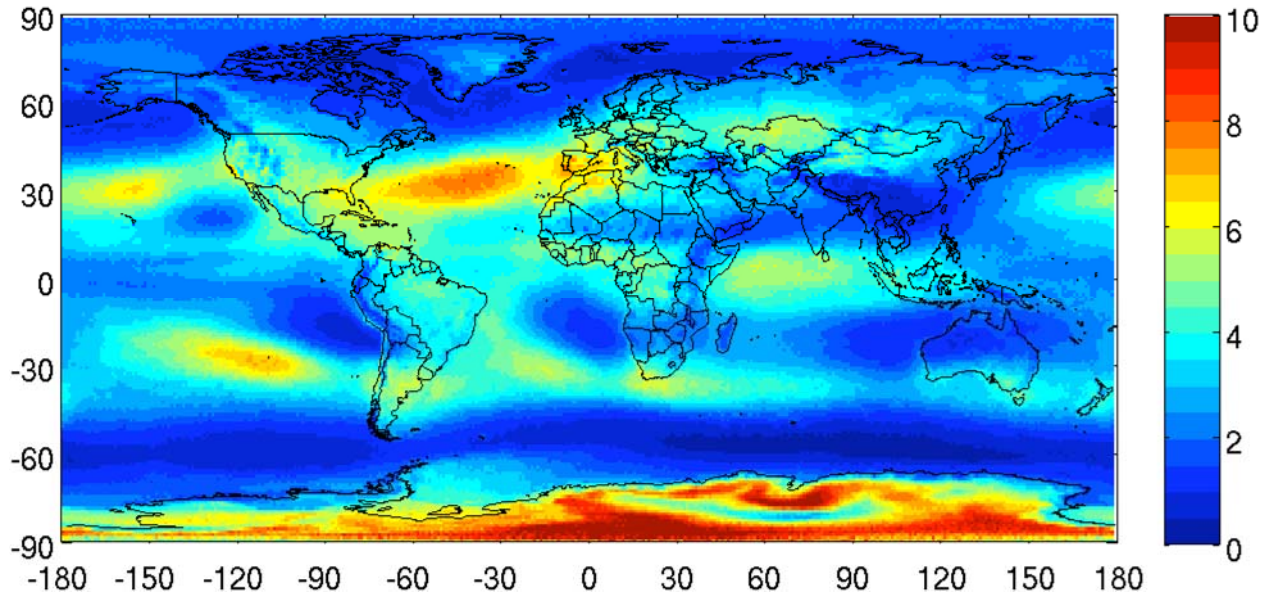


Figure 3: Global frequency of occurrence of potential persistent contrails having an impact on climate over the years 2003-2008 and integrated by the mean flight altitude in the upper troposphere.

Now, the AERO2k database not only provides vertical density of the air traffic. The distance flown by aircrafts forming contrails is proportional to the additional cloud coverage induced by contrails (Gierens, 1998). Accounting for the whole (horizontal and vertical) air traffic density, along with the climatological risk of formation, persistence and impact of contrails, provides a comparison between the total air traffic in the upper troposphere and the total air traffic in the upper troposphere producing contrails.

Both results (Fig.4) are normalized by the highest value over the globe. We see that the North-Atlantic Flight Corridor (NAFC) exhibits a second branch of comparable risk of formation of persistent contrails having an impact on climate. This effect is induced by the much higher potential contrail frequency of occurrence despite the lower air traffic density in the southern region of the NAFC.

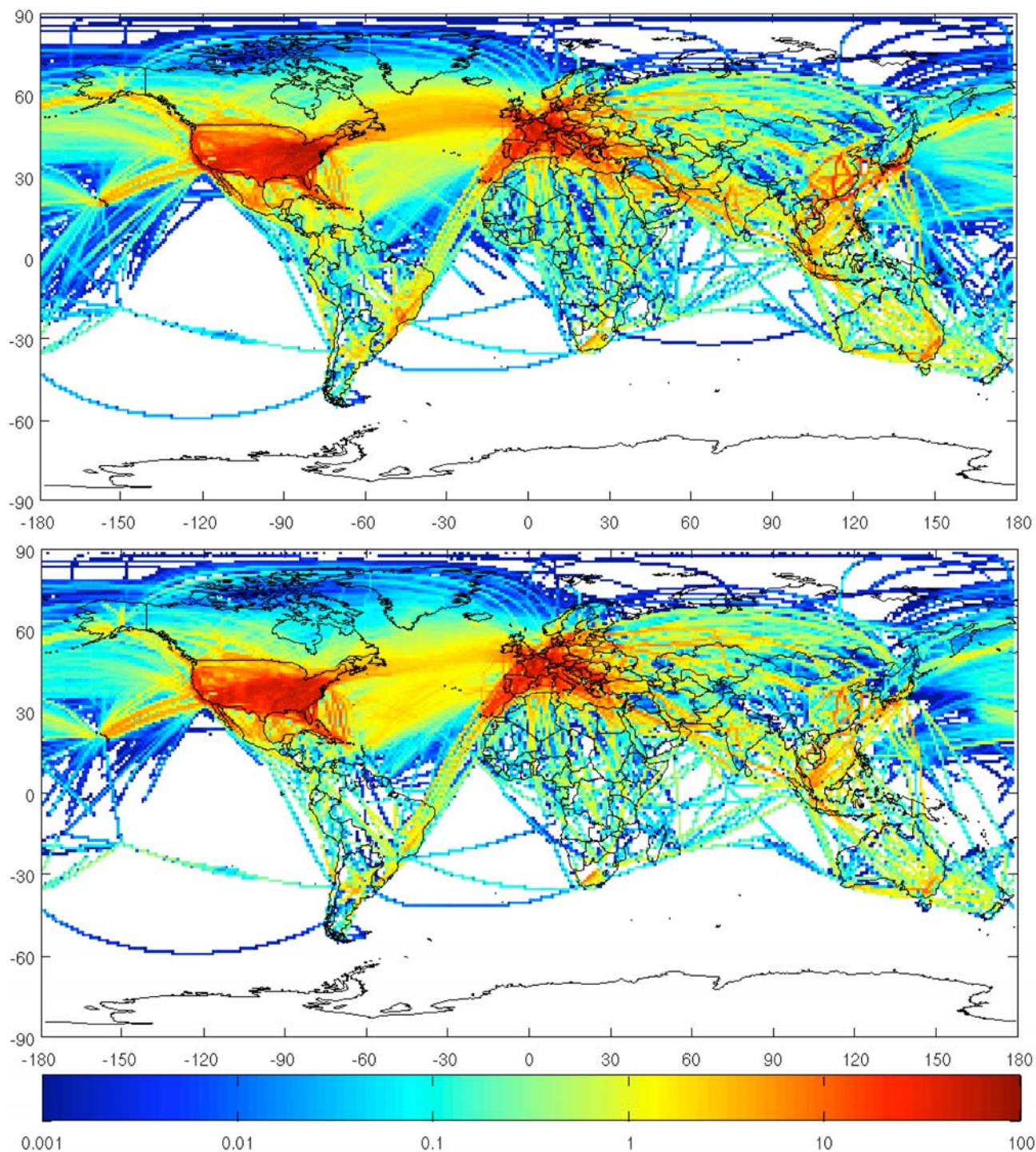


Figure 4: Density of air traffic in the upper troposphere (top) and density of potential persistent contrails having an impact on climate (bottom).

5 CONCLUSIONS

The synergy of ice supersaturation detection from MOZAIC and relative humidity profiles from AIRS was used to build a correction algorithm for a better determination of occurrence of ice supersaturation in the upper troposphere. Ice supersaturation occurrence over pressure layers in the upper troposphere is determined by AIRS over the whole globe over 6 years and expands regional MOZAIC results.

The combination with the AIRS-LMD cloud properties and the application of the Schmidt-Appleman criterion on AIRS relative humidity provides a climatology of the risk of formation, persistence and impact on climate of contrails. Occurrence of potential contrails has been determined

for situations with largest impact (zonal means of about 5% \pm 2%). There exists a rough agreement with analyses using ECMWF reanalyses, but AIRS provides more detailed horizontal structures. Weighted by air traffic density, provided by the AERO2k database, one result shows that the NAFC exhibits two branches of the air traffic with comparable risk of contrail impact on climate despite the lower air traffic density in the southern branch.

In the future we will consider comparisons with observations of contrails (Vazquez-Navarro et al., 2009) and more recent climatologies of ice supersaturation and potential contrails from models (Burkhardt et al., 2008) and radiosoundings (Dickson et al., 2009).

REFERENCES

- Burkhardt, U., B. Kärcher, M. Ponater, K. Gierens, and A. Gettelman, 2008 : Contrail cirrus supporting areas. *Geophys. Res. Lett.* **35**, L16808, doi :10.1029/2008GL034056.
- Dickson, N., K. Gierens, H. Rogers, and R. Jones, 2009 : Vertical spatial scales of ice supersaturation. *This conference proceedings*.
- Chahine, M.T., and Coauthors, 2006 : AIRS : Improving weather forecasting and providing new data on greenhouse gases. *Bull. Amer. Meteor. Soc.* **87**, 911-926.
- Eyers, C.J., P. Norman, J. Middel, M. Plohr, K. Atkinson, and R.A. Christou, 2004 : AERO2k global aviation emission inventories for 2002 and 2025. QinetiQ Ltd. Retrieved from http://www.aero-net.org/pdf-docs/AERO2K_Global_Aviation_Emissions_Inventories_for_2002_and_2025.pdf.
- Gierens, K., 1998 : How the sky gets covered with contrails. *Meteorol. Z.* **7**, 181-187.
- Gierens, K., U. Schumann, M. Helten, H.G.J. Smit, and A. Marengo, 1999 : A distribution law for relative humidity in the upper troposphere and lower stratosphere derived from three years of MOZAIC measurements. *Ann. Geophys.* **17**, 1218-1226.
- Gierens, K., U. Schumann, M. Helten, H. Smit, and P.-H. Wang, 2000 : Ice-supersaturated regions and sub-visible cirrus in the northern midlatitudes upper troposphere. *J. Geophys. Res.* **105**, D18, 22743-22753.
- Kahn, B.H., C.K. Liang, A. Eldering, A. Gettelman, Q. Yue, and K.N. Liou, 2008 : Tropical thin cirrus and relative humidity observed by the Atmospheric Infrared Sounder. *Atmos. Chem. Phys.* **8**, 1501-1518.
- Lamquin, N., C.J. Stubenrauch, and J. Pelon, 2008 : Upper tropospheric humidity and cirrus geometrical and optical thickness : relationships inferred from one year of collocated AIRS-CALIPSO data. *J. Geophys. Res.* **113**, D00A08, doi :10.1029/2008JD010012.
- Lamquin, N., K. Gierens, C.J. Stubenrauch, and R. Chatterjee, 2009 : Evaluation of upper tropospheric humidity forecasts from ECMWF using AIRS and CALIPSO data. *Atmos. Chem. Phys.* **9**, 1779-1793.
- Marengo, A., V. Thouret, P. Nédélec, H.G. Smit, M. Helten, D. Kley, F. Karcher, P. Simon, K. Law, J. Pyle, G. Poschmann, R. Von Wrede, C. Hume, and T. Cook, 1998 : Measurements of ozone and water vapour by in-service Airbus aircraft : the MOZAIC airborne program, an overview. *J. Geophys. Res.* **103**, 25631-25642.
- Sausen, R., K. Gierens, M. Ponater, and U. Schumann, 1998 : A diagnostic study of the global distributions of contrails part I : present day climate. *Theor. Appl. Climatol.* **61**, 127-141.
- Schumann, U., 1996 : On conditions for contrail formation from aircraft exhausts. *Meteorol. Z.* **5**, 4-23.
- Stubenrauch, C.J., S. Cros, N. Lamquin, R. Armante, A. Chédin, C. Crevoisier, and N.A. Scott, 2008 : Cloud properties from AIRS and evaluation with CALIPSO. *J. Geophys. Res.* **113**, D00A10, doi :10.1029/2008JD009928.
- Stubenrauch, C.J., S. Cros, A. Guignard, and N. Lamquin, 2009 : A 6-year global climatology from the Atmospheric InfraRed Sounder aboard the Aqua satellite : statistical analysis in synergy with CALIPSO and Cloudsat. *In prep.*
- Stuber, N., and P. Forster, 2007 : The impact of diurnal variations of air traffic on contrail radiative forcing. *Atmos. Chem. Phys.* **7**, 3151-3162.
- Susskind, J., C. Barnet, and J. Blaisdell, 2003 : Retrieval of atmospheric and surface parameters from AIRS/AMSU/HSB data in the presence of clouds. *IEEE Trans. Geosci. Remote Sens.* **41**, 390-409.
- Susskind, J., C. Barnet, J. Blaisdell, L. Iredell, F. Keita, L. Kouvaris, G. Molnar, and M. Chahine, 2006 : Accuracy of geophysical parameters derived from AIRS/AMSU as a function of fractional cloud cover. *J. Geophys. Res.* **111**, D09S17, doi :10.1029/2005JD006272.
- Vazquez-Navarro, M., H. Mannstein, and B. Mayer, 2009 : Lifecycle of contrails. *This conference proceedings*.

Aviation emissions under climate stabilization at 450ppmv and below

H. J. Preston^{*}, L. L. Lim, D. S. Lee and P. D. Hooper

Dalton Research Institute, Department of Environmental and Geographical Sciences, Manchester Metropolitan University, Manchester, United Kingdom

ABSTRACT: The climate change objectives and policies of the European Union are based upon the concept of climate stabilization, with the premise that the climate needs to be stabilized so that temperatures increase by no more than 2°C at 2100. However, the stabilization scenarios currently published do not prescribe where emissions reductions must come from to meet the stabilization of atmospheric CO₂. If the principle of stabilization is to continue to be used as a basis of climate policies, then it will be important to address where the emissions reductions will come from, and to what extent. This paper is a first look at how aviation may or may not be compatible with stabilization. It highlights that aviation emissions have the potential to consume a significant proportion of the emissions budget under stabilization.

Keywords: Aviation, stabilization scenarios, emissions

1 INTRODUCTION

The European Union's (EU's) climate change objectives and policies are based upon the concept of climate stabilization, within which there is the assumption that the climate needs to be stabilized so that temperatures increase by no more than 2°C (CEC, 2007). This paper attempts to determine what fraction of the emissions budget the aviation sector will consume under different growth and technology scenarios for a range of climate stabilization regimes. The aviation industry has until recent years received limited attention regarding its climate impacts, and was not allocated emission targets within the Kyoto Protocol (although it was addressed in Article 2.2 which stated that emissions from aviation and marine bunker fuels should be limited or reduced (UNFCCC, 1998). However, the industry is growing strongly and is projected to do so (projections from aircraft manufacturers predict a doubling of the global civil fleet size from ~20,500 aircraft in 2006 to ~40,500 in 2026 (Airbus, 2007 in Lee *et al*, 2009: 3522)), and whilst currently the climate forcing of the emissions the industry produce are fairly small in global terms (3.5% of total anthropogenic forcing excluding the effects of cirrus clouds), this will increase along with the growth in the industry (Lee *et al*, 2009: 3528). It is evident therefore, that focus on the industry will be important in future climate change policy. Such attention has already become apparent within the UNFCCC draft negotiating text (in preparation for the COP-15 in December), with the acknowledgement that all sectors (including international aviation and shipping) should contribute to limiting emissions (UNFCCC, 2009).

2 STABILIZATION SCENARIOS

Climate stabilization scenarios use an inverse modelling approach which calculates the required emissions and their rate of change, to achieve stabilization of atmospheric CO₂ concentrations at different levels (Wigley, 2003). There are a number of climate stabilization scenarios or profiles that have been published, with the first being in 1994 when Working Group 1 (WG1) of the IPCC published a set of stabilization profiles that stabilized atmospheric CO₂ concentrations at a variety

^{*} *Corresponding author:* Holly Preston, Centre for Aviation, Transport and the Environment, Manchester Metropolitan University, United Kingdom. Email: h.preston@mmu.ac.uk

of stabilization levels from 750 ppmv to 350 ppmv (IPCC, 1994 in Manne & Richels, 1997: 254). The objective of the profiles was to demonstrate what emissions would be required to reach such stabilization. Following from the WG1 profiles Wigley, Richels and Edmonds developed an alternative set of emissions profiles with the objective of achieving the concentration targets of the WG1 profiles (using the same attainment dates), but by using a different route to stabilization (Wigley et al, 1996). These stabilization scenarios are known as the WRE scenarios. In addition to the WG1 and WRE stabilization scenarios, the Greenhouse Gas Initiative (GGI) has developed another set of scenarios using data derived from the IPCC's SRES scenarios (which have been revised to reflect new information) (IIASA Greenhouse Gas Initiative, 2006). The scenarios include 11 stabilization scenarios for 8 comparable levels, with the lowest stabilization target being 480ppmv. As this paper looks at aviation emissions under stabilization at 450ppmv and below (see Hansen et al, 2008 who posit that a stabilization down to 350 ppm may be more appropriate level to avoid dangerous climate change), the GGI scenarios will not be discussed further.

The emissions and concentration data for the WRE stabilization profiles were taken from MAGICCv5.3 (Model for the Assessment of Greenhouse-gas Induced Climate Change), which is a suite of coupled gas-cycle, climate, and ice-melt models that can determine the changes in the greenhouse gas concentrations, global mean surface temperature and sea level resulting from anthropogenic emissions including CO₂, CH₄, N₂O, VOCs and SO₂ (Wigley, 2008). Figure 1 shows the CO₂ concentration profiles of the WRE stabilization profiles for 650 ppmv down to 350 ppmv. There is a steady increase in CO₂ concentrations that then plateau/stabilize at various dates depending on the stabilization target i.e. WRE450 CO₂ concentrations stabilize at ~2065, compared with WRE350 CO₂ concentrations that stabilize at ~2140.

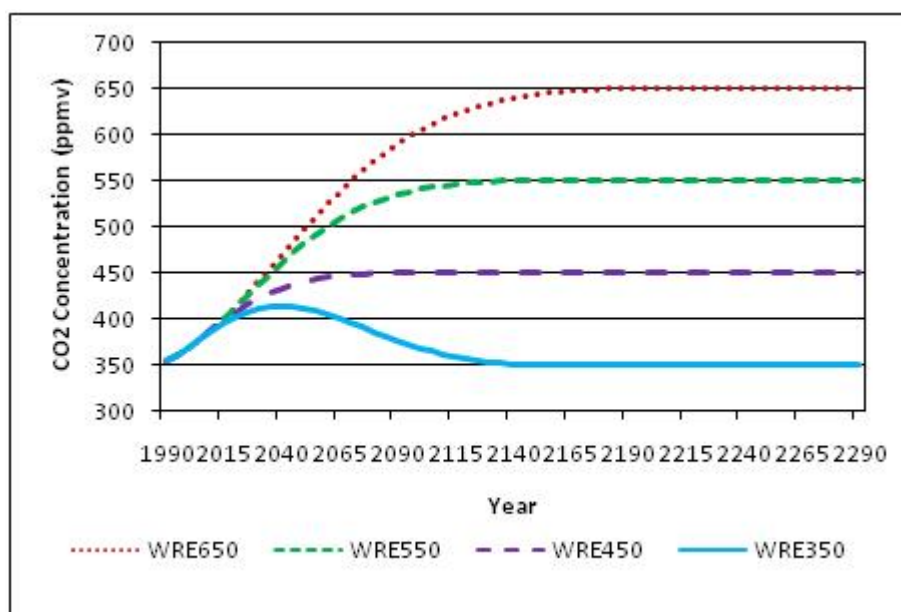


Figure 1. WRE stabilization profiles for CO₂ concentration

The corresponding emissions response for the WRE stabilization profiles are shown in Figure 2, which displays emissions for all scenarios showing a business-as-usual (BAU) pathway that then eventually declines. Again, there are different rates of decline for example, the emissions response under stabilization at 650 ppmv has a longer BAU pathway and a more gradual decline in emissions; compared with the emissions under 350 ppmv which has a very short BAU pathway and then a very rapid decline of emissions, requiring negative emissions at 2065 and then increasing again after 2140. The WRE350 profile has this negative emissions response as that is what would be required to meet the stabilization of atmospheric concentrations of CO₂ at 350 ppmv.

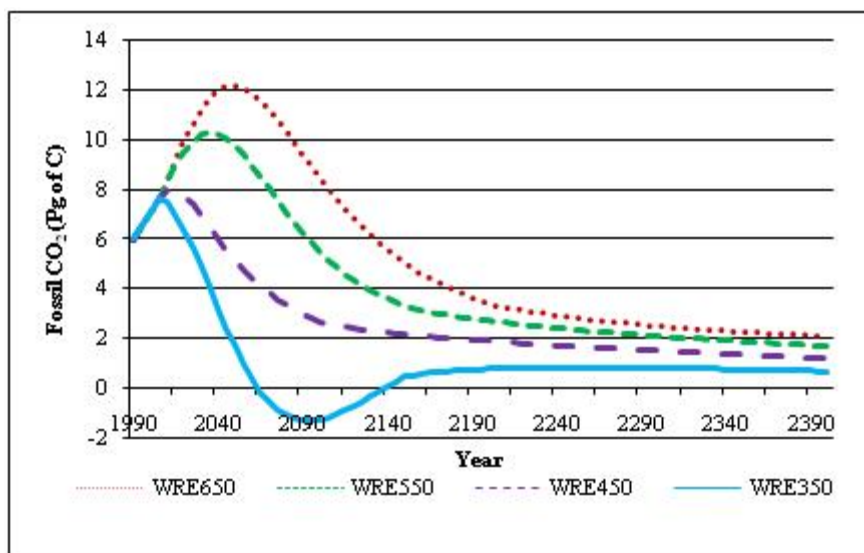


Figure 2. WRE stabilization profiles for emissions response

3 SCENARIOS OF AVIATION EMISSIONS UNDER A CLIMATE STABILIZATION REGIME

The stabilization scenarios do not prescribe from which sectors or sources that the emissions reductions must come from to meet the stabilization of atmospheric CO₂; rather they demonstrate what emissions reductions would be required to do so. If the principle of stabilization is to continue to be used as a basis of climate policies, then it will be important to address where the emissions reductions will come from, and to what extent. This paper aims to look at one part of one sector i.e. aviation emissions.

The aviation emissions data was taken from the European Commission's 6th Framework Project QUANTIFY whereby SRES-based scenarios were developed in a consistent manner for the whole transport sector (Owen & Lee, 2009). Owen and Lee (2009) have created 4 aviation scenarios that follow the assumptions of the SRES A1, A2, B1, B2 storylines. Figure 3 shows the projected aviation emissions for each pathway to 2100.

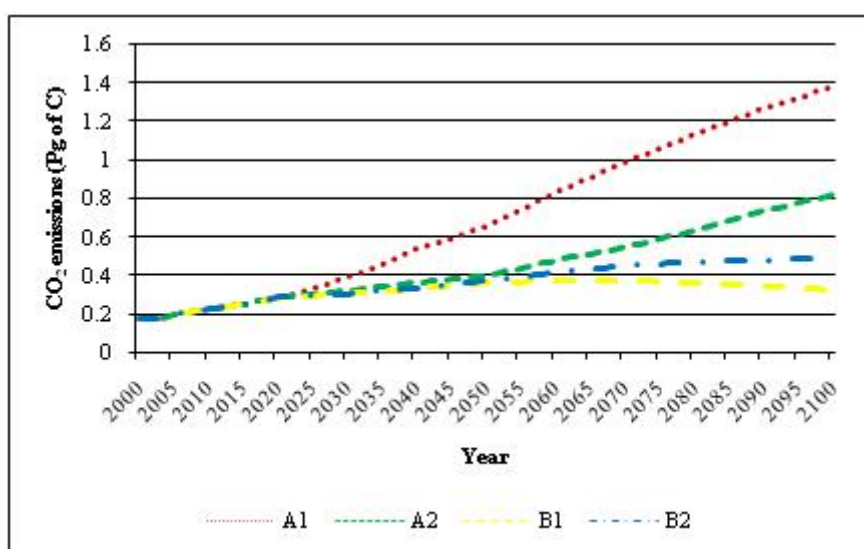


Figure 3. Projected aviation emissions pathway to 2100

Figure 3 shows that the aviation emissions pathways vary considerably depending upon the storyline assumptions. For example, the A1 emissions pathway shows a steady and significant in-

crease in the emissions reaching 1.4 Pg C yr^{-1} by 2100, especially when compared with the emissions pathway under the B1 scenario which only reaches 0.3 Pg C yr^{-1} by 2100. This is consistent with the SRES assumptions as under A1 there is an emphasis on very rapid economic growth and the rapid introduction of new technologies; compared with B1 in which there is an emphasis on environmental sustainability and the introduction of clean and resource efficient technologies (IPCC, 2000).

To compare the aviation emissions under climate stabilization policies, the CO_2 emissions of the 4 aviation scenarios were plotted with the emissions profiles of the WRE450 and WRE350 stabilization scenarios (see Figure 4). Figure 4 demonstrates that the emissions from the aviation sector will be taking an increasingly significant proportion of the total emissions under stabilization at 450 ppmv, and under 350 ppmv. The outlook is clearly unsustainable, especially under WRE350 where there is the requirement for negative emissions and aviation's emissions are set to continue to increase. Consequently, if aviation emissions were to take the path that the scenarios project, and if climate policies are based on an even more stringent stabilization target than 450 ppmv, then there is a clear incompatibility.

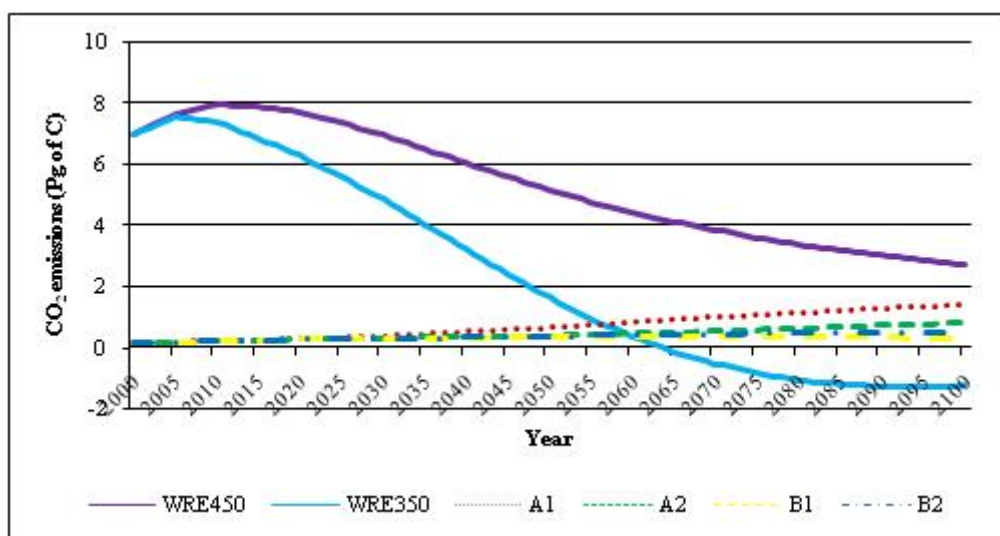


Figure 4. Projected aviation emissions to 2100 compared with WRE stabilization profiles

To demonstrate this further, Figure 5 shows the percentage aviation emissions contribution for A1, A2, B1 and B2 scenarios under the WRE450 stabilization scenario (the time-slices for 350 ppmv are not shown due to the fact that after 2055 the aviation sector takes up the entire emissions budget due to the negative emissions scenario).

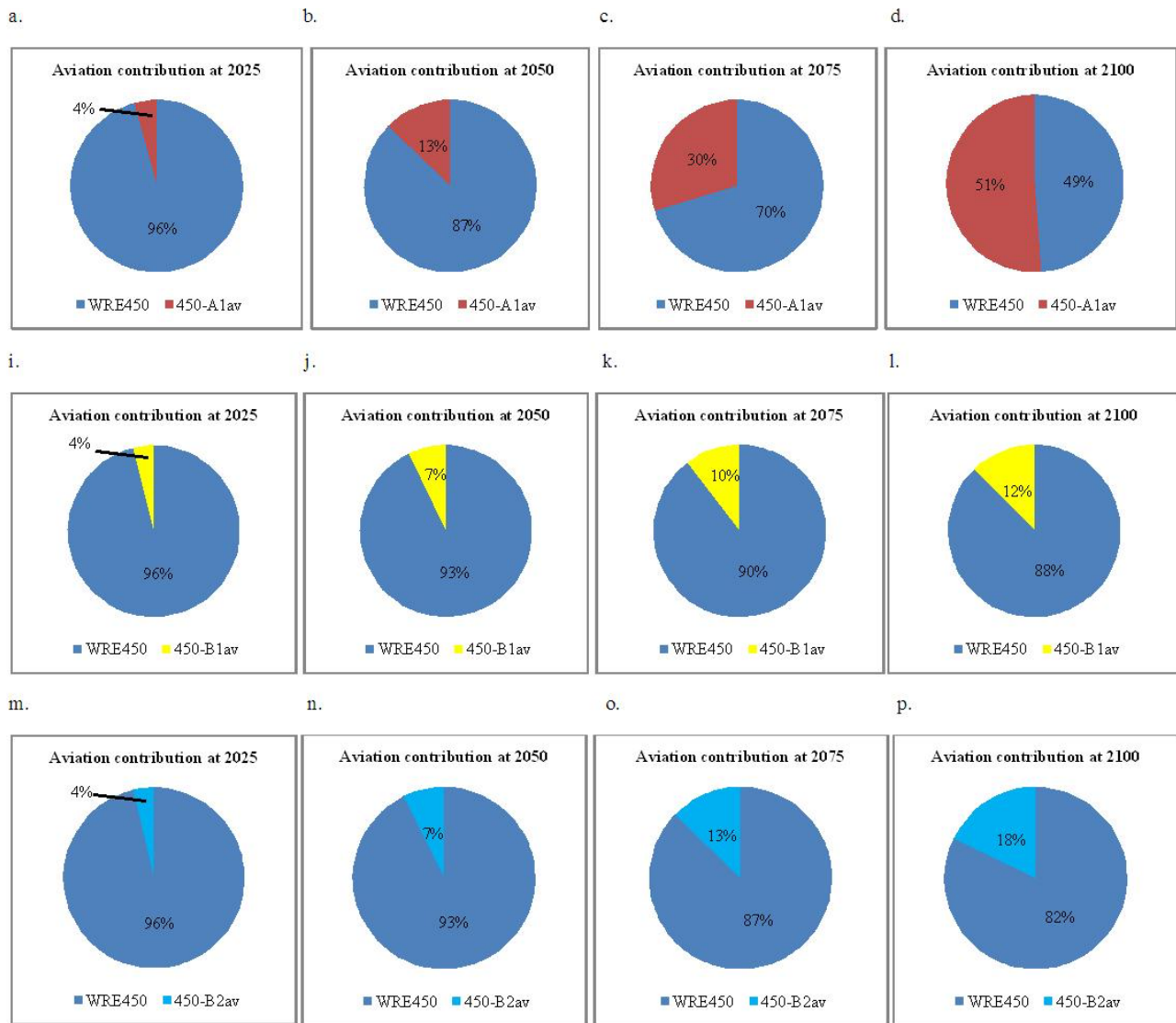


Figure 5. Percentage aviation emissions contribution for 450-A1av, 450-A2av, 450-B1av and 450-B2av scenarios under stabilization at WRE450

The pie charts in Figure 5 show the WRE emissions budget allowable under the WRE450 stabilization scenario for all sectors, with the percentage of the emissions budget that will be consumed by the aviation sector. For example, the time-slices for the 450-A1av scenario (a – d) show that aviation will take up a significantly increasing proportion of the emissions budget allowable under the stabilization regime, and by 2100 over 51% of the emissions budget will be consumed by the sector.

For the 450-B1av scenario (i – l), the percentage of emissions that will be consumed by the aviation sector is considerably smaller, reaching only 12% by 2100. This demonstrates that the feasibility or plausibility of a stabilization regime being successful may depend upon which pathway aviation takes, as some scenarios will be easier to implement when considering all the sectors. For example, under the 450-B1av scenario, there will be a larger proportion of the emissions budget available for other sectors than under the 450-A1av scenario.

4 AVIATION FORCING AND TEMPERATURE RESPONSE UNDER A CLIMATE STABILIZATION REGIME

To determine the forcing and temperature response of aviation CO₂ emissions under climate stabilization at 450 ppmv, the emissions for the 4 scenarios were run in LinClim, a linear climate response model (Lim *et al*, 2007). Figure 6 shows the temperature and response for all 4 scenarios.

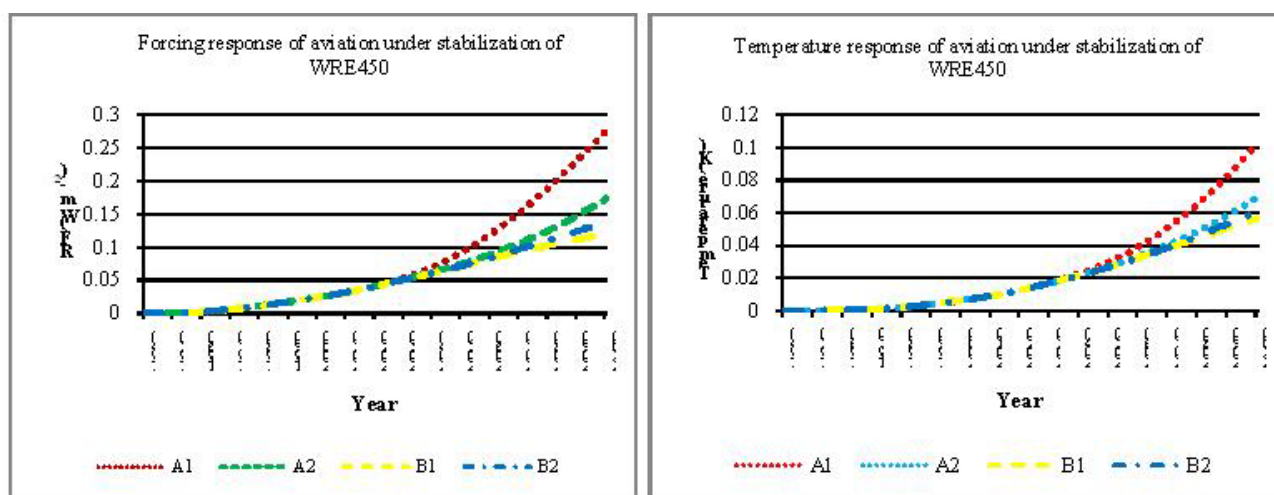


Figure 6. Forcing and temperature response of aviation under climate stabilization of WRE450

The graphs show the varying forcing and temperature response for the 4 aviation scenarios with the A1 scenario having the largest forcing and temperature increase; the temperature increasing by 0.1K in 2100. The B1 scenario has the smallest forcing and temperature response with the temperature increasing by just over 0.6K by 2100. If presented with this information alone, it could be concluded that the climatic impact from the aviation industry's emissions are minimal compared with other sectors. However, it is important to note that these data represent the temperature and forcing for CO₂ alone and aviation has other non-CO₂ RF effects. Therefore, the temperature response for the sector will be greater than the temperature response from just CO₂ alone.

5 DISCUSSION

This paper is a first look at how various aviation scenarios of growth and technological improvement may or may not be compatible with a 450 ppmv stabilization scenario. It is acknowledged that this approach uses a combination of SRES-based scenarios (A1, A2, B1, B2) along with stabilization scenarios, which might be considered to be a mix of inconsistent world outlooks. However the paper serves to illustrate the potential demand for aviation, and what may be required of aviation under policies based upon stabilization.

An important aspect of this paper is to demonstrate the use of modelled data when relating it to specific climate policies. Under EU climate policies, the aim is to reach a stabilization of greenhouse gas emissions so that temperatures do not exceed 2°C. The analysis tells the story of aviation taking an increasing and significant proportion of the emissions allowable under the stabilization profiles, a point which is of use to both the sector and other stakeholders in terms of expectations. Furthermore, the analysis enables a consideration of growth expectations of the sector versus the possibility and feasibility of emissions reductions in other sectors that still allows stabilization at 450 ppmv.

There are a number of questions that this analysis raises. Firstly, if climate policies are to be based upon the principle of climate stabilization, how is this to be achieved and how can the emissions budget be broken down between each of the sectors? One possible solution to this has been presented by Pacala and Socolow with their proposed 'Stabilization Wedges' which divides the emissions reduction budget into 7 equal wedges (representing an emissions reduction action) that could potentially be divided up between sectors or carbon reducing actions (Pacala & Socolow, 2004) e.g. transport sector could be one section/wedge.

Furthermore, as this work has demonstrated, when focusing on just one element of one sector, and only one of the greenhouse gases, under certain future pathways aviation alone has the potential to take up the significant proportion of the emissions budget. What are the potential contributions of the other sectors and the implications that they will have on policy? If this analysis were to be extended further to look at the whole transport sector under stabilization then the complexities of the issue become considerable since, for example, international shipping has similar growth expecta-

tions to 2050 (Buhaug *et al.*, 2009). Similarly, policy has mainly focused upon CO₂, if there were to be an emphasis upon the non-CO₂ emissions then again the potential climate impacts of the sector, as well as the uncertainties, are increased.

REFERENCES

- Airbus, 2007: Global Market Forecast 2006-2026. Airbus, France.
- Buhaug, Ø., Corbett, J.J., Endresen, V., Eyring, V., Faber, J., Hanayama, S., Lee, D.S., Lee, D., Lindstadt, H., Mjelde, A., Pålsson, C., Wanquing, W., Winebrake, J.J. & Yoshida, K. 2009: *Second Study on Greenhouse Gas Emissions from Ships*, International Maritime Organisation (IMO) London, UK
- CEC, 2007: *Communication from the Commission to the Council, The European Parliament, The European Economic and Social Committee, and the Committee of Regions*.
- International Institute for Applied System Analysis (IIASA), 2007: *GGI Scenario Database* available online at: <http://www.iiasa.ac.at/Research/GGI/DB/>
- Intergovernmental Panel on Climate Change (IPCC), 2000: *Special Report on Emissions Scenarios* Nakicenovic, N. & Swart, R. (Eds.), Cambridge University Press
- Hansen, J., Sato, M., Kharecha, P., Beerling, D., Berner, R., Masson-Delmotte, V., Pagani, M., Raymo, M., Royer, D.L. & Zachos, J.C. 2008: "Target Atmospheric CO₂: Where Should Humanity Aim?", *The Open Atmospheric Science Journal*, 2: 217 - 231
- Lee, D.S., Fahey, D.W., Forster, P.M., Newton, P.J., Wit, R.C.N., Lim, L.L., Owen, B. & Sausen, R. 2009: "Aviation and global climate change in the 21st century", *Atmospheric Environment*, 43: 3520 - 3537
- Lim, L.L., Lee, D.S., Sausen, R., & Ponater, M., 2007: "Quantifying the effects of aviation on radiative forcing and temperature with a climate response model", In: Sausen, R., Blum, A., Lee, D.S., & Brüning, C. (Eds.) *Proceedings of an International Conference on Transport, Atmosphere and Climate (TAC)*. Luxembourg, Office for Official Publications of the European Communities, ISBN 92-79-04583-0, 202-207
- Manne, A. & Richels, R. 1997: "On stabilizing CO₂ concentrations – cost-effective emissions reduction strategies", *Environmental Modeling and Assessment* 2: 251 - 265
- Owen, B. Lee, D.S. & Lim, L.L. 2009: "Flying into the future – aviation emissions scenarios to 2050". Submitted.
- Pacala, S. & Socolow, R. 2004: "Stabilization Wedges: Solving the climate problem for the next 50 years with current technologies", *Science*, 305
- United Nations Framework Convention on Climate Change (UNFCCC), 2009: *Ad Hoc Working Group on Long-term Cooperative Action under the Convention*, 6th Session, Bonn 1 – 12 June 2009 Available online at: <http://unfccc.int/resource/docs/2009/awglca6/eng/08.pdf>
- UNFCCC, 1998: *Kyoto Protocol to the United Nations Framework Convention on Climate Change*, available online at: <http://unfccc.int/resource/docs/convkp/kpeng.pdf>
- Wigley, T.M.L. 2008: *MAGICC/SCENGEN 5.3: User Manual (Version 2)*. Available online at: <http://www.cgd.ucar.edu/cas/wigley/magicc>
- Wigley, T.M. L. 2003: "Modelling climate change under no-policy and policy emissions pathways", *Working Party on Global and Structural Policies. OECD Workshop on the Benefits of Climate Policy: Improving Information for Policy Makers*.
- Wigley, T.M.L., Richels, R. & Edmonds, J.A. 1996: "Economics and environmental choices in the stabilization of atmospheric CO₂ concentrations", *Nature* 379: 240 - 243

Global temperature change from the transport sectors: Historical development and future scenarios

R.B. Skeie, J.S. Fuglestad^{*}, T. Berntsen, M.T. Lund, G. Myhre, K. Rypdal
CICERO – Center for International Climate and Environmental Research – Oslo, Norway

Keywords: Transport sectors, radiative forcing, temperature, historical emissions, scenarios

ABSTRACT: Transport affects climate directly and indirectly through mechanisms that cause both warming and cooling and operate on very different timescales. In this study, we calculate contributions to the historical development in global mean temperature for the main transport sectors (road transport, aviation, shipping and rail) based on estimates of historical emissions of a suite of gases, aerosols and aerosol precursors, and by applying knowledge about the various forcing mechanisms from detailed studies. Furthermore, we calculate the development in future global mean temperature for four transport scenarios consistent with the IPCC SRES scenarios. We also calculate contributions for a sensitivity test scenario and a mitigation scenario for aviation, which is consistent with the strategic research agenda of the Advisory Council for Aeronautics Research in Europe (ACARE) targets for greening of air transport.

There are large differences between the transport sectors in terms of sign and magnitude of temperature effects and with respect to the contributions from the long- and short-lived components. From pre-industrial times to year 2000, we calculate that transport in total has contributed 9% to a total net man-made warming of 0.76°C. The dominating contributor to warming is CO₂, followed by tropospheric O₃. By sector, road transport is the largest contributor; 11% of the warming in 2000 is due to this sector. Aviation has contributed 4% and rail ~1%. Shipping, on the other hand, has caused a net cooling up to year 2000, with a contribution of -7%, due to the effects of NO_x and SO₂ emissions. The total net contribution from the transport sectors to total man-made warming is ~15% in 2050, and reaches 20% in 2100 in the A1 and B1 scenarios. Throughout the 21st century, road transport remains the dominating contributor to warming, followed by aviation. In the aviation mitigation scenario, the temperature increase in 2050 is ~20% less than in the least warming scenario, B1. Due to the anticipated reduction in the sulphur content of fuels, the net effect of shipping switches from cooling to warming by the end of the century. There are significant uncertainties related to the estimates of historical and future net warming, mainly due to aerosol effects, cirrus, contrails and uncertainty in the climate sensitivity.

^{*} Corresponding author: Jan S. Fuglestad, CICERO, P.O. Box 1129, Blindern, N-0318 Oslo, Norway
Email: j.s.fuglestad@cicero.uio.no

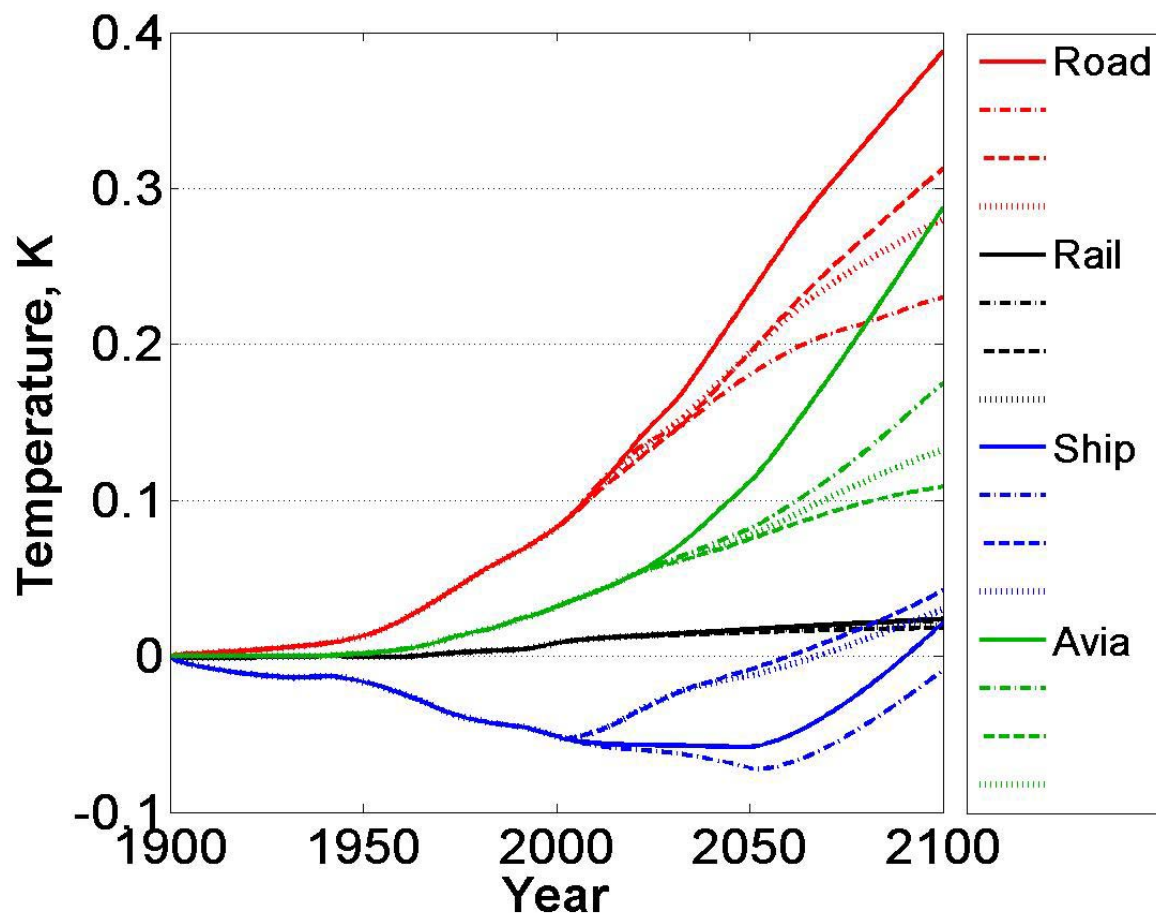


Figure 1. Global mean temperature change due to historical emissions from the transport sectors and future emissions following the four SRES scenarios: A1 (solid), A2 (dash-dot), B1 (dashed) and B2 (dotted).

REFERENCES:

Skeie, R.B., J.S. Fuglestad, T. Berntsen, M.T. Lund, G. Myhre, K. Rypdal, 2009: Global temperature change from the transport sectors: Historical development and future scenarios. *Atmospheric Environment*, in press. <http://dx.doi.org/10.1016/j.atmosenv.2009.05.025>

Indications of Distinctive Efficacies for Transport Related Ozone Perturbations

M. Ponater^{*}, S. Dietmüller

Deutsches Zentrum für Luft- und Raumfahrt, Institut für Physik der Atmosphäre, Oberpfaffenhofen, Germany

N. Stuber, K.P. Shine, E.J. Highwood, G. Rädel

Department of Meteorology, University of Reading, Reading, UK

Keywords: Ozone, Radiative Forcing, Climate Sensitivity, Efficacy

ABSTRACT: Two series of equilibrium climate change simulations forced by ozone change patterns from transport emissions have been performed with two climate models. It is investigated whether radiative forcings like this lead to climate sensitivity and efficacy parameters that are significantly different among each other and from a reference forcing caused by a homogeneous CO₂ increase. Identification of such differences is complicated by an unexpectedly strong dependence of the climate sensitivity on the strength of certain forcing patterns. Efficacy parameters calculated for the radiative forcings due to ozone increases resulting from aviation, shipping, and land transport emissions vary from unity by no more than 10%. Our results confirm earlier studies that hinted at the necessity to weight radiative forcings from different mechanisms individually in assessment studies, according to their efficacy, but more work is necessary before reliable efficacy parameters can be attributed to such forcings.

1 INTRODUCTION

For a quantitative inter-comparison of climate impact components, metrics of climate change are needed. As discussed by Fuglestad et al. (2009), some of these (like radiative forcing) are easy to obtain but difficult to observe in nature, while others (like temperature change) are physically more intuitive but usually hard to determine with the required accuracy. Despite known limitations, the concept of the radiative forcing of climate change has become a standard tool in global climate research (e.g., Shine et al., 1990; Forster et al., 2007) and it is still almost indispensable when small contributions to a total climate effect are to be quantified. However, some implicit basic assumptions have to be re-checked if the concept is applied to new forcing components. Distinctly non-homogeneous forcings have proved to be a conceptual challenge, as model simulations indicate that the fundamental semi-empirical equation linking global surface temperature change (ΔT_{sfc}) to global radiative forcing (RF)

$$\Delta T_{\text{sfc}} = \lambda \cdot \text{RF} \quad (1)$$

is often not fulfilled with a universal climate sensitivity parameter λ (e.g., Joshi et al., 2003; Cook and Highwood, 2004; Stuber et al., 2005). Hansen et al. (2005) have pointed out that in cases like this it may still be possible to define a component's (i) climate sensitivity parameter $\lambda^{(i)}$, from which an efficacy factors $r^{(i)} = \lambda^{(i)} / \lambda^{(\text{CO}_2)}$ can be derived, where $\lambda^{(\text{CO}_2)}$ indicates the climate sensitivity of a homogeneous CO₂ increase. This approach would modify Eq. (1) to

$$\Delta T_{\text{sfc}} = \lambda^{(i)} \cdot \text{RF} = r^{(i)} \cdot \lambda^{(\text{CO}_2)} \cdot \text{RF} \quad (2),$$

retaining a useful link of ΔT_{sfc} and RF if unique component efficacies $r^{(i)}$ can be determined. Note that both Eq. (1) and (2) imply that the climate sensitivity parameter for all forcings (including CO₂) does not depend on the magnitude of RF, i.e., that ΔT_{sfc} is strictly linear in RF. As shown in Hansen et al. (2005), however, even for CO₂ perturbations moderate deviations from this assumption are

^{*} *Corresponding author:* Michael Ponater, DLR-Institut für Physik der Atmosphäre, Oberpfaffenhofen, D-82230 Wessling, Germany. Email: Michael.ponater@dlr.de

apparent. Hence, in their paper the reference climate sensitivity, $\lambda^{(\text{CO}_2)}$, has been defined as the climate sensitivity to CO_2 doubling.

Ozone change patterns inferred from precursor emissions of certain transport sectors (aviation, shipping, road traffic) are distinctly non-homogeneous (both horizontally and vertically) and also distinctly different from sector to sector (Hoor et al., 2009). In our study we not only investigated whether different forcing patterns imply the existence of unique efficacies different from unity, but also to which extent the values obtained for $\lambda^{(i)}$ and $r^{(i)}$ are model dependent and method dependent. Moreover, we have checked whether the radiative forcing increases linearly with the amplitude of the ozone change pattern and whether it adds linearly across the sectors

$$\text{RF}(a \cdot \Delta\text{O}_3^{(j)}) = a \cdot \text{RF}(\Delta\text{O}_3^{(j)}), \quad \text{RF}(\sum \Delta\text{O}_3^{(j)}) = \sum \text{RF}(\Delta\text{O}_3^{(j)}) \quad (3\text{a,b}),$$

where (j) indicates the three transport sectors mentioned above. Finally, we have also considered whether the temperature response is additive across the sectors:

$$\Delta T_{\text{sfc}} = \sum \Delta T_{\text{sfc}}^{(j)} \quad (4)$$

Eq. (4) would be equivalent to requiring that the efficacy parameter of a combination of ozone perturbations can be obtained by linear combination of the respective parameters for individual sectors:

$$r = \sum (\text{RF}^{(j)} \cdot r^{(j)}) / \sum \text{RF}^{(j)} \quad (5)$$

We use the ozone change patterns presented by Hoor et al. (2009) as an non-interactive input to two climate models. The respective radiative forcings according to the IPCC are determined. The perturbations are then scaled to ensure statistical significant results for the equilibrium global temperature response and the radiative forcing according to the regression definition (Gregory et al., 2004). The resulting climate sensitivity and efficacy parameters are discussed with respect to their consistency with equations (1) to (5). The reasons for and consequences of deviations from the simple behaviour are suggested.

2 MODELS AND METHODS

Two models have been used for the simulations, viz., ECHAM4/ATT (Stenke et al., 2008) and the UK Met Office Unified Model (UM) (version HADSM3, Williams et al., 2001). Both are full-scale 3-dimensional climate models that are nonetheless economic enough to run many equilibrium climate change simulations including a slab ocean. Each of the runs is at least 45 years long. The first 20 simulation years (spin-up phase) are used to calculate radiative forcings and climate sensitivity parameters (RF_{greg} , λ_{greg}) from the regression method (Gregory et al., 2004). The climate response (e.g., ΔT_{sfc}) is calculated as the difference between the equilibrium states of a climate sensitivity run and a reference simulation. Radiative forcings according to the IPCC definition ('stratosphere adjusted forcing at the tropopause', RF_{adj}) are determined from an extra one-year simulation with the respective radiation code (Morcrette et al., 1986, for ECHAM; Edwards and Slingo, 1996, for UM).

An essential point is the necessity of scaling the original ozone perturbations because, both, the equilibrium temperature response (ΔT_{sfc}) and the parameters derived from the regression method (RF_{greg} , λ_{greg}) are associated with a statistical uncertainty that renders any simulation with radiative forcing values smaller than about 0.3 W/m^2 useless for calculating significant differences between climate sensitivity or efficacy parameters. This emphasizes the crucial role of the linearity assumption for the radiative forcing concept as described in the introduction. ECHAM/ATT as well as the UM have been run with ozone perturbations scaled by factors of 100 and 500. However, for reasons to be explained in section 3 the number of simulations had to be enhanced for ECHAM/ATT.

3 RESULTS

3.1 Radiative forcing and its linearity

The results of the radiative forcing calculations for those simulations performed by both models are summarized in Table 1. The RF values based on the regression method (3rd and 5th column) can only be given with sufficient reliability if the perturbations are scaled.

	ECHAM		UM	
	RF _{adj}	RF _{greg}	RF _{adj}	RF _{greg}
CO ₂ (doubling)	3.792	3.62	<i>3.76</i>	<i>4.04</i>
OZavi	0.019	-	<i>0.015</i>	-
OZavi (100)	1.593 (82)	1.47	<i>1.27 (85)</i>	<i>1.40</i>
OZavi (500)	5.730 (295)	5.51	<i>4.34 (289)</i>	<i>4.89</i>
OZrtr	0.034	-	<i>0.023</i>	-
OZrtr (100)	2.646 (77)	2.59	<i>1.94 (84)</i>	<i>2.05</i>
OZrtr (500)	9.051 (264)	8.32	<i>6.41 (278)</i>	<i>6.70</i>
OZshi	0.034	-	<i>0.023</i>	-
OZshi (100)	2.679 (78)	2.79	<i>1.93 (84)</i>	<i>2.27</i>
OZshi (500)	9.261 (269)	8.48	<i>6.36 (276)</i>	<i>6.91</i>
OZsum	0.088	-	<i>0.061</i>	-
OZall	0.087 (99%)	-	<i>0.060 (98%)</i>	-
OZsum (100)	6.918	6.85	<i>5.14</i>	<i>5.72</i>
OZall (100)	5.637 (81%)	5.54 (81%)	<i>4.11 (80%)</i>	<i>4.58 (80%)</i>
	[Wm ⁻²]	[Wm ⁻²]	[Wm ⁻²]	[Wm ⁻²]

Table 1: Radiative Forcing according to the IPCC definition and according to the regression definition for the scaled ozone perturbations from aviation (avi), road traffic (rtr), and shipping (shi), as calculated with the ECHAM and UM (marked by *italics*) climate models. Values in brackets indicate the enhancement factors for the forcings of the scaled perturbations, or the percentage by which the forcing of the sum of all perturbations [OZall(100)] is reduced compared to the sum of forcings of the individual perturbations [OZsum(100)].

Radiative forcing from CO₂ agrees well between the two models, but ozone forcings are generally larger in ECHAM than in UM. The regression method produces smaller radiative forcings for ECHAM but larger radiative forcings for UM, which may be explained by different feedbacks on the short time-scale (Gregory et al., 2004) for the two participating models. Additivity over the three sectors is almost perfect for the un-scaled ozone perturbations. However, as scaling increases saturation effects show up (particularly in the longwave part of the spectrum), which disturb the linearity in the ozone perturbation/radiative forcing relation. Radiative forcings for the factor 500 scaled patterns exceed the forcing of the un-scaled perturbation only by factors less than 300 in both models. Summarizing, substantial non-linearities in the radiative forcing only occur for excessive scaling.

3.2 Climate response: model dependence

Table 2 summarizes, for both participating models, the results of radiative forcing, climate sensitivity, and efficacy as determined using the regression method (RF_{greg}, λ_{greg}, r_{greg}). The reference climate sensitivity for CO₂ doubling is surprisingly similar when compared with model to model differences that have been found elsewhere (e.g., Joshi et al., 2003). However, there is no indication of a universal climate sensitivity parameter for either model. A similar conclusion can be drawn when the values are derived using the IPCC forcings (RF_{adj}, not shown). Moreover, except for the aviation ozone perturbation, the results inhibit a substantial non-linearity of the surface temperature response that is inconsistent with the concept outlined above. For the ECHAM model, in particular, the climate sensitivity and efficacy parameters seem to depend more on the scaling of a pattern than on its spatial structure. A straightforward conclusion about possible efficacy differences for the original (un-scaled) ozone perturbations is thus impossible from the simulations listed in Table 2. Only for aviation ozone these simulations do hint at an efficacy value systematically different from unity; however, in this case ECHAM and UM point in opposite directions, the first model suggesting a higher and the second on a lower efficacy.

	ECHAM				UM			
	ΔT_{sfc}	RF_{greg}	λ_{greg}	r_{greg}	ΔT_{sfc}	RF_{greg}	λ_{greg}	r_{greg}
CO ₂ (doubling)	2.73	3.62	0.78	1	<i>3.35</i>	<i>4.04</i>	<i>0.84</i>	<i>1</i>
OZavi (100)	1.17	1.47	0.87	1.11	<i>0.81</i>	<i>1.40</i>	<i>0.70</i>	<i>0.83</i>
OZavi (500)	4.83	5.51	0.87	1.11	<i>3.11</i>	<i>4.89</i>	<i>0.66</i>	<i>0.79</i>
OZrtr (100)	2.03	2.59	0.81	1.04	<i>1.60</i>	<i>2.05</i>	<i>0.86</i>	<i>1.02</i>
OZrtr (500)	8.57	8.32	1.03	1.31	<i>6.12</i>	<i>6.70</i>	<i>0.92</i>	<i>1.09</i>
OZshi (100)	1.92	2.79	0.73	0.93	<i>1.90</i>	<i>2.27</i>	<i>0.84</i>	<i>1.00</i>
OZshi (500)	8.79	8.48	1.06	1.36	<i>6.81</i>	<i>6.91</i>	<i>1.00</i>	<i>1.19</i>
OZall (100)	4.67	5.54	0.87	1.11	<i>3.53</i>	<i>4.58</i>	<i>0.82</i>	<i>0.97</i>
OZall (50)	2.52	3.10	0.85	1.09	-	-	-	-
	[K]	[Wm ⁻²]	[K/Wm ⁻²]		[K]	[Wm ⁻²]	[K/Wm ⁻²]	

Table 2: Radiative forcing, climate sensitivity, and efficacy according to the regression definition for the scaled ozone perturbations from aviation (avi), road traffic (rtr), and shipping (shi), calculated with the ECHAM and UM (*marked by italics*) climate models. The surface temperature response (2nd and 6th column) is the true equilibrium climate response and not derived through regression of the spin-up phase of a simulation (see text).

3.3 Nonlinearities in the forcing-response relationship

The unexpected and conceptually inconsistent variation of climate sensitivity and efficacy among patterns of the same structure but different scaling has been further explored for the ECHAM model for which this behaviour is most distinct. First, the number of simulations was enhanced to allow a more systematic investigation. Second, we determined the cloud radiative feedback as a likely candidate for the physical origin of the efficacy variations. Analysis confirms this hypothesis (Table 3).

	ΔT_{surf}	RF_{adj}	λ_{adj}	ΔCRF	$\Delta CRF/\Delta T_{\text{surf}}$
CO ₂ (1 W/m ²)	0.703	1.010	0.696	-0.127	-0.181
CO ₂ (doubling)	2.748	3.792	0.724	-0.340	-0.124
CO ₂ (tripling)	4.572	6.160	0.742	-0.355	-0.078
OZavi (50)	0.617	0.862	0.716	-0.082	-0.082
OZavi (100)	1.167	1.593	0.733	-0.196	-0.168
OZavi (200)	2.201	2.849	0.773	-0.110	-0.050
OZavi (500)	4.832	5.730	0.843	+0.562	+0.116
OZrtr (100)	2.032	2.646	0.768	-0.034	-0.017
OZrtr (150)	2.900	3.689	0.786	+0.129	+0.044
OZrtr (500)	8.586	9.051	0.949	+3.262	+0.380
OZshi (100)	1.925	2.679	0.719	-0.018	-0.009
OZshi (150)	2.833	3.743	0.757	+0.155	+0.055
OZshi (500)	8.793	9.261	0.949	+3.888	+0.442
OZall (50)	2.524	3.279	0.770	+0.062	+0.025
OZall (100)	4.673	5.637	0.829	+0.774	+0.165
	[K]	[Wm ⁻²]	[K/Wm ⁻²]	[Wm ⁻²]	[Wm ⁻² /K]

Table 3: Equilibrium temperature response, radiative forcing, climate sensitivity, and cloud radiative feedback for ECHAM simulations forced by CO₂ and ozone perturbations (from aviation (avi), road traffic (rtr), and shipping (shi)) with different scaling. Radiative forcing and climate sensitivity are calculated using the IPCC definition (see text). The cloud radiative feedback (ΔCRF) is the equilibrium change of cloud radiative forcing, relative to the reference run.

For all ozone perturbations, increasing scaling induces a gradual change from negative cloud radiative feedback for moderate scaling to ever stronger positive feedback for heavy scaling. This shift to a qualitatively different cloud feedback regime causes higher climate sensitivity in the simulations with heavy scaling of the original perturbation. It is also evident that the shift occurs earlier for shipping than for aviation ozone, suggesting a crucial influence of static stability changes in the lower troposphere and respective consequences for low level clouds. It is notable that the effect of a changing cloud feedback regime is also present, but much less distinct, in case of an increasing CO₂ forcing. Here, the cloud radiative feedback remains negative up to a forcing level of 6 W/m², though the specific cloud feedback per unit temperature response (last column in Table 3) slightly decreases. As a consequence, the climate sensitivity increase with an increasing CO₂ forcing remains comparatively moderate and consistent with what is reported by Hansen et al. (2005).

4 NON-LINEAR FIT FOR CLIMATE SENSITIVITY AND EFFICACY

The dependence of the cloud radiative feedback on strength and pattern of the forcing offers a physical explanation for the unexpected increase of climate sensitivity and efficacy with increasing forcing. Assuming the existence of terms of higher order (in RF) in Eq. (1), and requiring that λ approaches a constant value for small radiative forcing, implies that to describe the correlation of climate sensitivity and radiative forcing a parabolic fit (Figure 1) is to be preferred above a linear fit:

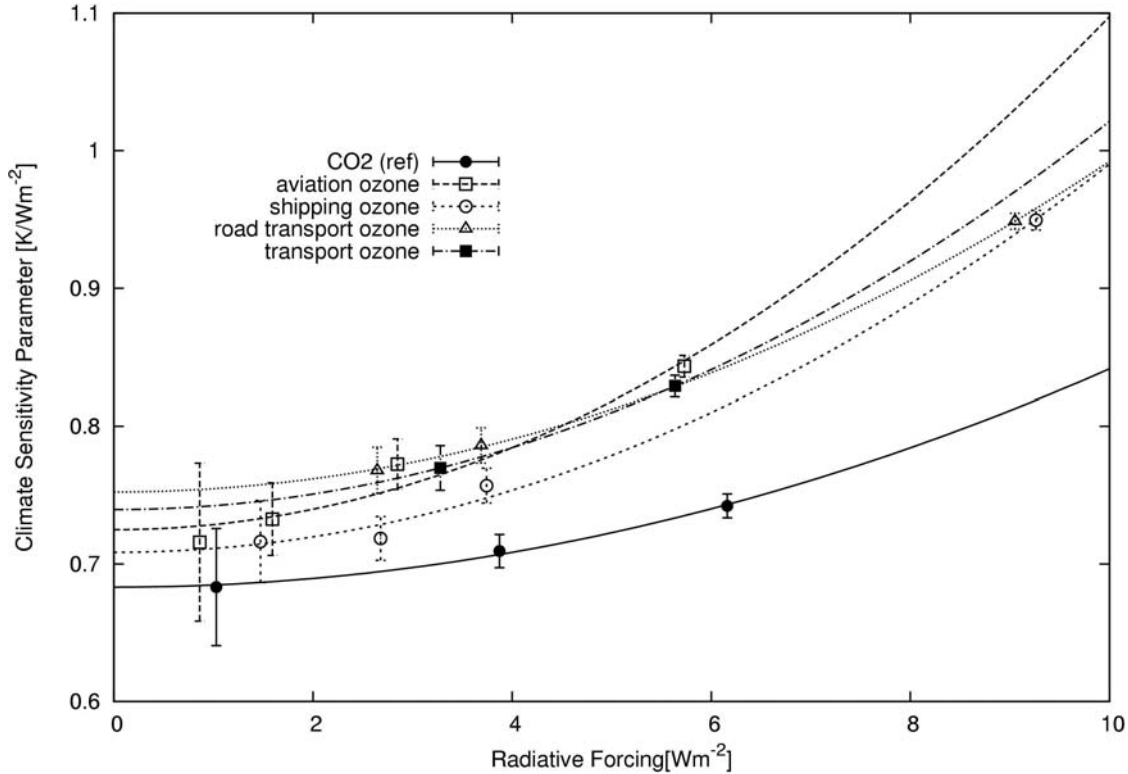


Figure 1: Dependence of the climate sensitivity parameter from the radiative forcing in the series of ECHAM simulations listed in Table 3. The symbols represent the individual simulations for CO₂, individual transport sector ozone, and combined transport ozone, respectively. The curves indicate quadratic fits to the individual simulation series. A linear fit is not adopted, in order to ensure that the curves approach horizontal lines as RF approaches zero. The uncertainty bars indicate the 95% confidence interval for the simulated climate sensitivities (which is growing wider as ΔT_{surf} and λ decrease).

By taking the interception of the fitted curves with the ordinate we approximate unique values of the climate sensitivity parameter (λ_{adj} , in this case) for the original (small) perturbations. We apply this definition for all forcings (incl. CO₂), thus diverging from Hansen et al. (2005) who deliberately calculate the efficacy with respect to CO₂ doubling. If we define the efficacy values as explained, all transport ozone efficacies exceed unity and deviate by less than 10%. This means a much smaller excess over unity than found in earlier work (e.g., Stuber et al., 2005), probably because the perturbation patterns used here are smoother compared to the idealized patterns used in previous studies.

	λ_{adj}	ϵ_{adj}
CO ₂	0.692	1
OZavi	0.725	1.048
OZrtr	0.752	1.088
OZshi	0.707	1.021
OZall	0.739	1.068
OZall	0.729	1.053
(approx)		
	[K/Wm ⁻²]	

Table 4: Climate sensitivity and efficacy parameters derived from the parabolic fit of the results from the ECHAM simulations with individual transport related ozone perturbation patterns. The last line includes values of the same parameters derived for transport ozone by linear combination of the RF weighted values from the individual sector contributions.

Table 4 summarizes the respective values for λ_{adj} and r_{adj} reached in this way. It is suggested that, qualitatively, the ozone change pattern from road traffic has the largest efficacy while shipping ozone has the lowest efficacy close to unity. Using equation (5) to calculate a combined efficacy for a simultaneous forcing involving all transport sectors (OZall(approx)) yields satisfactory agreement with the fitted efficacy from dedicated runs with the same combination of forcings (OZall).

5 CONCLUSIONS AND OUTLOOK

Results from two series of equilibrium climate change simulations with respect to ozone perturbations caused by emissions by the transport sector confirm earlier findings suggesting the existence of efficacies significantly deviating from unity for this kind of non-homogeneous radiative forcing. Differences from the reference case (homogeneous CO₂ increase) are, however, not as large as found in previous studies which used idealized perturbation patterns. Individual ozone patterns clearly tend to show up distinctive efficacy values but inter-model differences render quantitative conclusions only indicative. A strong dependence of the climate sensitivity on the strength of a radiative forcing has become obvious from the simulations analysed for this study; this has required an extra effort to quantify well-defined efficacy value for some of the perturbation patterns.

In view of the difficulties in determining method-independent efficacy values, the relatively small deviation of the efficacies of transport related ozone perturbations from unity (not larger than 10 %), and occasional qualitative contradictions between the results of the two participating climate models, care is required when introducing the efficacy values from our simulations in assessment studies (e.g., Fuglestad et al., 2008). They may be used to test how sensitive a comparison of transport sector climate impacts depends on including distinctive efficacies. A more comprehensive understanding, validation of key feedbacks, and a consensus between different climate models will be necessary, however, before we can claim for sure that climate impact assessments are improved by the use of distinctive efficacies.

6 ACKNOWLEDGEMENTS:

The QUANTIFY project is funded by the European Union within the 6th Framework Project under contract 003893.

REFERENCES

- Cook, J. and E.J. Highwood, 2004: Climate response to tropospheric absorbing aerosols in an intermediate general-circulation model. *Q. J. R. Meteorol. Soc.* 130, 175-191.
- Edwards, J.M., and A. Slingo, 1996: Studies with a flexible new radiation code. I: Choosing a configuration for a large scale model. *Q. J. R. Meteorol. Soc.*, 122, 689-719.
- Forster, P., et al., 2007: Changes in atmospheric constituents and in radiative forcing. In: *Climate change 2007: The physical science basis. Contribution of Working Group I to the 4th assessment report of the IPCC* (Eds.: Solomon, S., et al.), Cambridge Univ. Press, Cambridge, UK and New York, NY, USA.
- Fuglestad, J., T. Berntsen, G. Myhre, K. Rypdal, and R. B. Skeie, 2008: Climate forcing from the transport sectors, *PNAS* 105, 454-458, doi:10.1073/pnas.0702958104.
- Fuglestad, J., K.P. Shine, T. Berntsen, J. Cook, D.S. Lee, A. Stenke, R.B. Skeie, G.J.M. Velders, and I.A. Waitz, 2009: Transport impacts on atmosphere and climate: Metrics, *Atmos. Environ.*, in press, doi: 10.1016/j.atmosenv.2009.04.044.
- Gregory, J., et al., 2004: A new method diagnosing radiative forcing and climate sensitivity. *Geophys. Res. Lett.* 31, L03205, doi:10.1029/2003GL018747.
- Hansen, J., M. Sato, R. Ruedy, L. Nazarenko, A. Lacis, G.A. Schmidt, G. Russell, et al., 2005: Efficacy of climate forcings. *J. Geophys. Res.* 110, D18104, doi: 10.1029/2005GL022740.
- Hoor P., et al., 2009: The impact of traffic emissions on atmospheric ozone and OH: results from QUANTIFY. *Atmos. Chem. Phys.* 8, 3113-3136.
- Joshi, M.M., K.P. Shine, M. Ponater, N. Stuber, R. Sausen, and L. Li, 2003: A comparison of climate response to different radiative forcings in three general circulation models: towards an improved metric of climate change. *Clim. Dyn.* 20, 843-854, doi: 10.1007/s00382-003-0305-9.

- Morcrette, J.-J., L. Smith., and Y. Fouquart, 1986: Pressure and temperature dependence of the absorption in longwave radiation parameterizations. *Beitr. Phys. Atmos.*, 59, 455-469.
- Shine, K.P., et al., 1990: Radiative forcing of climate. In: *Climate change: The IPCC scientific assessment* (Eds.: Houghton, J.T., et al.), Cambridge University Press, Cambridge, New York, Melbourne, Sydney.
- Stenke, A., V. Grewe, V., M. Ponater, 2008: Lagrangian transport of water vapour and cloud water in the ECHAM4 GCM and impact on the cold bias. *Clim. Dyn.*, 31, 491-506, doi: 10.1007/s00382-007-0347-5.
- Stuber, N., M. Ponater, and R. Sausen, 2005: Why radiative forcing might fail as a predictor of climate change. *Clim. Dyn.* 24, 497-510, doi:10-1007/s00382-004-0497-7.
- Williams, K.D., C.A. Senior, and J.F.B. Mitchell, 2001: Transient climate change in the Hadley Centre models: The role of physical processes. *J. Clim.*, 14, 2659-2674.

Investigation of NO₂ Pollutions on Board of Research Aircraft (Some Results of QUANTIFY and POLARCAT Field Campaigns)

N. Sitnikov *, V. Sitnikova, A. Ulanovskiy, A. Lukyanov
Central Aerological Observatory, Russia

H. Schlager, A. Roiger, M. Scheiber, M. Lichtenstern and P. Stock
Deutsches Zentrum für Luft- und Raumfahrt, Oberpfaffenhofen, Germany

F. Ravagnani
Istituto di Scienze dell' Atmosfera e del Clima, Bologna, I-40129 Italy

Keywords: Air Pollutions, Ship Emissions, Nitrogen Oxides

ABSTRACT: The results of investigation of NO₂ pollutions on board of research aircraft Falcon (DLR, Germany) are presented. The measurements have been carried out by chemiluminescent nitrogen dioxide analyzer developed in Central Aerological Observatory (Russia). The data of NO₂ distribution have been obtained during QUANTIFY (West Europe, July 2007) and POLARCAT (Greenland, July 2008) field campaigns. NO₂ measurements over Greenland during POLARCAT field campaign have been carried out using ACCENT support. Different sources of nitrogen oxides are investigated. Some aspects of nitrogen dioxide distribution and transport are considered. Chemical transformation of nitrogen oxides inside ship plumes is observed and analyzed.

1 INTRODUCTION

Aircraft measurements of NO₂ atmospheric pollutions have been carried out using chemiluminescent nitrogen dioxide analyzer developed in Central Aerological Observatory (Russia). They were performed on board of research aircraft "Falcon" (DLR, Germany) during Quantify (July 2007, Brest, France) and POLARCAT (June 2008, Greenland) field campaigns. First one was concerned to ship emission measurements in the major European ship corridor. Ship emission is very important component of anthropogenic environmental pollution which gives considerable impact of greenhouse gases, aerosols and another substances to atmosphere. There are some publications concerning experimental investigations and modeling studies of ship emission (Corbett and Fischbeck, 1997, Schlager et al. 2006, Petzold et.al. 2006). Chemical transport models parametrization needs detail information about chemical and photochemical reactions in atmosphere of polluted regions including exhaust plumes. Simultaneous measurements of different gas species permit to investigate chemical and photochemical processes in atmosphere including the processes inside individual exhaust plume. Specially developed chemiluminescent nitrogen dioxide analyzer has a high time (~0.2 sec) and space (~20m) resolution, which is important to make correct measurements of NO₂ distribution in small size ship emission plumes. Another experience of using this instrument on board of research aircraft "Falcon" was in POLARCAT field campaign in June 2008 in Greenland. The objectives of the campaign are to investigate the impact of urban and forest fire emissions in the Arctic troposphere, mechanisms of fire plume spreading (dispersion, mixing), chemical and photochemical transformations in the fire plumes, and impact of forest fire emission transported by pyroconvection into the lower stratosphere.

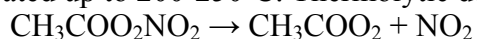
* Corresponding author: Nikolay Sitnikov, Central Aerological Observatory (CAO), Dolgoprudny, Moscow region, Russia. Email: sitnikov@caomsk.mipt.ru

2 METHOD AND INSTRUMENT

The instrument is based on chemiluminescent principle (Kinrade, 1991) that is interaction of NO₂ with luminol solution leads to light radiation in visible spectral range. The intensity of the light depends on the nitrogen dioxide concentration. This method is very fast and very sensitive to NO₂ but it has some interference in atmosphere. The highest interference is sensitivity to peroxyacetyl nitrate (PAN), which is about 25% of NO₂ sensitivity. For correct NO₂ measurements it must be taken into account. Another interference is the sensitivity to ozone. It is not so high (less than 0.5% of NO₂ sensitivity) and it can be excluded by additional O₃ measurements or using special ozone scrubber. Special design of the instrument permits to take into account PAN influence. Ozone influence is excluded using “Falcon” ozone data.

The block diagram of the instrument is shown in Fig.1. Main sensor (Sitnikov et.al 2005) consists of liquid pump with special valve, reaction chamber and photoelectric multiplier (Fig.1a). Liquid pump for circulating the liquid is a syringe filled with a chemiluminescent solution. Its plunger is slowly displaced by a reduction motor. In order to exclude the possibility of the chemiluminescent solution boiling at low pressures and the appearance of flow-velocity instabilities, valve is connected to the pump outlet. This valve obstructs the chemiluminescent solution flow; as a result, the pressure inside the syringe during the movement of the plunger always exceeds atmospheric pressure. A nipple manufactured from such neutral materials as silicone, teflon, polyethylene, etc., can serve as a valve. This design of the pump completely excludes the possibility of bubble formation and ensures a constant liquid flow at external pressures of 1 to 1000 mbar. The consumption of the chemiluminescent solution is determined only by the velocity of the plunger's motion and amounts to 2.5 ml/h; i.e., 10 ml of the solution sustains the operation of the instrument for 4 hours that is for usual duration of “Falcon” flight. The pump supplies the solution into the reaction chamber and onto a porous substrate. The exhausted solution drains off into a vessel positioned below the reaction chamber.

The instrument includes two channels (main and auxiliary) with two chemiluminescent sensors (Fig.1b). One of them (auxiliary channel) has PAN-NO₂ converter (thermolytic cell) which is heated up to 200-250°C. Thermolytic destruction of PAN provides increasing of NO₂ concentration:



This results in signal increasing in auxiliary channel because of different sensitivity to NO₂ and PAN. Simultaneous measurements in two channels permit to take into account the influence of PAN and increase the accuracy of NO₂ measurements. Ozone influence is corrected using the data of “Falcon” ozone measurements. Calibration of the instrument was performed in CAO and DLR. Fig.1c illustrates the process of measurements with correction taking into account PAN influence. Usually this correction was not high.

Air flow through the main and auxiliary channels (about 2 l/min) is provided by air pump with constant volume flow rate. The instrument is regulated by compact electronic block. It can operate in automatic regime. The data of measurements is recorded to internal flash memory. The instrument has RS232 interface for connection with computer or telemetry system.

Technical characteristics of the instrument:

The range of NO ₂ measurements	0.05 – 100 ppbv;
Time resolution	0.2 s
Weight	5 kg;
Power	50 W.

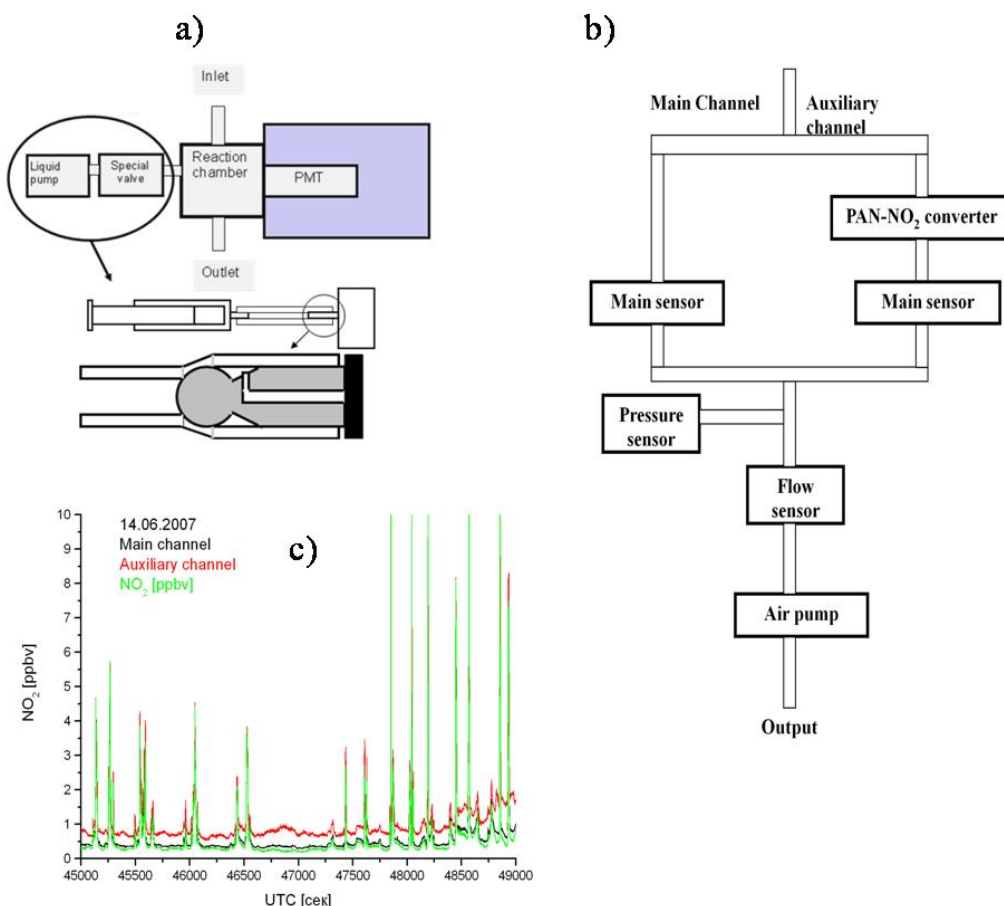


Fig.1. Block diagram of the main chemiluminescent sensor (a) and chemiluminescent nitrogen dioxide analyzer (b) and time series of signals (in terms of NO_2 concentration) in main channel (black), auxiliary channel (red) and NO_2 concentration corrected taking into account PAN influence (green).

3 RESULTS AND DISCUSSIONS

Eight scientific flights were fulfilled in June 2007 during Quantify project field campaign by scientific aircraft Falcon in different routes. The altitudes changed from several hundred meters to several kilometers, the duration of flights was 3 – 3.5 hours. The measurements were made above the Atlantic Ocean as in non polluted areas as in sea transport corridor, the most polluted regions of Europe. Distribution of some atmospheric species such as nitrogen oxides, CO, CO_2 , aerosols and others has been measured. NO_2 measurements were fulfilled by chemiluminescent nitrogen dioxide analyzer described above. Time response of the instrument was 0.2 sec. As the aircraft velocity was 100 m/sec, space resolution of NO_2 concentration measurements was about 20 m. Some results of nitrogen dioxide measurements are represented in Fig. 2-4.

The flight on 14th of June, 2007 was from Brest (France) to western coast of England as demonstrated in Fig.2. Different chemical components concentrations were measured in a dedicated exhaust plume of a large container ship (Atlantic Conveyor flight). During the flight the aircraft crossed the exhaust plume many times at different distances from the ship. Several trace species concentrations were measured for different life times of the exhaust plume (from 1 minute to several hours). Fig.2 represents NO and NO_2 concentrations measurements for the part of flight on the 14th of June, 2007. As the measurements were strictly synchronized we can determine dependence of NO_2 / NO_x ratio from the life time of the exhaust plume. The results of the calculation are represented in Fig.2b. As figure shows initial NO_2 / NO_x ratio is very low (about 0.1). Then it increased up to 0.6 – 0.7 during some minutes. This increasing is connected with fast chemical reaction of NO with ozone, and after that variation of NO_2 / NO_x ratio was not high during some hours.

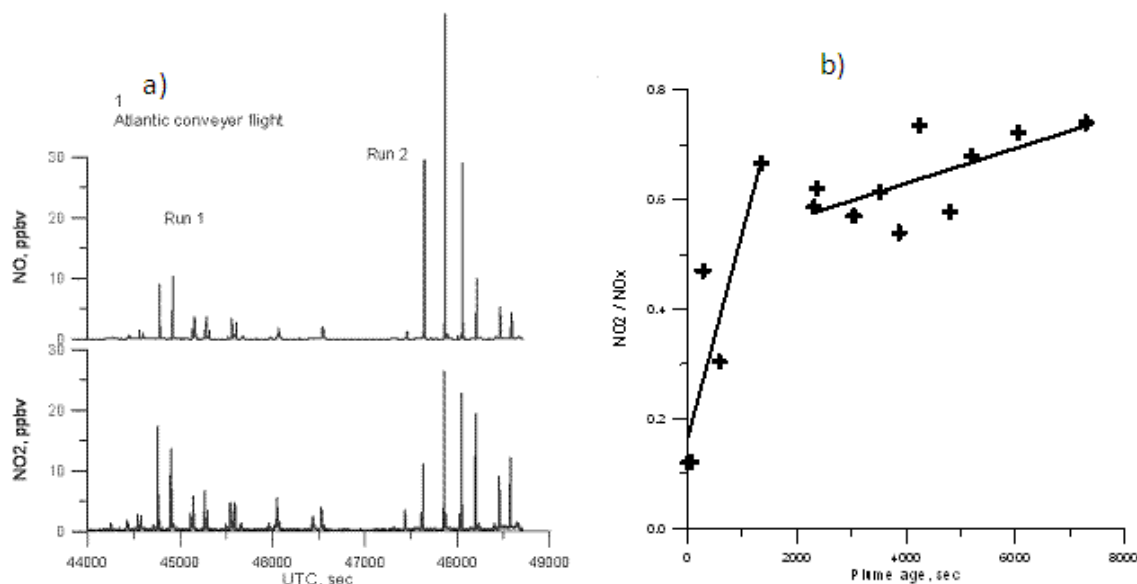


Fig.2. Time series of simultaneous NO and NO₂ measurements during Atlantic conveyor flight July 14, 2007 (a) and the ratio NO₂/NO_x versus plume age calculated from this data (b).

On the 17th of June there were two flights along English Channel from Brest to Bremen (Fig.3a) and back to Brest (Fig.3b). The first flight from Brest to Bremen was started early in the morning. The second flight from Bremen to Brest was several hours later. NO₂/NO_x ratios were calculated from the results of measurements in peaks of exhaust plumes of different ships. Fig.3c demonstrates the dependence of NO₂/NO_x ratio from the day time for both flights on the 17th of June. Decrease of the ratio with time most likely associated with dependence of photochemical reactions rate from the Sun radiation intensity. Average NO₂/NO_x ratio was 0.85 for the first flight and 0.64 for the second one. However NO₂/NO_x ratio of every flight has spreading in its values. This spreading is probably connected with different plume ages or different weather conditions in different points of the route.

The measurements demonstrated that NO₂ distribution in a major ship corridor near Western coast of Europe highly inhomogeneous. Background NO₂ concentrations were less than 0.5 ppbv. Local maximums which caused by ship emission were found about several tens of ppbv, sometimes more than 100 ppbv. Such concentrations were measured at altitudes less than 500 meters. At altitudes above 500 meters as a rule background NO₂ concentrations were measured.

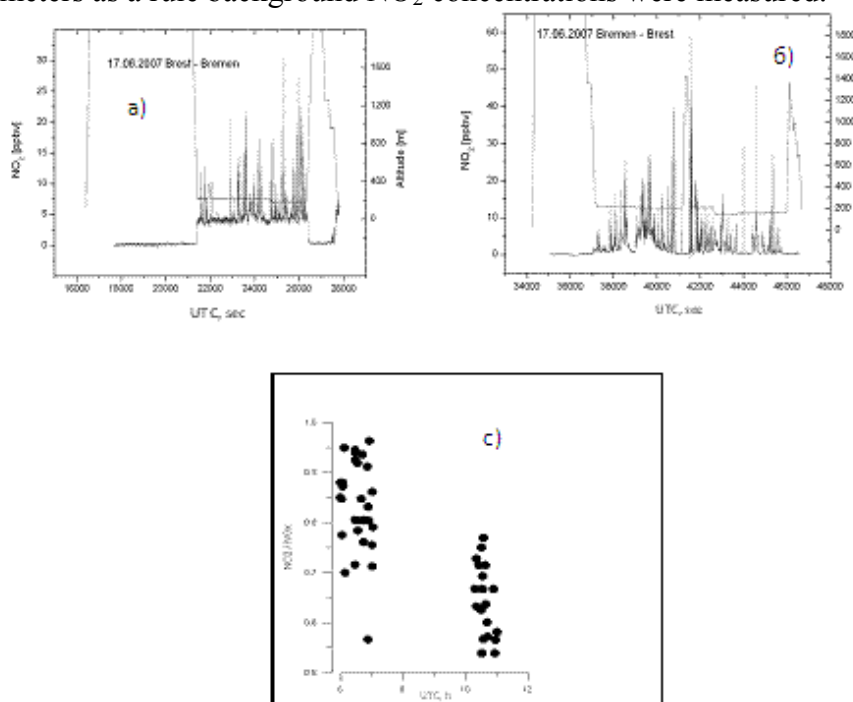


Fig.3. Time series of NO₂ concentration in ship corridor which is measured 17.06.2007 during the flights Brest-Bremen (a) and Bremen-Brest (b) and NO₂/NO_x ratio versus day time (c) calculated from NO₂ and NO local maxima.

Another experience of using nitrogen dioxide analyzer on board of research aircraft was during POLARCAT field campaign in June 2008. The campaign is based in Kangerlussuaq (Greenland). There were some flights with different routes to make measurements of atmospheric species from urban and forest fire emissions of North America and Siberia. In most of flights the measurements show very low NO₂ concentrations. There were nearly or lower the detection limit of the instrument (some tens of pptv). Maximal NO₂ concentration (about 200 pptv) has been observed during the flight of July 10, 2008. (Fig.4b) The flight was performed over the Greenland in North direction (Fig.4a) mainly in stratosphere. Fig.4c shows 10 days backward trajectories from initial points with increased NO₂ concentration. Considered air masses with increased NO₂ concentration have different origin. As trajectory analysis shows the origin of air masses with increased (in comparison with phone concentrations) NO₂ concentration is not connected with lower troposphere.

Then according to completed measurements, the considerable increasing of NO₂ concentration in Arctic connected with forest fire is not observed during POLARCT field campaign.

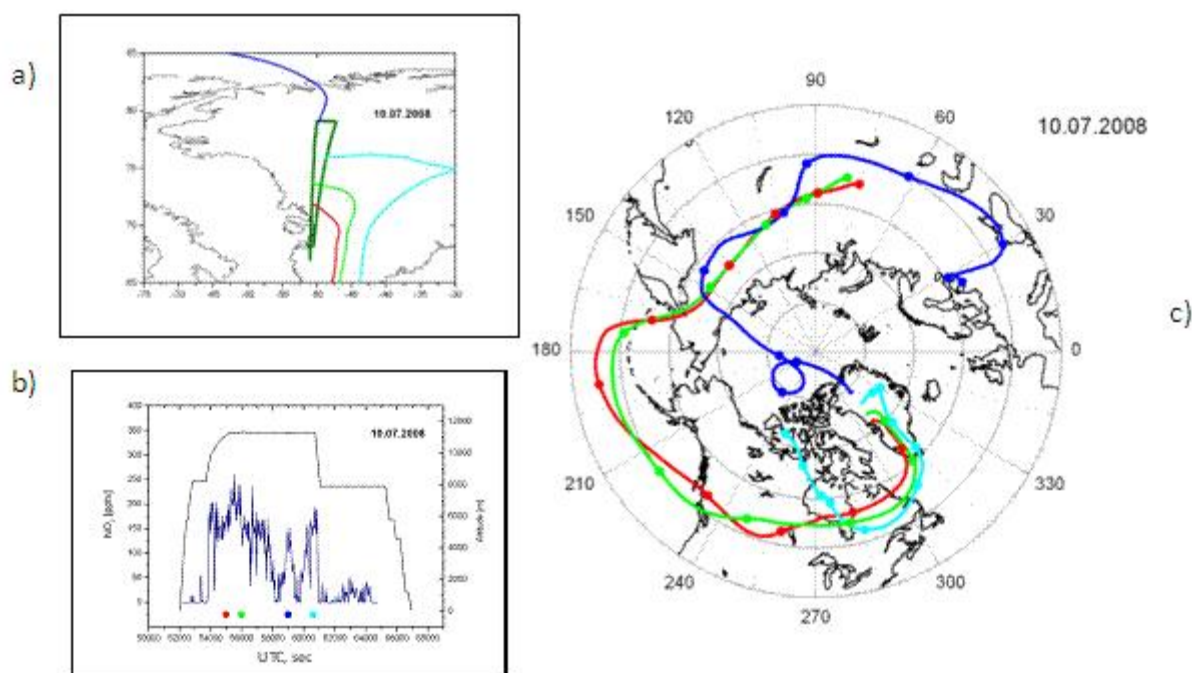


Fig.4. The route of research aircraft “Falcon” flight 10.07.2008 (a), time series of NO₂ measurements during this flight (b), 10 days backward trajectories of air masses plotted from initial points with maximal NO₂ concentration (c).

4 CONCLUSIONS

In the frame of European project QUANTIFY in Central Aerological Observatory Chemiluminescent Nitrogen Dioxide Analyzer for research aircraft have been developed and manufactured. NO₂ measurements on board of research aircraft “Falcon” during QUANTIFY (June 2007) and POLARCAT (July 2008) field campaigns have been carried out using developed instrument. NO₂ measurements in European ship corridor during QUANTIFY field campaign showed very inhomogeneous NO₂ distribution from concentrations < 0.5 ppbv up to 100 ppbv connected with ship emission. Data analysis of the of simultaneous NO and NO₂ measurements shows nitrogen oxides chemical transformation inside the individual exhaust plume.

5 ACKNOWLEDGEMENTS

Many thanks to “Falcon” team for the help during field campaigns. NO₂ measurements in POLARCAT field campaign have been carried out due to ACCENT support.

REFERENCES

- Corbett, J.J. and P.S. Fischbeck, 1997: Emissions from ships, *Science* 248, 3723-3731.
- Kinrade John D. Patent 5.015.590 US. // Scintrex Limited (Concord, CA), 1991.
- Petzold A., B. Weinzerl, M. Fiebig, Lichtenshtern M., P. Lauer, C. Gurk, K.Franke, E. Weingartner, 2006: Particle emissions from ship engines: emission properties and transformation in the marine boundary layer, *Proceedings of the TAC-Conference, June 26-29, 2006, 78-82, Oxford, UK.*
- Schlager H., R. Baumann, M. Lichtenstern, A. Petzold, F.n Arnold, M. Speidel, C. Gurk, H. Fisher, 2006: Aircraft-based trace gas measurements in a primary European ship corridor, *Proceedings of the TAC-Conference, June 26-29, 2006, 83-88, Oxford, UK.*
- Sitnikov N.M., A.O. Sokolov, F. Ravagnani, V.A. Yushkov and A.E. Ulanovskiy: A chemiluminescent balloon type nitrogen dioxide meter for tropospheric and stratospheric investigation (NaDA), *Instruments and Experimental Techniques Vol. 48, No. 3, 2005, pp. 400-405.*

High resolution simulations of aircraft condensation trails: Contrails Evolution and Diffusion

Sarrat, C.^{*}, R. Paugam¹, R. Paoli, D. Cariolle, L. Nybelen

*European Centre for Research and Advanced Training in Scientific Computation, CERFACS/CNRS,
Toulouse, France*

¹ *Now at Department of Geography, King's College London, London, UK*

Keywords: Contrails, Diffusion, transition contrail-to-cirrus

ABSTRACT: This study describes a high-resolution numerical simulation of the evolution of an aircraft condensation trail (contrail) and its transition into a contrail-cirrus. The results show the extension of the contrail over 3200m width during a few hours. In particular, we show that the vertically integrated optical thickness is maintained in the core of the contrail during four hours.

1 INTRODUCTION

Contrails and aircraft-induced cirrus clouds are the most uncertain contributors to the Earth radiative forcing, among all aircraft emissions, according to the latest estimations by Sausen, et al. (2005).

If the conditions for contrails formation and persistence are now well accepted ($RH_w > 100\%$ and $RH_i > 100\%$, where RH_w , RH_i are the ambient relative humidity with respect to water and ice, respectively), the details of the transformation of contrails, and in particular the critical phase of transition from linearly shaped contrails to widely spread cirrus, are still unclear.

One of the reasons for this uncertainty is the very complex dynamical and physical interactions that occur in aircraft wakes.

As proposed by Gerz et al. (1998), these interactions can be represented as four successive regimes. The two first regimes, (respectively the jet and vortex regimes) last a few minutes after emissions, and correspond to the interaction between the engines exhaust and the vortices generated by the wings, and the formation of the primary and secondary wakes. During the following minutes, the vortices breakup and generate turbulence (dissipation regime). During the last diffusion regime, the contrail evolution is controlled by the atmospheric background conditions. The aim of the present study is to carry out a direct dynamical large-eddy simulation of the diffusion regime where contrail-to-cirrus transition takes place.

2 MODEL PRESENTATION

The contrails simulations are performed with Meso-NH, a meteorological, non-hydrostatic meso-scale model (Lafore et al, 1998, see also <http://mesonh.aero.obs-mip.fr/mesonh/>).

The atmospheric Meso-NH model includes the wind components (u , v , w), the Turbulent Kinetic Energy (TKE) and the potential temperature (θ) as prognostic variables, whereas a dedicated microphysical scheme specific for contrails is implemented to simulate the ice crystal variable together with the condensation, evaporation and sedimentation process (see Paugam et al., 2009 for details).

The microphysical scheme adds three variables to the model: the number density of ice particles n_i , the mass density of the ice phase ρ_i and the water vapour density ρ_v .

We assume locally mono-dispersive and spherical ice particles within a computational cell which yield to the relation between ρ_i and the mean particle radius r_i :

^{*} *Corresponding author:* Sarrat, CERFACS, 42 avenue Coriolis, 31057 Toulouse. Email: sarrat@cerfacs.fr

$$\rho_i = \frac{4}{3} \pi r_i^3 \rho_{ice} n_i$$

We present here the simulation from 35 minutes to few hours after the aircraft release.

The model is initialized at 2120s using the outputs of Meso-NH simulations from Paugam et al. (2009).

A specific model configuration is used in order to maintain a synthetic turbulence that is representative of the background atmospheric turbulence at the tropopause level.

This is based on the 2 domain-nesting functionality of Meso-NH: in the father model, an unstable stratified shear flow is used to generate turbulent fluctuations of velocity and potential temperature.

These fluctuations are afterwards injected in the son model in which the contrail is simulated.

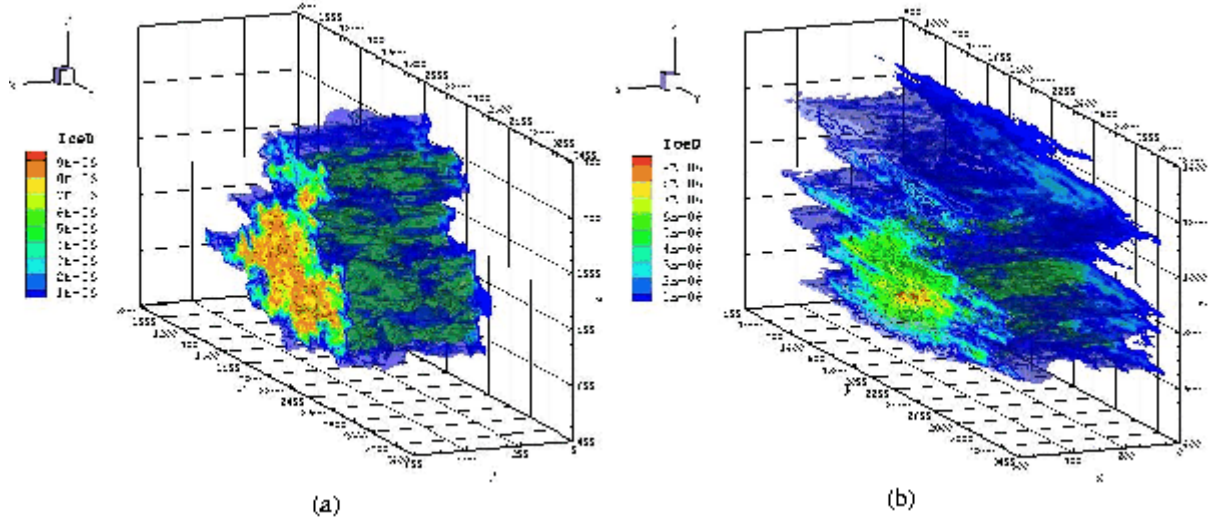
The dimensions of both domains are: $L_x = 500$ m, $L_y = 4000$ m and $L_z = 1500$ m, with the same resolution in the 3 directions ($\Delta x = \Delta y = \Delta z = 10$ m).

8 MODELING RESULTS

The Meso-NH simulations presented here correspond to the diffusion regime, i.e. the contrail-to-cirrus transition. Starting from 35 minutes after emission, the simulation lasts almost four hours.

Figure 1 presents the simulated ice density in a three dimensional figure, where the x axis is along the direction of the flight. Only a contrail fraction of 500 m is simulated as represented in Figure 1.

At $t=2120$ s (Figure 1a), the contrail core contains a large amount of ice, while the primary and secondary wakes are still visible. A few hours later, (at $t=10120$ s, Fig. 1b), the horizontal extension of the contrail perpendicularly to the aircraft trajectory increases from 1300 m to 3200 m. At this stage



of the diffusion regime, the primary and secondary wakes are almost merged.

Figure 1: Three-dimensional view of the contrail. The x-axis indicates the flight direction. The colored iso-surfaces represent the ice density: (a) at $t=2320$ s and (b) at $t=10120$ s.

The mean particle radius is displayed in Figures 2a and b. The larger particles are located at the top and the bottom of the contrail, where their number is lower: the ice particles grow faster because the water vapour available for condensation in the supersaturated ambient air is higher. On the other hand, in the contrail core, where most of the particles were trapped by the vortex, the growth is damped because the same amount of background water vapour has to be shared among more particles.

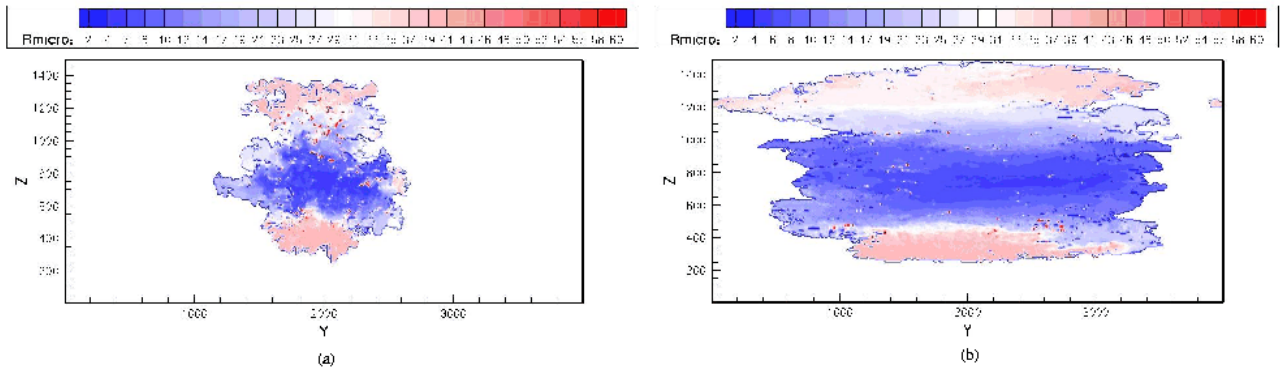


Figure 2: Vertical cross section at $x=250\text{m}$ of the ice particle mean radius: (a) at $t=2320\text{s}$ and (b) at $t=10120\text{s}$.

As shown in the Fig. 3, the vertically integrated optical thickness is maximum in the middle of the contrail, where the number of particles is the highest and rapidly falls next to the edge of the cloud. The optical depth remains rather high during the simulation, decreasing from 0.95 to 0.55, through the four hours of simulation in agreement the study of Jensen et al. (1998). In fact, even if the ice density decreases because of contrail spreading, the ice particles radius grows in such a way that the optical depth is maintained.

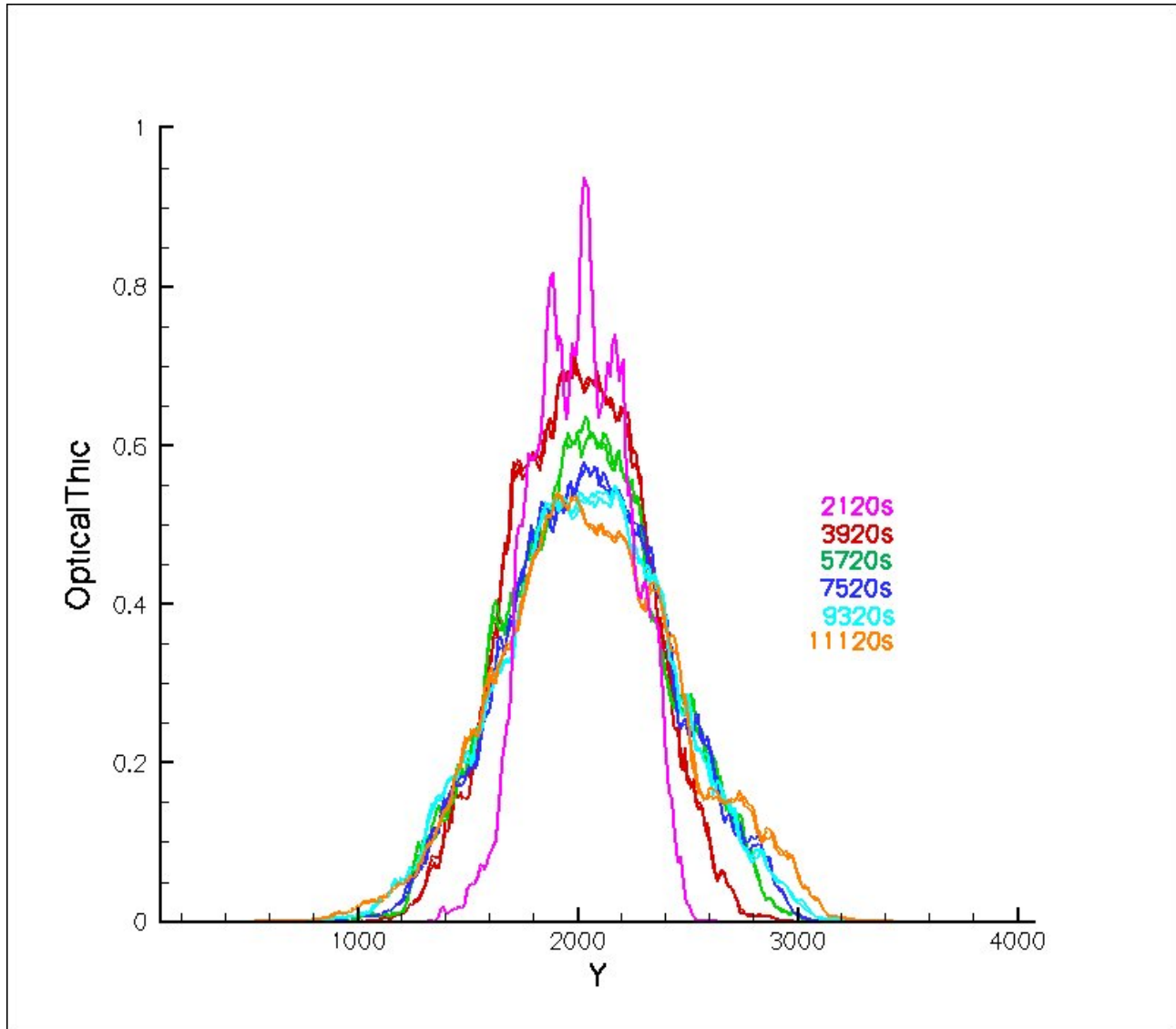


Figure 3: Contrail's optical thickness as a function of the horizontal axis, perpendicular to the flight direction. The optical thickness is integrated over the vertical direction. Colours identify time.

4 CONCLUSION

We use a three-dimensional non-hydrostatic meteorological model to describe the evolution of a contrail in the diffusion regime.

Four hours of the transition contrail to cirrus are simulated. The results show the horizontal contrail spreading over 3200 m width, while the vertical extent remains limited.

At this stage of the dissipation regime, the primary and secondary wakes are not separated any more.

The model is able to maintain a high optical depth because of the simultaneous decrease of ice density and increase of ice mean radius in the growing contrail, as the result of condensation of ambient water vapour.

The mean radius at the top and bottom of the cloud reaches 50 to 55 μm , allowing sedimentation. In this study, we don't activate the sedimentation parameterization, but we expect that the particles radius is large enough to have a fall velocity not negligible any more. As a consequence, the sedimentation impact of the vertical distribution will be addressed in a follow-up study.

5 ACKNOWLEDGEMENTS:

The authors would like to thank the French National Computing Centre for Higher Education (CINES) for the attribution of computational hours, used for this study.

REFERENCES

- Gerz, T., Dürbeck, T., and Konopka, P., 1998: Transport and effective diffusion of aircraft emissions, *J. Geophys. Res.*, 103, 25 905–25 914.
- Jensen, E., Ackerman, A., Stevens, D., Toon, O., and Minnis, P., 1998: Spreading and growth of contrails in a sheared environment, *J. Geophys. Res.*, 103, 31,557–31,567.
- Lafore, J., Stein, J., Bougeault, P., Ducrocq, V., Duron, J., Fischer, C., Hèreil, P., Mascart, P., Masson, V., Pinty, J.-P., Redelsperger, J., Richard, E., and de Arellano, J. V., 1998: The Meso-NH atmospheric simulation system. Part I: adiabatic formulation and control simulations, *Ann. Geophys.*, 16, 90–109.
- Paugam, R., Paoli, R., and Cariolle, D., 2009: Three-dimensional numerical simulations of the evolution of a contrail and its transition into a contrail-cirrus, *ACPD*, 9.
- Sausen, R., Isaksen, I., Grewe, V., Hauglustaine, D., Lee, D. S., Myhre, G., Khler, M. O., Pitari, G., Schumann, U., Stordal, F., and Zerefos, C., 2005: Aviation radiative forcing in 2000: an update on IPCC (1999), *Meteorol. Zeitschrift*, 14, 555–561.

The Effect of Ice Particles on the Tropospheric Ozone Budget via Heterogeneous Conversion processes

J. E. Williams^{*}, G.-J. van Zadelhoff and P.F.J. van Velthoven
Koninklijk Nederlands Meteorologisch Instituut, De Bilt, The Netherlands.

Keywords: Cirrus, Heterogeneous Processes, Future Emissions

ABSTRACT: Cirrus particles are ubiquitous throughout the mid- to upper troposphere and provide reactive surfaces onto which trace gas species may become either attached or chemically processed, thus modifying the chemical cycles active at high altitudes. Here we introduce two simple parameterizations for the description of the micro-physical properties of ice particle fields into a global 3D Chemistry Transport Model. We subsequently investigate the influence that the reversible loss of HNO₃ from the gas phase has on the tropospheric ozone budget. In contrast to previous studies there is a modest increase in the global tropospheric ozone burden, where there are stark hemispheric differences. By applying the EU-QUANTIFY 2050 aircraft emission scenarios using fixed meteorology for 2006 we show that the influence of heterogeneous scavenging becomes less important unless the available surface area upon which scavenging can occur would increase in the future.

1 INTRODUCTION

Ice particles form readily throughout the troposphere and may grow to significant sizes depending on both the ambient temperature and the partial pressure of water vapour. Once present they introduce both perturbations to the radiation budget and reactive surfaces upon which trace gas species may become either reversibly or irreversibly attached, depending on the chemical structure of the chemical species and their characteristic affinity for the ice surface. One such trace gas species which has a high affinity for being scavenged on ice is nitric acid (HNO₃). In the upper troposphere HNO₃ acts as an abundant reservoir species for reactive nitrogen, which, once oxidised, helps determine the *in-situ* formation of tropospheric ozone (O₃). By scavenging HNO₃ out of the gas-phase, a fraction of this reactive nitrogen is essentially removed (sequestered) from the gas phase, which has the potential to lower *in-situ* O₃ formation. Laboratory studies have determined the kinetic parameters needed to describe this reversible uptake and have found that saturation of the ice surface maybe accounted for by using a parameter to describe the maximum number of reactive sites available per cm² of ice surface (Cox et al, 2005). This uptake parameter is commonly known as the Langmuir uptake co-efficient. Here we introduce parameterizations into the global Chemistry Transport Model (CTM) TM4 for the calculation of the available reactive surface area utilizing the Ice Water Content (IWC) available from ECMWF meteorological data and investigate the effects of reversible scavenging of HNO₃ out of the gas phase.

2 DESCRIPTION OF THE CTM

The version of TM4 used in this study is similar to TM4_AMMA described in Williams et al (2009) apart from the application of updated heterogeneous uptake data for (e.g.) the scavenging of HCHO into cloud droplets. The gas phase conversion of N₂O₅ into HNO₃ involving water vapour is also included in the modified CBM4 scheme using the latest recommendations (Williams and Van Noije, 2008). For the present day simulations (denoted BASE and HNO₃_UP) the emissions are taken from the RETRO database (<http://retro.enes.org>) for anthropogenic and biogenic emissions and the GFEDv2 database (van der Werf et al, 2006) for biomass burning emissions. An injection

^{*} Corresponding author: Jason E. Williams, Koninklijk Nederlands Meteorologisch Instituut, Wilhelminalaan 10, 3732GK De Bilt, The Netherlands. Email: williams@knmi.nl

height of 2km is used in the tropics (20°N-20°S), which is typical of the injection heights seen in recent measurements (Labonne et al, 2007). Moreover, a daily cycle is imposed on the biomass burning cycle, which peaks at 2pm local time as has been determined by analysing satellite data with staggered overpass times (Boersma et al (2008)) and geostationary platforms (Roberts et al, 2009). For the future simulations (denoted 2050 and 2050_HNO3_UP) aircraft emissions for the year 2050 are applied as taken from the QUANTIFY emission database. The model uses a vertical resolution of 34 layers and a horizontal resolution of 3° x 2°, where ECMWF meteorological data is applied using an update frequency of 6 hours. A spin-up period of 6 months was used for each individual simulation.

3 RESULTS

3.1 The zonal distribution of ice particle

For the description of ice particles we introduce the parameterization of Heymsfield and McFarquar (1996) for the derivation of the Surface Area Density (SAD), and we use the resulting cross-sectional area (A_c) in the parameterization of Fu (1996) for the calculation the effective radii (R_{eff}). Both parameterizations use the ECMWF IWC for the derivation of the respective micro-physical properties of the ice particles. A scaling ratio of 10 was used to convert A_c into SAD as suggested by Schmitt and Heymsfield (2005), which constitutes a correction for randomly shaped particles rather than spherical particles. This is higher than the values of 2-4, which are more representative of spherical particles, used in previous CTM studies (Lawrence and Crutzen, 1998; von Kuhlmann and Lawrence, 2005). Both parameterizations have been validated against a host of different in-situ measurements (e.g. Heymsfield, 2003). Figures 1a and b show the resulting zonal distribution of both the R_{eff} and SAD values for seasons DJF and JJA, respectively. The largest R_{eff} values occur in the upper troposphere (UT) in the tropics and the lower troposphere at the poles, where there is a zonal shift between the seasons. For the SAD the highest values tend to occur in the lower troposphere above 65° latitude, as determined by the frequency at which particles occur throughout the season. Analysing daily fields reveals that values of R_{eff} ranging between 50-100µm can occur (not shown), although such sizes do not show up in the seasonal means. Depending on the lifetime of the ice particles, gravitational settling can occur for the larger particles, which will re-distribute any scavenged trace species to lower altitudes.

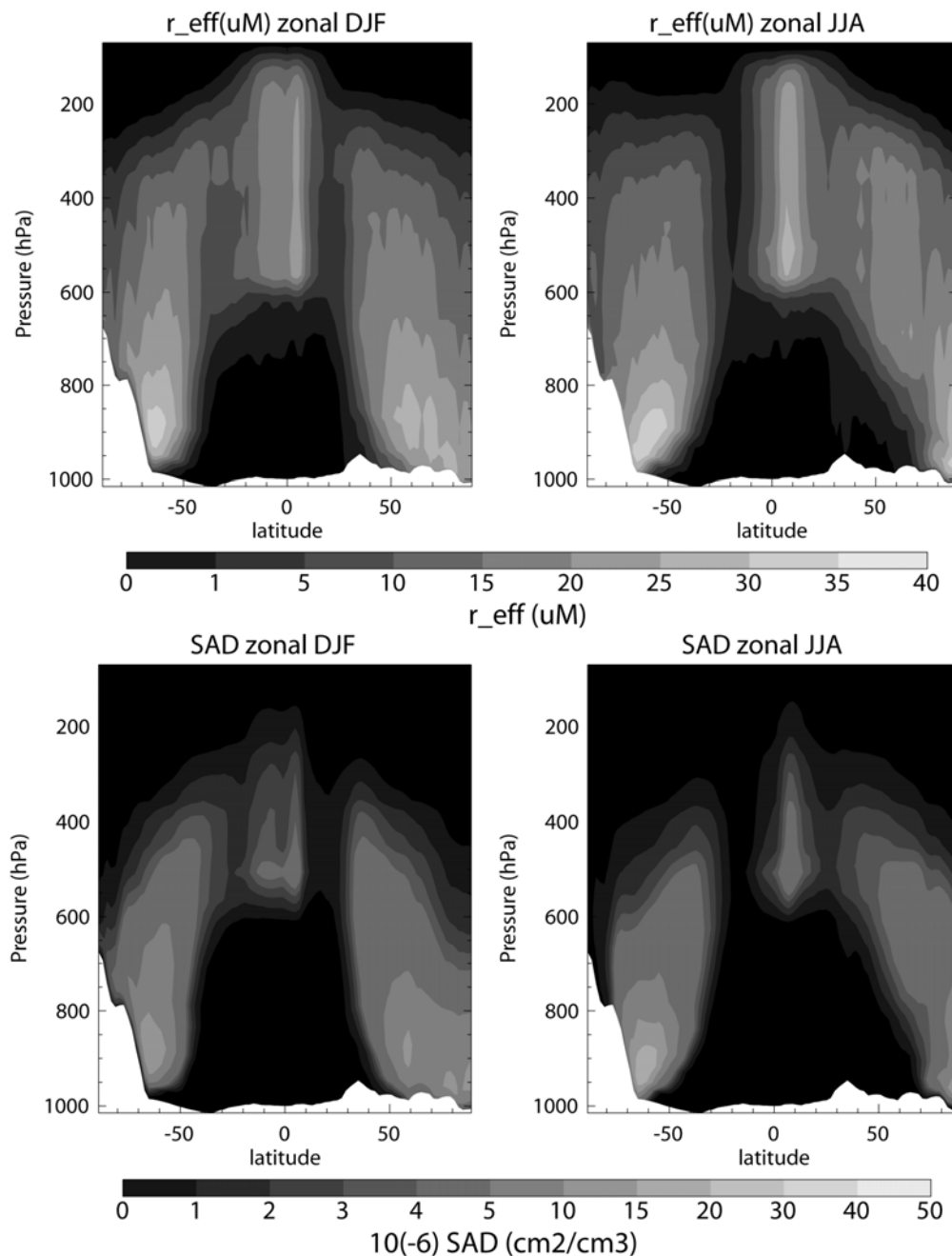


Figure 1: The zonal distribution of (top) R_{eff} and (bottom) SAD for seasons DJF and JJA when applying the chosen parameterizations for calculating the microphysical properties of ice fields online in TM4.

3.2 The effect of uptake of HNO_3 on ice surfaces for present day emissions

The uptake of HNO_3 on ice has been included in TM4 according to the latest recommendations given on the IUPAC website for chemical reaction data (www.iupac-kinetic.ch.cam.ac.uk), where the equilibrium rate is converted into a first-order absorption and desorption rate using the available SAD. It should be noted that trapping of HNO_3 by growing ice surfaces at low temperatures ($<210^\circ\text{K}$) as recently proposed by Kärcher et al (2009) is not included. Figure 2 shows the zonally integrated annual differences introduced for O_3 , NO_x , HO_x and the predominant nitrogen containing reservoir species. For the UT there are decreases in $[\text{HNO}_3]$ of $\sim 10\%$, with corresponding perturbations in $[\text{O}_3]$ of $\pm 2\%$. The differences in the lower troposphere are more moderate due to the higher temperatures which limit the available SAD. There is a clear difference in the simulated changes between the hemispheres as a result of higher $[\text{HNO}_3]$ (and $[\text{NO}_x]$) in the NH UT that are due to aircraft emissions. This uptake and subsequent release of HNO_3 causes an increase in $[\text{NO}_x]$ of between 2–5%, subsequently enhancing in-situ O_3 formation in the NH by a few percent. This is in contrast to previous studies, where decreases of between 40–60% have been simulated using NCEP meteorological data (von Kuhlmann and Lawrence, 2005). These authors did not provide in-

formation regarding the distribution of the available SAD, and no limit was placed on the number of reactive sites on the ice surface which can be occupied (*i.e.* saturation is ignored). Also a different uptake co-efficient was applied. In essence, the SAD values calculated here online in TM4 are low ($20\text{--}50\text{ }\mu\text{m}/\text{cm}^2$) compared to the range of values typically captured by in-situ measurements ($20\text{--}500\text{ }\mu\text{m}/\text{cm}^2$; Popp et al, 2004). This limits the amount of HNO_3 which can be scavenged out of the gas phase, where the low SAD is a result of the relatively large resolution adopted in the model and the ECMWF meteorological dataset (typically 1 km height in the UT). This could potentially be improved upon by introducing parameterizations of sub-grid processes (e.g.) for a more accurate description of aircraft contrails (which are currently ignored). Additional sensitivity tests including gravitational settling of large particles result in differences in NO_x of $\pm 1\%$ (not shown), due to the low fraction of HNO_3 removed from the gas phase. Inclusion of a fraction of irreversible loss ('Burial'), as proposed by Kärcher et al (2009), would enhance the effects presented here by providing a NO_x sink at high altitudes. Moreover, conversion of the NO_3 radical and irreversible loss of OH on the surface of ice particles were also tested and found to have relatively small effects on the composition of the UT.

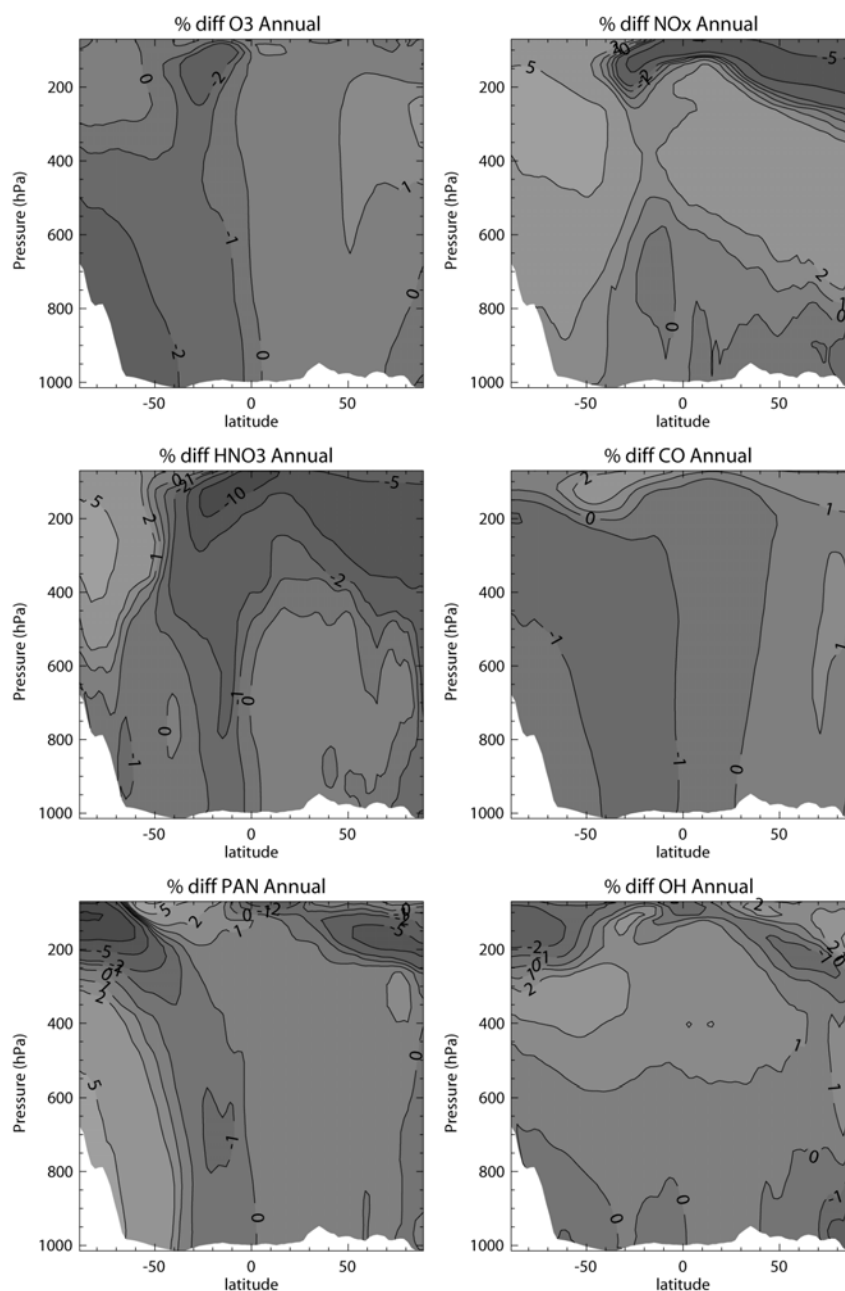


Figure 2: The zonally integrated annual differences in (a) O_3 , (b) NO_x , (c) HNO_3 , (d) CO , (e) PAN and (f) OH as a result of introducing heterogeneous uptake of HNO_3 on cirrus particles.

3.3 The effect of future aircraft emissions for the year 2050

The 2050 A1 future aircraft emissions as taken from the QUANTIFY project (www.pa.op.dlr.de/quantify) increase the annual global nitrogen budget by $\sim 4.5\text{Tg N}$, where the additional NO_x is predominantly injected between 200–600 hPa in the NH. Here we apply the meteorology for 2006 in order to differentiate the influence of increasing the aircraft emissions towards the future estimates from possible meteorological differences in future years. Figure 3 shows the resulting increases in the zonally integrated annual means for O_3 , NO_x and HNO_3 . For $[\text{NO}_x]$ increases of $>200\%$ occur between 200–400 hPa, which increases the tropospheric burden of O_3 by $\sim 10\%$. For HNO_3 , there are corresponding increases of up to $\sim 100\%$. Comparing Figs 1 and 3 shows that the largest increases in $[\text{HNO}_3]$ generally occur above the altitude at which the ice particle field exhibits its significant coverage.

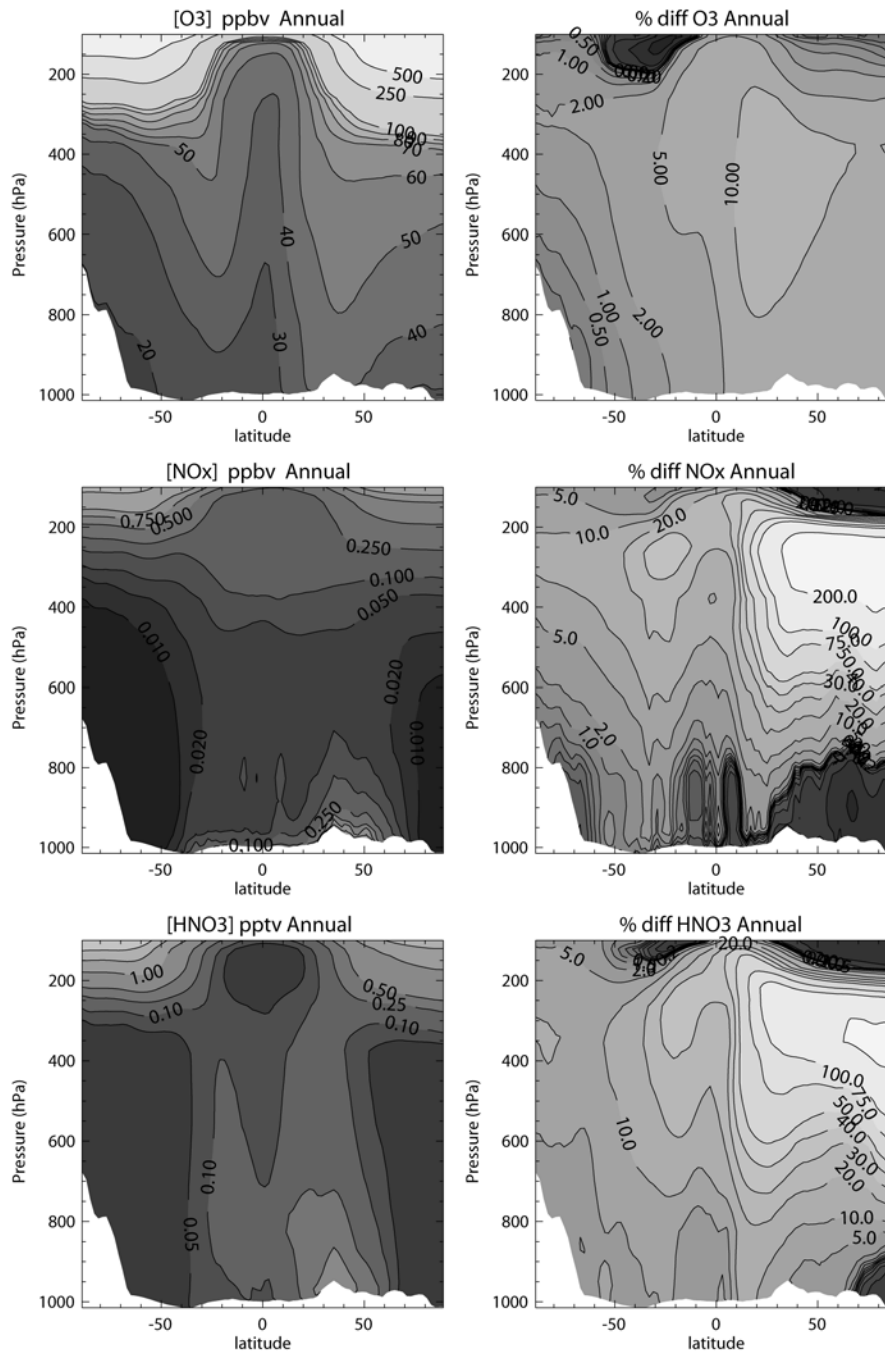


Figure 3: The zonally integrated annual means of (a) O_3 , (b) NO_x and (c) HNO_3 in the BASE simulation and the resulting differences as compared to the BASE_2050 simulation using 2006 meteorology.

3.4 The importance of heterogeneous scavenging with increased aircraft emissions

For the 2050_HNO3_UP simulation the perturbation in the *in-situ* production of ozone becomes

less important. Table 1 provides the global tropospheric burdens for O_3 , CO and HNO_3 for all of the simulations presented. Comparing the values for the BASE and 2050 simulations, it can be seen that the increase in $[\text{O}_3]$ substantially reduces the tropospheric burden of CO (although the corresponding future increase in CO emissions are not included in the simulation). For the solid $[\text{HNO}_3]$ the total integrated N scavenged onto ice surfaces increases +7% from 0.96 Tg yr^{-1} (present) to 1.03 Tg yr^{-1} (future). The percentage increase is less than that which occurs in the gas phase due to both saturation of the available ice surfaces and the differences in altitude between the SAD available and that where the largest increases in HNO_3 occur. The net effect on tropospheric O_3 is to reduce the observed increase which occurs in the present day scenario. In reality the changing climate could also impose an effect by modifying the SAD which is available, where increasing temperatures as a result of an increase in the radiative forcing from (e.g.) O_3 and a positive feedback due to enhanced evaporation (Dressler et al, 2008) would result in a decrease in the incidence of cirrus, thus diminishing the importance of such heterogeneous processes.

Table 1: The changes in the tropospheric burdens of O_3 , CO and HNO_3 due to heterogeneous scavenging of HNO_3 onto cirrus particles. All numbers are globally integrated values for the year 2006, where the HNO_3_{UP} and 2050_ HNO_3_{UP} values are given in parenthesis.

Trace Species	Present Tropo. Burden (Tg)	Future Tropo. Burden (Tg)
O_3	263.5 (275.5)	295.6 (294.6)
CO	305.7 (292.9)	274.3 (278.5)
HNO_3	0.645 (0.641)	0.649 (0.645)

4 CONCLUSIONS

In this study we have show that by incorporating simple parameterizations for calculating the micro-physical properties of cirrus particles in a global CTM, we can introduce seasonal and spatial variability in the ice particle fields as constrained by the meteorological input data available in the model. By introducing reversible scavenging of HNO_3 onto ice surfaces we have found that stark differences occur between the Northern and Southern Hemispheres with respect to the perturbation introduced to the in-situ formation of tropospheric O_3 . This effect is more modest than that found in previous studies, in that our study gives an increase in the tropospheric O_3 burden as a result of an increase in the availability of reactive nitrogen. The limited amount of scavenging of HNO_3 out of the gas phase means that the effect of de-nitrification due to the gravitational settling of large particles can be neglected. For a more accurate assessment of the global effects, the fraction of HNO_3 lost irreversibly into ice particles needs to be included, along with sub-grid parameterizations to describe the high SAD of contrail cirrus. This should amplify the effects presented here leading the a net global decrease in tropospheric O_3 . When adopting future aircraft emission estimates using fixed meteorology for 2006, we find that the fraction of HNO_3 scavenged out of the gas phase is reduced due to saturation effects on the ice surface. Therefore, without a corresponding increase in SAD due to climate changes, which is not likely considering that temperature is likely to increase, the influence of heterogeneous scavenging will become less important.

REFERENCES

- Boersma K. F., D. J. Jacob, H. J. Eskes, R. W. Pinder, J. Wang and R. J. van der A, 2008: Intercomparison of SCIAMACHY and OMI tropospheric NO_2 columns: Observing the diurnal evolution of chemistry and emissions from space, *J. Geophys. Res.*, 113, D16S26, doi:10.1029/2007JD008816.
- Cox, R. A., M. A. Fernandez, A. Symington, M Ullerstam and J. P. D. Abbatt, 2005: A kinetic model for up-take of HNO_3 and HCl on ice in a coated wall flow system, *Phys. Chem. Chem. Phys.*, 7, 3434-3442.
- Dressler, A. E., Z. Zhang and P. Yang, 2008: Water-vapor climate feedback inferred from climate fluctuations, 2003-2008, *Geophys. Res. Letts.*, 35, doi: 10.1029/2008GL035333.
- Grewe, V., M. Dameris, C. Fichter, and R. Sausen, 2002: Impact of aircraft NO_x emissions. Part 1: Interactively coupled climate-chemistry simulations and sensitivities to climate-chemistry feedback, lightning and model resolution, *Meteorologische Zeitschrift*, 11(3), 139ff.
- Heymsfield, A. J. and G. M. McFarquhar, 1996: High albedos of cirrus in the tropical pacific warm pool:

- Microphysical interpretations from CEPEX and from Kwajalein, Marshall Islands, *J. Atmos. Sci.*, 53, 2424-2451.
- Heymsfield, A. J., 2003: Properties of Tropical and Midlatitude Ice Cloud Particle Ensembles. Part II: Applications for Mesoscale and Climate Models, *J. Atmos. Sci.*, 60, 2592-2611.
- Kärcher, B., Abbatt, J. P. D., Cox, R. A., Popp, P. J. and Voigt, C., 2009: Trapping of trace gases by growing ice surfaces including surface-saturated adsorption, *J. Geophys. Res.*, 114, D11306, doi: 10.1029/2009JD011857.
- Labonne, M., F-M Breon and F. Chevallier, 2007: Injection height of biomass burning aerosols as seen from a spaceborne lidar, *Geophys. Res. Letts.*, 34, doi: 10.1029/2007GL029311.
- Lawrence, M. G., and P. J. Crutzen, 1998: The impact of cloud particle gravitational settling on soluble trace gas distributions, *Tellus*, 50B, 263-289.
- Popp, P.J., Gao, R.S., Marcy, T.P., Fahey, D.W., Hudson, P.K., Thompson, T.L., Kärcher, B., Ridley, B.A., Weinheimer, A.J., Knapp, D.J., Montzka, D.D., Baumgardner, D., Garrett, T.J., Weinstock, E.M., Smith, J.B., Sayres, D.S., Pittmann, J. V., Dhaniyala, S., Bui, T.P., and Mahoney, M., 2004 :Nitric Acid Uptake on Subtropical Cirrus Cloud Particles, *J. Geophys. Res.*, 109, D06, doi: 10.1029/2003JD004255.
- Roberts, G., M. J. Wooster, and E. Lagoudakis, 2009: Annual and diurnal biomass burning temporal dynamics, *Biogeosciences*, 6, 849-866.
- Von Kulmann, R., and M. G. Lawrence, 2006: The impact of ice uptake of nitric acid on atmospheric chemistry, *Atms. Chem. Phys.*, 6, 225-235.
- Williams, J. E., and T. P. C. van Noije, 2008: On the upgrading of the modified Carbon Bond Mechanism IV for use in global Chemistry transport Models, KNMI Scientific report WR 2008-02, pp 64.
- Williams, J. E., M. P. Scheele, P. F. J. van Velthoven, J-P. Cammas, V. Thouret, C. Galy-Lacaux and A. Volz-Thomas, 2009: The influence of biogenic emissions from Africa on tropical tropospheric ozone during 2006: a global modelling study, *Atms. Chem. Phys.*, 9, 5729-5749.
- Van der Werf, G. R., Randerson, J. T., Giglio, L., Collatz, G. J., Kasibhatla, P. S., and Arellano Jnr, A. F., 2006: Interannual variability in global biomass burning emissions from 1997 to 2004, *Atms. Chem. Phys.*, 6, 3423-3441.

Short-haul Flights and Climate Change: What are the Effects and Potential Alternatives?

R. Kaur*, C. Dey

Integrated Sustainability Analysis (ISA) Group, School of Physics, University of Sydney, Australia

Keywords: climate change, short-haul flights, integrated analysis, door-to-door emissions, policy-making.

ABSTRACT: Despite the economic crisis airline traffic for budget airlines grew by at least 10% in the beginning of 2009 (Ryanair, 2009; Easyjet, 2009). The growth in aviation can be attributed to the shift from full service carriers to budget airlines and as the industry is set to continue to grow this has important implications for climate change. Most literature focuses on modes of transport independent of each other. Realistically total journeys consist of a combination of transport modes as a consequence of time, cost and accessibility and policy making should involve a holistic approach in order to tackle climate change. This research involves a scenario analysis which involves calculating door-to-door emissions using a combination of different modes of transport between several origins within the UK to a destination in Europe. This provides a comparable analysis between budget airlines and full-service airlines; between hub airports and regional airports and between alternative modes of transport. Results show that trains are the best alternative in the context of door-to-door emissions however, results also show the necessity of an efficient infrastructure to and from regional airports to mitigate emissions. This paper concludes with a set of policy recommendations using a holistic approach.

1 INTRODUCTION

The impact of aviation on climate change is unique compared to other industries as aircraft engine emissions inject directly into the atmosphere which as research has shown has a greater effect on the environment than if the gases were emitted from the ground. The commercial aviation industry has been a fast growing industry and concerns are also growing in how to address its environmental impacts (Whitelegg, 2000; Bows & Anderson, 2007). Scientific uncertainty in quantifying these effects into a meaningful numerical value which policy makers require to mitigate these emissions poses a great challenge especially when emissions from aviation continue to grow.

Despite inclusion into the Kyoto Protocol, restrictions are only considered for domestic air travel (Oberthur, 2003). However, the majority of flights within Europe are international flights. In 2005, approximately 70% of total flights from the UK were destinations within Europe (CAA, 2007). With an increase of short-haul flights alternative modes of transports are being suggested in order to reduce green house gas emissions (ghge). International flights are set to continue to grow especially with budget airlines entering the medium-haul markets.

Since 1999, UK air traffic growth has been above the global average (Bows & Anderson, 2007). The UK accounts for a large proportion of the world's total aviation activity with a fifth of all international air passengers flying to or from a UK airport (DfT, 2003). The number of international passenger movements by air between 1995 and 2005 is illustrated in Figure 1:

* Corresponding author: Rajinder Kaur, Environmental Research and Consultancy Department, Civil Aviation Authority, London, WC2B 6TE, UK, rajinder.kaur@hotmail.co.uk

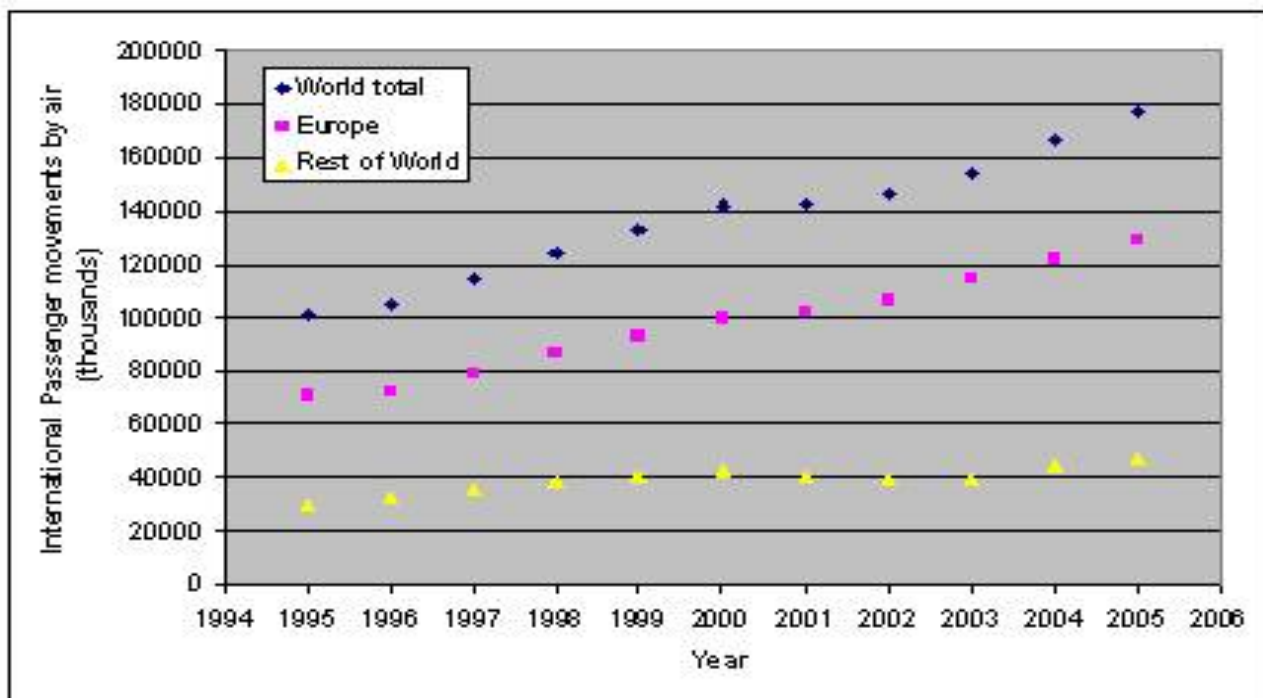


Figure 1. UK international passenger movements by air: 1995-2005 (DfT, 2006).

From Figure 1, the majority of international passenger movements are to and from Europe (approximately 70%) which is considered in this paper as short-haul. Furthermore, it shows that the increase of international passenger movements within the UK is attributed to short-haul flights. The number of international passengers from 2002 to 2005 increased by 31 million, 23 million additional passengers flying to Europe and about 8 million to the rest of the world.

It can be argued that this cause of growth can be attributed to the success of the low cost model used by budget airlines. Figure 2 (obtained from a report done by the CAA in 2006) illustrates the number of airport pairs from 1986 to 2005 comparing full-service airlines and budget airlines flown within the EU. It shows that from the mid 1990s airport pair numbers continued to grow rapidly for budget airlines relative to full-service airlines. This growth can be attributed to the increasing use of regional airports as well as using London (hub) airports. Between 1995 and 2005 the total traffic at regional airports grew from 46.6m to 94.7m, an average annual growth rate of 7.3% (CAA, 2006).

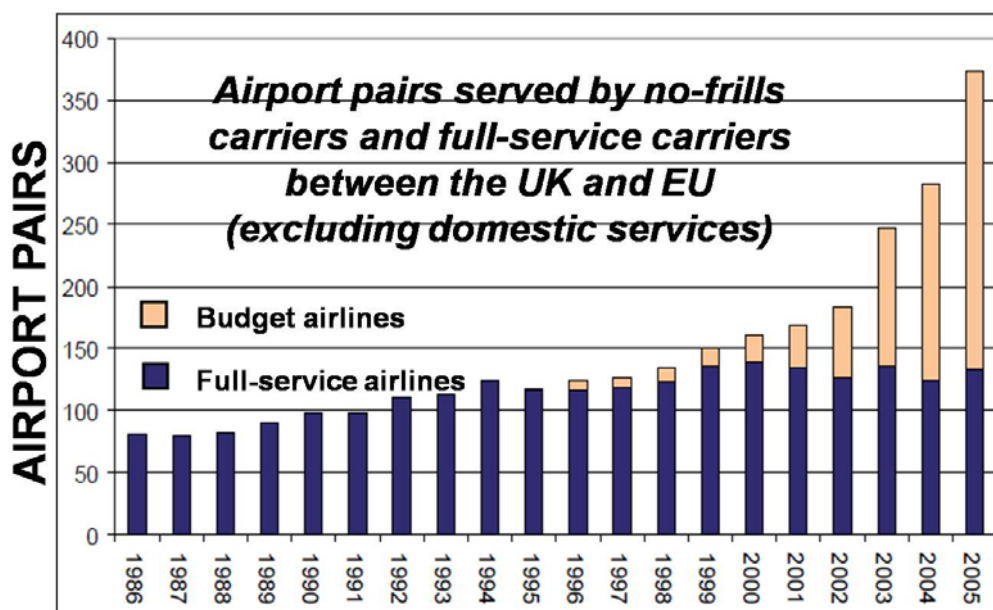


Figure 2. Airport pairs served by budget airlines between the UK and EU (excluding domestic services (CAA, 2006) (NB: CAA refers to budget airlines as 'no-frills' and also note this is for the EU and not all of Europe).

This paper analyses the effects of the changes within and its effect on climate change. The scope of the study consists of calculating the shift from full service airlines to budget airlines. This not only involves a change of airline, load capacity etc. but most importantly a shift of origin and destination airports i.e. hub versus regional. Most importantly, this research goes further and uses a holistic approach by calculating the door-to-door emissions from origin through to destination in the form of case studies. Literature read focuses on modes of transport independent of each other. Realistically, total journeys consist of a combination of transport modes as a consequence of time, cost and accessibility. Givoni and Banister (2006) discuss the potential benefits of airline and railway integration, through a mixture of substitution (i.e. replacing short-haul flights with high-speed rail) and complementation (better rail infrastructure to reach airports). However, their model was focused on Heathrow and discussed the potential benefits to hub airports if complementation was implemented. Finally, alternatives consisted of calculating different modes of transport i.e. substitution for the entire journey in each case study.

2 METHODOLOGY

A scenario analysis calculating the $\text{CO}_{2\text{equivalent}}$ of emissions for different combinations and sequences of modes of transport, including both full-service and budget airlines from regional and hub airports which are then compared and analysed. The scenario analysis uses a case study of holiday travellers travelling from the UK to the popular holiday destination Barcelona.

The scenario analysis considers three points of origins (Bristol, Bournemouth, Newcastle Upon Tyne). From each origin, holiday travellers have the following options to reach Barcelona via:

- a full-service airline flying from Heathrow airport (which included combinations of other modes of transport getting to and from the airport) to Barcelona airport (hub airport);
- a budget airline from Stansted (which included combinations of other modes of transport getting to and from the airport) to a regional airport in Girona and from there to Barcelona;
- regional airports (which included combination of other modes of transport getting to and from the airport) to a local airport in Girona and from there to Barcelona;
- alternative modes such as car, train, and coach for the entire journey.

The assumption of door-to-door was from each origin's train station to Barcelona train station. The budget airline Ryanair was used. The reasons for these different scenarios included to compare the emission differences between:

- Shifting from full-service carriers from Heathrow to budget airlines from Stansted
- Flying from regional airports versus flying from Stansted.
- Different combinations of modes of transport to and from the airport, to see if complementation could be feasible rather than complete substitution.
- Comparing the effects of flying versus potential alternatives over the ground.

The analysis is on the basis of a Boeing 737-400, a representative aircraft type for short-haul flights (Jardine, 2005). The emissions for a B737-400 are obtained from the Emissions Inventory Guidebook (EEA, 2001). Both the 'landing and take-off' (LTO) and 'climb cruise and descend' (CCD) distances are used to obtain the CO_2 emissions for the flight. The total CO_2 emissions from the LTO cycle of the B737-400 are equal to 2599.7 kg CO_2 . The total CO_2 emissions from the CCD cycle of the B737-400 depends on the quantity of fuel burnt, which is a function of the distance flown. From the amount of fuel used, the CO_2 emissions can be calculated. Each kg of fuel burnt produces 3.15 kg of CO_2 (Jardine, 2005). The total $\text{CO}_{2\text{equivalents}}$ /passenger.km for a short-haul flight can therefore be calculated as follows:

$$EPP = \frac{(LTO_{co2} + CCD_{co2}) \times RFI}{N_{seats} \times LF \times d} \quad (1)$$

where EPP is kg of $\text{CO}_{2\text{equivalent}}$ /pass.km; the LTO_{CO_2} and CCD_{CO_2} are in kg of CO_2 ; RFI is the radiative forcing index; N_{seat} is the number of seats an aeroplane contains; LF is the load factor and d is the distance. The RFI factor of 1.9 is used to convert the CO_2 emissions of the aircraft into

CO₂equivalent emissions and this figure is obtained from research on radiative forcing from aviation conducted by Sausen et al. (2005).

The difference between budget and full service airlines were seat capacity and load factor:

- A full-service airline has 160 seats and an average occupancy of 70% (ELFAA, 2005)⁸.
- Ryanair has 189 seats (Boukhari, 2007) and an average occupancy of 83% (ELFAA, 2005)

The emissions and assumptions associated with each mode of transport can be found in Table 1.

Ground-surface mode	Load factor	CO ₂ equivalent/p.km	Reference
Petrol car	1.58	0.20949	Lenzen (1999)
Train	50% full	0.038	ECCM (2007)
Coach	Not listed in reference	0.1	National Express (2005)

Table 1. CO₂equivalent values used for ground-surface modes of transport.

The following assumptions were used to calculate emissions from ground-surface modes of transport: the UK trains systems consists of 85% electric and 15% diesel trains, this composition was also used for Spanish train systems; the load factor for trains was 50%; the petrol car occupancy was of 1 person. (Note: the occupancy for the figure shown for a coach in Table 1 is unknown).

In total, there are 9 different scenarios with regard to full-service carriers to Barcelona and 3 different scenarios using alternative modes of ground-transport for the entire journey (see Figure 3). For budget airlines, there are 20 different scenarios generated by travelling from Bristol and Bournemouth to Barcelona. Newcastle Upon Tyne has 24 scenarios, since it is the only origin where its regional airport has a train connection (see Figure 4).

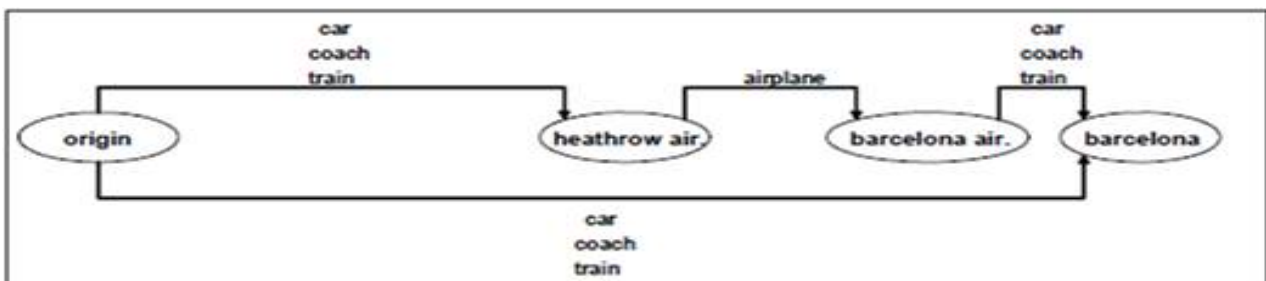


Figure 3. Different scenarios travelling to Barcelona via full-services airlines.

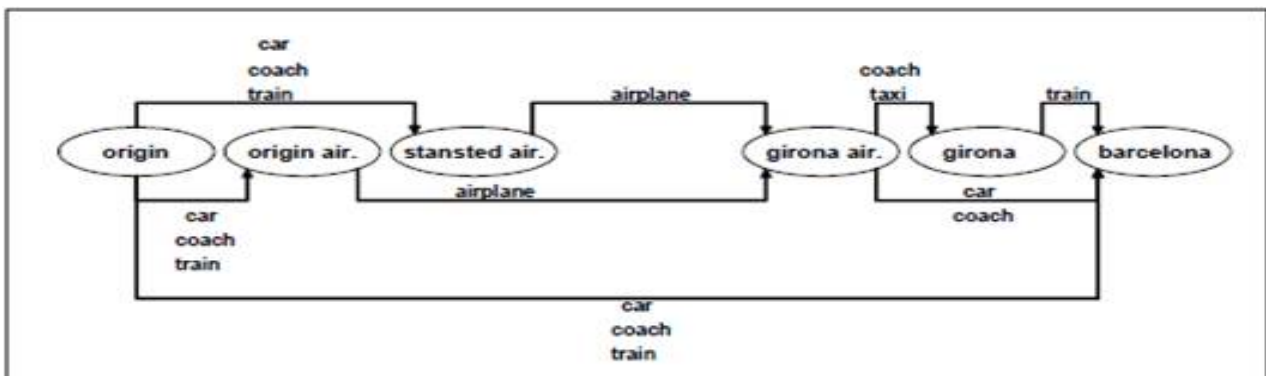


Figure 4. Total number of scenarios for travelling to Barcelona with budget airlines.

⁸ This data is obtained from a report of the European Low Fares Airline Association, which might be biased towards presenting data on budget airlines in favour of full-service airlines.

3 RESULTS

Figure 5 shows the results for all the different transport scenarios from Bournemouth, Bristol and Newcastle Upon Tyne to Barcelona. Scenario 1, 2 and 3 show the CO_{2equivalent} for travelling via car, train and coach to Barcelona, respectively. Scenarios 4 – 11 show the different options travelling via the regional airports. Scenario 12 – 23 show the different options travelling via Stansted and scenario 24 – 32 show the different scenarios flying with full-service airlines.

Figure 5 suggests that the CO_{2equivalent} is reduced if the market shifts from full-service airlines to budget airlines from regional airports. In addition, the scenario analysis shows that not only the air flight mode (regional, hub with budget or full-service) is an important determinant in total emissions, but also the different modes of transport to and from the airport have an important effect. The differences between the worst and best emission performance are large within each of the different methods of travelling. The worst performing scenarios for each of the three origin destinations (scenario 30 in Figure 5) is to drive by car to a hub airport and take a full carrier to Barcelona (374, 316, 313 kg CO_{2equivalent} for Newcastle Upon Tyne, Bournemouth and Bristol respectively). The fact that the full-service airline arrives closer to the destination does not outweigh the additional CO_{2equivalent} emissions from driving to the departure airport and the additional CO_{2equivalent} emissions from the flight in comparison to using a budget airline.

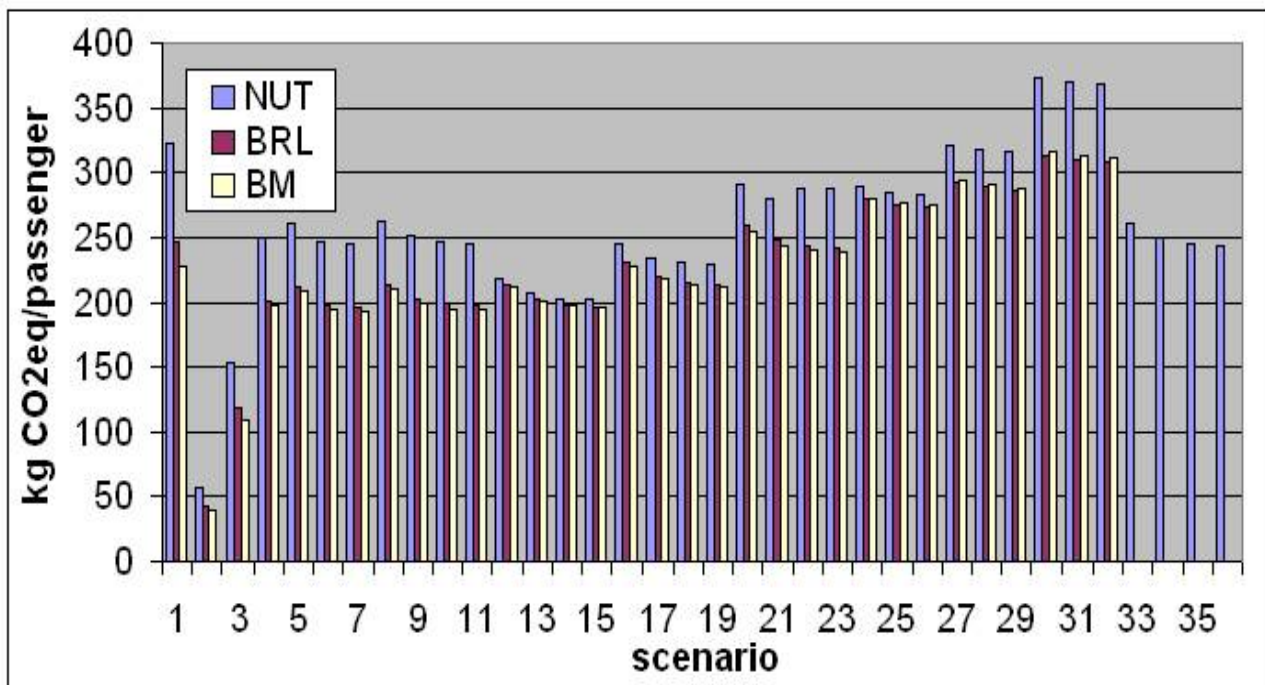


Figure 5. Total CO_{2equivalent} for one passenger for different scenarios travelling from the UK to Barcelona.

However, the best performing scenarios are different for the different origins. For Bournemouth and Bristol the best combination of transport modes consist of a bus to the regional airport and a train from Girona to Barcelona (193 and 196 kg CO_{2equivalent}, see scenario 7 in Figure 5), while for Newcastle Upon Tyne it is better to take the train from Newcastle Upon Tyne to Stansted and fly from there (187 kg CO_{2equivalent}, see scenario 15 in Figure 5) i.e. complementing the flight with train as the ground-transport. Furthermore, these results suggest that from a holistic perspective, reducing emissions in relative terms does not mean that there is one suitable mode of getting to and from the airport using existing infrastructure. Instead, different combinations might be required for different journeys whereby the location of the regional airports in comparison to the origin and destination is a major factor.

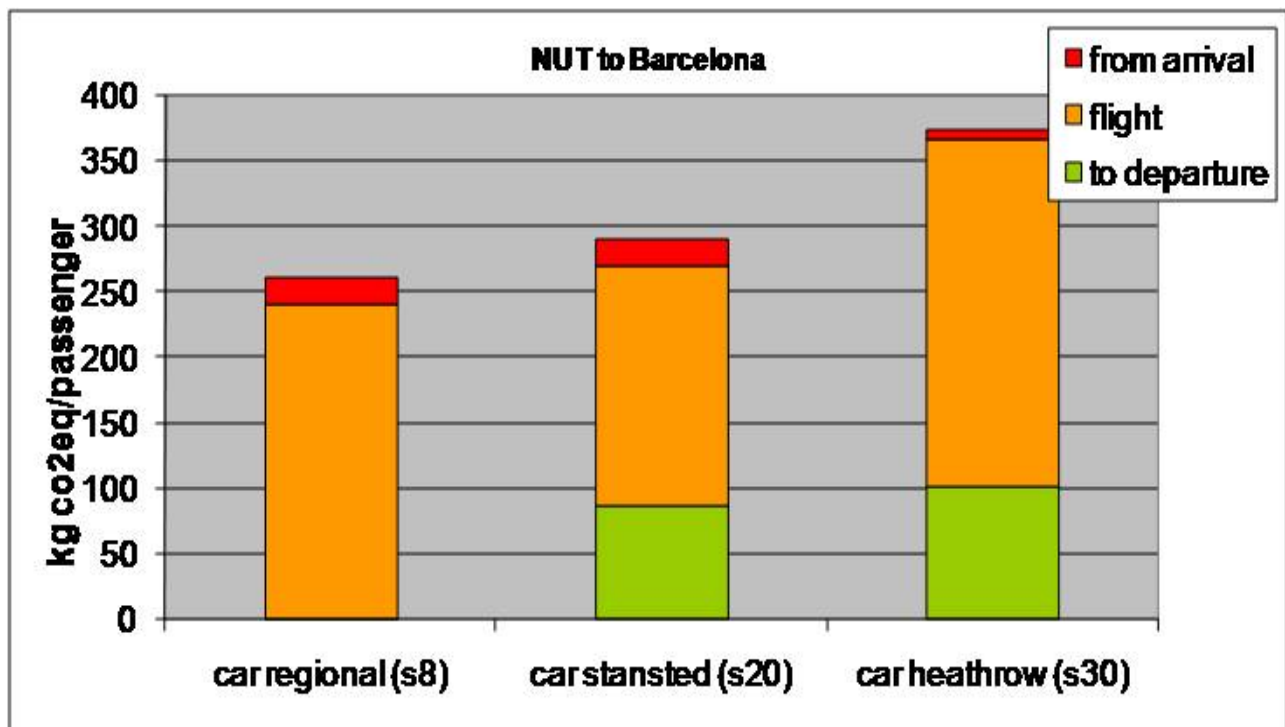


Figure 6. Total CO_{2eq} for one passenger travelling by car from Newcastle Upon Tyne to and from airports flying from the UK to Barcelona.

The results can also be used to compare the effects on CO_{2equivalent} emissions from 1) the journey from the origin to the departure airport, 2) the flight itself and 3) from the arriving airport to the destination. Figure 6 compares three different scenarios from Newcastle Upon Tyne to Barcelona whereby holiday travellers drive to and from the airports by car. For a budget flight from the regional airport (scenario 8 in Figure 5), this means that the CO_{2equivalent} emissions mainly take place from the arrival airport to the destination, while for budget or full-service airlines from London the emissions take place in the journey to the departure airport (scenario 20 and 30 in Figure 5). However, part of the emissions saved by using a regional airport are offset by the longer flight distance. In total, however, there is a 30% CO_{2equivalent} emissions saving if flown from a regional airport, while there is a 22% saving for flying with budget airlines in comparison to full-service airlines. These results suggest that the shift towards regional airports can save CO_{2equivalent} emissions, however the connection to and from the regional airports is crucial.

4 CONCLUSIONS AND RECOMMENDATIONS

Policy making should endeavour to tackle climate change by not looking at industries as sole entities but through an integrated approach. Trains are the best alternative in the context of substitution from door-to-door. There is a need for an efficient infrastructure to and from regional airports to reduce emissions. Regional airports may save emissions in comparison to full-service airlines via hubs however, this requires good public transport infrastructure. My final conclusion is that policy-making should focus on complementation of different modes of transport and to emphasise that these results show that there is no single combination of different modes which is suitable for all journeys – it depends on the distance of the origins and destinations relative to the airports.

Recommendations for further work include the following:

- Calculating the CO_{2equivalent} emissions by using more sophisticated and reliable method, which would be able to consider more accurately the effects of CO₂ emissions in the air (RFI was used as a quick and simple method in order to take into consideration the total impact of aviation).
- Emissions at airports – factoring in the contribution of emissions while waiting at airports, train stations, coach stations etc.
- Indirect emissions – a full life cycle analysis. Chester & Hovarth (2009) showed that the indirect emissions from onroad was an additional 63%, 155% for rail and 31% for aircraft systems.

- Cost and time – to see what effect this has on using a combination of different modes of transport and how factoring in reducing emissions from journeys can be effected by cost and time issues.
- Factoring other environmental impacts – climate change is not the only impact aviation has on the environment – noise and local air quality issues are also taken into consideration, but how are the trade-offs or comparing different impacts decided? What are the common indicators in comparing these in order to make decision-making less difficult?

Finally, in terms of policy it is crucial to consider high uncertainty, which is associated with these analyses. These uncertainties are partly the result of the scientific measures associated with analysing the effects of emissions on climate change. These uncertainties cannot be ignored, however need to be simplified in order to be able to form a basis for policy. Scientists focus on quantifying uncertainty in data for policy makers, however there is also uncertainty in applying this data. If an agreement is made at Copenhagen 2009 to cap international aviation emissions this is a positive step forward in tackling the impact of aviation on climate change.

5 ACKNOWLEDGEMENTS

I would like to thank Chris Dey for his help with this work. This research was conducted as part of my Masters thesis submitted in July 2007 at the University of Sydney as a post-graduate.

REFERENCES

- Boukhari, A., 2007: Low-cost airlines, Bryan, Garnier & Co., London, Paris & Geneva, 62.
- Bows, A. and Anderson, K. L., 2007: Policy clash: Can projected aviation growth be reconciled with the UK Government's 60% carbon-reduction target., *Transport Policy*, 14, 103-110.
- CAA 2006: No-Frills Carriers: Revolution or Evolution? A Study by the Civil Aviation Authority, CAA, London, 1-98.
- CAA, 2007: CAA Figures Show Increased Air Traffic at UK Airports in 2006.
- Chester, M. & Horvath, A., 2009: Environmental assessment of passenger transportation should include infrastructure and supply chains. *Environ. Res. Lett.* 4, 1-8.
- DfT, 2003: The Future of Air Transport, Aviation White Paper, London, 1-180.
- DfT, 2006: TSGB 2006 - List of Aviation data tables.
- ECCM, 2007: Emissions of trains and petrol cars in the UK, ECCM Ltd.
- EEA, 2001: UNECE/EMEP/EEA. The Emission Inventory Guidebook. Snap codes 080501-4, Vol. 2007.
- ELFAA, 2005: Low Fares Airlines and the Environment, European Low Fares Airline Association.
- Easyjet (2009) Quarter 1 2009 Interim Management Statement January 2009, January 2009, http://www.easyjet.com/common/img/q1_2009_interim_analyst_presentation.pdf, 1-22.
- Givoni, M. and Banister, D., 2006: Airline and railway integration, *Transport Policy*, 13, 386-397.
- Jardine, C. N., 2005: Part1: Calculating the Environmental Impact of Aviation Emissions.
- Lenzen, M., 1999: Total Requirements of energy and greenhouse gases for Australian transport, *Transportation Research Part D*, 4, 265-290.
- National Express, 2005: Emissions from busses and coaches, www.nationalexpress.co.uk, accessed March 2007.
- Oberthur, S., 2003: Institutional interaction to address greenhouse gas emissions from international transport: ICAO, IMO and the Kyoto Protocol, *Climate Policy*, 3, 191-205.
- Ryanair, 2009: 3rd Quarter Results 2009, February 2009 http://www.ryanair.com/site/about/invest/docs/2009/q3_2009_doc.pdf, 1-23.
- Sausen, R., Isaken, I., Grewe, V., Hauglustaine, D., Lee, D. S., Myhre, G., Kohler, M. O., Pitari, G., Schumann, U., Stordal, F. and Zerefos, C., 2005: Aviation radiative forcing in 2000: An update on IPCC (1999), *Meteorologische Zeitschrift*, 14, 555-561.
- Whitelegg, J., 2000: AVIATION: the social, economic and environmental impact of flying. Published by the Ashden Trust, London, 2000, 1-28.

Exploring the uncertainties involved in calculating temperature response from the transport sector

L.L. Lim^{*}, H.J. Preston, D.S. Lee

Dalton Research Institute, Department of Environmental and Geographical Sciences, Manchester Metropolitan University, United Kingdom

Keywords: climate response, transport, uncertainty

ABSTRACT: Simple climate models (SCMs) are useful tools for evaluating the climate impacts of anthropogenic emissions. As with any modelling exercise, it is important to identify and quantify the uncertainties in model results. For this study, the SCM, LinClim (Lim et al., 2007), was used to explore the sensitivity and uncertainties of various parameters involved in calculating global mean temperature response from the transport sector. The three main aspects of uncertainties explored in this paper are the effects due to the application of different background emission scenarios; the effects from the application of different carbon-cycle parameters and finally, the effects of tuning LinClim to different General Circulation Models (GCMs). Uncertainties in emissions scenarios and carbon-cycle parameters were investigated using transport emissions obtained from the EU Sixth Framework Project QUANTIFY (Quantifying the Climate Impact of Global and European Transport Systems); background scenarios from the Special Report on Emissions Scenarios (SRES); and carbon-cycle parameters derived from MAGICC (Wigley and Raper, 2001), the SCM used in the Intergovernmental Panel on Climate Change (IPCC) Fourth Assessment Report (AR4). Temperature response for the emission scenarios was then calculated using LinClim, by applying tuning parameters (climate sensitivity parameter, λ and lifetime of the temperature perturbation, τ) of different GCMs. The results highlighted that for the scenario A1B-AIM, the uncertainty parameter that gave rise to the highest range of CO₂ temperature response from the transport sector was the LinClim tuning parameters (0.27 K by 2100). The potential range of temperature response due to CO₂ transport emissions for the same scenario was 0.36–0.63 K, which represented ~13–19% of temperature rise due to all anthropogenic sources.

1 INTRODUCTION

Simple climate models have been used in many climate impact studies (e.g. in IPCC), and vary in complexity but are always more computationally efficient than GCMs. They can be used to investigate impacts from large perturbations such as all anthropogenic sources (IPCC, 2007), or small perturbations such as the aviation sector (Lee et al., 2009). The computational efficiency of SCMs make them ideal tools for determining the climate impacts of a wide range of emissions scenarios, and the results from such studies help policymakers to devise and assess possible mitigation strategies. It is therefore important that any SCM results include uncertainty ranges, to give a better, more complete picture to the policymakers.

Typically, SCMs use emissions as input to calculate atmospheric concentrations of greenhouse gases (GHGs) or precursors from which global radiative forcing (RF) may be calculated. Then, climate responses such as global mean temperature and sea level rise can be computed from these RF. Each step within this modelling exercise, from emissions forecasts to their potential impacts are bound by various uncertainties. In this study, the simple climate response model, LinClim (Lim et al., 2007, Lee et al., 2009), is used to explore the sensitivity and uncertainties involved in calculating temperature response of the carbon dioxide (CO₂) perturbation from the transport sector. LinClim has previously been used in the assessment of aviation (Lee et al., 2009) and shipping (Lee et al., 2007) impacts. The model has now been adapted to also account for climate impacts from road

^{*} *Corresponding author:* Ling Lim, Dalton Research Institute – CATE, Manchester Metropolitan University, Chester St, Manchester M1 5GD, UK. Email: l.lim@mmu.ac.uk

transport. For this study, we constrained our analysis to uncertainties due to background emission scenarios, carbon-cycle parameters and LinClim tuning parameters.

2 BACKGROUND CO₂ EMISSIONS AND CONCENTRATIONS

Background CO₂ emissions for this uncertainty analysis were taken from the IPCC SRES. The SRES scenarios follow four main storylines (A1, A2, B1, B2), each driven by different assumptions on “*demographic development, socio-economic development and technological change*”. Six integrated assessment models (AIM, ASF, IMAGE, MARIA, MESSAGE, MiniCAM) were then used to generate future GHG emissions based on these four storylines. The A1 storyline was further split into three groups characterized by the assumptions on technological developments: A1B (balanced), A1FI (fossil fuel intensive) and A1T (non-fossil energy sources). In total, 40 SRES scenarios were developed, with “*no single most likely, ‘central’, or ‘best-guess’ scenario*”. Six “*marker*” scenarios, which were considered by the SRES team as “*illustrative of a particular storyline*” were selected for use in large-scale climate models. However, these marker scenarios (A1B-AIM, A1FI-MiniCAM, A1T-MESSAGE, A2-ASF, B1-IMAGE and B2-MESSAGE) “*are no more or less likely than any other scenarios*” (IPCC, 2000).

Therefore, to fully capture the broad range of assumptions within the SRES storylines and modelling methodologies, the full suite of SRES scenarios should be used when calculating climate impacts using SCMs. However, for this study which focuses on uncertainty analysis, the A1B storyline was used as illustration of the possible range in temperature response due to CO₂ emissions from transport. Quantitatively, by the year 2100 for scenario A1B, the difference between the highest (20.6 Pg C/yr) and lowest scenarios (10.5 Pg C/yr) was 10.1 Pg C/yr. The marker scenario, A1B-AIM, produced a total anthropogenic CO₂ estimate of 13.5 Pg C/yr (IPCC, 2000).

The resulting background CO₂ concentrations from various A1B scenarios were modelled using MAGICC 5.3, the SCM used in IPCC AR4 (IPCC, 2007). MAGICC has a built-in carbon-cycle model that considers oceans, atmosphere and terrestrial carbon reservoirs. It also includes terrestrial feedbacks from temperature and atmospheric CO₂ concentration and three levels of model sensitivity (low, mid and high). The model sensitivity is dependent on the net flux due to land-use changes and CO₂ fertilization coefficient (Wigley, 1993). The temporal development of CO₂ concentrations for the A1B scenarios, under the assumptions of mid-range carbon-cycle with feedbacks is shown in Figure 1. At 2050, the difference between the highest (A1B-ASF) and the lowest (A1B-MESSAGE) CO₂ scenarios was 94 ppmv. This difference increased to 207 ppmv by the year 2100 (~56% of present day CO₂ levels), with A1B-ASF remaining as the highest scenario (924 ppmv) and A1B-AIM (717 ppmv) the lowest scenario.

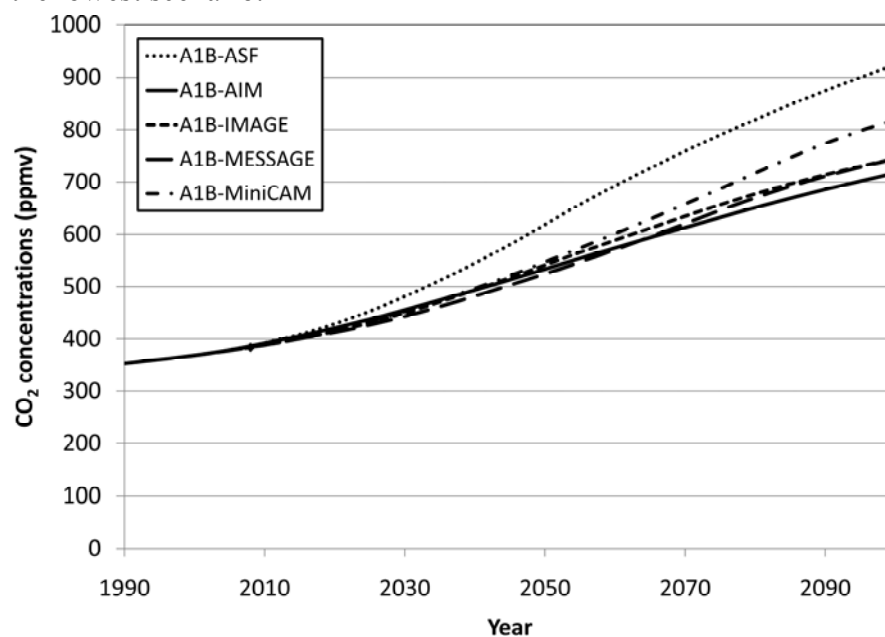


Figure 1: CO₂ background concentrations for A1B storyline (MAGICC 5.3, with feedbacks and mid-range carbon-cycle model)

The marker scenario A1B-AIM was also used as an illustration of the range of values various MAGICC carbon-cycle settings has on the background CO₂ concentrations (Figure 2). The range of uncertainty for carbon-cycle setting is not as high as those due to variations in emission scenarios. At 2050, the CO₂ concentrations range from 556 ppmv to 498 ppmv (difference of 58 ppmv) and at 2100, 773 ppmv to 609 ppmv (difference of 164 ppmv). As expected, there is a noticeable difference in CO₂ concentrations when feedbacks were included.

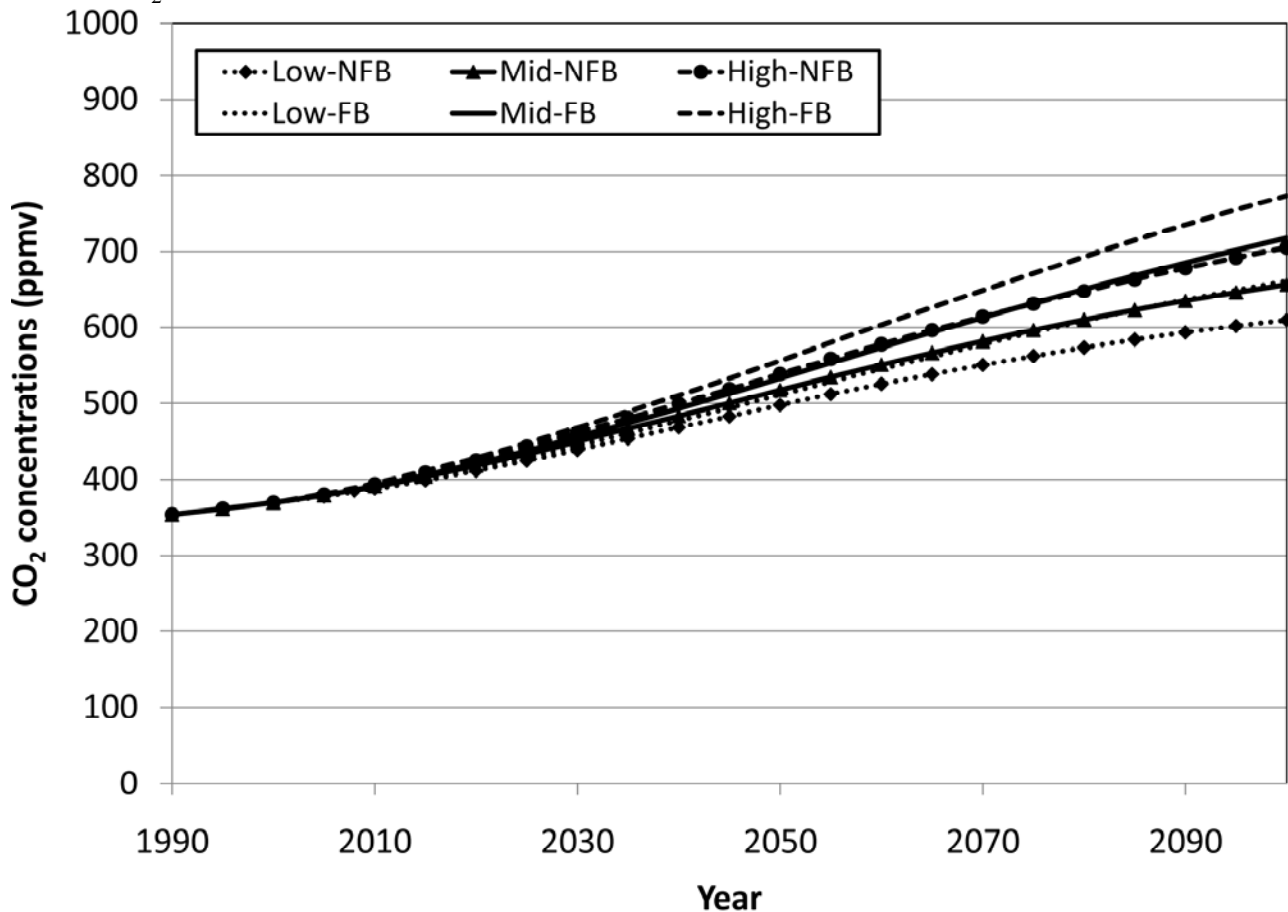


Figure 2: CO₂ background values for different carbon-cycle setting (Low, Mid, High; NFB – without feedbacks and FB – with feedbacks) for scenario A1B-AIM

3 TRANSPORT SECTOR CO₂ EMISSIONS AND CONCENTRATIONS

Emissions of CO₂ from the transport sector were taken from the project QUANTIFY. The transport emissions were divided into three broad categories: land transport (road, rail and inland shipping), maritime shipping, and aviation. These emissions were developed to be consistent with the SRES storylines of A1B, A2, B1 and B2. A mitigation aviation scenario (B1ACARE), which followed the SRES B1 storyline, was also generated.

This study only considered emissions from the main transport categories of road, maritime shipping, and aviation. Figure 3 illustrates the total CO₂ emissions from these categories by SRES storylines. Scenario A1B had the highest transport CO₂ emissions for all forecast period (2000 to 2100). Transport CO₂ emissions for A2, B1 and B2 for years 2015 to 2085 were in the same range of 2 to 3 Pg C/yr. Beyond this period, scenario A2 continued to rise to 3.4 Pg C/yr, while scenarios B1 and B2 remained relatively constant. As expected, scenario B1ACARE, which included a mitigation scenario for aviation, had lower CO₂ emissions and followed the trend of its parent B1 storyline. By the year 2100, transport represented ~41% of total background CO₂ emissions for scenario A1B, ~12% for A2, ~62% for B1 and ~20% for B2. At 2100, the difference between the highest (A1B) and lowest scenarios (B1ACARE) was 3.1 Pg C/yr.

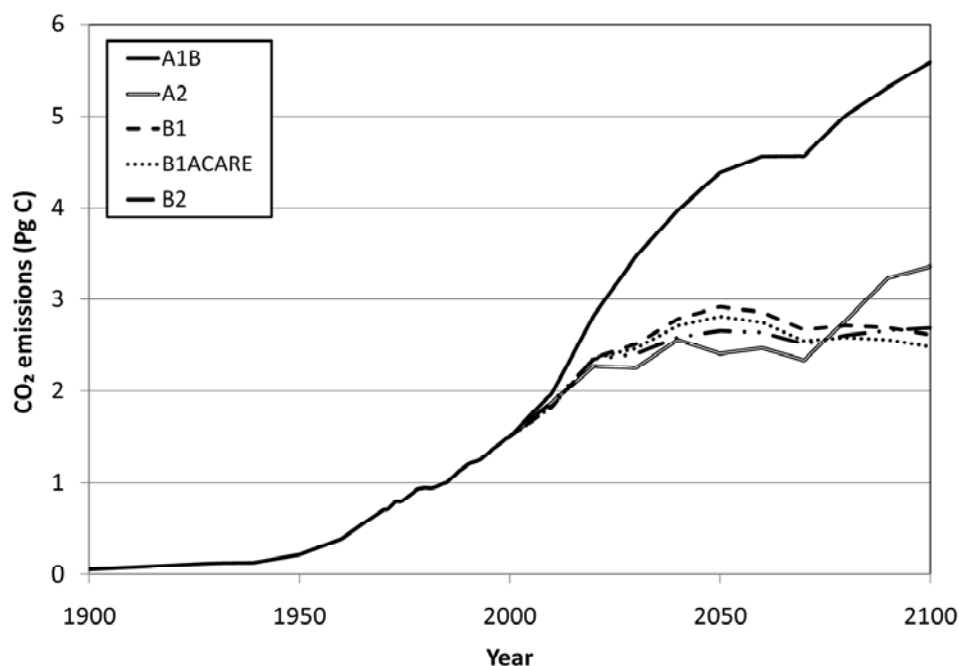


Figure 3: Total CO₂ transport emissions (road, maritime shipping and aviation) by SRES storylines

Figure 4 shows the split by transport category for scenario A1B, which is used as illustration for this study. Road sources were the largest contributors to CO₂ transport emissions; 76% at 2000, 71% at 2050 and 51% at 2100. The shipping and aviation emissions were very similar in magnitude, with each category contributing 0.18 Pg C/yr at 2000, 0.7 Pg C/yr at 2050 and 1.4 Pg C/yr at 2100. However, shipping had a longer history of CO₂ emissions when compared to aviation.

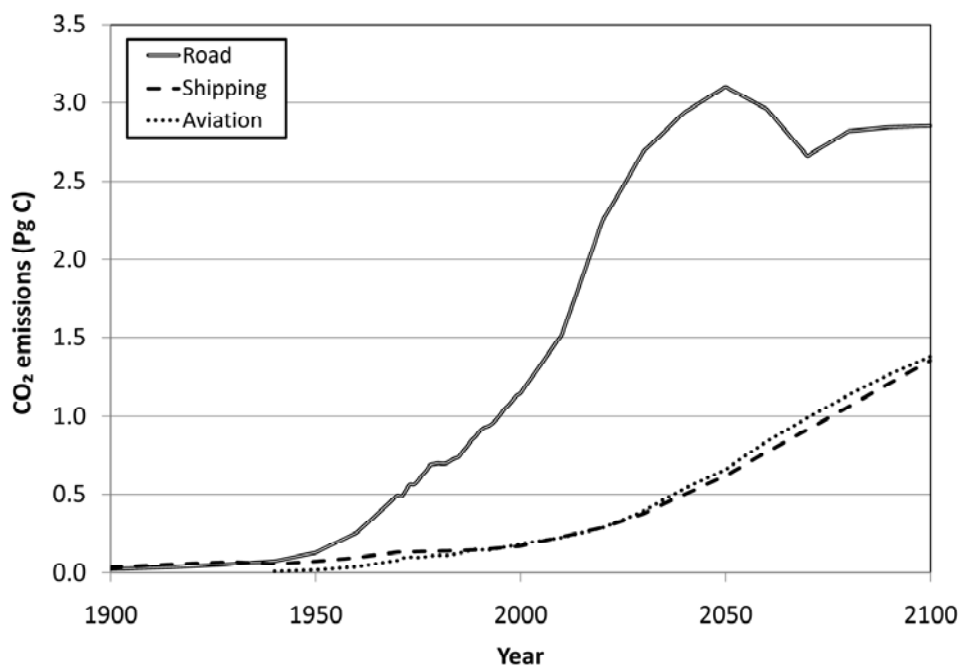


Figure 4: CO₂ emissions split by transport category for scenario A1B

Transport CO₂ concentrations were calculated explicitly from the emissions using LinClim's carbon-cycle model (Lim et al., 2007). The model is an impulse response function that approximates the results of the carbon-cycle model of Maier-Reimer and Hasselmann (1987). Figure 5 shows the results for scenario A1B by transport category. Between years 2000 to 2100, road transport accounted for 63–76% of total transport CO₂ concentrations, while shipping was 13–18%, and aviation was 11–19%. Assuming mid-sensitivity carbon-cycle with feedbacks, the total CO₂ transport concentrations represented 4–17% of background CO₂ concentrations; with road transport contributing 3–11% and shipping and aviation 0.07–3% each.

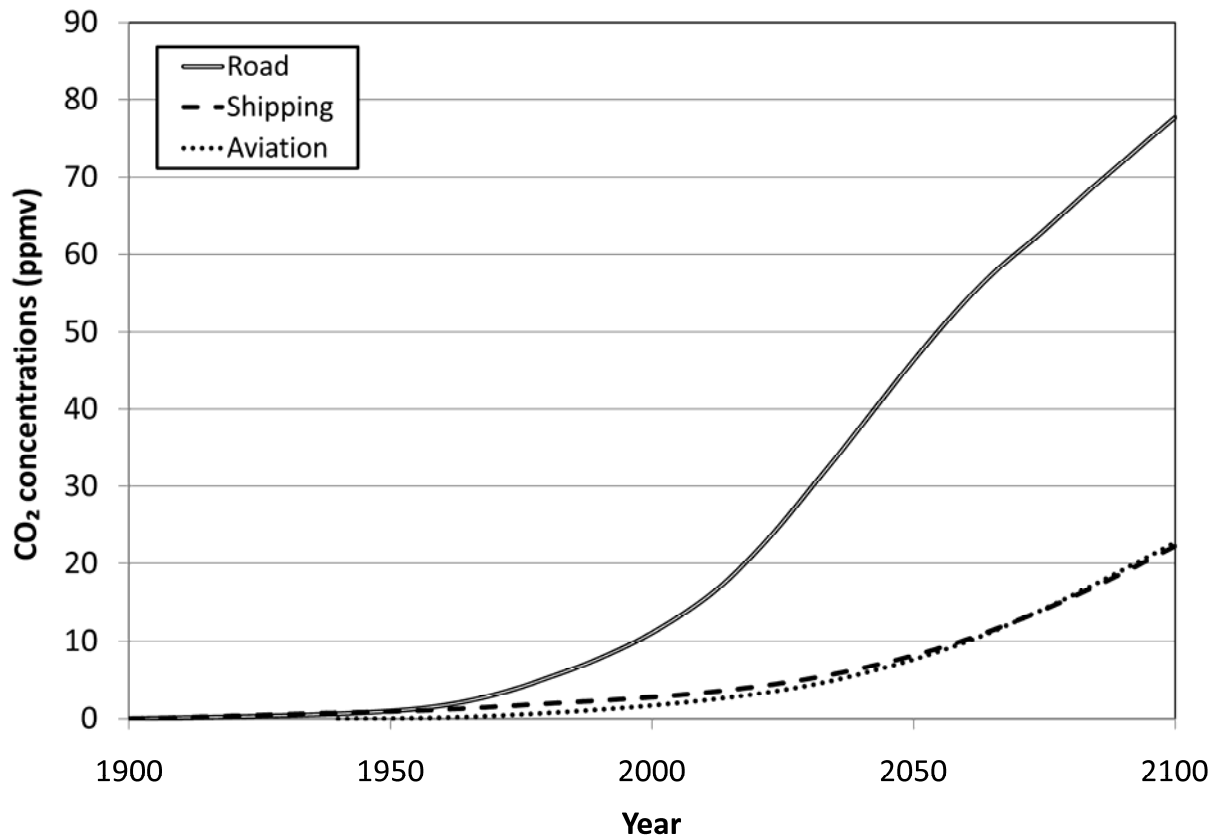


Figure 5: CO₂ concentrations split by transport category for scenario A1B

4 TRANSPORT SECTOR CO₂ RADIATIVE FORCING (RF) AND TEMPERATURE RESPONSE (ΔT)

Carbon dioxide RF in LinClim is calculated according to the simple function used in IPCC AR4 (Lim et al., 2007, IPCC, 2007). The resulting RF is then used in an impulse response function, which estimates the temperature response (ΔT) due to a specific perturbation. Temperature response is not only dependent on RF, but also two other parameters, the climate sensitivity parameter (λ) and lifetime of the temperature perturbation (τ). These parameters are derived or “tuned” to a specific GCM. Therefore, ΔT calculated by LinClim will emulate or evolve in the manner of its parent GCM. By default, LinClim uses tuning parameters from the GCM ECHAM4/OPYC3. To explore the uncertainty in calculating ΔT from transport, tuning parameters from other GCM were also developed. These parameters were derived using five sets of GCM temperature data from MAGICC 5.3. The five GCMs were NCAR’s CCSM3 and PCM, Hadley Centre’s HadCM3 and HadCM2, GFDL-CM2.0 and CSIRO’s Mk3.0.

4.1 Uncertainties due to background emissions (A1B storyline)

Table 1 shows RF summary for the A1B storyline calculated for each transport category using background CO₂ concentrations shown in Figure 1. The total transport CO₂ RF represented 13–19% of background RF in 2050 and 11–19% in 2100. At 2100, road sources had the biggest CO₂ RF difference, 0.14 W/m², between the highest (A1B-AIM) and lowest (A1B-ASF) scenario. Shipping and aviation, which had similar range of CO₂ concentrations (Figure 5), also had similar RF difference, 0.04 W/m². The ΔT results calculated by LinClim using ECHAM4/OPYC3 tuning parameters are also summarized in Table 1, with the temporal evolution depicted in Figure 6. The uncertainty range by 2100 was approximately 0.09 K. Over the 2000–2100 periods, road sources consumed 67–75% of the total transport ΔT budget, while shipping 14–24% and aviation 9–15%. Shipping had a higher ΔT compared to aviation because of its longer emissions history.

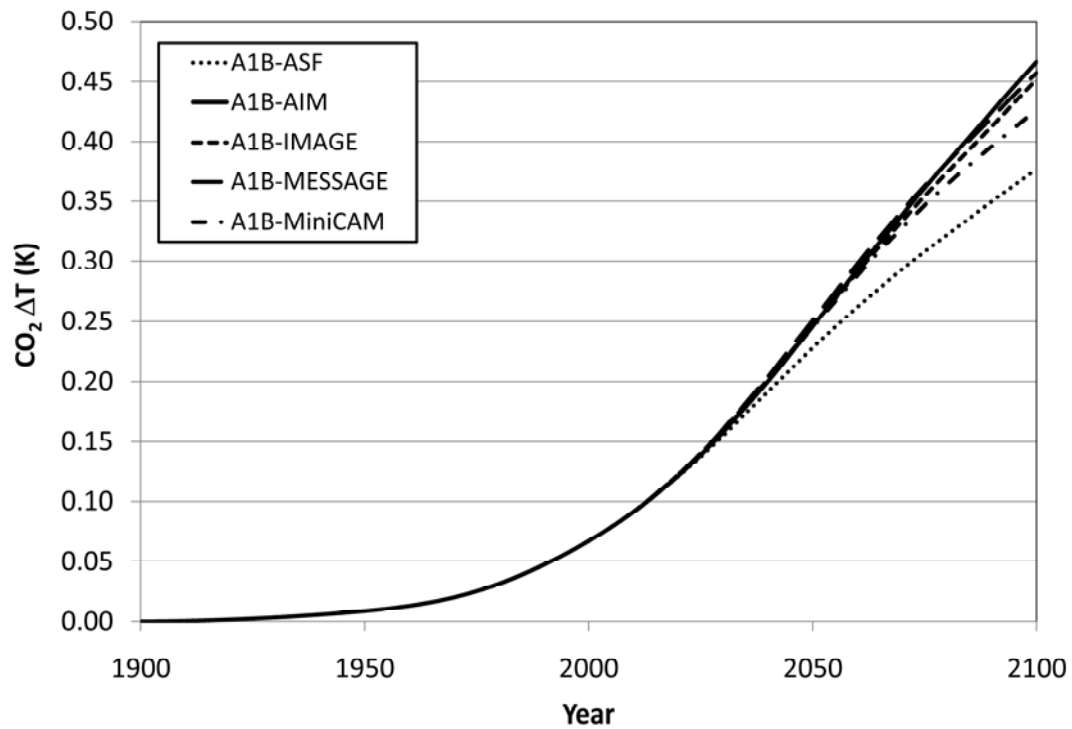


Figure 6: CO₂ total transport ΔT using background concentrations for A1B storyline as depicted in Figure 1

4.2 Uncertainties due to background concentrations (carbon-cycle settings, A1B-AIM scenario)

The total transport RF at 2050 and 2100, calculated using background CO₂ concentrations shown in Figure 2, are summarized in Table 1. Transport accounted for 17–22% of background RF in 2050 and 16–27% in 2100. High carbon-cycle with feedbacks on background concentrations resulted in the lowest transport RF. Figure 7 shows the range of ΔT results (tuned to ECHAM4/OPYC3) due to these RF variations. The transport CO₂ ΔT predictions for different carbon-cycle settings varied by 0.02 K in 2050, increasing to 0.09 K by 2100 (Table 1). The split between transport categories was similar to that reported in Section 4.1.

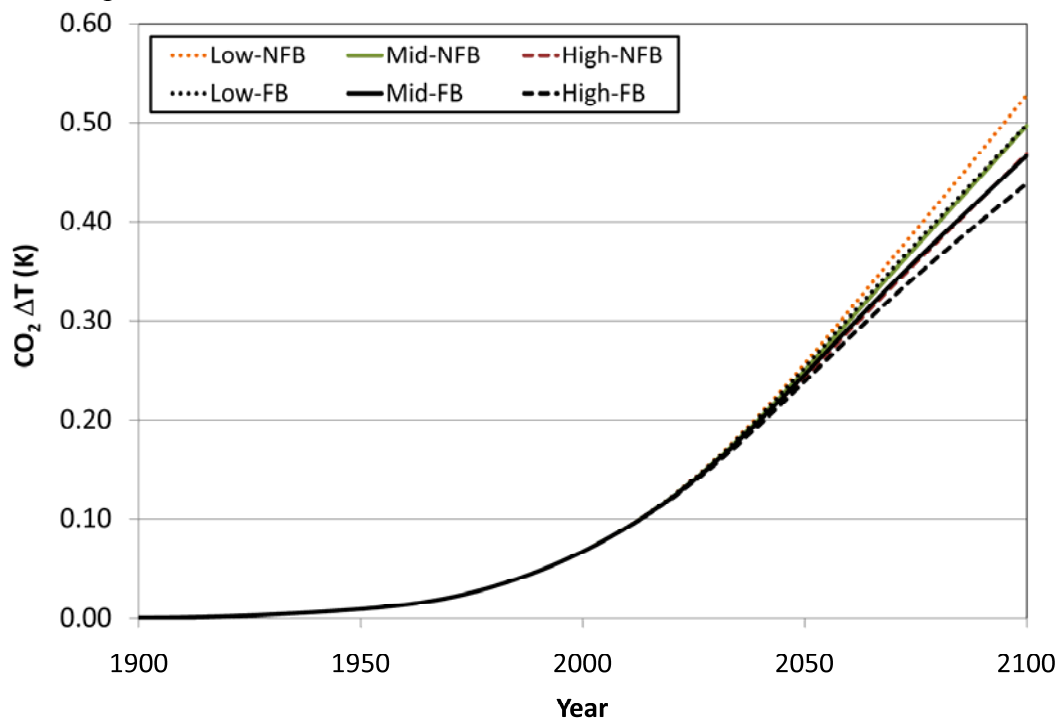


Figure 7: CO₂ total transport ΔT using background concentrations for scenario A1B-AIM as depicted in Figure 2

4.3 Uncertainties due to tuning parameters, λ and τ (A1B-AIM scenario)

Figure 8 shows the ΔT range calculated by LinClim when tuned to different GCMs. The RFs used to produce these ΔT were taken from the A1B-AIM scenario, Mid-FB background concentrations (Figure 2). A significant difference between the highest (CSIRO-Mk3.0) and lowest (ECHAM4/OPYC3) CO_2 ΔT was already observed in the year 2000. This uncertainty range of 0.11–0.067 K increased to 0.22–0.37 K in 2050 and 0.36–0.63 K in 2100 (Table 1). However, the tuning parameters from CM2.0 produced the highest ΔT in 2100, while CCSM3 the lowest. The split within the individual transport categories was again similar to that reported in Section 4.1.

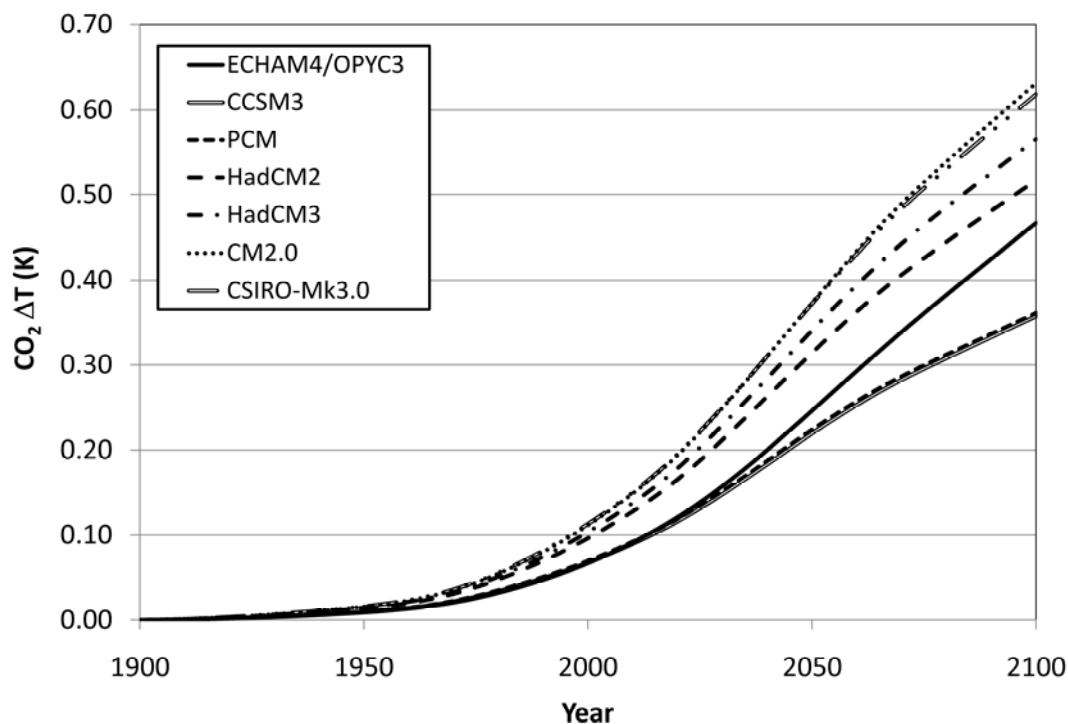


Figure 8: CO_2 total transport ΔT using different GCM tuning parameters for scenario A1B-AIM as depicted in Figure 2

5 SUMMARY AND FURTHER WORK

In this paper, we explored the uncertainty ranges involved in calculating CO_2 temperature response from the transport sector. A summary of the main results is shown in Table 1. The results demonstrated that considering only three uncertainty parameters for the scenario A1B-AIM, by the year 2100, the CO_2 temperature response from transport could range between 0.36–0.63 K. This represented ~13–19% of background temperature response. The uncertainty parameter that produced the highest range of temperature response was the tuning parameters (0.27 K by 2100), while background CO_2 emissions and carbon-cycle settings gave rise to uncertainty range of ~0.09 K by 2100.

Table 1: Summary of main results

Uncertainty parameters	Storyline/Scenario	RF (W/m^2)		ΔT (K)	
		2050	2100	2050	2100
Background emissions	A1	0.55 – 0.67	0.73 – 0.95	0.23 – 0.25	0.38 – 0.47
Background concentrations (carbon-cycle settings)	A1B-AIM	0.62 – 0.69	0.88 – 1.13	0.24 – 0.26	0.44 – 0.53
LinClim tuning parameters	A1B-AIM	-	-	0.22 – 0.37	0.36 – 0.63

This preliminary work demonstrated the importance of including uncertainty ranges to SCM results, especially if the results are to be used for policymaking. In the future, this work will be extended to include the full suite of SRES scenarios, to use tuning parameters from other AR4 GCMs and to also investigate other likely uncertainties in temperature response calculations.

6 ACKNOWLEDGEMENTS

This study was funded by the UK Department for Transport (DfT). Further support was given by the EU IP QUANTIFY.

REFERENCES

- IPCC, 2000: *Summary for Policymakers: Emissions Scenarios*. A Special Report of Working Group III of the Intergovernmental Panel on Climate Change. Based on a draft prepared by: N. Nakićenović, O. Davidson, G. Davis, A. Grübler, T. Kram, E. Lebre La Rovere, B. Metz, T. Morita, W. Pepper, H. Pitcher, A. Sankovski, P. Shukla, R. Swart, R. Watson, D. Zhou, Cambridge University Press, UK.
- IPCC, 2007: *Climate Change 2007. The Physical Science Basis*. S. Solomon, D. Qin, M. Manning, M. Marquis, K. Averyt, M.M.B. Tignor, H.L. Miller, Z. Chen (eds.), Contribution of Working Group I to the Fourth Assessment Report of the Intergovernmental Panel on Climate Change. Cambridge University Press, UK.
- Lee, D.S., L. Lim, V. Eyring, R. Sausen, Ø. Endresen, H.-L. Behrens, 2007: Radiative forcing and temperature response from shipping. R. Sausen, A. Blum, D.S. Lee and C. Brüning (eds.): *Proceedings of an International Conference on Transport, Atmosphere and Climate (TAC)*. Luxembourg, Office for Official Publications of the European Communities, ISBN 92-79-04583-0. 208–213.
- Lee, D.S., D.W. Fahey, P.M. Forster, P.J. Newton, R.C.N. Wit, L.L. Lim, B. Owen, R. Sausen, 2009: Aviation and global climate change in the 21st century. *Atmos. Environ.* 43, 3520–3537.
- Lim, L., D.S. Lee, R. Sausen, M. Ponater, 2007: Quantifying the effects of aviation on radiative forcing and temperature with a climate response model. R. Sausen, A. Blum, D.S. Lee and C. Brüning (eds.): *Proceedings of an International Conference on Transport, Atmosphere and Climate (TAC)*. Luxembourg, Office for Official Publications of the European Communities, ISBN 92-79-04583-0. 202–207.
- Maier-Reimer, E. and K. Hasselmann, 1987: Transport and storage of CO₂ in the ocean – An inorganic ocean-circulation carbon cycle model. *Clim. Dyn.* 2, 63–90.
- Wigley, T.M.L., 1993: Balancing the carbon budget. Implications for projections of future carbon dioxide concentration changes. *Tellus* 45B, 409–425.
- Wigley, T.M.L. and S.C.B. Raper, 2001: Interpretation of high projections for global-mean warming. *Science* 293, 451–454.

Abatement strategies to reduce air pollution from transport in Germany

U. Kugler^{*}, J. Theloke, B. Thiruchittampalam, T. Geftler, M. Uzbasich, R. Köble, R. Friedrich,
Institut für Energiewirtschaft und Rationelle Energieanwendung (IER), Universität Stuttgart, Germany

P. Builtjes, H. Denier van der Gon
TNO Build Environment and Geosciences (TNO), Utrecht, Netherlands

R. Stern
Freie Universität Berlin –(FUB), Geowissenschaften, Institut für Meteorologie, AG Troposphärische Umweltforschung, Berlin, Germany

W. Jörß
Institut für Zukunftsstudien und Technologiebewertung (IZT), Berlin, Germany

U. Dämmgen
Johann Heinrich von Thünen-Institut, Institut für Agrarrelevante Klimaforschung, Braunschweig, Germany

J. Appelhans
Umweltbundesamt, FG II 4.1, „Grundsatzfragen der Luftreinhaltung“, Dessau, Germany

Keywords: PM_{10/2.5}, Abatement strategies, road/offroad transport emissions, air pollution modelling

ABSTRACT: Large scale exceedances of PM₁₀ and NO₂ ambient air limit values will continue in Germany despite the implementation of national and international policies. An integrated approach has therefore been developed to assess different cost-effective mitigation strategies for all source groups on a national level. On-road and off-road transport emission abatement strategies such as more stringent emission limit values, cost internalisation, speed limits and levelling of fuel taxes can contribute to the overarching goal of an improved air quality.

1 INTRODUCTION

According to projected and modelled ambient air concentrations, large scale exceedances of PM₁₀ and NO₂ limit values in Germany will continue despite the implementation of current national and international legislation. On-road and off-road transport is one of the major sources of these exceedances, directly through NO_x and PM_{10/2.5} exhaust and non-exhaust emissions and indirectly by emissions of aerosol precursors. To be able to comply with the existing European limit values for PM₁₀ (and the expected ones for PM_{2.5}), it is therefore crucial to develop successful mitigation strategies that are not only considering all pollutants but also taking into account possible side effects on green house gases or noise.

In the PAREST research project (Particle Reduction Strategies) different cost-effective strategies on a national level are assessed to decrease air pollution caused by emissions of NO_x, SO₂, NH₃, NMVOC, PM₁₀ and PM_{2.5} and thus contribute to an improved air quality.

2 GENERAL METHODOLOGY

The methodology to assess abatement strategies for air pollution in Germany is as follows (Fig. 1).

^{*} Corresponding author: Ulrike Kugler, Institut für Energiewirtschaft und Rationelle Energieanwendung (IER), Universität Stuttgart, Heßbrühlstr. 49a, 70565 Stuttgart, Germany. Email: ulrike.kugler@ier.uni-stuttgart.de

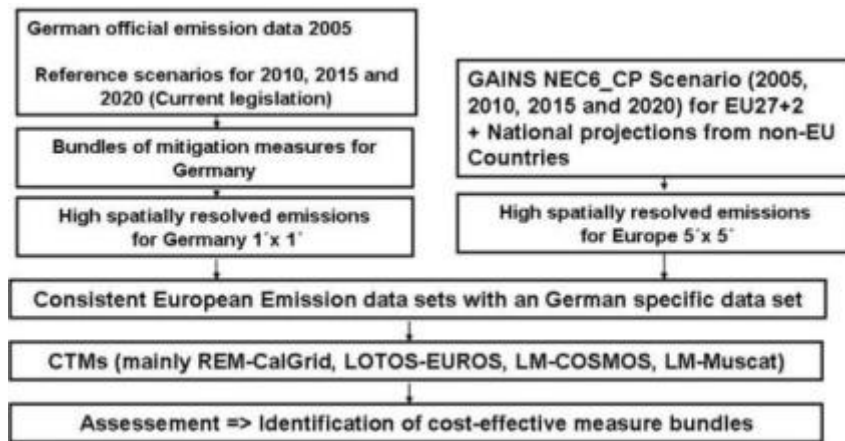


Figure 1. Methodology used for the assessment of abatement strategies for PM_{10} and $\text{PM}_{2.5}$ in Germany within the project PAREST

Emission inventory data for Germany in 2005 from the Umweltbundesamt, comprising all sectors, and reference scenario data for 2010, 2015 and 2020 comprising current legislation are used as a modelling basis. To the emissions of the reference scenario, different bundles of mitigation measures for sources such as on-road and off-road transport, electricity and heat production, other large and small combustion plants, agriculture and solvent use are applied to derive mitigation scenarios. All German emission scenarios are gridded to $1/60 \times 1/60$ (ca. 1 min x 1 min) with the help of proxy data such as road, railway and river networks, coordinates of point sources (airports, power plants and industrial plants), population and land use data (Thiruchittampalam, 2008). A quality check of those gridded emission maps was undertaken by experts of the German environmental agency UBA, an example is given in Figure 2.

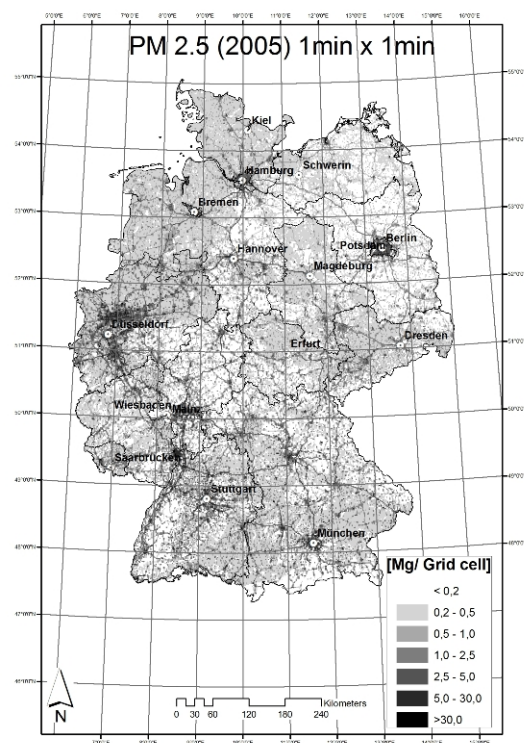


Figure 2. Highly resolved $\text{PM}_{2.5}$ emission map for Germany in 2005 (all sources, 1 min x 1 min)

For the European background, emission scenarios from GAINS from the NEC 6 scenario family (Amann et al. 2008) and national projections for non-EU countries are used. They are gridded on 5 min x 5 min (Denier van der Gon et al., 2009) and combined with the German emission data set to derive a consistent European emission data set (Fig. 3).



Figure 3. Highly resolved PM₁₀ emission map for Europe in 2020 (NEC6_CP, all sources, 5 min x 5 min)

To model the effect of mitigation strategies on air quality with the focus on PM₁₀ and PM_{2.5}, the chemical transport models (CTM) REM-CalGrid (major part of the modelling), LOTOS-EUROS, and COSMO-MUSCAT are used. A REM-CalGrid model result of PAREST is shown in Figure 4.

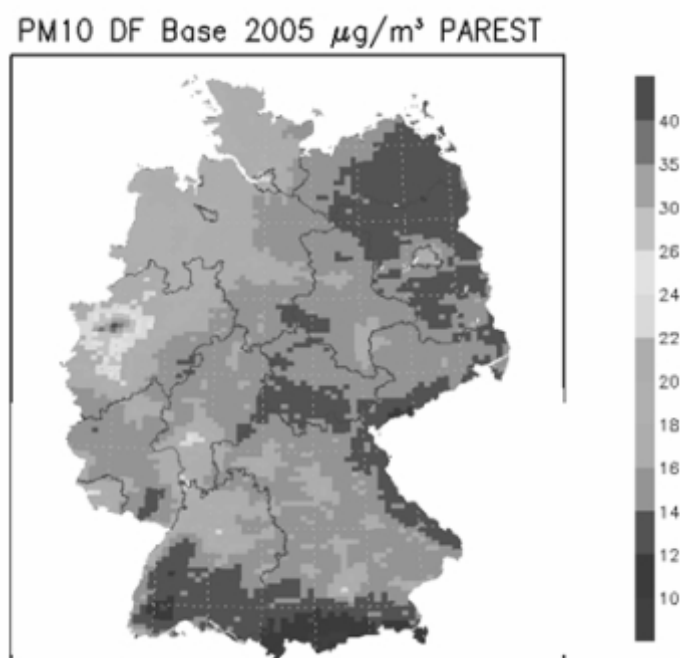


Figure 4. PM₁₀ concentration maps for Germany in 2005

The paper will focus on mitigation strategies for on-road and off-road transport emissions.

3 ASSESSMENT OF ABATEMENT MEASURES FOR ON-ROAD AND OFF-ROAD TRANSPORT

3.1 Off-road transport

Off-road transport such as rail and air traffic, inland and coastal shipping and mobile machines has gained importance in recent years due to their relatively high emissions of $PM_{10/2.5}$ and NO_x . In view of that, more stringent emission limit values were set out which will lead to a distinct decrease. Figure 5 shows that in the reference scenario, emissions of PM_{10} in 2020 will be more than halved compared to 2005. The majority of off-road PM_{10} emissions are caused by mobile machines (agricultural machinery, industrial and building machinery as well as household and gardening machinery).

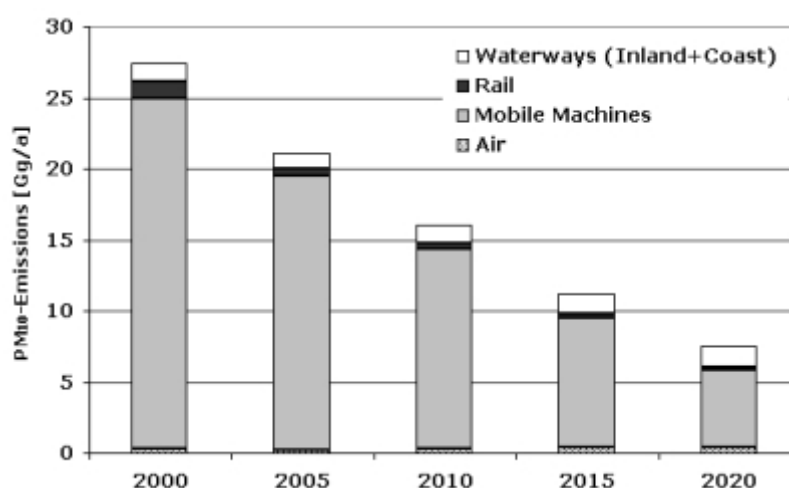


Figure 5. PM_{10} emissions in Germany from off-road sources in the reference scenario (2000-2020, UBA, 2009)

To assess further mitigation potentials for that sector, abatement measures were analysed for each subgroup. This was done on the basis of related research projects (Jörß et al., 2007; Theloke et al., 2007; Matthes et al., 2008), on literature reviews and on expert judgements. For each abatement measure, data sources, assumptions on reduction potentials, implementation degrees and mitigation costs as well as side effects on other environmental pollutants (e.g. CO_2) or stressors (e.g. noise) were documented and will be made available at the end of the project. The measures that were assessed for off-road sources in Germany are:

- More stringent emission limits (mobile machines, ships, trains)
- Limit values for evaporation emissions (gasoline machines)
- Ban on high emitting construction machines in cities ("Environmental Zone")
- Differentiation of rail track prices: trains with older emission standards pay more
- Cost internalisation of emission impacts from air traffic (fuel tax, emission trading scheme)

When all of these measures are applied, a maximum mitigation potential of 5% in 2020 is feasible for PM_{10} emissions of off-road sources (compared to the reference situation in 2020).

3.2 On-road transport

On-road transport such as passenger cars, light and heavy duty vehicles, busses and two-wheelers causes exhaust and evaporation emissions, but also non-exhaust emissions from the wear of road surfaces, tires and brakes and the resuspension of road dust. So far, resuspension emissions are not part of the official German inventory and were thus calculated on the basis of (Schaap et al., 2008) as input to the CTMs in PAREST. The results show that while PM_{10} diesel exhaust emissions are going to decrease due to more stringent emission limits (Euro 5/V and 6/VI), non-exhaust emissions are going to increase due to an increase in vehicle mileage (Fig. 6). By 2010, non-exhaust emissions are the major emission source for PM_{10} emissions from on-road transport.

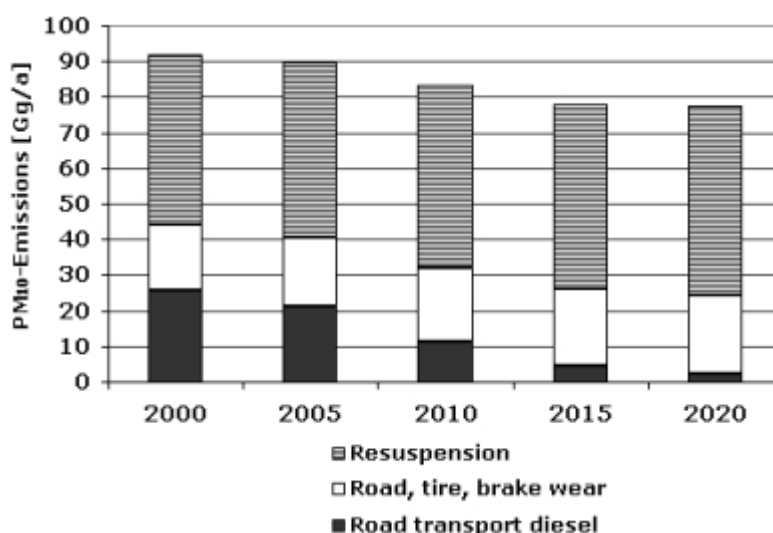


Figure 6. PM₁₀ emissions in Germany from on-road sources in the reference scenario (2000-2020, UBA, 2009)

As for the other sectors, mitigation measures were assessed for on-road emission sources:

- Limit values for evaporation emissions from motorcycles
- Retrofit of diesel passenger cars with particulate filters
- Speed limit of 120 km/h for motorways
- Speed limit of 30 km/h in cities
- Levelling of fuel taxes for diesel and gasoline
- Enhancing the use of bicycles in cities
- Use of low viscosity oil
- Use of low rolling resistance tyres

When all of these measures are applied, a maximum mitigation potential of 4% in 2020 is feasible for PM₁₀ emissions of on-road sources (compared to the reference situation in 2020).

4 CONCLUSION

An integrated approach on national level has been developed to assess reduction strategies for PM₁₀, PM_{2.5} and NO₂ for Germany. It is thus possible to assess the impact of mitigation measure bundles on ambient air quality. For on-road and off-road sources, a decrease in emissions is projected. With mitigation measures such as more stringent emission limit values for off-road machinery, cost internalisation in air transport, speed limits for cars and levelling of fuel taxes, a further decrease of 5% PM₁₀ emissions in 2020 compared to the reference situation is feasible. However, as the integrated approach comprises all emission source groups, most fitting cost-effective abatement strategies for air pollution can be designed.

5 ACKNOWLEDGEMENTS

This work is funded by Umweltbundesamt, Germany, in the frame of the research project PAREST (www.parest.de).

REFERENCES

- Amann, M., Bertok, I., Cofala, J., Heyes, C., Klimont, Z., Rafaj, P., Schöpp, W. and F. Wagner, 2008: *National Emission Ceilings for 2020 based on the 2008 Climate & Energy Package*. NEC Scenario Analysis Report Nr. 6, International Institute for Applied Systems Analysis (IIASA), Laxenburg, Austria
- Denier van der Gon, H., Visschedijk, A., van de Brugh, H., and M. Schaap (2009): *European emissions of PM_{2.5} and its precursors*. Presentation, Workshop 'Measurements and Modelling of PM_{2.5} in Europe', Bilthoven, the Netherlands

- Jörß, W., V. Handke, U. Lambrecht und F. Dünnebeil, 2007: *Emissionen und Maßnahmenanalyse Feinstaub 2000-2020 (Emissions and Assessment of Abatement Measures for Fine Particles 2000 – 2020)*. Final report, FKZ 204 42 202/2, Berlin, Germany
- Matthes, F.C., P. Markewitz, J. Diekmann, W. Eichhammer, S. Gores, V. Graichen, R.O. Harthan, P. Hansen, M. Kleemann, V. Krey, D. Martinsen, M. Horn, H.-J. Ziesing, W. Schade, B. Schlomann, C. Doll, N. Helfrich, N., and L. Müller, 2008: *Politikszennarien für den Klimaschutz IV (Policy Scenarios IV – Scenarios for the Projection Report 2007)*. Report No. 1/08, FKZ 205 46 434, Umweltbundesamt Dessau-Roßlau, Germany, ISSN 1862-4359
- Schaap, M., Manders, A.M.M., Hendriks, E.C.J., Cnossen, J.M., Segers, A.J.S., Denier van der Gon, H.A.C., Jozwicka, M., Sauter, F., Velders, G., Mathijssen, J., and P.J.H. Builtjes, 2008: *Regional Modelling of Particulate Matter for the Netherlands*. Technical Report BOP, Bilthoven, the Netherlands
- Theloke, J., B. Calaminus, F. Dünnebeil, R. Friedrich, H. Helms, A. Kuhn, U. Lambrecht, D. Nicklaß, T. Pregger, S. Reis and S. Wenzel, 2007: *Maßnahmen zur Einhaltung der Emissionshöchstmenge der NEC-Richtlinie – Maßnahmen zur weiteren Verminderung der Emissionen an NO_x und SO₂ und NMVOC in Deutschland (Measures to further reduce emissions of NO_x, SO₂, and NMVOCs in Germany)*. Report No. 36/07, FKZ 205 42 221, Umweltbundesamt Dessau-Roßlau, Germany, ISSN 1862-4804
- Thiruchittampalam, B., 2008: *High spatial and temporal resolution of emissions in Europe*. Presentation, TFEIP-Workshop, Milan
- UBA, 2009: German national emission inventory data base (ZSE). Umweltbundesamt, Dessau

ECATS - Mission of Association for an environmentally compatible air transport system

S. Matthes*, G. Erhardt, K. Gierens, A. Petzold,

Deutsches Zentrum für Luft- und Raumfahrt (DLR) – Institut für Physik der Atmosphäre Oberpfaffenhofen, Germany

P. Brok,

National Aerospace Laboratory (NLR), Netherlands

M. Hagström,

Swedish Defence Research Agency (FOI), Stockholm, Sweden

C. Helmis,

National Kapodistrian University of Athens, Greece

Ivar S. Isaksen,

University of Oslo, Norway

P. Laroche, X. Vancassel,

Office National d'Etudes et Recherches Aéronautiques (ONERA), France

D. Lee, D. Raper,

Manchester Metropolitan University, Manchester, United Kingdom

T. Panidis,

University of Patras, Greece

K. Mathioudakis, T. Tsalavoutas,

National Technical University of Athens, Greece

R. Kurtenbach, P. Wiesen,

Univ. Wuppertal, Germany

C. Wilson,

Univ. Sheffield, United Kingdom

P. Habisreuther, K. Schäfer, N. Zarzalis,

Karlsruhe Institute of Technology, KIT, Germany

Keywords: Aviation, emissions, environment, particulate matter, alternative fuels, climate impact, Association.

ABSTRACT: After 5 years of operation and collaboration the ECATS Network of Excellence (NoE) will now transform itself into a registered Association of European Research Establishments and Universities leading in the field of **aeronautics and the environment**. The transition from NoE to the Association will take place during 2010 and 2011. This future **ECATS Association** has the vision to support endeavours to make aviation more sustainable focussing on scientific expertise and exchange of information. ECATS' Virtual Fuel Centre focusses on alternative fuel characterisation allowing operating a premix burner, measuring flame velocities, expanding kinetic schemes and spray characterisation. ECATS' Airport Air Quality (AAQ) focus area provides an assessment of this highly interdisciplinary research field, and develops improved characterisation and approximation specifications for aviation particulate matter emissions. ECATS' third focus area is dealing with global impact of aviation and green flight. Close collaboration is exploited in order to provide updated estimates and synergies with other programmes established. The future ECATS Association provides an efficient framework for collaboration between universities and research establishments and helps making aviation more sustainable.

* Corresponding author: Sigrun Matthes, Deutsches Zentrum für Luft- und Raumfahrt (DLR) – Institut für Physik der Atmosphäre, Oberpfaffenhofen, D-82234 Weßling, Germany. Email: sigrun.matthes@dlr.de

1 INTRODUCTION

Reducing environmental impact of air transport with regard to emissions and noise is an important element in achieving the overall goals of Vision 2020 and the European Strategic Research Agenda (SRA). A coordinated collaborative effort is required, strengthened and guided by a single shared vision, through creation of a common network for research and technological development in order to overcome fragmentation. From this starting point the Network of Excellence (NoE) ECATS was brought to life in 2005, to harmonise and integrate European research aiming to help developing an environmentally compatible air transport system. Within the Network of Excellence ECATS a total of 12 partners – research establishments and universities - from 7 European Nations put their effort together to work jointly at an “Environmentally Compatible Air Transport System”. Partners within the Network of Excellence are Deutsches Zentrum für Luft- und Raumfahrt (DLR), National Aerospace Laboratory, Amsterdam (NLR), Office National d’Etudes et Recherches Aéronautiques (ONERA), Swedish Defence Research Agency (FOI), University of Sheffield (USFD), Manchester Metropolitan University (MMU), University of Norway (UiO), University of Wuppertal (BUW), National Technical University of Athens (NTUA), University of Patras (UP), the National Kapodistrian University of Athens (NKUA) and Karlsruhe Institute of Technology (KIT).

After five years of successful network activities ECATS Association furthers integrative work that started in the Network of Excellence (FP6). This future Association aims making aviation more environmentally compatible. Main objectives in the field of **aviation and environment** are: (a) Organize knowledge transfer including education, (b) Technological and scientific leadership in Europe, and (c) Contribute to technical and political debate. Working groups are defining individual business plans within specific thematic areas. The scope of this paper is to present activities of the future ECATS Association which is scheduled to be established in 2010 focussing on above activities.

2 ECATS APPROACH

ECATS Association will continue activities of the ECATS Network of Excellence. Network activities, hence Association activities, are covering three different Thematic Areas (TA): (1) Engine technology, near field plume and alternative fuels, (2) Local and regional aspects of air quality – Airport Air Quality (AAQ), and (3) Global aviation impact and Green Flight operations. Within all three thematic areas the Association is aiming to achieve primary objectives spelled out. Close collaboration and exchange between those multi-disciplinary thematic activities allow exploiting synergies for visibility and training activities.

This future **ECATS Association** has the vision to help making aviation more sustainable. Specifically, it will serve the following stakeholder’s needs: **a.** Build up, maintain and extend scientific expertise and, moreover, to further link and integrate scientific expertise in the different thematic areas and exploit the multi-disciplinary platform available in ECATS; **b.** Organise exchange of information in particular about experience and development of related research, e.g., on basis of workshops, reports and publications, education and training, and web-based information; **c.** Provide liaison between customers and experts to provide integrated and professional support; **d.** Foster to the technical, strategic and political debate, e.g., to initiate research on those topics identified to be relevant; **e.** Perform research work where identified to be crucial, e.g., short studies. Primary objectives of ECATS Association are to help building up and maintain scientific expertise in the field of aviation and environment.

Visibility for ECATS Association will be provided by further exploring the existing common web-portal, but also preparation of relevant documentation. Functionalities are internal and public areas which is guaranteeing effective communication for internal and external dissemination.

ECATS as a Network of Excellence fully provides thematic nucleus for scientific expertise by establishing thematic workpackages and tasks. Until end of 2011 a specific workprogramme is identified and implemented jointly by ECATS Consortium. Association activities are in-line with network workprogramme. Main focus is given on addressing open questions while exploiting full synergies with other programmes. Such synergies can be exploited by complementing own funding with other project funding.

3 FOCUS AREA 1: VIRTUAL FUEL CENTRE

ECATS holds unique expertise and technology in Europe with respect to fuel characterisation. Such characterisation is essential for exploring option on introducing alternative fuels into aviation. ECATS aim is to provide fuel characterization facilities for alternative fuels (XTL). The aviation fuel specification has developed over a number of years from the specification of kerosene for use in oil lamps. The specification has developed such that safety and supply of fuel are not compromised. However, the specification relies on properties of the fuel being within spec because other parameters are in spec and the fuel is generated in such a way that parameters are linked. By looking at alternative fuels it is important to identify which additional parameters need to be specified and how to check that the new fuels meet this specification.

Equipment to check a range of fuel functionalities needs to be assembled. Most of it is available but spread across Europe and not accessible to all partners. ECATS partners have evaluated which items are available and produced a virtual centre containing the equipment. The equipment contains all the standard specification equipment currently used and available within the major research establishments. ECATS has enhanced it by a range of additional facilities (some requiring modifications for application in the virtual fuel centre) such as: an engine simulator for the evaluation of fuel thermal stability at engine operating conditions, fuels injection facilities for the evaluation of spray composition, fuel auto ignition and flashback measurement facilities, combustion capabilities emissions reactivity measurement facilities, material compatibility facilities, alternative fuels modelling facility. During the early phase of the Network of Excellence ECATS capability has been enhanced and the ECATS Virtual Fuel Centre was established. Currently the ECATS Virtual Fuel Centre is commissioning a premixed burner and a rapid compression machine, it performs modifications to a bomb which is suited for measurements of flame velocities, and it develops kinetic schemes for improved representation of alternative fuels.

Specific work performed within ECATS' Virtual Fuel Centre comprises commissioning a premixed burner in a manner that it can be transported and operated in various European laboratories. To ensure that the facility is operated correctly a number of modifications were performed. A high speed Flame Ionization Detector (FID) is purchased and utilised in the facility setup to ensure that the facility is setup at the correct operating condition. A controllable hot plate is required to vary the inlet temperature to the burner and a calibrated syringe driver is required to deliver the alternative fuels. A partner within ECATS Virtual Fuel Centre possesses a bomb which is suited for measurements of laminar flame velocities. The bomb also enables optical access which is necessary in order to measure the stretch effect on the flame velocity (Markstein Number). The described experimental facility is currently only used for gaseous fuels. So, there are only minor modifications required in order to enable investigation of liquid fuels within the existing facility. Further work is being performed in order to achieve conditions representative of today's gas turbine engines. Additionally, modelling capabilities will continue to be developed. In particular, the historical way to represent kerosene combustion is to describe the fuel as a mixture of 70% n-dodecane and 30% aromatics. This needs to be developed to a more detailed description for alternative fuels. The fuels will include a narrow xTL cut, consisting mainly of relative low molecular weight n- and iso-paraffins, as a base case, and blends of the base case with appropriately selected single-ring aromatics, di-aromatics and naphthenes. A conventional wide kerosene cut, either neat or contaminated with a particular Fatty Acid Methyl Ester (FAME) mixture will also be considered. For each fuel a state-of-the-art detailed kinetic mechanism will be assembled and validated against laminar burning velocities, ignition time delays and stable species profiles from laminar premixed flames. Experimental data generated within the ECATS consortium or obtained from the open literature will be used for the validation procedure. ECATS Consortium has a significant and demonstrated capability in the development, assembly and validation of detailed kinetic mechanisms for hydrocarbon fuels. Additionally spray characteristics of alternative fuels will be assessed. Objective here is to enable the spray quality to be evaluated providing results on the fuels under consideration as well as a fuel spray testing protocol.

For above mentioned work close collaboration with fuel industry is exploited. Impact on the fuels' behavior to each of these additives (assuring fuel compliance with specification) is jointly characterized within ECATS virtual fuel centre by experimental and theoretical studies.

4 FOCUS AREA 2: AIRPORT AIR QUALITY

ECATS holds unique expertise and technology with respect to airport air quality. Activities focus on preparation of an state-of-the-art assessment providing a comprehensive overview, and a documentation of recent ECATS advancements, approaches, methodologies applied and remaining issues. Reliable information on mechanisms, dominating factors, impact and mitigation strategies in local and regional air quality is required. Relevant stakeholders in this domain are airport operators, local authorities but also airlines and engine manufacturers which are linked via various research programmes (see figure 1). ECATS Consortium follows three major activities within network and Association activities: (1) Assessment of AAQ relevant issues, (2) particulate matter characterisation within the frame of SAMPLE, and (3) improved First Order Approximation (FOA) for aviation particulate matter emissions.

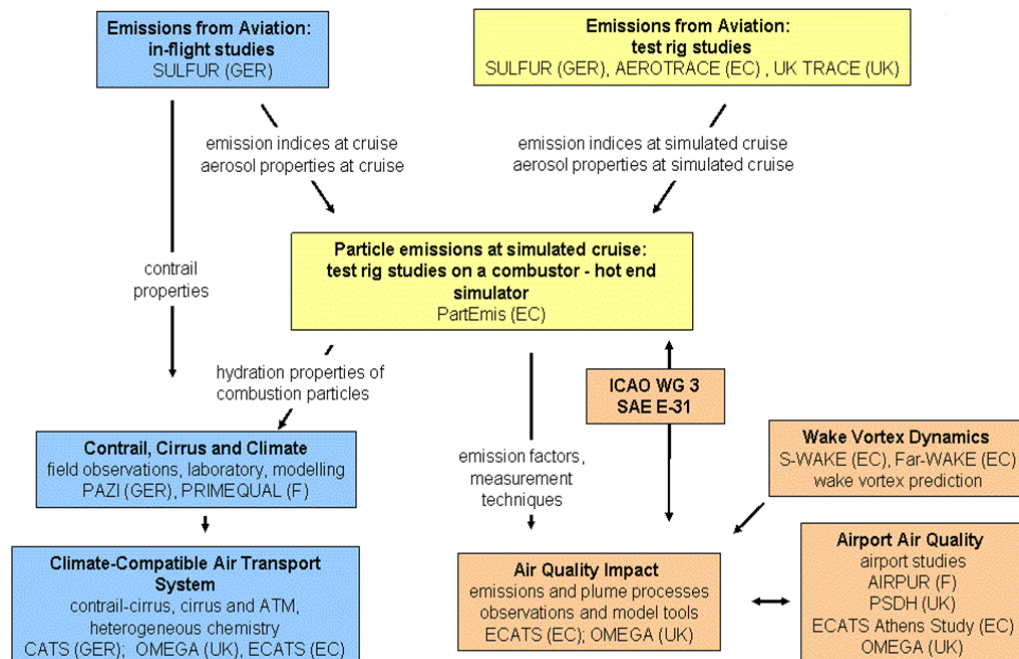


Fig 1: Activities on particulate matter emissions from aviation.

Regarding AAQ assessment, the main objectives are data interpretation of the ECATS airport campaigns and the further assessment of the impact of meteorology, source characteristics, atmospheric and emissions chemical properties on AAQ. In this framework, mitigation options in respect of AAQ will be studied with regards to technology, operational measures and economical measures, as well as source contributions and the evaluation and development of modelling tools. Regarding the SAMPLE II campaign, the role of the ECATS experts will be to further study the organic and inorganic matter emitted from aircraft engines. This work is expected to improve our understanding in this topic and to evaluate measurement methods in the framework of a new certification method based on the measurement of the mass and number of non-volatile particles. Furthermore, SAMPLE I and SAMPLE II results will build the basis for new Aerospace Recommended Practice (ARP) Guidelines for measuring particle emissions from aircraft engines. The new ARP which will be written in the next period will be sent in the ICAO CAEP/9 process to replace the outdated Smoke Number method by a modern methodology for engine certification issues. Regarding the First Order Approximation improvement for estimating particulate matter emission (PM) from aircraft, SAMPLE I and SAMPLE II results will be used together with literature data to improve the estimation of PM emissions from aircraft at the airport; the FOA will then become part of the ICAO Airport Air Quality Guidance Manual.

5 FOCUS AREA 3: GLOBAL AVIATION IMPACT AND GREEN FLIGHT

5.1 *Global Aviation Impact*

Despite the significant progress that has been made in reducing the specific emissions of aircraft, the absolute emissions have been increasing rapidly during the recent decades and are projected to continue to grow. Aviation CO₂ emissions in the EU nearly doubled over the period 1990 to 2005. Furthermore, aviation substantially impacts upon climate from non-CO₂ effects such as ozone formation and methane destruction from aviation's NO_x emissions, the formation of contrails and contrail cirrus, the emission of H₂O at high altitudes, emission of aerosols (e.g., soot) and aerosol precursors (e.g., SO_x), which are directly radiatively active and which modify cloudiness and cloud micro-physical and radiative properties.

The ultimate goal of ECATS is to contribute to solutions for a more environmentally sustainable aviation system. There are two principle pathways to that goal, namely (1) reducing the emissions and (2) reducing the climatic effects of the emissions. The first pathway proceeds mainly via novel technological solutions which are investigated in ECATS as one thematic area (TA1). The second pathway, reducing the climatic effects of emissions requires adapted flight operations that take into account the state of the atmosphere at the time and location of the specific emission.

ECATS thematic area Aviation climate impact and green flight (TA3) conducts research in order to increase the understanding of the effects of emissions in specific regions of the atmosphere. This research helps to reduce current uncertainties and helps to provide guidance to stakeholders and policy makers. In cases where uncertainties cannot be reduced substantially, for whatever reason, we explore the range of possibilities in order to allow robust decisions to be taken, i.e., decisions that work in almost all conceivable circumstances. ECATS work and achievements in TA3 help to develop operational mitigation strategies with respect to aviation's climate impact. One particular aspect is avoiding contrails that warm climate. Such contrails form in so-called ice supersaturated regions in the upper troposphere. Therefore we investigate properties of these regions and help aviation weather forecast to predict them in order to allow a flight routing that is able to take contrail effects into account. Another aspect is to investigate aviation global warming potential (GWP) due to NO_x emissions. Chemical impact of NO_x is highly non-linear. Short term warming effect due to ozone formation is compensated by a long-term indirect methane lifetime effect. The residuum of both effects depends also on assumed time horizon for evaluating climate impact.

5.2 *Green flight*

With air traffic growth, aviation's contribution to climate change may well increase. Proper modelling tools, realistic scenarios and databases are needed to assess the impact. Inefficiencies in the air traffic management (ATM) system and flight operations lead to a considerable amount of unnecessary fuel burn and emissions; approx 10% for Europe! ECATS establishes central databases and investigates operational measures to reduce fuel burn and emissions and to avoid sensitive regions in the atmosphere.

Flight time, fuel consumption and emissions can be reduced due to various enhancements in the field of air traffic management (ATM) and supporting communication, navigation, surveillance (CNS) techniques. ECATS' broad expertise and capabilities in this field include ATM, airport and flight simulators, and tools to assess environmentally friendly flight operations. ECATS' partners contribute to ongoing European ATM programmes like SESAR. Close linkages exist with EUROCONTROL. Current flight routing under cruise conditions is optimized against criteria such as punctuality and costs. Environmental effects are often not taken into account. ECATS' idea is to expand today's flight planning so that it becomes environmental flight planning. As a pre-requisite current flight planning tools have to be extended in order to be able to assess the climate impact of aviation, e.g. on contrail formation. This needs the involvement and commitment of stakeholders. Assessment of aviation impact on the environment requires reliable estimates on emissions for current and future fleet scenarios. ECATS combines expertise on flight planning and routing with aircraft, engine, combustion and propulsion technology in order to generate, adopt or compare global

emission inventories and scenarios. Such data was used in technological and environmental impact assessments within Europe, e.g. in the EC FP6 funded projects QUANTIFY and ATTICA.

6 CONCLUDING REMARKS

After having gained experience since the establishment of Network of Excellence ECATS in 2005 the ECATS Consortium now is stepping on to a future sustainable organisation structure, by establishing a registered Association. Founding members for this Association are the partners within the NoE ECATS. Other institutions are welcome to join this thematic Association which has spelled out scope to help making aviation more sustainable. Thematic focus areas of ECATS Association are alternative fuels, airport air quality and global aviation impact and green flight. ECATS will coordinate efforts for future research on aviation and environment within Europe.

In Spring 2010 ECATS Consortium has scheduled to apply for this registered Association ECATS. This future Association will provide an efficient framework for collaboration between universities and research establishment and help to make aviation more sustainable.

7 ACKNOWLEDGMENT

ECATS is a Network of Excellence (FP6) funded by EU under Contract ANE4-CT-2005-012284.

SPIDER model simulations of aircraft plume dilution

N. Dotzek*, S. Matthes, and R. Sausen

Deutsches Zentrum für Luft- und Raumfahrt (DLR), Institut für Physik der Atmosphäre, Oberpfaffenhofen, Germany

Keywords: Aircraft emissions, plume dilution, simplified chemistry, effective emission indices.

ABSTRACT: To include the effect of aircraft plume processes (effective emissions indices) in large scale chemistry transport models and climate-chemistry models, the instantaneous dispersion (ID) and single-plume (SD) approaches exist. We use the box model SPIDER to evaluate these two concepts. Its simplified NO_x-O₃ chemistry parameterises only the most relevant non-linear processes. SPIDER simulations for varying NO_x background reveal the largest difference between ID and SP approaches in clean-air conditions. For a NO_x background of $\sim 0.2 \text{ nmol mol}^{-1}$, the ID and SP approaches result in aviation-induced O₃ changes of opposite signs. Hence, this transition regime may require more attention in plume parameterisations applied in global atmospheric models.

1 MOTIVATION

Emissions from aircraft impact on global climate (cf. Brasseur et al., 1998; IPCC, 1999; Sausen et al., 2005). They are usually implemented in General Circulation Models (CGM) or Chemistry Transport Models (CTM) by an instantaneous dispersion of emitted matter over the large-scale grid boxes. Following Petry et al. (1998), this is called the instantaneous dispersion (ID) approach. The ID approach neglects non-linear chemical conversion processes in the evolving single plume. To resolve these by a plume model is called the single plume, or SP approach. However, detailed SP chemical modelling is computationally too demanding, both for more complex principle studies of plume-plume interactions, and for operational implementation in large-scale models.

To improve the ID approach in GCMS, Effective Emission Indices (EEIs) can be used (e.g., Möllhoff, 1996; Petry et al., 1998). These, and several other approaches to the problem, e.g., by Meijer et al. (1997), Meijer (2001), Karol et al. (1997, 2000), Kraabøl et al. (2000), Kraabøl and Stordal (2000) and Franke et al. (2008) applied detailed chemistry schemes. A simplified model was presented and validated by Dotzek and Sausen (2007) to evaluate various EEI concepts, and to perform studies of multi-plume interactions. This paper aims to (1) to apply this box model with simplified chemistry, the SPIDER (SP-ID Emission Relations) model, to various NO_x backgrounds and (2) to identify those NO_x background concentrations where the application of a more sophisticated single-plume approach yields results different from instantaneous dispersion approach.

2 MODEL DESIGN

In this study we use the SPIDER model which is a box model applying a simplified scheme for non-linear ozone production by aircraft NO_x emissions at cruise altitude. Motivated by the work by Petry et al. (1998) who applied a detailed chemistry scheme, we aim at computing plume dilution, and comparing of ID and SP results using a computationally efficient box model with greatly simplified chemistry. The resulting SPIDER model avoids explicit solution of the chemical rate equations. Chemistry enters the equations only in parameterized form by “dynamic forcing” terms, and the only species considered are NO_x and O₃. The model is described in more detail by Dotzek and Sausen (2007). The objectives were to apply the validated SPIDER model to multiple plume interactions or varying background NO_x fields, and to eventually evaluate different EEI approaches.

* *Corresponding author:* Dr. Nikolai Dotzek, Deutsches Zentrum für Luft- und Raumfahrt (DLR), Institut für Physik der Atmosphäre, Oberpfaffenhofen, 82234 Wessling, Germany. Email: nikolai.dotzek@dlr.de

2.1 SPIDER model setup

The main process to be covered by the SPIDER model is the non-linear production of O_3 by aircraft NO_x emissions at cruise altitude. Hence, the system of equations includes only these two species. The physical processes which are to be explicitly included in and resolved by the model within a typical GCM grid box volume are a) the emission of NO_x inside the GCM box, S_{NO_x} , b) non-linear production of ozone, P_{O_3} , and c) the decay of the NO_x and O_3 fields by conversion to reservoir species. For treatment of the SP approach, additionally the background (outer domain, superscript o) and plume fields (inner domain, superscript i) have to be integrated separately, and the entrainment of background matter by turbulent mixing at the growing-plume boundary enters the budget equations as another individual term.

As the SPIDER model equations are formulated for the plume dispersion regime (the far-field solution), they cannot resolve initial titration, which is a near-field plume process. The initial ozone level in the plume must be lowered slightly compared to the background state to provide the proper initialisation values for the early dispersion regime. Eqs. (1-4) specify the budget equations for the ID and SP concepts. Following the convention we denote extensive quantities by upper-case ($[NO_x]$ = mol, $[O_3]$ = mol) and intensive quantities by lower-case letters ($[no_x]$ = nmol mol⁻¹). Parameterisation of photochemical ozone production P_{O_3} applied for both approaches is presented below.

2.1.1 ID budget equations

In the following equations for instantaneous dispersion, dt denotes the temporal derivative d/dt :

$$d_t NO_x = S_{NO_x} \delta(t - t') - \frac{1}{\tau_{NO_x}} NO_x, \quad (1)$$

$$d_t O_3 = P_{O_3}(no_x) - \frac{1}{\tau_{O_3}} O_3. \quad (2)$$

The reference background state without aircraft emissions follows for $S_{NO_x} \equiv 0$. The decay, or conversion of NO_x and O_3 to reservoir species, is modelled as an exponential decay with fixed half-time periods τ ($\tau_{NO_x} = 10$ days, $\tau_{O_3} = 30$ days, cf. Köhler and Sausen, 1994).

2.1.2 SP budget equations

In the single-plume equations, each species must be treated with one budget equation for the plume (superscript i) and the background (superscript o). As the box model reference volume is one GCM grid box, the computation of entrainment in Eqs. (3-4) is terminated as soon as the plume volume V^i is equal to the reference volume V_{GCM} .

$$d_t NO_x^i = S_{NO_x} \delta(t - t') + NO_x^o / V^o d_t V^i - \frac{1}{\tau_{NO_x}} NO_x^i, \quad (3a)$$

$$d_t NO_x^o = - NO_x^o / V^o d_t V^i - \frac{1}{\tau_{NO_x}} NO_x^o, \quad (3b)$$

$$d_t O_3^i = P_{O_3}(no_x^i) + O_3^o / V^o d_t V^i - \frac{1}{\tau_{O_3}} O_3^i, \quad (4a)$$

$$d_t O_3^o = P_{O_3}(no_x^o) - O_3^o / V^o d_t V^i - \frac{1}{\tau_{O_3}} O_3^o. \quad (4b)$$

Eq. (3a) encompasses the case a fresh aircraft plume being emitted along the axis of an aged plume from another aircraft earlier on (cf. Kraabøl and Stordal, 2000; Dotzek and Sausen, 2007).

2.2 Parameterisation of $P_{O_3}(nox)$ terms

As treated in detail by, e.g., Johnson and Rohrer (1995), Brasseur et al. (1996), Grooß et al. (1998), and Meilinger et al. (2001), the production of ozone does not only depend on NO_x concentrations, but is a highly variable function of other species like O_3 itself, H_2O , CO , hydrocarbons, state vari-

ables p , and T , and the actinic flux J . A perfect parameterisation in this multidimensional phase space is impossible, and likely has prevented earlier simplified chemistry studies of plume dilution. However, the objective in developing the SPIDER model was to allow for principal studies of plume dilution, plume interaction, and methods to derive EEs. A parameterisation of O_3 production as a function of nitrogen oxides for some typical atmospheric conditions at cruise altitude following the data presented in the literature is possible. Aside from the NO_x concentration, also the solar elevation angle must be taken into account, in order to capture the diurnal cycle of photochemical ozone production. This non-linear production of ozone as a function of the ambient NO_x concentrations was parameterised by Dotzek and Sausen (2007) for the SPIDER model Eqs. (2) and (4), evaluating five different parameterisations of which curve D from the Brasseur et al. (1996) data was selected in the SPIDER model. It includes effects of the diurnal cycle, while the other curves are very similar in shape, and their variation comes mainly from different ambient chemical conditions. Note the non-linearity, or rather non-monotonicity, of all P_{O_3} curves. Low and very high NO_x concentrations are characterized by ozone depletion, while the peak ozone production is found in the range of 0.15 to 0.27 nmol mol⁻¹. The similarity of the curves in the upper troposphere gives us confidence that the SPIDER parameterisation of P_{O_3} is adequate for principal process studies.

2.3 Experimental model set-up

We perform a case study of ozone formation by an aircraft plume at about 10 km cruising altitude. This setting is similar to the original model cases of Möllhoff (1996) and was also used by Dotzek and Sausen (2007) to validate the SPIDER model. Without wind shear or cross-plume wind components, the exhaust of a typical B747 airplane is emitted as a line-source at 0800 LST (local solar time) in a $V_{GCM} = 50 \times 50 \times 1$ km³ reference volume. Ambient conditions are mid-latitude summer, $T = 218$ K and $p = 236$ hPa (about 10 km above sea level, ASL) in the North Atlantic flight corridor. The initial average values of NO_x and O_3 in the plume are chosen to be representative of the early dispersion regime (about 100 s after emission): for NO_x , 2.97 nmol mol⁻¹ and for O_3 196.5 nmol mol⁻¹ (Petry et al., 1998). Linear Gaussian plume growth is specified, so after $t_{ref} = 18$ h of dilution, the plume volume becomes equal to the reference volume V_{GCM} . The SPIDER model runs were performed for NO_x background concentrations of 0.05, 0.075, 0.1, 0.2, 0.5, 1, 2 and 3 nmol mol⁻¹, respectively. These cover the range from clean-air to strongly polluted environments.

3 RESULTS FOR VARYING BACKGROUND NO_x

In order to compare individual approaches for above model cases the temporal evolution of aircraft-induced O_3 change is presented as absolute values and per kilometre plume length along the flight path. Fig. 1 shows results for 0.05, 0.1, 0.2 and 1 nmol mol⁻¹ NO_x backgrounds. During the first few minutes after plume emission aircraft-induced ozone change is characterised by ozone titration within the plume due to very high NO_x concentration under all NO_x background conditions.

Both for the absolute change in O_3 and the change per kilometre flight path, it becomes obvious that the largest differences between the ID and SP approaches materialise for clean-air ambient conditions, that is, for NO_x background concentrations of less than about 0.1 nmol mol⁻¹. After an initial ozone titration in SP simulations, ozone production during the early phase (up to several hours) is higher in SP simulations, compared to ID calculations. More than 12 hours after emissions this changes, and finally ozone production in SP simulations is lower than in ID calculations.

For strongly polluted environments (1, 2, 3 nmol mol⁻¹, latter two not shown), the ID and SP simulations yield essentially identical results at the time when the plume attains the same volume as the GCM grid box. Interestingly, a transition regime can be identified for NO_x backgrounds of about 0.2 nmol mol⁻¹, in which the ozone productions of the ID and SP approaches at $t = t_{ref}$ are small, but have opposite signs. Here, during 24 hours after emission, the SP approach leads to a small net destruction of O_3 , while the ID approach leads to ozone production with a magnitude considerably larger than the destruction evaluated from the SP approach. This opposite sign of ozone change between SP and ID approach prevails from 4 hours after emission onward.

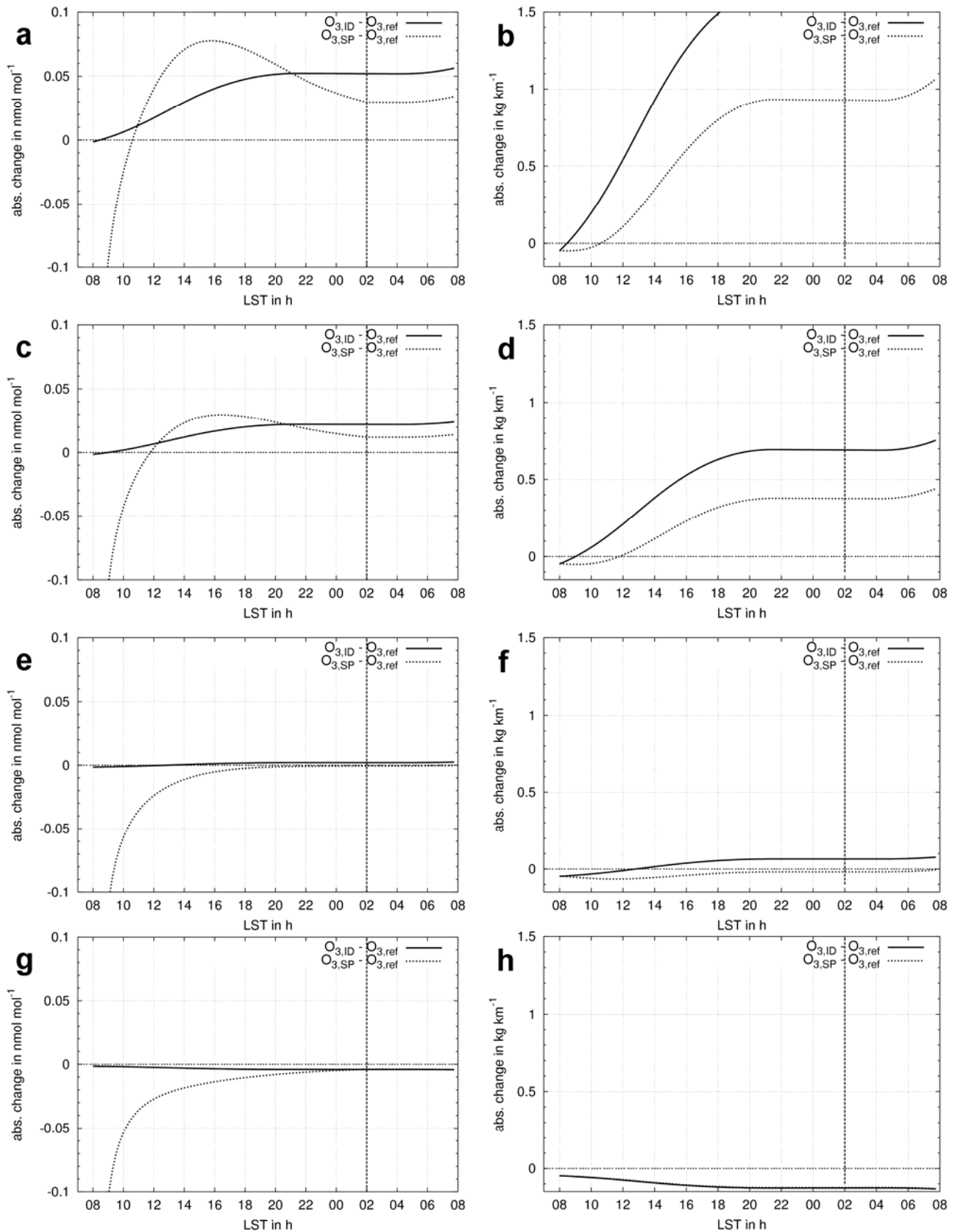


Figure 1. Aircraft-induced O_3 change as absolute change (left panels) and change per kilometre plume length along the flight path (right panels) compared to the background state for ID (solid) and SP simulations (dotted). Background NO_x concentrations increase from top to bottom: (a, b) 0.05 nmol mol^{-1} , (c, d) 0.1 nmol mol^{-1} , (e, f) 0.2 nmol mol^{-1} , and (g, h) 1 nmol mol^{-1} . Emission time was 0800 LST and after 18 h, the plume volume equals the GCM box volume (dashed line).

4 DISCUSSION

Depending on NO_x background concentrations, substantial differences between ID and SP approaches can occur. Differences in O_3 change observed in our results indicate that in the clean-air regime (below $0.1 \text{ nmol mol}^{-1}$) both ID and SP ozone productions are positive and show their largest absolute spreads. In the transition regime ($\sim 0.2 \text{ nmol mol}^{-1}$), an opposite sign can be observed between ID and SP approaches from several hours after emission on. This pattern prevails even after 18 hours of plume expansion to full GCM box volume. For more polluted regions, however, with NO_x backgrounds well above $0.2 \text{ nmol mol}^{-1}$, the ID and SP approaches yield increasingly similar results. Hence, for such conditions which can be found in the North Atlantic flight corridor, an ID approach may still be adequate and least time-consuming for application in GCMs or CTMs. Under clean-air conditions and in the transition regime, use of an ID approach would yield substantial differences from a more detailed SP approach, overestimating aviation-induced O_3 changes.

The simplifications made in the SPIDER model equations require some more discussion. The basic plume dilution processes were shown to be well-represented by Dotzek and Sausen (2007), in part even quantitatively. Some details are missing in the model which would require the complete set of chemical reactions – or an improved description of either the plume growth (being linear only on average, cf. Schumann et al., 1998) or the actinic flux in the P_{O_3} term. Nonlinear plume growth already has been implemented as an option in the model, but to facilitate comparison to the Dotzek and Sausen (2007) results, it was not considered here. Our model set-up does not include a typical diurnal cycle. For the parametric functions of P_{O_3} , a curve was selected from Brasseur et al. (1996) including a diurnal cycle. Future SPIDER versions will include a typical diurnal variation of these time scales, but this is a second-order effect with little consequence here.

For multi-plume interactions (Dotzek and Sausen, 2007), the net effect on the difference between ID and SP approaches critically depends on the age of the primary plume (and hence its NO_x and O_3 concentrations). Our present study with NO_x background variations across the whole GCM grid box, however, showed a consistent trend. The need for a more sophisticated description of plume processes in GCMs sets in at NO_x backgrounds of about $0.2 \text{ nmol mol}^{-1}$, first with a disparity of the signs of the (small) O_3 productions, and then with increasing magnitude for less polluted regions.

The inclusion of plume effects in the dispersion modelling of pollutants is not only relevant in aviation at cruise altitude, but also near the ground (Uphoff, 2008; Galmarini et al., 2008), for land transport (Ganev et al., 2008) and shipping (Franke et al., 2008). Several parameterisations to include these effects in mesoscale or general circulation models have been proposed recently. Cariolle et al. (2009) specifically addressed aircraft NO_x emissions in a similar setting as in our present paper. They track the plume air with NO_x concentrations above 1 nmol mol^{-1} by introducing a “fuel tracer” and a characteristic lifetime into their budget equations. Their detailed parameterisation confirms our results: Taking into account the plume processes consistently lowers the estimates of aircraft-induced O_3 production at cruise altitude in parts of the North Atlantic flight corridor.

5 CONCLUSIONS

Applying the SPIDER box model for various NO_x background concentrations illustrated:

- The largest differences between the ID and SP approaches occur for clean-air ambient conditions, that is, for NO_x background concentrations of less than about $0.1 \text{ nmol mol}^{-1}$;
- For strongly polluted environments, the ID and SP simulations yield essentially identical results at the time when the plume attains the same volume as the GCM grid box;
- A transition regime can be identified for NO_x backgrounds of about $0.2 \text{ nmol mol}^{-1}$ in which the ozone productions of the ID and SP approaches after 18 h are small, but have opposite signs.
- It appears necessary to also consider this transition regime in parameterisations of the ozone production by aircraft NO_x emissions at cruise altitude, in addition to the clean-air regime.

Future work will encompass simulations for a wider range of likely environmental conditions at cruise altitude to assess the robustness of our findings.

6 ACKNOWLEDGMENTS

This work was partly funded by the European Commission FP6: ND and RS were supported by the Integrated Project QUANTIFY under contract no. 003893 (GOCE) and SM was supported by the Network of Excellence ECATS under contract no. ANE-CT-2005-012284.

REFERENCES

- Brasseur, G. P., J.-F. Müller, and C. Granier, 1996: Atmospheric impact of NO_x emissions by subsonic aircraft: A three-dimensional model study. *J. Geophys. Res.*, 101 D, 1423-1428.
- Brasseur, G. P., R. A. Cox, D. Hauglustaine, I. Isaksen, J. Lelieveld, D. H. Lister, R. Sausen, U. Schumann, A. Wahner, and P. Wiesen, 1998: European scientific assessment of the atmospheric effects of aircraft emissions. *Atmos. Environ.*, 32(13), 2329-2418.
- Cariolle, D., D. Caro, R. Paoli, D. A. Hauglustaine, B. Cuénot, A. Cozic, and R. Paugam, 2009: Parameterization of plume chemistry into large-scale atmospheric models: Application to aircraft NO_x emissions. *J. Geophys. Res.*, 114, D19302, doi:10.1029/2009JD011873.
- Dotzek, N., and R. Sausen, 2007: SPIDER model process studies of aircraft plume dilution using simplified chemistry. In: Sausen, R., A. Blum, D. S. Lee and C. Brüning (eds.): *Proceedings of an International Conference on Transport, Atmosphere and Climate (TAC)*. Luxembourg, Office for Official Publications of the European Communities, ISBN 92-79-04583-0, 261-266.
- Franke, K., V. Eyring, R. Sander, J. Hendricks, A. Lauer, and R. Sausen, 2008: Toward effective emissions of ships in global models. *Meteorol. Z.*, 17(2), 117-129.
- Galmarini, S., J.-F. Vinuesa, and A. Martilli, 2008: Modeling the impact of sub-grid scale emission variability on upper-air concentration. *Atmos. Chem. Phys.*, 8, 141-158.
- Ganev, K., D. Syrakov, Z. Zlatev, 2008: New parameterization scheme for effective indices for emissions from road transport. *Ecol. Model.*, 217(3-4), 270-278.
- Groß, J.-U., C. Brühl, and T. Peter, 1998: Impact of aircraft emissions on tropospheric and stratospheric ozone. Part I: Chemistry and 2-D model results. *Atmos. Environ.*, 32(18), 3173-3184.
- IPCC, 1999: Aviation and the global atmosphere. – A special report of IPCC working groups I and III. (Penner, J. E., D. H. Lister, D. J. Griggs, D. J. Dokken, and M. McFarland (Eds.)). Intergovernmental Panel on Climate Change. – Cambridge University Press, Cambridge, UK and New York, NY, USA, 365 pp.
- Johnson, C., and F. Rohrer, 1995: NO_x and O₃ chemistry in the upper troposphere and lower stratosphere. In: Schumann (1995), 325-335.
- Karol, I. L., Y. E. Ozolin, and E. V. Rozanov, 1997: Box and Gaussian plume models of the exhaust composition evolution of subsonic transport aircraft in- and out of the flight corridor. *Ann. Geophys.* 15, 88-96.
- Karol, I. L., Y. E. Ozolin, A. A. Kiselev, and E. V. Rozanov, 2000: Plume transformation index (PTI) of the subsonic aircraft exhausts and their dependence on the external conditions. *Geophys. Res. Lett.* 27(3), 373-376.
- Kraabøl, A. G., and F. Stordal, 2000: Modelling chemistry in aircraft plumes 2: The chemical conversion of NO_x to reservoir species under different conditions. *Atmos. Environ.* 34, 3951-3962.
- Kraabøl, A. G., P. Konopka, F. Stordal, and H. Schlager, 2000: Modelling chemistry in aircraft plumes 1: Comparison with observations and evaluation of a layered approach. *Atmos. Environ.* 34, 3939-3950.
- Köhler, I., and R. Sausen, 1994: On the global transport of nitrogen oxides from emissions of aircraft. In: Schumann and Wurzel (1994), 193-198.
- Meijer, E. W., P. F. J. van Velthoven, W. M. F. Wauben, J. P. Beck, and G. J. M. Velders, 1997: The effects of the conversion of nitrogen oxides in aircraft exhaust plumes in global models. *Geophys. Res. Lett.* 24(23), 3013-3016.
- Meijer, E. W., 2001: Modeling the impact of subsonic aviation on the composition of the atmosphere. Ph. D. Thesis, Tech. Univ. Eindhoven, The Netherlands, 108 pp.
- Meilinger, S. K., B. Kärcher, R. von Kuhlmann, and T. Peter, 2001: On the impact of heterogeneous chemistry on ozone in the tropopause region. *Geophys. Res. Lett.* 28(3), 515-518.
- Möllhoff, M., 1996: Modellierung der chemischen Umwandlung reaktiver Flugzeugabgase im Tropopausenbereich unter Berücksichtigung ihrer Dispersion. Diploma thesis, Institut für Geophysik und Meteorologie, Universität zu Köln, 110 pp.
- Petry, H., J. Hendricks, M. Möllhoff, E. Lippert, A. Meier, A. Ebel, and R. Sausen, 1998: Chemical conversion of subsonic aircraft emissions in the dispersing plume: Calculation of effective emission indices. *J. Geophys. Res.* 103 (D5), 5759-5772.

- Sausen, R., I. Isaksen, V. Grewe, D. Hauglustaine, D. S. Lee, G. Myhre, M. O. Köhler, G. Pitari, U. Schumann, F. Stordal, and C. Zerefos, 2005: Aviation radiative forcing in 2000. An update on IPCC (1999). *Meteorol. Z.* 14, 555–561.
- Schumann, U., H. Schlager, F. Arnold, R. Baumann, P. Haschberger, and O. Klemm, 1998: Dilution of aircraft exhaust plumes at cruise altitudes. *Atmos. Environ.* 32, 3097–3103.
- Uphoff, M., 2008: Parametrisierung flugzeuginduzierter Vermischung in einem mesoskaligen Modell (Parameterisation of aircraft-induced mixing in a mesoscale model). Diplomarbeit, Universität Hamburg, 144 pp. [In German]

ECHAM5 simulations with the $\text{HO}_2 + \text{NO} \rightarrow \text{HNO}_3$ reaction

K. Gottschaldt*, C. Voigt¹, B. Kärcher

Deutsches Zentrum für Luft- und Raumfahrt (DLR) - Institut für Physik der Atmosphäre, Oberpfaffenhofen, Germany

¹also: Universität Mainz, Institut für Physik der Atmosphäre

Keywords: climate modelling, atmospheric chemistry, ozone, nitric acid

ABSTRACT: A HNO_3 -forming channel of the $\text{HO}_2 + \text{NO}$ reaction recently found in laboratory measurements (Butkovskaya et al., 2005, 2007) may significantly alter the concentration of HNO_3 , NO_x , O_3 and other trace gases in the tropopause region. This region is also significantly affected by air traffic NO_x emissions. Cariolle et al. (2008) adopted a pressure- and temperature dependent parameterisation of the rate constant to assess the impact of the $\text{HO}_2 + \text{NO} \rightarrow \text{HNO}_3$ reaction on trace gas concentrations in a 2-D stratosphere-troposphere model, and a 3-D tropospheric chemical transport model. We implemented the parameterisation of Cariolle et al. (2008) into the 3-D stratosphere-troposphere chemistry-climate model ECHAM5 / MESSy. Here we present results of our test runs, in support of planned studies of the effects of aircraft emissions on atmospheric chemistry.

1 BACKGROUND

The concentration of ozone in the upper troposphere and lower stratosphere region (UTLS) is mainly controlled by the reactive NO_x and HO_x cycles (figure 1).

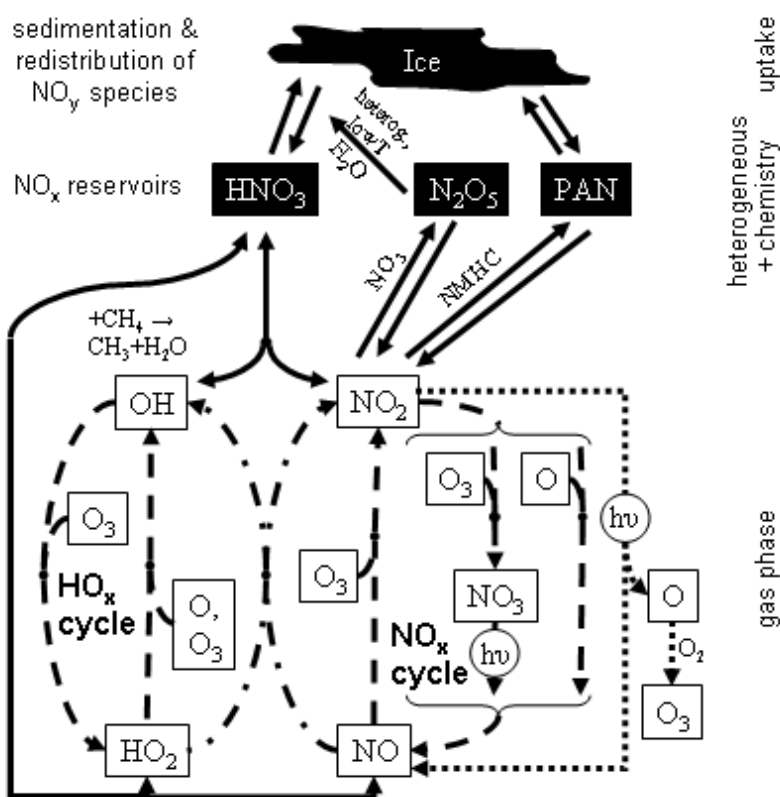


Figure 1. Major reactions in the UTLS involving ozone, methane NO_x , NO_y and HO_x . Solid lines represent reservoir reactions, dotted lines show reaction paths of ozone production, dashed paths indicate ozone destruction, and dash dot is neutral with respect to ozone.

* Corresponding author: Klaus Gottschaldt, Deutsches Zentrum für Luft- und Raumfahrt (DLR) - Institut für Physik der Atmosphäre, Oberpfaffenhofen, D-82234 Wessling, Germany. Email: klaus-dirk.gottschaldt@dlr.de

Aircraft NO_x emissions peak in the UTLS. Considering gas phase chemistry, the NO_x effect on ozone changes sign in the altitude range between about 12 and 18 km (Søvde et al., 2007). Below the tipping point, the ozone destructing NO_x cycle is bypassed via peroxy radicals. NO_x emissions lead to increased ozone production. Peroxy radicals and NO_2 photolysis are less important at higher altitudes. There aircraft NO_x emissions intensify the NO_x cycle, enhancing ozone destruction. NO_x may be removed from the system by heterogeneous reactions, but also by the recently discovered HNO_3 -forming channel of the $\text{HO}_2 + \text{NO}$ reaction (Butkovskaya et al., 2005, 2007):



with the rate constants k_1 and k_2 .

The $\text{HO}_2 + \text{NO}$ conversion has been assumed to have a temperature-dependent rate constant (Sander et al., 2003),

$$k_0 = k_1 + k_2 = 3.5 \cdot 10^{12} \cdot \exp\left(\frac{250}{T}\right) \quad (3)$$

with temperature T in [K]. In the following we study the effects of three different combinations of k_1 and k_2 on UTLS gas phase chemistry, extending the work of Cariolle et al. (2008).

2 BASE MODEL

We use the global chemistry-climate model ECHAM5 (Roeckner et al., 2003) / MESSy (Jöckel et al., 2006). Dynamics and chemistry are fully coupled. Our runs are based on the setup of Jöckel et al. (2006), but using MESSy version 1.6, with T42 / L90 resolution and the top layer centered at 0.01 hPa. Gas phase chemistry was calculated with the MECCA1 chemistry module (Sander et al., 2005), consistently from the surface to the stratosphere. However, the runs presented here were originally designed to find a parameterisation for correcting upper stratospheric chemistry in low resolution models. Therefore our chemical mechanism has full stratospheric complexity, but neglects the NMHC, sulfur, and halogen families in the troposphere. The initial conditions correspond to January 1978 and we evaluated twelve months, starting November 1978.

Figures 2a show the 12-month average of the zonal mean mixing ratios for HNO_3 , NO_x and O_3 , in the base model, run A. Reaction 1 is included with $k_1 = k_0$ (equation 3). The HNO_3 -forming channel (reaction 2) is ignored here, i.e. $k_2 = 0$.

3 EFFECTS OF THE $\text{HO}_2 + \text{NO} \rightarrow \text{HNO}_3$ REACTION

Simulation B differs to the base run just in k_1 and k_2 :

$$k_2 = \frac{k_0 \cdot \beta}{1 + \beta} \quad (4)$$

$$k_1 = k_0 - k_2 \quad (5)$$

with pressure p [Pa] in

$$\beta(p, T) = 0.01 \cdot \left(\frac{530}{T} + p \cdot 4.8 \cdot 10^{-6} - 1.73 \right). \quad (6)$$

Hence both reaction rates depend on temperature and pressure in this case. Equation 6 was proposed by Cariolle et al. (2008). It is based on an empirical fit to measurements and valid for dry conditions, in the range 93 - 800 hPa and 223 - 298 K. They noted deviations from equation 6 for temperatures above 298 K.

Figures 2b show the differences d between run B and the base model. The results are noisy, because both runs, A and B, were dynamic. They had all couplings between chemistry and meteorology switched on. Running the ECHAM model in a chemistry transport mode would have been better

suited for our sensitivity runs B and C, but this option was not available. Given the exploratory nature of this study, we believe the present approach is acceptable. Due to the different dynamics in both runs, a low background value in one model might coincidentally fall together with a high value in the other model. The biggest effects on HNO_3 , NO_x and O_3 correlate with rather small background mixing ratios. To filter out some noise, and to avoid random division by numbers close to zero, we normalized all values d by the locally highest background value:

$$d = \frac{v_B - v_A}{\max(v_A, v_B)} \cdot 100\% \quad (7)$$

v_A and v_B are the zonal mean mixing ratios of the same species, in the base run and model B, respectively. We get similar variations to the base model as Cariolle et al. (2008). They show results for March only. However, in another attempt to reduce noise, we evaluated 12 months instead of just March. Results for March display a similar pattern as the yearly mean, in our runs.

Inclusion of the HNO_3 forming channel results in a general HNO_3 increase, prompting an overall NO_x decrease. As expected, ozone correlates with NO_x variations below ≈ 12 km, while there is anticorrelation above ≈ 18 km.

Cariolle et al. (2008) applied equation 6 up to an altitude of 30 km, although it is only based on measurements for pressures corresponding to an altitude of about 15 km. Therefore we did not expect any problems for lower pressures and applied equation 6 up to 0.01 hPa (39 km). Similar to Cariolle et al. (2008), we get a locally pronounced HNO_3 increase about 15 km over the equator, followed by a region of smaller effects and another increase from 25 km upwards. However, in our model we note the biggest relative HNO_3 increase above 30 km. It remains unclear if this effect is real, an artefact due to the extrapolation of equation 6, or due to the very low background concentration in that altitude.

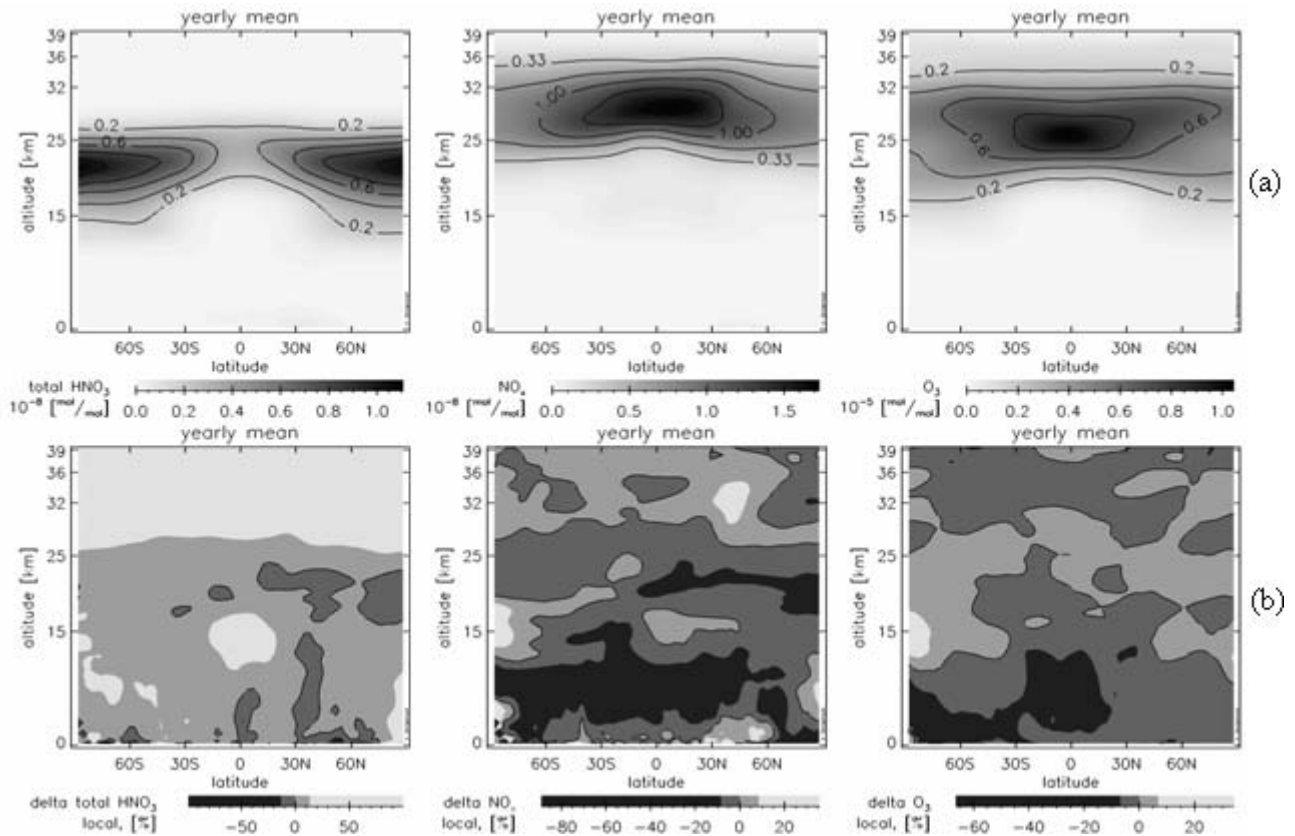


Figure 2: (a) Annual mean values of the zonal average concentrations of HNO_3 , NO_x and O_3 in base run A, without $\text{HO}_2 + \text{NO} \rightarrow \text{HNO}_3$ reaction; (b) Run B: deviations from A after inclusion of the dry HNO_3 reaction

4 CONCLUSIONS

The HNO_3 forming channel of the $\text{HO}_2 + \text{NO}$ reaction has the potential to alter UTLS chemistry significantly. Adding the dry $\text{HO}_2 + \text{NO} \rightarrow \text{HNO}_3$ reaction to our model resulted in a general increase of HNO_3 , a decrease of NO_x and related effects on ozone. The spatial pattern of variations confirms the results of Cariolle et al. (2008). However, it is not clear if the parameterisation used for the reaction rate is valid above 15 km. Measurements under stratospheric conditions are needed. At any rate, it is important to confirm the data set presented by Butkovskaya et al. (2005, 2007) by independent laboratory studies. A better noise reduction strategy and refined tropospheric chemistry in the model might be useful to study the impact of this reaction in more detail.

5 ACKNOWLEDGEMENTS

The authors thank Christoph Brühl, Georges Le Bras, Patrick Jöckel and the Messy-Team for their support.

REFERENCES

- Butkovskaya, N.I., Kukui, A., Pouvesle, N., and G. Le Bras, 2005: Formation of nitric acid in the gas-phase $\text{HO}_2 + \text{NO}$ reaction: Effects of temperature and water vapor. *J. Phys. Chem. A* 109, 6509–6520.
- Butkovskaya, N.I., Kukui, A., and G. Le Bras, 2007: Study of the HNO_3 forming channel of the $\text{HO}_2 + \text{NO}$ reaction as a function of pressure and temperature in the ranges 72 - 600 Torr and 223 - 323 K. *J. Phys. Chem. A* 111, 9047-9053.
- Cariolle, D., Evans, M.J., Chipperfield, M.P., Butkovskaya, N., Kukui, A., and G. Le Bras, 2008: Impact of the new HNO_3 -forming channel of the $\text{HO}_2 + \text{NO}$ reaction on tropospheric HNO_3 , NO_x , HO_x and ozone. *Atmos. Chem. Phys.* 8, 4061-4068.
- Jöckel, P., Tost, H., Pozzer, A., Brühl, C., Buchholz, J., Ganzeveld, L., Hoor, P., Kerkweg, A., Lawrence, M.G., Sander, R., Steil, B., Stiller, G., Tanarhte, M., Taraborrelli, D., van Aardenne, J., and J. Lelieveld, 2006: The atmospheric chemistry general circulation model ECHAM5/MESSy1: consistent simulation of ozone from the surface to the mesosphere. *Atmos. Chem. Phys.* 6, 5067–5104.
- Roeckner, E., Bäuml, G., Bonaventura, L., Brokopf, R., Esch, M., Giorgetta, M., Hagemann, S., Kirchner, I., Kornblüeh, L., Manzini, E., Rhodin, A., Schlese, U., Schulzweida, U., and A. Tompkins, 2003: *The atmospheric general circulation model ECHAM5*. Technical Report No. 349, Max-Planck-Institut für Meteorologie, Hamburg, Germany, ISSN 0937-1060, 127 pp.
- Sander, R., Kerkweg, A., Jöckel, P., and J. Lelieveld, 2005: Technical note: The new comprehensive atmospheric chemistry module MECCA. *Atmos. Chem. Phys.* 5, 445–450.
- Sander, S.P., Finlayson-Pitts, B.J., Friedl, R.R., Golden, D.M., Huie, R.E., Kolb, C.E., Kurylo, M.J., Molina, M.J., Moortgat, G.K., Orkin, V.L., and A.R. Ravishankara, 2003: *Chemical Kinetics and Photochemical Data for Use in Atmospheric Studies, Evaluation Number 14*. JPL Publication 02-25, Jet Propulsion Laboratory, Pasadena, CA.
- Søvde, O.A., Gauss, M., Isaksen, I.S.A., Pitari, G., and C. Marizy, 2007: Aircraft pollution – a futuristic view. *Atmos. Chem. Phys.* 7, 3621-3632.

Long-term 3D Simulation of Aviation Impact on Ozone Precursor Chemistry using MOZART-2

J. Hurley^{*},

Centre for Air Transport and the Environment, Manchester Metropolitan University, Manchester, United Kingdom

Keywords: Simulation, Aviation, Ozone, Chemistry, MOZART-2

ABSTRACT: Emission of aviation carbon dioxide (CO₂) and nitrogen oxides (NO_x) affects atmospheric composition through a complicated system of chemical reactions associated with ozone (O₃) and its precursors. The Model for Ozone and Related Chemical Tracers MOZART (version 2) is a three-dimensional global chemical transport model which considers 63 species as involved in some 170 reactions, with a scheme for ozone, nitrogen oxides and hydrocarbons – and hence is well-suited for quantifying the impact of aviation emissions upon atmospheric chemistry. In this preliminary study, a multi-year MOZART simulation is presented to analyse the behaviour of the aviation emission impact on important chemical fields such as O₃, hydroxide (OH), methane (CH₄), carbon monoxide (CO) and NO_x over a period of 10 years in such a chemical transport model, using QUANTIFY A1 emissions for 2000.

1 INTRODUCTION

1.1 Ozone Precursor Chemistry Pertinent to Aviation

Anything entering the global atmospheric system affects it in some way or another, however benign it may seem. In terms of chemical or aerosol emission, such as resulting from aircraft activity in the upper troposphere or lower stratosphere, it is obvious that adding species to a naturally clean region of the atmosphere will result in notable changes. These effects are predominantly expected to occur in the region of the emission perturbation – however due to atmospheric dynamics and circulation, may eventually affect large portions of the global atmosphere. In the specific case of aviation, the ozone family of species is most affected. It is thus important to quantify the effect that emission of aviation emissions on the atmosphere, taking ozone precursors as indicators of the perturbation.

From a first order, the largest deviations are expected in the regions in which aircraft activity is a maximum (see Section 1.3). This corresponds to the 1000 – 2000 Pa range (which converts to altitudes around 10 km) as there is a maximum of aircraft activity in that altitude range. Furthermore, the deviations should be focussed in the Northern mid-latitudes – again, in accordance with the large proportion of air traffic occurring in this region – and dominant features such as the North Atlantic flight corridor and point sources such as busy international hubs are expected to show prominent deviations.

As well, there are expected trends in the manner in which atmospheric trace species respond to emission of CO and NO_x from aircraft. The short-term response is linked to the set of reactions:



^{*} Corresponding author: Jane Hurley, Manchester Metropolitan University, Department of Environmental and Geographical Science, John Dalton Building, Chester Street, Manchester M1 5GD, United Kingdom. Email: j.hurley@mmu.ac.uk

whilst the long-term response is determined by the interplay between:



In the short-term (less than approximately 2 months), there is an increase in NO_x , O_3 and OH and a decrease in CH_4 . Over the long-term, the production of O_3 is overcome and there is a persistent destruction of O_3 . There persists a long-term destruction of CH_4 – however the long-term concentration of OH is dependent upon the balance between the O_3 and CH_4 destruction.

1.2 Overview of MOZART-2

The Model for Ozone and Related Chemical Tracers (MOZART, Horowitz, 2003) is a global chemical transport model which is driven by meteorological fields (generated either by a climate model or by measurement fields) to simulate the chemical composition of the troposphere and lower stratosphere (in version 2, used here) in T63LR resolution (roughly $2.8^\circ \times 2.8^\circ \times 19$ levels vertically extending to 1000 Pa).

The second version of MOZART, MOZART-2, considers 63 species as involved in some 170 reactions, with a scheme for ozone, nitrogen oxides and hydrocarbons –and is solved with a 20 minute time-step. It considers emissions such as surface emissions from fossil-fuel combustion, biomass burning, biogenic processes involving vegetation and soils, exchanges with oceans, aircraft emissions and production of NO_x from lightning. It also takes into account dynamical processes such as advective and convective transport, boundary layer mixing as well as phenomena such as cloudiness and precipitation, and allows for wet and dry deposition of chemical species.

MOZART-2 is not fully coupled – rather it is “one-way” coupled, such that atmospheric dynamics affect atmospheric chemistry but that the chemistry does not affect the dynamics. This enables study of specific chemical processes and attribution of changes in atmospheric constituents to changes in particular species – and hence is a good candidate for use in sensitivity studies.

1.3 Emissions Data

In order to isolate the impact of aviation emissions upon the atmospheric chemical system, it is important to differentiate between natural and anthropogenic (exclusive of aircraft) emissions, and those deriving from aviation.

Background emissions are taken as those provided default to MOZART-2, as detailed in Friedl (1997). The QUANTIFY A1 inventory (B. Owen, pers. comm.) compiled at the Centre for Air Transport and the Environment (CATE) has been used to detail the emissions from aviation into the atmospheric system. The CATE QUANTIFY A1 inventory considers the 2000 base-case (using IEA 2000 fuel- use statistics), as well as a range of future scenarios. It catalogues the distance flown, total fuel used, and mass of CO_2 , NO_x , and black carbon emitted per year in gridboxes of $1^\circ \times 1^\circ \times 610$ m (as flight levels). MOZART-2 requires NO_x and CO as input for aviation emissions – and as CO emissions are not catalogued in the QUANTIFY dataset, an emission index of 0.3 is used to scale the fuel emissions to estimate the emitted CO (B. Owen, pers. comm.). Figure 1 shows the average vertically-integrated global distribution of aviation emissions as well as the average latitude-altitude distribution of aviation emissions for CO and NO_x .

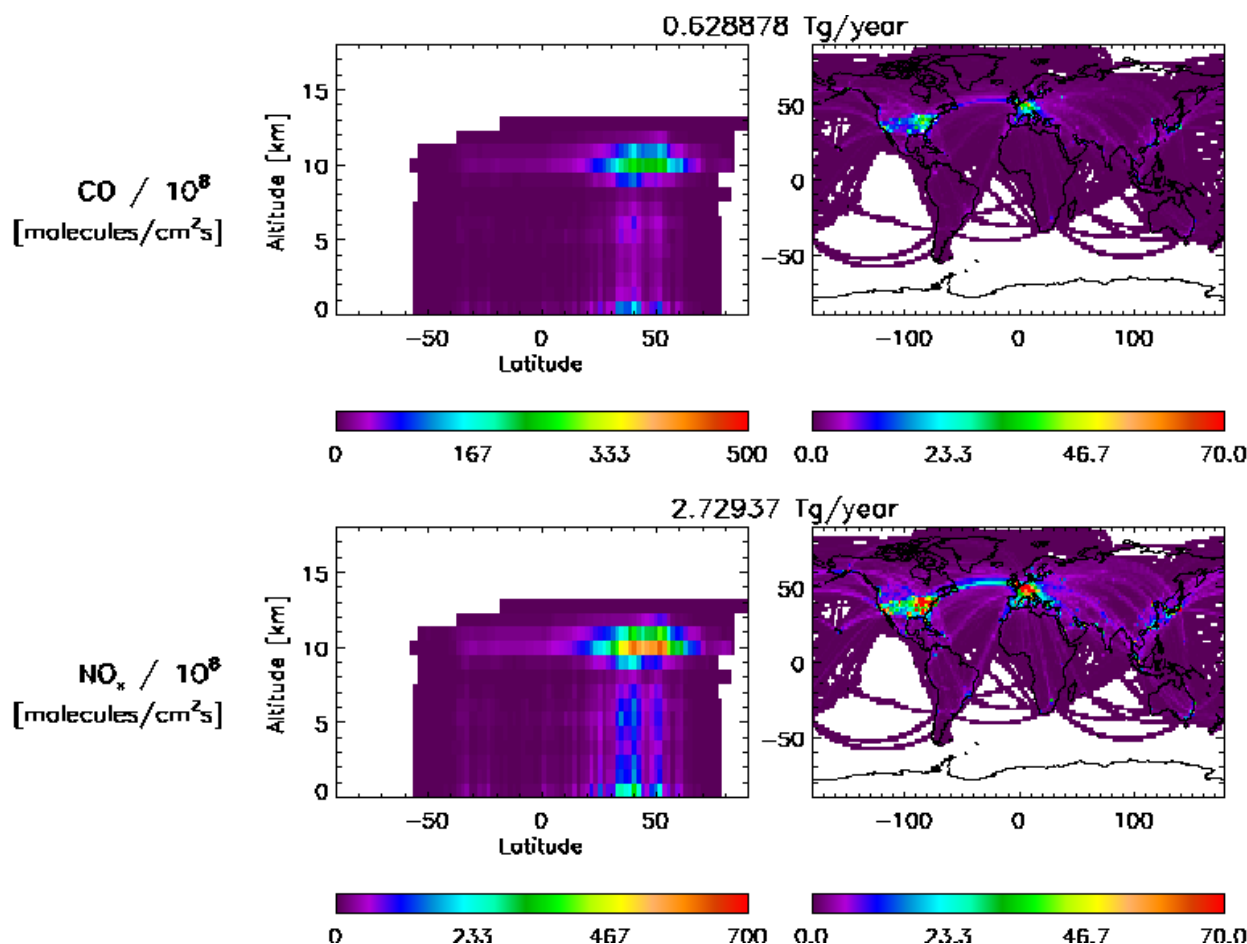


Figure 1. Aircraft emissions of CO (top panels) and NO_x (bottom panels) for CATE QUANTIFY inventory, averaged on both a latitude/altitude (left panels) and latitude/longitude (right panels) grid.

1.4 Simulation Approach

European Centre for Medium-Range Weather Forecasts (ECMWF, 2005) products for 2003 have been used for the dynamical and meteorological fields for all simulations, regardless of simulation year, so that the evolution of changes in chemistry due to changing aircraft emissions cannot be attributed to differences in synoptics specific to a particular year.

Difference between simulations with and without aviation emissions is used to isolate the impact of aviation emissions for ‘present-day’ conditions (2000). Thus, having run MOZART-2 with and without aircraft emissions (labelled ‘a’ for ‘with aircraft’ and ‘na’ for ‘with no aircraft’, the effect upon global chemistry and composition is studied, using the relative difference between the volume mixing ratios (vmr) of each chemical species studied (O₃, OH, nitrogen dioxide NO₂, CO and CH₄) for the simulations run with about without aircraft emissions is defined as

$$vmr_{rd}(x, y, z) = \frac{vmr_{na}(x, y, z) - vmr_a(x, y, z)}{vmr_{na}(x, y, z)} \times 100\% \quad (3)$$

where vmr_{rd} is the relative difference in vmr of the ‘no-aircraft’ (vmr_{na}) and ‘aircraft’ (vmr_a) cases, for longitude x , latitude y and altitude/pressure/level z . Whilst MOZART-2 outputs on hybrid-sigma pressure levels, all results here are presented on pressure levels, as they are more intuitively associable with altitudes – and because the aircraft emissions are given on altitude grids.

However, CH₄ is long-lived, taking upwards to 80 years to reach equilibrium in the atmosphere – a timeframe which is prohibitively out of range from a computational perspective. Hence, the CH₄ output by MOZART-2 after a typical single/several year run is not near to being in steady-state – which is why the unprocessed impact on CH₄ will be much less than expected. According to Fuglestad (1998), for a perturbed state from a simulation which is in chemical equilibrium, the perturbed steady-state concentration of CH₄, $[CH_4]_{ss}$, can be estimated using the concentration of

CH₄ from the equilibrated simulation, [CH₄]_{ref}, and the lifetimes τ for the perturbed and equilibrated simulations:

$$[CH_4]_{ss} = [CH_4]_{ref} \left(1 + 1.4 \frac{\tau_{per} - \tau_{ref}}{\tau_{ref}} \right) \quad (4)$$

This correction is applied to CH₄ fields output by MOZART-2 to extrapolate to the steady-state impact from the aviation perturbation.

In the current study, MOZART-2 is “spun-up” for a period of one year, and consequently run for a period of 10 years.

2 RESULTS

Timelines of the overall global burden as well as of the aircraft impact of each O₃ precursor are shown in Figure 2. The O₃ impact of aviation is dying away, as expected in the short-term, whilst the impact on all precursors appears to still be evolving and increasing – undoubtedly due to the longer CH₄ response.

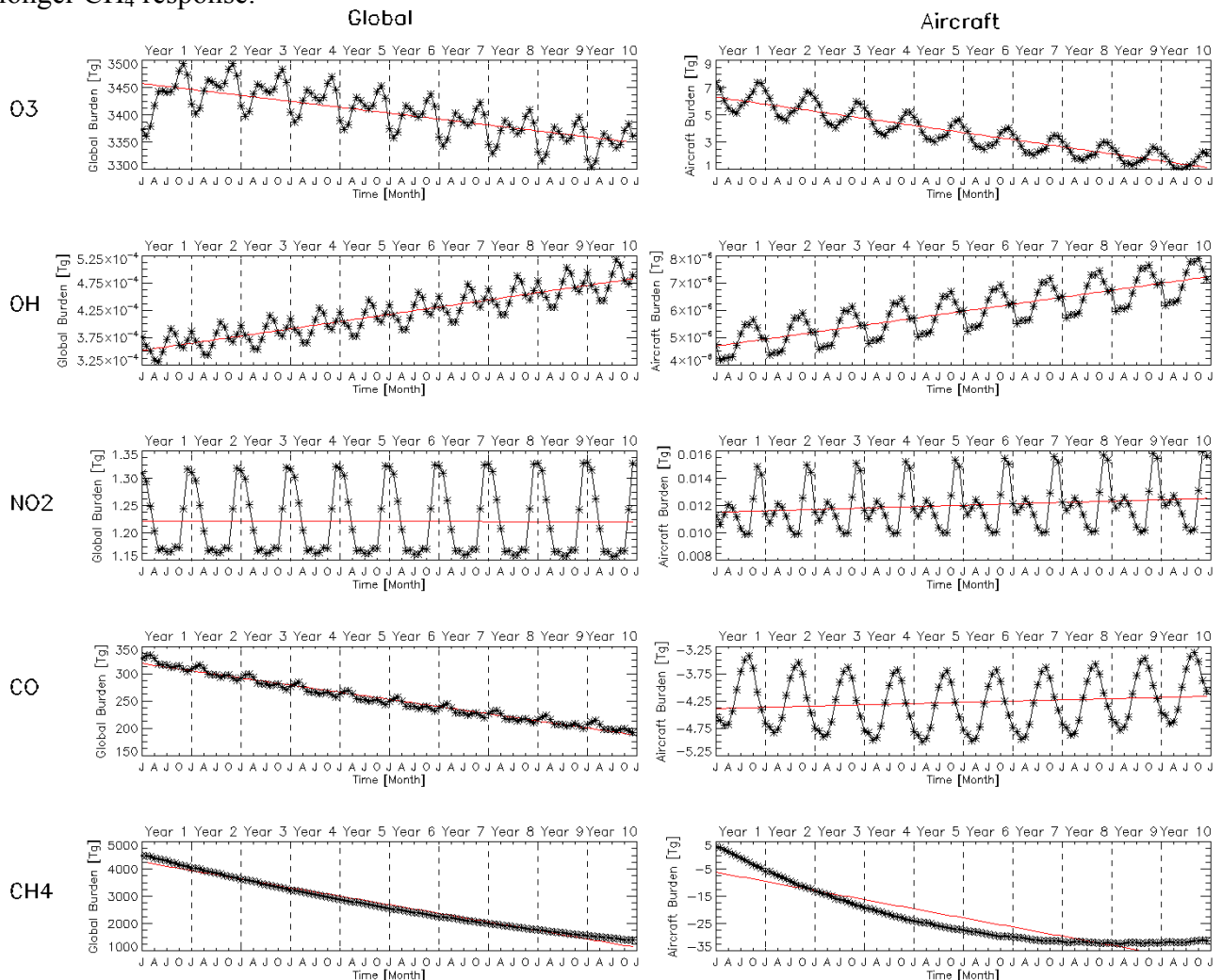


Figure 2. Global total burden (left panels) and burden attributable to aviation impact (right panels) as a function of simulated time.

Figure 3 shows the time evolution of the annual averages on a latitude/pressure grid of the aviation impact in terms of the relative difference from the base ‘no-aircraft’ state, for each species. In general, the changes in concentration due to inclusion of aviation emissions simulated by MOZART-2 agree with those expected from previous studies – quantifying values are tabulated in Table 1.

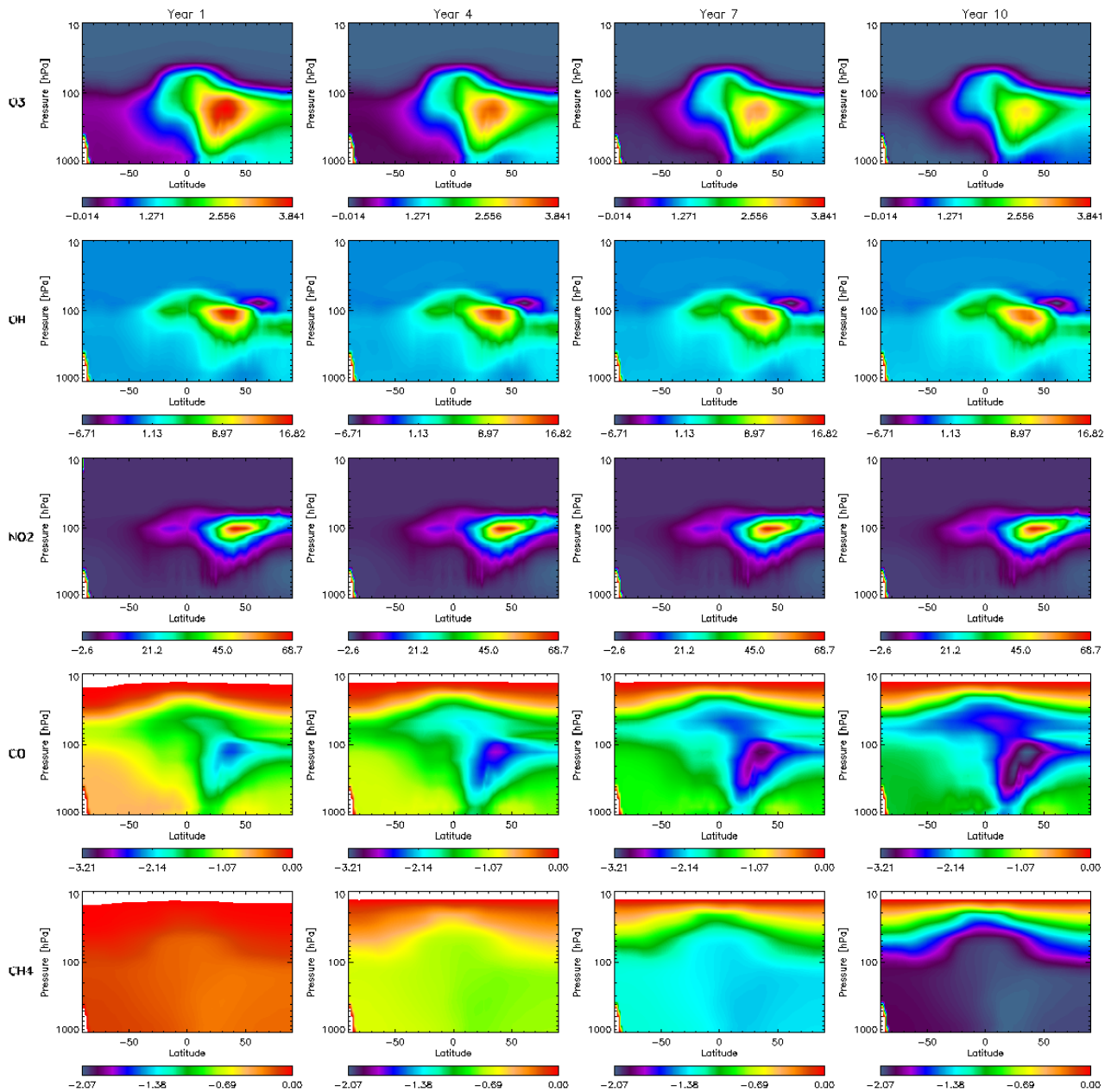


Figure 3. Relative differences in concentrations for O₃ precursor species (O₃ top, OH second, NO₂, third, CO fourth, and CH₄ bottom panels) due to the perturbation caused by aviation emissions.

Table 1. Volume mixing ratios for O₃ precursors as well as relative aviation impact, as expected from literature and outputted by MOZART-2. (eg. Brasseur et al., 1996; Kinnison et al., 2007; MIPAS, 2009)

Species	Absolute Volume Mixing Ratio Without Aviation		Aviation Impact, Change [%] Maximum / Mean	
	Expected	MOZART	Expected	MOZART
O ₃	0 – 8 ppm	0 – 15 ppm	4% / 1%	4% / 0.8%
OH	0.3 – 1.5 ppt	0 – 13 ppt	20% / 5%	17% / 0%
NO ₂	0 – 10 ppb	0 – 8 ppb	30% / 10%	65% / 0%
CO	30 – 200 ppb	14 – 202 ppb	? / ?	-3% / -1%
CH ₄ (steady-state)	0 – 3 ppm	0.3 – 1.6 ppm	? / -1%	-2% / -2%

As the CH₄ calculated by MOZART-2 is far from the final steady-state value, because the system is not in equilibrium for CH₄, Fuglestad's approximation has been applied for each year – and the steady-state concentration of CH₄ estimated, with and without aircraft, as well as the change in CH₄ due to aviation emissions in absolute volume-mixing-ratio and in relative difference, as shown in Figure 4. The steady-state CH₄ response appears to marginally grow in time.

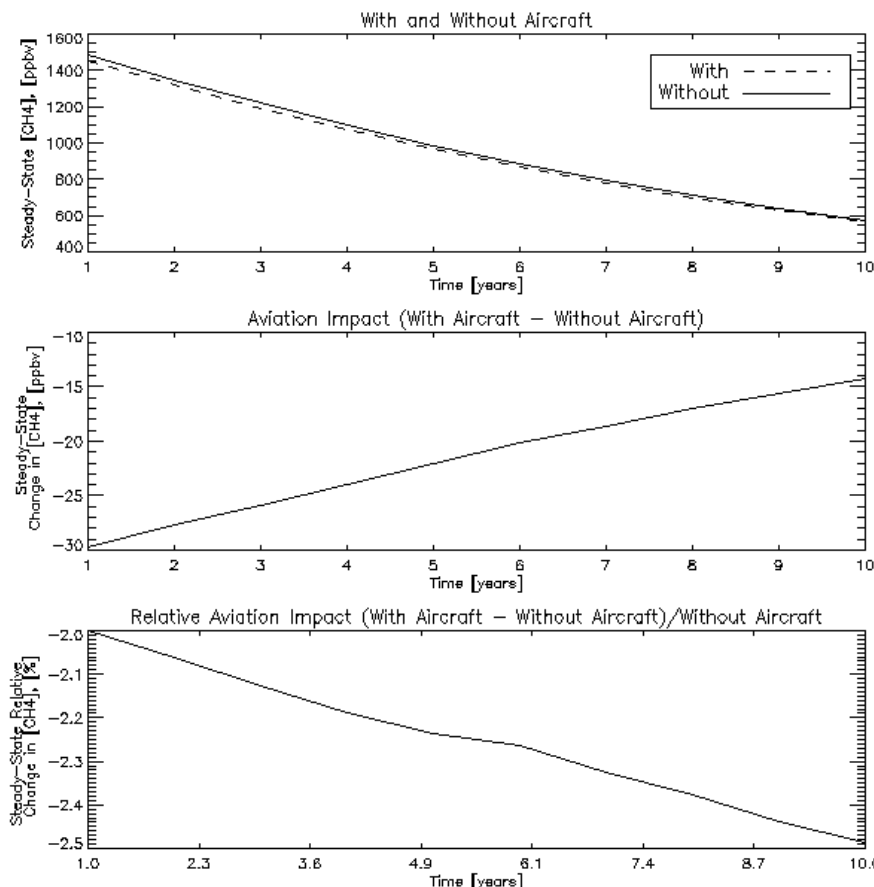


Figure 4. Estimates of steady-state concentration of CH₄ perturbation using Fuglestvedt (1998).

3 CONCLUSIONS

A long-term decade-long simulation of the impact of aviation emissions tabulated for 2000 on the chemistry of O₃ and its precursors has been carried out using the three-dimensional chemical transport model MOZART-2. As most O₃ precursors are short-lived, the difference between simulations with and without emissions seems sufficient to estimate the impact of aviation emissions; however CH₄, a long-lived species, must have a correction applied in order to quantify the steady-state impact. The relative changes in concentration predicted by MOZART-2 agree well with those determined by previous studies.

REFERENCES

- Brasseur, G., J. Müller, and C. Granier, 1996: Atmospheric impact of NO_x emissions by subsonic aircraft: A three-dimensional study, *J. Geophys. Res.*, 101, pp.1423 – 1428.
- ECMWF website, accessed 25 February 2009: <http://www.ecmwf.int/>, 2005.
- Friedl, R. (ed.), 1997: Atmospheric Effects of Subsonic Aircraft-Interim Assessment Report of the Advanced Subsonic Technology Program, NASA Reference Publication 1400, 143 pp.
- Fuglestvedt, J., T. Berntsen, I. Isaksen, H. Mao, X. Liang, and W. Wang, 1999: Climatic forcing of nitrogen oxides through changes in tropospheric ozone and methane; global 3D model studies, *Atmos. Env.*, 33, pp. 961 – 977, 1998.
- Horowitz, L., S. Walters, D. Mauzerall, L. Emmons, P. Rasch, C. Granier, X. Tie, J. Lamarque, M. Schultz, and G. Tyndall, 2003: A global simulation of tropospheric ozone and related tracers: Description and evaluation of MOZART, version 2.J. *Geophys. Res.*, 108, 4784, doi: 10.1029/2002JD002853.
- Kinnison, D., G. Brasseur, S. Walters, R. Garcia, D. Marsh, F. Sassi, V. Harvey, C. Randall, L. Emmons, J. Lamarque, P. Hess, J. Orlando, X. Tie, W. Randel, L. Pan, A. Gettelman, C. Granier, T. Diehl, U. Nie-meier, and A. Simmons, 2007: Sensitivity of chemical tracers to meteorological parameters in the MOZART-3 chemical transport model, *J. Geophys. Res.*, 112, D20302, doi:10.1029/2006JD007879.
- MIPAS webpage at University of Oxford, accessed 17 July 2009: <http://www.atm.ox.ac.uk/group/mipas/L2OXF/index.html>, 2009.

QUANTIFY model evaluation of global chemistry models: carbon monoxide

C. Schnadt Poberaj^{*9}, J. Staehelin

Institute for Atmospheric and Climate Science, ETH Zürich, Switzerland

R. Bintania, P. van Velthoven

Royal Netherlands Meteorological Institute (KNMI), Atmospheric Composition Research, De Bilt, the Netherlands

O. Dessens

Centre for Atmospheric Science, Department of Chemistry, University of Cambridge, United Kingdom

M. Gauss, I.S.A. Isaksen

University of Oslo, Department of Geosciences, Oslo, Norway

V. Grewe, P. Jöckel

DLR-Institut für Physik der Atmosphäre, Oberpfaffenhofen, Germany

P. Hoor

Institut für Physik der Atmosphäre, Johannes Gutenberg-Universität Mainz, Mainz, Germany

B. Koffi, D. Hauglustaine

Laboratoire des Sciences du Climat et de l'Environnement, Gif-sur-Yvette, France

D. Olivie

Centre National de Recherches Météorologiques (CNRM), Toulouse, France

Keywords: model evaluation, global chemistry models, carbon monoxide, emissions

ABSTRACT: In the EU Integrated project QUANTIFY, atmospheric chemistry models (ACMs) are one of the major tools to improve the understanding of key processes relevant for the effects of different transportation modes, and their representation in global models. The performance of the ACMs has been tested through comparisons with the ETH model evaluation global database for the upper troposphere and lower stratosphere. Data from measurement campaigns, ozone soundings, and surface data have been processed to support an easy and direct comparison with model output. Since model evaluation focuses on the year 2003, observational data to compare model data with are the SPURT campaign and the commercial aircraft program MOZAIC. The model evaluation indicates a particular problem in the simulation of carbon monoxide. If QUANTIFY emissions inventories are used, models significantly underestimate its tropospheric abundance at northern hemispheric middle latitudes and subtropical latitudes. Potential causes will be discussed.

1 INTRODUCTION

Global atmospheric chemistry models (ACMs), i.e. chemistry transport models (CTMs) and chemistry-climate models (CCMs) have become standard tools to study tropospheric and stratospheric photochemistry and the impact of different emission sources onto the atmospheric composition including scenarios for future emission changes. Studies based on such models were a central element in scientific assessments of the impact of present and future air traffic emissions (Brasseur et al., 1998; Penner et al., 1999; NASA, 1999). In the EU FP6 Integrated Project (IP) QUANTIFY (Quantifying the Climate Effect of Global and European Transport Systems) ACMs are used to improve the understanding of the relative effects of different transportation modes on the atmospheric com-

^{*} Corresponding author: Christina Schnadt Poberaj, Institute for Atmospheric and Climate Science, Universitaetstrasse 16, ETH Zurich, CHN, 8092 Zurich, Switzerland. Email: christina.schnadt@env.ethz.ch

position, and their representation in global models. For instance, the impact of present-day traffic emissions on atmospheric ozone and the hydroxyl radical (OH) was evaluated by Hoor et al. (2009). To estimate the reliability of the models and hence of the studies investigating the impact of traffic emissions, it is highly relevant to evaluate how well the models reproduce available observations. A first comprehensive model evaluation of ACMs operated by different groups in Europe was carried out by Brunner et al. (2003; 2005) in the framework of the EU project TRADEOFF. Brunner et al. (2003; 2005) compared model results with trace gas observations from several aircraft campaigns for the period 1995–1998. The present study uses updated versions of the models applied in Brunner et al. (2003; 2005). This paper focuses on the simulation of carbon monoxide (CO), one of the major atmospheric pollutants in densely populated areas, chiefly from exhaust of combustion engines by traffic, but also by incomplete burning of other fuels in industry. In the free troposphere, it has an indirect radiative forcing effect by elevating concentrations of tropospheric ozone through CO oxidation. Model results are compared to data from the commercial aircraft program MOZAIC (Marenco et al., 1998), as well as to aircraft campaign data. The next section summarises the main model characteristics, the boundary conditions used, and the methodology. Results of the model evaluation are shown in Section 3. Conclusions are presented in Section 4.

2 MODELS, DATA, AND METHODOLOGY

Within QUANTIFY model evaluation results from six models were compared with observational data. Four models are CTMs using prescribed operational ECMWF data to simulate meteorological conditions (TM4, p-TOMCAT, OsloCTM2, and MOCAGE) and two are CCMs (LMDzINCA and ECHAM5/MESSy), which were nudged toward operational ECMWF fields.

An overview of the main model characteristics is given in Hoor et al., 2009 (their Table 4), and in Table 1 for MOCAGE and ECHAM5/MESSy. The model setups are described in detail in Hoor et al. (2009) for TM4, p-TOMCAT, OsloCTM2, and LMDzINCA, in Teyss  dre et al. (2007) for MOCAGE, and in J  ckel et al. (2006) for ECHAM5/MESSy.

To force the models toward a realistic atmospheric state, emissions from different source categories were considered in the QUANTIFY numerical simulations. These are described in detail in Hoor et al. (2009). Emissions for the three transport sectors road, shipping, and air traffic were considered. The road traffic emissions inventory was developed within the QUANTIFY project. Except for a sensitivity simulation by OsloCTM2 (which used emissions from the POET project), the emissions used in this study are based on a draft version (Borken and Steller, 2006) (QUANTIFY preliminary, see Table 2 for CO emissions). An overview of CO emissions considered in the QUANTIFY

Table 1: Main characteristics of ECHAM5/MESSy and MOCAGE.

Model	MOCAGE	ECHAM5/MESSy
Operated	CNRM	MPICHEM
Model type	CTM	CCM (nudged)
Meteorology	ECMWF OD	ECMWF OD
Hor. resolution	T21	T42
Levels	60	90
Model top (hPa)	0.07	0.01
Transport scheme	Williamson & Rasch	Lin & Rood
Convection	Bechtold et al. (2001)	Tiedke-Nordeng
Lightning	Climatology	Price and Rind + Grewe
Transp. species	65	82
Total species	82	108
Gas phase reactions	186 + 47	178 + 57
Het. reactions	9	10 (PSC) + 26 (wet-phase)
Stratosph. chemistry	yes	yes
NMHC chemistry	yes	yes
Lightning NO _x (TgN/yr)	5	5

Table 2. CO emissions used in the QUANTIFY model simulations and comparison with TRADEOFF emissions (Brunner et al., 2003) (in Tg CO/yr). (*) Compare number in Hoor et al. (2009), their Table 1.

Species	Emission source	TRADEOFF	QUANTIFY preliminary	QUANTIFY final	OSLO POET
CO	Road traffic		73	110	196
	Ships		1.3	1.3	0.1
	Air traffic		1.1	1.1	
	Other anthropogenic		108	108	114
	Domestic burning (DB)		237	237	237
	Biomass burning (BB)	700	508	508	309
	Total anthr. fossil fuel (anthr.+road+ships+air)		183	220	310
	Total anthr. fossil fuel + DB	650	420	457	547
	Vegetation + soil	200	65*	65*	178
	Total	1550	993	1030	1034

simulations is given in Table 2.

Model output was generated and analysed with respect to trace gas observational data using point-by-point output, i.e. at each simulation time step, the instantaneous tracer fields were linearly interpolated to the positions of coinciding observations (Brunner et al., 2003; 2005). This method allows for a very close comparison with observations and fully accounts for the specific meteorological conditions of the measurements. By each modelling group the years 2002 and 2003 were simulated. 2002 was taken as spin-up, the year 2003 provided the base year for comparison with observations and sensitivity simulations (Hoor et al., 2009).

Model results were compared to data from the commercial aircraft program MOZAIC (Marengo et al., 1998), as well as to data from the SPURT (German: SPURenstofftransport in der Tropopausenregion) campaign (Engel et al., 2006). From MOZAIC, the one-minute averages of the CO measurements were evaluated. The 2003 SPURT campaigns took place in February, April, and July 2003 over Europe (Engel et al., 2006; their Fig. 4). Besides CO, ERA40 potential vorticity (PV) interpolated onto SPURT coordinates was used to distinguish between tropospheric and stratospheric air. The SPURT data were time averaged to yield one minute averages.

3 EVALUATION OF MODEL PERFORMANCE

Average model biases ($\text{mean}_{\text{model}} - \text{mean}_{\text{obs}} / \text{mean}_{\text{obs}} * 100\%$) and root-mean-square (RMS) differences E of point-to-point model results and measurements are shown in Table 3 for the February 2003 SPURT campaign for the lowermost stratosphere (LMS, $\text{PV} > 2 \text{ PVU}$) and the upper troposphere (UT, $p < 500 \text{ hPa}$ and $\text{PV} < 2 \text{ PVU}$). Additional information on model performance can be summarised in a Taylor diagram (Taylor, 2001; Brunner et al., 2003): the correlation coefficient R , the centred pattern RMS difference E' between a test vector f (model) and a reference vector r (observations), and the ratio of the standard deviations (σ_f / σ_r) of the two vectors are all indicated by a single point in a two-dimensional plot. For example, in Fig. 1a, the test point by MOCAGE (MO) refers to a correlation coefficient $R=0.87$, a normalised standard deviation $\sigma_f / \sigma_r=0.95$ (smaller modelled than observed σ), relatively large centred RMS difference (distance between reference and test point, only qualitative statement possible), and a skill score of > 0.9 (parabolic line of constant skill). For more details on the underlying algebra and relationships between statistical quantities see Taylor (2001) and Brunner et al. (2003) for the used definition of the skill score.

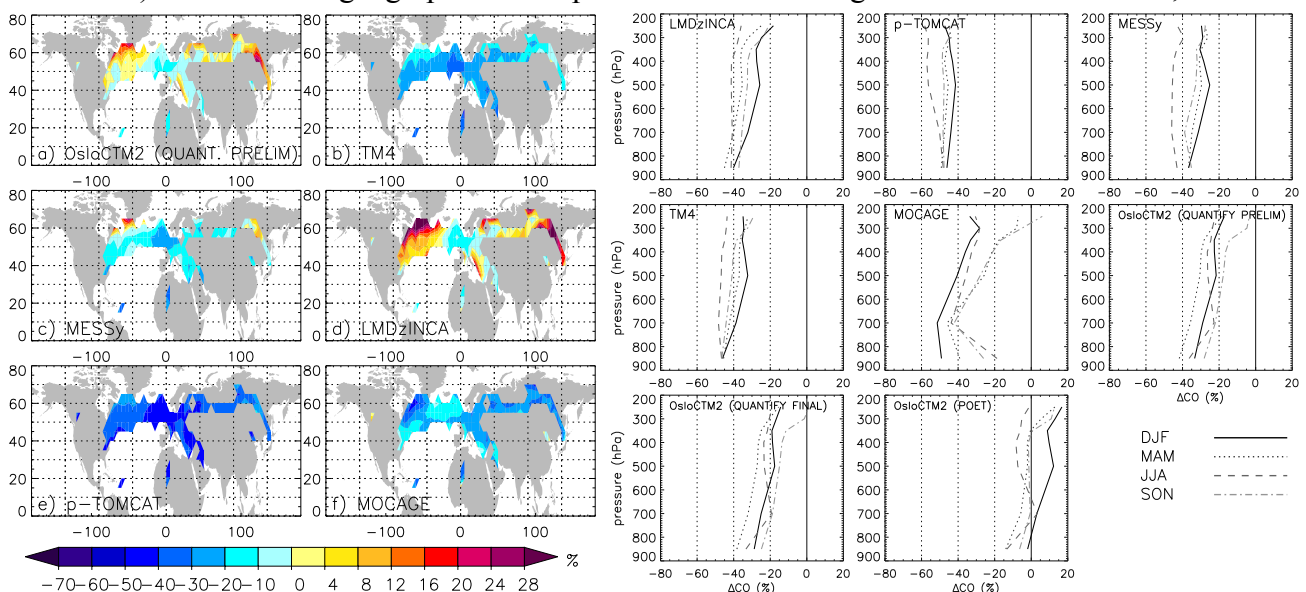
Upper tropospheric CO is underestimated by most models in all campaign months ($\approx -5\%$ to -50%) except for OsloCTM2 (POET), for which a positive deviation of 10% to $\approx 35\%$ is found. At higher altitudes in the LMS, negative biases are either significantly reduced or they turn to positive deviations. OsloCTM2, which exhibits positive biases in the UT, shows increased positive deviations from observations in the LMS. It could be suspected that the relatively low CO emissions from road traffic used in the QUANTIFY preliminary simulations (Table 2) might be responsible for the negative bias of most models. However, the negative deviations are not reduced or

Table 3: Mean model biases of CO (in %) for the 2003 SPURT campaigns for the lowermost stratosphere (PV > 2 PVU) (upper part) and the middle to upper troposphere (p < 500 hPa and PV < 2 PVU). Grey shading indicates negative deviation of a model mean from the respective observational value.

Model/Variable	February	April	July
Lowermost stratosphere (LMS)			
OsloCTM2 (POET)	83±47	61±51	30±52
OsloCTM2	24±29	18±37	3±39
TM4	-13±21	-7±22	-22±27
p-TOMCAT	-27±19	-30±25	-44±23
MOCAGE	-13±26	32±58	-17±24
LMDzINCA	27±39	19±43	-3±38
ECHAM5/MESSy	-1±20	-4±25	-25±25
Upper troposphere (UT)			
OsloCTM2 (POET)	35±55	37±59	10±54
OsloCTM2	-7±37	0±43	-11±41
TM4	-29±20	-17±30	-34±28
p-TOMCAT	-40±14	-43±23	-52±22
MOCAGE	-26±13	28±61	-19±30
LMDzINCA	-12±37	-5±50	-22±34
ECHAM5/MESSy	-18±27	-10±29	-33±28

eliminated when using QUANTIFY final road emissions, which are $\approx 50\%$ higher than the preliminary emissions (Fig. 1b, compare OsloCTM2 simulations PRELIM and FINAL). Hence, the different performance of OsloCTM2 using POET emissions (Table 3, Fig. 1b) can probably not be (fully) explained by the higher road traffic CO emissions. Possibly, emissions of non-methane volatile organic compounds (NMVOCs), which are an additional non-negligible source of CO (IPCC, 2001), may play a role: in the POET emissions inventory these are known to be significantly higher over polluted regions than in other inventories. The altitude dependency of biases is largely reflected by MOZAIC profiles: as presented for Frankfurt, Germany, relative differences show a positive slope with altitude (Fig. 1b). This effect might be connected to an insufficient vertical resolution of the models to resolve the vertical CO gradient across the tropopause.

Using MOZAIC cruise level data, which are mostly representative of the LMS, similar biases as over Europe were identified on the hemispheric scale in all seasons (Fig. 1a for DJF, other seasons not shown). Note that the geographical bias patterns are not homogeneous for most models,



a) b) Figure 1: Mean model biases for 2003 MOZAIC data (model-MOZAIC) (in %). a) Horizontal distribution from cruise level data at 300 hPa – 170 hPa, DJF 2003, biases only plotted if at least 20 measurements available in $5^\circ \times 5^\circ$ grid boxes; b) vertical profiles for Frankfurt, Germany, for DJF (black solid line), MAM (dark grey dotted line), JJA (grey dashed line), and SON (light grey dash-dotted line).

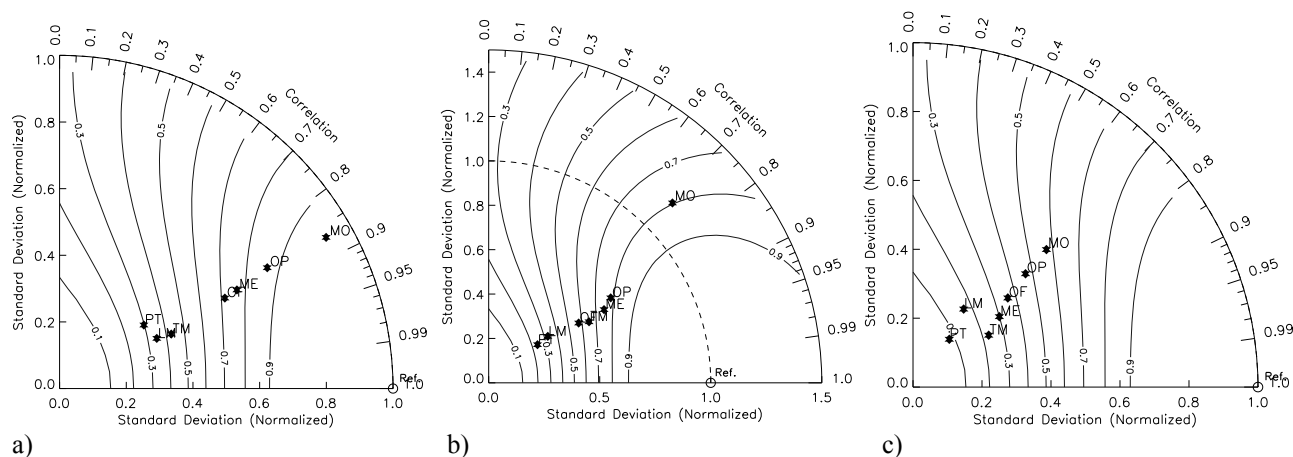


Figure 2: Taylor diagrams of the comparison between observed and modelled CO for the SPURT campaigns 2003. a) February, b) April, and c) July 2003. Letters denote models: OP (OsloCTM2 with POET emissions), OF (OsloCTM2 with preliminary QUANTIFY emissions), TM (TM4), PT (p-TOMCAT), ME (ECHAM5/MESSy), MO (MOCAGE), and LM (LMDzINCA).

but show maximum negative deviation over Europe and smaller negative or even positive biases over Eastern USA and Siberia. This is due to regional features in the observed distribution, namely a CO maximum over Europe and relatively low mixing ratios over northern America and East Siberia (not shown), which are not fully captured by the models.

CO has a sufficiently large photochemical lifetime of 1–3 months in the troposphere (IPCC, 2001) to be transported on the hemispheric scale (e.g., Stohl et al., 2002). Thus, not surprisingly, the Taylor diagrams reveal high correlation coefficients in winter and spring 2003 ($0.8 \leq R \leq 0.9$) (Fig. 2a and b). In July, only somewhat smaller correlations ($0.5 < R \leq 0.8$) are probably due to the fact that models cannot reproduce small-scale convective events that were encountered during the flights (Hegglin, 2004). However, most models underestimate observed data variability ($\sigma_f/\sigma_r < 1$), probably also related to inability to reproduce small- or regional-scale features in the observations.

4 CONCLUSIONS

Carbon monoxide is a compound with a rather long lifetime in the troposphere. It is emitted by several emission sources, formed by VOC oxidation and transformed to carbon dioxide by oxidation with OH radicals. Furthermore, vertical and horizontal mixing affects its concentrations. We regard the following processes as most critical to explain the partial disagreement between numerical simulations performed within QUANTIFY and available measurements:

- Tropospheric CO concentrations depend on the applied emissions inventories. While model biases are not affected by either the use of preliminary or final QUANTIFY traffic emissions, the agreement between measurements and model results is improved when using the set of POET CO emissions compared to when using QUANTIFY preliminary or final emissions. However, it remains an open question what the cause(s) for the better model performance of the simulation with POET emission is (are). Additionally, the biomass burning emissions inventory used, which is representative for the year 2000 (specifications see Hoor et al., 2009) may not reflect atmospheric conditions in 2003, as it is known that 2002/2003 biomass burning emissions were anomalously high in the extratropical northern hemisphere (e.g., Yurganov et al., 2005).
- CO can be formed from VOC oxidation. This source is expected to be different from model to model adding additional uncertainty in the comparison between simulations and measurements.
- The sharp vertical gradient in CO concentration across the tropopause is an additional challenge for global simulations. The results indicate that current model resolution may be insufficient to resolve this gradient.

In a further study the information from ozone and nitrogen concentrations will be used to shed more light in the reliability of the numerical simulations performed within QUANTIFY.

REFERENCES

- Brasseur, G. P., R.A. Cox, D. Hauglustaine, I. Isaksen, J. Lelieveld, D.H. Lister, R. Sausen, U. Schumann, A. Wahner, and P. Wiesen, 1998: European scientific assessment of the effects of aircraft emissions. *Atmos. Environ.*, 32, 2329–2418.
- Brunner, D., J. Staehelin, H.L. Rogers, M.O. Köhler, J.A. Pyle, D.A. Hauglustaine, L. Jourdain, T. K. Berntsen, M. Gauss, I. S. A. Isaksen, E. Meijer, P. van Velthoven, G. Pitari, E. Mancini, V. Grewe, and R. Sausen, 2005: An evaluation of the performance of chemistry transport models –Part 2: Detailed comparison with two selected campaigns. *Atmos. Chem. Phys.*, 5, 107–129.
- Brunner, D., J. Staehelin, H.L. Rogers, M.O. Köhler, J.A. Pyle, D. Hauglustaine, L. Jourdain, T.K. Berntsen, M. Gauss, I.S.A. Isaksen, E. Meijer, P. van Velthoven, G. Pitari, E. Mancini, V. Grewe, and R. Sausen, 2003: An evaluation of the performance of chemistry transport models by comparison with research aircraft observations. Part 1: Concepts and overall model performance. *Atmos. Chem. Phys.*, 3, 1609–1631.
- Engel, A., H. Bönsch, D. Brunner, H. Fischer, H. Franke, G. Günther, C. Gurk, M. Hegglin, P. Hoor, R. Königstedt, M. Krebsbach, R. Maser, U. Parchatka, T. Peter, D. Schell, C. Schiller, U. Schmidt, N. Spelten, T. Szabo, U. Weers, H. Wernli, T. Wetter, and V. Wirth, 2006: Highly resolved observations of trace gases in the lowermost stratosphere and upper troposphere from the Spurt project: an overview. *Atmos. Chem. Phys.*, 6, 283–301.
- Eyers, C., P. Norman, J. Middel, M. Plohr, S. Michot, K. Atkinson, and R. Christou, 2004: AERO2K Global Aviation Emissions Inventories for 2002 and 2025. Tech. Rep. 04/01113, QinetiQ, <http://elib.dlr.de/1328>.
- Hegglin, M.I., 2004: Airborne NO_y-, NO- and O₃-measurements during SPURT: Implications for atmospheric transport, dissertation, Diss. ETH No. 15553, 209 pp.
- Hoor, P., J. Borken-Kleefeld, D. Caro, O. Dessens, O. Endresen, M. Gauss, V. Grewe, D. Hauglustaine, I.S.A. Isaksen, P. Jöckel, J. Lelieveld, E. Meijer, D. Olivie, M. Prather, C. Schnadt Poberaj, J. Staehelin, Q. Tang, J. van Aardenne, P. van Velthoven, and R. Sausen, 2009: The impact of traffic emissions on atmospheric ozone and OH: results from QUANTIFY. *Atmos. Chem. Phys.*, 9, 3113–3136.
- IPCC (Intergovernmental Panel on Climate Change), 2001: Climate change 2001: The scientific basis, Contribution of Working Group 1 to the Third Assessment Report, edited by: Houghton, J. T., Cambridge University Press, Cambridge, United Kingdom and New York, NY, USA, 891 pp.
- Jöckel, P., H. Tost, A. Pozzer, C. Brühl, J. Buchholz, L. Ganzeveld, P. Hoor, A. Kerkweg, M. Lawrence, R. Sander, B. Steil, G. Stiller, M. Tanharte, D. Taraborrelli, J. van Aardenne, and J. Lelieveld, 2006: Evaluation of the atmospheric chemistry GCM ECHAM5/MESSy: Consistent simulation of ozone in the stratosphere and troposphere. *Atmos. Chem. Phys.*, 6, 5067–5104.
- Marengo, A., V. Thouret, P. Nédélec, H. Smit, M. Helten, D. Kley, F. Karcher, P. Simon, K. Law, J. Pyle, G. Poschmann, R. Von Wrede, C. Hume, and T. Cook, 1998: Measurement of ozone and water vapour by Airbus in-service aircraft: The MOZAIC program, An overview. *J. Geophys. Res.*, 103, 25631–25642.
- NASA, 1999: Atmospheric Effects of Aviation, A Review of NASA's Subsonic Assessment Project. National Academy Press, Washington, D.C., 41 pp.
- Penner, J. E., D. Lister, D. Griggs, D. Docken, and M. MacFarland (Eds), 1999: IPCC Special Report on Aviation and the Global Atmosphere. Cambridge University Press, New York, 373 pp.
- Stohl, A. S. Eckhardt, C. Forster, P. James, and N. Spichtinger, 2002: On the pathways and timescales of intercontinental air pollution transport, *J. Geophys. Res.*, 107, D23, 4684, doi:10.1029/2001JD001396.
- Taylor, K.E., 2001: Summarizing multiple aspects of model performance in a single diagram. *J. Geophys. Res.*, 106, 7183–7192.
- Teyssède, H., M. Michou, H. L. Clark, B. Josse, F. Karcher, D. Olivié, V.-H. Peuch, D. Saint-Martin, D. Cariolle, J.-L. Attié, P. Nédélec, P. Ricaud, V. Thouret, R. J. van der A, A. Volz-Thomas, and F. Chéroux, 2007: A new tropospheric and stratospheric Chemistry and Transport Model MOCAGE-Climat for multi-year studies: evaluation of the present-day climatology and sensitivity to surface processes. *Atmos. Chem. Phys.*, 7, 5815–5860.
- Yurganov, L.N., P. Duchatelet, A. V. Dzholi, D. P. Edwards, F. Hase, I. Kramer, E. Mahieu, J. Mellqvist, J. Notholt, P. C. Novelli, A. Rockmann, H. E. Scheel, M. Schneider, A. Schulz, A. Strandberg, R. Sussmann, H. Tanimoto, V. Velazco, J. R. Drummond, and J. C. Gille, Increased Northern Hemispheric carbon monoxide burden in the troposphere in 2002 and 2003 detected from the ground and from space, *Atmos. Chem. Phys.*, 5, 563–573.

Properties of Ice-Supersaturated Layers Based on Radiosonde Data Analysis

S. L. Baughcum^{*}, M. Y. Danilin
The Boeing Company, Seattle, WA, USA

L. M. Miloshevich, A. J. Heymsfield
National Center for Atmospheric Research, Boulder, CO, USA

Keywords: ice supersaturation, contrail, cirrus, radiosonde

ABSTRACT: In order to better understand upper tropospheric humidity and formation of persistent contrails, we analyzed radiosonde sounding data from selected stations of the US National Weather Service for a five year period. We used 55,177 individual corrected Vaisala RS80-H profiles over 15 USA stations from September 2000 to September 2005 for our analysis. These corrections are critical when investigating ice supersaturation in the upper troposphere. Using these corrected measurements for each season and location, we calculated key parameters of ice supersaturated layers (ISSLs): geometric thickness, frequency, and number of ice supersaturated layers per profile along with their probability distributions. The implications of these results are discussed in relation to contrail formation and mitigation.

1 INTRODUCTION

For contrails to form, the modified Appleman criterion (Schumann, 1996) which relates propulsion efficiency, fuel properties and ambient conditions must be satisfied. While supersaturation with respect to ice is not required to form a contrail, it is necessary for the contrail to persist for long times. Spichtinger et al. (2003) evaluated radiosonde data of relative humidity over Lindenberg, Germany and showed that the mean ice supersaturated layer (ISSL) thickness was 560 ± 610 meters. Rädcl and Shine (2007) performed a similar analysis for radiosonde sites in the United Kingdom and showed an ISSL thickness of 900-1300 m. Mannstein et al. (2005) suggested that small changes in flight altitude could move an aircraft out of the ISSL and reduce contrail impact.

In this paper, we evaluate ISSL properties over the United States with particular emphasis on conditions where contrails will both form and persist.

2 APPROACH

Radiosonde data for 13 sites [Blacksburg, Boise, Buffalo, Denver, Flagstaff, Grand Junction, Miami, Norman, Peachtree, Reno, Salt Lake City, Springfield, and Wilmington] in the continental United States plus Lihue (Hawaii) and Fairbanks (Alaska), were obtained from the US National Weather Service for the time period from September 2000 to September 2005. These soundings were made every 12 hours, recorded temperature and relative humidity with respect to water every 6 seconds, and used Vaisala RS80-H sondes. A total of 55,177 soundings were processed with 4,657 profiles rejected mostly because of sensor icing.

A temperature dependent error correction (Wang et al., 2002) and a time-lag correction (Miloshevich et al., 2004) are required for the RS80-H sondes when processing humidity data at the cold temperatures usually encountered in the upper troposphere. The response times of RS92, RS80-H and RS80-A radiosondes are shown in Figure 1a. Figure 1b shows an example highlighting that the time-lag correction can be critical when investigating ice supersaturation in the upper troposphere and that the temperature dependent correction alone is not enough. We use a very simple

^{*} Corresponding author: Steven L. Baughcum, Boeing Company, MC 0R-MT, P. O. Box 3707, Seattle, WA 98124 USA. Email: Steven.L.Baughcum@boeing.com

definition of an ISSL as a layer where the relative humidity with respect to ice (RHi) is greater than 100%. We define a contrailing ISSL (CISSL) as an ISSL where the Appleman criterion is satisfied as well.

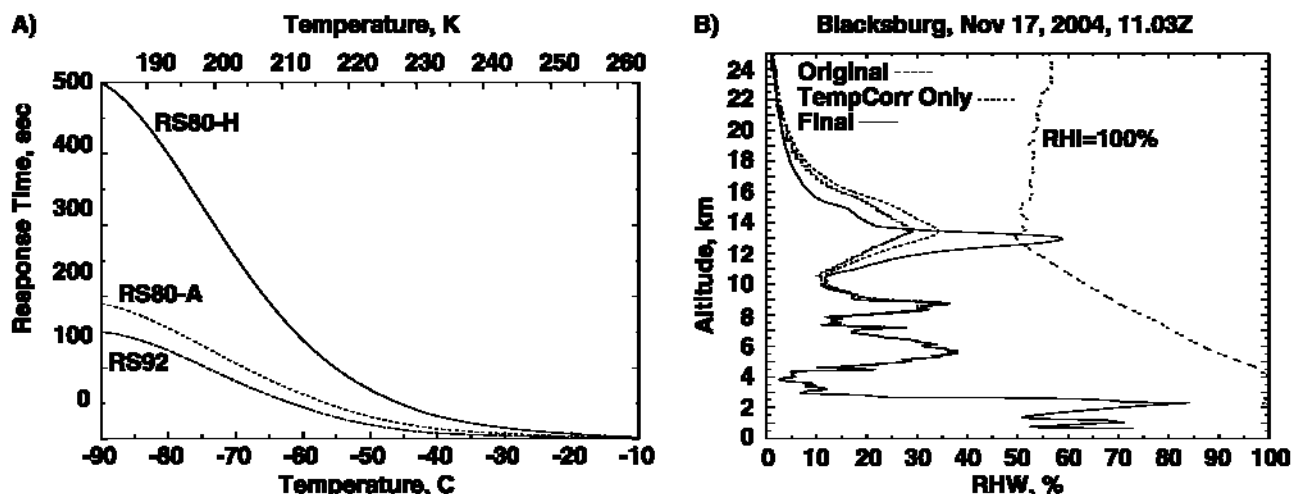


Figure 1. a.) The response time of RS92, RS80-H, and RS80A radiosondes as a function of temperature. b.) The vertical profiles of relative humidity for Blacksburg, VA, on 17 November 2004 at 11Z for the uncorrected data (dashed line labelled as Original), temperature dependence correction only (dotted line labelled as TempCorr only), and with both the temperature dependent and time-lag corrections (solid line labelled as Final). The dashed line on the right corresponds to ice supersaturation [$RHi = 100\%$] for the measured temperature profile.

3 RESULTS

Ice supersaturated regions can occur at temperatures which are too warm for contrail formation. This is illustrated in Figure 2 which shows the average probability of ice supersaturation (marked as no Appleman) over Denver (Colorado), in the summer and winter as a function of altitude. Superimposed on the plots is the probability profile when the modified Appleman criterion is applied to identify cases where contrails would form. For these plots, a propulsion efficiency of 30% was assumed. At the higher, colder altitudes, most ISSLs will also lead to contrails but at the lower altitudes (especially in summer) many ISSLs are too warm to form contrails. Similar analyses were done for all the sites but these will be discussed in more depth in a future publication. This figure illustrates the importance of the modified Appleman criterion and the difference between ISSL and contrailing ISSLs (CISSLs).

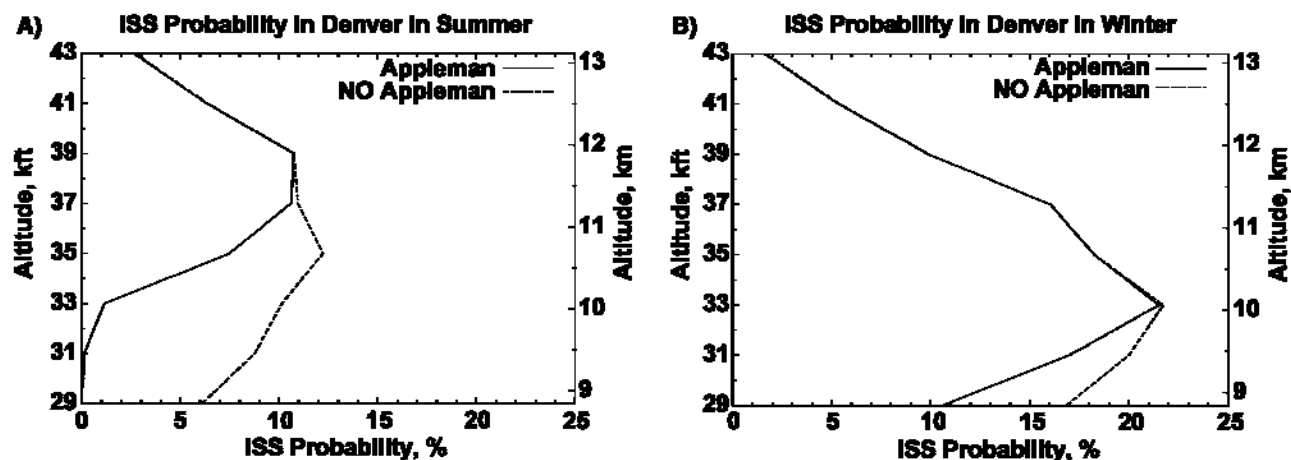


Figure 2. Ice supersaturation probability as a function of altitude over Denver (Colorado) for summer (left panel) and winter (right panel). The solid and dashed lines correspond to the probability with and without the modified Appleman criterion for contrail formation, respectively.

Figure 3a shows the probability distribution of the CISSL thickness over Denver at 35 kft (10.7 km, flight level 350) over the 5 year data period. Figure 3b depicts vertical profiles of the median CISSL thickness over the 15 US locations studied. These results reveal that the median CISSL thickness changes from 0.7–1.2 km at 9 km to 0.3–0.8 km at 13 km, which is consistent in general with the earlier findings of Spichtinger et al. (2003) and Rädcl and Shine (2007) for ISSLs over Europe. The studies use different geographical locations, different time periods and different methodologies hampering direct comparison of results.

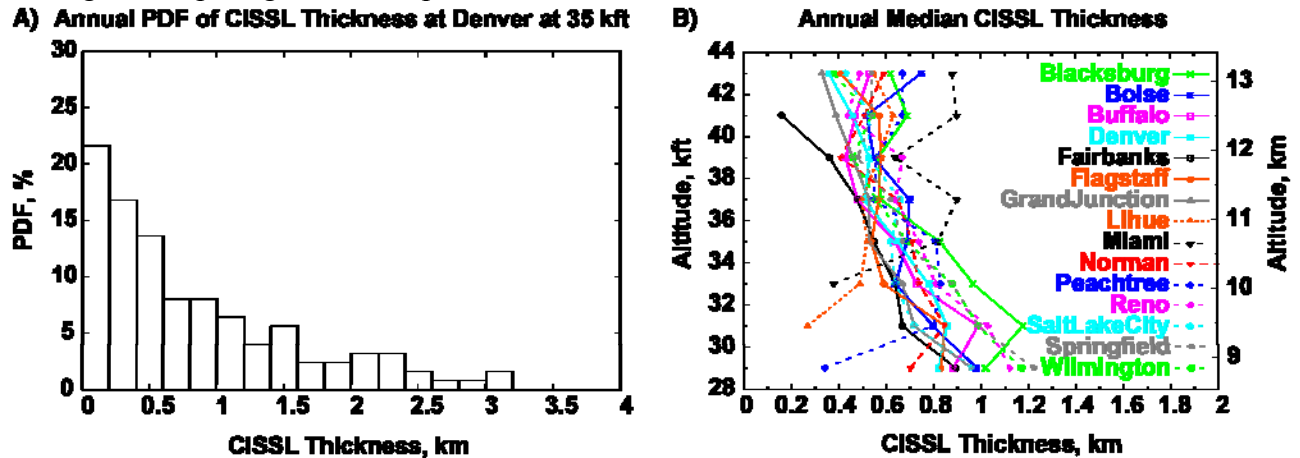


Figure 3. a.) The probability distribution function of the CISSL thickness over Denver (Colorado) at flight level 350 (35 kft or 10.7 km altitude) over the 5 year data period. b.) Annual median thickness of contrailing ISSL as a function of altitude for the 15 sites studied.

We analyzed the number of ice supersaturated layers per profile in the altitude range 5–18 km for all cases. There is a single ISSL approximately half of the time when ice supersaturation is observed anywhere in that altitude, regardless of whether the Appleman criterion is met. When contrailing cases only are considered, there is a single layer 70–80% of the time. As shown in Figure 4, this conclusion seems to be independent of the location. This large proportion of single CISSLs may challenge the random overlap assumptions used in global models studying contrail issues in which the prediction of contrails at one layer are assumed to not affect the presence of contrailing layers above or below.

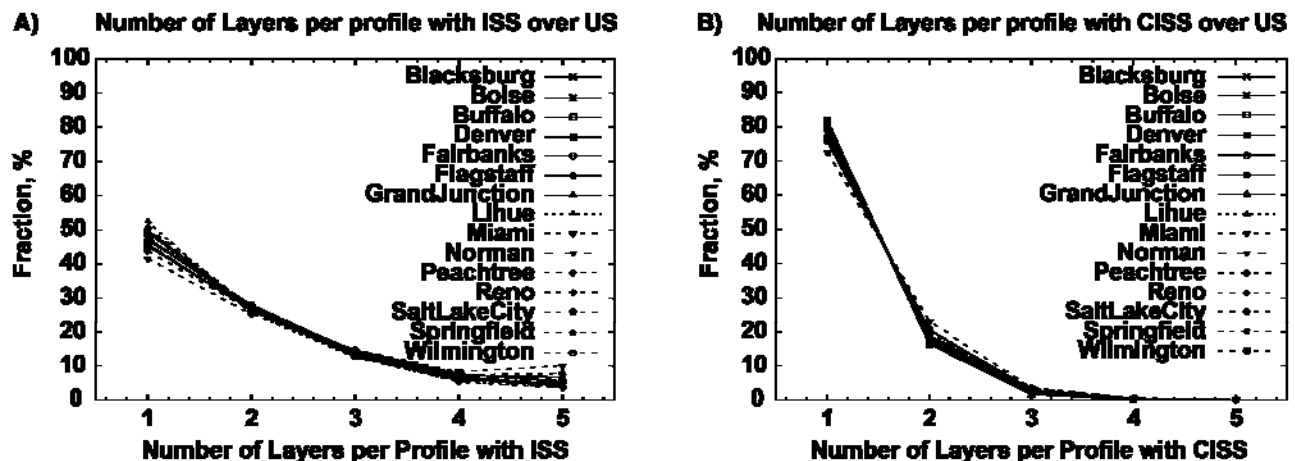


Figure 4. The relative probability as a function of number of ice supersaturated layers without (left panel) and with (right panel) the Appleman criterion over 15 US locations.

Using these results, we can explore how changes in altitude might alter the probability of contrail formation. As an example, we examine the radiosonde data at flight level 350 (35 kft or 10.7 km altitude) for all the sites. For each profile where a contrail would have formed at this flight level, we evaluate the probability distribution of forming a contrail for altitude changes in intervals of ± 1 kft (the current minimum cruise altitude change that might be considered). This was repeated for each radiosonde location. Figure 5 shows the cruise altitude change as a function of the latitude of the station location in order to reduce the contrail probability by half. The results show that changes of 2–4 kft would have reduced the probability by half for those cases where a contrail would have formed at 35 kft altitude. Note that these results should be used with caution for contrail avoidance,

since our radiosonde measurements do not contain any information about the horizontal extent of CISSLs. In order to avoid contrails in real life we need to know near-real-time RHI fields. So, better data and RHI forecasting techniques would be needed. Our results illustrate that, if contrails must be reduced, a viable option could be to change altitude enroute to fly above or below the CISSL. Although requiring much better humidity data than now exists, this may be a much easier solution rather than designing airplanes and the air space system for new cruise altitudes where contrails would never form.

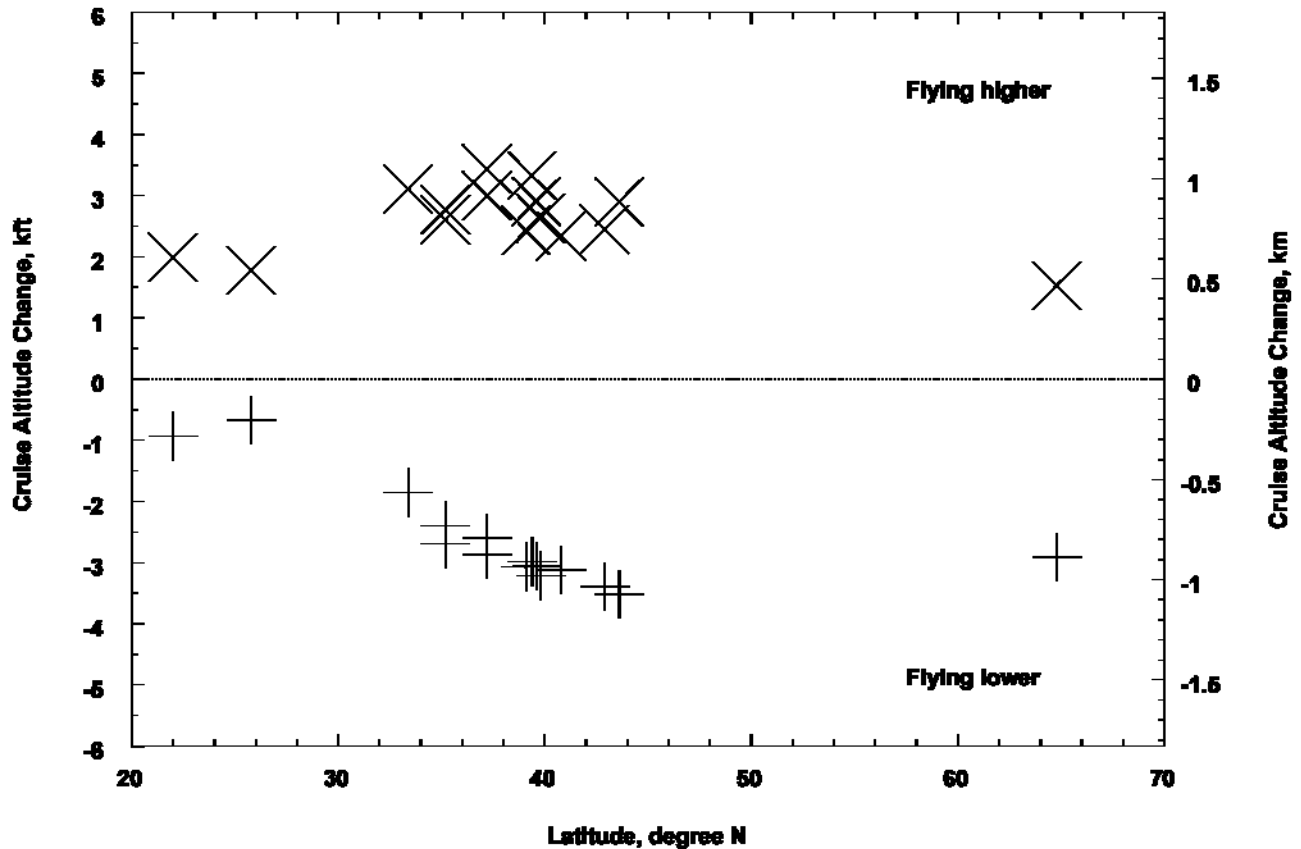


Figure 5. Cruise altitude changes required to halve the persistent contrail formation for flights at flight level 350 (35 kft or 10.7 km altitude) as a function of latitude, for flying higher (X) and for flying lower (+).

4 CONCLUSIONS AND RECOMMENDATIONS

The modified Appleman criterion is important in interpreting ice supersaturated layer (ISSL) results for contrails, particularly at warmer temperatures. Usually only a single ISSL was observed for which a persistent contrail could form. This suggests that random overlap assumptions used in some global models may not correctly predict such behaviour and should be used with caution in evaluating contrail mitigation options. The median contrailing ISSL thickness was found to be 0.7–1.2 km near 9 km altitude dropping to 0.3–0.8 km at 12–13 km altitude. If an aircraft is flying in a contrailing ISSL, changing the flight level by 2–4 kft may reduce the contrail probability significantly.

Much more reliable observational data on relative humidity at multiple cruise altitudes for different locations are needed. Multiple measurements at different altitudes in the same geographical region and for different regions are needed to better constrain atmospheric models and understand mitigation options. Simultaneous measurements of humidity and cirrus properties are needed to better interpret supersaturation events. Better predictive capabilities for RHI in near real time will be needed to identify areas where contrails would form.

REFERENCES

- Mannstein, H., P. Spichtinger, K. Gierens, 2005: A note on how to avoid contrail cirrus. *Transport. Res. Part D* 10, 421–426.
- Miloshevich, L. M., A. Paukkunen, H. Voemel, and S. J. Oltmans, 2004: Development and validation of a time-lag correction for Vaisala radiosonde humidity measurements. *J. Atmos. Oceanic Technol.*, 21, 1305–1327, doi:10.1175/1520-0426
- Rädel, G, and K. P. Shine, 2007: Evaluation of the use of radiosonde humidity data to predict the occurrence of persistent contrails. *Q.J.Roy.Meteor.Soc.* 133: 1413.1423 DOI: 10.1002/qj.128.
- Schumann, U., 1996: On conditions for contrail formation from aircraft exhausts. *Meteorol. Z.* 5, 4–23.
- Spichtinger, P., K. Gierens, U. Leiterer, and H. Dier, 2003: Ice supersaturation in the tropopause region over Lindenberg, Germany. *Meteorol. Z.* 12, 143–156.
- Wang, J. H., H. L. Cole, D. J. Carlson, E. R. Miller, K. Beierle, A. Paukkunen, and T. K. Laine, 2002: Corrections of humidity measurement errors from the Vaisala RS80 radiosonde - Application to TOGA COARE data. *J. Atmos. Ocean. Tech.*, 19, 981–1002.

Condensation Trails in the regional Climate Model CCLM

A. Ferrone*, P. Marbaix, R. Lescroart, J.-P. van Ypersele

Université catholique de Louvain, Institut d'astronomie et de géophysique G. Lemaître, Louvain-la-Neuve, Belgium

Keywords: Regional Climate Modeling, Contrails, cirrus clouds, aviation climate impacts

ABSTRACT: The aviation sector is one of the fastest growing sectors in the world, and its recent inclusion in the EU-ETS aims at limiting the growth of its CO₂ emissions. However this policy does not take into account the non- CO₂ effects of aviation, including the impact of NO_x on ozone and methane as well as condensation trails (contrails) and their evolution into cirrus clouds, the so-called “aircraft induced cloudiness” (AIC). The regional climate model CCLM is used in order to quantify the impacts of aviation on climate in Europe. A parameterization was added that creates supplementary ice clouds when the mete-orological conditions permit to create contrails and the air is ice-supersaturated. A first test case is performed, which gives an appreciation of the potential AIC over Europe (i.e. it assumed that planes are flying everywhere). This experiment shows that some regions, like the Scandinavian peninsula but also the English Channel and the North-Sea are more prone to form contrails than other. Then a run has been performed based on real flight distributions, which shows that the model is capable of capturing some important patterns that have also been observed in observation studies of linear contrails in satellite images.

1 INTRODUCTION

Under well defined conditions (see Schumann, 2000) the hot and moist engine exhaust gases of airplanes at cruise level trigger the formation of condensation trails (contrails) in the wake of the aircraft. If the surrounding air is ice-supersaturated these contrails become persistent and transform into cirrus clouds and can persist for several hours (IPCC,1999).

It has been shown (IPCC, 1999, IPCC, 2007) that this so-called aircraft induced cloudiness (AIC) has a warming impact on climate, although the magnitude of the impact is not well determined. This study aims at modeling the contrail formation and their evolution into cirrus clouds with the regional climate model CCLM (Cosmo model in CLimate Mode) over Europe. A regional model has been chosen as its cloud microphysics are generally more detailed than in global climate models. The higher resolution of the model (20km x 20km) permits a more detailed representation of small-scale structures like contrails. The global contrail coverage is spatially very inhomogeneous. Therefore Europe has been chosen as a model domain as it presents very high coverage due to the high traffic density over this region.

First a description of how air-traffic influences the cirrus cloudiness is given, followed by a description of regional model CCLM that is used for this study. Next the parameterization that has been introduced into the model to represent contrails is described and results for the potential contrail cover and for a case based on real movement data are presented. Finally we will conclude and give an outlook of the project.

2 MODEL DESCRIPTION

For this paper the regional climate model CCLM is used, which is based on the numerical weather production model COSMO (formerly LM, see Steppeler et al., 2003) used operationally amongst others by the German Weather Serviced (DWD). An overview of the climate version can be found in Will et al. (2009).

* *Corresponding author:* Andrew Ferrone, Université Catholique de Louvain (UCL) –Institut d’astronomie et de géophysique Georges Lemaître (ASTR), Louvain-la-Neuve B-1348 Belgium Email: andrew.ferrone@uclouvain.be

The model configuration is similar to the configuration used for the consortial runs of the CLM-Community: The model version is 3.14 with 0.2° resolution and 40 vertical levels on a rotated longitude-latitude grid (140x160 grid points). The domain covers entire Europe, spanning from Iceland to Northern Greece and Southern Spain to the Northern Tip of the Scandinavian peninsula. At the boundaries the model is forced by NECP re-analysis (Kistler et al. 2001). The model is run from the year 2005.

We use a two-category and one-moment ice-microphysics in CCLM, with prognostic cloud ice and water vapor mixing-ratios. A detailed description can be found in Doms et al. (2005). As in the present paper the focus is on the high troposphere, where only ice-clouds are present, we will give a short description of the formation and depletion of ice-crystals in the scheme. At very low temperatures, below 248.15 K ice crystals are assumed to form at ice-saturation, whereas at higher temperature, up to 267.15 K it is assumed that water-saturation is needed to condensate crystals, which permits high supersaturation to be reached in the model. Once the initial ice-crystals are formed they can grow by water vapor uptake until the ice-saturation level is reached.

Ice-crystals in the scheme can also be formed by the freezing of supercooled clouds droplets below 236.15 K. The main sink of ice in the high troposphere in the scheme is sublimation, when the air gets ice-subaturated, with a rate depending on the saturation deficiency. At lower altitudes the autoconversion and collection process are also parameterized in the model.

3 PARAMETRIZATION OF AIC IN CCLM

The left-hand side of figure 1 shows the growth of cloud ice in an large eddy simulation (LES) done by Lewellen and Lewellen (2001) for different super saturation value of ambient humidity and for different types of airplanes (two and four reactors). Especially for low supersaturation values an initial decrease in ice content can be seen, which is due to an adiabatic warming as the vortices created by the airplane entail the formed ice crystals to lower altitudes and thus warmer temperatures, followed by an increase of ice mass, as air masses are mixing and water vapour from the surrounding air is being fixed on the initial crystals.

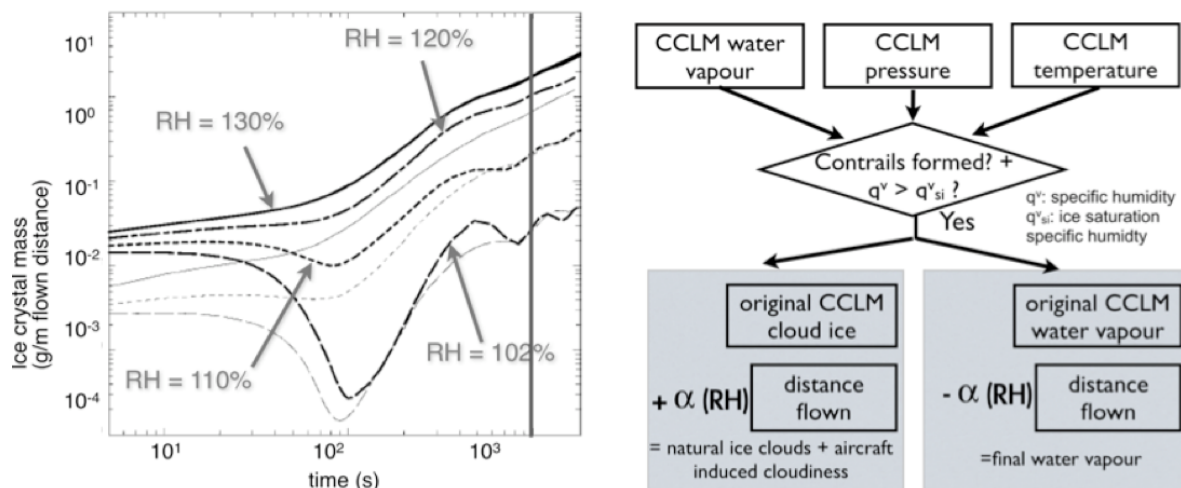


Figure 1: Left side: Ice crystal mass (in g/m of flown distance) as a function of time in the wake of two different types of aircraft, a two-engined one (thin lines) and a four-engined ones (thick lines), done by Lewellen and Lewellen (2001), for different supersaturation values. Right side: Schematic of contrail parametrization introduced in CCLM (see text for description). The parameter alpha is determined by values at 1000 s indicated by the red line on the left graph.

These processes are happening at spatial scales that are not resolved in the climate model. That is why the results of the LES simulation by Lewellen and Lewellen (2001) are introduced in the microphysics of the model if the Appleman-Schmidt criterion is fulfilled and the air is ice-supersaturated (i.e. if persistent contrails are forming). The left side of figure 1 shows that the importance of the supersaturation is an order of magnitude higher than the type of airplane, and in this approach the values given by Lewellen and Lewellen (2001) are linearly interpolated for the different supersaturations, whereas no distinction is made for different airplanes.

As the values in figure 1 are given per flown kilometers, they will be multiplied by the distance flown in the corresponding grid-box. The introduction of the additional ice due to aviation in the microphysics of the model, permits a coherent treatment of the evolution and advection of AIC with natural cirrus clouds and it permits the growth of contrails into cirrus clouds.

4 FIRST RUNS WITH THE CONTRAIL PARAMETRIZATION

4.1 Runs with homogeneous flight distribution

In order to analyze the differences in the potential to form contrails in different regions a first experiment has been made in which an airplane has been assumed to fly in every gridbox at every timestep. The results thus give us an appreciation of the potential additional cirrus cloud cover due to aviation.

The left-hand side of figure 2, gives the additional high (above 8km) cloud cover in the run with the contrail parametrization and a control run where this parametrization was not used, averaged for 2005. The impact on the high clouds is a strong local increase of the cover (up to 5%), which seems to correspond to a recent study done with a GCM that includes the transformation of contrails into cirrus clouds (Burkhardt et al., 2008). This, as well as the difference of magnitude of the direct output of the parametrization and the additional ice formed after going through the microphysics scheme of the model (see the vertical slices on the right side of figure 2 that follow the black line in the left of figure 2) seem to indicate that the model can simulate the transition from contrails to cirrus clouds. The vertical slices also show that contrails in this case are formed mainly between 8 000 to 12 000 m, which is the altitude at which most supersaturation is observed.

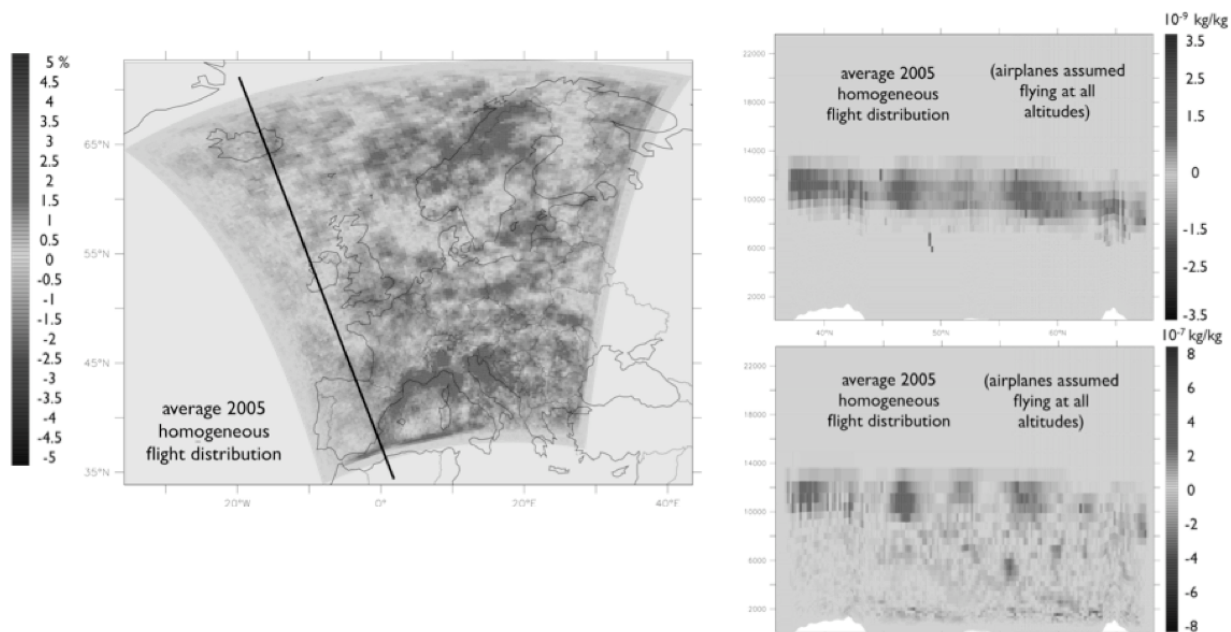


Figure 2 : Left side: Difference of the high cloud cover between a run with contrails and the reference run (in % of coverage) average on 2005, in which airplanes are assumed to fly in every grid box at every timestep, it thus gives a potential contrail cover. Right side: The vertical slices below show the direct output of the contrail parametrization averaged over 2005 (upper graph, in kg of ice per kg of air) as well as the increase of the ice mixing ratio as a function of altitude (lower graph, in kg of ice, per kg of air)

The increase is higher around the Mediterranean coast and the Scandinavian Peninsula, whereas the North Sea shows a rather low potential to form contrails. In Central Europe, the model shows a high potential over the South of the British Isles, the Channel and the Benelux, whereas Central France and large parts of Germany have a lower potential.

The four graphs on the left-hand side of figure 3 give the evolution of the potential contrail cover averaged over three months for the four seasons. The upper plot on the right side of figure 3 shows the average additional high cloud cover over the region for every month. The potential cover is highest in winter, as the temperatures are very low thus favoring the creation of supersaturation and lowest in June. The lower plot on the right-hand side figure 3 shows the diurnal cycle of the cover-

age, which shows a peak around midday in the annual average. This peak may be related to the onset of convection around this time and can also be seen in the summer average of the diurnal cycle. The predominance of convection with warmer temperatures can also explain the more inhomogeneous distribution of the potential cover in April, May June and July August September in the left side of figure 3.

The upper plot on the right-hand side of figure 3, gives the seasonal evolution of the potential AIC coverage, showing a maximum in winter and a minimum around June. This corresponds to the observed variation of supersaturated areas in this region.

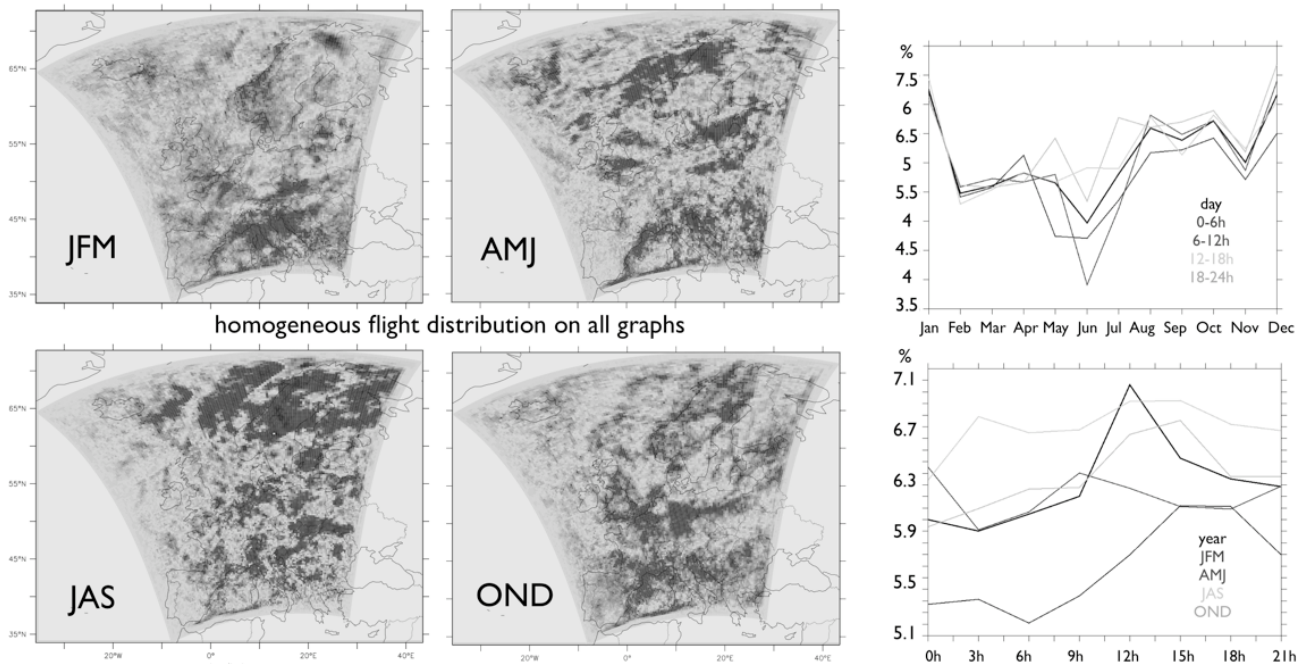


Figure 3: Left side: The four graphs show the evolution of the potential contrail cover averaged over three months (in % of coverage) for January, February March, (JFM), April Mai June (AMJ), July August September (JAS), October, November, December (OND), for the homogenous case (see text). Right side: The upper plot shows the evolution of the average additional high cloud cover over the region as a function of time (in % of coverage) The black line gives the monthly average considering all timesteps. In gray (from darker to lighter gray) only 0-6h (6-12h, 12-18h, 18h-24h) values are considered. The lower plot shows the average of AIC coverage (in % of coverage) as a function of time of day. In black (from darker to lighter gray) the whole year (JFM, AMJ, JAS, OND) is averaged.

4.2 Runs with real flight distribution

One run has been done where the flight distribution over Europe is based on data from the AERO2k database (Eyers et al., 2004). This database gives the flown distance for 2002 on a grid by $1^\circ \times 1^\circ$ and 500 ft vertical resolution. A first step was to downscale the grid on the model grid, which has a resolution of $0.2^\circ \times 0.2^\circ$. The values were uniformly distributed by the area of coverage of the different grid cells, in a way that the sum of distances remains unchanged.

The right hand side of figure 4 shows us the additional high cloud cover (above 8 km) in this case based on real flight distribution. A comparison with figure 2 shows that the pattern is now much more inhomogeneous, and in particular over Northern Europe AIC in the model is much lower, which is due to a reduced flight density over this areas, compared to Central Europe.

The left hand side of figure 4 gives the observed coverage averaged from 2000-2005 of linear contrails from satellite observations by Meyer et al. (2002). We can first see that this coverage is much lower compared to the AIC as given by CCLM, which is as expected. A comparison shows that the model is capable of capturing some important patterns such as the high cover over Western and the lower cover over Eastern part of France. Also the higher cover over the Benelux and the lower cover over Germany is captured. However the high increase over Spain is absent in the model which may be due to the proximity of the boundary data which do not represent supersaturation.

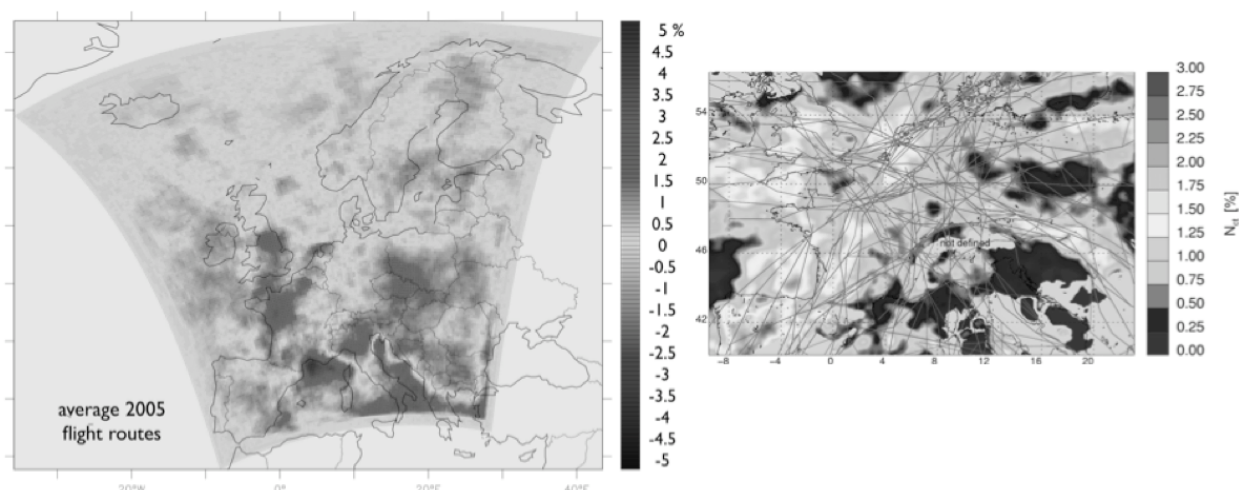


Figure 4 : Left side: Difference of the high cloud cover between a run with contrails and the reference run (in % of coverage) average on 2005, the distribution of flight movements is based on AERO2k (Eyers et al., 2002). Right side: Observation of linear contrail coverage from satellite observations from Meyer et al. (2002).

5 CONCLUSION AND OUTLOOK

This first investigation of aircraft induced cloudiness with the regional climate model CCLM shows that the model is able to reproduce some characteristic patterns of contrail coverage. The seasonal and diurnal cycle reproduced by the model is also in accordance with observed evolution of ice-supersaturated regions in the considered region.

The impact on the high clouds shows a strong local increase of the cover (up to 5%), which seems to correspond to a recent study done with a GCM that includes the transformation of contrails into cirrus clouds (Burkhardt et al., 2008).

This, as well as the difference of magnitude of the direct output of the parametrisation and the additional ice formed (see vertical slices) seem to indicate that the model can simulate the transition from contrails to cirrus clouds

Although these first runs show encouraging results a detailed validation of the simulated contrail coverage and the supersaturation in the model is still to be done.

Next steps of the project will be to perform sensitivity studies (e.g. of the calibration factor α in the parametrisation and of flight altitude), followed by impact studies of contrails on, for example, the diurnal temperature range, the cloud radiative forcing, the total cloud cover (including low level clouds) and the solar insolation.

6 ACKNOWLEDGMENTS

A. Ferrone is supported by the Belgian National Fund for Industrial and Agricultural (FRIA). P. Marbaix and B. Matthews are supported by the Belgian Science Policy Office through the project Aviation and the Belgian Climate Policy: Integration Options and Impacts (Science for a sustainable development SD/CP/01A)

REFERENCES

- ABCi: W. Hecq, S. Meyer, J. Van Mierlo, J. Matheys, C. Macharis, T. Festraets, J.P. van Ypersele, A. Ferrone, P. Marbaix, B. Matthews, Aviation and the Belgian Climate Policy: Integration Options and Impacts: Final report, phase I, Belgian Public Planning Service Science Policy Rue de la Science 8 - Wetenschapsstraat B-1000 Brussels 87p., 2008
- Burkhardt, U., B. Kärcher, M. Ponater, K. Gierens, and A. Gettelman, Contrail cirrus supporting areas in model and observations, *Geophys. Res. Lett.*, 35, L16808, doi:10.1029/2008GL034056, 2008

- Doms, G. and Forstner, J.: Development of a kilometer-scale NWP system: LMK, COSMO Newsletter, 4, 159–167, 2004
- Eyers C., P. Norman, J. Middel, M. Plohr, S. Michot, and K. Atkinson, AERO2k Global Aviation Emissions Inventories for 2002 and 2025, 2004
- IPCC: J. E. Penner, D. H. Lister, D. J. Griggs, D. J. Dokken, and M. McFarland, editors, Aviation and the Global Atmosphere, Cambridge University Press, Cambridge, United Kingdom and New York, NY, USA, 1999
- IPCC: S. Solomon, D. Qin, M. Manning, Z. Chen, M. Marquis, K. Averyt, M. Tignor, and H. Miller, editors, Climate Change 2007: The Physical Science Basis. Contribution of Working Group I to the Fourth Assessment Report of the Intergovernmental Panel on Climate Change, Cambridge University Press, Cambridge, United Kingdom and New York, NY, USA, 2007
- Kistler, R., E. Kalnay, W. Collins, S. Saha, G. White, J. Woollen, M. Chelliah, W. Ebisuzaki, M. Kanamitsu, V. Kousky, H. van den Dool, R. Jenne, and M. Fiorino: The NCEP-NCAR 50-Year Reanalysis: Monthly Means CD-ROM and Documentation. Bull. Amer. Meteor. Soc., 82, 247–268, 2001
- Lee, D.S., D.W. Fahey, P.M. Forster, P.J. Newton, R.C.N. Wit, L.L. Lim, B. Owen, and R. Sausen, Aviation and global climate change in the 21st century, Atmospheric Environment, doi: 10.1016/j.atmosenv.2009.04.024, 2009
- Lewellen D. C. and W. S. Lewellen, The effects of aircraft wake dynamics on contrail development, Journal of the Atmospheric Sciences, 58(4), pp. 390–406, 2001
- Meyer R., H. Mannstein, R. Meerkötter, P. and Wendling, Contrail and cirrus observations over Europe from 6 years of NOAAVHRR data, EUMETSAT Meteorological Satellite Conference, edited by EUMETSAT, vol. EUM P 36, pp. 728–735, 2002
- Sausen R. and I Isaksen and V. Grewe and D. Hauglustaine and D. S. Lee and G. Myhre and M. O. Köhler and G. Pitari and U. Schumann and F. Stordal and and C. Zerefos, 2005. Aviation radiative forcing in 2000: An update on IPCC. Meteorologische Zeitschrift, Vol. 14, 555–561, 2000
- Schumann U., Influence of propulsion efficiency on contrail formation. Aerosp. Sci. Technol, 4(6), pp. 391–401, 2000
- Steppeler, J., Doms, G., Schättler, U., Bitzer, H.W., Gassmann, A., Damrath, U., Gregoric, G., Meso-gamma scale forecasts using nonhydrostatic model LM, Meteorological Atmospheric Physics, 82, 75–96, 2003
- Will A., M. Baldauf, B. Rockel, A. Seifert, Physics and Dynamics of the COSMO-CLM, Meteorol. Z., submitted, 2008

Some evidence of aviation fingerprint in diurnal cycle of cirrus over the North Atlantic

K. Graf*, H. Mannstein, B. Mayer, U. Schumann

Deutsches Zentrum für Luft- und Raumfahrt, Institut für Physik der Atmosphäre, Oberpfaffenhofen, Germany

Keywords: Contrail, Contrail Cirrus, Aviation

ABSTRACT: The diurnal cycle of aviation in the North Atlantic Region (NAR; 45° W – 10° W, 45° N – 55° N) shows a unique fingerprint dominated by two maxima due to rush-hours in westbound resp. eastbound air traffic. We investigate the hypothesis that this signature can be found also in the diurnal cycle of cirrus coverage. Air traffic data were kindly provided by EUROCONTROL with adequate temporal and spatial resolution for this investigation. The cirrus cover is derived from Meteosat-8/9 SEVIRI data with a spatial resolution of about 5 km and a temporal resolution of 15 min using the cirrus detection algorithm MeCiDA (Krebs et al., 2007). Aviation induced cloud cover changes are derived from diurnal cycle of cirrus cover observed in NAR. We developed several response functions representing the effect of air traffic on cirrus coverage and applied fitting methods for determination of the fit parameters representing the statistical lifetime and the amount of AIC in NAR. Application of the fitting procedures to the air traffic density (ATD) allows us to reproduce the signature of cirrus coverage observed in cirrus coverage. The results are robust for investigations of sub regions of NAR with different signatures of initial ATD and shifts in the occurrence of maxima. Several satellite scenes illustrate the statistical behaviour in single scenes.

1 DATASETS – CIRRUS COVERAGE AND AIR TRAFFIC DENSITY

The MSG cirrus detection algorithm MeCiDA (Krebs et al., 2007) using seven infrared channels of MSG-SEVIRI is applied, delivering a time series of cirrus coverage for the considered region with a temporal resolution of 15 minutes.

* *Corresponding author:* Kaspar Graf, Deutsches Zentrum für Luft- und Raumfahrt, Institut für Physik der Atmosphäre, Oberpfaffenhofen, Germany. Email: Kaspar.Graf@dlr.de

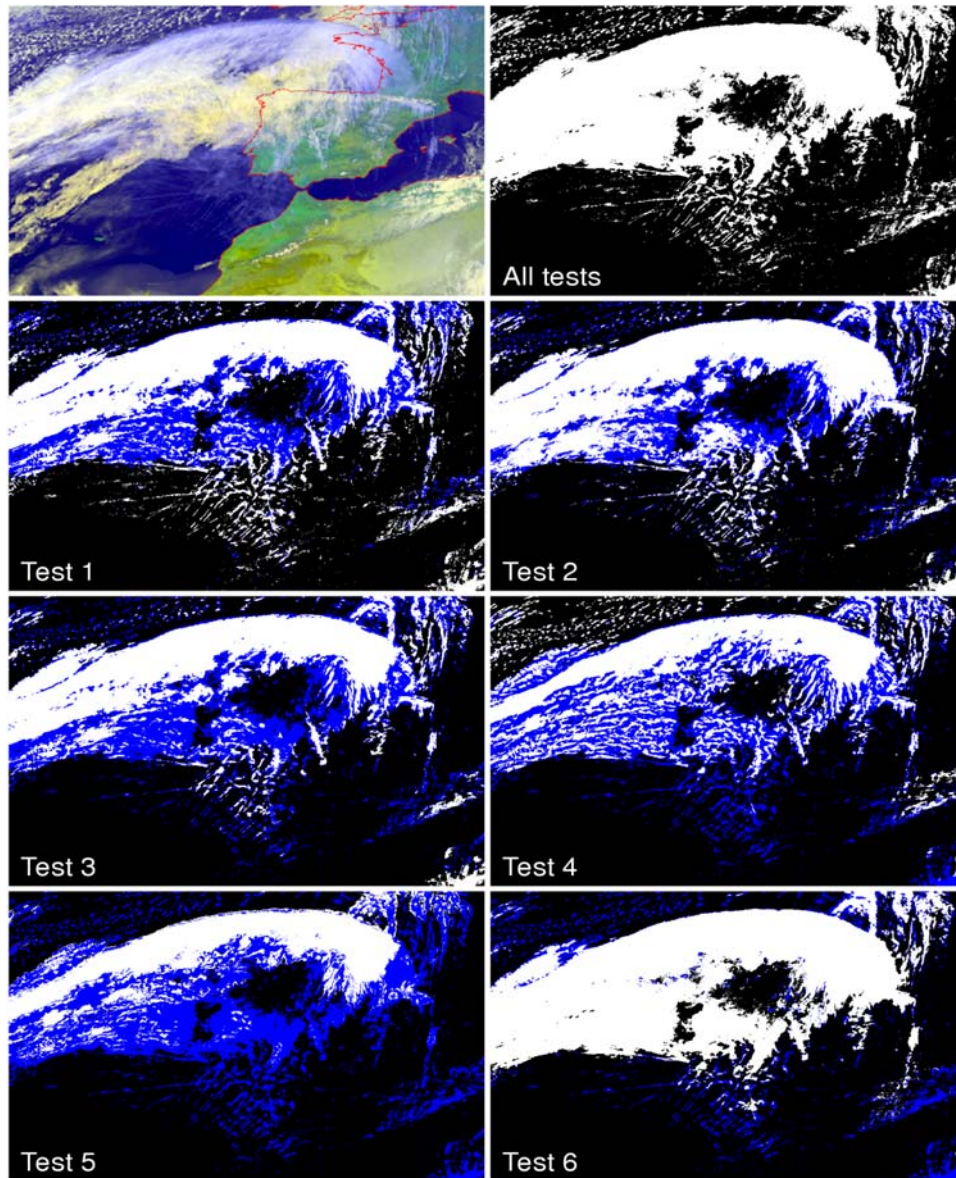


Figure 1. Top left: False color composited of an exemplary cirrus scene. Top right: MeCiDA cirrus classification. The resulting cirrus classification is a combination of six individual cirrus tests which are combined by a logical “OR”, see Krebs et al. (2007).

Based on this time series the diurnal cycle of cirrus coverage in NAR can be obtained. Missing time steps (e.g. satellite malfunction) are interpolated. The diurnal cycle for several sub regions of NAR is determined similarly. The algorithm was applied to a four year time period (02/2004 –01/2008). Within the ESA-DUE Project CONTRAILS, EUROCONTROL provided a dataset of air traffic density (ATD) for six weeks in 2004 with a temporal resolution of 15 min and a spatial resolution of $0.25^\circ \times 0.25^\circ$ for the region shown in figure 2.

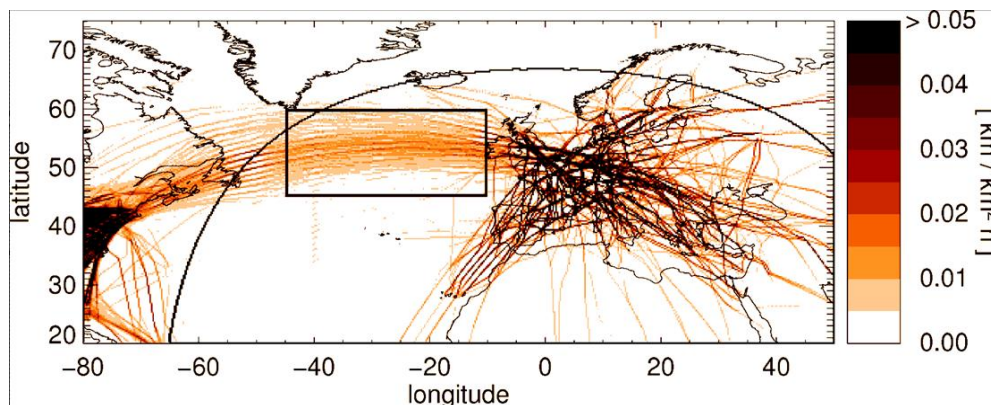


Figure 2. Mean air traffic density in Europe and the North Atlantic. The region NAR is marked by the box. The curve is representing the 75° satellite zenith angle of Meteosat-8/9.

This dataset allows the determination of a representative diurnal cycle of ATD in the NAR, showing a peak at 4 am (UTC) representing the eastbound transatlantic rush hour whereas the peak at 4 pm represents the maximum in westbound traffic.

2 METHOD

The mean diurnal cycle of cirrus coverage shows a pattern similar to a delayed ATD diurnal cycle.

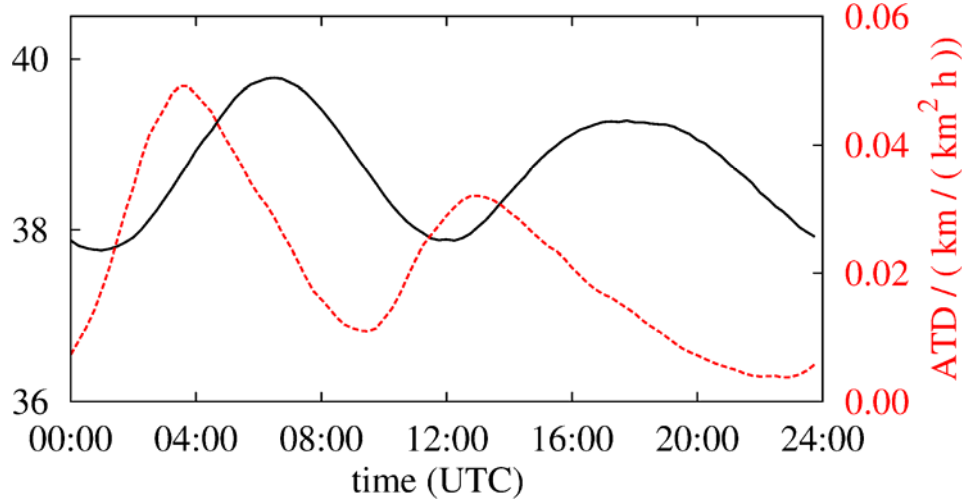


Figure 3. Mean diurnal cycle of air traffic density in NAR (red) and observed cirrus coverage in the same region (black) for 2004.

The diurnal cycle of cirrus coverage can be described as a composite of a constant background, a natural diurnal cycle and an AIC component:

$$C(t) = C_{mean} + C_0(t) + c_{AIC}(t)$$

The natural diurnal cycle $C_0(t)$ is either assumed to be negligible or assumed to be identical to the one observed in the corresponding South Atlantic Region SAR. The AIC contribution to the cirrus cover at time t , $c_{AIC}(t)$ can be expressed statistically as a superposition of all air traffic events in the past,

$$c_{AIC}(t) = \int_{-\infty}^t a(t') \cdot r(t-t') dt',$$

where r is representing the mean AIC at time t triggered by an air traffic event at time t' . For quantification of AIC, we use several response functions $r(t)$ representing this answer of cirrus cover to an air traffic event:

$$r_1(t) = s \cdot \delta(t - \tau), \quad \delta(t) = 0 \text{ for } t \neq 0, \quad \int_{-\infty}^{\infty} \delta(t) dt \equiv 1$$

$$r_2(t) = \begin{cases} s \cdot t \cdot e^{-\lambda \cdot t} & \text{for } t \geq 0 \\ 0 & \text{for } t < 0 \end{cases}$$

$$r_3(t) = b \cdot t^c \cdot e^{-d \cdot t} \cdot e^{-f \cdot t^2}$$

$$r_4(t) = b \cdot t^c \cdot e^{-d \cdot (t-f)^g}$$

Based on the ATD, the coefficients of the response functions are least-square-fitted to the cycle in cirrus coverage (see Fig. 4)

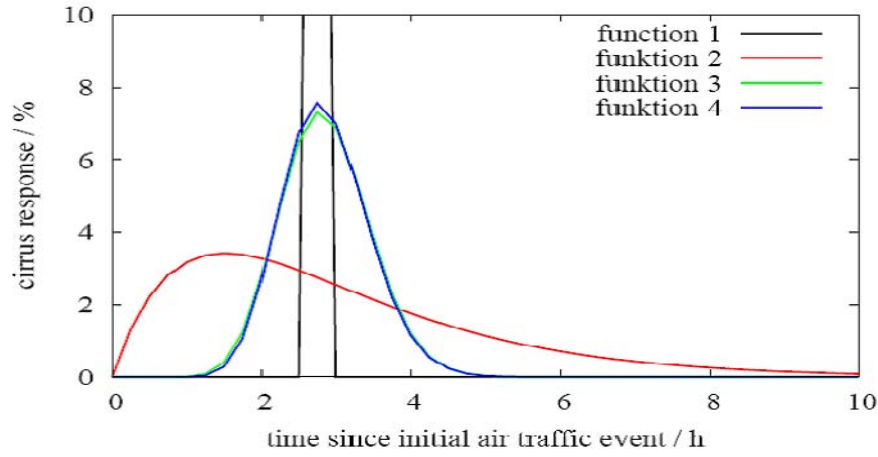


Figure 4. Shape of the different response functions declared in the text.

3 RESULTS

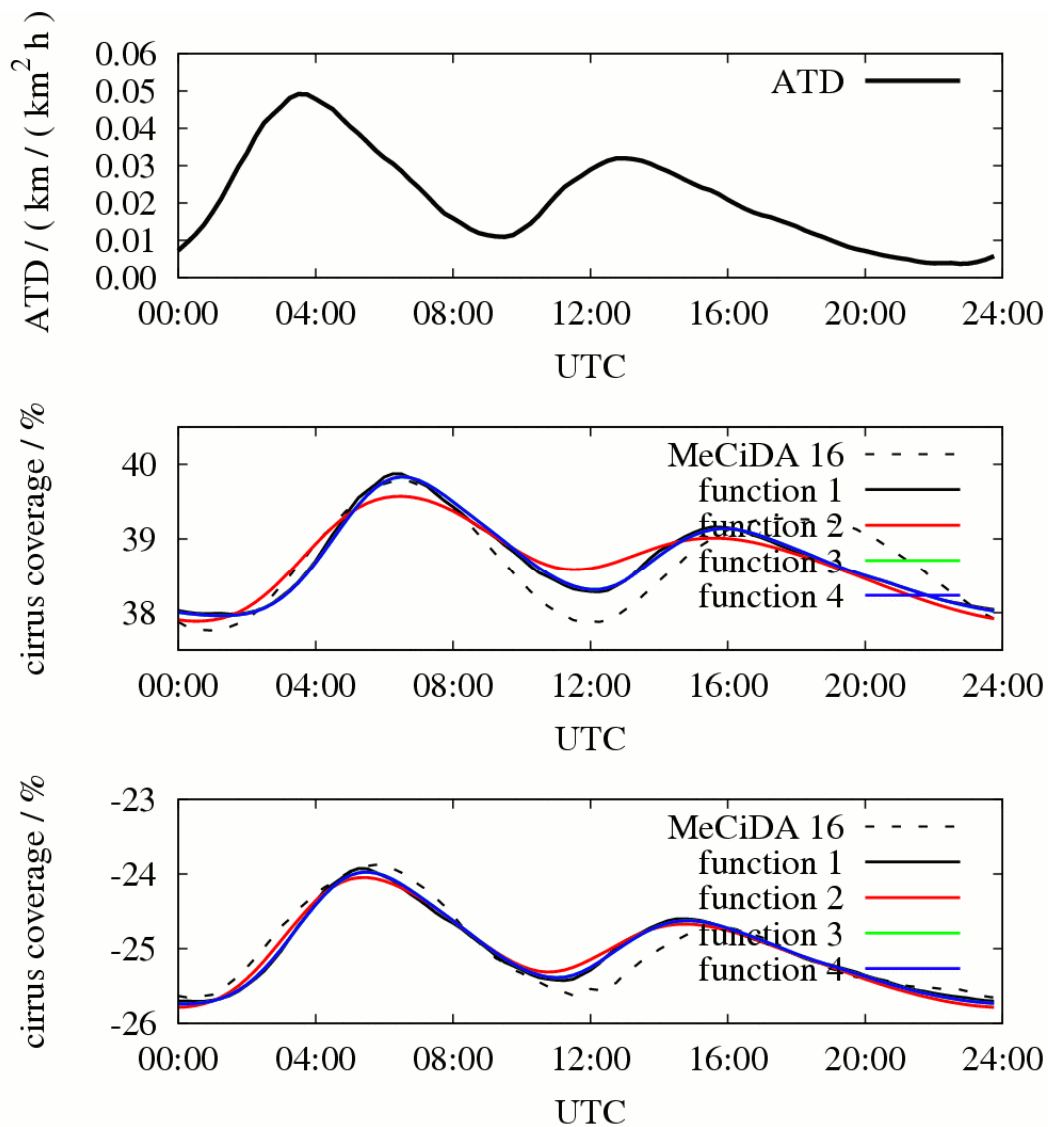


Figure 5. Diurnal cycle of ATD in NAR, based on six weeks in 2004 (top), observed and fitted diurnal cycle of cirrus coverage for the cases $C_0(t) = 0$ (middle) and $C_0(t) = C_{SAR}(t)$ (bottom).

On figure 5, the fitting results based on the ATD input (top) are shown for the case $C_0(t) = 0$ (middle) and $C_0(t) = C_{SAR}(t)$ (bottom). It is obvious that the fitting result is different for each response function. In general, the fitting procedure performs better for the case $C_0(t) = C_{SAR}(t)$.

Table 1. Fitting results for response functions r_1 , r_2 , r_3 and r_4 as declared in the text.

nr	$C_0(t)$	C_{Mean}	s	τ in h	-	-	-	ρ	Δc	c_{AIC}
1	0	0.378	0.416	2.75	-	-	-	0.871	0.003	0.0083
1	SAR	-0.259	0.392	1.75	-	-	-	0.946	0.017	0.0083
			s	λ	-	-	-			
2	0	0.375	0.061	0.66	-	-	-	0.790	0.0038	0.0119
2	SAR	-0.26	0.145	1.11	-	-	-	0.940	0.0019	0.0098
			b	c	d	f	-			
3	0	0.378	0.0044	7.05	0.345	0.71	-	0.867	0.0031	0.0095
3	SAR	-0.259	0.0864	2.89	0.428	0.39	-	0.949	0.0017	0.0089
			b	c	d	f	g			
4	0	0.378	0.5605	17.39	1.50	2.25	1.60	0.870	0.0031	0.0092
4	SAR	-0.259	3.7676	4.51	1.10	1.61	1.48	0.949	0.0017	0.0089

The fit parameters are shown in table 1. For fit function 1 (simple delay), best fits are obtained for a time shift of 1.75 resp. 2.75 h. The 24-h mean AIC in NAR is 0.83% in both cases. For the other response functions, AIC amounts to about 0.8 – 1.2%, depending on which assumption for $C_0(t)$ is used. All results shown here are based on data from February – December 2004, as for the following years no representative ATD dataset is available so far.

4 CONSISTENCY

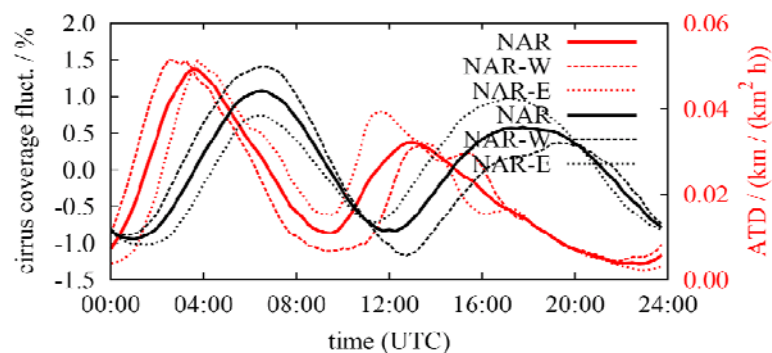


Figure 6. Diurnal cycle of ATD (red) and cirrus coverage (black) for the sub regions NAR-W and NAR-E, the western resp. eastern part of NAR.

The peak representing ATD in eastbound direction occurs earlier in the western part of NAR than in the eastern one, whereas the westbound peak occurs earlier in the eastern part of the NAR. This unique (i.e. non-meteorological) behaviour can be retrieved in the cirrus coverage as well (Fig. 6).

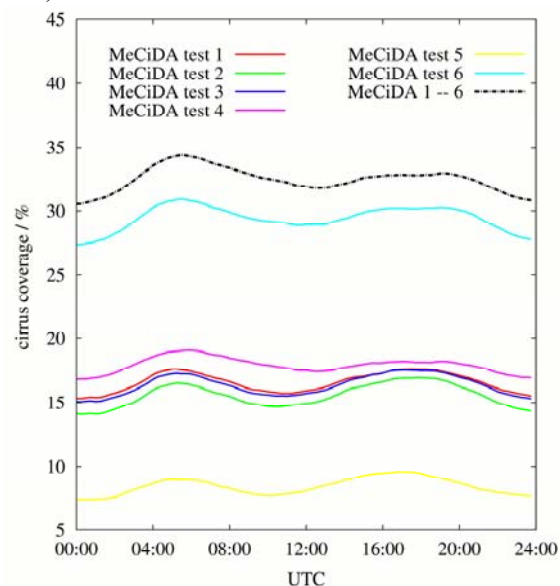


Figure 7. Diurnal cycle of cirrus coverage derived by the six individual cirrus tests of MeCiDA for NAR, 2004.

MeCiDA consists of six individual cirrus tests based on different channel combinations of MSG-SEVIRI. These tests are combined by a logical “OR”. Applying each test alone to a data-subset, the diurnal cycle in cirrus coverage is consistent with the total MeCiDA result (see figure 7). Therefore, artefacts due to a “diurnal-cycle sensitive” channel (e.g. the ozone channel $9.3\ \mu\text{m}$) are excluded. Furthermore, periodic oscillations of MSG around its nominal position were analysed. The frequency of these oscillations would not cause a diurnal cycle.

5 EXAMPLE AND OUTLOOK

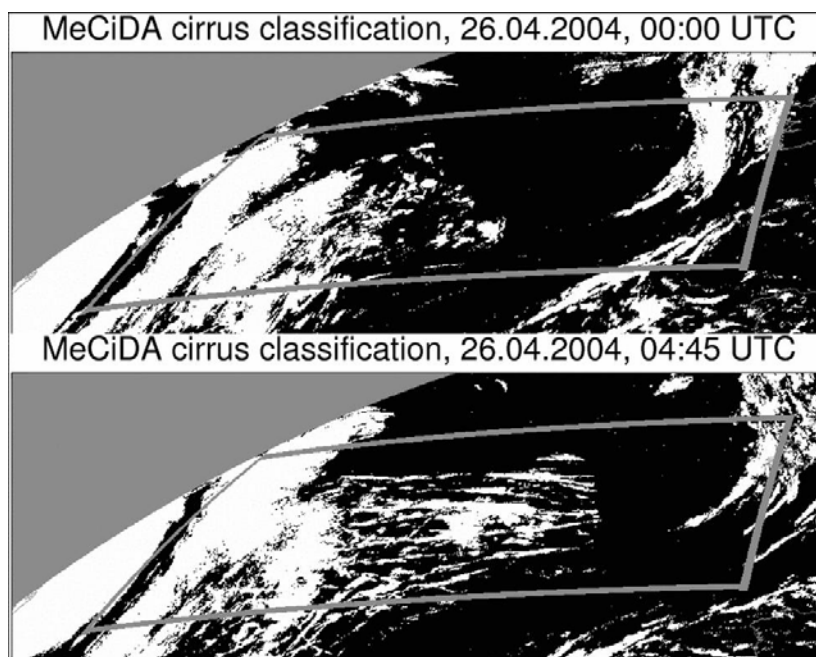


Figure 8. Cirrus scenes derived with MeCiDA.

The visibility of AIC in satellite data is illustrated by the two scenes shown in figure 8: At 0:00 UTC, ATD is low and the last peak was 10 hours ago. Therefore, no significant ATD fingerprints are visible in the satellite scene. At 4:45 UTC, the westbound ATD has passed the region two hours ago and triggered AIC in the NAR. In the following time, this AIC is decreasing until the eastbound ATD triggers new AIC formation. Further work is needed for a better identification and understanding of natural contributions in diurnal cycle of cirrus coverage in NAR as well as SAR.

The HALO campaign “ML-CIRRUS” will address the validation of diurnal cycle in AIC. So far, analysis is based on an ATD dataset of several weeks. A complete ATD dataset is needed for a more detailed consistency check and for comparisons with the Contrail and Cirrus Prediction tool CoCiP (Schumann, 2009).

6 ACKNOWLEDGEMENT

We thank S. Rentsch for data handling support. Meteosat 8/9 data were provided by EUMETSAT via the German Sensing data center at DLR and air traffic data were provided by EUROCONTROL, both within the ESA-DUE project CONTRAILS. The work performed was part of the DLR projects PAZI 2 and CATS, and the BMBF project UFO within Klimazwei.

REFERENCES

- Krebs, W., H. Mannstein, L. Bugliaro, and B. Mayer, 2007, Technical note: A new day- and night-time Meteosat Second Generation Cirrus Detection Algorithm MeCiDA. *Atmos. Chem. Phys.*, 7, 6145-6159
Schumann, U., 2009: A Contrail Cirrus Prediction Tool. In: Sausen, R. et al. (eds.): *Proceedings of an International Conference on Transport, Atmosphere and Climate (TAC-2)*. Aachen, Maastricht, 2009, in press

Aviation and ship soot as freezing nuclei of water/sulfate cloud droplets

E. Kireeva*, O. Popovicheva, N. Persiantseva
Institute of Nuclear Physics, Moscow, Russia

N. Shonija, T. Khokhlova
Dept. of Chemistry, Moscow State University, Moscow, Russia

Keywords: immersion freezing nucleation, soot aerosols, aviation and ship emission

ABSTRACT: Laboratory study of heterogeneous freezing of water/sulfate droplets induced by immersed aviation and ship soot particles is reviewed. In order to identify the impact of individual transport soot particles on the droplet freezing efficiency a set of well-characterized laboratory soots with different properties are analyzed along with aviation and ship soots. This laboratory approach allows the identification of the properties for the most effective immersion freezing nuclei. The maximum temperature shift due to heterogonous freezing in respect to homogeneous freezing is found to be 10°C for hydrophobic soot immersed into sulfuric acid solution droplets. Aviation and ship – emitted aerosols cannot be referring as effective immersions freezing nuclei in both water and sulfuric acid droplets due to high hygroscopicity and water soluble fraction on their surface.

1 INTRODUCTION

The major source of uncertainties in assessing aerosol indirect effects on climate is the emission of soot aerosols. Transport - emitted aerosols may act as effective ice nuclei impacting the Earth's climate indirectly by changing the properties and lifecycle of clouds. The commonly observed carbon-containing particles in cirrus ice crystals indicate that aerosol particles can stimulate the process of ice formation in the atmosphere. It is assumed that aerosols after the evaporation of contrail ice crystals can change the microphysical properties of cirrus clouds (Strom and Ohlsson, 1998). Heterogeneous ice formation in cirrus clouds due to immersed soot aerosols can occur at noticeably lower degrees of water supersaturation than those required for the homogeneous formation of sulfate aerosols (DeMott et al., 1997).

However, the effects of aviation and ship soot emission on freezing the cloud droplets along with the mechanism that could lead to heterogeneous ice nucleation by soot particles at the cirrus level are not clear. The field observations of transport emission particulates and their influence on freezing ability are much limited because of the great difficulties in direct measurements of soot aerosols involved in ice cloud formation. This situation is complicated by the fact that soot particles emitted into atmosphere from aircrafts and ships have a wide range of a natural variability with respect to physico-chemical properties including the composition and extent of hygroscopicity. Laboratory approach can provide relevant information to establish the link between physico-chemical properties of soot particles and their freezing activity.

This work is devoted to laboratory studies of heterogeneous freezing of water and sulfate droplets induced by immersed soot. Along with original transport soot (aviation and ship residuals) a set of well-characterized laboratory soots with various extent of hydroscopicity is investigated. The median freezing temperature of an ensemble of water and sulfate droplets with soot immersed demonstrates a clear impact of soot wetting, hydrophilicity, and water soluble fraction. The characteristics of soot particles active in the immersion freezing mode are thereby suggested. The efficiency of

* Corresponding author: Elena Kireeva, Institute of Nuclear Physics, Moscow, Russia. Email: elenakireeva2@gmail.com

aviation and ship soot as freezing nuclei in water/sulfate cloud droplets in the atmosphere is reported.

2 EXPERIMENTAL SECTIONS

2.1 Aviation and ship soot sampling

A sampling campaign for monitoring a number of seagoing transport ships was undertaken in the framework QUANTIFY EU project in the Odessa port. Ship emitted particulates were collected during a few months onboard of a diesel-powered marine tanker using distillate diesel oil fuel. A high-volume bulk aerosol sampler mounted at the ship end-of-pipe was used. Diesel fuel typically contained not more than 0.5% of sulfur and 0.01% of ash. Aircraft engine combustor (AEC) soot was produced by a combustor of a modern gas turbine engine, model D30-KU, operating at cruise combustion conditions on a test facilities in CIAM, Moscow (Popovicheva et al., 2004). The engine fuel was aviation kerosene TC1 containing 0.11 % of sulfur and less than $10^{-4}\%$ of metals.

2.2 Immersion freezing experiments

Detailed description of freezing experiment is given in Popovicheva 2008. To obtain statistically reliable data the freezing of an ensemble of 100 microdroplets of 0.13 μm was examined in a cooled cell. For preparation of the soot suspensions the agglomerates of the size less than 80 μm was used; a particle number density in the microdroplets was 2.5 wt %. As a measure of the freezing efficiency a difference between the median freezing temperature of an ensemble of pure microdroplets and ones from soot suspensions, ΔT_f , was assumed. ΔT_f for pure water droplets and 10 wt% sulfuric acid solution droplets was obtained $-11.5 \pm 2.1^\circ\text{C}$ and $-21 \pm 2.5^\circ\text{C}$, respectively. A set of well-characterized soots with different properties, water-soluble fraction and extent of hygroscopicity were analyzed. It includes lamp soot (LS), furnace black (FB), thermal soot (TS), Printex, and acetylene black (AB) which were produced by combustion of liquid fuel in a lamp and furnace, by the pyrolysis of natural gas and by explosion of acetylene, respectively.

3 FREEZING OF WATER DROPLETS WITH SOOT IMMERSED

3.1 Soot behaviour in water

The key physical characteristic impacting the water droplet freezing efficiency is the soot particle distribution in water that is influenced by the mass density and size of soot agglomerates, and wetting characteristics. In the case of soot particles of high mass density, like FB soot, the sedimentation instability (see fig.1a) limits the freezing efficiency of droplets. AB soot with a low mass density creates the sedimentation stable suspension with particles homogeneously distributed over droplet volume; these particles have the property of floating and water droplets with AB soot are uniformly dark (see fig.1b). The sedimentation stable water/soot suspensions with homogeneously distributed over droplet volume particles provide the appreciable freezing efficiency, near 4.7°C . Moreover, there is a correlation between wetting ability of the soot surface and the floating properties of soot agglomerates. For a given mass density, soot characterized by a smaller contact angle is more wettable and therefore its particles more easily sediment on the droplet bottom. It is found that the wettability of soot is in good correlation with their hygroscopicity which is determined from water adsorption isotherms (Persiantseva et al., 2004).

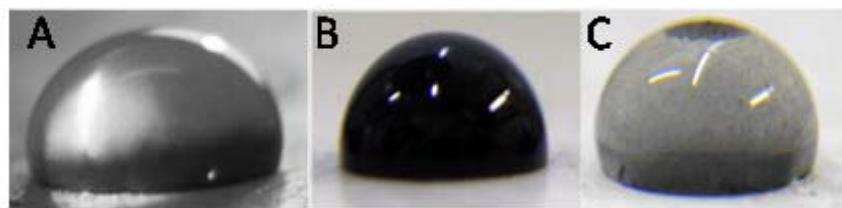


Figure 1. Water droplets with different soot behavior: a) sedimentation instable droplet of FB soot, b) sedimentation stable droplet of AB soot, c) AEC soot droplet with two separated fraction of particles.

Aviation and ship soots have the highest mass density, their particles are partly deposited on the droplet bottom or concentrate at the top (see fig. 1c). This distribution over the droplet is in accordance with findings that aviation soot contains two fractions, one is hydrophobic and other is hydrophilic because of the large amount of water-soluble impurities (Popovicheva et al., 2004).

3.2 Extent of soot hygroscopicity and freezing efficiency

Adsorption of water vapor is a sensitive tool to establish the link between the freezing mechanism and soot surface hydration characteristics. Therefore in this work the water uptake as a function of the relative humidity is measuring by a gravimetric method to identify the extent of soot particle hygroscopicity. The fundamental theory of water adsorption on soots assumes that, due to low dispersion energy between water molecules and graphite platelets, there is a strong dependence on the presence of hydrophilic sites, so called primary adsorption sites (oxygen-containing active sites). It is assumed that sites of the adsorption of water molecules are also sites for ice formation. So, the extent of soot hydrophilicity is the second key characteristics relating to immersion freezing efficiency. Our study shows the strong correlation between the numbers of oxygen containing active sites on the soot surface and the freezing efficiency of water droplets with soot immersed.

Hydrophobic particles of TS soot consist mainly from elemental carbon with negligible number oxygen-containing sites. These particles do not promote ice nucleation in the immersion freezing mode. Fig. 2A shows the freezing frequency of pure water droplets versus droplets with TS soot immersed. There is a negligible shift, 0.4°C , in the freezing temperature in respect to pure water droplets (see Table 1).

Table 1. Freezing efficiency (ΔT_f) of droplets with soots immersed and soot water soluble fraction (WSF).

Soots	ΔT_f of water droplets, $^{\circ}\text{C}$	ΔT_f of sulfate droplets, $^{\circ}\text{C}$	WSF, %
Ship soot	0.2	2	18
Aviation (AEC) soot	0.9	4	13.5
Furnace Black (FB)	4.2	7.2	0.1
Lamp soot (LS)	3.9	6.5	0.4
Thermal soot (TS)	0.9	6	0.5
Printex		8.8	0.1

The maximum freezing efficiency is about 4.2°C was obtained for FB soot. This soot contains a significant number of oxygen-containing functional groups but not covered totally by hydrophilic sites and soluble compounds. Therefore, a relatively low polar surface is preferable for the ice formation as compared with polar surfaces on which the dipoles of water molecules are predominantly oriented in parallel with one another, thus enhancing the free energy of new phase nuclei formation. Hence, hydrophilic soot is preferable for heterogeneous ice formation. The similar freezing efficiency of 3.9°C was observed for LS soot with the same extent of hygroscopicity (Table 1).

However, if the soot surface contains the high water-soluble inorganic/organic fraction (the case of hygroscopic soots) the active sites may be sensible to dissolution after the particle has become immersed into water. Soluble coverage changes the mechanism of water uptake from water cluster growth on the active sites to the dissolution into soluble surface material. Then, we may predict the reduction of potential ice nucleation ability for really hygroscopic soot.

Both aviation and ship soots are characterized by high water soluble fraction, 13.5% and 18% respectively. Additionally, the WSF of aviation soot contains 3.5 wt% of sulfates which are easily washed by water. Such high WSF leads to extremely high water uptake up to 40 and 500 water monolayers for aviation and ship soots, respectively (Popovicheva et al., 2004; 2009). And therefore the freezing efficiency of these soots are not exceed 0.9°C (Table 1). The histogram of freezing frequency of water droplets with ship soot immersed confirms this finding (fig. 2A).

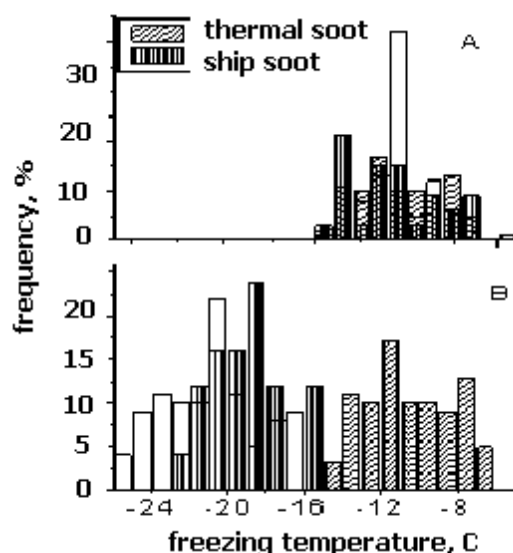


Figure 2. Freezing frequency of A) pure water droplets and droplets with TS and ship soot immersed, of B) pure 10 wt % sulfuric acid droplets and droplets with TS and ship soot immersed.

4 FREEZING OF SULFATE DROPLETS WITH SOOT IMMERSED

The immersion freezing efficiency of polluted water droplets is determined by the water molecule ability to form hydrogen bonds with the soot surface. In sulfuric acid droplets the soot surface attracts sulfates due to electrostatic or dispersion forces. Mechanism of sulfate interactions is determined by acidic and basic properties of the soot surface. In our study a set of soots with different soot surface acidity is analyzed in respect to heterogeneous freezing efficiency. The maximum of freezing efficiency of 8.8°C is observed for Printex soot with basic surface properties. ΔT_f of the neutral soot surface of TS and LB is similar, 6°C and 6.5°C , respectively. Ship soot is characterized by extremely acid surface. For this soot ΔT_f is not exceed 2°C . The histograms of the freezing frequency of ship and TS soot polluted sulfuric acid droplets in respect to pure ones are shown in fig.2B. The comparison of freezing of water and sulfate droplets with TS soot immersed shows the significant difference. Such difference indicates the different mechanism of sulfate/soot and water/soot interactions. Ship soot is found to act as poor ice nuclei in both water and sulfate droplets (fig. 2 A,B). The adsorption of sulfate ions leads to subsequent decrease of the acid concentration in the droplets that relates with a shift of the droplet freezing temperature to more warm value. Therefore, the final significant effect of soot immersion into sulfuric acid droplets is observed.

5 DISCUSSION AND CONCLUSIONS

The link between soot physico-chemical properties and immersion freezing efficiency is established. Soot behaviour in water and extent of soot hydrophilicity determine the water droplet immersion freezing. We suggest that these factors could be considered as key requirements for immersion freezing of cloud droplets together with the wetting parameter and a number of active sites. Deposition of the soot particles on the droplet bottom due to sedimentation instability or on the droplet surface due to a poor wettability limits the efficiency of heterogeneous freezing. Hydrophobic soot with negligible active sites does not promote ice nucleation in the immersion freezing mode. Soluble coverage changes the mechanism of water uptake from water cluster growth on the active sites to the dissolution into soluble surface material. Highly soluble surface compounds of hygroscopic soot, such as sulfates, may be easily dissolved in water leading to losing the potential freezing efficiency. The most efficient immersion freezing nuclei in the atmospheric water cloud droplets is hydrophilic soot with a significant number of oxygen-containing functional groups but not covered totally by hydrophilic sites and soluble compounds. Quantitatively, we may add the maximum efficiency obtained for hydrophilic soot 4.2°C , to 4.7°C found for a homogeneous sus-

pension of soot and conclude a highest effect about 9°C for the best immersion freezing nuclei which may be hypothesized on the bases of our experimental results.

The efficiency of sulfate droplet immersion freezing is determined by the surface chemistry of soot particles namely by a number of acid and basic groups on the surface. Hydrophobic soot with negligible active sites and hydrophilic soot with a number of oxygen-containing functional groups are proposed to act as the most efficient immersion ice nuclei in the sulfate droplets. Hydrophilic soot with significant number of active sites slightly attracts sulfate ions from solution and can not change significantly the acid concentration. Particles of aviation and ship soot are not efficient ice nuclei both in water and sulfuric acid droplets because of the large amount of WSF dissolving in droplet environment.

6 ACKNOWLEDGEMENTS

This research was funded by EU FP6 Project QUANTIFY-TTC 003893.

REFERENCES

- DeMott, P.J., Rogers, D.C., Kreidenweis, S.M., 1997: The susceptibility of ice formation in upper tropospheric clouds to insoluble aerosol components. *J. Geophys. Res.* **102** (D16), 19575–19584.
- Persiantseva, N.M., Popovicheva, O.B., Shonija, N.K., 2004: Wetting and hydration of insoluble soot particles in the upper troposphere. *J. Environ. Monit.* **6**, 939–945.
- Popovicheva, O.B., Persiantseva, N.M., Lukhovitskaya, E.E., Shonija, N.K., Zubareva, N.A., Demirdjian, B., Ferry, D., Suzanne, J., 2004: Aircraft engine soot as contrail nuclei. *Geophys. Res. Lett.* **31**, L11104.
- Popovicheva, O.B., Kireeva, E.D., Persiantseva, N.M., Khokhlova, T.D., Shonija, N.K., Tishkova, B., Demirdjian, B., 2008: Effect of soot on immersion freezing of water and possible atmospheric implications. *Atmospheric Research* **90**, 326–337.
- Popovicheva, O.B., Kireeva, E. D., Shonija, N. K., Zubareva, N. A., Persiantseva, N. M., Tishkova V., Demirdjian, B., Moldanová, J., V. Mogilnikov, V. Ship particulate pollutants: characterization in terms of environmental implications. *J. Environ. Monit.* Doi:10.1039/B908180A
- Strom, J. and S. Ohlsson, 1998: In situ measurements of enhanced crystal number densities in cirrus clouds caused by aircraft exhaust. *J. Geophys. Res.* **103**, 11355–11361.

Large Eddy Simulation of Persistent Contrails

A.D. Naiman^{*}, S.K. Lele, F. Ham, J.T. Wilkerson, M.Z. Jacobson
Stanford University, Stanford, CA, USA

Keywords: large eddy simulation, contrails, climate modelling

ABSTRACT: A study of three-dimensional contrail evolution has been conducted using a large eddy simulation (LES) model. The LES solves the incompressible Navier-Stokes equations with a Boussinesq approximation for buoyancy forces. Contrail ice particles are modelled using a Lagrangian tracking approach along with a microphysical model of growth due to ice deposition and sublimation. Initial condition flow fields approximate the wake of a commercial jet one second after the aircraft has passed. We present results of simulations to 1200 seconds after emission. We find that higher levels of turbulence and shear promote mixing of the aircraft exhaust with ambient air, resulting in faster growth of contrail ice particles and wider dispersion of the exhaust plume when the ambient air is supersaturated. These results provide sensitivity information that is used to refine a subgrid model of aircraft exhaust plume dynamics for use within a global climate model.

1 INTRODUCTION

Aircraft are unique among anthropogenic sources of air pollution in that they consume much of their fuel at a cruise altitude near the tropopause, where exhaust has a long residence time and conditions are conducive to the formation of condensation trails (contrails). The effect of contrails and related aviation-induced cloudiness on climate is highly uncertain. The most recent assessment of the effect of aviation on global radiative forcing lists the level of scientific understanding as “low” for linear contrails and as “very low” for induced cloudiness (Lee et al., 2009). The range of estimates for these effects is large, and if the upper end of the range was realized, it would nearly double the overall forcing of aviation.

This paper presents work that is aimed at reducing the uncertainty in these estimates related to understanding the formation and persistence of contrails. We present results from a large eddy simulation (LES) model of contrails that tracks ice particles using a Lagrangian approach. The model has been used to simulate contrail development from 1 to 1200 seconds after emission by a passing commercial jet aircraft under several atmospheric conditions.

2 LES MODEL OVERVIEW

Several researchers have modelled contrail development using an LES approach, including Lewellen and Lewellen (2001), Paoli and Garnier (2005), Huebsch and Lewellen (2006), Shirgaonkar and Lele (2007). Our LES code solves the three-dimensional, incompressible Navier-Stokes equations with a Boussinesq approximation for buoyancy forces on an unstructured grid. The numerical scheme uses a finite volume spatial discretization and an implicit fractional-step method for time advancement, with second order accuracy in both space and time (Mahesh et al., 2004; Ham et al., 2007). Contrail ice particles are modelled using a Lagrangian tracking approach and a microphysical model of growth due to ice deposition and sublimation, similar to Paoli et al., (2004).

The computational domain is stationary with respect to the ground, so the computation represents a temporal simulation in a triply periodic domain. The coordinate axes are positioned such that the y -axis is vertical (opposite gravity), the z -axis points in the flight direction, opposite the cruise velocity, and the x -axis is the cross-stream direction. The coupled fluid equations are listed below, where $\mathbf{u} = u\mathbf{i} + v\mathbf{j} + w\mathbf{k}$ is the velocity vector, ρ is the fluid density, p is the fluid pressure, \mathbf{g} is the

^{*} *Corresponding author:* Alexander D. Naiman, Department of Aeronautics and Astronautics, Stanford University, Durand Building Room 267, 496 Lomita Mall, Stanford, CA 94305, USA. Email: anaiman@stanford.edu

gravitational acceleration vector, μ is the dynamic viscosity of air, θ is the potential temperature, κ is the thermal diffusivity of air, and D_v is the diffusivity of water vapour in air.

$$\nabla \cdot \mathbf{u} = 0 \quad (1)$$

$$\rho_0 \frac{D\mathbf{u}}{Dt} = -\nabla p + \rho' \mathbf{g} + \mu \nabla^2 \mathbf{u} \quad (2)$$

$$\rho' = \frac{-\rho_0 \theta'}{\theta_0} \quad (3)$$

$$\frac{D\theta'}{Dt} = -\frac{d\theta}{dy} v + \kappa \nabla^2 \theta' + \omega_T \quad (4)$$

$$\frac{DY'}{Dt} = -\frac{dY}{dy} v + D_v \nabla^2 Y' + \omega_Y \quad (5)$$

$$\omega_T = -\omega_Y L \quad (6)$$

In addition to the typical set of incompressible Navier-Stokes equations (Equations 1-2) with a Boussinesq approximation (Equation 3), two scalar diffusion equations are solved for potential temperature and water vapour density. We decompose these scalars into a reference part (θ_0 , Y_0), an altitude-varying part ($\theta(y)$, $Y(y)$), and a perturbation part (θ' , Y'). The altitude-varying part is prescribed to be a constant gradient for both variables. The diffusion equations are solved for the perturbation part of the scalars (Equations 4-5). Equations 4-5 also include source terms (ω_T , ω_Y) resulting from a coupling to the microphysical equations and related according to Equation 6, where L is the latent heat of sublimation of ice.

Contrail ice particles are modelled using a Lagrangian tracking approach and a microphysical model of growth due to ice deposition and sublimation. Particles are currently tracked as tracers of the background fluid. This approximation is suitable at early phases of contrail development, when particle relaxation time $\tau_p = 4\rho_p r_p^2 / 18\mu$ is short compared to flow time scales due to small particle sizes (particle radius r_p 1-10 μm). For the late stages of simulation, when the largest particles grow to 100 μm , the effects of sedimentation and particle drag will be added in the future.

The model of microphysical growth is described in detail in Shirgaonkar and Lele (2007). In summary, each ice particle is treated as a spherical nucleus over which ice has deposited. Each computational particle represents a collection of physical particles. Coagulation and coalescence are neglected and re-nucleation is allowed. Particle radius changes due to deposition or sublimation of water to or from the particle surface. The growth rate of a single ice particle is calculated using a simple diffusion model from Kärcher et al. (1996). Growth rates are calculated for each computational particle and integrated over the time step. The source term, ω_Y , is then calculated by integrating the source of water vapour in each Eulerian control volume.

3 SIMULATION DESCRIPTION

Each case described here was simulated as follows. First, a background field of periodic, decaying turbulence was generated. This background field was then scaled such that the energy matched the inertial subrange spectra $E(k) = 1.7\epsilon^{2/3} k^{-5/3}$ at the peak wavenumber, $k_p = 4$, for the given case turbulent dissipation rate, ϵ . The 2-D wake one second downstream of a Boeing 767, calculated by the Boeing Company and provided by Dr. Steven L. Baughcum, was added to the background field. A series of unstructured, periodic grids was used to simulate the development of the contrail, with grid resolution maximized near the contrail structure and decreased out to the domain boundaries. Results on each grid were interpolated to the next. Maximum resolution ranged from 0.37 m during the early stages of the simulation to 2.96 m in the latest stage. Similarly, total domain size ranged from $400 \times 400 \times 400 \text{ m}^3$ to $3200 \times 1600 \times 400 \text{ m}^3$ as the simulation progressed. Grid sensitivity studies showed little variation in results due to these transitions from one grid to the next.

For all of the cases considered here, the potential temperature gradient is stable ($d\theta/dy = 2.5$ K/km) and the water vapour gradient approximates a constant ambient relative humidity with respect to ice (RH_i) of 130%. Ambient conditions were consistent with a cruise altitude of 10.5 km in a standard atmosphere. The peak exhaust temperature was 4.4 K, the peak exhaust water vapour density was 1.14×10^{-4} kg/m³, and the peak particle number density was 85,000 per cm³. A total of 8×10^6 computational particles, each representing 2.73×10^8 physical particles, were tracked, giving a total of 5.8×10^{12} per m in the flight direction, and each was initialized with a radius of 0.1 μ m. Four cases were simulated, varying the intensity of both ambient turbulence and vertical wind shear. The cases are summarized in Table 1.

Table 1. Summary of simulation cases, which vary initial ambient turbulence and vertical wind shear.

Case		Turbulent Dissipation Rate (m ² /s ³)	Vertical Shear (s ⁻¹)
A	Baseline	0.0001	0
B	High turbulence	0.001	0
C	Moderate shear	0.0001	0.005
D	High shear	0.001	0.01

4 LES RESULTS

The following figures show results from the four simulation cases. Figure 1 shows two sets of plots for case A, the baseline case, and for case C, the moderate shear case – the upper plots are flight-direction averaged contours of ice water content, while the lower plots are vertically integrated ice area density. For the lower plots, the domain has been duplicated in the flight direction in order to give an impression of the contrail as it would appear in the sky.

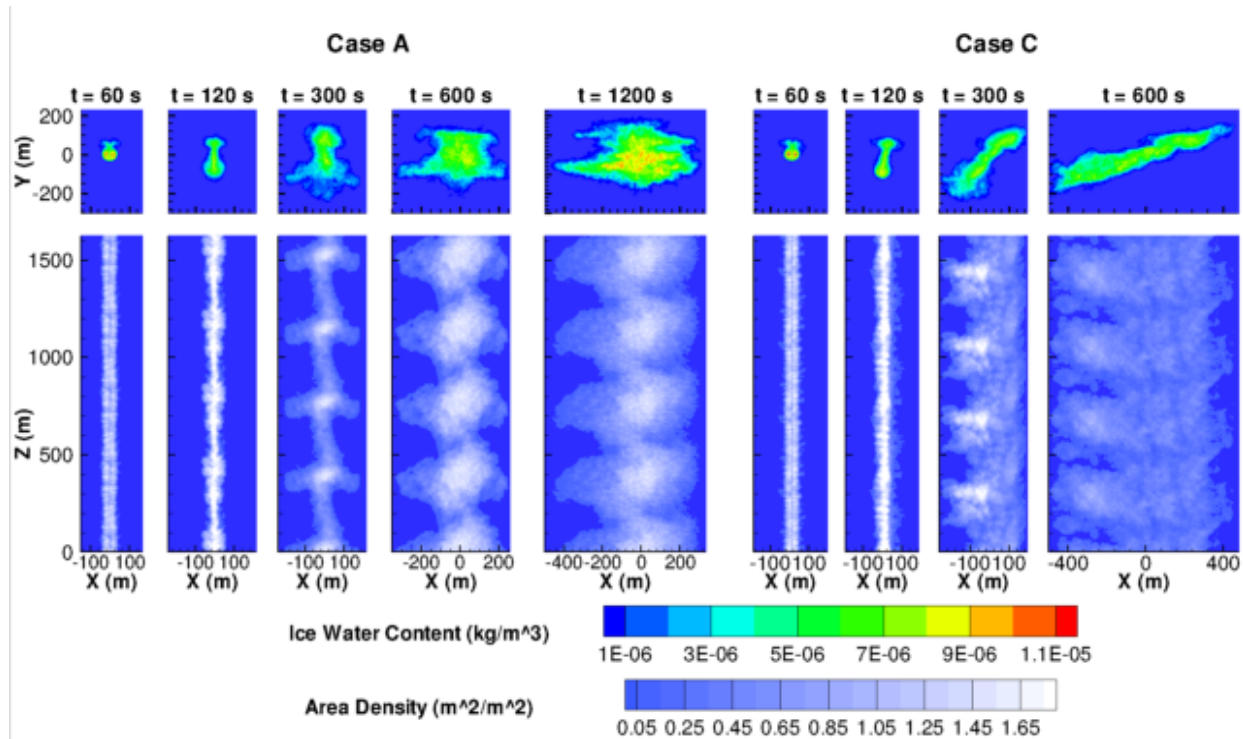


Figure 1. Left plots are for case A, right plots are for case C. Upper plots are flight-direction averaged contours of ice water content. Lower plots are vertically integrated ice area density. Scales and contour levels are identical on all plots.

The overall development of the contrail is as expected. The wake vortices dominate the early flow field and much of the contrail descends with the wake, leaving behind a vertical curtain that detrains due to buoyancy. As the Crow instability develops, the vortices are perturbed from their initial linear shapes and eventually link. The pinching off of vortex loops leads to periodic, puffy shapes in the linear contrail. At late times, the decaying ambient turbulence field continues to spread the contrail plume.

Comparison of cases A and C in Figure 1 shows that moderate shear has little effect on vortex behaviour. The vortex wake descends at approximately the same rate, and develops the Crow instability, again forming periodic puffs. As development continues, the contrail is spread horizontally by the vertical shear. An increase in mixing is evident, shown by the reduced separation between the periodic puffs at later times. This mixing is driven by the vertical shear, which reduces the rate at which the ambient turbulent field decays.

Figure 2 shows a comparison of the flight-direction averaged contours of ice water content at the end of the simulation, $t = 1200$ s, for each of the four cases. The intensity of the ambient turbulence and the vertical shear have a large effect on the contrail cross-sectional shape at late times. More intense ambient turbulence increases cross-sectional area as higher mixing rates spread the contrail (cases A and B). When vertical shear is present, however, it dominates horizontal spreading (cases C and D). These effects are important to understanding the climate impact of contrails, since the horizontal and vertical thicknesses of contrails directly affect the cloud fraction and optical depth attributed to these anthropogenic clouds.

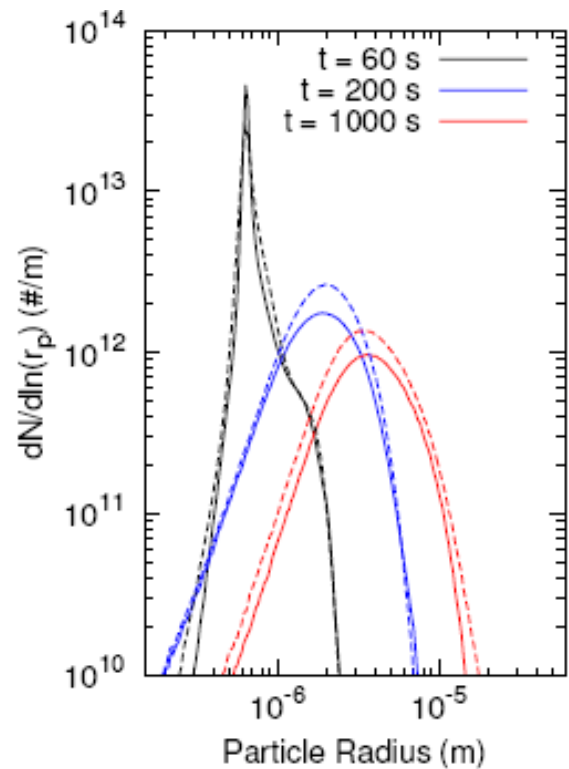
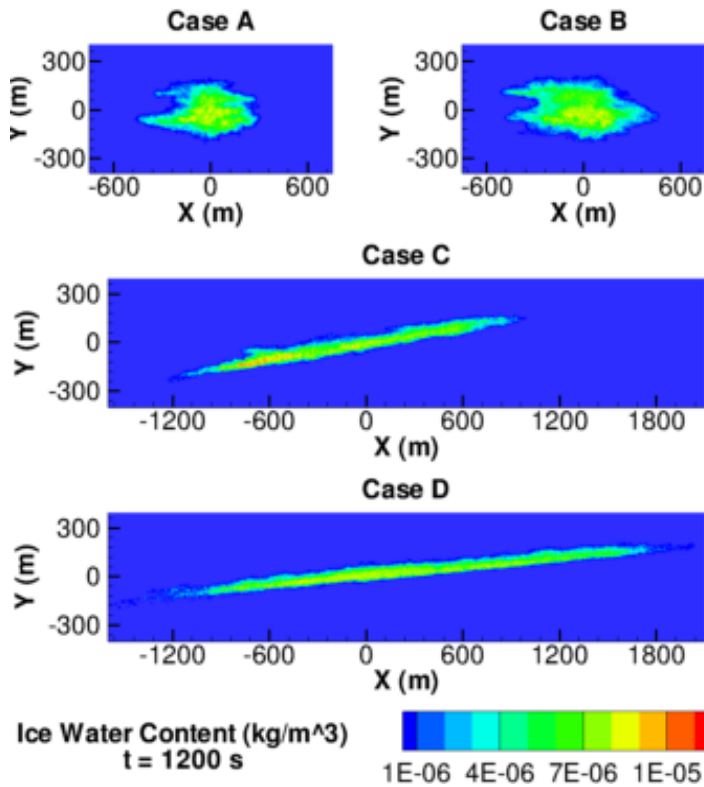


Figure 2. Flight-direction averaged contours of ice water content for each case after 1200 seconds of simulation time.

Figure 3. Particle radius distributions at three times during the simulation. Solid lines are for case A, dashed lines are for case D.

Figure 3 shows the size distribution of ice particles integrated over the domain at three times during the simulation for cases A and D. In both cases, as the contrail ages, the spectrum widens and the peak moves to higher radii as ice particles grow. The distribution peak is higher for case D at late times, reflecting the increased ice growth for this case as explained below.

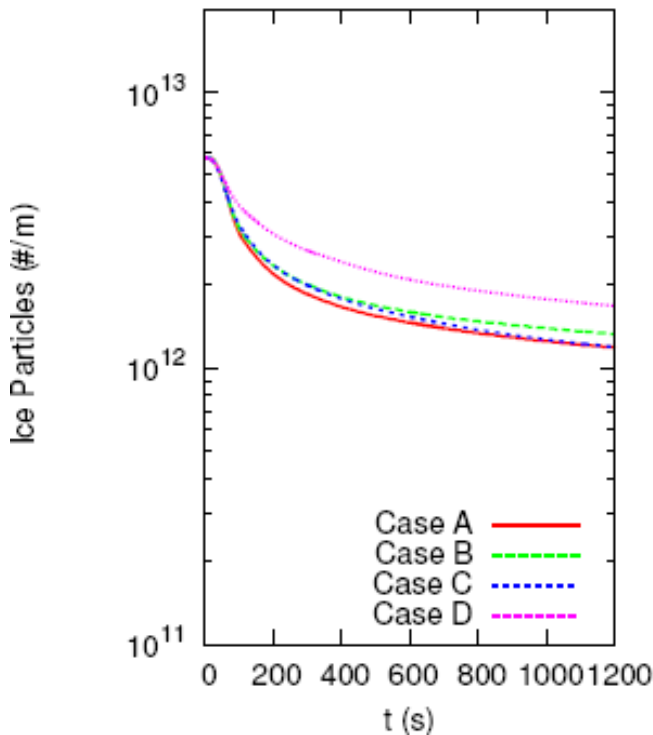


Figure 4. Time history of the domain integrated number of surviving ice particles for each case over 1200 seconds of simulation time.

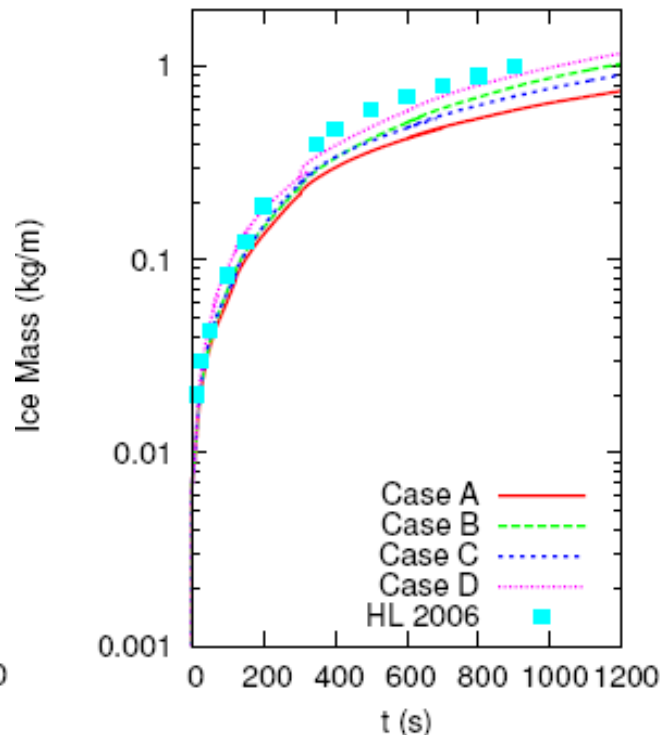


Figure 5. Time history of the domain integrated ice mass for each case over 1200 seconds of simulation time. The HL 2006 data is drawn from Huebsch and Lewellen (2006) for comparison.

Figures 4 and 5 show time history plots of domain-integrated ice statistics. As Huebsch and Lewellen (2006) noted, different turbulent realizations produce variations on the order of 10% in these statistics, so some care should be taken in interpreting the significance of differences between cases.

Figure 4 shows the number of surviving ice particles (that is, ice nuclei from which not all of the ice has sublimated) normalized by the domain length in the flight direction for each case. The number surviving in cases A–C is not significantly different, but case D showed 35% more surviving particles than any of the other cases. Two reasons are likely for this result. First, case D experienced more mixing of ambient air into the contrail than the other cases due to increased forcing of turbulence by its higher shear intensity. Second, the plume experienced more mixing of ambient air into the contrail because of its larger surface area due to its elongated shape. Since the ambient air is highly supersaturated with respect to ice, more mixing into the contrail makes more water vapour available for deposition to particles, resulting in fewer particles completely sublimating.

Figure 5 shows the ice water content normalized by the domain length in the flight direction for each case. The total amount of ice deposited during the simulation seems to depend most on the initial level of ambient turbulence, with cases A and C resulting in less ice than cases B and D. The magnitude of ice present at the end of the simulations is similar for each case, and matches well with results presented by Huebsch and Lewellen (2006) under similar conditions. This comparison provides confidence in our results, since the Huebsch and Lewellen simulation used a different LES code that included a binned microphysics model.

5 CONCLUSIONS

Our simulations of persistent contrails show the expected results and agree well with previous work. An initial set of four sensitivity cases has shown that ice growth is relatively insensitive to ambient turbulence levels produced by both a decaying isotropic turbulence field and by a linear vertical wind shear. These results have been assimilated into a subgrid contrail model (Naiman et al., 2009) to track contrails within a global climate simulation (Jacobson et al., 2009).

Additional LES cases will vary simulation parameters including aircraft size and engine configuration, and will study the effect of additional microprocesses such as sedimentation. Further study of the sensitivity of contrails to atmospheric and aircraft parameters will allow refinement of the subgrid contrail model for use in future climate studies. Furthermore, these high fidelity simulations will help establish confidence that the low fidelity subgrid contrail model captures the contrail dynamics that are relevant to climate model simulations.

6 ACKNOWLEDGEMENTS

This work was supported by the Partnership for AiR Transportation Noise and Emissions Reduction (PARTNER) and the Federal Aviation Administration (FAA) under award number DTFAWA-05-D=0006. Any opinions, findings, and conclusions or recommendations expressed in this material are those of the authors and do not necessarily reflect the views of PARTNER or the FAA. This research is also supported in part by the National Science Foundation through TeraGrid resources provided by LONI and NCSA. The initial flow field was provided by Dr. Steven L. Baughcum of the Boeing Company.

REFERENCES

- Jacobson, M.Z., J.T. Wilkerson, A.D. Naiman, and S.K. Lele, 2009: Quantifying the effects of aircraft on climate with a model that treats the subgrid evolution of contrails from all flights worldwide. *J. Geophys. Res. – Atmos.*, in review.
- Ham, F., K. Mattsson, G. Iaccarino, and P. Moin, 2007: Towards Time-Stable and Accurate LES on Unstructured Grids. *Lect. Notes Comput. Sci. Eng.* 56, 235-250.
- Huebsch, W.W., and D.C. Lewellen, 2006: Application of LES and binned microphysics for sensitivity study on contrail evolution. In: Sausen, R., A. Blum, D.S. Lee, and C. Brüning (eds.): *Proceedings of an International Conference on Transport, Atmosphere, and Climate (TAC)*. Luxembourg, Office for Official Publications of the European Communities, ISBN 92-79-04583-0, 167-172.
- Kärcher, B., Th. Peter, U.M. Biermann, and U. Schumann, 1996: The initial composition of jet condensation trails. *J. Atmos. Sci.* 53, 3066-3083.
- Lee, D.S., et al., 2009: Aviation and global climate change in the 21st century. *Atmos. Environ.* 43, 3520-3537.
- Lewellen, D.C., and W.S. Lewellen, 2001: The effects of aircraft wake dynamics on contrail development. *J. Atmos. Sci.* 58, 390-406.
- Mahesh, K., G. Constantinescu, and P. Moin, 2004: A numerical method for large-eddy simulation in complex geometries. *J. Comput. Phys.* 197, 215-240.
- Naiman, A.D., S.K. Lele, J.T. Wilkerson, and M.Z. Jacobson, 2009: A Subgrid Contrail Model for use in Large-Scale Atmospheric Simulations, in preparation.
- Paoli, R., J. Helie, and T. Poinsot, 2004: Contrail formation in aircraft wakes. *J. Fluid Mech.* 502, 361-373.
- Paoli, R., and F. Garnier, 2005: Interaction of exhaust jets and aircraft wake vortices: small-scale dynamics and potential microphysical-chemical transformations. *C.R. Physique* 6, 525-547.
- Shirgaonkar, A.A., and S.K. Lele, 2007: Large eddy simulation of early stage aircraft contrails. Technical Report No. TF-100, Flow Physics and Computational Engineering Group, Department of Mechanical Engineering, Stanford University, 208 pp.

Uptake of nitric acid in ice crystals in persistent contrails

D. Schäuble*, C. Voigt, B. Kärcher, P. Stock, H. Schlager

Deutsches Zentrum für Luft- und Raumfahrt, Institut für Physik der Atmosphäre, Oberpfaffenhofen, Germany

M. Krämer, C. Schiller, R. Bauer, N. Spelten

Institut für Stratosphärenforschung, FZ Jülich, Jülich, Germany

M. de Reus, M. Szakáll, S. Borrmann

Institut für Physik der Atmosphäre, Johannes-Gutenberg Universität Mainz, Mainz, Germany

U. Weers, T. Peter

Institut für Atmosphäre und Klima, ETH Zürich, Zürich, Switzerland

Keywords: Nitric acid, Partitioning, Uptake, Contrails, Cirrus

ABSTRACT: This is a short version of Schäuble et al. (2009) published in ACPD. In November 2006 cirrus clouds and almost 40 persistent contrails were probed with in situ instruments over Germany and Northern Europe during the CIRRUS-III campaign. At altitudes between 10 and 11.5 km and temperatures of 211 to 220 K contrails with ages up to 8 hours were detected. These contrails had a larger ice phase fraction of total nitric acid ($\text{HNO}_{3,\text{ice}}/\text{HNO}_{3,\text{tot}} = 6\%$) than the ambient cirrus layers (3 %). The differences in ice phase fractions between developing contrails and cirrus are likely caused by high plume concentrations of HNO_3 prior to contrail formation and large ice crystal number densities in contrails. The observed decrease of nitric acid to water molar ratios in ice with increasing mean ice particle diameter suggests that ice-bound HNO_3 concentrations are controlled by uptake of exhaust HNO_3 in the freezing plume aerosol in young contrails and subsequent trapping of ambient HNO_3 in growing ice particles in older (age > 1 h) contrails.

1 INTRODUCTION

In the tropopause region the ozone budget is influenced by heterogeneous processes such as the uptake of nitric acid (HNO_3) in cirrus clouds. Results from a global chemistry transport model indicate that HNO_3 uptake in cirrus ice particles and subsequent particle sedimentation has the potential to remove HNO_3 irreversibly from this region, leading to a large-scale reduction of gas phase HNO_3 concentrations (von Kuhlmann and Lawrence, 2006). At typical upper tropospheric NO_x levels the irreversible removal of gaseous HNO_3 reduces the concentrations of the ozone precursor nitrogen oxide ($\text{NO}_x = \text{NO} + \text{NO}_2$) and thus net ozone production rates. Reductions in local ozone concentrations of up to 14 % are found in chemistry box model studies (Meier and Hendricks, 2002).

During several field campaigns from the tropics to the Arctic the interaction of HNO_3 and cirrus ice crystals was experimentally investigated (e.g. Weinheimer et al., 1998; Popp et al., 2004; Voigt et al., 2006). Voigt et al. (2006) summarized these measurements in terms of average nitric acid to water molar ratios ($\mu = \text{HNO}_{3,\text{ice}}/\text{H}_2\text{O}_{\text{ice}}$) in cirrus ice particles and ice-bound fractions of total nitric acid ($\Phi = \text{HNO}_{3,\text{ice}}/\text{HNO}_{3,\text{tot}}$). Kärcher and Voigt (2006) explained the inverse temperature trend of the μ and Φ data by means of a model describing nitric acid uptake in growing ice crystals (trapping).

Simulations by Kärcher et al. (1996) indicate the formation of high levels of HNO_3 in jet aircraft exhaust plumes prior to contrail formation. E.g. Arnold et al. (1992) measured gas phase HNO_3 in young aircraft plumes. The efficient transfer of gaseous HNO_3 into plume aerosols and ice particles during contrail formation is demonstrated by Kärcher (1996) by means of microphysical simulations. Gao et al. (2004) measured HNO_3 in ice particles of a WB-57 aircraft contrail in the subtro-

* Corresponding author: Dominik Schäuble, Deutsches Zentrum für Luft- und Raumfahrt (DLR) – Institut für Physik der Atmosphäre, Oberpfaffenhofen, D-82234 Wessling, Germany. Email: dominik.schaeuble@dlr.de

ics at 14 – 15 km altitude. They observed HNO_3 in contrail particles at temperatures below 205 K, presumably in the form of NAT, but did not explicitly report ice phase HNO_3 concentrations.

An experimental quantification of the HNO_3 content in contrail ice particles as a function of mean ice particle size, a proxy for the microphysical age of persistent contrails, is lacking. So our observations provide an unprecedented data set on the uptake of HNO_3 in persistent contrails.

2 INSTRUMENTATION

During the CIRRUS-III campaign in November 2006, the Enviscope Learjet performed 5 flights at latitudes between 48°N and 68°N with instruments measuring NO_y , H_2O , small ice crystal size distributions, and condensation nuclei (CN). Total and gas phase NO_y were measured based on the chemiluminescence technique with a forward- and a backward-facing inlet, respectively. We calculated the concentration of particulate (in our case essentially ice phase) reactive nitrogen, $\text{NO}_{y,\text{ice}} = (\text{NO}_{y,\text{forw}} - \text{NO}_{y,\text{back}}) / \text{EF}_{\text{NO}_y}$, in contrails with a size-dependent relationship for the enhancement factor $\text{EF}_{\text{NO}_y}(d)$ (Belyaev and Levin, 1974). Nitric acid was directly measured during the flight on 28 November (nylon filter technique). The HNO_3 concentration on 24 and 29 November was derived from NO_y observations and the HNO_3 to NO_y ratio (0.45 ± 0.2) detected on 28 November. This ratio is in good agreement with previous observations in midlatitudes (e.g. Talbot et al., 1999).

In young contrails NO_x constitutes the major fraction of NO_y . A microphysical plume model study (Meilinger et al., 2005) including detailed heterogeneous aerosol and ice phase chemistry indicates that the chemical conversion into HNO_3 is small in contrails in terms of the gas phase HNO_3/NO_y ratio ($\approx 1\%$) within the first ten hours after emission due to heterogeneous dehydroxylation and production of HONO. In such contrails the gas phase HNO_3 concentration is supposed to be controlled by entrainment of ambient HNO_3 . Thus, we used the ambient HNO_3 concentration as an approximation for the concentration inside contrails. In cirrus clouds as well as in contrails, HNO_3 is assumed to account for 100 % of NO_y in ice particles. The uptake of PAN and HONO on ice crystals is probably small compared to HNO_3 (Bartels-Rausch et al., 2002) and N_2O_5 and HO_2NO_2 are quickly photolyzed during daytime.

Total water was measured with the forward-facing inlet of the Fast In situ Stratospheric Hygrometer (FISH) (Zöger et al., 1999) and water vapour was detected with a TDL instrument (OJSTER). The Forward Scattering Spectrometer Probe FSSP-100 (Borrmann et al., 2000) measured the number concentration and size distribution of particles with diameters of 2.8 – 29.2 μm .

Contrails were identified from distinct simultaneous short-term increases in the time series of the concentrations of $\text{NO}_{y,\text{gas}}$, $\text{NO}_{y,\text{tot}}$, CN (> 5 nm diameter, not discussed here), and ice particles. Lower limits of 0.1 nmol/mol for $\Delta\text{NO}_{y,\text{gas}}$ and 100 cm^{-3} for ΔCN enabled a separation of contrails from cirrus clouds that were not affected by aviation within the last 8 h of their lifetime. Contrails often exhibit significant spatial inhomogeneities in structure and dilution properties. The spatially random sampling of contrails and merging of several individual contrails introduce considerable uncertainty in the exact determination of contrail age from plume dilution data which is difficult to quantify.

3 NITRIC ACID PARTITIONING AND ICE WATER CONTENT IN CONTRAILS

European Centre for Medium-Range Weather Forecasts analyses indicate that the top regions of frontal cirrus layers were probed on 24 and 29 November, whereas on 28 November the observations originate from deeper inside cirrus clouds. Figure 1 shows a typical time series of data from the flight on 24 November over Germany.

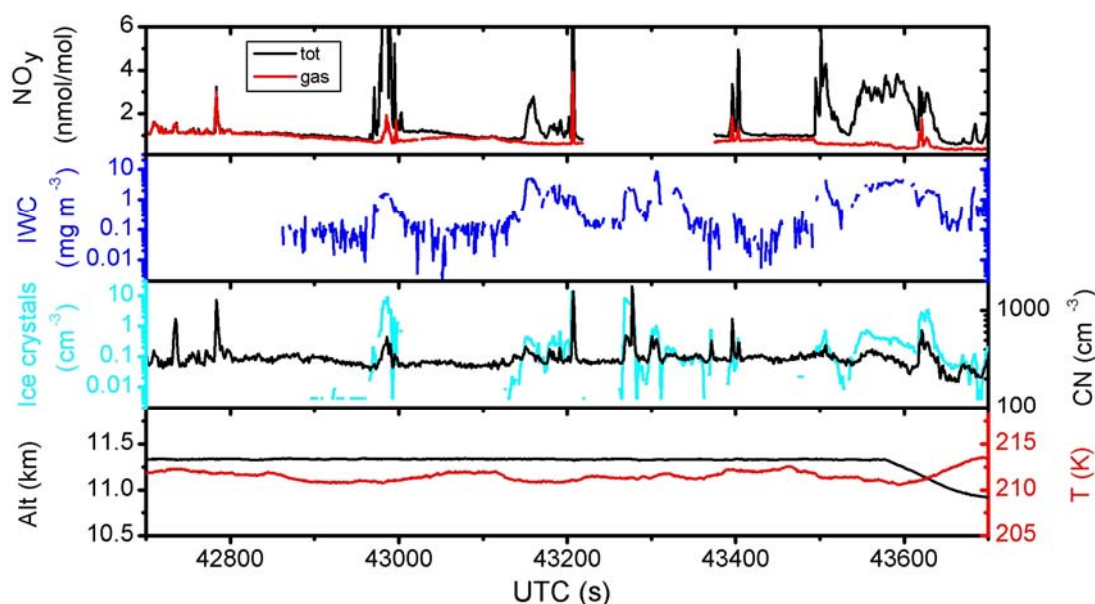


Figure 1. Time series of gas phase and total NO_y , ice water content (IWC), number densities of ice particles with approximate diameters between 2.8 and 29.2 μm , CN ($> 5\text{nm}$) concentration, as well as altitude and temperature for a period of the flight on 24 November 2006. Exhaust plume at 42,780 s, contrails at approximately 42,980 s, 43,200 s, 43,400 s, and 43,620 s, and cirrus clouds around 43,150 s and 43,550 s. Gaps in the NO_y measurements are due to calibration procedures.

On average, contrails were found to have larger Φ values than the cirrus layers under similar conditions. This is illustrated by means of the probability density function of Φ (Fig. 2a). At temperatures between 211 and 220 K, contrail ice particles contained on average 6 % (cirrus 3 %) of the total nitric acid.

Twelve young contrails with $\Delta\text{NO}_{y,\text{gas}} > 0.75$ nmol/mol, corresponding to ages $< 1\text{h}$, had even larger ice phase nitric acid fractions (9 %). The maximum Φ measured in contrails was 22 %. The gas phase equivalent mixing ratio of nitric acid in ice, $\text{HNO}_{3,\text{ice}}$, is 14 pmol/mol in contrails compared to 6 pmol/mol in the cirrus layers. The mean $\text{HNO}_{3,\text{ice}}$ in the young contrails is 21 pmol/mol.

Figure 2b (top panel) shows the temperature dependence of the ice phase molar ratios of nitric acid and water (μ) in contrails (red circles) and in the surrounding cirrus layers (grey circles) that were not recently influenced by aviation. The μ values generally increase with decreasing temperature, as the probability of HNO_3 molecules to escape from the growing ice surfaces after adsorption is reduced at low temperatures leading to more efficient trapping of HNO_3 (Kärcher and Voigt, 2006).

The curves are results from the trapping model by Kärcher et al. (2009). The dashed and solid model curves were computed for HNO_3 partial pressures of 3×10^{-8} hPa and 6×10^{-8} hPa, respectively, roughly capturing the range of measured values occurring in contrails and cirrus (see above). The trapping model bounds the observed mean μ values in cirrus (black squares) very well at 211–220 K. The model assumes temperature-dependent mean ice particle growth rates (net supersaturations) to estimate steady-state molar ratios. Deviations of individual data points from the mean model curves are likely caused by variable growth/sublimation histories of the observed ice particles. Further, the μ of small ice crystals may be strongly influenced by the composition of the freezing aerosol resulting in values exceeding the means (Sect. 4). The mean $\text{HNO}_3/\text{H}_2\text{O}$ molar ratio in contrails of 4×10^{-6} is found to be approximately twice as large as in the cirrus layers (2×10^{-6}).

Figure 2b (bottom panel) illustrates the IWC of contrails and cirrus clouds versus temperature. The difference between the CIRRUS-III IWCs and the climatological means (solid curve) by Schiller et al. (2008) are discussed in Schäuble et al. (2009). The contrails have a slightly larger mean IWC (red squares) than the cirrus clouds, 1.8 and 1.3 mg m^{-3} , respectively. The IWC of young contrails 2.9 mg m^{-3} is more than twice the cirrus mean. The H_2O aircraft emissions become unimportant for contrails older than a few minutes, according to plume dilution estimates (Gerz et al., 1998). Differences between contrail and cirrus IWCs are expected to diminish over time as most of the H_2O in contrail ice condenses from the ambient air during ice particle growth.

We additionally report a striking difference between measured contrail and cirrus cloud ice particle number densities in the FSSP-100 size range 2.8–29.2 μm in diameter, 1.5 cm^{-3} and 0.21 cm^{-3} ,

respectively. Figure 3a shows the increase of the ice-bound nitric acid fraction with increasing ice crystal number densities in contrails (means in black). Together this is one explanation for the larger Φ in contrails compared to cirrus.

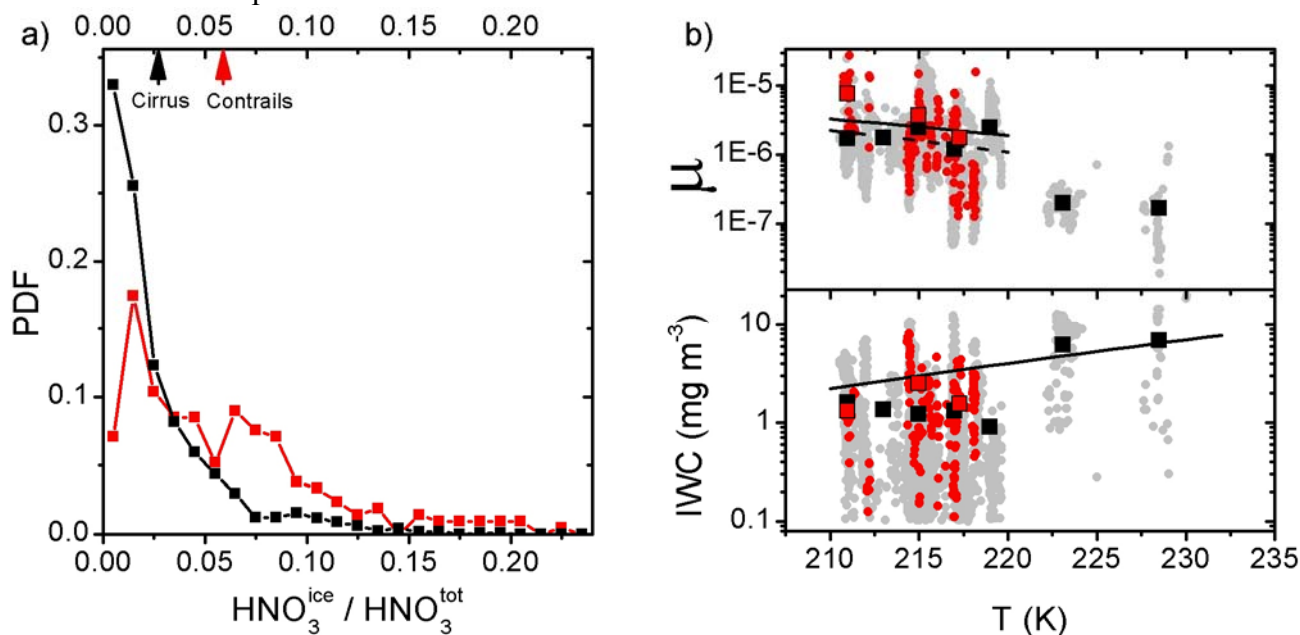


Figure 2. a) Normalized probability density function of the ice phase fraction of total HNO_3 , Φ , for contrails (red) and cirrus clouds (black). Arrows indicate the means for the temperature range (211–220 K) where contrails occurred. b) The temperature dependence of the (top) molar ratio of nitric acid to water in ice particles ($\mu = \text{HNO}_{3,\text{ice}}/\text{H}_2\text{O}_{\text{ice}}$) and (bottom) ice water content (IWC) of contrails (red circles) and cirrus clouds (grey circles). Squares are means over 2 K temperature bins. Curves are model results, see text for details. The curve in the bottom panel depicts the mean cirrus IWCs based on a large number of in situ measurements at midlatitudes (Schiller et al., 2008).

4 NITRIC ACID UPTAKE IN DEVELOPING CONTRAILS

Given the limited amount of contrail data, it is unclear whether the systematic differences in ice phase fraction and molar ratios in ice presented in Section 3 are representative. Nevertheless, sorting the molar ratio data as a function of the mean ice particle size enables us to study the HNO_3 uptake process in contrails in more detail.

Figure 3b shows the molar ratios (grey circles) along with the mean (black squares) and median (grey squares) values of the contrails probed during CIRRUS-III as a function of the mean ice particle diameter. We associate rough estimates of the contrail age with the mean diameter based on the gas phase ΔNO_y data (Schumann et al., 1998), as indicated in the figure. In persistent contrails, the mean size increases due primarily to uptake of H_2O from the gas phase (depositional growth). The measurements show a clear trend of decreasing μ with increasing mean size or age. Young contrails with ages 10–15 min and mean diameters $7\text{ }\mu\text{m}$ have a mean $\mu \approx 10^{-5}$, while older contrails with ages $> 1\text{ h}$ and mean diameters $> 10\text{--}15\text{ }\mu\text{m}$ exhibit values closer to the mean 2×10^{-6} of the cirrus data. How are the high molar ratios in young contrails brought about? We argue that a high concentration of HNO_3 entered the ice particles already during contrail formation, when they are very small (mean diameters $1\text{ }\mu\text{m}$), leading to very high molar ratios. Subsequent depositional growth increases the size per ice particle, while trapping in young contrails (mean diameters $1\text{--}10\text{ }\mu\text{m}$) only adds a small contribution to the HNO_3 content per particle; both effects cause μ to decrease in this phase of contrail development. Further growth to larger sizes diminishes the role of the initially high molar ratios and trapping takes over the dominant part in determining μ . These processes are illustrated by the model curves as explained in detail in Schäuble et al. (2009).

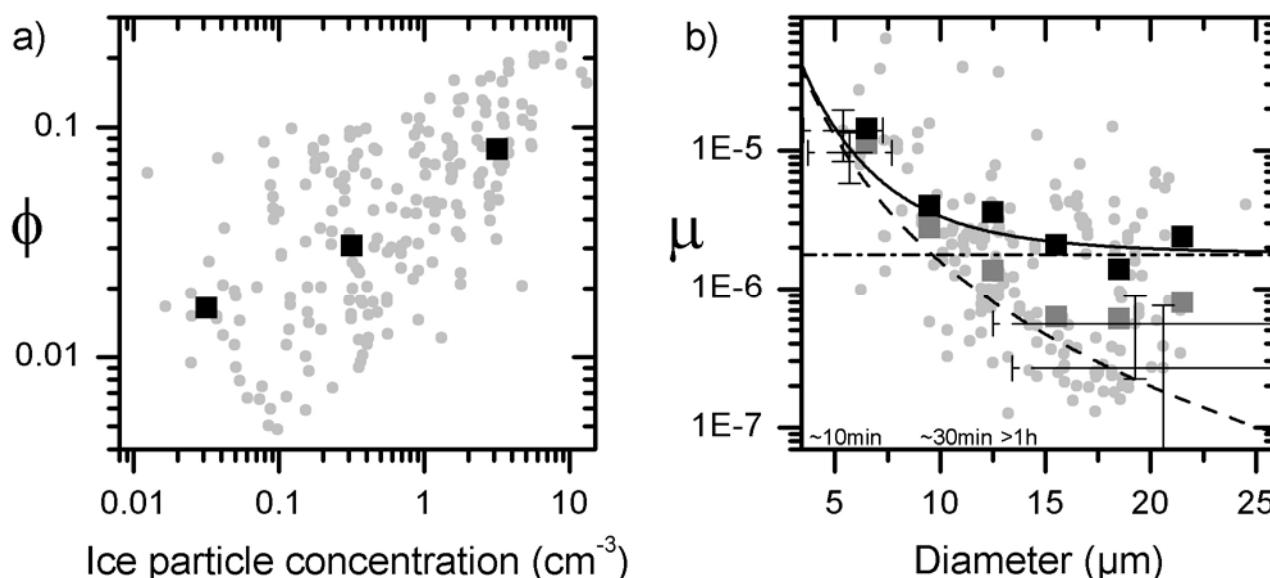


Figure 3. a) Ice-bound nitric acid fraction versus ice crystal number density for mean ice particle diameters between 2.8 and 29.2 μm . b) Molar ratios of nitric acid to water in contrail ice particles μ versus mean ice particle diameter. A detailed description is given in Schäuble et al. (2009).

5 SUMMARY AND CONCLUSIONS

During the CIRRUS-III field campaign gas phase and ice phase reactive nitrogen, ice water content, and ice crystal size distributions were measured in contrails and cirrus at midlatitudes close to the tropopause. The temperatures and HNO_3 partial pressures were in the ranges 210 – 230 K and $3 - 6 \times 10^{-8}$ hPa, respectively. The observed uptake of HNO_3 in ice particles residing in the top layers of frontal cirrus clouds confirms previous results from airborne field campaigns carried out in polar, midlatitude, and sub-tropical regions (Voigt et al., 2006).

On average the probed contrails contained twice as much ice-bound HNO_3 as the cirrus clouds within 211 – 220 K, 14 pmol/mol and 6 pmol/mol, respectively. Thus, the mean fraction of total HNO_3 in ice particles was considerably larger in the contrails (6 %) than in the cirrus layers (3 %). In young contrails (approximate age < 1 h) this fraction was even higher (9 %). The measured molar ratios of HNO_3 and H_2O in contrail ice particles exceeded 10^{-5} for small particle sizes, or contrail ages. For older contrails, molar ratios approached the mean value of 2×10^{-6} detected in the cirrus layers. Averaged over all detected contrails regardless of age, this caused the mean molar ratios in contrails to be about twice as large as in the cirrus clouds.

Motivated by our study, contrails may be regarded as an atmospheric laboratory to study HNO_3 uptake during ice particle growth. Our data show that ice phase $\text{HNO}_3/\text{H}_2\text{O}$ molar ratios decrease during contrail ageing. This dependence was explained by uptake of high levels of HNO_3 into the freezing aerosol particles during ice formation in contrails and subsequent trapping of relatively low levels of ambient HNO_3 in growing contrail ice particles. In young contrails with ages < 1 h or mean diameters < 10 μm , the ice phase HNO_3 concentrations are therefore largely controlled by the jet engine NO_x and OH emission indices. More airborne measurements with extended instrumentation are needed to study the dependence of HNO_3 uptake on HNO_3 partial pressure and to better quantify ice particle size distributions in developing contrails.

The results of this study help constrain chemical-microphysical models simulating heterogeneous chemistry in persistent contrails in order to constrain the impact of plume processing of NO_x emissions on the chemical production or loss of ozone.

REFERENCES

- Arnold, F., J. Scheid, T. Stipl, H. Schlager, and M.E. Reinhardt, 1992: Measurements of jet aircraft emissions at cruise altitude I: the odd-nitrogen gases NO , NO_2 , HNO_2 and HNO_3 , *Geophys. Res. Lett.*, 19, 2421 – 2424.

- Bartels-Rausch, T., B. Eichler, P. Zimmermann, H. W. Gäggeler, and M. Ammann, 2002: The adsorption of nitrogen oxides on crystalline ice, *Atmos. Chem. Phys.*, 2, 235 - 247.
- Belyaev, S.P. and L. M. Levin, 1974: Techniques for collection of representative aerosol samples, *J. Aerosol Sci.*, 5, 325 - 338.
- Borrmann, S., B. P. Luo, and M. Mishchenko, 2000: Application of the T-matrix method to the measurement of aspherical (ellipsoidal) particles with forward scattering optical particle counters, *J. Aerosol Sci.*, 31, 789 - 799.
- Gao, R. S., P. J. Popp, D. W. Fahey, T. P. Marcy, R. L. Herman, E. M. Weinstock, D. Baumgardner, T. J. Garrett, K. H. Rosenlof, T. L. Thompson, T. P. Bui, B. A. Ridley, S. C. Wofsy, O. B. Toon, M. A. Tolbert, B. Kärcher, T. Peter, P. K. Hudson, A. J. Weinheimer, and A. J. Heymsfield, 2004: Evidence that nitric acid increases relative humidity in low-temperature cirrus clouds, *Science*, 303, 516 - 520.
- Gerz, T., T. Dürbeck, and P. Konopka, 1998: Transport and effective diffusion of aircraft emissions, *J. Geophys. Res.*, 103, 25905 - 25913.
- Kärcher, B., 1996: Aircraft-generated aerosols and visible contrails, *Geophys. Res. Lett.*, 23, 1933 - 1936.
- Kärcher, B. and C. Voigt, 2006: Formation of nitric acid/water ice particles in cirrus clouds, *Geophys. Res. Lett.*, 33, L08806, doi10.1029/2006GL025927.
- Kärcher, B., M. M. Hirschberg, and P. Fabian, 1996: Small-scale chemical evolution of aircraft exhaust species at cruising altitudes, *J. Geophys. Res.*, 101, 15169 - 15190.
- Kärcher, B., J. P. D. Abbatt, R. A. Cox, P. J. Popp, and C. Voigt, 2009: Trapping of trace gases by growing ice surfaces including surface-saturated adsorption, *J. Geophys. Res.*, 114, D13306, doi:10.1029/2009JD011857.
- Meier, A. and J. Hendricks, 2002: Model studies on the sensitivity of upper tropospheric chemistry to heterogeneous uptake of HNO_3 on cirrus ice particles, *J. Geophys. Res.*, 107, 4696, doi10.1029/2001JD000735.
- Meilinger, S. K., B. Kärcher, and Th. Peter, 2005: Microphysics and heterogeneous chemistry in aircraft plumes - high sensitivity on local meteorology and atmospheric composition, *Atmos. Chem. Phys.*, 5, 533 - 545, 2005.
- Popp, P.J., R. S. Gao, T. P. Marcy, D. W. Fahey, P. K. Hudson, T. L. Thompson, B. Kärcher, B. A. Ridley, A. J. Weinheimer, D. J. Knapp, D. D. Montzka, D. Baumgardner, T. J. Garrett, E. M. Weinstock, J. B. Smith, D. S. Sayres, J. V. Pittman, S. Dhaniyala, T. P. Bui, and M. J. Mahoney, 2004: Nitric acid uptake on subtropical cirrus cloud particles, *J. Geophys. Res.*, 109, D06302, doi10.1029/2003JD004255.
- Schäuble, D., C. Voigt, B. Kärcher, P. Stock, H. Schlager, M. Krämer, C. Schiller, R. Bauer, N. Spelten, M. de Reus, M. Szakáll, S. Borrmann, U. Weers, T. Peter, 2009: Airborne measurements of the nitric acid partitioning in persistent contrails, *Atmos. Chem. Phys. Discuss.*, 9, 1 - 22.
- Schiller, C., M. Krämer, A. Afchine, N. Spelten, and N. Sitnikov, 2008: Ice water content of Arctic, midlatitude, and tropical cirrus, *J. Geophys. Res.*, 113, D24208, doi10.1029/2008JD010342.
- Schumann, U., H. Schlager, F. Arnold, R. Baumann, P. Haschberger, and O. Klemm, 1998: Dilution of aircraft exhaust plumes at cruise altitudes, *Atmos. Environ.*, 32, 3097 - 3103.
- Talbot, R.W., J. E. Dibb, E. M. Scheuer, Y. Kondo, M. Koike, H. B. Singh, L. B. Salas, Y. Fukui, J. O. Ballenthin, R. F. Meads, T. M. Miller, D. E. Hunton, A. A. Viggiano, D. R. Blake, N. J. Blake, E. Atlas, F. Flocke, D. J. Jacob, and L. Jaegle, 1999: Reactive nitrogen budget during the NASA SONEX mission, *Geophys. Res. Lett.*, 26, 3057 - 3060.
- Voigt, C., H. Schlager, H. Ziereis, B. Kärcher, B. P. Luo, C. Schiller, M. Krämer, P. J. Popp, H. Irie, and Y. Kondo, 2006: Nitric acid in cirrus clouds, *Geophys. Res. Lett.*, 33, L05803, doi10.1029/2005GL025159.
- von Kuhlmann, R. and M. G. Lawrence, 2006: The impact of ice uptake of nitric acid on atmospheric chemistry, *Atmos. Chem. Phys.*, 6, 225 - 235.
- Weinheimer, A. J., T. L. Campos, J. G. Walega, F. E. Grahek, B. A. Ridley, D. Baumgardner, C. H. Twohy, B. Gandrud, and E. J. Jensen, 1998: Uptake of NO_y on wave-cloud ice particles, *Geophys. Res. Lett.*, 25, 1725 - 1728.
- Zöger, M., A. Afchine, N. Eicke, M. T. Gerhards, E. Klein, D. S. McKenna, U. Mörschel, U. Schmidt, V. Tan, F. Tuitjer, T. Woyke, and C. Schiller, 1999: Fast in situ stratospheric hygrometers: A new family of balloon-borne and airborne Lyman- α photofragment fluorescence hygrometers, *J. Geophys. Res.*, 104, 1807 - 1816.

Peculiarities of airplane vortex wakes and condensation trails interaction and their mathematical modeling

A.N. Zamyatin^{*}, V.T. Dedesh, R.L. Kagarmanov
Gromov Flight Research Institute (GFRI)

A.I. Zhelannikov
N.E.Zhukovski Military-air engineering academy

Keywords: vortex wakes, condensation trails, mathematical modeling

ABSTRACT: The unique photos, demonstrating air flow peculiarities in aircraft aerodynamic wake vortex, are presented in the report. On the bases of these materials analysis and also basing on obtained in flight the quantitative data and calculation wake models results, there are presented the patterns of air flow development and structure in aircraft aerodynamic wake. It is shown that scheme of formed aircraft wake vortex structure could be presented as two independent air flow areas. These areas are separated by closed current surface. First – more spacious area corresponds to practically plane spiral flows, consisting of two vortices of opposite direction. The second one is located in the small area of vortices axis and corresponds to spatial flow with circumferential flow velocities, analogous to solid body rotation and with intensive alternating axial flows. Presented in the report are pictures, obtained in real flight conditions with the help of visualization, demonstrating interaction of wake vortex and contrail for aircraft of different types. It is shown that depending on engine location at the aircraft, the contrail could practically do not interact with aerodynamic wake, mainly being captured by external vortex flow and dissipated at relatively small distances from aircraft. Contrail could also being captured by external vortex flow, then got to vortices nuclei and hold by them rather long. Examples of mathematical modeling of a vortex wakes of the airplane, based on MDV utilization are presented in the report, in view of influence of engines jets and conditions of an atmosphere. As an example of wakes calculation for airplanes A - 310, A - 380 and SSJ-100, the qualitative agreement of results of calculations and visualization of streams in wakes is shown. It indicates a possibility of usage and perfection of this method of calculation for the purposes of model creation, account of wake vortices interaction with contrails both in near and far wake, down to their destruction.

1 AIRFLOW STRUCTURE IN AIRCRAFT WAKE

Schematic of airplane wake development could be divided into several stages: vortex pair formation, inviscid development, disturbances development, viscid development, destruction. Qualitatively, the flow patterns within one stage are identical for all aircraft and flight conditions. In the first stage the vortex sheet rolling-up after the wing occurred with followed vortex system formation, converting then in the pair of contrary rotating vortices. Airflow structure at this stage depends on circulation distribution along the wing. Local aerodynamics peculiarities could noticeably influence wake formation.

The second stage of wake development is characterized by availability of formed pair of intensive vortices. During this stage, viscosity influence on vortex cinematic characteristics is practically absent, vortex system geometry is changed insignificantly and vortex system descends with small, slow varying speed.

The third stage of wake development features varying geometry of vortices axis while its cinematic characteristics remain the same as in previous stage.

Both geometry and cinematic wake characteristics are varied in the forth stage. Explosive distor-

^{*} *Corresponding author:* Andrey N. Zamyatin, Gromov Flight Research Institute, Zhukovsky t., Moscow Reg., 140186 Russia. Email: frizamyatin@mail.ru

tions start to develop.

Finally, the fifth stage features qualitative change of vortex structure of wake and its conversion either in closed distorted vortical rings or in attenuating disturbances.

The structure of formed wake vortex of airplane in the second, third and fourth stages of development could be divided schematically in two independent flow zones. These zones are separated by closed current surface. First – more spacious zone corresponds to practically flat vortical flow, consisting of two vortices of opposite direction. The second one is located in the small zone near vortices axis and corresponds to spatial flow with circumferential flow velocities, analogous to solid body rotation with intensive axial flows. This scheme of wake vortex air flow is good illustrated by experimental results.

With the help of vortex flow visualization in vertical cross section the dynamics of vortex wake development after freely flying model of A-300 aircraft, launched by catapult is shown in Figure 1.1. The process of spiral-like rolling-up of vortex in wake after aircraft half-wing is absolutely evident. It could be seen in vortex center the not visualized flow zone – vortex nucleus, bounded by closed current surface. The nucleus remains invisible because this closed current surface is impermeable.

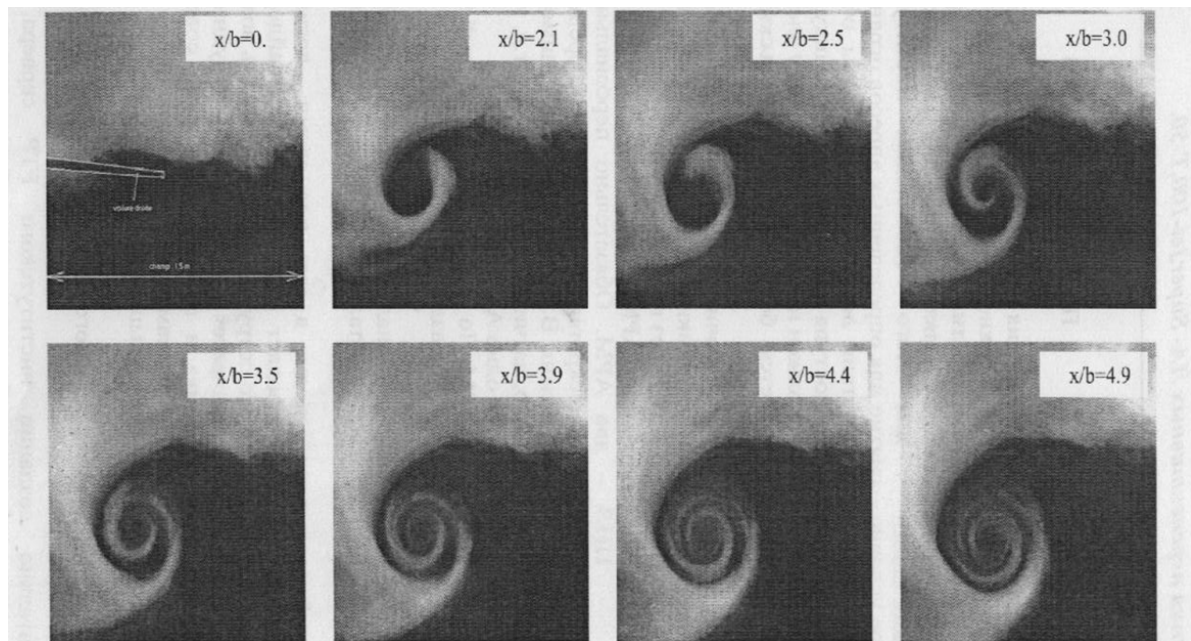


Figure 1.1 The dynamics of vortex wake development after freely flying model of A-300 aircraft. Analogous flow pattern could be seen in real flights also. Both visualized external flat vortical flow and not visualized vortices nuclei are clearly seen in B-767 airplane wake after flyover through the cloud, see Figure 1.2.



Figure 1.2 Natural visualization of B-767 wake

Having shot a gala firework, the C-17A airplane continuous its flight (Fig. 1.3). Large smoke of pyrotechnics had visualized air flow in wake. Both external vortex motion in wake and free from smoke vortices nuclei could be seen absolutely clear.



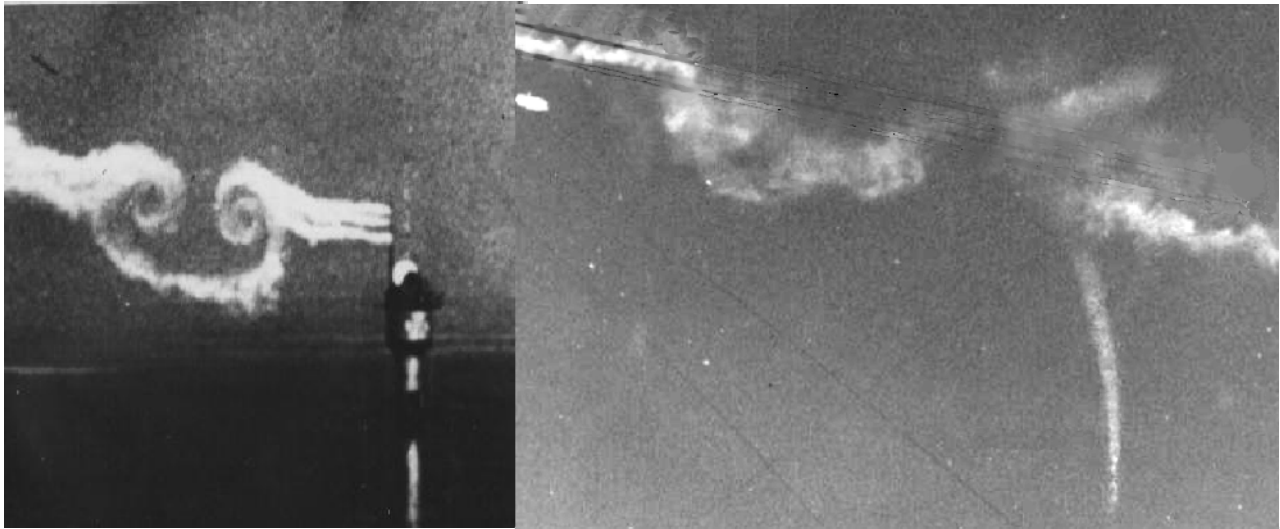
Figure 1.3 Artificial visualization of C-17A wake

Visualization of one of vortices in BAe-146 airplane wake had occurred during fly over upward smoke stream, see Figure 1.4. Both zones of air flow in airplane wake again could be observed distinctly.

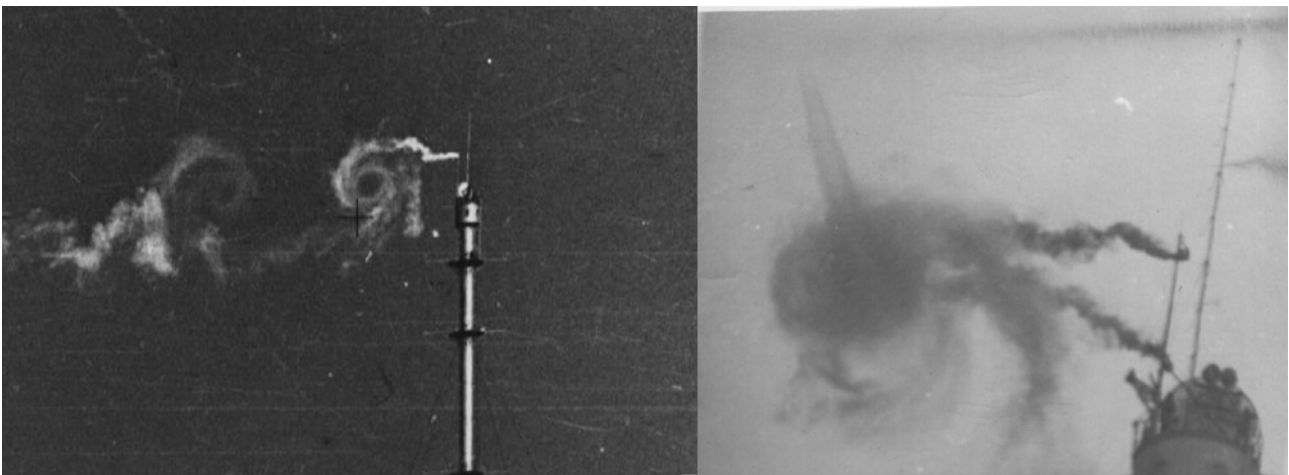


Figure 1.4 Visualization of one of vortices in BAe-146-200A wake at fly over an upward smoke stream

Artificial visualization of external zone of wake vortex was made in special flight research with the help of smoke cartridges, installed in a mast. Pictures of smoke capturing by wake vortices of L-39 and Tu-124 airplanes are shown in Figure 1.5.



L-39



Tu – 124

Figure 1.5 Smoke visualization of a wake with the help of cartridges, installed in a mast

Again external flow in wake vortex is clearly observed and closed current surface on nucleus boundary prevents air flow visualization in vortices nuclei.

The flow in vortices nuclei could be visualized only in case of visualization source location immediately in vortex nucleus or with the help of wake formation process visualization, that is during visualization of vortex sheet rolling-up.

Sufficiently sharp visualization of flow in vortex nucleus was obtained with the help of artificial visualization, when one of smoke cartridges installed in the mast occurred in the vortex nucleus. Pattern of such flow is shown in Figure 1.6. It is shown the sequence of pictures of aircraft wake smoke visualization, made sideways with small time interval. Red circles depict flow area of visualized vortex pair in case when smoke source has got in nucleus of one of vortices. Both zones of flow were visualized in example presented.



Figure 1.6. Visualization of nuclei zone, when the smoke source has got in nucleus (L-39)

Artificial visualization of vortices by smoke generators located at 70...90 % of wing half span provides smoke penetration into vortices nuclei. Nuclei in turn hold smoke inside closed current surface and make the wake visible up to it destruction.

Shown in Figure 1.7 are the smoke visualization of vortices of L-39 and Tu-124 wakes. Smoke generators, mounted in 80% of half wing span under each wing provided vortices nuclei visualization up to wake destruction.

Tu-124



L-39

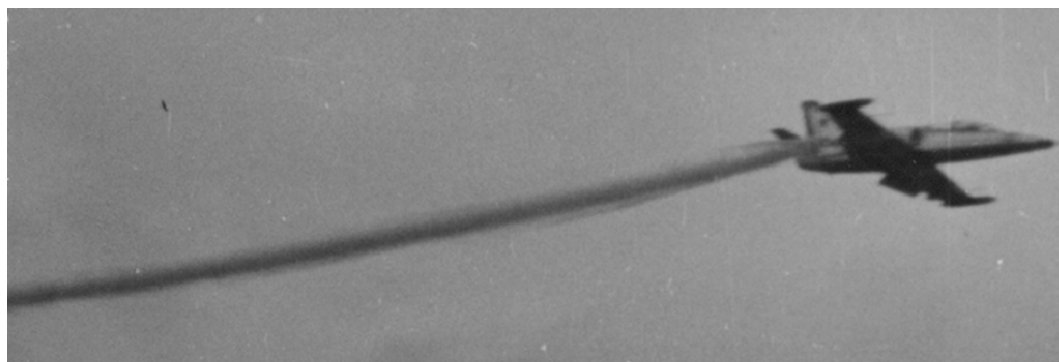


Figure 1.7 Smoke visualization of vortices nuclei

At certain meteorological conditions, the areas of over tenuity become visible. As an example the natural visualizations of zones in nuclei of vortices and also zones over the wings are presented in the next Figure 1.8.



Figure 1.8 Natural visualization of vortex nucleus zone and external zone of flat vortical flow (B-777)
Natural visualization of vortex nucleus zone could expand for long distances up to wake destruction, while conditions for it existence persist. Also observed in the picture is an external flow, visualization of which occurred as a result of local cloudiness capturing.

2 AIRCRAFT WAKE VORTICES INTERACTION WITH CONDENSATION TRAILS

Contrails could be captured by vortex flow, penetrate into vortices nuclei and to be hold by it rather long, could be captured by external vortex flow or could practically do not interact with vortex wake depending from aircraft configuration – engines location on the aircraft.

The first situation, when contrails are captured by external vortical flow and penetrate into vortices nuclei and hold by it rather long is illustrated in the Figure 2.1. This picture is observed in case of aircraft with several engines, installed under the wings, like B-747, IL-86 aircraft etc.

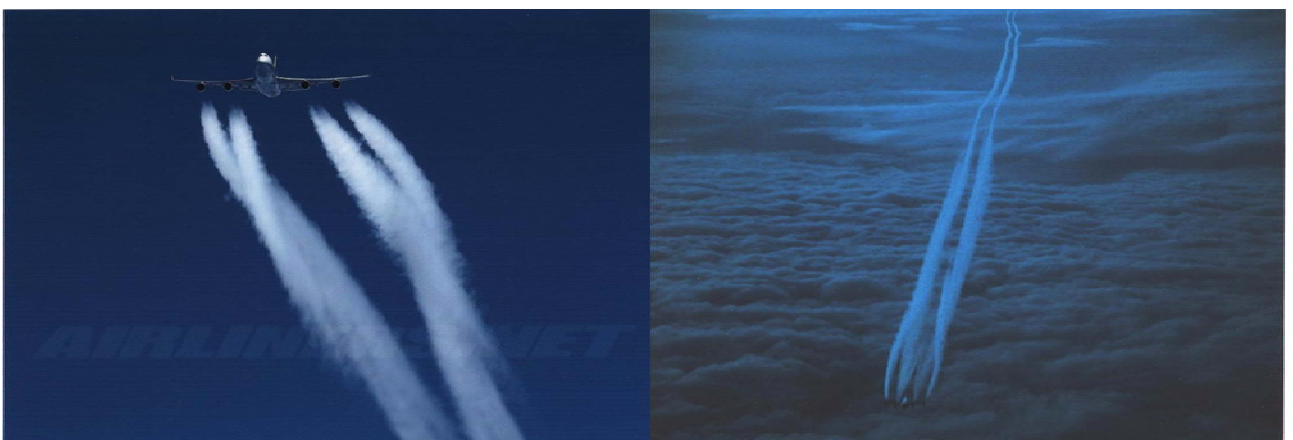


Figure 2.1 Capture of contrail by both zones of vortex wake (B-747) (two engines under each wing)
It is evident that contrail capture by vortex flows of aircraft vortex wake occurs at the pictures presented. Engines location is such that vortex wake captures contrail both by it external vortical flow and by vortices nuclei. It seems that conditions for stable existence of contrail disappear and the flow becomes invisible in external zone of vortices at a distance of 5...10 wing spans.

Conditions for stable existence of contrail persist inside closed surface of vortex nucleus and the flow remains to be visible for many kilometers after the airplane (see Figure 2.2).



Figure 2.2 Existence of contrail in nuclei zone at long distance behind IL-86

Shown on the pictures presented is the sufficiently extended visualization of airplane vortex wake, occurred as a result of contrail capture by vortices nuclei what make it possible to trace the development of a wave instability of vortex pair and to observe explosive vortices destructions. But it seems impossible to give an answer to the question of airplane wake vortex destruction influence on captured contrail existence and its conversion in cirrus clouds without additional research.

In case of airplane with engines location one by one under each wing, like B-767, B-777 airplanes, the contrail, as a rule, is captured only by an external zone of vortex flow and exists for a short time. Taking into account the relative geometric position of engines and vortices in B-777 or B-767 airplanes wake the contrail penetration into vortices nuclei is unlikely for airplanes of such configuration. The picture of B-777 aircraft wake in real flight, presented in the Figure 2.3, confirms that, but for more precise results with quantitative data, the additional specially prepared researches are necessary.

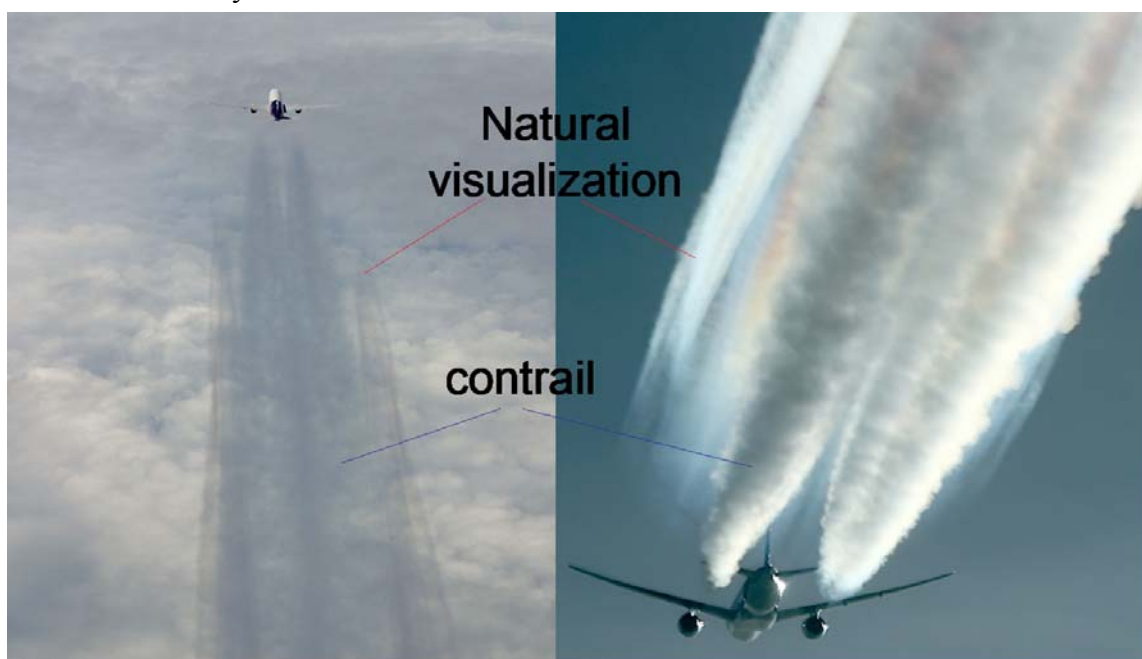


Figure 2.3 Capture of contrail by external vortical zone (B-777) (one engine under each wing)

There is no evident capture of contrail by vortex flow for the airplane with configuration analogous to Tu-154, as it follows from picture on Figure 2.4.



Figure 2.4 Without capture of contrails by vortex wake (Tu-154)
Used photographic materials are taken from internet and received by authors.

3 MATHEMATICAL MODELING OF A VORTEX WAKES OF THE AIRPLANE , BASED ON MDV UTILIZATION IN VIEW OF INFLUENCE OF ENGINES JETS

3.1 Problem statement. Discrete vortex method

Considered here is the unsteady flow of an ideal incompressible fluid past an aircraft flying at the speed W_∞ (Figure 3.1). The motion of the aircraft and deflection of its control surfaces and high-lift devices are performed in an arbitrary way. The aircraft's surface is considered impermeable. The flow is potential everywhere outside of the aircraft and vortex wakes generated by flow separation from its surface. The vortex wakes represent thin vortex sheets, i.e., surfaces of discontinuity for the tangential component of the velocity. The lines of flow separation are specified.

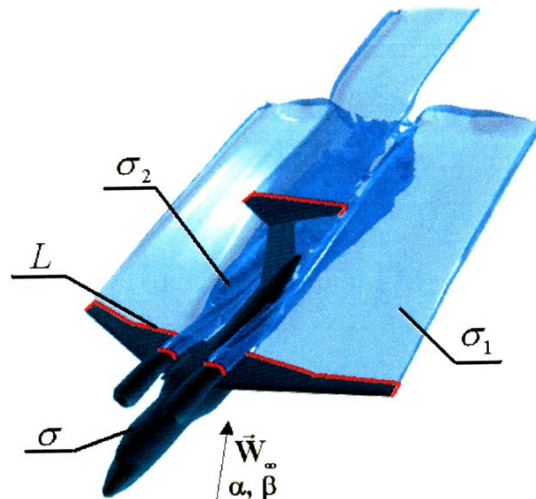


Figure 3.1. Computational model.

Let us denote the lifting and control surfaces of an aircraft together with its engine nacelles by σ , the free vortex sheet shed from the lifting and control surfaces by σ_1 , the surface of the exhaust jet by σ_2 . The lines of the sheet's shedding are labeled L .

From a mathematical point of view, the problem at hand is reduced to obtaining in a suitable coordinate system the unsteady fields of the velocities $\vec{W}(\vec{r}, t)$ and pressures $p(\vec{r}, t)$, which must satisfy the following conditions and equations:

- The perturbation velocity potential $U(\vec{r}, t)$ at every time moment outside of the surfaces σ , σ_1 and σ_2 must satisfy the Laplace equation

$$\Delta U = 0, \quad (3.1)$$

- On the surface σ , the flow tangency condition must be met:

$$\frac{\partial U}{\partial n} = -\vec{W}_\infty \vec{n}; \quad (3.2)$$

- On the vortex wake's surfaces σ_1 and σ_2 , being the tangential discontinuity surfaces, the condition of zero pressure jump across the wake at every its point and the no-flow condition through the surface must be satisfied:

$$p^+ = p^-, \quad W_n^+ = W_n^- = V_n, \quad (3.3)$$

where V_n is the normal component of the velocity on the surface σ_1 .

- At the separation lines, the Chaplygin-Zhukovsky condition concerning velocity finiteness must be met:

$$\vec{W}_n(\vec{r}, t) \rightarrow 0. \quad (3.4)$$

- At infinity, the disturbances die away:

$$\Delta U \rightarrow 0, \quad \text{at } \vec{r} \rightarrow \infty; \quad (3.5)$$

- For relation between velocity and pressure, the Bernoulli equation is used:

$$p = p_\infty + \frac{\rho W_\infty^2}{2} - \frac{\rho W^2}{2} - \rho \frac{\partial U}{\partial t}. \quad (3.6)$$

When solving the problem, the potential $U(\vec{r}, t)$ or $U(M, t)$ is sought in the form of the double-layer potential

$$U(M_0) = \vec{W}_\infty(t) + \sum_{i=1,2} \frac{1}{4\pi} \int_{\sigma_i} \frac{\partial}{\partial \vec{n}_M} \left(\frac{1}{MM_0} \right) g_i(M, t) d\sigma_M, \quad (3.7)$$

where $g_i(M, t)$ is the density of the double-layer potential on the surface σ . In this case the fluid velocity at every point not lying on the surfaces σ , σ_1 and σ_2 is determined by the formula

$$\vec{W}(M_0, t) = \vec{W}_\infty + \sum_{i=1,2} \frac{1}{4\pi} \int_{\sigma_i} \nabla_{M_0} \left(\frac{\partial}{\partial \vec{n}_M} \left(\frac{1}{r_{MM_0}} \right) \right) g_i(M, t) d\sigma_M. \quad (3.8)$$

Relationship (3.8) is also true on the surfaces σ , σ_1 and σ_2 if the integrals involved in it are meant as hypersingular in the sense of Hadamard's finite value. It will be recalled that the double-layer potential undergoes a jump on surfaces where it is defined, but its normal derivative is continuous. Correspondingly, the velocity field has a jump in the tangential velocity component on the surfaces of the schematized aircraft and its wake, whereas the normal component on these surfaces is continuous.

To satisfy conditions (3.3), we seek such a solution where the surfaces $\sigma_1(t)$ and $\sigma_2(t)$ consist of points moving together with the fluid, and the density of the double-layer potential, $g_i(M, t)$, at

every such point does not depend on time. Suppose that at each instant of time $\tau \leq t$ a fluid particle leaves the line of wake-shedding, $M(s)$, where s is the arc length, and at the instant t occupies the position $M(s, \tau, t)$, and at each instant t the totality of the points $M(s, \tau, t)$ forms the surface of the vortex wakes $\sigma_1(t)$ and $\sigma_2(t)$. In this case the equation of motion for these surfaces takes the form:

$$\frac{\partial \vec{r}(s, \tau, t)}{\partial t} = \vec{W}(M(s, \tau, t), t), \tau \leq t, s : M(s) \in L \quad (3.9)$$

with the initial conditions

$$\vec{r}(s, \tau, t) \Big|_{t=\tau} = \vec{r}_{M(s)}, \quad (3.10)$$

where $\vec{r}(s, \tau, t)$ and $\vec{r}_{M(s)}$ are the position vectors of the points $M(s, \tau, t)$ and $M(s)$, respectively, whereas for the function $g_2(M, t)$ the following relation is true:

$$g_2(M(s, \tau, t), t) \equiv g_2(s, \tau), \tau \leq t, s : M(s) \in L \quad (3.11)$$

Condition (3.2) is equivalent to the equation

$$\frac{1}{4\pi} \sum_{i=1}^2 \int_{\sigma_i} \frac{\partial}{\partial \vec{n}_{M_0}} \frac{\partial}{\partial \vec{n}_M} \left(\frac{1}{r_{MM_0}} \right) g_i(M, t) d\sigma_{i,M} = f(M_0), M_0 \in \sigma_1, \quad (3.12)$$

where $f(M_0) = -\vec{W}_\infty \vec{n}(M_0)$.

Finally, the interrelation between the functions $g_1(M, t)$ and $g_2(s, t)$ is described by the following formula, resulting from the integrability condition for the velocity field:

$$g_2(s, t) = g_1(M(s), t), s : M(s) \in L. \quad (3.13)$$

Thus, the problem of unsteady separated flow of an ideal fluid past an aircraft is reduced to the solution of the closed system of equations (3.9)-(3.13) for the functions $\vec{r}(s, \tau, t)$, $g_1(M, t)$, $g_2(s, \tau)$. With that, if these functions are the solution of the indicated equations, the potential $U(M, t)$ defined by formula (3.7), the corresponding velocity field $\vec{W}(M, t)$ defined by expression (3.8), and the pressure $p(M, t)$ determined by integral (3.6) satisfy conditions (3.1)-(3.6).

The aircraft's geometry was represented with a combination of thin plates and solid elements. The wing and other lifting surfaces are presented schematically as their surfaces, whereas the fuselage and engine nacelles are modeled with solid elements. The plates and solid elements, in turn, are modeled with a double layer of continuously distributed doublet singularity approximated with the network of discrete closed vortex frames. In this case, rectangular vortex frames (cells) are used. Located along the contour of each cell are vortex filaments, whose intensities are unknown. These vortex filaments induce velocities in accordance with the Biot-Savart law. The resulting velocity field is sought in the form of the sum of the velocities induced by all vortex frames modeling the body's surface and its wake and the velocity of the oncoming flow:

$$\vec{W}(\vec{r}, t_k) = \sum_{i=1}^N \Gamma_i(t_k) \vec{W}_i(\vec{r}) + \sum_{m,l} \Gamma_{ml}^1 \vec{W}_{mlk}(\vec{r}) + \vec{W}_\infty, \quad (3.14)$$

$$\vec{W}_i(\vec{r}) = \frac{1}{4\pi} \oint_{\vec{r} \in \partial \sigma_i} \frac{[\vec{r} - \vec{r}_0] \times d\vec{l}}{[\vec{r} - \vec{r}_0]^3}.$$

Thereafter the problem is reduced to determining the intensities of the vortex frames representing the body Γ_i and vortex wake $\Gamma_{m,l}$, along with the coordinates of corner points of the vortex frames, $\vec{r}_{m,l}$. For determining intensities Γ_i for each vortex frame, a control point (collocation point) is established in a special way, for which the flow tangency condition is written. As a result, one obtains the following system of algebraic equations for Γ_i :

$$\sum_{i=1}^N \Gamma_i(t_k) \omega_{ij} = f_j^k, \quad j=1 \dots N, \quad (3.15)$$

$$\omega_{ij} = \vec{W}_i(\vec{r}_j) \vec{n}_j, \quad f_j^k = \left[- \sum_{m,l} \Gamma_{ml}^1 \vec{W}_{mlk}(\vec{r}_j) - \vec{W}_\infty \right] \vec{n}_j. \quad (3.16)$$

When simulating the vortex wake, it is assumed that the vortex frames moves together with fluid particles, and as this takes place, their intensities $\Gamma_{m,l}$ remain constant:

$$\vec{r}_{ml}(t_k) = \vec{r}_{ml}(t_{k-1}) + \vec{W}(\vec{r}_{ml}(t_{k-1}), t_{k-1}) \Delta t, \quad l < k \quad (3.17)$$

At each instant of time, a new vortex cell forms with its two corner points lying on the separation line:

$$\vec{r}_{kl}(t_k) = \vec{r}_l^L, \quad (3.18)$$

and the intensity of the vortex filament of the newly shed frame is determined through the intensities of the vortex filaments lying on the body's surface and having with it a common side:

$$\Gamma_{ml} = \Gamma_{i^+}(t_m) - \Gamma_{i^-}(t_m). \quad (3.19)$$

In formulas 3.14-3.19, l is the number of the segment of the separation line left by the frame $b_{m,l}$, m is the point in time at which the frame leaves the line.

Thus, the solution of the problem is obtained by time stepping until the specified end of computation. At each step, the loads are computed through the Cauchy-Lagrange integral.

The problem in hand is solved by the DVM according to which a flow-immersed body and its wake are replaced with systems of bounded and free vortices (Figure 3.2). In this case, the closed rectangular vortex frames (cells) are used as hydrodynamic singularities (Figure 3.3).

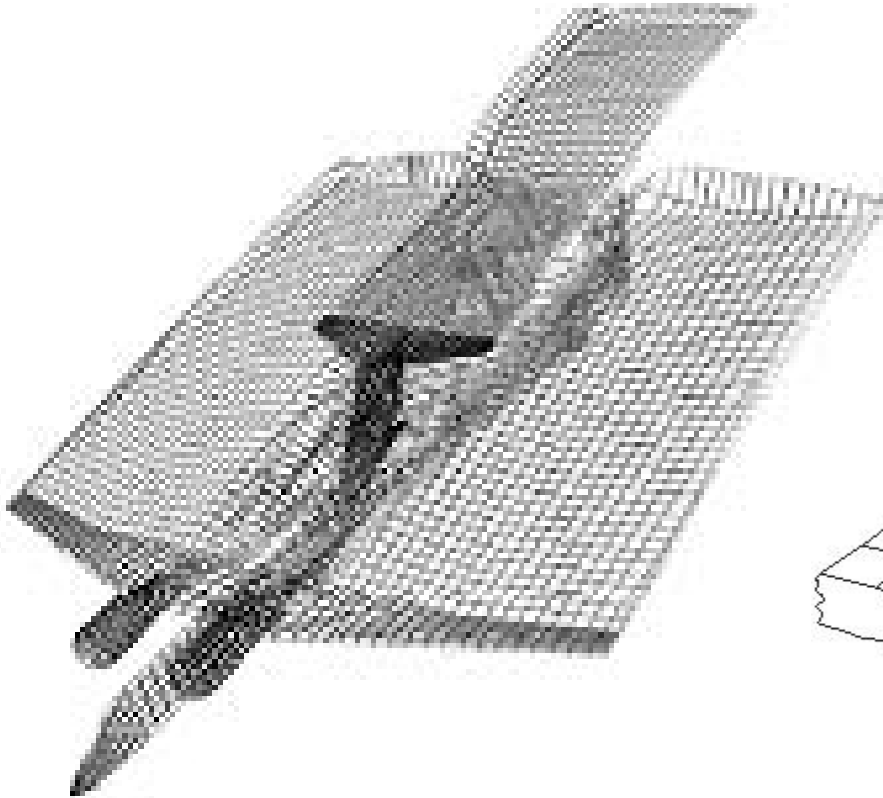


Figure 3.2. System of vortex frames.

Positioned along the contour of each cell i is a vortex filament whose intensity is unknown. The vortex filaments induce velocities according to the Biot-Savart law. The combined velocity field is

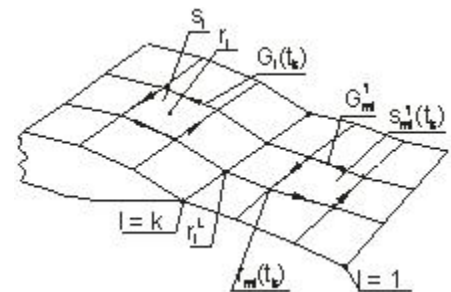


Figure 3.3. Closed vortex frames.

sought as the sum of the velocities induced by all vortex frames modeling the body's surface and its wake and the velocity of the oncoming flow:

$$\vec{W}(\vec{r}, t_k) = \sum_{i=1}^N \Gamma_i(t_k) \vec{W}_i(\vec{r}) + \sum_{m,l} \Gamma_{ml}^1 \vec{W}_{mlk}(\vec{r}) + \vec{W}_\infty, \quad (3.20)$$

$$\vec{W}_i(\vec{r}) = \frac{1}{4\pi} \oint_{\vec{r} \in \partial\sigma_i} \frac{[\vec{r} - \vec{r}_0] \times d\vec{l}}{[\vec{r} - \vec{r}_0]^3}.$$

Thereafter the problem is reduced to determination of the intensities of the vortex frames representing the body Γ_i and vortex wake $\Gamma_{m,l}$ along with the coordinates of the corner points of the vortex frames $\vec{r}_{m,l}$. For determination of intensities Γ_i for each vortex frame, a control point (collocation point) is specified in a special way, for which the flow tangency condition is written. As a result, one obtains the following system of algebraic equations in Γ_i :

$$\sum_{i=1}^N \Gamma_i(t_k) \omega_{ij} = f_j^k, \quad j = 1, N \quad (3.21)$$

$$\omega_{ij} = \vec{W}_i(\vec{r}_j) \vec{n}_j, \quad f_j^k = \left[- \sum_{m,l} \Gamma_{ml}^1 \vec{W}_{mlk}(\vec{r}_j) - \vec{W}_\infty \right] \vec{n}_j. \quad (3.22)$$

When modeling the vortex wake, it is assumed that the vortex frames moves together with fluid particles and as this takes place their intensities $\Gamma_{m,l}$ remain constant:

$$\vec{r}_{ml}(t_k) = \vec{r}_{ml}(t_{k-1}) + \vec{W}(\vec{r}_{ml}(t_{k-1}), t_{k-1}) \Delta t, \quad l < k. \quad (3.23)$$

At each instant of time, a new vortex cell is formed with its two corner points lying on the separation line (3.24):

$$\vec{r}_{kl}(t_k) = \vec{r}_l^L, \quad (3.24)$$

and the intensity of the vortex filament on the newly shed frame is determined through the intensities of the vortex filaments lying on the body's surface and having with it a common side:

$$\Gamma_{ml} = \Gamma_{i^+}(t_m) - \Gamma_{i^-}(t_m). \quad (3.25)$$

In formulas (3.20)-(3.25), l is the number of the segment of the separation line left by the frame $b_{m,l}$, m is the point in time at which the frame leaves the line.

Thus, the solution of the problem is obtained by time stepping until the specified final time step is made. At each step, the loads are computed through the Cauchy-Lagrange integral. These loads are averaged over time when needed.

3.2 Aircraft geometry representation

The schematic representation of an aircraft's geometry is an important part of modeling the flow around the aircraft and its vortex wake. The present report generalizes the approaches of many researchers employing the DVM. Among the types of aircraft representation developed up to now, the following three are the most popular and successful: plate-element, solid-element and hybrid representations.

The plate-element representation idealizes an aircraft as an array of thin plates. Each solid element of the aircraft (fuselage, engine nacelles) is represented by two mutually perpendicular plates ("cruciform scheme"). This simplest representation gives good results in many cases, including the prediction of the behavior of an aircraft encountering the wake of another aircraft.

The solid-element representation considers all components of an aircraft (fuselage, engine nacelles, wing, stabilizer, fin) as a combination of solid elements. This is the most complicated representation, but it practically always gives good results, especially in predicting the motion of aircraft.

Presently, the most popular aircraft representation is the hybrid one. In this case the fuselage and engine nacelles are considered as solid elements, whereas the horizontal tail, fin and other lifting and control surfaces are treated as thin plates. Experience has shown that the best results are obtainable if the element representing the wing is bent according to its mean-camber surface.

3.3 The characteristics of the near vortex wake behind some aircraft

For predicting of flow around aircraft and obtaining the characteristics of their vortex wakes, nonlinear unsteady theory, based on the DVM was employed. Some works contain the results of computation of aircraft near wakes with the help of linear and nonlinear steady theories. The computational results for the near vortex wake were obtained using a nonlinear unsteady theory, the most general and universal.

Shown in Figure 3.4 is the near vortex wave in view of influence of engines jets generated by the A-310 aircraft at $\alpha = 7^\circ$. Thin plates were used to represent the lifting and control surfaces of the aircraft, solid elements modeled the fuselage and engine nacelles. The high-lift devices are deflected for landing. From calculation results it is visible, that in near vortex wave engines jets generated by the A-310 practically do not interact with vortex wake.

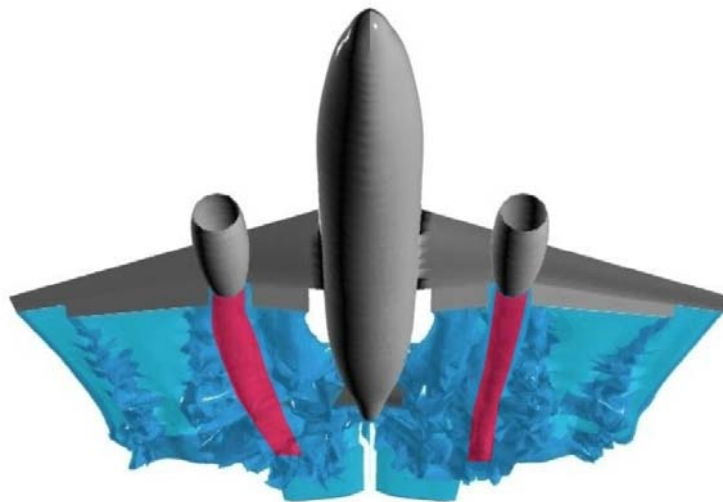


Figure 3.4. Vortex wave generated by the A-310 aircraft at $\alpha = 7^\circ$.

The near vortex wake of the A-380 aircraft at $\alpha = 7^\circ$ in view of influence of engines jets can be seen in Fig. 3.5. Thin plate representation is used for its lifting and control surfaces, the fuselage and engine nacelles are modeled with solid elements. The wing's high-lift devices are in takeoff configuration. It is visible from calculation results, that in near vortex wave engines jets generated by the A-380 starts to be captured by external vortical zone of A-380 aircraft vortex wake.

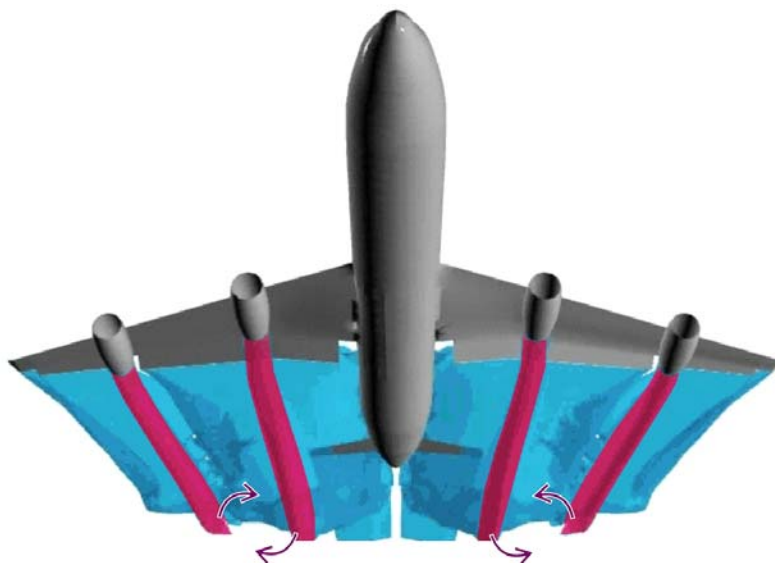


Figure 3.5. Vortex wake of the A-380 aircraft at $\alpha = 7^\circ$

Figure 3.6 presents the near vortex wake behind the SSJ-100 aircraft at $\alpha = 20^\circ$ in view of influence of engines jets; lifting and control surfaces are modeled with thin plates, and engine nacelles - with solid elements. In this case capture of the engines jets by near vortex wake also takes place.

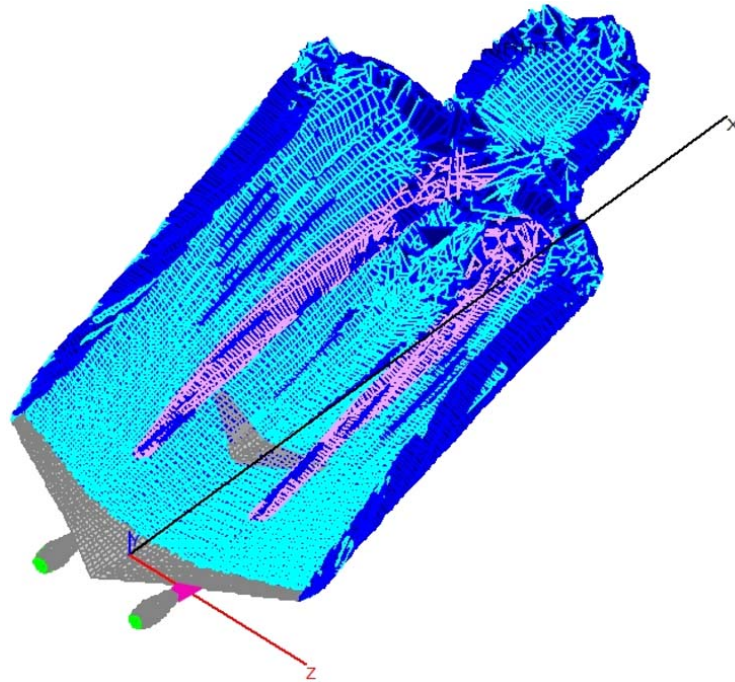


Figure 3.6. Near vortex wake behind the SSJ-100 aircraft at $\alpha = 20^\circ$

4 CONCLUSIONS

- The analysis of different aircraft wake flow visualization patterns testifies that engines contrails and vortex wake could interact with each other depending on aircraft configuration. This process is essential and it should be taken into account during evaluation of contrail characteristics.
- There is a possibility to model the processes of interaction of vortex wakes with condensation trails by numerical methods, for example by MDV.
- Researches of far interaction of wake and contrails including mathematical modeling will help to study the processes of contrails existence and destruction.

REFERENCES

- Aubakirov, T.O., Belotserkovsky, S.M., Zhelannikov, A.I., Nisht, M.I., 1997: *Nonlinear wing theory and its applications*, Almaty, Gylm, 448 pp
- Belotserkovsky, S.M., Dvorak, A.V., Zhelannikov, A.I., Kotovsky, V.N., 1987: *Computer-based simulation of turbulent jets and wakes*. In: *Problems of turbulent flows*, Nauka, Moscow
- Belotserkovsky, S.M., Kotovsky, V.N., Nisht, M.I., Fedorov, R.M., 1988: *Mathematical simulation of separated flows about bodies*, Nauka, Moscow, 232 pp
- Vyshinsky, V.V., Sudakov, G.G., 2006: *Vortex wake of an aircraft in a turbulent atmosphere*, Proc TsAGI # 2667, 155 pp
- Zhelannikov, A.I., 2007: A simplified methodology for computing the far vortex wake behind trunk-route aircraft, Scientific Bulletin of Moscow State Technical University of Civil Aviation, Aeromechanics and Strength # 111, 16 – 21
- Zamyatin, A.N., Soudakov, G.G., 2002: *Colloquium 433, Dynamics of Trailing Vortices*, Theoretical and experimental investigations of external turbulence effect on aircraft vortex wake, Euromech RWTH Aachen, Book of Abstracts, Aachen, Germany
- Babkin, V.I., Belotserkovsky, A.S., Turchak, L.I., Zamyatin, A.N., 2008: *Wake vortex flight safety systems for aircrafts*, Nauka, Moscow, Russia, 373 pp
- Zamyatin A.N., 1991: *Proceedings of the aircraft wake vortices conference*, Real research of different class airplane vortex wakes, U.S.Department of transportation FAA, Washington, DC, USA

Do radiative forcings of methane and ozone cancel out? - A case study from the last IMO Greenhouse gas study

Jérôme Hilaire*, Ruben Rodriguez de Leon, David S. Lee
Dalton Research Institute, Manchester Metropolitan University, UK

Keywords: Shipping, NO_x emissions, Atmospheric composition, Climate impacts, IMO GHG Study 2, MOZART-2, GCTM, Edwards&Slingo, RTM.

ABSTRACT: This modelling work aims at quantifying the perturbation resulting from international maritime transport emissions of nitrogen oxides on the lower atmospheric composition and radiative forcing. We use the emission dataset created for the new IMO Greenhouse gas study as input to the tropospheric GCTM MOZART-2. We further run the Edwards & Slingo Radiative Transfer Model to assess impacts on the radiative forcing. The IMO emissions of nitrogen oxides are large compared to previous assessments (about 8Tg(N).yr⁻¹ in this study, compared to about 4Tg(N).yr⁻¹ before). These emissions cause significant perturbations in ozone (35mW.m⁻²) and methane (-45mW.m⁻²) which in turn result in a significant radiative forcing. However, it is likely that these impacts are overestimated because the non-linearity introduced by subgrid scale plume processes that are not accounted.

1 INTRODUCTION

International shipping is undeniably a cornerstone of the global economy. However, it is an increasing environmental problem that consumes large quantities of fossil fuel and releases significant amounts of atmospheric pollutants leading to acidification, eutrophication, premature mortality [Corbett *et al*, 2007] and climate change. In addition, the CO₂ emissions from international shipping (the largest fraction) are not covered under the Kyoto Protocol (Article 2.2).

Indeed, by emitting nitrogen oxides (NO_x), carbon monoxide (CO) and volatile organic compounds (VOCs) in the marine boundary layer and through complex chemical processes, these molecules contribute to the formation of ozone (O₃) and the depletion of methane (CH₄) which induce climate change.

Several studies [Corbett *et al*, 2001], [Endresen *et al*, 2003], [Eyring *et al*, 2005], [Eyring *et al*, 2009] have presented different values resulting from a large range of shipping emissions. However, all patterns looks similar.

This study focuses on the trade-off between impacts of ozone and methane on the climate stemming from a shipping perturbation induced by emissions calculated for IMO [Buhaug, *et al*, 2009]. First, the methodology is presented, the results from the simulations are discussed and finally, conclusions are drawn.

2 METHODOLOGY

In order to carry this research, shipping emissions are provided to a Global Chemistry-Transport Model (MOZART-2 [Horowitz *et al*, 2003]). MOZART-2 is a tropospheric chemical transport model accounting for the most important processes occurring in the lowermost part of the atmosphere. This version of the model calculates the global distribution of 63 gas-phase chemical species over a T63 (roughly equivalent to 1.875° × 1.875°) grid and 47 hybrid vertical levels ranging from the surface to about 10 hPa. In addition, the model time step for chemistry and transport is set to 15

* Corresponding author: Jérôme Hilaire, PhD Student, Dalton Research Institute, MMU, UK. Email: j.hilaire@mmu.ac.uk

minutes. The dynamical meteorological data are provided from the ECMWF Operational Analysis data for 2003. Chemical species are transported by several physical processes. Advection is performed using a flux-form semi-Lagrangian scheme [Lin and Rood, 1996] with a pressure fixer. Vertical diffusion is treated with the Holstag and Boville parametrization [Holtslag and Boville, 1993] and convection is split into two schemes: deep convection [Hack, 1994] and shallow convection [Zhang and McFarlane, 1995]. Dry and wet deposition is parameterised in the model. Stratospheric concentrations of 7 long-lived species are constrained by relaxation toward climatological values. Details on the treatment of the gas-phase chemical mechanisms and transport processes are described by [Horowitz et al, 2003].

The perturbed chemical species values constitute then an input to a Radiative Transfer Model (RTM) (Edwards & Slingo [Edwards and Slingo, 1996]) that estimates the change in the Earth's radiative balance and thus the impact on climate. The Edwards & Slingo RTM has been tested over a significant number of studies. Radiative fluxes are performed using the δ -Eddington form of the two-stream equations in both the short-wave and long-wave regions of the spectrum.

This study makes use of the emission dataset created for the new IMO Greenhouse study [Buhaug et al, 2008-2009]. Two 1-year spin-up simulations are run, one with the IMO emissions and the other one without. After this, two new simulations are started but this time with initial conditions provided by the spin-up simulations.

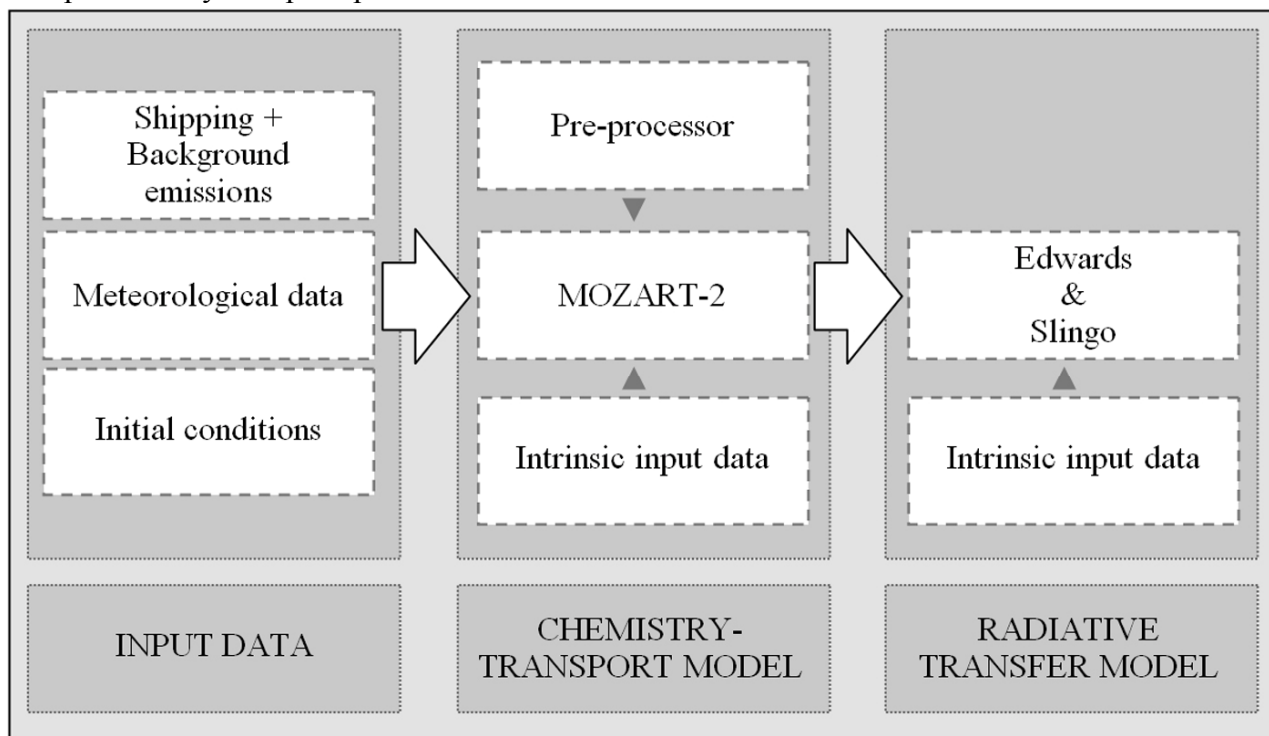


Fig 2.1 – Schema of modelling system

3 IMPACTS ON ATMOSPHERIC COMPOSITION AND RADIATIVE FORCING

In this case study, emissions from the recent IMO Greenhouse gas study are employed. These emissions are larger than estimated in previous studies. For instance, NO_x emissions are 7.3 Tg(N)/yr which is almost twice the amount of nitrogen oxides used in the past (eg 3.10 in [Eyring et al, 2007], 4.38 in [Fuglestad et al, 2008]). Emissions of VOCs are also larger than previous estimations (see **Fig 3.1**). Shipping NO_x emissions correspond to about 15% of the total anthropogenic NO_x emissions. Background emissions are from the GEMS study [Schultz and Stein, 2006]. Emission totals of CH_4 and NO_x , are in good agreement with the Fourth assessment report from the IPCC [cf Chapter 7]. Whereas spin-up simulations are run with prescribed methane lower-boundary concentrations, the following simulations account for CH_4 emissions (516 Tg(CH_4)/yr).

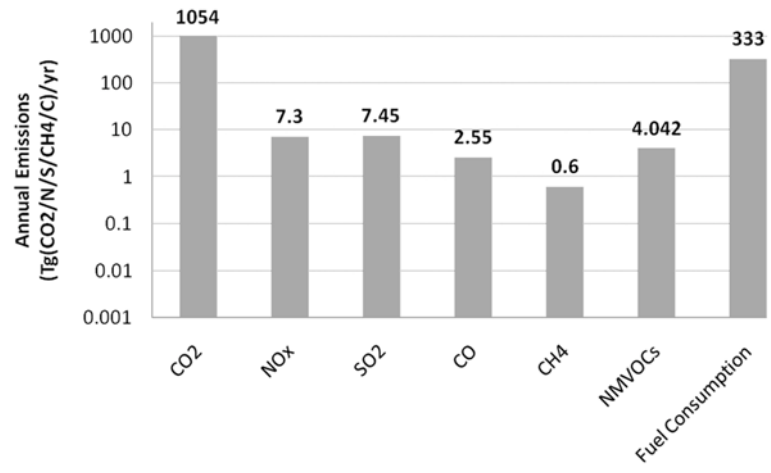
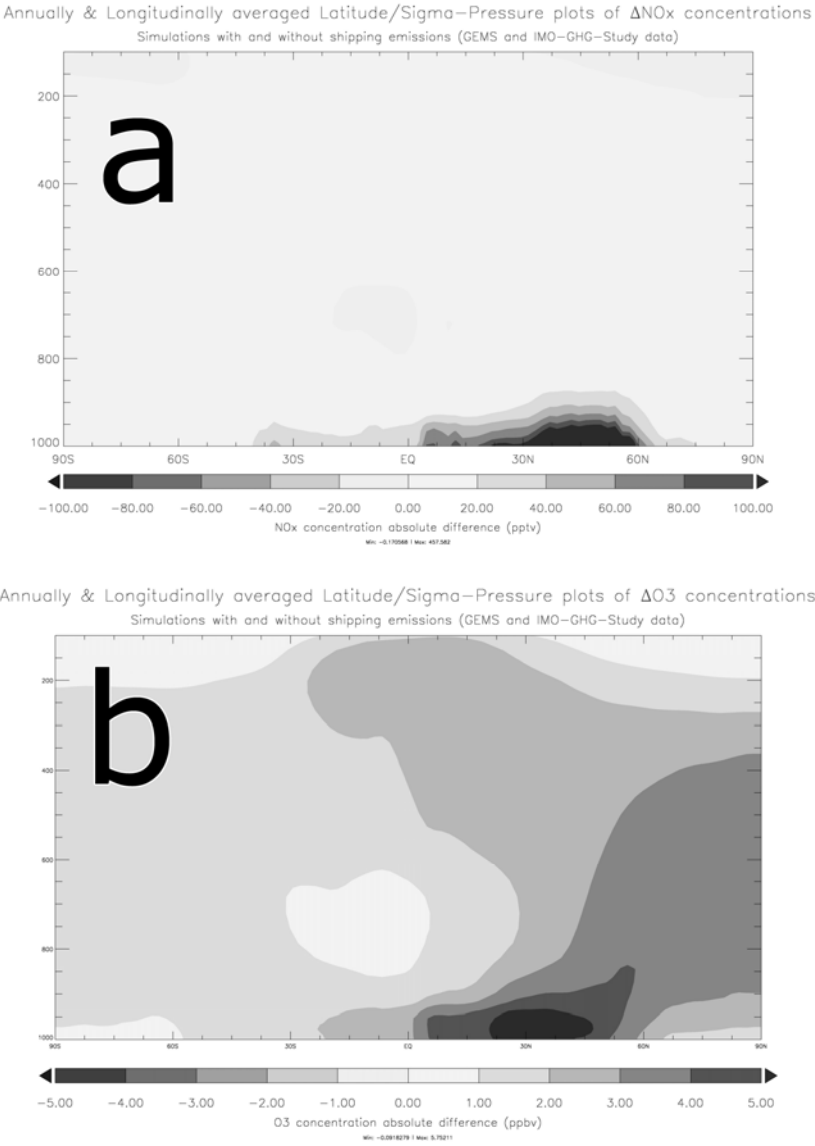


Fig 3.1 – Annual total shipping emissions for different chemical species. [Source: IMO GHG Study 2009]

The magnitude of the ozone shipping perturbation resulting from the difference between the 2 simulations is consistent with previous studies [Eyring et al, 2007] when differences in NO_x emissions are accounted for. The pattern is also in good agreement (see Fig 3.2). However, the impact on the methane lifetime is larger and quite significant. Indeed, according to the model, it could be reduced by about 0.9 year. This means that once methane would reach steady state it could have been globally reduced by more than 250 ppbv. Even though this value is large compared with the ones presented in a recent assessment of shipping impacts [Eyring et al, 2009], it still belongs to the range of magnitude.



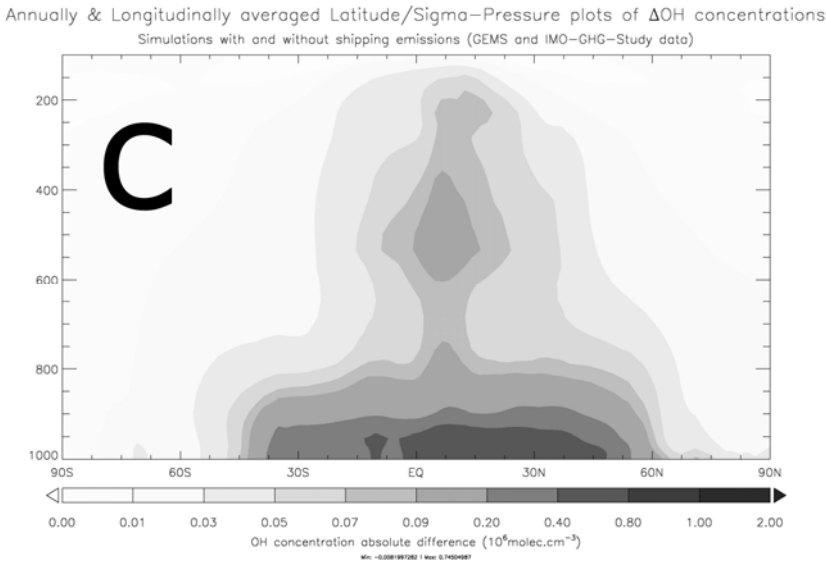


Fig 3.2 – Annual and longitudinal average of atmospheric chemical species. a. nitrogen oxides – b. ozone – c. hydroxyl radical

Table 3.1 – Annually averaged methane lifetimes

Simulation	Methane lifetime
1. With shipping emissions	9.48
2. Without shipping emission	10.4
Difference between simulations (1 – 2)	-0.92

Because of the formation of ozone and the depletion of methane due to emissions of nitrogen oxides, the radiative forcing from shipping ozone is positive whereas the radiative forcing of shipping methane is negative.

Using LinClim [Lim et al, 2005] to normalize the results, we find a global radiative forcing from ozone of 35 mW.m^{-2} and radiative forcing from methane is -45 mW.m^{-2} . The sum of these 2 components results in a small negative value. However, although, these radiative forcings operate on similar latitudinal scales, but they also present some variability ranging from 0.02 mW.m^{-2} in the northern tropical and the southern polar regions to -20 mW.m^{-2} near the southern tropic (see Fig 3.3).

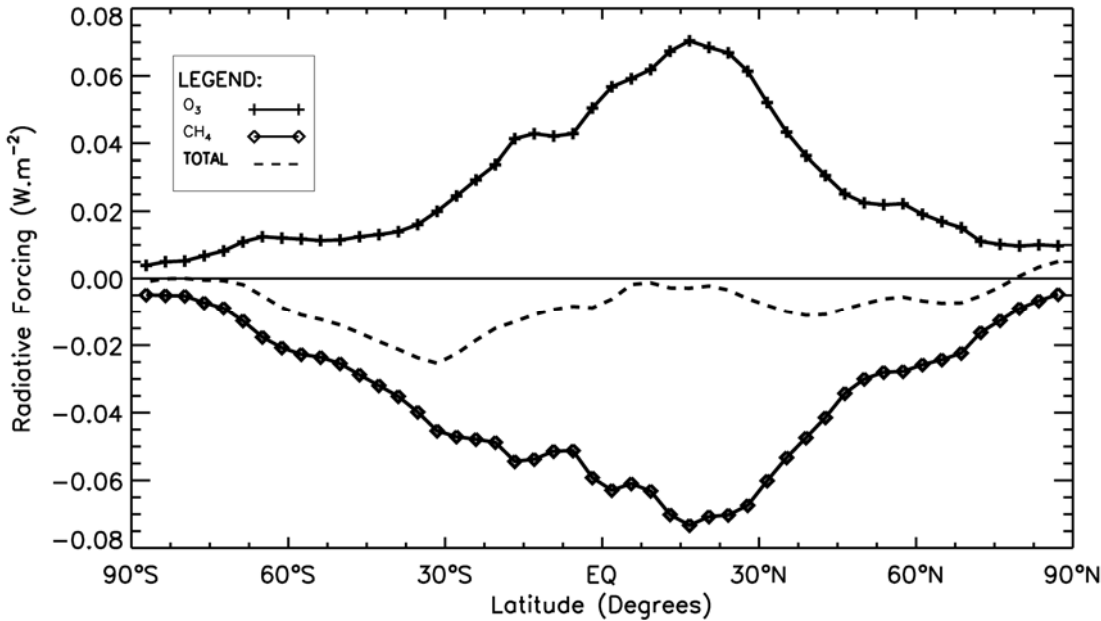


Fig 3.3 – Annual radiative forcing from total shipping in 2007.

4 CONCLUSIONS AND PERSPECTIVES

The magnitudes of the ozone and methane perturbations are larger than previous studies but they scale linearly to the emitted NO_x (about 2 times higher). However the methane lifetime perturbation is at the higher end of the range of values of previous studies. Although the radiative forcings of ozone and methane are globally of the same order of magnitude, the latitudinal plot (**Fig 3.3**) shows some variability which can be significant depending on the location. As a consequence, these radiative forcings do not necessarily cancel out regarding position (a map would give more details). Also, a subgrid scale parameterisation would probably reduce errors inherent to coarse resolution modelling [Franke et al, 2007], [Cariolle et al, 2009].

It would be interesting to look at the whole set of radiatively active components in the future to foresee the impacts of shipping.

Implementing the recent findings on halogen-mediated ozone destruction in the model could also give a different atmospheric composition. And especially, it could lead to another ozone perturbation. [Read et al, 2008]

REFERENCES

- Buhaug, Ø., J.J. Corbett, Ø. Endresen, V. Eyring, J. Faber, S. Hanayama, D.S. Lee, D. Lee, H. Lindstad, A.Z. Markowska, A. Mjelde, D. Nelissen, J. Nilsen, C. Palsson, J.J. Winebrake, W.-Q. Wu and K. Yoshida, 2009: Second IMO GHG study; International Maritime Organization (IMO) London, UK
- Corbett, J. J. and J.J. Winebrake, 2003: Updated emissions from ocean shipping
- Corbett, J. J., J.J. Winebrake, E.H. Green, P. Kasibhatla, V. Eyring and A. Lauer, 2007: Mortality from Ship Emissions: A Global Assessment
- Cariolle, D., D. Caro, R. Paoli, D.A. Hauglustaine, B. Cuenot, A. Cozic and R. Paugam, 2009: Parametrization of plume chemistry into large-scale atmospheric models: application to aircraft NO_x emissions [*in preparation*]
- Edwards, J. M and Slingo, A., 1996: Studies with a flexible new radiation code. I: Choosing a configuration for a large-scale model
- Endresen, Ø., E. Sørsgard, J.K. Sundet, S.B. Dalsoren, I.S.A. Isaksen, T.F. Berglen and G. Gravir, 2003: Emission from international sea transportation and environmental impact
- Eyring, V., H.W. Kohler, J. van Ardenne and A. Lauer, 2005: Emissions from international shipping 1. Past 50 years
- Eyring, V., D.S. Stevenson, A. Lauer, F.J. Dentener, T. Butler, W.J. Collins, K. Ellingsen, M. Gauss, D.A. Hauglustaine, I.S.A. Isaksen, M.G. Lawrence, A. Richter, J.M. Rodriguez, M. Sanderson, S.E. Strahan, K. Sudo, S. Szopa, T.P.C. van Noije and O. Wild, 2007: Multi-model simulations of the impact of international shipping on Atmospheric Chemistry and Climate in 2000 and 2030
- Eyring, V., I.S.A. Isaksen, T. Bernsten, W.J. Collins, J.J. Corbett, Ø. Endresen, R.G. Grainger, J. Moldanova, H. Schlager and D.S. Stevenson, 2009: Transport impacts on atmosphere and climate: Shipping
- Franke, K., V. Eyring, R. Sander, J. Hendricks, A. Lauer and R. Sausen, 2007: Towards Effective Emissions of Ships in Global Models
- Fuglestad, J., T.K. Bernsten, I.S.A. Isaksen, H. Mao, X.-Z. Liang, and W.-C. Wang, 1999: Climatic forcing of nitrogen oxides through changes in tropospheric ozone and methane; global 3D model studies
- Horowitz, L. W., S. Walters, D.L. Mauzerall, L.K. Emmons, P.J. Rash, C. Granier, X. Tie, J.-F. Lamarque, M.G. Schultz, G.S. Tyndall, J.J. Orlando and G.P. Brasseur, 2003: A global simulation of tropospheric ozone and related tracers: Description and evaluation of MOZART, version 2
- Lim, L. L., D.S. Lee, R. Sausen and M. Ponater, 2005: Calculating radiative forcing and temperature changes from aviation effects with a climate response model
- Read, K., A.S. Mahajan, L.J. Carpenter, M.J. Evans, B.V.E. Faria, D.E. Heard, J.R. Hopkins, J.D. Lee, S.J. Moller, A.C. Lewis, L. Mendes, J.B. McQuaid, H. Oetjen, A. Saiz-Lopez, M.J. Pilling and J.M.C. Plane, 2008: Extensive halogen-mediated ozone destruction over the tropical Atlantic Ocean
- Schultz, M. G. and Stein, O., 2006: GEMS (GRG) Emissions for 2003 reanalysis simulations. Technical report, MPI-M Hamburg, 2006

Aerosol optical properties

D.M. Peters^{*}, R.G. Grainger, G. Thomas

Sub-Department of Atmospheric, Oceanic and Planetary Physics, University of Oxford, UK

Keywords: aerosol optical properties, aerosol refractive index

ABSTRACT: Traditionally the atmospheric physics department at the University of Oxford has applied optimal estimation techniques for the retrieval of atmospheric properties of gases; temperature, pressure and volume mixing ratio from satellite measurements. This paper describes the latest novel application of these techniques in deriving aerosol optical properties in laboratory experiments. Two examples are given; a spectral resolved technique allows an aerosol refractive index to be derived over a wide wavelength range and a method of deriving single particle refractive index and size from a novel aerosol instrument suitable for in situ aerosol monitoring.

1 OPTIMAL ESTIMATION; A GENERIC METHOD

Optimal estimation has a long history in use in remote sensing. The advantage over other methods is the ability to provide the highest information content for a retrieval problem. This is achieved by using a model that contains all the known physics of the problem and prior knowledge of the measurement. In addition the method provides error estimates on the parameter(s) of interest. The following paragraphs provide a quick overview of the method; for a detailed discussion of the method refer to Rodgers (2000).

Measurement(s), \mathbf{y} are related to the state, \mathbf{x} by physics. This is represented by the forward model, $\mathbf{F}(\mathbf{x})$. Hence the relationship of the state to measurement can be described by the equation:

$$\mathbf{y} = \mathbf{F}(\mathbf{x}) \quad (1)$$

We need to invert our measurements to find the state, \mathbf{x} (i.e. refractive index, and particle size in the examples to follow). We also use the best knowledge of the solution, \mathbf{x}_a before the measurement was made, thus the problem is to solve the inverse model:

$$\mathbf{x} = \mathbf{F}^{-1}(\mathbf{y}, \mathbf{x}_a) \quad (2)$$

To do this we minimise the cost function Φ , to find the state \mathbf{x} :

$$\Phi(\mathbf{x}) = (\mathbf{x} - \mathbf{x}_a)^T \mathbf{S}_{\mathbf{x}_a} (\mathbf{x} - \mathbf{x}_a) + (\mathbf{y} - \mathbf{F}(\mathbf{x}))^T \mathbf{S}_{\mathbf{y}}^{-1} (\mathbf{y} - \mathbf{F}(\mathbf{x})) \quad (3)$$

And we find our estimated state, $\hat{\mathbf{x}}$ is given by:

$$\hat{\mathbf{x}} = \mathbf{x}_a + \mathbf{S}_{\mathbf{x}_a} \mathbf{K}_{\mathbf{x}}^T \mathbf{S}_{\mathbf{y}}^{-1} (\mathbf{y} - \mathbf{F}(\hat{\mathbf{x}})) \quad (4)$$

Where the weighting function $\mathbf{K}_{\mathbf{x}}$ is:

$$\mathbf{K}_{\mathbf{x}} = \frac{\partial \mathbf{F}}{\partial \mathbf{x}}. \quad (5)$$

Equation 4 and 5 are generally by the Levenberg-Marquardt algorithm (Gauss-Newton and the gradient descent iteration methods). For details of how the uncertainty estimates are calculated see Rodgers (2000).

^{*} *Corresponding author:* Dr Daniel Peters, University of Oxford, AOPP, Clarendon laboratory, South parks road, OX1 3PU, UK. Email: dpeters@atm.ox.ac.uk

2 AEROSOL REFRACTIVE INDEX

The following section shows the application of this optimal estimation to determining the spectrally dependent refractive index of aerosols in a test cell.

2.1 Method

The extinction cross section of an aerosol in the cell is related to the optical transmission by:

$$T(\lambda) = e^{-\beta(\lambda)x} \quad (6)$$

Where, $T(\lambda)$ is the transmission, $\beta(\lambda)$ the volume extinction coefficient, x path length though the test cell at the wavelength λ . The extinction coefficient can be calculated if we assume Mie theory and know the particle size distribution from the equation:

$$\beta(\lambda) = \int_0^{\infty} \sigma_{ext}(r, m(\lambda), \lambda) n(r) dr \quad (7)$$

Where, σ_{ext} is the extinction coefficient (assuming Mie theory), r is the particle radius, $m(\lambda)$ the refractive index and $n(r)dr$ the number of particles between radii r and $r + dr$.

In this application of the optimal estimation method the forward model $\mathbf{F}(\mathbf{x})$ represents equations 6 and 7, with the state vector, \mathbf{x} containing the size distribution and refractive index. The measurement vector \mathbf{y} contains the spectrally resolved transmission measurement.

Experimental setup Figure outlines the basic configuration of the experiments undertaken. The aerosol is generated (the method is chosen based on the aerosol type) and the aerosol introduced to aerosol test cell. The aerosol cell has optical windows fitted, allowing the aerosol absorption to be measured via the Fourier Transform Spectrometer, FTS. Particle size distribution of the aerosol is then determined using techniques insensitive to particle refractive index and the aerosol vented into a fume cupboard. The configuration also included a water bath to allow the relative humidity to be controlled.

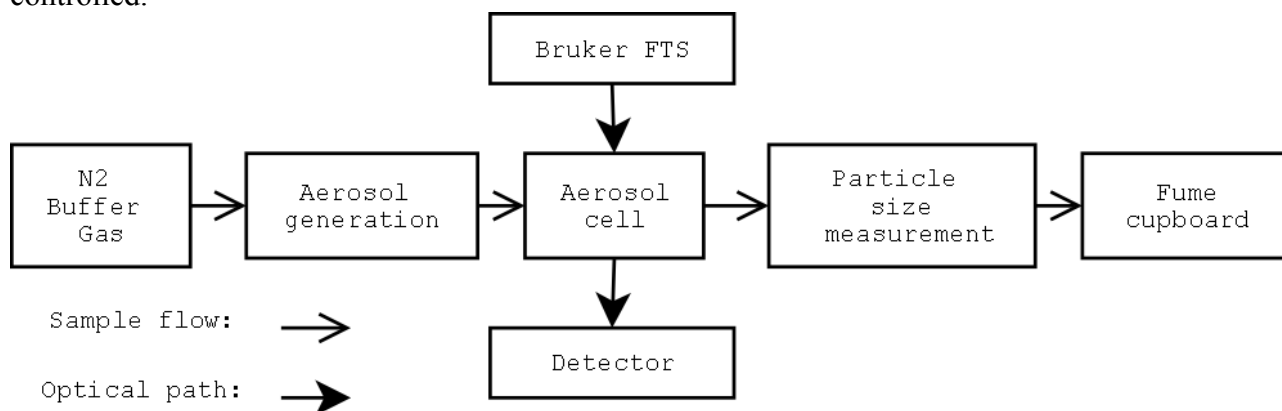


Figure 1. Simplified diagram of experimental configuration.

All of the measurements were undertaken at the Molecular spectroscopy facility at the Rutherford Appleton laboratory, a UK NERC funded facility. The aerosol cell used has an optical path length of 30 cm. Future work is planned to use a multi-pass cell to look at black carbon aerosol optical properties. Spectral intensity measurements are made using a Bruker FTS. Measurements of the detected spectrum are obtained with and without the aerosol to calculate the transmission spectrum, $T(\lambda)$. The method has been described in detail by Thomas (2005). A correction is made to the transmission spectrum to remove water and carbon-dioxide gas absorption lines; this was achieved via a separate retrieval of these gas species concentrations.

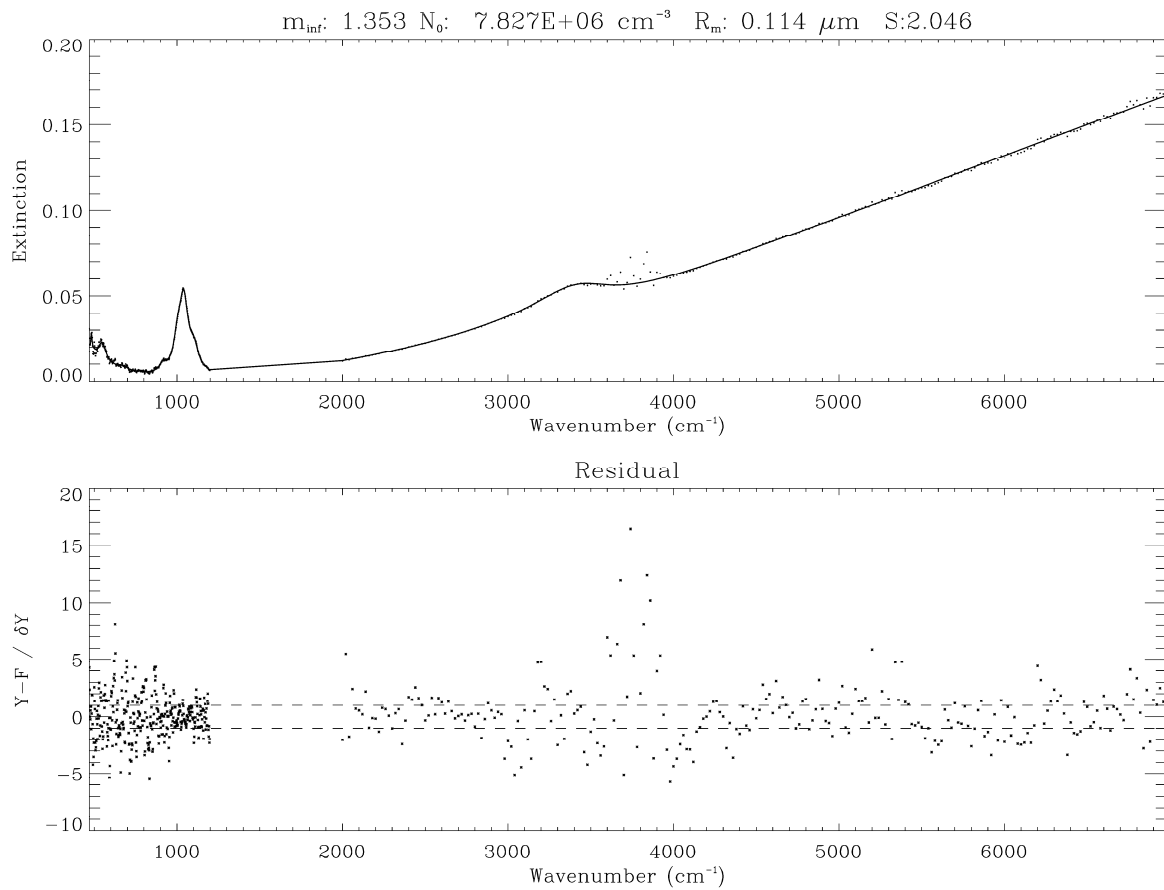


Figure 2. Top plot: Measured spectra (dots) and fitted spectra (lines). Bottom plot: fitted residual.

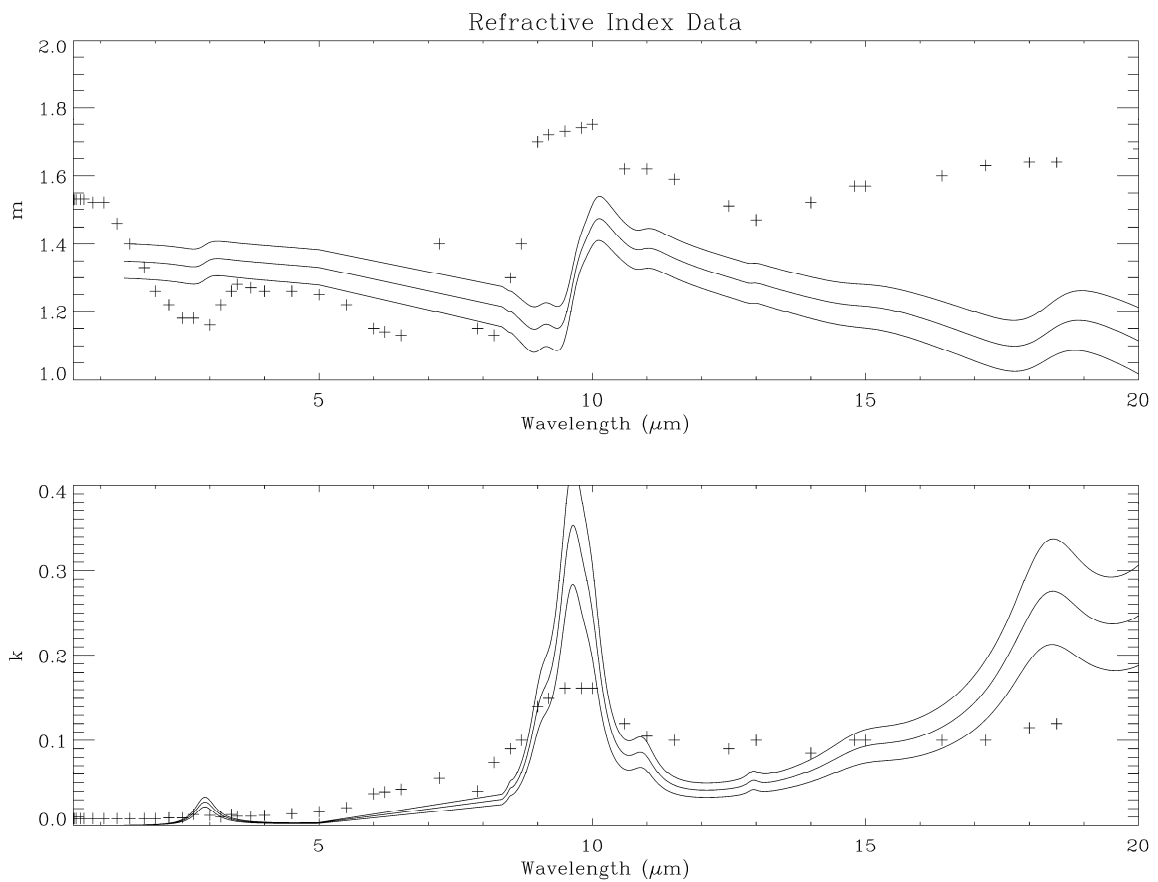


Figure 3. Inverted complex refractive example for Cape Verde dust (central black line). Surrounding two black lines indicates estimated uncertainties. Crosses show the existing published data [2]. Note these are still preliminary results.

2.2 Results

The refractive index of the aerosol from the measured absorption spectra has been determined using this method. This is the first time that the spectral dependent refractive index has been measured on a real mineral aerosol in the laboratory, past measurements are based on collected samples pressed into KBr pellets, for example Shettle (1979). An example of the measurement and forward model fit is shown in Figure , the associated refractive index in Figure . These are preliminary results; the final results may differ and will be published after further validation work. Further results have been published using this method by Irshad (2009) for sea salt aerosols.

3 A NOVEL INSTRUMENT

The angular scattering of radiation by a particle is not only dependent on its size and shape, but also on its refractive index. Traditionally, this dependence has been viewed as a hindrance to the performance of optical particle counters, as it requires assumptions to be made about the refractive index to allow size estimates to be calculated. Instruments such as the Wyoming OPC use white light and carefully positioned detectors to minimize the sensitivity of the instrument to particle refractive index (Dashler 2003). The SPARCLE instrument represents a shift in measurement principle to actively using this dependence to gain more information about the aerosol particles. Additionally, data analysis is performed on a particle-by-particle basis in the SPARCLE system. This enables the attribution of particles' sources (by their refractive index) to different size ranges this cannot be done using the Wyoming OPC system, where the returned data are simply the number of counts per channel.

3.1 Method

There are two key innovations that form the basis of the SPARCLE instrument. Firstly the use of a solid state detector array within a small, autonomous in situ instrument to provide a high resolution measurement of particle scattering on single particles. Secondly the analysis scheme employed by the instrument is completely original. This is to our knowledge the first numerical retrieval scheme which provides both the particle radius and the complex refractive index from a measurement of light in the Mie scattering regime. The development of such an algorithm and its application to actual measurements represents a new state-of-the-art in optical particle measurement.

Sensitivity to both refractive index and size allows measurement of the single scatter albedo on each particle (by assuming Mie theory). This is a significant advantage as SPARCLE is the first instrument to be able to make this measurement on single particles in the atmosphere.

3.2 Results

The instrument uses two detectors; a fast sensitive photomultiplier tube (PMT) and a linear detector array (LDA). The LDA records individual particle phase functions and the PMT measures over a wide angular range to provide sensitivity to the smallest particles. Thus the forward model; $F(\mathbf{x})$ relates the detectors measured phase function via mie theory to the particle size and refractive index, the state vector \mathbf{x} . The optimal position of the detectors has been determined by calculation of the number of degrees of freedom to allow the highest instrument performance to be obtained i.e. the best ability to distinguish size and refractive index. The Figure demonstrates that real part of the refractive index and particle size are obtainable up to a lower size limit of around $0.1\mu\text{m}$ in radius. The real and imaginary parts of the refractive index and the particle size are available for particles sizes of $0.2\mu\text{m}$ in radius and above.

The current prototype instrument is able to detect and measure the phase function of test particles and has been field tested. Further work is required to increase the LDA sensitivity. The current set up is limited by digitization noise. Low noise pre-amplification is required to ensure the detectors are dark current limited hence obtaining the highest instrument sensitivity. The increased instrument sensitivity will allow the instrument to reach it's full potential in determining single particle optical properties.

4 CONCLUSIONS

Two examples of the application of optimal estimation are given. The Aerosol refractive index of Cape Verde dust has been successfully retrieved. The method is unique as it provides spectrally resolved refractive index data from a real aerosol, current published measurements have only been made on bulk samples. This work is soon to be expanded to include black-carbon aerosol. This will allow the investigation of the applicability of the widely used of mie theory, which assumes spherical particles to predict the radiative forcing of this aerosol type despite it being far from spherical. A novel method to determine individual particle refractive index has been described, and this is very much work in progress (subject to funding). The method shows potential to determine single scatter albedo, particle refractive index and size on individual particles for the first time. These new methods show great potential in characterisation of transport particulate (in particular black carbon) emissions from transport sources both in the field and for laboratory studies.

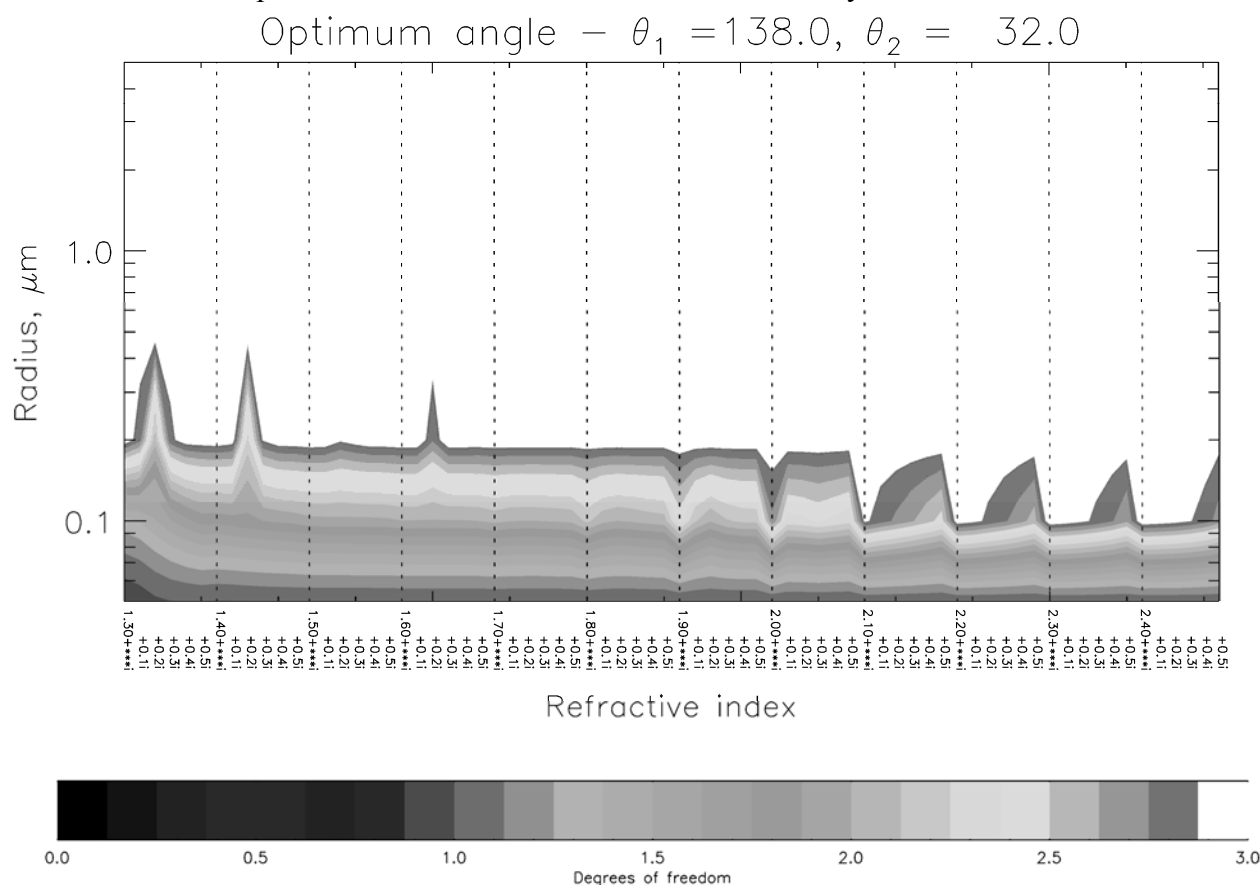


Figure 4. Optimal instrument calculated performance.

REFERENCES

- Dashler T., et al., 2003, Thirty years of in situ stratospheric aerosol size distribution measurements from laramie, wyoming (41°n), using balloonborne instruments. *J. Geophys. Res.*, 104, D5, 4167
- Shettle E.P. and Fenn R.W. 1979 Models for the aerosols of the lower atmosphere and the effects of humidity variations on their optical properties. Technical Report AFGL-TR-79-0214, Air Force Geophysics Laboratory
- Thomas G. E., Bass S. F., Grainger R. G., and Lambert A., 2005, Retrieval of aerosol refractive index from extinction spectra with a damped harmonic-oscillator band model. *Applied Optics*, 44, 7, 1332-1341
- Rodgers C. D., 2000: *Inverse methods for atmospheric sounding: Theory and practice Vol 2*. World scientific publishing Co., ISBN-10: 981022740X, 240 pages
- Irshad R., Grainger R. G., Peters D. M., McPheat R. A., Smith K. M., and Thomas G., 2009, Laboratory measurements of the optical properties of sea salt aerosol, *Atmos. Chem. Phys.*, 9, 221-230

Distinctive Efficacies of the Components Contributing to Total Aviation Climate Impact

M. Ponater*

Deutsches Zentrum für Luft- und Raumfahrt, Institut für Physik der Atmosphäre, Oberpfaffenhofen, Germany

Keywords: Aviation Climate Impact, Contrails, Water Vapour, Efficacy

ABSTRACT: Separate climate sensitivity simulations were run for all important non-CO₂ radiative forcing contributions from aviation (except for contrail cirrus), aiming at the quantification of an individual efficacy parameter for each component. All simulations were performed with the same climate model, E39A. The necessity to scale the original perturbations complicates a straightforward determination of efficacy values, particularly for aviation ozone. The results presented here indicate that a radiative forcing from water vapour increase caused by supersonic aviation would have a similar efficacy than CO₂. Ozone changes induced by subsonic aviation and methane changes appear to have an efficacy larger than CO₂, but the enhancement is moderate (~1.05). For line-shaped contrails we find an efficacy substantially smaller (~0.6) than CO₂ in agreement with previous results. The (small) water vapour increase expected from subsonic aviation shows reduced efficacy (~0.7), too. Similar studies with other climate models are desirable in view of probable model dependency.

1 INTRODUCTION

Aviation impacts on climate in a variety of ways. Radiatively active atmospheric trace gases are changed either directly by aircraft emissions (e.g., CO₂, water vapour) or indirectly (e.g., O₃, CH₄) if atmospheric chemistry is modified by emitting reactive components such as NO_x or aerosols. A further change of the Earth's radiative balance is caused by emissions (water vapour, aerosols) that modify cloudiness, e.g., cirrus coverage and optical properties. According to well-established IPCC practice, all these climate impact components have been compared, quantitatively, in terms of their radiative forcing (e.g., Penner et al., 1999; Lee et al., 2009). In order to account for the differential lifetime of the various tracers when assessing their integrated future impact, more sophisticated metrics such as the Global Warming Potential or the Global Temperature Potential (Fuglestad et al., 2009) have to be used which, however, are also calculated based on the radiative forcing. The fundamental role of radiative forcing (RF) originates from the empirical equation

$$\Delta T_{\text{sfc}} = \lambda \cdot \text{RF} \quad (1)$$

linking RF linearly to the equilibrium change of global mean surface temperature (ΔT_{sfc}) through an assumed constant, the climate sensitivity parameter λ . There has been mounting evidence that, in particular in case of non-homogeneous perturbations (e.g., Joshi et al., 2003), individual climate sensitivity parameters ($\lambda^{(i)}$) different from the basic climate sensitivity due to a homogeneous CO₂ increase ($\lambda^{(\text{CO}_2)}$) may emerge. Hansen et al. (2005) have proposed to define efficacy parameters ($r^{(i)}$) for such perturbations, retaining the relation given by Eq. (1) in a more comprehensive expression:

$$\Delta T_{\text{sfc}} = \lambda^{(i)} \cdot \text{RF} = r^{(i)} \cdot \lambda^{(\text{CO}_2)} \cdot \text{RF} \quad (2).$$

Hereafter we will present results from climate sensitivity simulations driven by aviation related RFs (from aviation induced ozone, methane, water vapour, contrails), in an attempt to assign unique efficacy parameters to such forcings. This extends earlier efforts (Ponater et al, 2006, 2007) that lacked consistency in the sense that results were compiled from various model systems. Here, all

* Corresponding author: Michael Ponater, DLR-Institut für Physik der Atmosphäre, Oberpfaffenhofen, D-82230 Wessling, Germany. Email: Michael.ponater@dlr.de

simulations have been run with the ECHAM4/ATTILA (E39A) model system described by Stenke et al. (2008). This model involves enhanced vertical resolution around the tropopause and a Lagrangian advection scheme for water vapour and cloud water which makes it especially suitable to describe forcings and feedbacks in the upper troposphere and lower stratosphere region.

2 THE SCALING PROBLEM

As shown by Lee et al. (2009), an estimate of total RF from aviation for the year 2005 conditions amounts to about 50 mW/m^2 . (Note that this value excludes contrail cirrus, for which a reliable RF best estimate has not yet been provided. Thus, this effect is not covered in the present paper either). Individual contributions to the total aviation RF remain generally lower than 30 mW/m^2 . Forcings of this magnitude are too small to cause a statistically significant temperature signal in equilibrium climate change simulations and to derive robust values of the climate sensitivity parameter and the efficacy according to Eq. (1, 2). Thus, strong scaling of respective emissions or concentration changes is unavoidable in order to ensure significant signals. Conceptually, the climate sensitivity parameters ($\lambda^{(i)}$) in Eq. (2) are expected to be independent from the magnitude of the forcing, so RF scaling ought to be a straightforward procedure. Moderate deviations from this basic assumption have been pointed out even in the CO_2 case for a number of climate models (e.g., Senior and Mitchell, 2000; Boer and Yu, 2003; Hansen et al., 2005). Nevertheless, calculation and attribution of distinctive efficacies $r^{(i)}$ remains possible as long as their deviation from unity is sufficiently large to neglect a small uncertainty in $\lambda^{(\text{CO}_2)}$. Indeed, Hansen et al. (2005) defined $\lambda^{(\text{CO}_2)}$ with respect to a 50% CO_2 increase over a (pre-industrial) background concentration of 291 ppmv as their reference, paying little heed to the magnitude deviation of some other forcings when interpreting their efficacy values for a larger number of effects. In agreement with previous results, the E39A model used for the simulations reported hereafter shows a relatively small variability of $\lambda^{(\text{CO}_2)}$ with increasing RF: Its value is 0.70, 0.72, and 0.74 K/Wm^{-2} as $\text{RF}(\text{CO}_2)$ increases from 1.01 over 3.79 to 6.16 W/m^2 .

However, as pointed out in a companion study to the present paper (Ponater et al., this volume), it is not guaranteed that such robustness of λ exists for other forcing agents as well. Equilibrium climate change simulations with E39A, forced by ozone change patterns resulting from transport emissions, yielded a climate sensitivity increase of up to 30 % for the same pattern if the forcing was heavily scaled. Hence, in that case the efficacy proved to be more dependent on the scaling of a pattern than on its structure. While the problem could be solved by diagnostic analysis and more simulations, the respective experience suggests to limit the amount of scaling, keeping the RF at values around 1 W/m^2 (or smaller). A less welcome side effect of this decision to restrict the scaling factors is that the regression method for deriving the RF and the climate sensitivity (Gregory et al., 2004; Hansen et al., 2005) can no longer be applied due to an insufficient signal to noise ratio. However, it will be shown here that useful results can be obtained on the basis of the classical IPCC definition of RF (stratosphere adjusted radiative forcing) and the associated $\lambda^{(i)}$, and $r^{(i)}$ values.

3 RESULTS

3.1 Simulation dedicated to individual aviation forcing components

Table 1 lists the relevant parameters for each simulation run with the E39A climate model for this study. The climate sensitivity of a CO_2 increase by 72.3 ppmv (yielding about 1 W/m^2 radiative forcing) is used as a reference, as in the simulations dedicated to methane increase, aviation water vapour increase, and contrails forcings were scaled to a similar magnitude. Note that this means a slight deviation from the way the CO_2 reference value was reached in the companion study dealing with transport related ozone increase (Ponater et al., this volume). The difference is insignificant, however: The climate sensitivity of a 1 W/m^2 CO_2 radiative forcing results as 0.696 K/Wm^{-2} with an estimated 95 % confidence interval of 0.02 K/Wm^{-2} , while the climate sensitivity of CO_2 approximated via the nonlinear fit applied in that companion study is 0.692 K/Wm^{-2} . We further recall that the efficacy of aviation ozone according to Ponater et al., this volume, is about 1.05. This is close to the values directly derived from the two aviation ozone simulations (O3 and O4, using a scaling factor of 50 and 100, respectively) as given Table 1.

	RF_{adj}	ΔT_{sfc}	λ_{adj}	r_{adj}
CO ₂ (1 W/m ²)	1.010	0.703	0.696	1
OZavi (30) – O1	0.540	-	-	-
OZavi (40) – O2	0.704	-	-	-
OZavi (50) – O3	0.862	0.617	0.712	1.02
OZavi (100) – O4	1.593	1.167	0.733	1.05
CH ₄ (1 W/m ²)	1.053	0.760	0.722	1.04
CH ₄ (2 W/m ²)	2.123	1.576	0.742	1.07
Contrails (80, $\tau=0.3$) – C1	0.609	-	-	-
Contrails (80, $\tau=0.4$) – C2	0.833	0.385	0.462	0.66
Contrails (100, $\tau=0.3$) – C3	0.694	0.297	0.427	0.61
Contrails (100, $\tau=0.4$) – C4	0.928	0.383	0.413	0.59
WatVap_avia_sub (750) – H1	0.442	0.223	0.505	0.72
WatVap_avia_sub (1000) – H2	0.555	0.273	0.492	0.71
WatVap_avia_super (20) – HS	0.585	0.428	0.732	1.05
	[Wm ⁻²]	[K]	[K/Wm ⁻²]	

Table 1: Radiative forcing, global mean surface temperature change, climate sensitivity, and efficacy as found in equilibrium climate change simulations with the E39A model. Forcing types are a homogeneous CO₂ increase, the aviation ozone change pattern (OZavi) as given by Hoor et al. (2009), scaled by various factors, a homogeneous CH₄ increase, scaled contrails, and two patterns of aviation induced water vapour increase (see text). In case of the O1, O2, and C1 perturbations, only the stratosphere adjusted radiative forcing (RF_{adj}) was calculated.

Two simulations were performed with two different amounts of homogeneous CH₄ concentration increase to yield either about 1 W/m² (+3.11 ppmv) or about 2 W/m² (+8.6 ppmv) radiative forcing, respectively. Similar to the CO₂ case, the climate sensitivity of a methane perturbation shows only little dependency on the scaling. The moderate efficacy enhancement of CH₄ versus CO₂ changes is consistent with results reported by Hansen et al. (2005), but there have also been examples of climate models with a CH₄ efficacy smaller than that of CO₂ (Berntsen et al., 2005).

When based on a realistic air traffic density, line-shaped contrails provide only a small radiative forcing (< 15 mW/m²), hence their amount must be scaled substantially. In the only study that has attempted to estimate an efficacy of contrail forcing before (Ponater et al., 2005), a 2050 aviation inventory was scaled by a factor 20, still yielding a radiative forcing as low as 0.2 W/m². In that study the contrail optical depth was not scaled, rather the varying optical depth values (yielding a mean around 0.1) from the contrail parameterisation scheme of Ponater et al. (2002) were retained. This resulted in a marginally significant surface temperature response just sufficient for the purpose of deriving an interpretable efficacy change. Even higher scaling of air traffic density can hardly be recommended, as the contrail coverage pattern may be influenced by excessive scaling as soon as saturation effects for certain regions show up. Hence, for the contrail simulations discussed in this study (Table 1) we decided to scale both air traffic density (contrail coverage) and contrail optical depth in order to reach a larger global contrail radiative forcing around 1 W/m². The basic inventory was the same as in Ponater et al. (2002), referring to 1992 aviation density, which was scaled by factors of 80 or 100, while contrail optical depth τ was prescribed to a uniform value of 0.3 or 0.4.

The three contrail driven equilibrium climate change simulations C2, C3, and C4 (Table 1), slightly varying with respect to the choice of scaling, all indicated a similar climate sensitivity parameter around 0.45 K/Wm⁻², suggesting that the resulting efficacy of about 0.6 has some degree of robustness. The value also agrees with the one estimated by Ponater et al. (2005) with a (slightly) different climate model and, as explained above, a somewhat different simulation setup. In view of the higher degree of model dependency for the efficacy parameter that has been found in studies dealing with, e.g., ozone change patterns (Joshi et al., 2003; Berntsen et al., 2005), the indications for a substantially reduced efficacy of contrails are strong indeed.

Two simulations for the present study (H1, H2, Table 1) were dedicated to the water vapour change induced by subsonic aviation. The respective concentration increase pattern is characterised by a distinct maximum in the northern hemisphere lowermost stratosphere (Ponater et al., 2006, their Fig. 3). Typical radiative forcings of a perturbation of this magnitude are very small (below 2 mW/m² for present day aviation, Lee et al., 2009), and a large scaling has to be applied in order to increase the respective response in equilibrium climate change simulations to acceptable levels of statistical significance. The simulations H1 and H2 consistently suggest an efficacy substantially

smaller than the CO₂ reference for this type of forcing. The estimated value is about 0.7, which does not agree with the efficacy suggested in Ponater et al. (2006) for aviation water vapour (1.14). The latter value was, however, derived from a water vapour concentration change pattern induced by a hypothetical supersonic air fleet in the stratosphere (Søvde et al., 2007), which is characterised by a different structure and a much higher basic radiative forcing of around 35 mW/m² (Myhre et al., 2009). In order to confirm whether the different concentration change pattern causes the difference in efficacies we repeated with E39A the simulation forced by the supersonic aviation water vapour increase scaled with a factor 20 (HS, Table 1). The respective efficacy parameter is 1.05, which is hardly distinguishable from 1 in a statistical sense, given the relatively small forcing of 0.585 W/m².

Summarizing, there are at least two contributions to aircraft climate impact whose forcing may be associated with an efficacy significantly different from unity, line-shaped contrails and water vapour induced by subsonic aviation.

3.2 Simulations dedicated to forcings from combined individual components

The usefulness of introducing distinctive efficacies in assessment studies would greatly increase if they can serve as linear weighting factors in case that the response to a combined perturbation (e.g., aviation total impact) is to be derived from the individual response components.

$$\Delta T_{\text{sfc,comb}} = r_{\text{comb}} \cdot \lambda^{(\text{CO}_2)} \cdot \text{RF}_{\text{comb}} \quad ; \quad r_{\text{comb}} = \sum(\text{RF}^{(i)} \cdot r^{(i)}) / \sum \text{RF}^{(i)} \quad ; \quad \text{RF}_{\text{comb}} = \sum \text{RF}^{(i)} \quad (3)$$

This possibility was explored by some simulations forced by more than one of the individual impact contributions (Table 2). Our guideline in choosing appropriate combinations has been not to diverge too far from the standard. For this purpose perturbations with smaller forcing had to be employed (O1, O2, C1, Table 1), for which no dedicated efficacy values from individual simulations had been determined. However, this investigation was built on the hypothesis of unique efficacies for each component anyway, which were assumed according to the last section: 1.05 for water vapour from supersonics and ozone, 0.6 for contrails, and 0.7 for water vapour from subsonics.

	RF _{adj}	ΔT _{sfc}	λ _{adj}	r _{adj}	r _{adj} (comb)
CO ₂ (1 W/m ²)	1.010	0.703	0.696	1	-
O1 + C1	1.122 (98%)	0.683	0.609	0.86	0.83
O2 + C3	1.409 (100%)	0.854	0.606	0.87	0.82
O1 + H1	0.983 (100%)	0.609	0.620	0.89	0.89
O2 + HS	1.294 (100%)	0.994	0.768	1.10	1.05
C1 + H1	1.037 (98%)	0.494	0.476	0.68	0.65
C1 + HS	1.201 (100%)	0.716	0.596	0.86	0.82
C1 + O1 + H1	1.577 (99%)	0.935	0.593	0.85	0.79
	[Wm ⁻²]	[K]	[K/Wm ⁻²]		

Table 2: Radiative Forcing, surface temperature response, climate sensitivity, and efficacy of simulations using more than one aviation impact components. The designations in the 1st column refer to aviation ozone (O), contrail (C), and aviation water vapour (H) perturbations, whose individual forcing and response parameters are given in Table 1. 4th column is the efficacy derived from the actual λ_{adj} values, 5th column the efficacy reached through linear combination according to Equation 3 (see text).

Going through Table 2 it can be noted first (2nd column) that the contributing radiative forcings are almost perfectly additive, a necessary precondition for the linearization of efficacies (Eq. 3) to work. Second, the efficacy parameter for the combined perturbation always takes a value between the contributing component efficacies, except for “O2+HS”, where both component efficacies are assumed as equal (1.05) and should also be equal to the combined efficacy in an ideal case. However, as all efficacy parameter values are subject to a statistical uncertainty (which I do not give here due to lack of space), this is still an acceptable degree of non-linearity. The efficacy parameter of a combined perturbation calculated by linear combination of the contributing individual efficacy values (Table 2, last column) are close to the efficacy parameters from the actual climate model simulations forced by the combined perturbation, but with a tendency towards underestimation. This can be related to the fact that the simulations driven by the combined perturbations have, in general, larger forcings. As we already know, for most perturbations larger forcing inhibits higher efficacy. All in all, deviations from the linearity concept behind Eq. 1 to 3 appear to be limited for radiative forcings below 1.5 W/m². This provides some confidence in using individual efficacies as

weighting factors when the respective perturbations and forcings are combined. The method should be suitable even more so for assessing the present-day aviation climate impact.

4 DISCUSSION AND CONCLUSIONS

Evidence of a distinctive efficacy for at least some individual aviation forcing components poses the question, which feedback mechanisms are at the root of such anomalous effects. The reasons may be different from perturbation to perturbation and also different from model to model. This paper restricts to a brief look at the contrail case, for which the efficacy deviates strongest from the CO₂ reference. As mentioned, Ponater et al. (2005) found a quantitatively similar efficacy reduction for contrails in a previous version of the climate model applied here. Their explanation was, that due to the absence of contrail radiative forcing over the Arctic (where there is only little air traffic) the temperature response at these latitudes is weakened. This entails reduced ice-albedo feedback and reduced global climate sensitivity. The same effect is also apparent, but to a less extent, in the E39A simulations presented here (not shown). Further analysis reveals, however, that the radiative feedback of natural clouds to a contrail forcing also significantly deviates in comparison to a respective CO₂ driven simulation.

	λ_{adj}	$\Delta\text{CRF}(\text{sw})$	$\Delta\text{CRF}(\text{lw})$	ΔCRF	$\Delta\text{CRF}/\Delta T_{\text{surf}}$
CO ₂ (1 Wm ⁻²)	0.696	-0.659	+0.532	-0.127	-0.181
Contrails (80, $\tau=0.4$) – C2	0.462	-0.296	-0.058	-0.354	-0.919
Contrails (100, $\tau=0.3$) – C3	0.423	-0.262	-0.111	-0.373	-1.255
Contrails (100, $\tau=0.4$) – C4	0.413	-0.365	-0.110	-0.475	-1.240
	[K/Wm ⁻²]	[Wm ⁻²]	[Wm ⁻²]	[Wm ⁻²]	[Wm ⁻² /K]

Table 3: Climate sensitivity, shortwave, longwave, and net radiative feedbacks of natural clouds, and the specific net cloud feedback for the E39A equilibrium climate change simulations driven by CO₂ increase and by scaled forcing of line-shaped contrails (see text). The corresponding global mean surface temperature response can be found in Table 1. The radiative feedback of natural clouds has been taken as the difference of the radiative forcing of natural clouds between the respective simulation and the control simulation.

Table 3 presents the radiative feedback related to changes in natural cloudiness for the three contrail simulations already discussed in Section 3.1, together with the CO₂ increase simulation scaled to 1 W/m² forcing. The latter exhibits negative cloud feedback in the solar spectrum (i.e., enhanced shortwave cooling) and positive cloud feedback in the terrestrial spectrum (i.e., enhanced longwave warming) yielding a comparatively small net cooling effect. In the contrail driven simulations both shortwave and longwave feedback components are negative, resulting in a stronger negative net feedback. It is notable that in simulations C2, C3, and C4 natural cirrus cloud coverage decreases at latitudes and altitudes where contrails are present, while in the CO₂ driven simulation cirrus cloud coverage increases in the same regions (not shown). As natural cirrus clouds provide a warming of the climate system it is consistent that the climate sensitivity of a perturbation should be reduced if it acts to remove cirrus coverage. The contrails produced by the parameterisation of Ponater et al. (2002) warm the upper troposphere and reduce the relative humidity, which could easily lead to the effect that they offset part of their own positive radiative forcing by allowing less natural cirrus than in an atmosphere without contrails. Whether this is an effect reflecting the role of contrails in the real world correctly must remain an open question at this stage.

It can be concluded that efficacy anomalies for some individual effects of aircraft total climate impact are significant, require further research, and deserve attention when determining the balance of effects in aviation assessment studies. Respective indications are obvious for contrails and should be taken into consideration in forthcoming studies of contrail cirrus (see Burkhardt et al., 2010), as its presumably higher radiative forcing makes knowledge of its efficacy even more relevant. The simulations presented here and in the dedicated paper of Ponater et al., this volume, do not confirm the distinct efficacy increase suggested for aviation ozone by previous studies that used idealized ozone change patterns in extra-tropical latitudes (e.g., Stuber et al., 2005). For all aviation impact components more model studies are clearly required in order to allow more reliable conclusions.

ACKNOWLEDGEMENTS:

This study was funded within the QUANTIFY project supported by the European Union within the 6th Framework Project under contract 003893.

REFERENCES

- Berntsen, T., J. Fuglestad, M. Joshi, K.P. Shine, N. Stuber, M. Ponater, R. Sausen, D.A. Hauglustaine, and L. Li, 2010: Response of climate to regional emissions of ozone precursors: sensitivities and warming potentials, *Tellus* 57B, 283-304.
- Burkhardt, U., B. Kärcher, and U. Schumann, 2010: Global modelling of contrail and contrail cirrus climate impact, *Bull. Am. Meteorol. Soc.*, in press.
- Boer, G.J. and B. Yu, 2003: Climate sensitivity and climate state, *Clim. Dyn.* 21, 167-176, doi: 10.1007/s00382-003-0323-7.
- Fuglestad, J., et al., 2009: Transport impacts on atmosphere and climate: Metrics, *Atmos. Environ.*, in press, doi: 10.1016/j.atmosenv.2009.04.044.
- Gregory, J., et al., 2004: A new method diagnosing radiative forcing and climate sensitivity. *Geophys. Res. Lett.* 31, L03205, doi:10.1029/2003GL018747.
- Hansen, J., M. Sato, R. Ruedy, L. Nazarenko, A. Lacis, G.A. Schmidt, G. Russell, et al., 2005: Efficacy of climate forcings. *J. Geophys. Res.* 110, D18104, doi: 10.1029/2005GL022740.
- Hoor P., et al., 2009: The impact of traffic emissions on atmospheric ozone and OH: results from QUANTIFY. *Atmos. Chem. Phys.* 9, 3113-3136.
- Joshi, M., K.P. Shine, M. Ponater, N. Stuber, R. Sausen, and L. Li, 2003: A comparison of climate response to different radiative forcings in three general circulation models: towards an improved metric of climate change. *Clim. Dyn.* 20, 843-854, doi: 10.1007/s00382-003-0305-9.
- Lee, D.S., D.W. Fahey, P.M. Forster, P.J. Newton, R.C.N. Wit, L.L. Lim, B. Owen, R. Sausen, 2009: Aviation and global climate change in the 21st century, *Atmos. Environ.* 43, 3520-3537.
- Myhre, G., et al., 2009: Intercomparison of radiative forcing calculations of stratospheric water vapour and contrails. *Meteorol. Z.* 18, 585-596, doi: 10.1127/0941-2948/2009/0411.
- Penner, J., D.H. Lister, D.J. Griggs, D.J. Dokken, M. McFarland (Eds.), 1999: Aviation and the Global Atmosphere, Special Report of the Intergovernmental Panel on Climate Change, Cambridge Univ. Press, 365pp.
- Ponater, M., S. Marquart, R. Sausen, 2002: Contrails in a comprehensive global climate model: Parameterisation and radiative forcing results. *J. Geophys. Res.* 107, 4164, doi:10.1029/2005JD22580.
- Ponater, M., S. Marquart, R. Sausen, U. Schumann, 2005: On Contrail Climate Sensitivity. *Geophys. Res. Lett.* 32, L10706, doi:10.1029/2005GL22580.
- Ponater, M., S. Pechtl, R. Sausen, U. Schumann, G. Hüttig, 2006: Potential of the cryoplane technology to reduce aircraft climate impact: A state of the art assessment. *Atmos. Environ.* 40, 6928-6944, doi:10.1016/j.atmosenv.2006.06.036.
- Ponater, M., V. Grewe, R. Sausen, U. Schumann, S. Pechtl, E.J. Highwood, N. Stuber, 2007: Climate sensitivity of radiative impacts from transport systems. In: *Proceedings of an International Conference on Transport, Atmosphere and Climate (TAC)* (Eds. R. Sausen et al.), European Communities, Oberpfaffenhofen, Germany, 320pp.
- Shine, K.P., et al., 1990: Radiative forcing of climate. In: *Climate change: The IPCC scientific assessment* (Eds.: Houghton, J.T., et al.), Cambridge University Press, Cambridge, New York, Melbourne, Sydney.
- Stenke, A., V. Grewe, V., M. Ponater, 2008: Lagrangian transport of water vapour and cloud water in the ECHAM4 GCM and impact on the cold bias. *Clim. Dyn.*, 31, 491-506, doi: 10.1007/s00382-007-0347-5.
- Stuber, N., M. Ponater, and R. Sausen, 2005: Why radiative forcing might fail as a predictor of climate change. *Clim. Dyn.* 24, 497-510, doi:10-1007/s00382-004-0497-7.
- Senior, C.A., and J.F.B. Mitchell, 2000: The time dependence of climate sensitivity. *Geophys. Res. Lett.* 27, 2685-2689.
- Søvde, O.A., M. Gauss, I.S.A. Isaksen, G. Pitari, and C. Marizy, 2007: Aircraft pollution – a futuristic view. *Atmos. Chem. Phys.* 7, 3621-3632.

Aviation NO_x Global Warming Potential

Agnieszka Skowron^{*}, David S. Lee, Jane Hurley

Dalton Research Institute, Manchester Metropolitan University, John Dalton Building, Chester Street, Manchester, M1 5GD, United Kingdom

Keywords: GWP, aviation NO_x emissions, O₃ non-linearity

ABSTRACT: The dual approach of using 2D and 3D Chemical Transport Models (CTMs) was adopted to deal with the temporal discrepancies of aircraft O₃ and CH₄ responses. A series of pulse and sustained experiments over 100-year horizons of aircraft O₃ and CH₄ for a range of aviation NO_x emission rates were carried out. Observed at a global scale, the non-linear aircraft O₃ response with respect to aircraft NO_x emissions rates may hold the key for understanding the discrepancy between reported aviation NO_x GWPs.

1 INTRODUCTION

The Global Warming Potential (GWP), since it was introduced at the first Intergovernmental Panel on Climate Change (IPCC) scientific assessment in 1990 (IPCC, 1990) became widely and deeply accepted as an appropriate measure by the user community. Usage of the GWP is the established method for comparing the potential impact of emissions of different long-lived greenhouse gases on climate under the Kyoto Protocol. A GWP is defined as the integrated radiative forcing from a unit emission of a gas over a certain defined time horizon relative to the unit emission of a reference gas (by convention, CO₂) over the same time horizon. The GWP places emissions of gases with different lifetimes and radiative properties on a common scale. This leads to weaknesses and uncertainties (Smith and Wigley, 2000a, b; Fuglestad et al., 2003; Shine et al., 2005a, b, 2007), which are challenges particularly for short-lived species and their precursors, e.g. the aviation NO_x emissions (IPCC, 1999).

The coupled NO_x-O₃-CH₄ system, as affected by aviation NO_x emissions, results in a short-term O₃ positive radiative forcing and a long-term O₃ and CH₄ negative responses. Nonetheless the overall radiative forcing induced by current day emissions of aviation NO_x is positive (Lee et al., 2009). These processes act on different spatial and temporal scales, which is why defining a unanimous result describing the impact of aviation NO_x on climate remains challenging and controversial.

IPCC AR4 WGI recently summarized studies that attempted to define an aviation NO_x GWP (Forster et al., 2007). Only three studies were identified, which yielded NO_x GWPs for aviation of: 100 (Derwent et al., 2001), 130 (Wild et al., 2001), and -3 (Stevenson et al., 2004). In addition, a recent study of Köhler et al. (2008) produced aviation NO_x GWP of 68. These GWPs have recently been re-evaluated by Fuglestad et al. (2009), yielding values of -2.1, 71, 6.9.

Such a wide range of results make it difficult to recommend an aviation NO_x GWP for formulating policy (Faber et al., 2008). These few and disparate values of aviation NO_x GWP are the motivation of this study, in which a preliminary attempt of unravelling these apparent disagreements is presented.

2 METHODOLOGY

One of the fundamental difficulties in calculating a GWP for aviation NO_x is that the timescales of responses of O₃ enhancement and CH₄ depletion are very different, such that the CH₄ results are often parameterized rather than fully calculated, since long integration times of the order of several

^{*} *Corresponding author:* A. Skowron, Dalton Research Institute-CATE, Manchester Metropolitan University, Faculty of Science and Engineering, John Dalton Building, Chester St, Manchester M1 5GD, UK. Email: a.skowron@mmu.ac.uk

CH₄ lifetimes (~ 8 – 10 years) are required – and such simulations are computationally expensive. We adopt a dual approach of using 2D and 3D CTMs to deal with the temporal discrepancies of responses.

The Two-dimensional Chemistry Model (TROPOS) is a latitudinally-averaged two-dimensional Eulerian global tropospheric chemistry model (Hough, 1989, 1991), with a domain which extends from pole-to-pole (24 latitudinal grid cells) and from the surface to an altitude of 24 km (12 vertical layers). TROPOS is driven by chemistry, emissions, transport, removal processes and upper boundary conditions. The revised values of emissions, thermal and photolysis reactions rates, cross-sections and quantum yield are applied and based on recent evaluations. This 2D CTM has the disadvantage of not fully representing atmospheric transport, but has the advantage of a complex chemical scheme and being computationally efficient such that many long-term integrations (of the order of 100 years) are easily achieved.

The Model for Ozone and Related Tracers, version 2 (MOZART-2) (Horowitz et al., 2003) is a state-of-the-art global 3D CTM. The model has been used at a T63LR resolution (~ 1.875° x 1.875°) and has a vertical domain of 47 layers which extends upward to around 10 hPa. The chemical scheme provides a detailed study of the distribution and budget of tropospheric ozone and its precursors. MOZART-2 is driven by meteorological fields from the European Centre for Medium Range Weather Forecasting (ECMWF), with schemes accounting for dynamical and removal processes, emissions, as well as boundary layer parameterizations.

Qualitative comparisons between basic characteristics of ozone precursor distributions produced from MOZART-2 (as a 3D CTM) and TROPOS (2D CTM) simulations were used to justify employing TROPOS to carry out long-term simulations, as TROPOS is capable of reproducing many of the broad-scale features simulated by the more-complete MOZART-2 model. Thus, it was possible to run TROPOS simulations for many perturbations of different magnitudes and natures. The series of pulse and sustained experiments over 100 year horizons of aircraft O₃ and CH₄ for a range of aviation NO_x rates were calculated.

All TROPOS integrations were run for a 103 years, where the ‘spin-up’ constitutes the first two years, beginning at January 2000 from realistic initializations. The sustained aviation simulation, with aircraft emissions of 2.8 Tg NO₂, was differenced against to the base case (without aircraft). The pulse emission experiments, on the other hand, had pulses applied globally for a period of a year during the third year of simulation, having aircraft emission rates ranging from 1.0 to 5.0 Tg N. A simulation having 2.8 Tg of aviation NO₂ (0.85 Tg N) is taken to be the base case for each pulse size.

3 RESULTS AND DISCUSSION

In all cases, the positive short-term O₃, negative long-term CH₄ and negative long-term O₃ responses were observed, the different shapes and magnitudes of behaviour reflect the varying natures of the individual experiments.

3.1 TROPOS vs MOZART-2

The 2D CTM reliability was justified with 3D CTM results. Figure 1 presents the distributions (latitude vs altitude) of O₃ and CH₄. A good agreement between these two models in terms of absolute and aircraft perturbation patterns is observed.

The largest mixing ratios of O₃ occur around the 20 km, where the photolysis of molecular oxygen is more intensive than in the lower parts of the atmosphere. The CH₄ distribution follows the emission sources, which explains the maximum in number densities observed at mid-to-high latitudes of the Northern Hemisphere (where the higher emission rates occur). This maximum in CH₄ is compounded by the fact that the removal of CH₄ by OH is slower in the mid-to-high latitudes, than in the tropics because of the temperature dependence of CH₄+OH reaction.

The aircraft perturbation distributions display well-known patterns. Aviation NO_x results in an increase in O₃ concentration. This response is observed mainly in the air traffic corridors, as O₃ is rather short-lived, with its lifetime of weeks. The increased concentrations of OH, caused by the O₃ enhancement, act to remove CH₄ from the atmosphere (the CH₄+OH reaction is the main removal path for tropospheric CH₄). The CH₄ is well-mixed through the globe, due to its long lifetime,

which is why its observed decline is distributed globally.

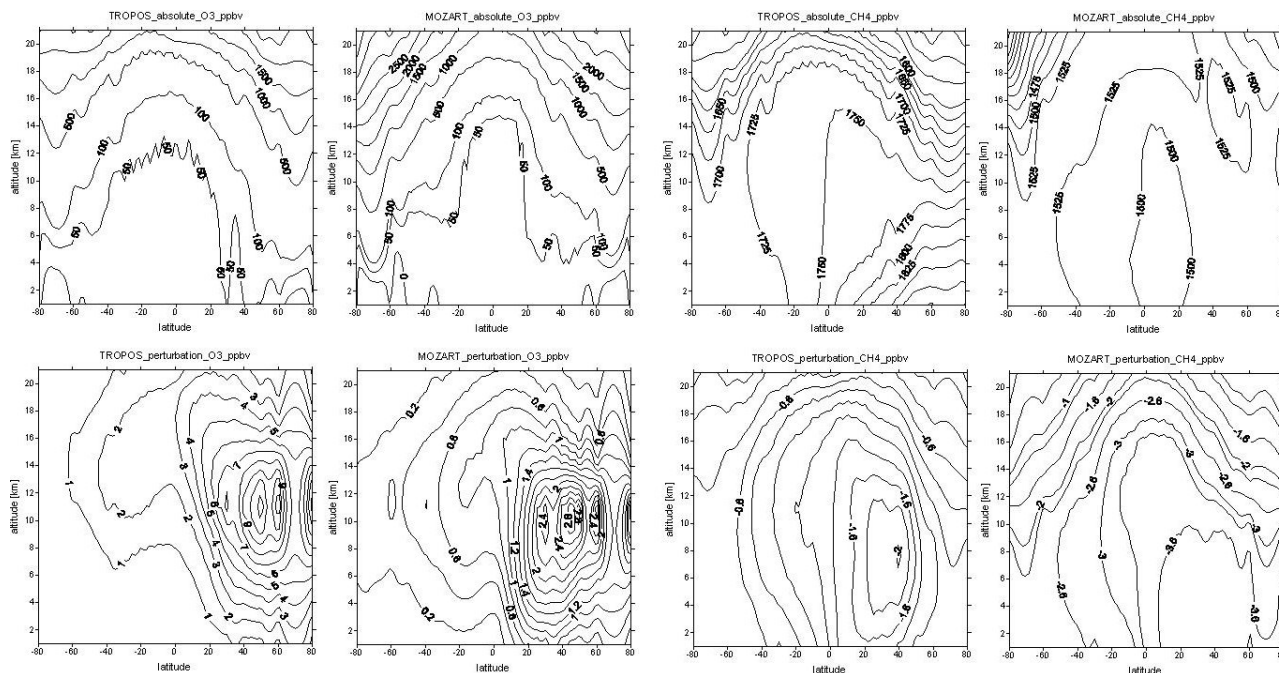


Figure 1: The distribution (latitude vs altitude) of O_3 and CH_4 (respectively from left to right) for absolute (first row) and aircraft perturbation (second row) values in TROPOS and MOZART-2.

The pattern of aircraft O_3 perturbation is in good agreement between the 2D and 3D simulations, despite the fact that O_3 production from aviation NO_x seems to be more efficient in TROPOS (higher maximum values). This can be explained by the 2D model shortcomings – for example, too coarse a spatial resolution can result in the transport of NO_x into remote environments and hence O_3 production in these NO_x -limited environments (Johnson and Derwent, 1996; Derwent et al., 2001).

The 2D CTM results were also compared with measurements. As most of the experiments in this study are designed as a long-term simulations, it is important to know how well TROPOS is able to represent the variability of species, especially methane (a well-mixed gas of lifetime = ~ 10.05 years in TROPOS), over decades. Figure 2 presents the modelled methane volume mixing ratios from the two lowest layers for three chosen latitude bands as compared with the observations of Dlugokencky et al. (2003) during the period 1983–2007. The values represent the monthly means and multiple observation points were included to show the variability within each latitude band. There is a good agreement between model and observational shapes, magnitudes and phases of the seasonal variations of methane concentrations; also the growth rate with time is well represented. While in the Southern Hemisphere the first and second of the model layers are overlapped, in the Northern Hemisphere some disparities are noticed. This is mainly due to the surface methane emissions, whose main sources occur in the northern latitudes (emissions are immediately mixed through the model surface grid cells, while in reality it takes a finite time to distribute around the latitude circle (Hough, 1991)), as well as by the fact that the air is mixed much better at the southern, especially high, latitudes.

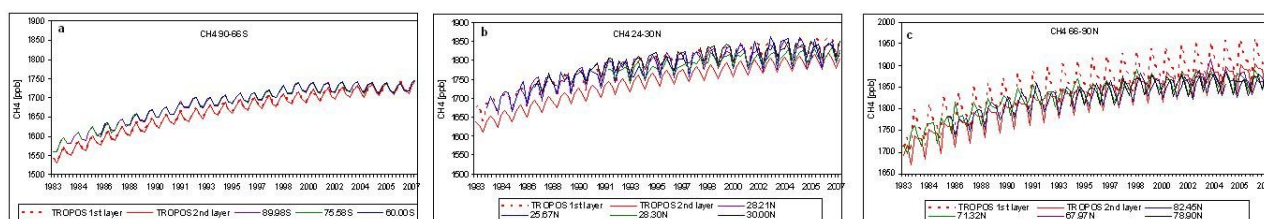


Figure 2: TROPOS vs measurements from Dlugokencky et al. (2003): the temporal variation of methane mixing ratio at chosen sites of the world. The dashed red curve is the model surface layer; the solid red curve is the model second vertical layer. The sites are: (a) South Pole, Antarctica, 89.98°S; Halley Station, Antarctica, 75.58°S; Syowa Station, Antarctica, 69.00°S, (b) Sand Island, Midway; 28.21°N; Key Biscayne, Florida; 25.67°N; Tenerife, Canary Islands; 28.30°N; Pacific Ocean; 30.00°N, (c) Pallas-Sammaltunturi, GAW Sta-

tion, 67.97°N; Barrow, Alaska, 71.32°N; Ny-Alesund, Svalbard, 78.90°N; Alert, Nunavut, 82.45°Nhttp://www.esrl.noaa.gov/gmd/dv/site/PAL.html.

3.2 Sustained Simulation

Figure 3 presents the evolution of O_3 and CH_4 perturbations over 100 years from a 2.8 Tg NO_2 sustained aviation experiment from TROPOS. We can observe the positive O_3 and negative CH_4 responses. The continuous input of aviation NO_x emissions keeps the burden of O_3 at certain level; the long-term O_3 is also pronounced and it manifests as a small (~ 1.2 Tg O_3 within the 90 years) reduction in the positive aviation O_3 perturbation. The CH_4 response for constant aircraft emission is the continual decline of its tropospheric mass, until approximately the seventieth year of simulation, when CH_4 reaches its equilibrium. CH_4 , as a long-lived gas, needs a few decades (the steady reduction of ambient CH_4 takes place with a 9.9 year CH_4 perturbation lifetime) to reach steady-state, while O_3 response is ‘instantaneous’.

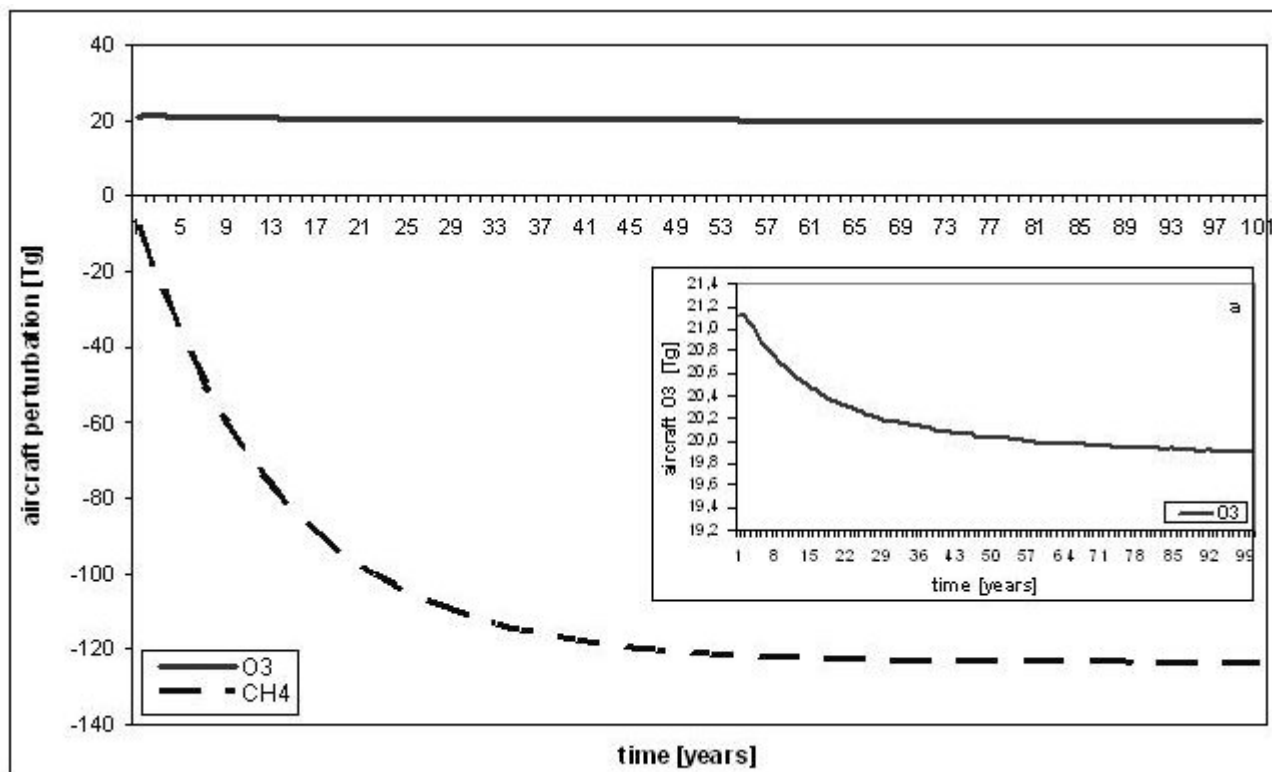


Figure 3: The time evolution of perturbations in the global burdens of ozone and methane over the 100 year horizon from the 2.8 Tg NO_2 sustained aviation experiment. The secondary O_3 is observed (a).

3.3 Pulse Simulations

Pulses are widely accepted and used to define and understand the mechanisms of complex NO_x chemistry. They are also utilized in order to assess the NO_x impact on climate through the GWP approach.

The year-long pulses are sources of easily visible short-term positive O_3 , long-term negative CH_4 and long-term negative O_3 perturbations (Fig. 4). The temporal scales of its responses are clearly shown. After each pulse, the O_3 enhancement immediately becomes noticeable, and persists for a relatively brief period, (~ 3 years); then, a year after the pulse, the negative peak response of CH_4 takes place – and, finally, at the fifth year after the pulse, the long-term negative O_3 peak response develops. It takes few decades for both CH_4 and long-term O_3 to return to their equilibrium values; the pulse size plays an important role in the length of their recovery.

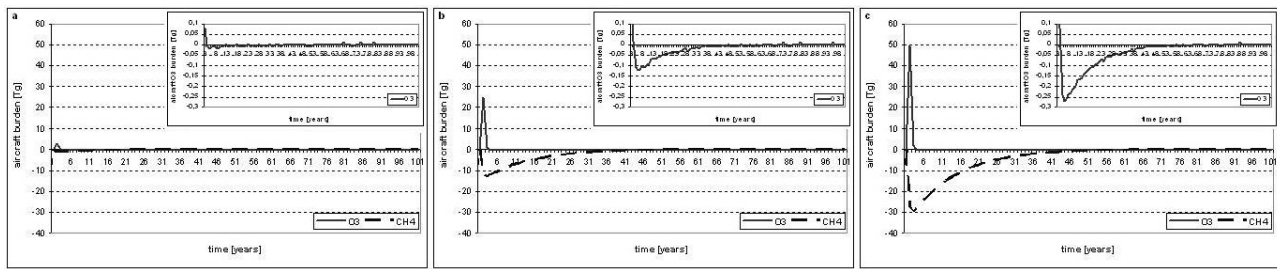


Figure 4: The time evolution of ozone and methane responses from the aircraft NO_x pulse experiments. Three different aircraft NO_x rates are presented: (a) 1.0 Tg N, (b) 2.5 Tg N, (c) 5.0 Tg N.

It is immediately visible how, with increasing rates of emission of aviation NO_x , the methane response increasingly dominates over the positive O_3 perturbation. The proportion of O_3 burden to CH_4 burden decreases with higher NO_x : for 1.0 Tg N, the O_3 burden constitute 14.5% of the CH_4 perturbation, whilst for 2.5 Tg N and 5.0 Tg N, it falls to 12.7% and 11.1% of the CH_4 response, respectively. The integrated burden of CH_4 becomes more pronounced than that of O_3 . The ‘production’ of O_3 seems to saturate with respect to NO_x .

The positive O_3 response weakens with larger aircraft NO_x perturbations. This leads to a non-linear behaviour of aviation O_3 , which is presented in Figure 5. Previously, mainly linear characteristics of O_3 for a various aircraft emissions were shown (Grewe et al., 1999; IPCC, 1999; Köhler et al., 2008). The non-linear response is expected from the chemistry (Lin et al., 1988; Bernsten et al., 2005), but it has not been demonstrated so clearly before on a global scale. While the capacity of the troposphere to generate O_3 from NO_x is gradually declining, the non-linearity of methane burden destruction is much weaker; nevertheless it is also observed.

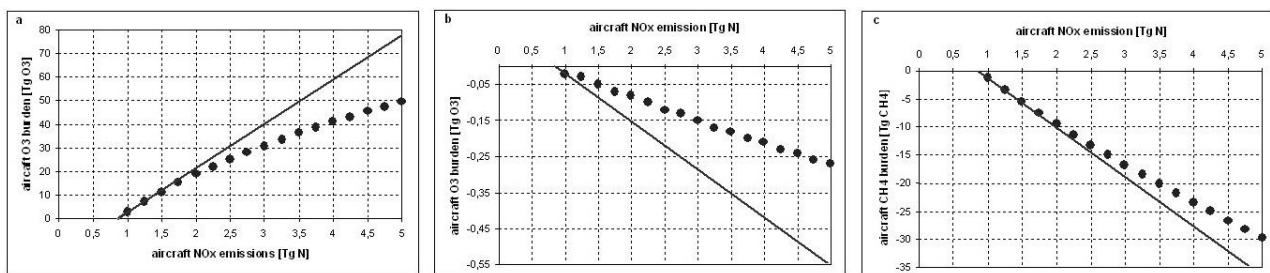


Figure 5: The modelled peak of pulse for (a) short-term O_3 , (b) long-term O_3 and (c) CH_4 (dots) from a range of aircraft NO_x emissions rates. The line presents the linear solution.

4 CONCLUSIONS AND FURTHER WORK

These results imply that the O_3 response due to aircraft emissions, as observed on a global scale, is linked to the rate of emission of aircraft NO_x – and that the discrepancy between previously published NO_x GWPs may possibly be linked to the non-linear response of O_3 to aircraft NO_x emissions, particularly when the variances amongst the various experimental designs are taken into account.

These 2D CTM simulations give a unique view of NO_x chemistry perturbations, which cannot be easily achieved through 3D studies, as which long-term simulations are computationally prohibitive. It is important to carry out similar pulse experiments with a 3D CTM to confirm the results and trends suggested by this 2D CTM study.

In the next step of the work, the pulse aircraft perturbation values of O_3 and CH_4 will be translated into radiative forcings and consequently the AGWPs and GWPs will be defined for a series of aircraft NO_x rates and a range of time horizons.

REFERENCES

- Bernsten, T. K., J. S. Fuglestad, M. M. Joshi, K. P. Shine, N. Stuber, M. Ponater, R. Sausen, D. A. Hauglustaine, and L. Li, 2005: Response of climate to regional emissions of ozone precursors: Sensitivities and warming potentials. *Tellus, Series B: Chemical and Physical Meteorology*, 57, 283–304.

- Derwent, R. G., W. J. Collins, C. E. Johnson, and D. S. Stevenson, 2001: Transient behaviour of tropospheric ozone precursors in a global 3-D CTM and their indirect greenhouse effects. *Climatic Change*, 49, 463-487.
- Dlugokencky, E. J., S. Houweling, L. Bruhwiler, K. A. Masarie, P. M. Lang, J. B. Miller and P. P. Tans, 2003: Atmospheric methane levels off: Temporary pause or a new steady-state? *Geophysical Research Letter*, 30.
- Faber, J., Greenwood, D., D. Lee, M. Mann, P. M. de Leon, D. Nelissen, B. Owen, M. Ralph, J. Tilston, A. van Velzen, G. van de Vreede, 2008: Lower NO_x at higher altitudes. Policies to reduce the climate impact of aviation NO_x emission. Delft: CE Delft.
- Forster, P., V. Ramaswamy, P. Artaxo, T. Berntsen, R. Betts, D. W. Fahey, J. Haywood, J. Lean, D. C. Lowe, G. Myhre, J. Nganga, R. Prinn, G. Raga, M. Schulz, R. Van Dorland, 2007: Changes in atmospheric constituents and in radiative forcing. In 'Climate Change', *Fourth Assessment Report of Working Group I of the Intergovernmental Panel on Climate Change*, Cambridge University Press, UK.
- Fuglestvedt, J. S., T. K. Berntsen, O. Godal, R. Sausen, K. P. Shine, and T. Skodvin, 2003: Metrics of climate change: Assessing radiative forcing and emission indices. *Climatic Change*, 58, 267-331.
- Fuglestvedt, J. S., K. P. Shine, T. Berntsen, J. Cook, D. S. Lee, A. Stenke, R. B. Skeie, G. J. M. Velders, and I. A. Waitz, 2009: Transport impacts on atmosphere and climate: Metrics. *Atmospheric Environment*.
- Grewe, V., M. Dameris, R. Hein, I. Köhler, and R. Sausen, 1999: Impact of future subsonic aircraft NO_x emissions on the atmospheric composition. *Geophysical Research Letters*, 26, 47-50.
- Horowitz, L. W., S. Walters, D. L. Mauzerall, L. K. Emmons, P. J. Rasch, C. Granier, X. Tie, J. F. Lamarque, M. G. Schultz, G. S. Tyndall, J. J. Orlando, and G. P. Brasseur, 2003: A global simulation of tropospheric ozone and related tracers: Description and evaluation of MOZART, version 2. *Journal of Geophysical Research D: Atmospheres*, 108.
- Hough, A. M., 1989: The development of a two-dimensional global tropospheric model. 1. The model transport. *Atmospheric Environment*, 23, 1235-1261.
- Hough, A. M., 1991: Development of a two-dimensional global tropospheric model: model chemistry. *Journal of Geophysical Research*, 96, 7325-7362.
- IPCC, 1990: Climate Change: The Intergovernmental Panel on Climate Change, Cambridge University Press, Cambridge, UK.
- IPCC, 1999: *Aviation and the Global Atmosphere*. J.E. Penner, D.H. Lister, D.J. Griggs, D.J. Dokken and M. McFarland (Eds). Intergovernmental Panel on Climate Change, Cambridge University Press, UK.
- Johnson, C. E. and R. G. Derwent, 1996: Relative radiative forcing consequences of global emissions of hydrocarbons, carbon monoxide and NO_x from human activities estimated with a zonally-averaged two-dimensional model. *Climatic Change*, 34, 439-462.
- Köhler, M. O., G. Rädcl, O. Dessens, K. P. Shine, H. L. Rogers, O. Wild, and J. A. Pyle, 2008: Impact of perturbations to nitrogen oxide emissions from global aviation. *Journal of Geophysical Research D: Atmospheres*, 113.
- Lee, D. S., D. W. Fahey, P. M. Forster, P. J. Newton, R. C. N. Wit, L. L. Lim, B. Owen, and R. Sausen, 2009: Aviation and global climate change in the 21st century. *Atmospheric Environment*, 43, 3520-3537.
- Lin, X., M. Trainer, and S. C. Liu, 1988: On the nonlinearity of the tropospheric ozone production. *Journal of Geophysical Research*, 93.
- Shine, K. P., J. S. Fuglestvedt, K. Hailemariam, and N. Stuber, 2005a: Alternatives to the Global Warming Potential for comparing climate impacts of emissions of greenhouse gases. *Climatic Change*, 68, 281-302.
- Shine, K. P., T. K. Berntsen, J. S. Fuglestvedt, and R. Sausen, 2005b: Scientific issues in the design of metrics for inclusion of oxides of nitrogen in global climate agreements. *Proceedings of the National Academy of Sciences of the United States of America*, 102, 15768-15773.
- Shine, K. P., T. K. Berntsen, J. S. Fuglestvedt, R. B. Skeie, and N. Stuber, 2007: Comparing the climate effect of emissions of short- and long-lived climate agents. *Philosophical Transactions of the Royal Society A: Mathematical, Physical and Engineering Sciences*, 365, 1903-1914.
- Smith, S. J. and T. M. L. Wigley, 2000a: Global Warming Potentials: 1. Climatic implications of emissions reductions. *Climatic Change*, 44, 445-457.
- Smith, S. J. and T. M. L. Wigley, 2000b: Global Warming Potentials: 2. Accuracy. *Climatic Change*, 44, 459-469.
- Stevenson, D. S., R. M. Doherty, M. G. Sanderson, W. J. Collins, C. E. Johnson, and R. G. Derwent, 2004: Radiative forcing from aircraft NO_x emissions: Mechanisms and seasonal dependence. *Journal of Geophysical Research D: Atmospheres*, 109.
- Wild, O., M. J. Prather, and H. Akimoto, 2001: Indirect long-term global radiative cooling from NO_x emissions. *Geophysical Research Letters*, 28, 1719-1722.

Vertical spatial scales of ice supersaturation and probability of ice supersaturated layers in low resolution profiles of relative humidity

N.C. Dickson¹, K. Gierens^{2*}, H.L. Rogers¹, R.L. Jones¹

1) *Centre for Atmospheric Science, University of Cambridge, Cambridge, UK*

2) *DLR Oberpfaffenhofen, Institut für Physik der Atmosphäre, Germany*

Keywords: Ice supersaturated regions, Radiosondes

ABSTRACT: We present an analysis of the vertical extension of ice supersaturated regions based on high resolution, corrected humidity data from British radiosonde launch stations (2002-2006). Additionally, we provide a probabilistic description of the occurrence of ice supersaturated layers in low resolution profiles of relative humidity. The results bear an importance for operational strategies of contrail avoidance.

1 INTRODUCTION

To avoid formation of persistent contrails means to avoid flights through ice supersaturated regions (ISSRs). Based on an analysis of the vertical extension of ISSRs obtained from 14 months of radiosonde data from Lindenberg, Germany, Mannstein et al. (2005) proposed that a substantial fraction of flights in ISSRs can be avoided by changing flight levels by 1-2 levels, because the supersaturated layers over Lindenberg turned out to be shallow on average (about 650 m). However, radiosonde data from Spitzbergen (Treffeisen et al., 2007) and southern England (Rädel and Shine, 2007) seem to indicate larger vertical extensions of ISSRs which would render the Mannstein et al. avoidance strategy more difficult to implement or less successful. We present new statistical evidence for ISSR vertical extent, utilising in-situ observations from UK Met Office high resolution radiosonde stations. We show layer depth statistics and demonstrate that over this extended data set most ISSR layers are fairly shallow. Hence the avoidance strategy of Mannstein et al. can well be confirmed; however, for weather prediction models with their usually low resolution layers in the tropopause region it will be more difficult to correctly predict ISSRs unless their vertical resolution is improved. In order to estimate the true occurrence frequency of ISSRs in low resolution data, we additionally derive from the radiosonde data set a probabilistic description of the occurrence of ice supersaturated layers in low resolution profiles of relative humidity.

2 PROCESSING OF RADIOSONDE DATA

2.1 Selection of launch stations

From the UK Met Office global radiosonde data-set we selected a sub-set of nine radiosonde stations, sited predominantly around the UK but with three non-UK stations (Gibraltar, St. Helena and the Falkland Islands) that have recorded vertical profiles at a high vertical resolution, i.e. every two seconds. Profiles for a five year period, from 1st January 2002 to 31st December 2006, from nine UK Met Office radiosonde launch stations as shown in Table 1, were used to study the vertical extent of ISS layers. For the nine stations used, launches were typically twice daily at local times of 1200h and 2400h. The only exception to this was St. Helena, which recorded approximately one launch per day, with approximately 20-25 launches per month.

* *Corresponding author:* Klaus Gierens, DLR-Institut für Physik der Atmosphäre, Oberpfaffenhofen, D-82234 Wessling, Germany. Email: Klaus.Gierens@dlr.de

Table 1: A summary of UK Met Office high resolution radiosonde observations (1st January 2002 to 31st December 2006) used in this study. Observations were generally performed using the Vaisala RS80 up to mid-2005 with the RS92 instrument used thereafter [UK Met Office].

Station	Location	Launches (2002-06)	Radiosonde type
Albemarle	1.88°W, 55.02°N	3546	RS80/RS92
Camborne	5.329°W, 50.218°N	3981	RS80/RS92
Castor Bay	6.503°W, 54.503°N	3234	RS80/RS92
Herstmonceux	0.319°E, 50.89°N	3771	RS80/RS92
Lerwick	1.183 °W, 60.139°N	3957	RS80/RS92
Watnall	1.25 °W, 53.005°N	3804	RS80/RS92
Gibraltar	5.35°W, 36.15°N	3429	RS80
St Helena	5.667°W, 15.933°S	1189	RS80
Falkland Islands	58.45°W , 51.817°S	3551	RS80

2.2 Correction

The Vaisala RS80-H radiosonde was in service with UK Met Office launch stations until approximately mid-2005, when the RS92 type radiosonde entered service. The exact changeover date was launch station dependent, but from the beginning of 2006 all observations used here were made with the RS92 radiosonde. Both RS80 and RS92 are subject to different systematic errors and as such these instruments have different correction algorithms. The RS80-H has specific issues over temperature dependency, chemical contamination, sensor ageing and measurement time lag, leading to a dry bias. To account for the resulting bias in observations, the correction presented by Wang et al., (2002) was used. RS92 observations are also subject to a dry bias, in this case due to the lack of a radiation shield, leading to solar heating of the humidity sensor [Vömel et al., 2006]. There is less information regarding RS92 accuracy and only a few correction methods are available, however, a study by Vömel et al., (2006) was applied here to correct for the observation dry bias. It is worthy of note, that in many profiles, ISS events would not be observed if it were not for application of the correction algorithms [see also Rädcl and Shine, 2007]. Data contaminated by sensor icing and data from pressure layers containing the tropopause have been discarded from the study.

3 RESULTS

3.1 Occurrence of ice supersaturation

Figure 1a describes the seasonal changes with relation to launch station and the inter-annual variation, respectively, from stations in the British Isles. These data show that ISS, of any layer thickness, is likely to occur with a probability of between 13% and 25% in the winter and 9% and 17% in the summer. These statistics are similar to those presented in Rädcl and Shine (2007) which presents ISS events occurring at a frequency of 15-25% and 9-12% in the winter and summer respectively. Occurrence of ISS and seasonal trends in the troposphere, presented in Rädcl and Shine (2007) and Vaughan et al (2006), support the findings here.

The same analysis is performed on the data from stations outside of the British Isles. 1b shows the ISS occurrence statistics from the St Helena, Gibraltar and Falkland Islands stations and is compared to the monthly mean from the six British Isles based stations. St Helena demonstrates a low occurrence of ISS, and this can not simply be explained by the paucity of data from this station. The Gibraltar and Falkland Island stations show variation in the monthly mean in line with expectations.

Gibraltar shows in general a smaller probability of ISS occurrence compared with the British Isles stations, but with a summer low of two percent and a winter high of 13% the seasonality trends are similar. The Falkland Islands, with its southerly mid-latitude location shows similar lows and highs in the same season, albeit south hemisphere season, as the British Isles data.

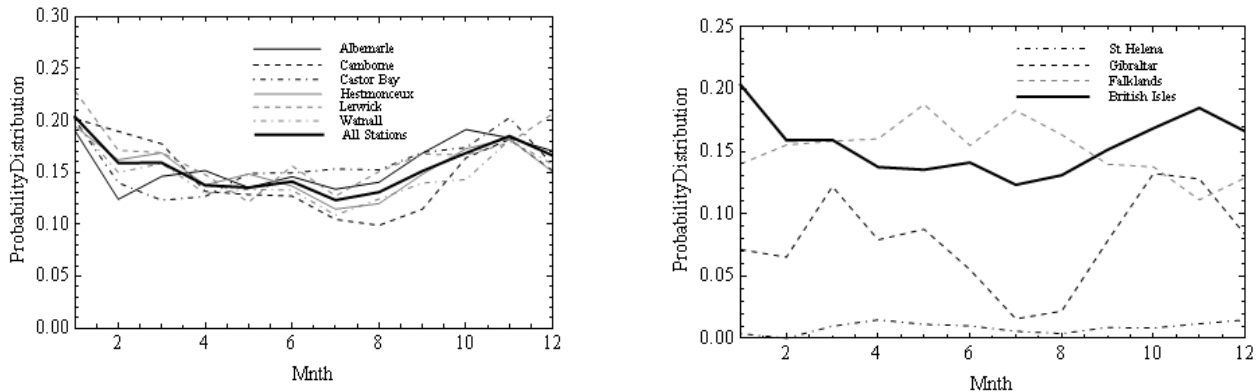


Figure 1. (a) Frequency of occurrence of ice supersaturated layers in radiosonde profiles from 6 launch station on the British Isles; (b) same as (a) but for Gibraltar, St Helena and the Falkland Islands.

3.2 Vertical extension of ice supersaturated layers

To investigate the vertical extensions of ISSRs and their statistics, each radiosonde profile is interrogated for ISS. Once an ISS event is identified then the depth is recorded. The British Isles dataset is used (2002–2006) to generate a radiosonde station centric subset of ISS events. These subsets are divided into bins of 100 metre layer depths and initially this gives a frequency distribution as described by 2. The difference between stations is remarkably small and there is evidence of an exponential-type distribution. The majority of layers are shallower than 1500 m, accounting for 81 to 87 percent of data and 27 to 34 percent of layers are less than 100 metres deep. The remaining layers occur in sizes up to 4500 metres with on average 11 percent are in the size range 1500 to 3000 metres and with 5% greater than 3000 metres. The distributions are similar for the three considered launch stations outside the UK, and the annual and seasonal variations are weak except for the shallowest layers.

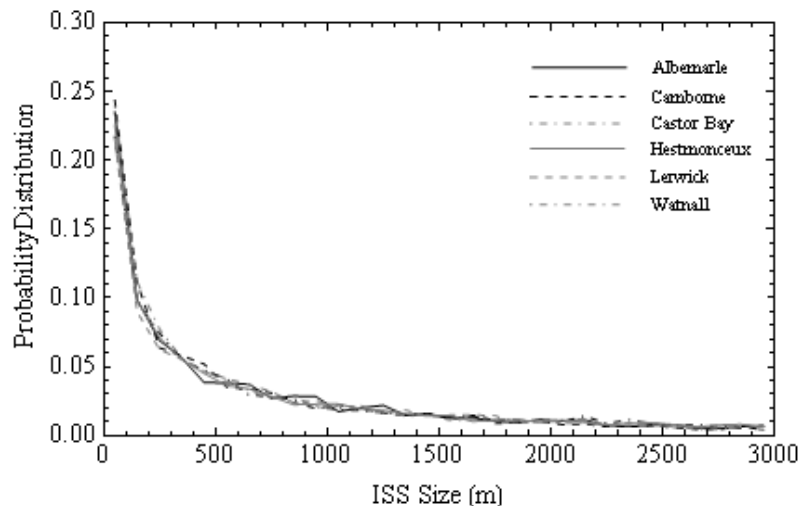


Figure 2. Probability distribution function of vertical layer depths of ice supersaturated layers detected in radiosonde humidity profiles at 6 launch station in the UK.

3.3 Probabilistic description of the occurrence of shallow ice supersaturated layers embedded in low-vertical resolution humidity profiles

The analysis was based on 30,462 radiosonde profiles separated into 50 and 100 hPa layers which gave totals of 152,310 50 hPa and 60,924 100 hPa pressure layers. For each pressure layer we determined the fraction of single humidity measurements that showed ice supersaturation in that layer together with the average relative humidity over that layer. The relation between these quantities is shown in Figure 3.

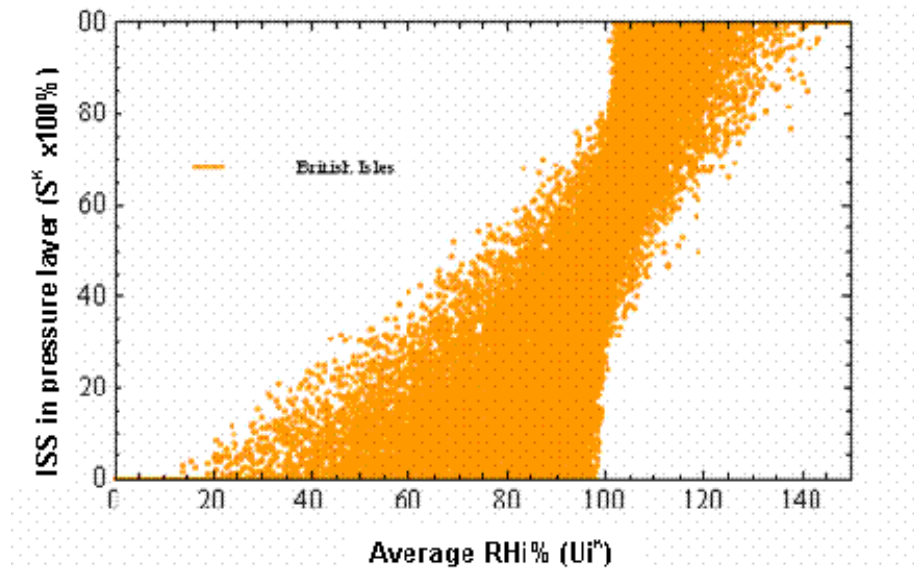


Figure 3. The fraction of humidity measurements indicating ice supersaturation vs. the corresponding average relative humidity wrt ice for 50 hPa pressure layers over the British Isles.

These data have been grouped together in 5% RH_i bins, and the mean of the fractional ISS occurrence has been computed for each bin. This resulted in the following s-shaped relationship:

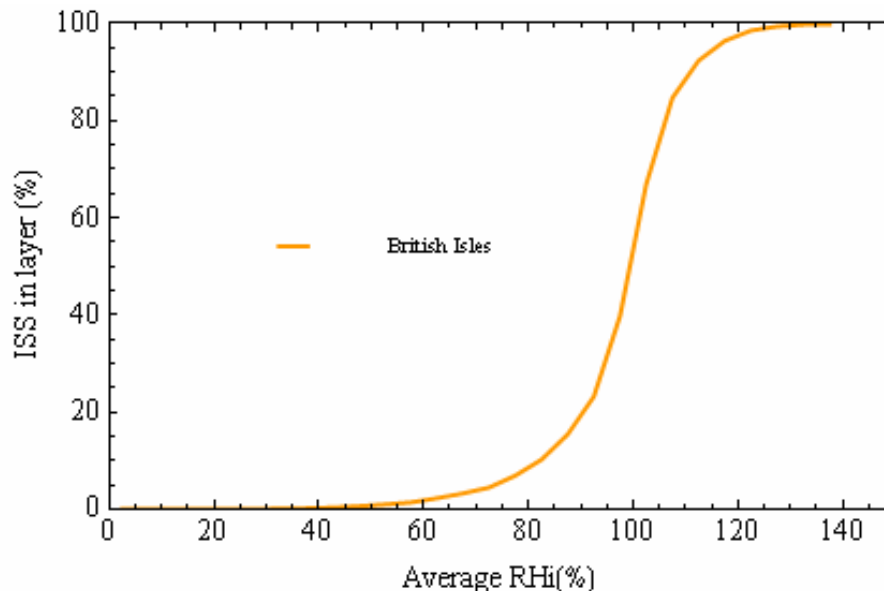


Figure 4. The average fraction of ice supersaturation in thick layers vs. the average RH_i in that layer displays an s-shaped relation.

The maximum standard deviation from the s-curve is 0.18, determined from the whole British Isles data set. In comparison to this, variations due to geographical location, annual and seasonal variation, and vertical location of the considered pressure layer, are all smaller, such that this s-curve can be considered as representative for all cases. We have additionally developed a simple mathematical description of the s-curve, based on the observed data. This will be presented elsewhere.

4 CONCLUSIONS

After analysing 5 years of high-vertical resolution radiosonde humidity profiles obtained from 9 launch stations on the British Isles and three from elsewhere (Gibraltar, St Helena, and Falkland Islands) we arrived at the following results:

- Ice supersaturated layers occur on average in 15–20% of all radiosonde profiles over the British Isles and the Falkland Islands, i.e. mid-latitude stations. The ISS frequency is very low at the tropical site of St Helena, and intermediate at Gibraltar.

- The vertical extension of ice supersaturated layers obeys a roughly exponential probability distribution; that is, most layers are shallow, such that aircraft can often avoid flying in ice supersaturated air by switching their flight level by one standard step up or down.
- Humidity profiles in low vertical resolution, e.g. from radiosonde archives (standard pressure levels) or from satellite data can be corrected to determine a probable ISS frequency using the s-shaped relationship derived from the data. The mathematical model that we have developed will simplify such an exercise.

These results bear some implications not only for strategies of operational contrail avoidance, as indicated, but also for (aviation) weather forecast which must be able to reliably predict ice supersaturated layers. The predominant shallowness of these layers makes it necessary either to improve the vertical resolution of weather models in the upper troposphere region (which will occur as soon as computer power allows it) or to introduce means and measures that describe the vertical sub-grid scale variability. The latter is in particular worth of consideration in climate models with their generally lower vertical resolution. The application of the s-shaped relationship may be a way forward into this direction.

5 ACKNOWLEDGEMENT

This research was funded by the UK research council NERC at the University of Cambridge, in collaboration with QinetiQ, and was supported by the DLR project CATS. It contributes further to the German UFO project and to the European Network of Excellence ECATS.

REFERENCES

- Mannstein, H., P. Spichtinger, and K. Gierens, 2005: A note on how to avoid contrails. *Transportation Res. Part D* 10, 421-426.
- Rädel, G., and K.P. Shine, 2007: Evaluation of the use of radiosonde humidity data to predict the occurrence of persistent contrails. *Quart. J. Roy. Meteorol. Soc.*, 133, 1413-1423.
- Treffeisen, R., R. Krejci, J. Ström, A.C. Engvall, A. Herber, and L. Thomason, 2007: Humidity observations in the Arctic troposphere over Ny-Alesund, Svalbard based on 15 years of radiosonde data. *Atmos. Chem. Phys.*, 7, 2721-2732.
- UK Meteorological Office, 2006: UK High Resolution Radiosonde Data, [Internet]. British Atmospheric Data Service (BADC). Available from <http://badc.nerc.ac.uk/data/rad-highres/>
- Vömel, H., H. Selkirk, L. Miloshevich, J. Valverde-Canossa, J. Valdés, E. Kyrö, W. Kivi, W. Stolz, G. Peng, J.A. Diaz, 2007: Radiation dry bias of the Vaisala RS92 humidity sensor. *J. Atmos. Ocean. Techn.*, 24, 953-963.
- Wang, J.H., H.L. Cole, D.J. Carlson, E.R. Miller, K. Beierle, A. Paukkunen, T.K. Laine, 2002: Corrections of humidity measurement errors from the Vaisala RS80 radiosonde - Application to TOGA COARE data. *J. Atmos. Ocean. Techn.*, 19, 981-1002.

Impact on air quality of a 90 km/h speed limit during PM10 episodes

P. Viaene^{*}, W. Lefebvre, K. Van de Vel, S. Janssen, G. Cosemans, K. De Ridder, I. De Vlieger, C. Mensink, L. Schrooten, J. Vankerkom
VITO, Mol, Belgium

F. Fierens
Belgian Interregional Environment Agency, Brussels, Belgium

T. Van Mierlo
Flemish Government Department of Environment, Nature and Energy, Section Air and Climate, Brussels, Belgium

F. Blommaert
Flemish Environmental Agency, Antwerp, Belgium

Keywords: road transport, smog, emission reduction

ABSTRACT: During smog episodes Flemish legislation imposes a 90 km/h speed limit on certain stretches of the highway network. In this contribution to TAC-2 we present the results of a study in which we assess the effects of this measure on air quality and compare the effect to other more stringent measures such as banning heavy duty vehicles or cars older than EURO-3 from the highways.

1 INTRODUCTION

To protect the health of its citizens the European Community has defined air quality guidelines to limit particulate matter (PM₁₀) concentrations such as the “cleaner air for Europe” directive (2008/50/EG) which states that the daily average PM₁₀ concentration may not exceed 50 µg/m³ for more than 35 days a year. According to Article 24 of this directive, EU member states have to devise action plans stating which type of actions are taken in case threshold values are likely to be exceeded, in order to diminish both the risk and the duration of such exceedances. Within this context the Flemish government decided to adopt a speed limit of 90 km/h instead of 120 km/h on certain high way sections during PM₁₀ smog episodes.

2 METHODOLOGY

To assess the effect of the speed limit measure and compare this effect to that of more severe measures the air quality during 2 smog episodes was modelled for a reference situation where no speed limit is imposed and a number of scenario's using a suite of models (Figure 1) that can calculate the effect of different emission scenario's on air quality in enough detail to discern the short range effects that are to be expected.

Besides the reference run using the normal emissions, the study considered the following scenario's:

- the speed limit is reduced to 90 km/h in line with Flemish legislation to a selection of the highway network;
- the speed limit of 90 km/h is applied to all the highways in Flanders and Brussels;
- scenario 1 and all heavy duty vehicles of euro-classes 0, 1 and 2 are banned and not replaced by newer heavy duty vehicles;
- scenario 1 and all heavy duty vehicles are taken off the road;

^{*} Corresponding author: Peter Viaene, VITO, Boeretang 200, B-2400 Mol, Belgium. Email: peter.viaene@vito.be

- scenario 1 and all cars, of euro-classes 0, 1 and 2 are taken off the road and not replaced by newer vehicles.

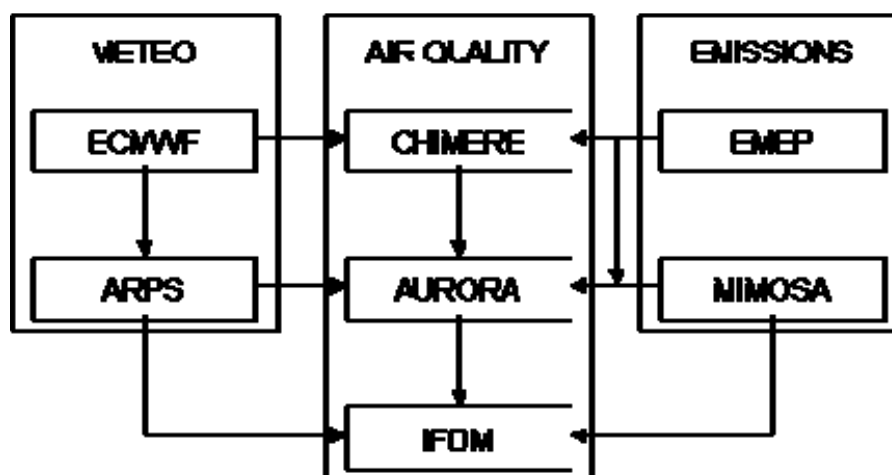


Figure 1. The coupled modelling system used for this study.

3 EMISSIONS

For the road traffic emissions, MIMOSA4 the most recent version of the MIMOSA model (Mensink et al., 2000, Vankerkm et al., 2005) was used. This model generates hourly traffic emissions for different types of pollutants, such as PM₁₀ and PM_{2.5} for Flanders. Based on the modelled number of different types of vehicles for each road, MIMOSA calculates the corresponding emissions by splitting up the total number of vehicles into different categories, depending on e.g. weight, EURO class, ... This distribution is based on statistical data on the vehicle fleet in Flanders. In order to calculate these emissions, the COPERT-IV methodology has been used. Emissions due to cold start and loss by evaporation are also modelled and for particulate matter the model takes into account non-tailpipe emissions due to brake-, tire- and road wear.

The MIMOSA model sets the traffic speed based on the type of road (rural, urban, highway,...). For the purpose of this study, the model was adapted so that different speed limits can be imposed for different parts of the road network. The speed limits can also be specified for individual EURO classes and vehicle types in order to allow for maximum flexibility in the scenario definition.

In the study we also looked at elementary carbon (EC). As EC is not modelled by MIMOSA the EC emissions were estimated from the PM_{2.5} emissions by multiplying these by 0.7. This high fraction is reasonable in view of the fleet composition in Flanders where the vast majority of cars has a diesel engine.

For the non-traffic emissions, the EPER-database is used, except for Flanders. For this last region, the emissions are those from the Emissie-Inventaris Lucht (EIL), the so-called ‘Kernset’. More information on the used emissions can be found in Maes et al. (2009).

The reduction in the average emission for each of the scenario’s can be found in Table1 below.

Table 1. The mean traffic emissions for NO_x, PM₁₀ and PM_{2.5} for the different scenario's relative to the emission for the reference run in % of the reference values.

	NO _x	PM ₁₀	PM _{2.5}
Scenario 1	95.91	94.04	93.15
Scenario 2	91.28	87.32	85.43
Scenario 3	81.64	86.42	84.63
Scenario 4	52.07	76.17	73.52
Scenario 5	81.42	70.54	69.73

4 AIR QUALITY MODELLING

For the air quality modelling both the AURORA and the IFDM models were used. The AURORA air quality model (Mensink et al., 2001) is a prognostic 3-dimensional Eulerian chemistry-transport model, designed to simulate urban- to regional-scale concentration fields. The IFDM model (Cosemans et al., 1992) on the other hand is a bi-Gaussian plume model used to describe the local dispersion of traffic emissions. The modelling approach consists of a number of one way nested runs starting with the boundary condition and initial conditions from a regional model run for a domain covering Europe at a resolution of 25 km over intermediate resolutions of 15 and 9 km to arrive at modelling results for a resolution of 3 km for the Flemish region. The 3 km AURORA concentrations are then after correction for the road emissions taken as background concentrations for runs with the IFDM model. To obtain detailed results along the highways the IFDM run calculates results for the points of a 1 km resolution regular grid combined with those of an irregular grid along the roads with a resolution varying from 50 to 800 m. The meteorological input required for the air quality modelling at the different resolutions was calculated with the ARPS model (Xue et al., 2000).

As can be expected the improvement of the average air quality in Flanders due to limiting the speed on selected stretches of the highways to 90 km/h is rather small. For this scenario the concentrations of NO₂ and PM are reduced by less than one percent (Table 2). The effect on the concentrations is more pronounced along the highways (Figure 2) where the concentration decreases up to 8% for NO₂ and 3% for PM. In this study we also looked at the changes in the elementary carbon concentration. Here we found a reduction of up to 30% in the immediate vicinity of highways and of 10% up to 1.2 km away from the highway.

Table 2. The percent change in average concentration for Flanders in NO₂, PM₁₀ and PM_{2.5} for the different scenario's relative to the reference run.

	NO ₂	PM ₁₀	PM _{2.5}
Scenario 1	-0.87	-0.12	-0.22
Scenario 2	-1.87	-0.26	-0.50
Scenario 3	-7.60	-0.45	-0.80
Scenario 4	-10.91	-0.54	-0.95

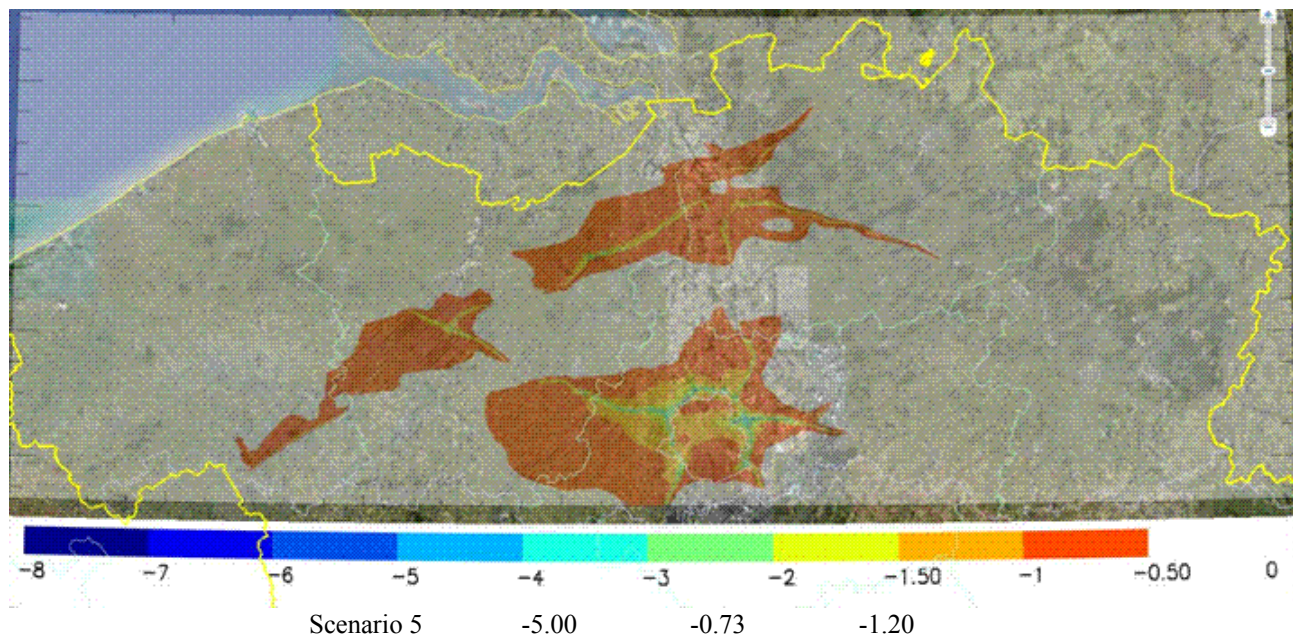


Figure 2. Percent change of the average modelled PM_{2.5} concentration for scenario 1 compared to the reference situation for the whole smog episode of December 2007.

By combining the modelled concentration changes with a population density map, one can also assess the changes in population exposure as shown in Figure 3. It can then be seen that scenario 1 results in a 0.5% decrease in PM_{2.5} concentration for 50 % of the population. For 5% of the population the PM_{2.5} concentration decreases by 1.3%.

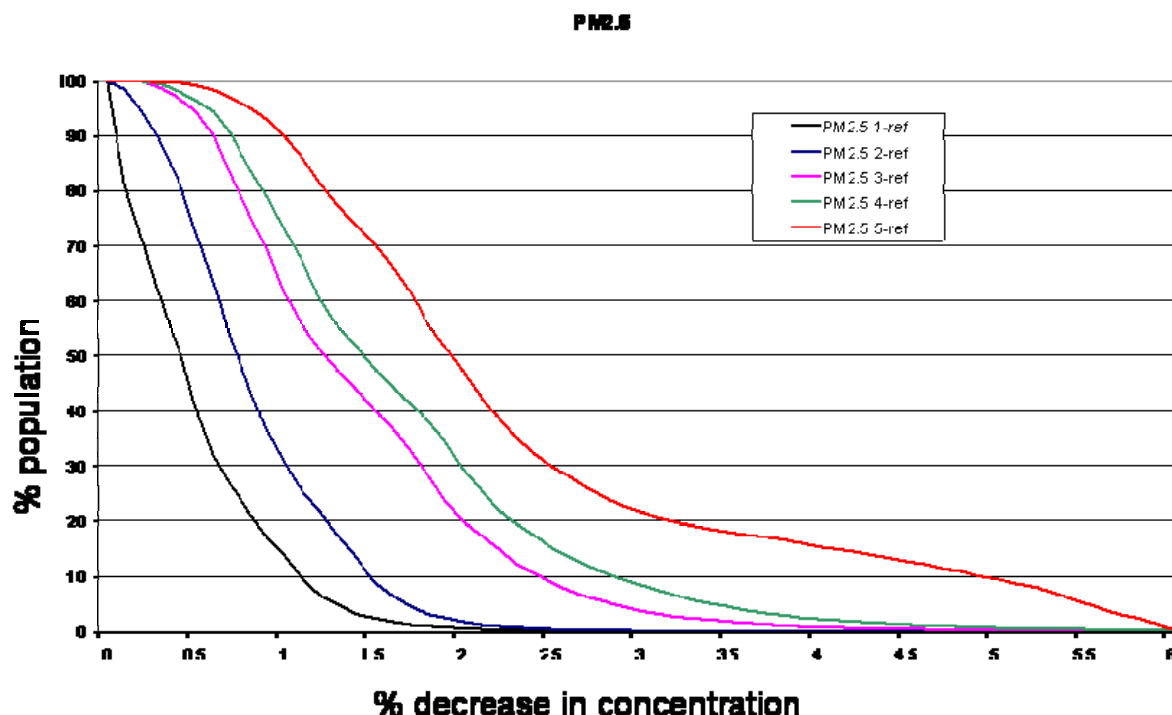


Figure 3. Percentage of the population for which a certain decrease in concentration of PM_{2.5} is valid for the different scenario's.

5 CONCLUSIONS

According to the results of this study enforcing a speed limit of 90 km/h on some of the high ways in Flanders during smog episodes has a limited effect on PM and NO₂ concentration levels for the region as a whole. The effect is however more significant if one accounts for the fact that the population density can be high along highways and if we focus on elementary carbon which is believed to be one of the more detrimental components of PM. In general this study demonstrates that modelling tools can help the administration to evaluate and compare different policies for improving air quality.

REFERENCES

- Cosemans, J., Kretzschmar J., Maes G., 1992: The Belgian Immission Frequency Distribution Model IFDM Proceedings of the DCAR workshop on objectives for the next generation of practical short range atmospheric dispersion models. May 6-8, 1992, Risoe, Roskilde, Denmark.
- Maes, J., Vliegen, J., Van de Vel, K., Janssen, S., Deutsch, F., De Ridder, K., Mensink, C., 2009: Spatial surrogates for the disaggregation of CORINAIR emission inventories, Atmospheric Environment, Volume 43, Issue 6, February 2009, 1246-1254.
- Mensink, C., De Ridder, K., Lewycky, N., Delobbe, L., Janssen, L., Van Haver, P., 2001: Computational aspects of air quality modelling in urban regions using an optimal resolution approach (AURORA). Large-scale scientific computing – lecture notes in computer science, 21791, 299-308.
- Mensink, C., De Vlieger, I. and Nys, J., 2000: An urban transport emission model for the Antwerp area. Atmospheric Environment, 34, 4595-4602.
- Naser, T.M., Kanda, I., Ohara, T., Sahamoto, K., Kobayashi S, Nitta, H. and Nataami, T., 2009: Analysis of traffic-related NO_x and EC concentrations at various distances from major roads in Japan, Atmospheric Environment, 41, 2379-2390, doi:10.1016/j.atmosenv.2009.02.002
- Vankerkom, J., Lefebvre, F., De Vlieger, I., Cornelis, E., Schrooten, L., Peetermans, E., Puttemans, C. and Verlinden, K., 2005: Gecombineerd gebruik van verkeerstellingen en TRIPS/32 modeloutput binnen MIMOSA: implementatie, validatie en afstemming met TEMAT en FOD mobiliteit (MIMOSA 3), Studie uitgevoerd in opdracht van ANIMAL, 2005/IMS/R/168, VITO, Mol, Belgium.
- Xue, M., Droegemeier, K. K. and Wong, V., 2000: The Advanced Regional Prediction System (ARPS) - A multiscale nonhydrostatic atmospheric simulation and prediction tool. Part I: Model dynamics and verification. Meteor. Atmos. Physics., 75, 161-193.

Participants - Photo



Participants List

Mr Víctor Daniel Archilla Prat
INSTITUTO NACIONAL DE TECNICA
AEROESPACIAL
Ctra de Ajavir, Km 4
28850 Torrejón de Ardoz (Madrid)
ESPAÑA
archillapv@inta.es

Mrs Ingrid Arts

Dr Artur Jerzy Badyda
Faculty of Environmental Engineering
Warsaw University of Technology
ul. Nowowiejska 20
00-653 Warszawa, Poland
artur.badyda@is.pw.edu.pl

Yves Balkanski

Dr Steven L. Baughcum
Boeing Company
P. O. Box 3707, MC 0R-MT
Seattle, WA 98124, USA
Steven.L.Baughcum@boeing.com

Dr Terje Berntsen
Dept. of Geosciences/CICERO,
University of Oslo
PO Box 1022 Blindern, 0315 Oslo, Norway.
t.k.berntsen@geo.uio.no

Dr Andreas Beyersdorf
NASA Langley Research Center
Science Directorate
Mail Stop 483
Hampton, VA
23681
andreas.j.beyersdorf@nasa.gov

Mr Bert Borst

Dr Bram Bregman
KNMI
Climate and Seismology
Climate Services
P.O. box 201
3730 AE De Bilt
The Netherlands
bregman@knmi.nl

Dr Frits J.J. Brouwer
KNMI
Director-General KNMI
P.O. box 201
3730 AE De Bilt
The Netherlands
Frits.Brouwer@knmi.nl

Dr Claus Brüning
European Commission
claus.bruning@ec.europa.eu

Dr Ulrike Burkhardt
Institut für Physik der Atmosphäre
DLR Oberpfaffenhofen
Germany
ulrike.burkhardt@dlr.de

Mrs Audrey Crespin
CERFACS-meteofrance
42 avenue Gaspard Coriolis
31007 Toulouse Cedex 01
crespin@cerfacs.fr

Drs Rob Cuelenaere

Dr Mauro Dall'Amico
Deutsches Zentrum für Luft- und
Raumfahrt (DLR)
Institut für Physik der Atmosphäre
(IPA)
Oberpfaffenhofen
Germany
Mauro.DallAmico@dlr.de

Dr Stig Dalsøren

Department of Geosciences, Metos
Forskningsparken, 0349 Oslo, Norway.
stigbd@geo.uio.no

Drs Ing Bart de Mooij**Dr Martijn de Ruyter de Wildt**

KNMI
Postbus 201
3730 AE De Bilt
The Netherlands
ruijterd@knmi.nl

Ir Piet de Wildt**Dr Benjamin Demirdjian**

CINaM, UPR CNRS 3118
Campus de Luminy - case 913
13288 MARSEILLE CEDEX 09
FRANCE
demirdjian@cinam.univ-mrs.fr

Dr Olivier Dessens

University of Cambridge
Centre for Atmospheric Science
Department of Chemistry
Lensfield Road
CB2 1EW CAMBRIDGE
UK
olivier.dessens@atm.ch.cam.ac.uk

Mrs Odette Deuber

Faculty of Management, Economics and Social
Sciences, University of Cologne, Germany
odettedeuber@gmx.de

Mrs Simone Dietmueller

Deutsches Zentrum für Luft- und Raumfahrt
e.V.
Institut für Physik der Atmosphäre
Oberpfaffenhofen
D-82234 Wessling
simone.dietmueller@dlr.de

Dr Nikolai Dotzek

DLR-IPA
Oberpfaffenhofen
82234 Wessling
Germany
nikolai.dotzek@dlr.de

Dr Kostas Eleftheratos

Laboratory of Climatology and
Atmospheric Environment, Faculty of
Geology and Geoenvironment,
University of Athens, 15784 Athens,
Greece
kelef@geol.uoa.gr

Dr Gabriele Erhardt

DLR Institut für Physik der Atmosphäre
Oberpfaffenhofen, 82234 Wessling,
Germany
gabriele.erhardt@dlr.de

Dr Veronika Eyring

Deutsches Zentrum fuer Luft- und
Raumfahrt (DLR)
Institut für Physik der Atmosphäre
Oberpfaffenhofen
82234 Wessling
Germany
veronika.eyring@dlr.de

Mr Andrew Ferrone

Institut d'astronomie et de géophysique
G. Lemaître (ASTR)
Université catholique de Louvain
(UCL)
2, chemin du cyclotron
1348 Louvain-la-Neuve
Belgium
andrew.ferrone@uclouvain.be

Mrs Christine Fichter

DLR - Institut fuer Physik der
Atmosphaere
Oberpfaffenhofen
D-82234 Wessling
Germany
christine.fichter@dlr.de

Dr Paul Fortuin

Dr Jan Fuglestedt

CICERO, P.O. Box. 1129 Blindern,
N-0318 Oslo, NORWAY
j.s.fuglestedt@cicero.uio.no

Dr Georgi Gadzhev

Institute of Geophysics, Bulgarian Academy of
Sciences (BAS)
Acad. G. Bonchev str. bl. 3, 1113 Sofia,
Bulgaria
tel: (+359) 2 979 3708
fax: (+359) 2 971 3005
ggadjev@geophys.bas.bg

Dr Klaus M. Gierens

Institut für Physik der Atmosphäre
DLR Oberpfaffenhofen
D-82234 Weßling, Germany
klaus.gierens@dlr.de

Dr Klaus-Dirk Gottschaldt

Institute for Atmospheric Physics
DLR Oberpfaffenhofen
82234 Weßling
Germany
klaus-dirk.gottschaldt@dlr.de

Mr Kaspar Graf

Deutsches Zentrum fuer Luft- und Raumfahrt
(DLR)
Institut fuer Physik der Atmosphaere,
Oberpfaffenhofen, Germany
kaspar.graf@dlr.de

Mrs Emily Gray

Centre for Air Transport and the Environment
(CATE) Manchester Metropolitan University
Ground Floor, John Dalton Building
Chester Street
Manchester, M1 5GD
United Kingdom
eeekg20@bath.ac.uk

Dr Volker Grewe

Institut für Physik der Atmosphäre
DLR-Oberpfaffenhofen
82234 Weßling, Germany
volker.grewe@dlr.de

Dr Mohan Gupta

Federal Aviation Administration
800 Independence Ave.
Washington, DC 20591
mohan.l.gupta@faa.gov

Dr. H.W. Haak

Dr Tomas Halenka

Charles University, Dept. of
Meteorology and Environment
Protection,
V Holesovickach 2,
180 00 Prague, Czech Republic
tomas.halenka@mff.cuni.cz

Mr Pieter Hammingh

Netherlands Environmental Assessment
Agency - PBL
Antonie van Leeuwenhoeklaan 9
3721 MA Bilthoven
+31-(0)30-2742025
pieter.hammingh@pbl.nl

MSc. S. Hassing

Mr Falk Heinen

German Federal Ministry for the
environment, nature Conservation and
Nuclear Safety
Alexanderstraße 3
11055 Berlin
falk.heinen@bmu.bund.de

Mr Harry Hemmer

DLR German Aerospace Center
Institute of Propulsion Technology
Linder Hoehe
51147 Koeln
harry.hemmer@dlr.de

Dr Scott C. Herndon

Aerodyne Research, Inc.
45 Manning Road
Billerica, MA 01821-3976
USA
herndon@aerodyne.com

Mr Jerome D. J.-M. Hilaire

Centre for Air Transport and the Environment,
Manchester Metropolitan University,
Chester street,
M1 5GD
MANCHESTER
UK
j.hilaire@mmu.ac.uk

Mrs Margit Hildebrandt

Forschungszentrum Jülich
ICG-1
52425 Jülich
m.hildebrandt@fz-juelich.de

Dr Chris Hume

Airbus - UK
Future Projects Office
Building 07L, Module 5
Filton
Bristol BS99 7AR
UK
chris.hume@airbus.com

Ivar Isaksen**Mrs Tina Jurkat**

Deutsches Zentrum für Luft- und Raumfahrt
e.V.
Institut fuer Physik der Atmosphaere
Muenchner Strasse 20
D-82234 Wessling, Germany
Tina.Jurkat@dlr.de

Prof Bernd Kärcher

Deutsches Zentrum für Luft- und Raumfahrt
Institut für Physik der Atmosphäre
Oberpfaffenhofen
D-82234 Wessling
bernd.kaercher@dlr.de

Mrs Rajinder Kaur

School of Physics
University of Sydney
NSW 2006
Australia
rajinder.kaur@hotmail.co.uk

Mrs Elena Kireeva

Institute of Nuclear Physics Lomonosov
Moscow State University
lenahome1@yandex.ru

Mrs Angelika Klein

Flughafen Düsseldorf GmbH
Nachbarschaftsdialog und
Immissionsschutz
Postfach 300363
40403 Düsseldorf
a.klein@dus-int.de

Dr Robert Koelemeijer**Dr Marcus Köhler**

Department of Geography
King's College London
Strand Campus
London, WC2R 2LS
United Kingdom
marcus.koehler@kcl.ac.uk

Dr Martina Krämer

Forschungszentrum Jülich
Institut für Chemie und Dynamik der
Geosphäre
ICG 1: Stratosphäre
Arbeitsgruppe Wolken
52425 Jülich, Deutschland
m.kraemer@fz-juelich.de

Mrs Miriam Kuebbeler

Forschungszentrum Jülich
ICG 1: Stratosphäre
Arbeitsgruppe Wolken
52425 Jülich, Deutschland
m.kuebbeler@fz-juelich.de

Mrs Ulrike Kugler / Kummer

IER - Institute of Energy Economics
and the Rational Use of Energy
Universität Stuttgart
Hessbrühlstr. 49a
70565 Stuttgart, Germany
Phone +49-711-685 87824
Fax +49-711-685 87873
uk@ier.uni-stuttgart.de

Dr Ralf Kurtenbach

University of Wuppertal
Faculty of Mathematics and Natural Sciences
Department of Chemistry
Laboratory for Physical Chemistry
H.13.04
Gaußstraße 20
42119 Wuppertal (Germany)
kurtenba@uni-wuppertal.de

Mr Nicolas Lamquin

Laboratoire de Météorologie Dynamique
CNRS/IPSL
nicolas.lamquin@gmail.com

Mrs Janine Leunessen

KNMI
Wilhelminalaan 19
3732GK De Bilt
The Netherlands
janine.leunessen@knmi.nl

Dr Ling Ling Lim

CATE, Manchester Metropolitan University,
John Dalton East, Chester St,
Manchester M1 5GD,
UK
l.lim@mmu.ac.uk

Mrs Marianne Tronstad Lund

CICERO - Center for International Climate and
Environmental Research, Oslo
P.B.1129 Blindern, 0318 Oslo, Norway
m.t.lund@cicero.uio.no

MSc. M. Lunter

Mark Major

EU European Commission

Dr Hermann Mannstein

Deutsches Zentrum für Luft- und Raumfahrt,
Institute of Atmospheric Physics,
Oberpfaffenhofen,
82230 Wessling,
Germany
Hermann.Mannstein@dlr.de

Dr Philippe Marbaix

Institut d'Astronomie et Géophysique
Université catholique de Louvain
philippe.marbaix@uclouvain.be

Dr Sigrun Matthes

Institut Physik der Atmosphäre,
Oberpfaffenhofen
82334 Wessling
sigrun.matthes@dlr.de

Dr Volker Matthias

Institute for Coastal Research
GKSS Research Center
Max-Planck-Strasse 1
21502 Geesthacht, Germany
volker.matthias@gkss.de

Mrs Jessica Meyer

Forschungszentrum Jülich GmbH
ICG-1: Stratosphäre
52425 Jülich
j.meyer@fz-juelich.de

Dr Richard C. Miake-Lye

Aerodyne Research, Inc.
45 Manning Road
Billerica, MA 01821-3976
USA
rick@aerodyne.com

Patrick Minnis

Mr Cees Molenaars

KNMI, Senior advisor Communications
/spokesman
De Bilt, The Netherlands
cees.molenaars@knmi.nl

Ir Marcel Molendijk

Mr Alexander D. Naiman

Durand Building Room 267
496 Lomita Mall
Stanford University
Stanford, CA 94305
USA
anaiman@stanford.edu

Dr Laurent Nybelen

CERFACS
42, avenue Gaspard Coriolis
31057 TOULOUSE
FRANCE
nybelen@cerfacs.fr

Dr Dirk Olivie

CNRM
Centre National de Recherches
Météorologiques
Météo-France
42, avenue Gaspard Coriolis
31057 Toulouse
France
dirk.olivie@cnrm.meteo.fr

Dr Roberto Paoli

CERFACS
42 Avenue Gaspard Coriolis
31057 Toulouse
France
paoli@cerfacs.fr

Prof Joyce E. Penner

University of Michigan
2455 Hayward St.
Ann Arbor, MI 48109-2143
penner@umich.edu

Dr Daniel Peters

AOPP University of Oxford
Clarendon Laboratory
Parks Road
Oxford
OX1 3PU
United Kingdom
dpeters@atm.ox.ac.uk

Mrs Rachel Pike

Centre for Atmospheric Science
Department of Chemistry
Lensfield Road
Cambridge
CB2 1EW
United Kingdom
rachel.pike@atm.ch.cam.ac.uk

Dr Michael Ponater

Deutsches Zentrum für Luft- und
Raumfahrt
Institut für Physik der Atmosphäre
Oberpfaffenhofen, Germany
D-82230 Wessling
michael.ponater@dlr.de

Dr Olga Popovicheva

Institute of Nuclear Physics
Moscow State University
119991
Moscow
Russia
olga.popovicheva@gmail.com

Prof Michael John Prather

3329 Croul Hall
Dept of Earth System Science, UC
Irvine
Irvine, CA 92697-3100
USA
mprather@uci.edu

Dr Gaby Radel

University of Reading
Department of Meteorology
Earley Gate, P.O. box 243
Reading, RG1 5ES
UK
g.radel@reading.ac.uk

Dr Mattia Righi

Deutsches Zentrum fuer Luft- und
Raumfahrt (DLR)
Institut für Physik der Atmosphäre
Oberpfaffenhofen
82234 Wessling
Germany
Mattia.Righi@dlr.de

Dr Ruben Rodriguez De Leon

Centre for Air Transport and the
Environment
Manchester Metropolitan University
John Dalton Building,
Chester Street,
Manchester, M1 5GD
r.deleon@mmu.ac.uk

Mrs Jenny Ryman

Transportstyrelsen
Vikboplan 7
SE-601 73 Norrköping
SWEDEN
jenny.ryman@transportstyrelsen.se

Dr Nikolay Sitnikov

Central Aerological Observatory /
Pervomayskaja str., 3, Dolgoprudny,
Moscow reg., Russian Federation,
141700
sitnikov@caomsk.mipt.ru

Prof Robert Sausen

Deutsches Zentrum für Luft- und Raumfahrt
(DLR)
Institut für Physik der Atmosphäre
Oberpfaffenhofen
D-82234 Wessling
Germany
robert.sausen@dlr.de

Mrs Agnieszka Skowron

Centre for Air Transport and the
Environment (CATE)
Manchester Metropolitan University
John Dalton Building
Chester Street
Manchester
M1 5GD
United Kingdom
a.skowron@mmu.ac.uk

Dr Andrew Sayer

Atmospheric, Oceanic and Planetary Physics
Department of Physics
University of Oxford
Parks Road
Oxford
OX1 3PU
sayer@atm.ox.ac.uk

MinDiriG Hubert Steinkemper

Mrs Alice Suri

Federal Office of Civil Aviation
(FOCA)
Aviation Policy and Strategy
Environmental Affairs
3003 Bern
Switzerland
alice.suri@bazl.admin.ch

Mr Dominik Schauble

Deutsches Zentrum für Luft- und Raumfahrt
Institut für Physik der Atmosphäre
Münchner Straße 20
82234 Weßling
Dominik.Schaeuble@dlr.de

Dr Saadat Syed

Pratt & Whitney
MS 162-24
400 Main Street
East Hartford
CT 06108
saadat.syed@pw.utc.com

Dr Christina Schnadt Poberaj

Institute for Atmospheric and Climate Science
Universitätstrasse 16
ETH Zürich, CHN
CH-8092 Zurich
Switzerland
christina.schnadt@env.ethz.ch

Dr Simon Unterstrasser

Institut für Physik der Atmosphäre
DLR Oberpfaffenhofen, Wessling
simon.unterstrasser@dlr.de

Prof Ulrich Schumann

Deutsches Zentrum für Luft- und Raumfahrt
Institut für Physik der Atmosphäre
Münchner Str. 20
82234 Oberpfaffenhofen
Germany
ulrich.schumann@dlr.de

Mr Malte Uphoff

Meteorologisches Institut
ZMAW, Universität Hamburg
Bundesstr 55
20146 Hamburg, Germany
malte.uphoff@zmaw.de

Mrs Miranda Van Brussel-Verzoo

KNMI
Climate and Seimology
Climate and Chemistry
P.O. Box 201
3730 AE De Bilt
The Netherlands
verzoo@knmi.nl

MSc. H. van Hoorn**Mrs Margarita Vazquez-Navarro**

Institut für Physik der Atmosphäre
Deutsches Zentrum für Luft- und Raumfahrt
Oberpfaffenhofen
82234 Weßling
Germany
Margarita.Vazquez@dlr.de

Mr Peter Viaene

VITO
Boeretang 200
B-2400 Mol
Belgium
peter.viaene@vito.be

Dr Christiane Voigt

DLR-Institut fuer Physik der Atmosphaere
Oberpfaffenhofen
D-82234 Wessling
Germany
Christiane.Voigt@dlr.de

Dr Andreas Waibel

Lufthansa German Airlines
FRA CP/U
Airportring, LAC B0.612
D-60546 Frankfurt/Main
andreas.waibel@dlh.de

Dr Ernie Weijers

Energy research Centre of the Netherlands
(ECN)
P.O. Box 1
1755ZG Petten
The Netherlands
weijers@ecn.nl

Mr Gillian Mary Whelan

University College Cork, Geography
Department, College Road, Western
Road, Cork, Ireland
whelan.gillian@student.ucc.ie

Drs (MSc) Jan Wijmenga**Mrs Laura Wilcox**

Department of Meteorology,
University of Reading,
Earley Gate, PO Box 243,
Reading, RG6 6BB
UK
l.j.wilcox@reading.ac.uk

Mr Jordan Wilkerson

Civil & Environmental Engineering
Atmosphere / Energy
Yang & Yamazaki Environment &
Energy
Stanford University
473 Via Ortega, 390A, MC 4020
Stanford, CA 94305-4020
wilkejt1@stanford.edu

Dr Jason Williams

Royal Netherlands Meteorological
Institute
Wilhelminalaan 10
3732GK
De Bilt
Netherlands
williams@knmi.nl

Dr Andrey Zamyatin

Gromov Flight Research Institute/
Zhukovsky t., Moscow Reg., 140186
Russia
frizamyatin@mail.ru

Index of Authors

- AAFEX Science Team 21
 Anderson B. 21
 Appelhans J. 134
 Arnold F. 57
 Bauer R. 197
 Baughcum S.L. 169
 Berntsen T. 93
 Beyersdorf A. 21
 Bintania R. 163
 Blommaert F. 245
 Borrmann S. 57, 197
 Brok P. 140
 Brouwer F.J.J. 16
 Builtjes P. 134
 Campmany E. 75
 Cariolle D. 108
 Carrico C.M. 51
 Cosemans G. 245
 Cros S. 80
 Dämmgen U. 134
 Danilin M.Y. 169
 De Reus M. 197
 De Ridder K. 245
 De Vlieger I. 245
 Dedesh V.T. 63, 203
 Demirdjian B. 38
 DeMott P.J. 51
 Denier van der Gon H. 134
 Dessens O. 163
 Dey C. 119
 Dickson N.C. 239
 Dietmüller S. 95
 Dörnbrack A. 57
 Dotzek N. 146
 Eichler H. 57
 Eleftheratos K. 45
 Erhardt G. 140
 Evstigneev A.A. 63
 Faccineto A. 38
 Ferrone A. 174
 Fierens F. 245
 Focsa C. 38
 Frey W. 57
 Fridell E. 38
 Friedrich R. 134
 Fuglestad J.S. 93
 Gadzhev G. 33
 Ganey K. 33
 Gauss M. 163
 Gayet J.-F. 57
 Geftler T. 134
 Gierens K. 140, 239
 Gottschaldt K. 153
 Goubeyre C. 57
 Graf K. 180
 Grainger R.G. 75, 222
 Grewe V. 163
 Habisreuther P. 140
 Hagström M. 140
 Ham F. 191
 Hamburger T. 57
 Hauglustaine D. 163
 Helms C. 140
 Herndon S.C. 26
 Heymsfield A.J. 169
 Highwood E.J. 95
 Hilaire J. 217
 Holzäpfel F. 57
 Hooper P.D. 86
 Hoor P. 163
 Hurley J. 157, 233
 Isaksen I.S.A. 140, 163
 Jacobson M.Z. 191
 Janssen S. 245
 Jöckel P. 163
 Jones R.L. 239
 Jordanova G. 33
 Jörß W. 134
 Jurkat T. 57
 Kagarmanov R.L. 203
 Kärcher B. 153, 197
 Kaur R. 119
 Khokhlova T. 186
 Kiose S.N. 63
 Kireeva E. 51, 186
 Knighton W.B. 26
 Köble R. 134
 Koehler K.A. 51
 Koffi B. 163
 Krämer M. 57, 197
 Kreidenweis S.M. 51
 Kübbeler M. 57
 Kugler U. 134
 Kurtenbach R. 140
 Lamquin N. 80
 Lanshin A.I. 63
 Laroche P. 140
 Lavrov M.A. 63
 Lee B. 26
 Lee D.S. 86, 126, 140, 217, 233
 Lefebvre W. 245
 Lele S.K. 191
 Lescroart R. 174
 Lichtenstern M. 57, 102

- Lim L.L. 86, 126
Lukyanov A. 102
Lund M.T. 93
Mannstein H. 180
Marbaix P. 174
Mathioudakis K. 140
Matthes S. 140, 146
Mayer B. 180
Mensink C. 245
Meyer J. 57
Miake-Lye R.C. 26
Miloshev N. 33
Miloshevich L.M. 169
Minnis P. 45
Mogilnikov V.P. 63
Moldanová J. 38
Molleker S. 57
Myhre G. 93
Naiman A.D. 191
Nevzorov A.N. 63
Nybelén L. 108
Olivie D. 163
Panidis T. 140
Paoli R. 108
Paugam R. 108
Pavlova E.G. 63
Persiantseva N. 186
Peter T. 197
Peters D.M. 222
Petters M.D. 51
Petzold A. 57, 140
Ponater M. 95, 227
Popov V.V. 63
Popovicheva O. 38, 186
Popovicheva O.B. 51, 63
Preston H.J. 86, 126
Prodanova M. 33
Rädel G. 95
Raper D. 140
Ravegnani F. 102
Rodriguez de Leon R. 217
Rogers H.L. 239
Roiger A. 102
Rypdal K. 93
Santoni G. 26
Sarrat C. 108
Sausen R. 146
Sayer A.M. 75
Schäfer K. 140
Schäuble D. 57, 197
Scheibe M. 57
Scheiber M. 102
Schiller C. 197
Schlager H. 57, 102, 197
Schmale J. 57
Schnadt Poberaj C. 163
Schneider J. 57
Schrooten L. 245
Schumann U. 57, 69, 180
Shine K.P. 95
Shonija N. 51, 186
Sitnikov N. 102
Sitnikova V. 102
Skeie R.B. 93
Skowron A. 233
Smit H. 80
Spelten N. 197
Staehelin J. 163
Stern R. 134
Stock P. 102, 197
Stubenrauch C.J. 80
Stuber N. 95
Syrakov D. 33
Szakáll M. 197
Tenishev R.Kh. 63
Theloke J. 134
Thiruchittampalam B. 134
Thomas G. 222
Timko M.T. 26
Tishkova V. 38
Todorova A. 33
Tsalavoutas T. 140
Ulanovskiy A. 102
Uzbasich M. 134
Van de Vel K. 245
Van Mierlo T. 245
Van Velthoven P.F.J. 112, 163
van Ypersele J.-P. 174
Van Zadelhoff G.-J. 112
Vancassel X. 140
Vankerkom J. 245
Viaene P. 245
Voigt C. 57, 153, 197
Voronich I.V. 63
Weers U. 197
Wiesen P. 140
Wilkerson J.T. 191
Williams J.E. 112
Wilson C. 140
Wood E.C. 26
Yu Z. 26
Zamyatin A.N. 203
Zarzalis N. 140
Zerefos C.S. 45
Zhelannikov A.I. 203